

Ф — Фізика і
Х — хімія
Т — твердого
Т — тіла

№ 1
2023
Том
Vol. 24



P — Physics and
C — Chemistry of
S — Solid
S — State

Міністерство освіти і науки України
Прикарпатський національний університет імені Василя Стефаника
Фізико-хімічний інститут
Навчально-дослідний центр напівпровідникового матеріалознавства

Ministry of Education and Science of Ukraine
Vasyl Stefanyk Precarpathian National University
Physical-Chemical Institute
Research & Education Center of Semiconductor Material Science

ISSN 1729-4428

ФІЗИКА І ХІМІЯ ТВЕРДОГО ТІЛА

PHYSICS AND CHEMISTRY OF SOLID STATE

№ 1
2023
Том
Vol. 24

Журнал ФХТТ індексується міжнародними наукометричними базами WoS (починаючи із 2017 р.)
та Scopus (індексація матеріалів із 2018 р.)

Журнал включено у категорію А Реєстру фахових видань України:
Галузь науки: хімічні (02.07.2020), технічні (02.07.2020), фізико-математичні (24.09.2020)
Спеціальності: 102 (02.07.2020) 132 (02.07.2020) 104 (24.09.2020) 105 (24.09.2020)

Рекомендовано до друку Вченою радою
Прикарпатського національного університету імені Василя Стефаника

Свідоцтво про державну реєстрацію
КВ № 24247-14087ПР від 27.09.2019

Certificate of State Registration
КВ No. 24247-14087 ПР from 27.09.2019

Передплатний індекс: 22938

Subscription index: 22938

© Прикарпатський національний університет імені Василя Стефаника, 2023
Фізико-хімічний інститут, 2023

Адреса редакції:
Прикарпатський національний університет
імені Василя Стефаника,
вул. Шевченка, 57,
Івано-Франківськ,
76018, Україна
Тел.: +380 (342) 596082
Факс.: +380 (342) 531574
E-mail: pcss@pnu.edu.ua
<https://journals.pnu.edu.ua/index.php/pcss>

Editorial address:
Vasyl Stefanyk Precarpathian National University,
57, Shevchenko Str.,
Ivano-Frankivsk,
76018, Ukraine
Tel.: +380 (342) 596082
Fax.: +380 (342) 531574
E-mail: pcss@pnu.edu.ua
<https://journals.pnu.edu.ua/index.php/pcss>

Vasyl Stefanyk Precarpathian National University
Physical-Chemical Institute
Research & Education Center of Semiconductor Material Science

Scientific Journal
“Physics and Chemistry of Solid State”

EDITORIAL BOARD

EDITOR-IN-CHIEF

Lyubomyr Nykyruy (Ivano-Frankivsk, Ukraine)

EDITORS

Andriy Zagorodnyuk (Ivano-Frankivsk, Ukraine)

Bogdan Ostafiychuk (Ivano-Frankivsk, Ukraine)

Grzegorz Wisz (Rzeszów, Poland)

EDITORIAL BOARD MEMBERS

Physics&Mathematical Sciences

Belyaev O. (Kyiv, Ukraine), **Bester M.** (Rzeszów, Poland), **Budzulyak I.** (Ivano-Frankivsk, Ukraine), **Fodchuk I.** (Chernivtsi, Ukraine), **Ilchuk H.** (Lviv, Ukraine), **Galuschak M.** (Ivano-Frankivsk, Ukraine), **Gasyuk I.** (Ivano-Frankivsk, Ukraine), **Gurevich Yu.** (Mexico, Mexico), **Holovko M.** (Lviv, Ukraine), **Klyui M.** (Changchun, China), **Korbutyak D.** (Kyiv, Ukraine), **Kovalenko O.** (Dnipro, Ukraine), **Labuz M.** (Rzeszów, Poland), **Lishchynskyy I.** (Ivano-Frankivsk, Ukraine), **Malashkevich G.** (Minsk, Belarus), **Parashchuk T.** (Krakow, Poland), **Ploch D.** (Rzeszów, Poland), **Protsenko I.** (Sumy, Ukraine), **Rubish V.** (Uzhhorod, Ukraine), **Sabat K.** (Bhopal, India), **Saliy Ya.** (Ivano-Frankivsk, Ukraine), **Strikha M.** (Kyiv, Ukraine), **Swiatek Z.** (Krakow, Poland), **Wal A.** (Rzeszów, Poland)

Chemical Sciences

Babanly M. (Baku, Azerbaijani), **Fochuk P.** (Chernivtsi, Ukraine), **Gladyshevskii R.** (Lviv, Ukraine), **Gorichok I.** (Ivano-Frankivsk, Ukraine), **Lobanov V.** (Kyiv, Ukraine), **Myronyuk I.** (Ivano-Frankivsk, Ukraine), **Nedilko S.** (Kyiv, Ukraine), **Shyichuk O.** (Bydgoszcz, Poland; Ivano-Frankivsk, Ukraine), **Tatarchuk T.** (Ivano-Frankivsk, Ukraine), **Tomashyk V.** (Kyiv, Ukraine), **Turovska L.** (Ivano-Frankivsk, Ukraine), **Zinchenko V.** (Odessa, Ukraine)

Technical Sciences

Ahiska R. (Ankara, Turkey), **Anatychuk L.** (Chernivtsi, Ukraine), **Ascheulov A.** (Chernivtsi, Ukraine), **Dashevsky Z.** (Beer-Sheva, Israel), **Kharchenko M.** (Kharkiv, Ukraine), **Kogut I.** (Ivano-Frankivsk, Ukraine), **Kryuchyn A.** (Kyiv, Ukraine), **Novosyadlyy S.** (Ivano-Frankivsk, Ukraine), **Romaka V.** (Lviv, Ukraine), **Uhrin R.** (New Jersey, USA), **Zukowski P.** (Lublin, Poland)

TECHNICAL EDITOR

Yurchyshyn L. (Ivano-Frankivsk, Ukraine)

Synthesis and Properties of Silicon Carbide (Review)	5
<i>L.M. Soltys, I.F. Mironyuk, I.M. Mykytyn, I.D. Hnylytsia, L.V. Turovska</i>	
Band Structure Calculation and Optical Properties of Ag₃AsS₃ Crystals	17
<i>M.Ya. Rudysh, O.V. Smitiukh, G.L. Myronchuk, S.M. Ponedelnyk, O.V. Marchuk</i>	
X-ray diffractometric study of HDPE/GaAs and HDPE/GaAs composites	23
<i>N.N. Gadzhieva, G.B. Ahmadova, S.Z. Melikova, F.G. Asadov</i>	
Free Vibration Analysis of Composite Cylindrical Shell Reinforced with Silicon Nano-Particles: Analytical and FEM Approach	26
<i>M. J. Jweeg, E. K. Njim, O. S. Abdullah, M. A. Al-Shammari, M. Al-Waily, S. H. Bakhy</i>	
The effect of orthophosphoric acid on energy-intensive parameters of porous carbon electrode materials	34
<i>N.Ya. Ivanichok, P.I. Kolkovskiy, A.M. Soltys, V.M. Boychuk, V.I. Mandzyuk, L.S. Yablon, B.I. Rachiy</i>	
Studies on structural, optical nonlinearity and antibacterial activity of Piperazine (bis) p-toluenesulfonate single crystal for optical limiting and biological applications	46
<i>K. Balakrishnan, S. Sakthy Priya, A. Lakshmanan, P. Surendran, Karthik Kannan, P. Geetha, G. Vinitha, P. Praveen Kumar, P. Rameshkuma</i>	
Synergistic properties of β-Ga₂O₃ nanowire arrays	56
<i>M.V. Naumenko, R.M. Balabai</i>	
Nonlinear features of the transition of a liquid crystalline mixture into an isotropic state under the action of alcohol vapors	64
<i>Z. Mykytyuk, H. Barylo, I. Kremer, Y. Kachurak, O. Samoilo, I. Kogut</i>	
Periodic nanostructures induced by point defects in Pb_{1-x}Sn_xTe	70
<i>Ya. Saliy, L. Nykyruy, G. Cempura, O. Soroka, T. Parashchuk, I. Horichok</i>	
Effect of synthesis methods and comparative study of structural properties of micro and nano Ferrites	77
<i>A. T. Pathan, A. M. Shaikh, S.K. Sushant, Shridhar N. Mathad</i>	
Peculiarities of structural, electrokinetic, energetic, and magnetic properties semiconductive solid solution Lu_{1-x}V_xNiSb	84
<i>Yu. Stadnyk, V.A. Romaka, L. Romaka, P. Demchenko, A. Horyn, O. Poplavskiy, V. Pashkevych, P. Haraniuk</i>	
Influence of metal atom substitution on the electronic and optical properties of solid-state Cd_{0.75}X_{0.25}Te (X= Cu, Ag and Au) solutions	92
<i>A.I. Kashuba</i>	
A theoretical model for estimation of work function reduction for MXenes with hydroxyl termination	102
<i>M. V. Strikha, D. V. Antoniuk</i>	
Magnetic properties and nanocrystallization behavior of Co-based amorphous alloy	106
<i>Yu. Nykyruy, S. Mudry, Yu. Kulyk, V. Prunitsa, A. Borysiuk</i>	
Adsorption of Sr(II) cations onto titanium dioxide, doped with Boron atoms	114
<i>I. Mironyuk, H. Vasylyeva, I. Prokipchuk, I. Mykytyn</i>	
Transport phenomena in CdTe:Cl and CdTe:Cu – calculation from the first principles	126
<i>O. Malyk</i>	
Solar cells based on CdTe thin films (Part II)	134
<i>T.M. Mazur, M.P. Mazur, I.V. Vakaliuk</i>	
Electron and hole spectrum taking into account deformation and polarization in the quantum dot heterostructure InAs/GaAs	146
<i>H.Ya. Bandura, I.V. Bilynskiy, R.Ya. Leshko</i>	
Influence of gadolinium doping on structural properties of carbon nanotubes	153
<i>R.G. Abaszade, M.B. Babanli, V.O. Kotsyubynsky, A.G. Mammadov, E. Gür, O.A. Kapush, M.O. Stetsenko, R.I. Zapukhlyak</i>	
About synthesis mechanism of periodic oxide nanocrystallites on surface of single-crystal InP	159
<i>S. Kovachov, I. Bohdanov, I. Bardus, D. Drozhcha, K. Tikhovod, A. Khrekin, V. Bondarenko, I. Kosogov, Y. Suchikova</i>	
Catalytic oxidation of acetone and ethanol on a platinum wire	166
<i>A.S. Chernenko, V.V. Kalinchak, A.K. Kopyyka, M.V. Roziznanyi, A.V. Fedorenko</i>	
Fabrication and Tailoring the Structural and Dielectric Characteristics of GO/Sb₂O₃/PMMA/PC Quaternary Nanostructures For Solid State Electronics Nanodevices	173
<i>D. A. Sabur, M. A. Habeeb, A. Hashim</i>	
An optical absorption of the composite with the nanoparticles, which are covered by the surfactant layer	181
<i>N.A. Smirnova, M.S. Maniuk, A.V. Korotun, I.M. Titov</i>	

Laser-modified nanocrystalline NiMoO₄ as an electrode material in hybrid supercapacitors	190
<i>O.M. Popovych, I.M. Budzulyak, M.M. Khemii, R.V. Ilnytskyi, L.S. Yablon, D.I. Popovych, I.I. Panko</i>	
Direct magnetic and surface relief patterning using carbazole-based azopolymer	197
<i>O. Paiuk, A. Meshalkin, A. Stronski, E. Achimova, C. Losmanschii, V. Botnari, A. Korchovyi, M. Popovych</i>	
Synthesis and Photoluminescence characterization of Sr₃La(AlO)₃(BO₃)₄:Eu³⁺,Sm³⁺ Phosphor for W-LED	202
<i>R.M. Yerojwar, N. S. Kokode, C. M. Nandanwar, D. K. Ingole</i>	
Corr.-Member NAS of Ukraine, Prof. Ostafiychuk B.K. celebrate 75 anniversary	208
Prof. Kogut I.T. celebrate 70 anniversary	211
Information for authors	213

L.M. Soltys¹, I.F. Mironyuk¹, I.M. Mykytyn¹, I.D. Hnylytsia², L.V. Turovska³

Synthesis and Properties of Silicon Carbide (Review)

¹*Vasyl Stefanyk Precarpathian National University, Ivano-Frankivsk, Ukraine, soltys86@gmail.com*

²*Ivano-Frankivsk National Technical University of Oil and Gas, Ivano-Frankivsk, Ukraine*

³*Ivano-Frankivsk National Medical University, Ivano-Frankivsk, Ukraine*

Silicon carbide is an extremely hard material that exhibits exceptional corrosion resistance as well as thermal shock resistance. Its high mechanical properties determine the increased performance of materials based on it. The combination of high thermal conductivity and low thermal expansion coefficient determines the stability of silicon carbide at high heating rates and under stationary thermal conditions. To date, significant progress has been made in the development of methods for the synthesis of various materials based on silicon carbide. The main synthesis methods that scientists use in their research are the sol-gel method, sintering, pyrolysis, microwave synthesis, chemical vapor deposition, etc. The use of "green" techniques in the synthesis of SiC has gained wide popularity due to environmental friendliness, renewability, and ease of implementation. This review analyzes modern research in the field of silicon carbide synthesis published in peer-reviewed professional journals.

Key words: silicon carbide, polytype, "green" synthesis, ceramic nanomaterials.

Received 14 September 2022; Accepted 31 January 2023.

Content

Introduction

1. Crystal structure of silicon carbide
2. Physical properties of silicon carbide
3. Chemical properties of silicon carbide
4. Silicon carbide synthesis methods

Conclusions

Introduction

Silicon carbide plays an important role in many industries and various areas of production due to its exceptional physical and chemical properties and characteristics. Among the most significant properties are the following: low density, high thermal conductivity, very low coefficient of friction, refractoriness, low coefficient of thermal expansion, high chemical, corrosion and radiation resistance, high hardness, etc. [1, 2].

Silicon carbide has improved ballistic characteristics, since it has excellent mechanical properties, including strength, fracture toughness and hardness, so it is used in the production of bulletproof vests and composite armor

[3,4]. Silicon carbide is used in the metallurgical industry as a refractory material, in the production of abrasive, cutting and grinding tools, in the nuclear power industry, in the production of jewelry, in heating elements, in electronics, etc. [5].

Silicon carbide has such electronic properties as high thermal and electrical conductivity, high ion mobility and high electron drift velocity. It is these properties that contribute significantly to making SiC based materials the best for applications in electronic devices such as power electronics, field emission, sensors, etc. [5]. In addition, SiC is used as blue and ultraviolet diodes due to its ability to emit high intensity and stable ultraviolet and blue-green light. Nanotechnology-based silicon carbide is becoming

an increasingly economical and efficient material in engineering and industry. Thus, the use of SiC in optoelectronics, microelectronics, nanodevices, nanocomposites, hydrophobic devices, biomedical technology is important and useful for humanity [5].

Silicon carbide and mesoporous structures based on it are actively used in many catalytic applications, in the field of optical spin defects, and as substrates for growing other wide gap semiconductors [6].

Materials based on silicon carbide absorb microwaves well due to their thermal and chemical stability, as well as good resistance to the environment [7].

All these properties and applications pose an extremely important task for scientists to develop efficient and economical methods for the synthesis of high-quality crystals, films, and porous structures of silicon carbide.

In this work, the goal was to elucidate the possibilities of modern methods for the synthesis of silicon carbide, especially the preparation of nanoparticles in the form of whiskers, rods, fibers, tubes, etc. with cubic and hexagonal crystal structure.

I. Crystal structure of silicon carbide

Silicon carbide is known as a wide bandgap semiconductor that exists in many different polytypes. All polytypes have a hexagonal framework with a carbon atom located above the center of the triangle of silicon atoms and below the silicon atom belonging to the next layer [8]. The distance between neighboring silicon or carbon atoms is approximately 3.08 Å for all polytypes. The carbon atom is in the center of a tetragonal structure outlined by four neighboring silicon atoms, so that the distance between the C atom and each of the Si atoms is the same and is 1.89 Å. The difference between the polytypes lies in the stacking order of successive double layers of carbon and silicon atoms. Fig. 1 shows the stacking sequence for the most common silicon carbide polytypes [9]. If the first double layer is called position A, the next layer that can be placed according to the closed

packed structure will be placed at position B or position C. Different polytypes will be built by permuting these three positions.

In 1947, Ramsdell systematically identified different types of silicon carbide. The type of SiC was marked as nX, where "X" represents the Bravais lattice, including cubic (C), hexagonal (H), and rhombic (R), and "n" indicates the number of diatomic layers contained in one lattice period [10]. That is, the number indicates the periodicity, and the letter indicates the resulting structure. Cubic 3C, hexagonal 4H and 6H, and rhombohedral R are the most common atomic arrangements in SiC. Silicon carbide has only one type of cubic (3C) SiC, which is called β -SiC, and all hexagonal and rhombohedral hexahedra can be called α -SiC [5]. The 3C-SiC polytype has the ABCABC... or ACBACB... stacking sequence, the 4H stacking sequence is ABCB..., the 6H stacking sequence is ABCACB..., and the 15R stacking sequence is ABCABCBCABACBCB... (Fig. 2) [9]. There are about 250 polytypes, some of which have a stacking period of several hundred double layers [10].

II. Physical properties of silicon carbide

Since silicon carbide is a ceramic material, it has excellent properties such as corrosion resistance, wear resistance, high strength, and high hardness. SiC also has good high-temperature properties, in particular, oxidation resistance, high thermal conductivity, and low thermal expansion coefficient [10].

In electronics, silicon carbide materials are valued for their wide bandgap [10]. The bandgap for various modifications of SiC can be in the range from 2.72 to 3.34 eV. The large bandgap makes it possible to create semiconductor devices on its basis that remain operational at temperatures up to 600°C.

Silicon carbide single crystals doped with group V impurities (nitrogen, phosphorus, arsenic, antimony, bismuth), as well as lithium and oxygen, have *n*-type conductivity and green color. Group III elements (boron,

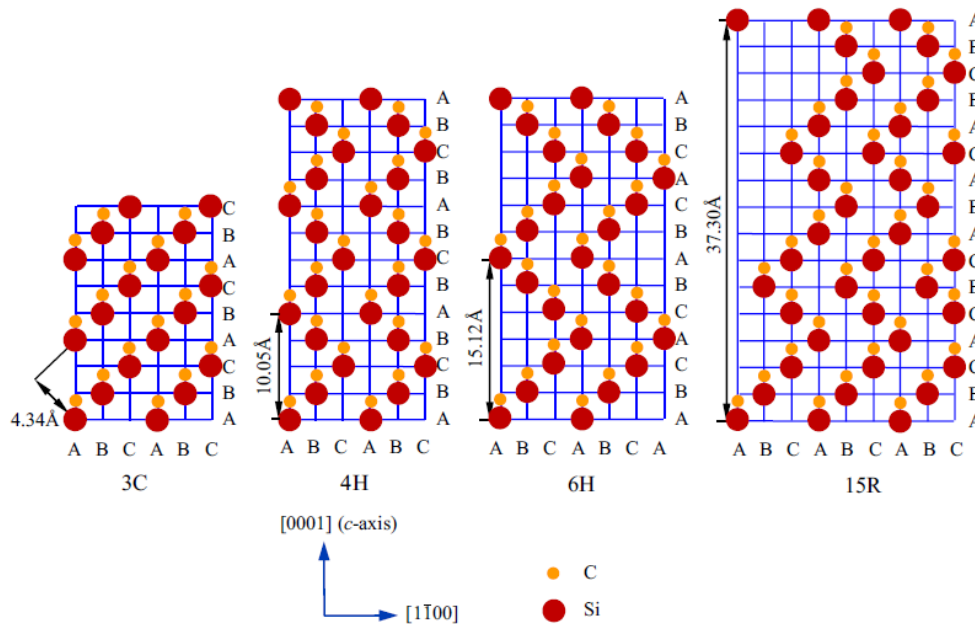
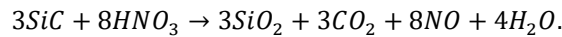
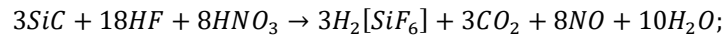


Fig. 1. Sequence of stacking double layers 3C-, 4H-, 6H- and 15R-SiC [9].

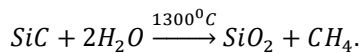
aluminum, gallium, indium) and group II elements (beryllium, magnesium, calcium) are acceptors; therefore, SiC crystals doped with them have *p*-type conductivity and blue or black color. When the composition deviates from stoichiometric towards an increase in the silicon content, the crystals have an *n*-type electrical conductivity, and with an excess of carbon, they have a *p*-type conductivity [1].

SiC is one of the hardest known materials with a pressure of about 25 GPa, similar to B₄C (boron carbide). Only diamond (60-120 GPa) and cubic boron nitride (borazon 40 GPa) are much harder [1]. The Mohs hardness of silicon carbide is 9.2, the Vickers microdensity hardness is 3000-3300 kg/mm², and the Knoop hardness is 2670–2815 kg/mm.

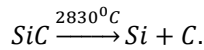
Silicon carbide does not melt, but sublimates at about



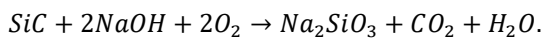
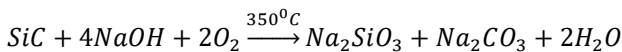
Highly superheated steam decomposes silicon carbide:



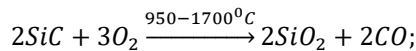
Silicon carbide is a very stable substance and decomposes in an inert atmosphere only at very high temperatures:



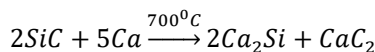
In the presence of oxygen and alkali, silicon carbide dissolves:



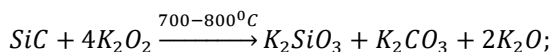
When heated, silicon carbide reacts with oxygen [11]:



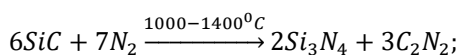
with active metals:



and their peroxides:



with nitrogen:



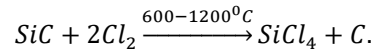
with halogens:

2700°C. When heated in air, SiC forms a strong surface film of SiO₂, which prevents its oxidation up to 1850°C for short periods of time (hours) and up to 1500°C for a long time (days). Thus, SiC is one of the most oxidation-resistant non-oxide ceramics [1].

III. Chemical properties of silicon carbide

Silicon carbide has high chemical resistance and stands out for its resistance to oxidation among many heat-resistant alloys and chemical compounds [11]. It oxidizes significantly only at temperatures above 800°C.

Concentrated acids oxidize silicon carbide, and acid solutions dissolve silicon carbide:



IV. Silicon carbide synthesis methods

Silicon carbide crystals are almost completely absent in nature, but natural silicon carbide is known to occur as moissanite. Natural moissanite was first discovered in 1893 as a small component of a meteorite in Arizona by Dr. Ferdinand Henri Moissan, after whom the material was named in 1905. Rare on Earth, silicon carbide is found throughout the universe as stardust around carbon-rich stars [12].

Due to the low prevalence in nature, synthesized silicon carbide is used. The first large-scale production of silicon carbide was started by Edward Goodrich Acheson in 1890. Acheson tried to make artificial diamonds by heating a mixture of clay (aluminum silicate) and powdered coke (carbon) in an iron vessel. He called the blue crystals formed in this case carborundum, believing that this is a new compound of carbon and aluminum, similar to corundum. Acheson patented a process for making silicon carbide powder on February 28, 1893. Perhaps he called the material "carborundum" by analogy with corundum, another very hard substance [1,10]. The Acheson method (synthesis temperature of about 2500°C) is considered the most popular method for the synthesis of silicon carbide.

Today, the synthesis of silicon carbide nanoparticles has become widespread among scientists around the world. There are many developed methods for the synthesis of silicon carbide nanoparticles, for example: sintering [13–19], combustion [20,21], selective method [22], sol-gel method [23–26], hydrothermal acid leaching [27], pyrolysis [28–30], pyrohydrolysis [31], low temperature synthesis [32,33], microwave synthesis [34–37], chemical vapor deposition [38–42], in situ growth [43,44], electric arc synthesis [45,46], etc.

Let us consider in detail the most common methods for the synthesis of silicon carbide nanoparticles.

Currently, the synthesis of nanomaterials using natural resources attracts much attention, since this is an environmentally friendly, less harmful, and economically profitable step towards the "green" synthesis of nanomaterials [47,48]. Many scientists use rice husks in their experiments on the synthesis of silicon carbide nanoparticles. Rice is the staple food of over half of the world's population, and rice husks are the main agricultural by-product of rice production. It is usually disposed of by burning or burying it in the ground, which results in wasted energy, greenhouse gas pollution, etc. Rice husk mainly contains lignin, cellulose, and hydrated silica, so it is a natural reservoir for nanostructured silica and its derivatives [48].

In [49], the synthesis of silicon carbide whiskers by the stacking method was proposed (Fig. 2). The experiment consisted of two groups: using a mixture of graphene and rice husk ash (RHA-G) and using only rice husk ash (RHA). Fig. 2a,e shows the original method of placing the reagents in a graphite crucible. Next, the growth of SiC whiskers on graphene after heat treatment at 1400°C is shown (Fig. 2b,f). Fig. 2c,g shows the separation between the graphene layer (upper part) and the initial silicon layers (lower part). As a result (Fig. 2d,h), SiC samples were obtained after decarbonization of the graphene layer. The diameter of the synthesized whiskers of silicon carbide was 30-120 nm.

In a similar study [50], silicon carbide whiskers were also synthesized using rice husk ash and graphene. For this, rice husk ash and graphene were mixed in a weight ratio of 1:1. 300 mg of the resulting mixture was poured into a graphite crucible with a lid and placed in a tube furnace heated to 1450°C at a heating rate of 5°C/min and held for 2 hours. The resulting samples were decarbonized at 700°C for 2 hours and then treated with hydrofluoric acid to remove residual ions and SiO₂. The synthesized SiC whiskers had a diameter of 50-150 nm and a length of several 10 μm.

In [48], β-SiC was synthesized from rice husks by magnesiothermic reduction at a relatively low temperature of 600°C. To do this, rice husks were thoroughly washed with distilled water to remove dirt, and then dried at a temperature of 80°C for 2 hours. After that, it was washed several times with distilled water and dried overnight. Rice husks were annealed in a tube furnace at 600°C for 1 hour in an argon atmosphere to carbonize and remove small organic molecules, then further boiled in HCl (1 mol/L) for 4 hours to remove metal impurities, and then dried at a temperature of 80°C for 3 hours. To synthesize silicon carbide nanoparticles, carbonized rice husk and magnesium powders were mixed at a molar ratio of SiO₂/Mg = 1:2.5, hermetically sealed into a stainless steel container, which was placed in a tube furnace, and heated to 600°C at a heating rate of 5°C/min under a continuous flow of argon for 3 hours. After that, the products were immersed in HCl (1 mol/L) with stirring to remove MgO, washed with distilled water until neutral pH, calcined in air at 700°C for 1 hour to remove residual carbon, and washed with HF to remove residual SiO₂. As a result, a light green powder of SiC nanoparticles with a particle size of 20-30 nm was obtained.

In [51], microsilica particles were obtained by burning rice husks at a temperature of 700°C, acid leaching to remove inorganic impurities, and, finally, mechanical ball milling for 0, 18, 36, and 72 hours to reduce the particle size. The SEM images showed that the particle size decreases with increasing grinding time, resulting in a particle diameter of less than 2.0 μm.

Another "green" precursor for the synthesis of silicon carbide nanoparticles is barley husk, since it is widely available, and its agricultural waste contains a large amount of nanostructured silica. In [52], SiC nanoparticles were obtained by a simple high-temperature synthesis using barley husks (Fig. 3).

Due to its high availability, corn cobs are also used as a raw material for the synthesis of silicon carbide. The

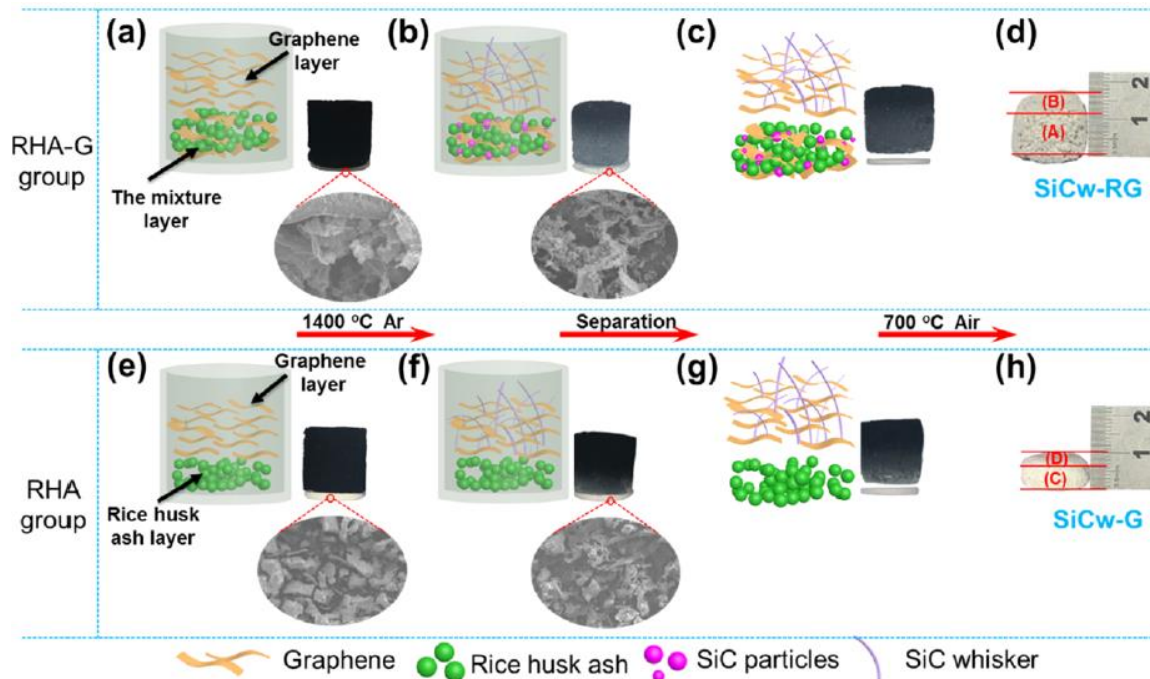


Fig. 2. Scheme for the synthesis of silicon carbide whiskers [49].

authors of [53] synthesized silicon carbide from corn cobs by the sol-gel method. For this, crushed corn cobs were pyrolyzed at a temperature of 600°C to obtain corn cob ash. 10 g of ash was dissolved in 60 ml of 2.5 M NaOH and refluxed at 80°C for 3 hours. The pH of the cooled solution was adjusted to 7.0 with 2.5 M H₂SO₄ to form a silica hydrogel and incubated for 12 hours. The gel was centrifuged at 4000 rpm for 5 minutes. The supernatant was removed, and the resulting silica was washed with deionized water and dried in an oven at 80°C. A mixture of silica, activated carbon and magnesium powder in a ratio of 1:0.2:0.88 was transferred to a crucible, pyrolyzed at 600°C for 8 hours, and reheated to 500°C after cooling at room temperature for 30 minutes. The resulting solid was leached with acid (5 M HCl), and the solution was left to stand for 1 hour. The solution was filtered, the solid was washed several times with deionized water and dried in an oven overnight at 100°C to obtain SiC.

In [54], a technology was developed for using printed circuit board waste as a precursor of silicon and carbon to obtain silicon carbide nanoparticles. The preparation process contained three optimized steps: 1) prewash with 3 mol/L nitric acid at 60°C for 96 hours; 2) low temperature pyrolysis at 500°C to decompose the epoxy resin into carbon; 3) high temperature pyrolysis at a temperature of 1600°C (in situ carbothermal reduction) to

obtain pure SiC nanoparticles. Fig. 4 shows the morphology of the obtained SiC using a scanning electron microscope (the pyrolyzed powder was additionally heated to 1500, 1600, and 1700°C). The particle size ranged from several tens to hundreds of nanometers.

In [55], hollow spheres of silicon carbide were synthesized. To do this, SiO₂ was uniformly applied to dry yeast as a biological template by the sol-gel method, and the internal substances of the yeast were removed at a temperature of 700°C to obtain a hollow silicon template. RF aerogel (source of carbon) was then used to wrap the silicone template. After carbonization, a carbon thermal reduction reaction was carried out at a temperature of 1400°C to obtain SiC hollow spheres. And in [36], silicon carbide was synthesized by microwave sintering using graphene as a carbon source and ethyl orthosilicate as a silicon source. First, SiO₂ particles were deposited in situ on the graphene surface by the sol-gel method, and then one-dimensional silicon carbide nanowires were obtained by the thermal reduction reaction. The optimum sintering temperature is 1500°C, holding time is 40 min.

In [56], silicon carbide was obtained by reaction-bonding sintering with the addition of nanosized carbon black and microspherical carbon. Inert carbon particles remained after the process of infiltration of molten silicon and were consumed in reaction with residual silicon at

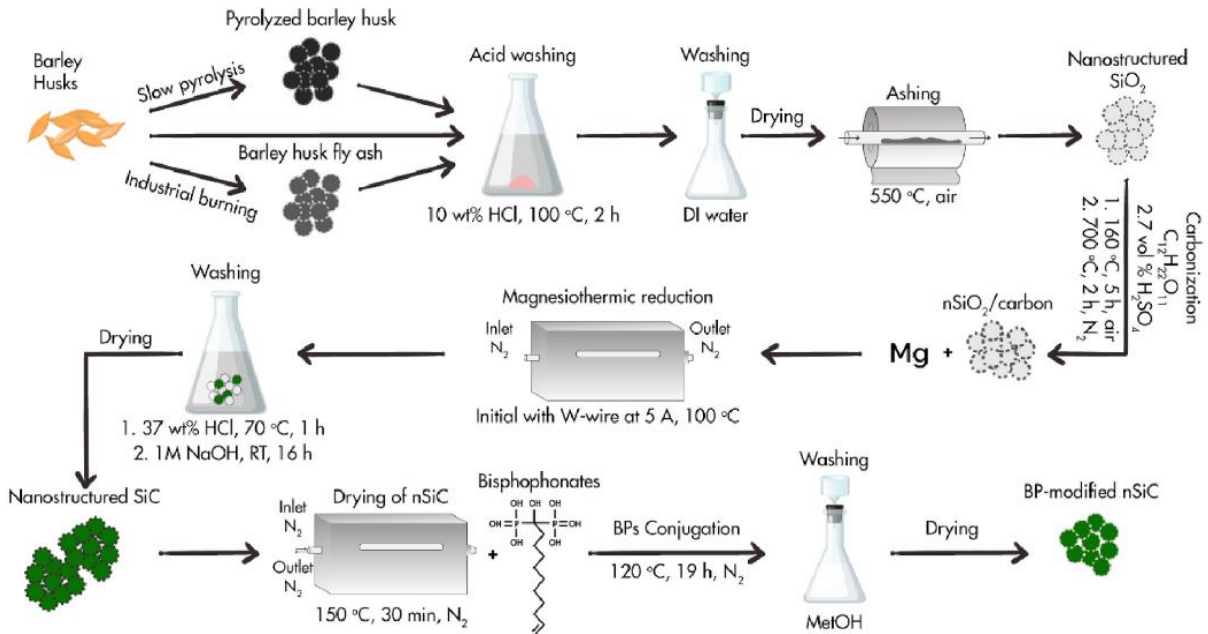


Fig. 3. Graphic scheme for the synthesis of nanostructured silicon carbide [52].

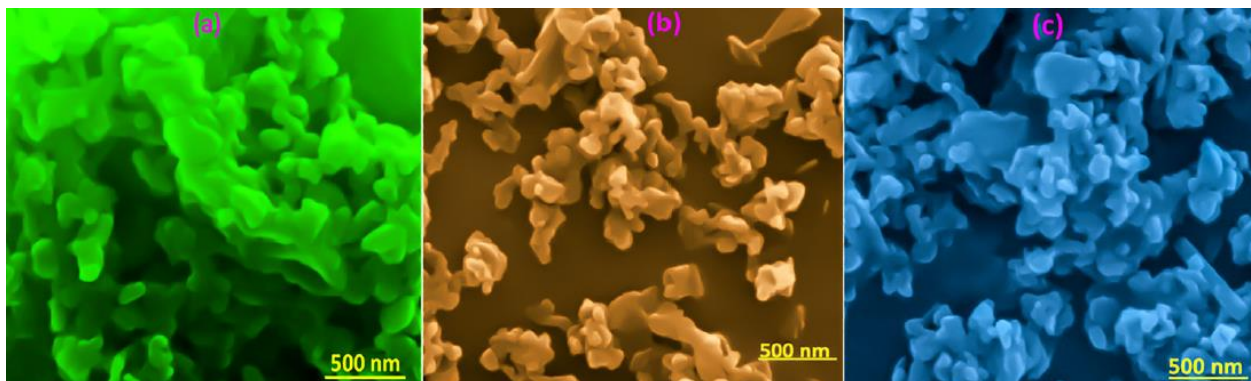


Fig. 4. SEM images of SiC-1500 (a); SiC-1600 (b) and SiC-1700 (c) [54].

high temperature. At a temperature of 1850°C, the residual carbon decreased to almost zero, which was accompanied by 6% Si as a result of continuous infiltration of Si in the second soaking step. A hardness of 25.3 GPa and a Young's modulus of 443 GPa were achieved. It has been found that the sintering process consists of a fast direct reaction by infiltration and a slow reaction by diffusion, potentially resulting in SiC with a very low residual Si content.

In [57], silicon carbide was synthesized by calcining tissue and glass microspheres at high temperature. The results show that a higher synthesis temperature can improve SiC crystallinity, form more whiskers, and reduce the content of impurities. The synthesized products at 1600°C have excellent microwave absorption properties. Also a good material for microwave absorption is porous silicon carbide foams synthesized in [58] as a result of the reaction of phenolic resin and silicon powder by the replica method using polyurethane foam followed by sintering. SiC foams have also been modified by adding various microwave absorbing additives such as ZrO_2 , Fe_3O_4 , and NiO.

In [59], cubic 3C-SiC was synthesized at different temperatures (1600°C, 1650°C, and 1700°C) using graphite flakes and microfine silica by the carbothermal reduction method. The grown SiC structures were observed in two different morphologies, namely ribbon-type (diameter 2-5 μm) and rod-type (diameter $\leq 2 \mu\text{m}$). The ribbon-type morphology was formed on the surface of the graphite flakes at a relatively low temperature (1600°C), and the rod-type morphology was formed at a higher temperature ($\geq 1650^\circ\text{C}$) between the interlamellar spaces of the graphite flakes.

In [60], amorphous and crystalline SiC nanoparticles were synthesized by laser ablation (wavelength 1064 nm) of microsized SiC powder in water and ethanol. The analysis showed the amorphous nature of SiC nanoparticles with an average particle size of 44 nm in water and crystalline nature of 6H-SiC nanoparticles with an average particle size of 18 nm in ethanol. The direct and indirect bandgaps for SiC nanoparticles according to absorption spectra in the UV-visible range in water were 5.3 and 3.03 eV, respectively, and in ethanol, 4.9 and 3.05 eV, respectively.

In [46], an AC multi-arc plasma device was developed for continuous gas-phase synthesis of ultra-small silicon carbide nanoparticles (Fig. 5). SiC nanoparticles with an average size of 7-10 nm were obtained by decomposition of triethylsilane in an AC multi-arc plasma (Ar, H_2 , and N_2 were used as buffer gases).

In [61], the detonation synthesis of silicon carbide is presented. Simulation of detonation on a continuum scale showed that the detonation wave energy transfer is completed within 2-9 μs , depending on the location of the measurement within the detonating explosive charge. Carbon and added elemental silicon in the detonation products remained chemically reactive up to 500 ns after the passage of the detonation wave, indicating that carbonaceous detonation products can participate in the synthesis of silicon carbide with sufficient carbon-silicon interaction. Controlled charge detonation with 3.2 wt% of elemental silicon, carried out in an argon environment, leads to the formation of ~ 3.1 wt% of β -SiC in the condensed detonation products. In a similar study [62], the same scientists added polycarbosilane to a mixture of 1,3,5-trinitro-1,3,5-triazinane and 2,4,6-trinitrotoluene, which was then detonated in a closed chamber filled with an inert gas. X-ray diffraction analysis of detonation soot showed the presence of crystalline silicon with a diamond cubic structure and cubic silicon carbide along with amorphous material.

In [63], SiC membranes were synthesized by additive sintering using NaA zeolite residues (sodium, aluminum, and silicon oxides) as additives. Zeolites are among the largest cation exchangers [64]. With such additives, the particles are more tightly connected due to the formation of new phases. The SiC powder was ground in a ball mill with NaA residues (NaA content: 6, 8, 10, 12, and 14 wt%) and activated carbon powder (activated carbon content: 0, 5, 10, 15, and 20 wt%) for 2 hours. After sieving, an 8 wt% polyvinyl alcohol solution was added to the mixture. Next, the samples were sintered in an atmospheric air from 850°C to 1050°C and gradually cooled to room temperature. The use of NaA zeolite residues has effectively reduced the cost of production and improved the performance of ceramic membranes. SiC membranes have shown high resistance to cyclic thermal shock, strong long-term acidity, and caustic corrosion [63].

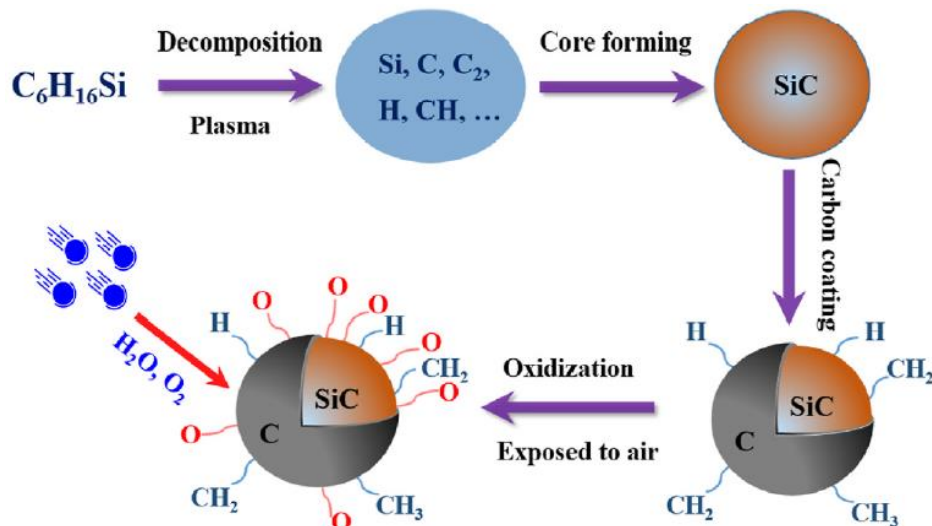


Fig. 5. Formation of SiC nanoparticles in an AC multi-arc plasma [46].

The authors of [65] studied the effect of the addition of TiO₂ nanoparticles [66,67] on the physicomechanical properties of a silicon carbide composite. The samples were made without pressure at a temperature of 1900°C. The results have shown that the addition of TiO₂ nanoparticles up to 4.5 wt% inhibits excessive growth of SiC grains. According to research data, composites were affected by density, synthesized phases, as well as their distribution in the matrix, and grain size. The highest density was 98.7%, Young's modulus was 401.2 GPa and hardness was 27.1 GPa.

In [68], SiC/SiO₂ nanowires were synthesized from silica fume [69] and sucrose by carbothermal reduction. To do this, silica fume (as a source of silicon) and sucrose (as a source of carbon) were mixed in a molar ratio of 1:4. NaCl and NaF were used as the molten salt medium. Silica and sucrose were mixed with salt and placed in a graphite crucible covered with a lid, and then kept at a temperature of 1300-1500°C for 4 hours in an argon flow. After cooling in a furnace to room temperature, the reacted mass was washed several times with hot distilled water and filtered to leach out the remaining salts. After drying at 100°C for 12 hours, the obtained samples were heated at 700°C for 3 hours in air to remove residual carbon. The resulting nanowires were a heterostructure composed of a 3C-SiC core 100 nm in diameter and a 5-10 nm thick amorphous SiO₂ shell layer.

Many studies of methods for obtaining silicon carbide are devoted to synthesis by chemical vapor deposition.

In [70], β-SiC nanowires were synthesized by catalyst-free chemical vapor deposition using silicon, trace nanoscale SiO₂ particles, and phenolic resin powders. To do this, the SiO₂ nanopowder was ultrasonically dispersed in ethanol to obtain a SiO₂-alcohol suspension. The suspension was then added to the Si powder and then stirred for 30 minutes, resulting in a Si-SiO₂ mixture. Thereafter, the phenolic resin powder and the dried Si-SiO₂ mixture were blended for 30 minutes. The final mixture was heated at 1400°C for 3 hours in a small corundum crucible with a lid embedded in a large closed corundum crucible filled with graphite powder. The synthesized β-SiC nanowires were well crystallized, had different morphology (chain, bamboo-shaped, and linear), lengths up to tens of microns, and diameters of 80-650 nm.

In a similar study [42], SiC nanowires were also synthesized by simple chemical vapor deposition at high temperatures using silicon, phenolic resin, and ZrB₂ powder. A mixture of phenol formaldehyde resin powder, Si powder, and ZrB₂ powder was stirred at 310 rpm for 30 minutes using a QM-3SP4 ball mill. The well-blended mixture was placed in a small corundum crucible and covered with a lid. The small crucible was then placed in the larger crucible and coated with graphite powder. A large crucible containing the mixture was fired at 1400°C for 3 hours. Since a large corundum crucible with an excess of graphite powder was sealed, the gases in the crucibles mainly consisted of CO and N₂ (from a protective atmosphere), which contributed to the formation of SiC nanowires.

The authors of [71] proposed a new chemical vapor deposition process in which gaseous SiO and toluene vapor react to form SiC in the presence of iron oxide as a

catalytic component. One side of the alumina plate used as the substrate was wetted with an iron (III) nitrate aqueous solution, then dried and heated to 800°C in air. Thus, a layer of iron oxide with a thickness of about 5 μm was deposited as a catalytic component. Next, 300 mg of granular SiO was poured into an alumina crucible with an internal volume of 15 mL, and an alumina support plate and the above-mentioned iron oxide deposited alumina plate were placed on granular SiO, which were then placed on the support plate (Fig. 6). The crucible in this state was placed in an electric furnace, and the air in the furnace was replaced with argon. Then, the crucible was heated to a temperature of 1450°C for a given time, while toluene vapor was continuously fed into the crucible. Thus, various SiC coatings along with fibrous materials were formed at those places on the alumina plates where iron oxide was deposited. The fibrous material is composed of fibrous SiC as well as a spherical substance containing Fe and can be easily removed mechanically from the SiC coating.

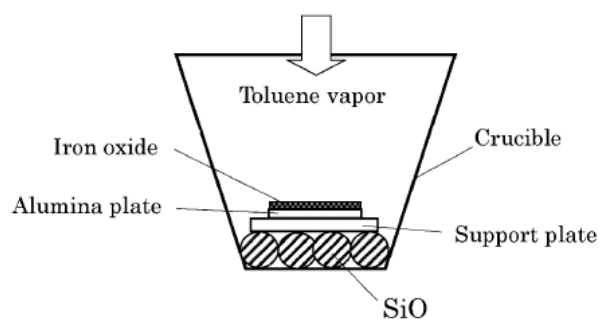


Fig. 6. Scheme for the SiC coating [71].

In [39], a SiC fiber was synthesized at atmospheric pressure in a horizontal hot wire CVD reactor (Fig. 7). A coil of tungsten wire with a diameter of $17.8 \pm 0.1 \mu\text{m}$ was used as a heating element and a substrate for SiC deposition. CH₃SiCl₃ (purity > 98%) was used as a precursor, the flow rate of which was controlled by supplying a diluent gas through a thermostatic bubbler. H₂ and Ar were used as diluent gases. The substrate temperature was measured through a viewing window inside the reactor using a SYG WGG2-201 optical pyrometer with an error of $\pm 20^\circ\text{C}$, and the corresponding temperature of the reactor wall was measured with a Lutron TM902C digital thermometer with an error of $\pm 1^\circ\text{C}$. Before introducing CH₃SiCl₃ into the reactor, an external heating jacket was used to preheat the reactor wall to 150°C, and a dilution gas was used to purge the reactor for 30 minutes at a flow rate of 400 sccm. During SiC deposition, the W wire speed and the flow rate of CH₃SiCl₃ were separately maintained at 2 cm/s and 600 sccm, while the diluent gas flow rate varied from 800 to 1600 sccm. By controlling the input power, all deposition processes were carried out at a substrate temperature of 1000°C.

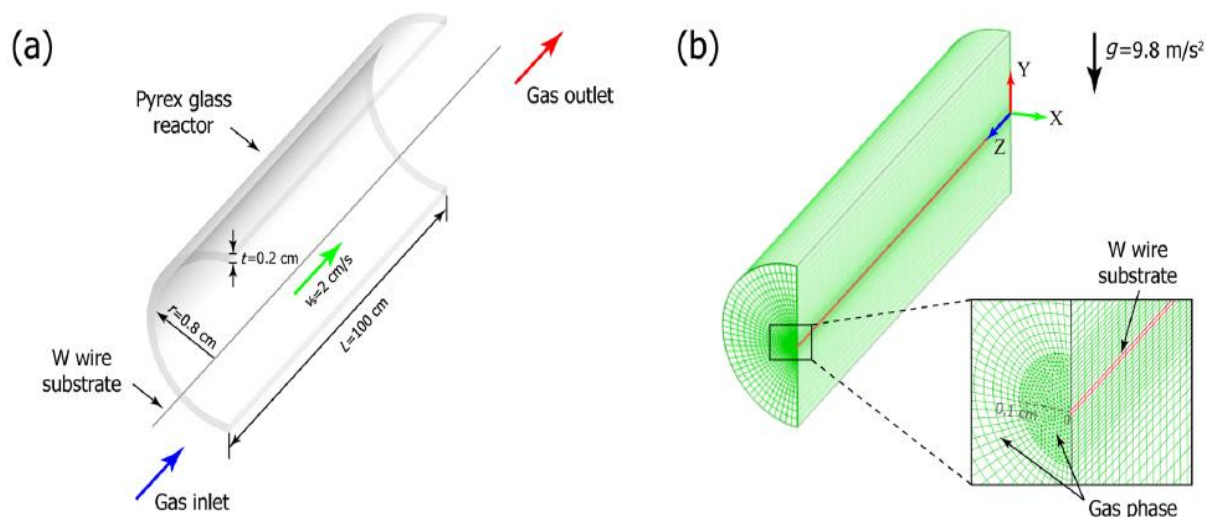


Fig. 7. Schematic diagrams of the CVD reactor [39].

Conclusions

Silicon carbide is a widely used material with unique physical and chemical properties. In particular, high hardness (~25 GPa), high compressive strength (~3.5 GPa), and low density make SiC an attractive option for many applications at high temperatures and in corrosive environments. The most important problems in the synthesis of silicon carbide are the low sinterability of SiC due to the presence of covalent bonds and its low self-diffusion. Therefore, the sintering of silicon carbide must be carried out at a very high temperature. New modern heating technologies such as microwave, plasma and laser heating allow the reaction to be carried out at a low temperature, which reduces preparation costs and significantly reduces reaction time. Today, the concept of "green" synthesis is very popular, involving the development of renewable, non-toxic and environmentally friendly materials based on silicon carbide. Therefore, scientists actively study ways to

synthesize SiC nanoparticles using biomass. Due to their excellent characteristics, silicon carbide nanoparticles have a high potential for application in many aspects, in particular, use in structural and functional composites, catalysts, fluorescent biomarkers, bioadhesives, etc.

Soltys L.M. – PhD (Chemical Sciences), Head of Educational Laboratories of the Department of Chemistry, Associate Professor at the Department of Chemistry, Vasyl Stefanyk Precarpathian National University;
Mironyuk I.F. – Doctor of Chemical Sciences, Professor, Head of the Department of Chemistry, Vasyl Stefanyk Precarpathian National University;
Mykytyn I.M. – PhD (Technical Sciences), Associate Professor at the Department of Chemistry, Vasyl Stefanyk Precarpathian National University;
Hnylytsia I.D. – PhD (Technical Sciences), Associate Professor at the Department of Welding, Ivano-Frankivsk National University Technical of Oil and Gas;
Turovska L.V. – PhD (Chemical Sciences), Associate Professor at the Department of Medical Informatics, Medical and Biological Physics, Ivano-Frankivsk National Medical University.

- [1] A.J. Ruys, I.G. Crouch, *Siliconized Silicon Carbide* (Elsevier Ltd., 2021); ISBN 9780081028698.
- [2] J. Lamon, *Properties and Characteristics of SiC and SiC/SiC Composites*, *Compr. Nucl. Mater.* Second Ed. 7, 400 (2020); <https://doi.org/10.1016/B978-0-12-803581-8.11717-5>.
- [3] L. Bracamonte, R. Loutfy, I.K. Yilmazcoban, S.D. Rajan, *Design, Manufacture, and Analysis of Ceramic-Composite Armor* (Elsevier Ltd, 2016); ISBN 9780081004258.
- [4] A. Tariq, A.; Shakir, M.F. *Ceramic Composites* (LTD, 2021); ISBN 9780128219843.
- [5] M.A.H. Mohd Sohor, M. Mustapha, J. Chandra Kurnia, *Silicon Carbide – from Synthesis to Application: A Review*, *MATEC Web Conf.*, 131, 1 (2017); <https://doi.org/10.1051/mateconf/201713104003>.
- [6] S. Gryn, T. Nychyporuk, I. Bezverkhyy, D. Korytko, V. Iablokov, V. Lysenko, S. Alekseev, *Mesoporous SiC with Potential Catalytic Application by Electrochemical Dissolution of Polycrystalline 3C-SiC*, *ACS Applied Nano Materials*, 1(6), 2609 (2018); <https://doi.org/10.1021/acsnm.8b00301>.
- [7] Z. Wu, H. Zheng, G. Zhang, Y. Deng, Z. Meng, H.U. Wahab, *Synthesis of Diameter-Fluctuating Silicon Carbide Nanowires for Excellent Microwave Absorption*, *Mater. Chem. Phys.*, 244, 122648 (2020); <https://doi.org/10.1016/j.matchemphys.2020.122648>.
- [8] Tsunenobu Kimoto, James A. Cooper, *Fundamentals of Silicon Carbide Technology: Growth, Characterization, Devices, and Applications* (John Wiley & Sons Singapore Pte. Ltd, Singapore, 2014); <https://doi.org/10.1002/9781118313534.ch1>.

- [9] R. Wu, K. Zhou, C.Y. Yue, J. Wei, Y. Pan, *Recent Progress in Synthesis, Properties and Potential Applications of SiC Nanomaterials*, Prog. Mater. Sci., 72, 1 (2015); <https://doi.org/10.1016/j.pmatsci.2015.01.003>.
- [10] Y. Wang, S. Dong, X. Li, C. Hong, X. Zhang, *Synthesis, Properties, and Multifarious Applications of SiC Nanoparticles: A Review*, Ceram. Int., 48(7), 8882 (2022); <https://doi.org/10.1016/j.ceramint.2021.12.208>.
- [11] J.E. House, *Inorganic Chemistry* (Elsevier, 2020); ISBN 9780128143698.
- [12] H.K. Henisch, R. Roy, *Silicon Carbide—1968* (Elsevier, 1969); ISBN 9780080067681.
- [13] X. Ren, B. Ma, F. Qian, W. Yang, G. Liu, Y. Zhang, J. Yu, Q. Zhu, *Green Synthesis of Porous SiC Ceramics Using Silicon Kerf Waste in Different Sintering Atmospheres and Pore Structure Optimization*, Ceram. Int., 47(18), 26366 (2021); <https://doi.org/10.1016/j.ceramint.2021.06.047>.
- [14] E. Padovano, C. Badini, K. Mergia, J. Barcena, *Thermophysical and Radiative Properties of Pressureless Sintered SiC and ZrB₂-SiC Laminates*, Ceramics International, 44 (13), 2018, 15050 (2018); <https://doi.org/10.1016/j.ceramint.2018.05.135>.
- [15] M. Liu, X. Yang, J. Guo, L. Zhang, *Fabrication of SiC Foam Ceramics at a Low Sintering Temperature by Adding Fly Ash*, Ceram. Int. 48(20), 30462 (2022); <https://doi.org/10.1016/j.ceramint.2022.06.326>.
- [16] J. Gu, S.H. Lee, V.H. Vu, J. Yang, H.S. Lee, J.S. Kim, *Fast Fabrication of SiC Particulate-Reinforced SiC Composites by Modified PIP Process Using Spark Plasma Sintering – Effects of Green Density and Heating Rate*, J. Eur. Ceram. Soc., 41(7), 4037 (2021); <https://doi.org/10.1016/j.jeurceramsoc.2021.02.025>.
- [17] D. Feng, Q. Ren, H. Ru, W. Wang, S. Ren, C. Zhang, *Mechanical Properties and Microstructure Evolution of SiC Ceramics Prepared from the Purified Powders*, Mater. Sci. Eng.: A, 802, 140443 (2021); <https://doi.org/10.1016/j.msea.2020.140443>.
- [18] R. Ma, J. Shi, W. Lin, J. Chen, *Synthesis and Sintering of Nanocrystalline SiC Ceramic Powders*, Mater. Chem. Phys., 253, 123445 (2020); <https://doi.org/10.1016/j.matchemphys.2020.123445>.
- [19] E. Eray, V. Boffa, M.K. Jørgensen, G. Magnacca, V.M. Candelario, *Enhanced Fabrication of Silicon Carbide Membranes for Wastewater Treatment: From Laboratory to Industrial Scale*, J. Memb. Sci., 606, 118080 (2020); <https://doi.org/10.1016/j.memsci.2020.118080>.
- [20] A.S. Mukasyan, *Properties and Applications of Silicon Carbide* (InTech Open, 2011); <https://doi.org/10.5772/15620>.
- [21] M. Xia, H. Guo, M.I. Hussain, *Controllable Combustion Synthesis of SiC Nanowhiskers in a Si-C-N System: The Role of the Catalyst*, Applied Sciences, 10(1), 252 (2019); <https://doi.org/10.3390/app10010252>.
- [22] Z. Han, H. Zhu, Y. Zou, J. Lu, F. Zhu, Q. Ning, *Band Gap Regulation and a Selective Preparation Method for Single-Walled Silicon Carbide Nanotubes*, Results Phys., 38, 105658 (2022); <https://doi.org/10.1016/j.rinp.2022.105658>.
- [23] F.W. Aldbea, S.A. Alameen, C.V. Vázquez, A. Sharma, M. Kraini, A.A. Ahmed, P.K. Singh, *Structural Analysis of Silicon Carbide Prepared from Two Types of Carbon Sources*, Mater. Today, Proc. 49, 3711 (2020); <https://doi.org/10.1016/j.matpr.2021.10.119>.
- [24] Z. Pan, C. Weng, M. Gao, W. Lin, L. Gao, H. Zhu, J. Chen, *Syntheses and Photoluminescence Properties of SiC Nanowires with Different Colors*, J. Alloys Compd., 842, 155768 (2020); <https://doi.org/10.1016/j.jallcom.2020.155768>.
- [25] M. Zeraati, K. Tahmasebi, A. Irannejad, *Formation of SiC Nanocrystals Prepared by Sol-Gel Processing of Green Carbon Sources and DFT Calculations*, J. Nanostructures, 10(3), 660 (2020); <https://doi.org/10.22052/JNS.2020.03.019>.
- [26] M. Zeraati, V. Alizadeh, G. Sargazi, H. Kazemian, *Sol-Gel Synthesis of Silicon Carbide on Silicon Pyramids: A Promising Candidate for Supercapacitor Electrodes*, J. Mater. Sci. Mater. Electron., 32(17), 22319 (2021); <https://doi.org/10.1007/s10854-021-06718-4>.
- [27] J. Xiao, L. Zhang, J. Yuan, Z. Yao, L. Tang, Z. Wang, Z. Zhang, *Co-Utilization of Spent Pot-Lining and Coal Gangue by Hydrothermal Acid-Leaching Method to Prepare Silicon Carbide Powder*, J. Clean. Prod., 204, 848 (2018); <https://doi.org/10.1016/j.jclepro.2018.08.331>.
- [28] Q. Wen, Z. Yu, R. Riedel, *The Fate and Role of in Situ Formed Carbon in Polymer-Derived Ceramics*, Progress in Materials Science, 109, 100623 (2020); <https://doi.org/10.1016/j.pmatsci.2019.100623>.
- [29] B. Santhosh, E. Ionescu, F. Andreolli, M. Biesuz, A. Reitz, B. Albert, G.D. Sorarù, *Effect of Pyrolysis Temperature on the Microstructure and Thermal Conductivity of Polymer-Derived Monolithic and Porous SiC Ceramics*, J. Eur. Ceram. Soc., 41(2), 1151 (2021); <https://doi.org/10.1016/j.jeurceramsoc.2020.09.028>.
- [30] Y. Wang, X. Pei, H. Li, X. Xu, L. He, Z. Huang, Q. Huang, *Preparation of SiC Ceramic Fiber from a Photosensitive Polycarbosilane*, Ceram. Int., 46(18), 28300 (2020); <https://doi.org/10.1016/j.ceramint.2020.07.333>.
- [31] C.M. Senger, K.F. Anschau, L. Baumann, A.L.H. Muller, P.A. Mello, E.I. Muller, *Eco-Friendly Sample Preparation Method for Silicon Carbide Using Pyrohydrolysis for Subsequent Determination of Tungsten by ICP-MS*, Microchem. J., 171, 106781 (2021); <https://doi.org/10.1016/j.microc.2021.106781>.
- [32] X. Li, W. Yang, J. Sang, J. Zhu, L. Fu, D. Li, L. Zhou, *Low-Temperature Synthesizing SiC on Diamond Surface and Its Improving Effects on Thermal Conductivity and Stability of Diamond/Al Composites*, J. Alloys Compd., 846, 156258 (2020); <https://doi.org/10.1016/j.jallcom.2020.156258>.

- [33] A. Gubernat, W. Pichór, R. Lach, D. Zientara, M. Sitarz, M. Springwald, *Low-Temperature Synthesis of Silicon Carbide Powder Using Shungite*, Boletín de la Sociedad Española de Cerámica y Vidrio, 56(1), 39 (2017); <https://doi.org/10.1016/j.bsecv.2016.04.003>.
- [34] F. Zhang, Y. Chen, S. Wei, Y. Si, H. Wang, R. Zhang, G. Wang, L. Song, B. Fan, *Microwave Heating and Mechanism for Seed-Induced Synthesis of SiC*, Mater. Today Commun., 31, 103846 (2022); <https://doi.org/10.1016/j.mtcomm.2022.103846>.
- [35] C.C. Lee, S.M. Kahar, C.H. Voon, *Microwave Synthesis of Silicon Carbide Nanowhiskers: Effect of Molar Ratio*, Mater. Today Proc., 37(2), 119 (2020); <https://doi.org/10.1016/j.matpr.2020.04.571>.
- [36] Q. Qin, J. Chen, M. Song, F. Cao, Y. Li, F. He, Z. Liu, G. Zhu, Q. Diao, *Preparation of SiC Nanowires Based on Graphene as the Template by Microwave Sintering*, J. Alloys Compd., 910, 164746 (2022); <https://doi.org/10.1016/j.jallcom.2022.164746>.
- [37] C.H. Voon, B.Y. Lim, S.C.B. Gopinath, H.S. Tan, V.C.S. Tony, M.K. Md Arshad, K.L. Foo, U. Hashim, *Green Synthesis of Silicon Carbide Nanowhiskers by Microwave Heating of Blends of Palm Kernel Shell and Silica*, IOP Conf. Ser. Mater. Sci. Eng., 160(1), 012057 (2016); <https://doi.org/10.1088/1757-899X/160/1/012057>.
- [38] M. Zhang, H. Ling, W. Zhang, H. Bian, H. Lin, T. Wang, Z. Li, A. Meng, *Preparation, Superior Field Emission Properties and First Principles Calculation of Electronic Structure of SiC Nanowire Arrays on Si Substrate*, Mater. Charact., 180, 111413 (2021); <https://doi.org/10.1016/j.matchar.2021.111413>.
- [39] S. Liu, X. Luo, B. Huang, P. Li, Y. Yang, *Role of H₂ and Ar as the Diluent Gas in Continuous Hot-Wire CVD Synthesis of SiC Fiber*, J. Eur. Ceram. Soc. 42(7), 3135 (2022); <https://doi.org/10.1016/j.jeurceramsoc.2022.02.038>.
- [40] B. Zhumadilov, G. Suyundykova, G. Partizan, A. Kenzhegulov, B. Medyanova, B. Aliyev, *Structure and Morphology of SiC Nanostructures Synthesized on Cu Films*, Mater. Today Proc., 31, 417 (2019); <https://doi.org/10.1016/j.matpr.2020.01.385>.
- [41] A. Baux, A. Goillot, S. Jacques, C. Heisel, D. Rochais, L. Charpentier, P. David, T. Piquero, T. Chartier, G. Chollon, *Synthesis and Properties of Macroporous SiC Ceramics Synthesized by 3D Printing and Chemical Vapor Infiltration/Deposition*, J. Eur. Ceram. Soc., 40(8), 2834 (2020); <https://doi.org/10.1016/j.jeurceramsoc.2020.03.001>.
- [42] Q. Zhang, Z. Sun, X. Liu, J. Sun, R. Yu, X. Liu, *Synthesis of SiC Nanowires by a Simple Chemical Vapour Deposition Route in the Presence of ZrB₂*, Ceram. Int., 46(8), 12249 (2020); <https://doi.org/10.1016/j.ceramint.2020.01.274>.
- [43] H. Zhu, X. Li, Z. Dong, Y. Cong, G. Yuan, Z. Cui, *In Situ Growth of Dense SiC Nanowires on Structural Defined Carbon Fibers without Sacrificing Flexibility*, Ceram. Int., 46(16), 26017 (2020); <https://doi.org/10.1016/j.ceramint.2020.07.094>.
- [44] Z. Zhang, J. Tan, L. Cheng, W. Yang, *In-Situ Growth of Silicon Carbide Nanofibers on Carbon Fabric as Robust Supercapacitor Electrode*, Ceram. Int., 47(17), 24652 (2021); <https://doi.org/10.1016/j.ceramint.2021.05.187>.
- [45] J. Zhou, C. Wang, M. Song, X. Chen, W. Xia, *Simple Synthesis of Ultrafine Amorphous Silicon Carbide Nanoparticles by Atmospheric Plasmas*, Mater. Lett., 299, 130072 (2021); <https://doi.org/10.1016/j.matlet.2021.130072>.
- [46] C. Wang, J. Zhou, M. Song, X. Chen, Y. Zheng, C. Yang, W. Xia, W.; Xia, W., *Fabrication of Ultra-Small SiC Nanoparticles with Adjustable Size, Stoichiometry and Photoluminescence by AC Multi-Arc Plasmas*, Ceram. Int., 48(1), 632 (2022); <https://doi.org/10.1016/j.ceramint.2021.09.142>.
- [47] L. Soltys, O. Olkhovyy, T. Tatarchuk, M. Naushad, *Green Synthesis of Metal and Metal Oxide Nanoparticles: Principles of Green Chemistry and Raw Materials*, Magnetochemistry, 7(11), 145 (2021); <https://doi.org/10.3390/magnetochemistry7110145>.
- [48] J. Su, B. Gao, Z. Chen, J. Fu, W. An, X. Peng, X. Zhang, L. Wang, K. Huo, P.K. Chu, *Large-Scale Synthesis and Mechanism of β -SiC Nanoparticles from Rice Husks by Low-Temperature Magnesiothermic Reduction*, ACS Sustain. Chem. Eng., 4(12), 6600 (2016); <https://doi.org/10.1021/acssuschemeng.6b01483>.
- [49] J. Chen, Q. Kong, Z. Liu, Z. Bi, H. Jia, G. Song, L. Xie, S. Zhang, C.M. Chen, *High Yield Silicon Carbide Whiskers from Rice Husk Ash and Graphene: Growth Method and Thermodynamics*, ACS Sustain. Chem. Eng., 7(23), 19027 (2019); <https://doi.org/10.1021/acssuschemeng.9b04728>.
- [50] J.P. Chen, G. Song, Z. Liu, Q.Q. Kong, S.C. Zhang, C.M. Chen, *Preparation of SiC Whiskers Using Graphene and Rice Husk Ash and Its Photocatalytic Property*, J. Alloys Compd., 833, 155072 (2020); <https://doi.org/10.1016/j.jallcom.2020.155072>.
- [51] D.F. Hincapié-Rojas, A. Rosales-Rivera, P. Pineda-Gomez, *Synthesis and Characterisation of Submicron Silica Particles from Rice Husk*, Green Mater., 6(1), 15 (2018); <https://doi.org/10.1680/jgrma.17.00019>.
- [52] O. Haluska, A. Rahmani, A. Salami, P. Turhanen, J. Vepsäläinen, R. Lappalainen, V.P. Lehto, J. Riikonen, *Plant-Based Nanostructured Silicon Carbide Modified with Bisphosphonates for Metal Adsorption*, Microporous Mesoporous Mater., 324, 111294 (2021); <https://doi.org/10.1016/j.micromeso.2021.111294>.
- [53] A.N.R. Alfonso, J.R. Salazar, J.J. Monserate, M.M. Sarong, *Potential for Photovoltaic Cell Material by Green Synthesis of Silicon Carbide from Corn Cob through Magnesiothermic Reduction*, Int. J. Energy Prod. Manag., 5(1), 14 (2020); <https://doi.org/10.2495/EQ-V5-N1-14-23>.

- [54] J. Yang, J. Feng, W. Li, X. Chen, X. Liu, J. Ruan, R. Qiu, Y. Xiong, S. Tian, *A Resource-Utilization Way of the Waste Printed Circuit Boards to Prepare Silicon Carbide Nanoparticles and Their Photocatalytic Application*, *J. Hazard. Mater.*, 373, 640 (2019); <https://doi.org/10.1016/j.jhazmat.2019.03.115>.
- [55] J. Zhou, B. Wei, Z. Yao, H. Lin, R. Tan, W. Chen, X. Guo, *Preparation of Hollow SiC Spheres with Biological Template and Research on Its Wave Absorption Properties*, *J. Alloys Compd.*, 819, 153021 (2020); <https://doi.org/10.1016/j.jallcom.2019.153021>.
- [56] N.L. Zhang, J.F. Yang, Y.C. Deng, B. Wang, P. Yin, *Preparation and Properties of Reaction Bonded Silicon Carbide (RB-SiC) Ceramics with High SiC Percentage by Two-Step Sintering Using Compound Carbon Sources*, *Ceram. Int.*, 45(12), 15715 (2019); <https://doi.org/10.1016/j.ceramint.2019.04.224>.
- [57] R. Tan, J. Zhou, Z. Yao, B. Wei, Z. Li, *A Low-Cost Lightweight Microwave Absorber: Silicon Carbide Synthesized from Tissue*, *Ceram. Int.*, 47(2), 2077 (2021); <https://doi.org/10.1016/j.ceramint.2020.09.040>.
- [58] S. Kumari, R. Kumar, P.R. Agrawal, S. Prakash, D.P. Mondal, S.R. Dhakate, *Fabrication of Lightweight and Porous Silicon Carbide Foams as Excellent Microwave Susceptor for Heat Generation*, *Mater. Chem. Phys.*, 253, 123211 (2020); <https://doi.org/10.1016/j.matchemphys.2020.123211>.
- [59] M. Raju, S. Sen, D. Sarkar, C. Jacob, *Synthesis of 3C-Silicon Carbide 1D Structures by Carbothermal Reduction Process*, *J. Alloys Compd.*, 857, 158243 (2021); <https://doi.org/10.1016/j.jallcom.2020.158243>.
- [60] E.P. Shuaib, G.K. Yogesh, D. Sastikumar, *Amorphous and Photoluminescent Crystalline Silicon Carbide Nanoparticles Synthesized by Laser Ablation in Liquids*, *Mater. Today Proc.*, 50, 2745 (2020); <https://doi.org/10.1016/j.matpr.2020.08.453>.
- [61] M.J. Langenderfer, Y. Zhou, J. Watts, W.G. Fahrenholtz, C.E. Johnson, *Detonation Synthesis of Nanoscale Silicon Carbide from Elemental Silicon*, *Ceram. Int.*, 48(4), 4456 (2022); <https://doi.org/10.1016/j.ceramint.2021.10.231>.
- [62] M.J. Langenderfer, W.G. Fahrenholtz, S. Chertopalov, Y. Zhou, V.N. Mochalin, C.E. Johnson, *Detonation Synthesis of Silicon Carbide Nanoparticles*, *Ceram. Int.*, 46(5), 6951 (2020); <https://doi.org/10.1016/j.ceramint.2019.11.064>.
- [63] Q. Jiang, J. Zhou, Y. Miao, S. Yang, M. Zhou, Z. Zhong, W. Xing, *Lower-Temperature Preparation of SiC Ceramic Membrane Using Zeolite Residue as Sintering Aid for Oil-in-Water Separation*, *J. Memb. Sci.*, 610, 118238 (2020); <https://doi.org/10.1016/j.memsci.2020.118238>.
- [64] L.M. Soltys, I.F. Mironyuk, T.R. Tatarchuk, V.I. Tsinurchyn, *Zeolite-Based Composites as Slow Release Fertilizers (Review)*, *Phys. Chem. Solid State*, 21(1), 89 (2020); <https://doi.org/10.15330/pcss.21.1.89-104>.
- [65] M. Khodaei, O. Yaghobizadeh, H.R. Baharvandi, A.A. Shahraki, H. Mohammadi, *The Effect of Nano-TiO₂ Additions on the Densification and Mechanical Properties of SiC-Matrix Composite*, *Ceram. Int.*, 46(5), 6477 (2020); <https://doi.org/10.1016/j.ceramint.2019.11.128>.
- [66] I.F. Mironyuk, L.M. Soltys, T.R. Tatarchuk, V.I. Tsinurchyn, *Ways to Improve the Efficiency of TiO₂-Based Photocatalysts (Review)*, *Phys. Chem. Solid State*, 21(2), 300 (2020); <https://doi.org/10.15330/pcss.21.2.300-311>.
- [67] I.F. Mironyuk, L.M. Soltys, T.R. Tatarchuk, K.O. Savka, *Methods of Titanium Dioxide Synthesis (Review)*, *Phys. Chem. Solid State*, 21(3), 462 (2020); <https://doi.org/10.15330/pcss.21.3.462-477>.
- [68] J. Zhang, S. Yan, Q. Jia, J. Huang, L. Lin, S. Zhang, *Preparation of SiC/SiO₂ Core-Shell Nanowires via Molten Salt Mediated Carbothermal Reduction Route*, *Phys. E Low-Dimensional Syst. Nanostructures*, 80, 19 (2016); <https://doi.org/10.1016/j.physe.2016.01.002>.
- [69] I.F. Myronyuk, V.O. Kotsyubynsky, T.V. Dmytrotso, L.M. Soltys, V.M. Gun'ko, *Atomic Structure and Morphology of Fumed Silica*, *Phys. Chem. Solid State*, 21(2), 325 (2020); <https://doi.org/10.15330/pcss.21.2.325-331>.
- [70] X. Chen, Y. Qin, Q. Jia, Q. Zhang, Y. Zhou, X. Liu, *Synthesis of Blue-Green Photoluminescent β -SiC Nanowires via a Simple Catalyst-Free CVD Technique*, *Mater. Lett.*, 234, 187 (2019); <https://doi.org/10.1016/j.matlet.2018.09.101>.
- [71] N. Murakawa, M. Eguchi, K. Tatsumi, *Synthesis of SiC Coating from SiO by a Chemical Vapor Deposition (CVD) Process*, *Journal of the Ceramic Society of Japan*, 125(3), 85 (2017); <https://doi.org/10.2109/jcersj2.16203>.

Л.М. Солтис¹, І.Ф. Миронюк¹, І.М. Микитин¹, І.Д. Гнилиця², Л.В. Туровська³

Синтез та властивості силіцій карбїду (огляд)

¹Прикарпатський національний університет імені Василя Стефаника, Івано-Франківськ, Україна, soltys86@gmail.com

²Івано-Франківський національний технічний університет нафти і газу, Івано-Франківськ, Україна

³Івано-Франківський національний медичний університет, Івано-Франківськ, Україна

Силіцій карбїд надзвичайно твердий матеріал, який проявляє виняткову корозійну стійкість, а також стійкість до теплових ударів. Його високі механічні характеристики визначають підвищену роботоздатність матеріалів на його основі. Поєднання великої теплопровідності та низького коефіцієнта термічного розширення зумовлюють стійкість силіцій карбїду при великих швидкостях нагріву та в умовах стаціонарного теплового режиму. На сьогодні існує значний прогрес у розвитку методів синтезу різноманітних матеріалів на основі силіцій карбїду. Основними методами синтезу, які використовують науковці у своїх дослідженнях, є золь-гель метод, спікання, піроліз, мікрохвильовий синтез, хімічне осадження з парової фази тощо. Широкої популярності набуло використання «зелених» методик у синтезі SiC, через екологічність, відновлюваність та простоту виконання. У даному огляді зроблено аналіз сучасних досліджень у галузі синтезу силіцій карбїду, які опубліковані у рецензованих фахових виданнях.

Ключові слова: силіцій карбїд, політип, «зелений» синтез, керамічні наноматеріали.

M.Ya. Rudysh^{1,2,3}, O.V. Smitiukh¹, G.L. Myronchuk¹, S.M. Ponedelnyk¹, O.V. Marchuk¹

Band Structure Calculation and Optical Properties of Ag_3AsS_3 Crystals

¹Lesya Ukrainka Volyn National University, Lutsk, Ukraine, myronchuk.halyna@vnu.edu.ua

²J. Dlugosz University in Częstochowa, Częstochowa, Poland

³Ivan Franko National University of Lviv, Lviv, Ukraine

In the study, band structure calculation in the points of high symmetry of the first Brillouin zone and alongside the lines that connect them has been derived by using CASTEP programs in which the pseudopotential method with the basis in the form of plane-waves is realized. The calculated value of the lattice parameters using GGA functional is well correlated with experimental data. According to the band diagram that was built for the Ag_3AsS_3 crystal using GGA method, band gap has an indirect type. The calculated value of the band gap is $E_g = 1.22$ eV. The experimental value of the band gap obtained by Tauc's method is $E_g^{ind} = 2.01$ eV, $E_g^{dir} = 2.17$ eV. Full and partial density of $N(E)$ states for contributions of separate atoms has been calculated. As a result, the top of the valence band is formed by $3p$ -states of S atoms and the bottom of the conduction band is formed by $5s$ -states of Ag atoms and $3p$ -states of S atoms.

Keywords: Ag_3AsS_3 , band structure, density functional theory, optical spectrum.

Received 14 September 2022; Accepted 16 February 2023.

Introduction

The Ag_3AsS_3 (proustite) crystals are interesting due to their physical properties and potential of technical application [1–5]. They have been investigated as prospective materials for electronics because they are piezoelectrics, pyroelectrics, as well as thermal and photosensitive semiconductors. The Ag_3AsS_3 crystal is characterized by a dark conductivity of hole mechanism and high resistivity [6–9]. According to the requirements that are for non-linear optical materials in IR region, Ag_3AsS_3 is an acentric single crystal with large non-linear-optical coefficients $d_{31} = 10.4$ pm/V, that is approximately 1.1 times larger than a commercially used AGS ($d_{31} = 30$ times d_{36} in KDP, $d_{22} = 50$ times d_{36} in KDP), high refractive index (~ 3.0), large negative birefringence in the IR region of the spectrum and high transparency in a wide range (0.6–13 μm except a strong absorption band at 1600 cm^{-1}) [3–5].

In order to understand all processes and phenomena better, we need to have more information at crystal

structure of materials and their change under the influence of external fields. The considerable importance has data about electronic band structure with which certain properties can be associated. This study is devoted to the band structure calculation of the Ag_3AsS_3 crystals by *ab initio* methods.

I. Calculation method

The calculations have been carried out by using Cambridge Serial Total Energy Package (CASTEP) program [10] based on the density functional theory (DFT) [11]. The program implements the pseudopotential method with a basis in the form of plane-waves. All electrons of atoms were divided to the two groups: valence electrons (determine the main properties) and core electrons (inert). Ag $4d^{10} 5s^1$, S $3s^2 3p^4$, As $4s^2 4p^3$ electronic configurations have been used as valence electrons. The core electrons together with nuclear charge were counted in pseudopotential. The ultrasoft Vanderbilt

pseudopotential [12] was used in the calculations which, in comparison with the norm-conserving pseudo potential, require a smaller number of plane-waves (smaller basis). The exchange–correlation interaction was considered as a generalized gradient approximation (GGA) in the form of Perdew–Burke–Ernzerhoff (PBE) parametrization [13]. The cut-off energy of plane waves was chosen to be equal to 350 eV. Integration was carried out on a $3 \times 3 \times 3$ k-mesh chosen according to the Monkhorst–Pack scheme [14]. The Kohn–Sham equation was solved self-consistently. This procedure was carried out until the energy difference of the system in successive steps reached a value of 24×10^{-7} eV. For optimization of the crystal structure Broyden–Fletcher–Goldfarb–Shanno (BFGS) algorithm was used [15]. The structure was optimized until the forces acting on each ion were greater than 0.02 eV/Å and the total energy of the system coincided with an accuracy of 5×10^{-6} eV/atom, the maximum pressure was 0.02 GPa, and the maximum ion displacement was 5.0×10^{-4} Å.

Band structure calculations were performed for the high-symmetry points of the first Brillouin zone and along the lines connecting them. For the Ag_3AsS_3 crystal, the band structure calculations have been performed along the Brillouin zone in the direction $\Gamma \rightarrow \text{A} \rightarrow \text{H} \rightarrow \text{K} \rightarrow \Gamma \rightarrow \text{M} \rightarrow \text{L} \rightarrow \text{H}$.

II. Results and discussion

2.1. Crystal structure

The unit cell of the pure Ag_3AsS_3 crystal consists of 42 ions that are formed by three types of atoms. The crystal belongs to the trigonal symmetry (hexagonal scalenohedral $-3m$ crystal class) and has a space group C_{3v}^6 (space group No.161) [16].

The structural parameters of investigating compound are presented in Table 1 and 2. As can be seen from Table 1, calculated (by using GGA functional method) and measured values [16] for the lattice parameters correlate well. The general view of the unit cell is presented in Fig. 1.

2.2. Electronic band structure of the Ag_3AsS_3 crystal

Band structure calculation that determines certain properties of material have been carried out by using the GGA method. Band diagram $E(k)$ was built along the directions that connect the special points of the first Brillouin zone ($\Gamma \rightarrow \text{A} \rightarrow \text{H} \rightarrow \text{K} \rightarrow \Gamma \rightarrow \text{M} \rightarrow \text{L} \rightarrow \text{H}$). The view of the first Brillouin zone of the investigating crystal is presented in Fig. 2.

Band diagram that was built for the Ag_3AsS_3 crystal is presented in Fig. 3 (a). As can be seen in Fig. 3 (a), the Ag_3AsS_3 crystal has an indirect band gap.

The top of the valence band is located in the center of Brillouin zone (point $\Gamma(0; 0; 0)$). The bottom of the conduction band is formed by two broad sub bands (0 – 6 eV and 1.2 – 8 eV). The lower levels of the valence band formed by narrow sub bands nearby 10, 13 and 14.5 eV. Previously the electronic band structure of the Ag_3AsS_3 crystal had been calculated within the tight-binding method with the correction with experimental data [17]. The general view of $E(k)$ in the work [17] depicts peculiarities of the band diagram that we calculated using

DFT. The calculated value of the band gap using GGA method is $E_g = 1.22$ eV. At the same time, the experimental value of the band gap calculated by Tauc’s method (Fig.4) is $E_g^{ind} = 2.01$ eV and $E_g^{dir} = 2.17$ eV. These results are consistent with the works [1, 18].

Table 1.

The experimental structure parameters of the Ag_3AsS_3 crystal and theoretically calculated ones (optimized with GGA functional).

Parameter	GGA	Exp.[16]
$a = b(\text{Å})$	10.783	10.813
$c(\text{Å})$	9.456	8.691
$\alpha(^{\circ})$	90	90
$\beta(^{\circ})$	90	90
$\gamma(^{\circ})$	120	120
$V(\text{Å}^3)$	952.297	880.199

Table 2.

Fractional atomic coordinates of the Ag_3AsS_3 crystal given in the work [16].

Atom	Site	x/a	y/b	z/c
Ag	18b	0.2483	0.2980	0.2194
As	6a	0	0	0
S	18b	0.2129	0.0926	0.3743

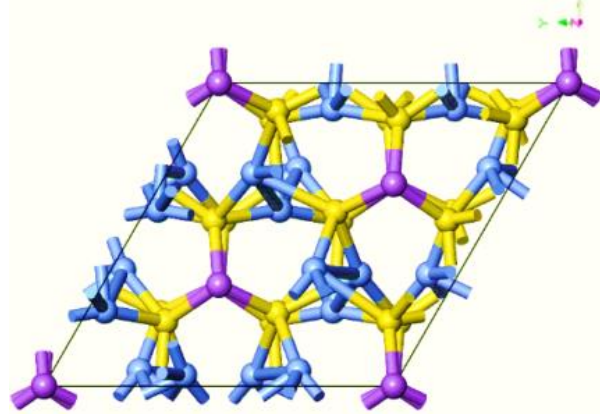


Fig.1. The projection of the unit cell of the Ag_3AsS_3 crystal on the xy plane.

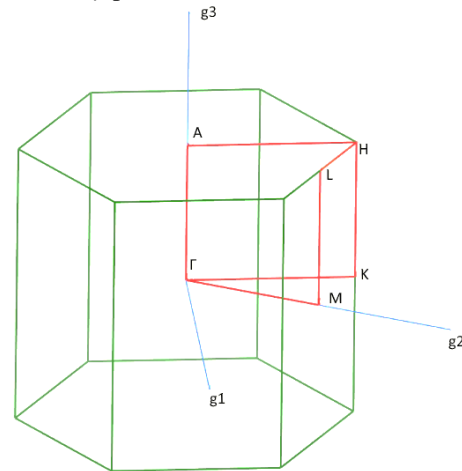


Fig.2. The view of the first Brillouin zone of the Ag_3AsS_3 investigating crystal: $\Gamma(0;0;0)$; $\text{A}(0;0;1/2)$; $\text{H}(-0.333; 0.667; 0)$; $\text{K}(-0.333; 0.667; 0)$; $\text{L}(0; 1/2; 1/2)$; $\text{H}(-0.333; 0.667; 1/2)$ – points of high symmetry, g_1 , g_2 , and g_3 – directions of axes in the reciprocal lattice.

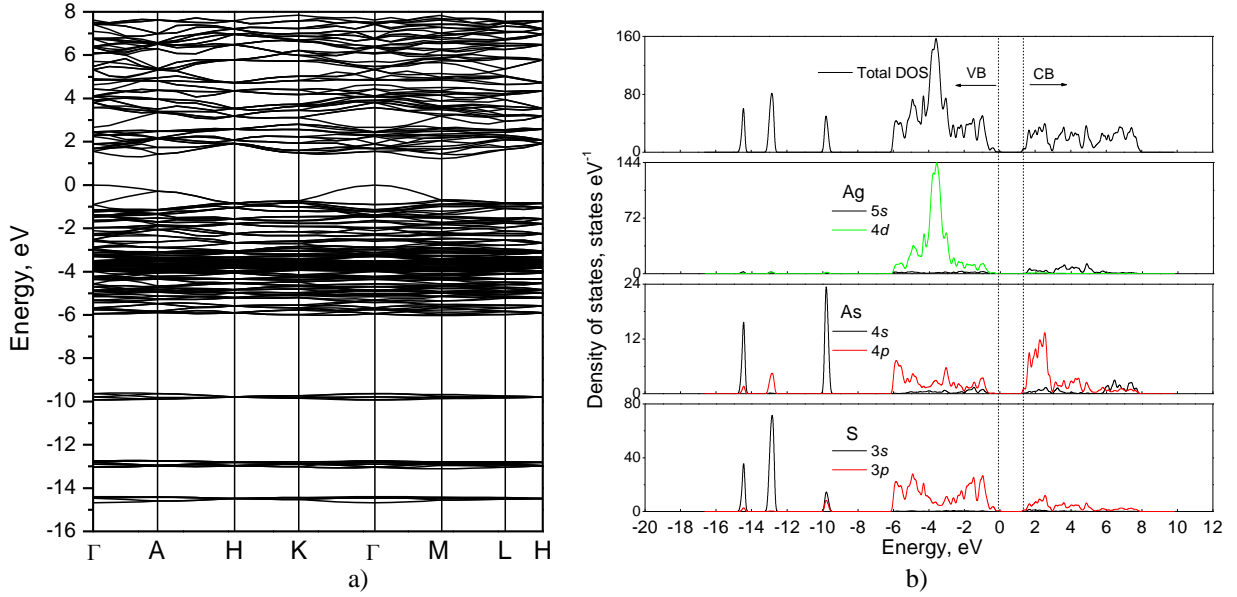


Fig.3. The electronic structure (a) and density of states (b) of the Ag_3AsS_3 crystal obtained with using GGA functional.

For detailed study of origin of energy levels, we calculated total and partial density of states (PDOS) $N(E)$ for contributions of individual atoms (Fig.3(b)). As can be seen in Fig.3(b), the top of the valence band is formed by 3-*p*-states of S atoms. They together with 4*p*-states of As atoms form the broad band from 0 to -6 eV. The intensive peak around -5 eV corresponds to 4*d*-states. The valence states around -10 eV are formed by core As 4*s*-electrons. At energy -13 eV the localized level is formed by 3*s*-states of sulfur with a minor contribution of As 4*p*-electrons. At energy -14.5 eV the narrow peak is formed by 3*s* and 4*s*-states of As and S, respectively. The bottom of conduction band is formed by 5*s*-states of Ag and 3*p*-states of S. It worth noting that the origin of electronic levels that create a band gap is correlated to the results obtained in the work [17].

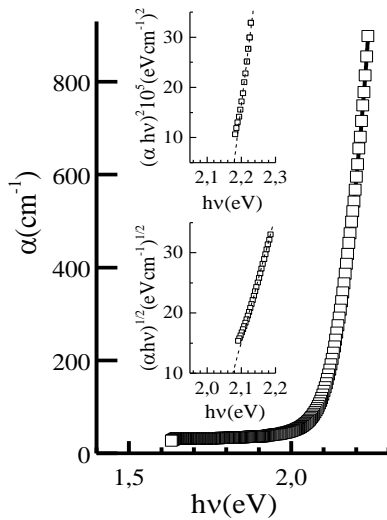


Fig. 4. Spectral dependence of the absorption coefficient of Ag_3AsS_3 .

2.3. Optical properties

The results of band structure calculation may be used for an analysis of optical properties of materials. It is well-

known that optical properties of materials are determined with dielectric function ϵ that depends on frequency $\epsilon(\omega)$ (energy). The function is complex and consist of real $\epsilon_1(\omega)$ and imaginary $\epsilon_2(\omega)$ parts. For the Ag_3AsS_3 crystal optical properties are obtained from the frequency dependence of the complex dielectric function $\epsilon(\omega) = \epsilon_1(\omega) + i\epsilon_2(\omega)$, where $i = \sqrt{-1}$. It is also known that the real part of dielectric function explains refractive properties and is related to the refractive index. The imaginary part $\epsilon_2(\omega)$ explains processes of light absorption in the material and associated with transitions of electrons to higher energy levels during light absorption [19]. The frequency dependence of the imaginary part of the dielectric function $\epsilon_2(\omega)$ is calculated using equation (1) by integrating in *k*-space the elements of the dipole matrix operator between the filled states in the valence band and the empty states of the conducting band levels

$$\epsilon_2(\omega) = \frac{2\pi e^2}{\Omega \epsilon_0} \sum_{k,v,c} |\langle \psi_k^c | u \mathbf{r} | \psi_k^v \rangle|^2 \delta(E_k^c - E_k^v - E), \quad (1)$$

where E is energy; u the vector of polarization of incident beam; ψ_k^c and ψ_k^v are a wave functions of the conduction band and valence band in *k*-space, respectively; Ω is volume of a unit cell; e is the electron charge; ϵ_0 the dielectric constant for vacuum; \mathbf{r} is electron position operator.

The real $\epsilon_1(\omega)$ can be obtained from an imaginary dielectric function. For this, the well-known Kamers-Kronig relation is used. The relation connects the spectral dependence of the real and imaginary parts of the dielectric function [20]:

$$\epsilon_1(\omega) = 1 + \frac{2}{\pi} \int_0^\infty \frac{\epsilon_2(\omega') \omega' d\omega'}{\omega'^2 - \omega^2}. \quad (2)$$

The spectrum of the real $\epsilon_1(\omega)$ and imaginary $\epsilon_2(\omega)$ parts was calculated using GGA functional. The frequency dependence of ϵ_1 and ϵ_2 calculated for the light wave polarization directions $E \parallel Z$ and $E \perp Z$ are shown in Fig.5. As shown in figure, the dielectric function is characterized

by significant anisotropy, which is determined by the difference in the positions of the bands and their intensities. Also, for the comparison of dielectric function Fig.5 contain its experimentally obtained real and imaginary part reported in [17]. The theoretical dielectric functions are consistent with the experimental. Insignificant deviations can be related to not taking into account indirect transitions. According to group theoretical analysis performed within the dipole approximation [21] the allowed inter band transitions in the center of first Brillouin zone between electronic states (without spin consideration) are following: $\Gamma_1 \rightarrow \Gamma_3$, $\Gamma_3 \rightarrow \Gamma_1$, $\Gamma_2 \rightarrow \Gamma_3$, $\Gamma_3 \rightarrow \Gamma_2$ for $E \perp Z$, and $\Gamma_1 \rightarrow \Gamma_1$, $\Gamma_2 \rightarrow \Gamma_2$, $\Gamma_3 \rightarrow \Gamma_3$ for $E \parallel Z$. As expected, the dielectric function for $E \perp Z$ polarization of light the is more instance than for $E \parallel Z$ polarization. This is confirmed by the larger amount of allowed transitions in Γ point.

From spectral dependence of real and imaginary parts of dielectric functions we can obtain other optical properties also, for instance, a refractive index $n(\omega)$, the coefficient of extinction $k(\omega)$ which are related to each other as follows $N = n + ik$.

In the work, n and k are calculated using following formulas [22]:

$$n = \sqrt{\frac{(\varepsilon_1^2 + \varepsilon_2^2)^{1/2} + \varepsilon_1}{2}}, \quad k = \sqrt{\frac{(\varepsilon_1^2 + \varepsilon_2^2)^{1/2} - \varepsilon_1}{2}}. \quad (3)$$

Frequency dependence of refractive index n_i and the extinction coefficient k_i of the Ag_3AsS_3 crystal is presented in Fig.6.

Other parameter that is related to the dielectric function is the absorption coefficient of material α . It is obtained from expression:

$$\alpha = \frac{2k\omega}{c}, \quad (4)$$

and it indicates the part of lost energy loss due to the passage of the wave through the material.

It can be seen from the figure that the calculated dependence of the absorption coefficient of the crystal is characterized by an increase in α with increasing photon energy, reaching a maximum at an energy of approximately 8.5 eV, followed by a rapid decrease. Also, it is worth noting that the studied crystal has a large value of the absorption coefficient α , which lies within the range of $1-3 \times 10^5 \text{ cm}^{-1}$. A similar high value was previously obtained for other crystals of group I-III-VI₂, which is also of the order of 10^5 cm^{-1} [23,24].

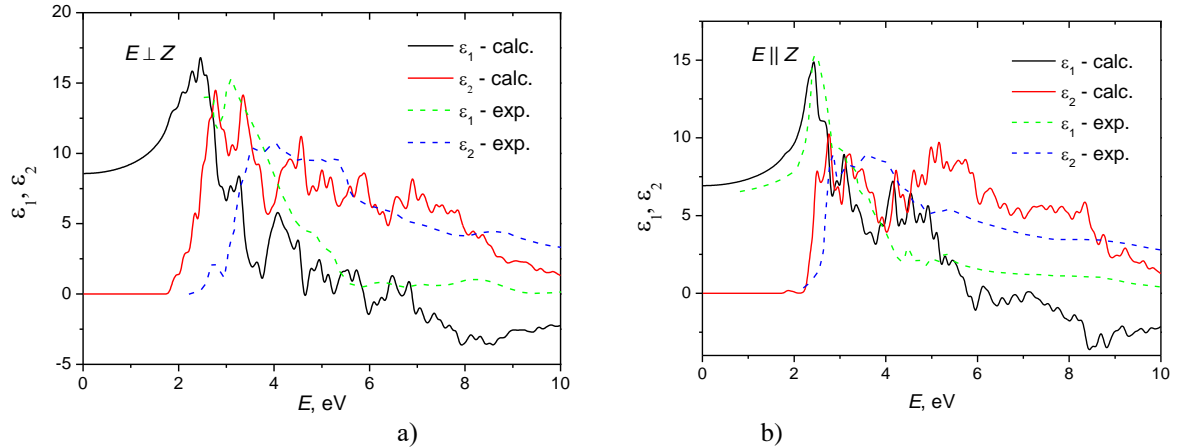


Fig.5. The spectral dependence of the real and imaginary parts of the dielectric function are calculated using the GGA functional for the directions of light polarization (a) $E \perp Z$ and (b) $E \parallel Z$ (experimental data taken from work [16]).

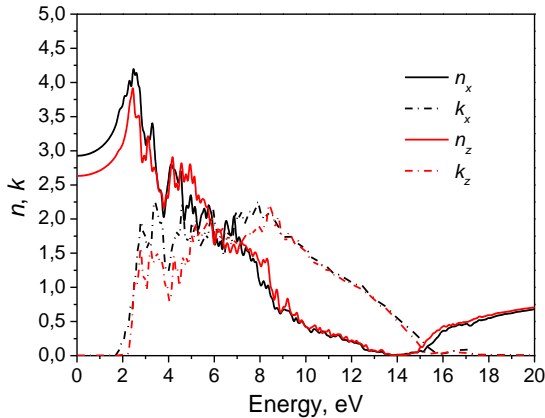


Fig.6. Spectral dependence of the refractive index n and the extinction coefficient k of the Ag_3AsS_3 crystal calculated using the GGA functional.

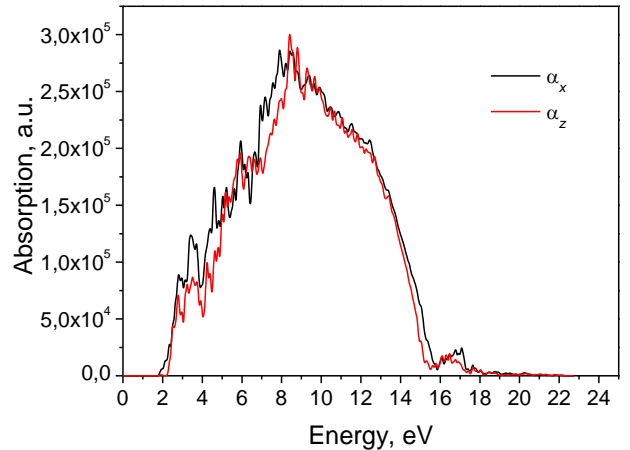


Fig.7. Spectral dependence of absorption coefficient α of the Ag_3AsS_3 crystal for directions $E \perp Z$ and $E \parallel Z$ calculated using the GGA functional.

Conclusions

In the study, the band structure calculation in the points of high symmetry of the first Brillouin zone and along the lines connecting them have been prepared using CASTEP program based on pseudo potential method with basis in the form of plane waves. The calculated and measured parameters of the lattice are correlated well. According to the band structure of the Ag₃AsS₃ crystal that was built using GGA functional method, the band gap is indirect. The calculated value of band gap is $E_g = 1.22$ eV. The experimental value of band gap estimated by Tauc's method is $E_g^{ind} = 2.01$ eV and $E_g^{dir} = 2.17$ eV, respectively. The full and partial density of states $N(E)$ for contributions of individual atoms have been calculated. As a result, the top of the valence band formed by 3p-states of S and the bottom of the conduction band formed by 5s-states of silver and 3p-states of sulfur. A spectral dependences of the optical function has been calculated. Shown a good agreement with the experimental data.

Acknowledgments

This work was supported by the PRELUDIUM 15 program of Polish National Science Center (Grant No. 2018/29/N/ST3/02901).

Rudysh M.Ya. – Candidate of Physical and Mathematical Sciences, senior researcher of the Department of General Physics of Ivan Franko Lviv National University;
Smitiukh O.V. – candidate of chemical sciences, senior laboratory technician of the Department of Chemistry and Technologies, Faculty of Chemistry, Ecology and Pharmacy of Lesya Ukrainka Volyn National University;
Myronchuk G.L. – doctor of physical and mathematical sciences, professor, director of the educational-scientific physical-technological institute of Volyn National University named after Lesya Ukrainka;
Ponedelnyk S.M. – graduate student of Volyn National University named after Lesya Ukrainka;
Marchuk O.V. – candidate of chemical sciences, docent of the Department of Chemistry and Technologies, Faculty of Chemistry, Ecology and Pharmacy of Lesya Ukrainka Volyn National University.

- [1] V.V. Zalamai, A.V. Tiron, I.G. Stamov, S.I. Beril, *Wavelength modulation optical spectra of Ag₃AsS₃ crystals in the energy gap*, *Optical Materials*, 129, 112560 (2022); <https://doi.org/10.1016/j.optmat.2022.112560>.
- [2] H. Lin, W.B. Wei, H. Chen, X.T. Wu, Q.L. Zhu, *Rational design of infrared nonlinear optical chalcogenides by chemical substitution*, *Coord. Chem. Rev.* 406, 213150 (2020); <https://doi.org/10.1016/j.ccr.2019.213150>.
- [3] Kui Wu, Shilie Pa., *A review on structure-performance relationship toward the optimal design of infrared nonlinear optical materials with balanced performances*, *Coord. Chem. Rev.* 377, 191 (2018); <https://doi.org/10.1016/j.ccr.2018.09.002>.
- [4] Fei Liang, Lei Kang, Zheshuai Lin, and Yicheng Wu, *Mid-Infrared Nonlinear Optical Materials Based on Metal Chalcogenides: Structure-Property Relationship Cryst.*, *Growth Des.*, 17(4), 2254 (2017); <https://doi.org/10.1021/acs.cgd.7b00214>.
- [5] A. Abudurusuli, J. Li, S. Pan, *A review on the recently developed promising infrared nonlinear optical materials*, *Dalt. Trans.* 50, 3155 (2021); <https://doi.org/10.1039/D1DT00054C>.
- [6] V. Kavaliukė, T. Šalkus, A. Kežionis, M.M. Pop, I.P. Studenyak, *Ag₃AsS₃-As₂S₃ composite: Detailed impedance spectroscopy study*, *Solid State Ionics*, 383, 115971 (2022); <https://doi.org/10.1016/j.ssi.2022.115971>.
- [7] V. S. Bilanych, R. Yu. Buchuk, K. V. Skubenyh, I. I. Makauz, I. P. Studeniak, *Relaxation Processes in Silver Containing Superionic Composites in the System Ag₃AsS₃-As₂S₃*, *Physics and Chemistry of Solid State*, 13 (3), 625 (2012). Rezhym dostupu: http://nbuv.gov.ua/UJRN/PhKhTT_2012_13_3_12. (In Ukrainian)
- [8] V. A. Bordovsky, N. Yu. Gunia, R. A. Castro, *High-frequency dielectric study of proustite crystals Ag₃AsS₃*, *Journal of Physics: Conference Series*, 572, 012019 (2014); <https://doi.org/10.1088/1742-6596/572/1/012019>.
- [9] O.V. Smitiukh, O.V. Marchuk, Y.M. Kogut, V.O. Yuhymchuk, N.V. Mazur, G.L. Myronchuk, S.M. Ponedelnyk, O.I. Cherniushok, T.O. Parashchuk, O.Y. Khyzhun, K.T. Wojciechowski, A.O. Fedorchuk, *Effect of rare-earth doping on the structural and optical properties of the Ag₃AsS₃ crystals*, *Optical and Quantum Electronics*, 54:4, 224 (2022); <https://doi.org/10.1007/s11082-022-03542-w>.
- [10] S.J. Clark, M.D. Segall, C.J. Pickard, P.J. Hasnip, M.J. Probert, K. Refson, M.C. Payne, *First principles methods using CASTEP*, *Z. Kristallogr.* 220, 567 (2005); <https://doi.org/10.1524/zkri.220.5.567.65075>.
- [11] P. Hohenberg, W. Kohn, *Inhomogeneous Electron Gas*, *Phys. Rev.* 136, B864 (1964); <https://doi.org/10.1103/PhysRev.136.B864>.
- [12] D. Vanderbilt, *Soft self-consistent pseudopotentials in a generalized eigenvalue formalism*, *Phys. Rev. B.* 41, 7892 (1990); <https://doi.org/10.1103/PhysRevB.41.7892>.
- [13] J.P. Perdew, A. Zunger, *Self-interaction correction to density-functional approximations for many-electron systems*, *Phys. Rev. B* 23, 5048 (1981); <https://doi.org/10.1103/PhysRevB.23.5048>.
- [14] H.J. Monkhorst and J.D. Pack, *Special points for Brillouin-zone integrations*, *Phys. Rev. B*, 13, 5188 (1976); <https://doi.org/10.1103/PhysRevB.13.5188>.
- [15] B.G. Pfrommer, M. Côté, S.G. Louie, M.L. Cohen, *Relaxation of Crystals with the Quasi-Newton Method*, *Journal of Computational Physics*, 131, 233 (1997); <https://doi.org/10.1006/jcph.1996.5612>.
- [16] A. Gagor, A. Pawłowski, A. Pietraszko, *Silver transfer in proustite Ag₃AsS₃ at high temperatures: Conductivity and single-crystal X-ray studies*, *J. Solid State Chem.* 182(3), 451 (2009); [DOI:10.1016/j.jssc.2008.11.005](https://doi.org/10.1016/j.jssc.2008.11.005).

- [17] Ya.O. Dovgii, I.V. Kityk, *Band Structure and Nonlinear Optical Susceptibilities of Proustite (Ag_3AsS_3)*, Phys. Stat. Sol. (b), 166, 395 (1991); <https://doi.org/10.1002/pssb.2221660208>.
- [18] Marvin J. Weber, *Handbook of optical materials* (CRC Press, 2002).
- [19] Mark Fox, *Optical properties of solids* (Oxford University Press, Oxford (2001)).
- [20] M. Dressel, B. Gompf, D. Faltermeier, A.K. Tripathi, J. Pflaum and M. Schubert, *Kramers-Kronig-consistent optical functions of anisotropic crystals: generalized spectroscopic ellipsometry on pentacene*, Opt.Express 16, 19770- (2008); <https://doi.org/10.1364/OE.16.019770>.
- [21] Ya.O. Dovhyj I.V. Kityk, *The electronic structure and optics of the nonlinear crystals*. 176 p. (Monograph. – Lviv. Svit publisher. 1996).
- [22] Sonali Saha, T.P. Sinha and Abhijiti Mookerjee, *Electronic structure, chemical bonding, and optical properties of paraelectric $BaTiO_3$* , Phys. Rev. B 62, 8828 (2000); <https://doi.org/10.1103/PhysRevB.62.8828>.
- [23] M.Ya. Rudysh, P.A. Shchepanskyi, A.O. Fedorchuk, M.G. Brik, V.Yo. Stadnyk, G.L. Myronchuk, E.A. Kotomin, M. Piasecki, *Impact of anionic system modification on the desired properties for $CuGa(S_{1-x}Se_x)_2$ solid solutions*, Computational Materials Science, 196, 110553 (2021); <https://doi.org/10.1016/j.commatsci.2021.110553>.
- [24] M.Ya. Rudysh, M. Piasecki, G.L. Myronchuk, P.A. Shchepanskyi, V.Yo. Stadnyk, O.R. Onufriv, M.G. Brik, *AgGaTe₂ – The thermoelectric and solar cell material: Structure, electronic, optical, elastic and vibrational features*, Infrared Physics and Technology, 111, 103476 (2020); <https://doi.org/10.1016/j.infrared.2020.103476>.

М.Я. Рудиш^{1,2,3}, О.В.Смітюх¹, Г.Л. Мирончук¹, С.М.Понедельник¹, О.В. Марчук¹

Зонна структура та оптичні властивості кристалів Ag_3AsS_3

¹Волинський національний університет імені Лесі Українки, Луцьк, Україна, myronchuk.halyna@vnu.edu.ua

²Гуманітарно-природничий університет імені Яна Дугоша в Ченстохові, Ченстохова, Польща

³Львівський національний університет імені Івана Франка, Львів, Україна

У роботі проведено розрахунок зонної структури у точках високої симетрії першої зони Бріллюена і вздовж ліній, що їх з'єднують за допомогою програми CASTEP в якій реалізований псевдо потенціальний метод з базисом у вигляді плоских хвиль. Розраховані значення параметрів ґратки з використанням GGA функціоналів добре узгоджуються з експериментальними даними. Згідно зонної діаграми, побудованої використовуючи GGA метод для кристала Ag_3AsS_3 , заборонена зона є непрямого типу. Розраховане нами значення ширини забороненої зони становить $E_g = 1,22$ еВ. Експериментальне значення ширини забороненої зони оціненої методом Тауца становить $E_g^{ind} = 2,01$ еВ, $E_g^{dir} = 2,17$ еВ.

Розраховано повну та парціальну густини станів $N(E)$ для внесків окремих атомів встановлено, що вершина валентної зони утворена 3p-станами сірки, а дно зони провідності утворене 5s-станами срібла та 3p-станами сірки.

Ключові слова: Ag_3AsS_3 , зонна структура, теорія функціонала густини, оптичні спектри.

N.N. Gadzhieva¹, G.B. Ahmadova², S.Z. Melikova¹, F.G. Asadov¹

X-ray diffractometric study of HDPE/GaAs and HDPE/GaAs<Te> composites

¹*Institute of Radiation Problems of Ministry of Science and Education Republic of Azerbaijan, Baku, Azerbaijan;*

²*Institute of Physics of of Ministry of Science and Education Republic of Azerbaijan, Baku, Azerbaijan
esevincmelikova9513@gmail.com*

High-density polyethylene sheets (HDPE), HDPE/GaAs and HDPE/ GaAs<Te> composites with GaAs and GaAs<Te> semiconductor fillers were studied by X-ray diffractometry at room temperature. The degree of crystallization of these samples was calculated and it was determined that the inclusion of fillers in the polymer matrix (x=1-10% composite) leads to an increase in the degree of crystallization by 1.3-1.4 times. The obtained results are explained by the change of the upper molecular structure of the polymer.

Keywords: high density polyethylene, GaAs, GaAs<Te>, composites, X-ray diffractometry method.

Received 16 November 2022; Accepted 27 January 2023.

Introduction

It is known that the introduction of new fillers leads to the expansion of the possibility of using composite materials. From this point of view, polymer-semiconductor filler polymer composite materials are of special interest [1-3]. The introduction of semiconductor fillers into the polymer matrix leads to changes in its structure and properties. From this aspect, composites based on high-density polyethylene HDPE/GaAs and HDPE/GaAs<Te> semiconductor fillers are important [4,5]. Using these materials as modifying additives for polymers can lead to the production of new composites with different properties. X-ray diffraction (XRD) analysis is the most reliable experimental method for obtaining information about the structure and dynamics of the crystal lattice of solid bodies. It gives a three-dimensional image of macromolecules, which is necessary for understanding the features of structure formation in polymer composites. An important technological application of XRD analysis is the measurement of the degree of crystallinity in polymer composites. This method is considered an ideal analytical method for studying any type of sample. The reviewed article presents the results of X-ray diffractometric analysis of

HDPE/GaAs and HDPE/GaAs<Te> composites.

I. Experimental part

The diffractograms of the primary HDPE, HDPE/xwt.% GaAs and YSPE/x wt.% GaAS<Te> (x=1-10% composite) layers were obtained on a D2 Phaser (Bruker company, Germany) x-ray diffractometer. CuK α source and Ni filters were used during the experiment. The values of the degree of crystallization in the studied samples were calculated by the program. This method allows to monitor structural changes caused by the introduction of microparticles into the composition of the polymer matrix [6].

II. Discussion of results

The diffractogram of the initial HDPE (1) layer is given in figure 1 (a). As can be seen from Figure 1(a), the initial HDPE layers are characterized by a set of reflections: $2\theta=220$ and 240 . The given lines are characteristic lines for HDPE polymer.

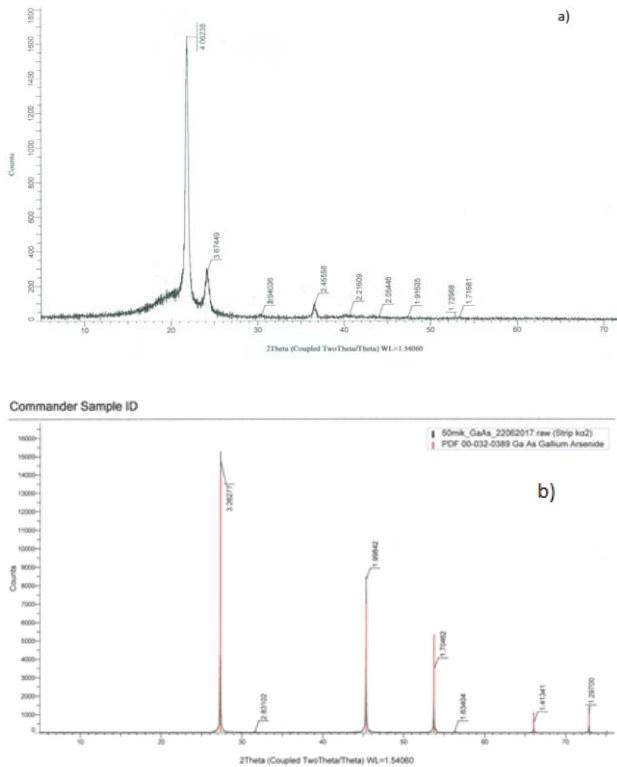


Fig. 1. Diffractograms of HDPE (a) and GaAs (b) samples.

Incorporating 2 wt.% GaAs microparticles into the matrix results in stronger 270 and 450 as well as weaker lines compared to the new 53.50 and 72.50. The observed new lines belong to GaAs (Fig. 1b). When GaAs alloyed with 2 wt.% tellurium is included in the matrix, the same diffraction lines (reflexes) are observed in the diffractogram, they are distributed as in HDPE/GaAs. When the concentration of microparticles included in the composition of the polymer matrix is increased from 2 wt.% to 6 wt.%, the diffraction lines shift (Fig. 2 and 3). The strongest lines are considered to be: $2\theta=27$; 45 and 53.50.

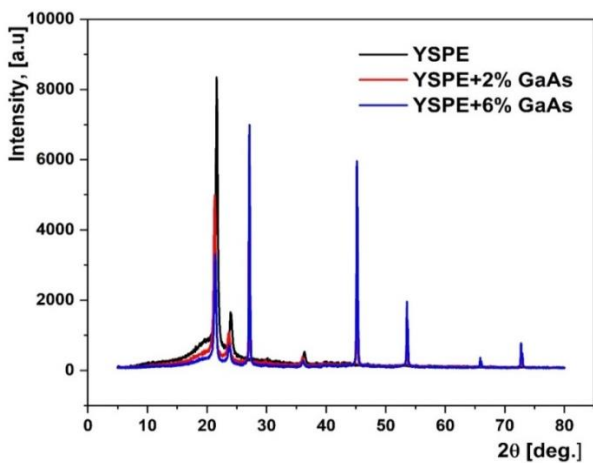


Fig. 2. Comparative diffractograms of HDPE polymer matrix, HDPE/2wt%GaAs and HDPE/6wt%GaAs composites.

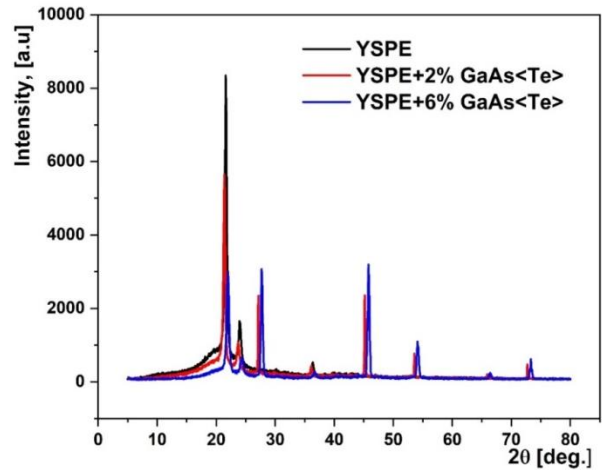


Fig. 3. Comparative diffractograms of HDPE polymer matrix, HDPE/2wt%GaAs<Te> and HDPE/6wt%GaAs<Te> composites.

At this time, a noticeable change in the intensities of the lines of the crystalline phase of HDPE is observed. Based on the data, the degrees of crystallization of the primary HDPE layer, HDPE/GaAs and HDPE/GaAs<Te> composite layers were calculated using a known program. At this time, it was determined that with increasing concentration, the degree of crystallization of HDPE/GaAs composite materials increased by 1.3 times (from 54 to 71.4%) compared to the initial sample, and in HDPE/GaAs<Te> composites by ~1.4 times (from 54 to 73.9%) increases (table).

Table 1.
Crystallization degree values of HDPE, HDPE/wt.%GaAs and HDPE/wt.%GaAs<Te> composites

№	Sample	Crystallization degree,%
1	HDPE	54
2	HDPE/2wt.%GaAs	68,7
3	HDPE/6wt.%GaAs	71,4
4	HDPE/2wt.%GaAs<Te>	70,2
5	HDPE/6wt.%GaAs<Te>	73,9

The observed increase in the degree of crystallization is due to the possibility of a decrease in the size of the crystallites and an increase in their dispersion. The obtained experimental results are in good agreement with the results of Fourier-IR spectroscopic studies [7, 8].

Thus, on the basis of comparative X-ray diffractometric analysis, it was determined that the degree of crystallization of composite layers increases by x=12-16% compared to the degree of crystallization of primary layers. The observed effects are related to the change of the molecular structure and degree of crystallization (K) of the polymer, so that GaAs and GaAs<Te> fillers with a dispersion of 50 μm increase the degree of crystallization in polyethylene composites (these microparticles play a central role in crystallization) and the molecular structure of the polymer. it plays the role of creating a structure in its change. The increase in the degree of crystallization can occur due to the formation of the third transition phase [7].

According to X-ray results, AB (aligned bonds) have a three-dimensional structure with a periodicity of $\lambda=50-60$ nm [4]. AB is an integral part of highly oriented PE. For HDPE fibers, the quantity λ corresponds to the length of the trans-sequences in the crystalline region of the lamellae. Apparently, the concentration of 2-6 wt.% of GaAs microparticles and 2-8 wt.% of GaAs<Te> microparticles in HDPE leads to an increase in the amount of AB in the transitional crystalline layer of HDPE. This is due to the fact that at these concentrations GaAs and GaAs<Te> microparticles act as centers of additional crystallization. When the concentration of microparticles of fillers in HDPE increases, the sizes of clusters become larger than the values of periodicity.

Conclusion

Pure HDPE, GaAs, GaAs<Te>, HDPE/GaAs and HDPE/ GaAs<Te> composites with semiconductor filler were studied by diffractometry method. Crystallization degrees of these samples were calculated. It was determined that the inclusion of fillers in the polymer matrix leads to an increase in the degree of crystallization. This increase is related to the change of the upper molecular structure of the polymer.

Gadzhieva N.N. – Dr.S., Assoc. Professor;
Ahmadova G.B. – Ph.D. Doctoral student;
Melikova S.Z. – Ph.D in Physics, Assoc.Professor;
Asadov F.G. – Ph.D in Physics.

- [1] O.E.Gouda, A.S.Haiba, *Measurements of dielectrics of High Density Polyethylene-Nanocomposites*, Measurement, 134, p.624 (2019); <https://doi.org/10.1016/j.measurement.2018.10.029>.
- [2] R.Hsissou, R.Seghiri, Z.Benzekri, *Polymer composite materials: A comprehensive review*, Composite Structures, 262, 113640 (2021); <https://doi.org/10.1016/j.compstruct.2021.113640>.
- [3] Q.E.Efendiyev, N.N. Gadzhieva, T.M. İlyaslı, R.F.Abbasova, F.F.Yaxyaev, *Structure of Polyethylene Films Containing Copper Nanoparticles*, Journal of Applied Spectroscopy, 73(3), 462 (2006); <https://doi.org/10.1007/s10812-006-0101-5>.
- [4] A.M. Magerramov, Structural and radiation modified electret, piezoelectric properties of polymer composites. Baku, "Elm", 323 (2001).
- [5] E.M.Godzhaev, A.M.Magerramov, S.S.Osmanova, M.A.Nuriev, E.A.Allakhyarov, *Charge state of compositions based on polyethylene with semiconductor filler TeInSe*, Electronic processing of materials, 2, 84 (2007).
- [6] Zhiyong Wei, Ping Song, *Chapter 14 - Crystallization Behavior of Semicrystalline Polymers in the Presence of Nucleation Agent*, Crystallization in Multiphase Polymer Systems, 433 (2018); <https://doi.org/10.1016/B978-0-12-809453-2.00014-1>.
- [7] M.I.Aliev, N.N. Gadzhieva, G.B.Ahmadova, *Fourier-IR study of the high-density polyethylene composites with semiconductor fillers GaAs and GaAs<Te>*, International Journal of Composite Materials, 1), 1 (2014); <https://doi.org/10.5923/j.cmaterials.20140401.01>.
- [8] M.I.Aliyev, N.N.Gadzhieva, G.B.Akhmedova, *Optical absorption spectra of high-density polyethylene composite films with semiconductor fillers GaAs and GaAs<Te>*, Transactions of Azerbaijan National Academy of Sciences (physics and astronomy), 34(2), 43 (2014).

Н.Н. Гаджієва¹, Г.Б. Ахмадова², С.З.Мелікова¹, Ф.Г. Асадов¹

Рентгенівське дифрактометричне дослідження композитів HDPE/GaAs та HDPE/GaAs<Te>

¹Інститут радіаційних проблем Міністерства науки і освіти Азербайджанської Республіки, Баку, Азербайджан

²Інститут фізики Міністерства науки і освіти Азербайджанської Республіки, Баку, Азербайджан,
esevincmelikova9513@gmail.com

Листи поліетилену високої щільності (HDPE), композити HDPE/GaAs і HDPE/ GaAs<Te> з напівпровідниковими наповнювачами GaAs і GaAs<Te> досліджували методом рентгенівської дифрактометрії при кімнатній температурі. Розраховано ступінь кристалізації цих зразків і встановлено, що включення до полімерної матриці наповнювачів (x=1-10% складу) призводить до збільшення ступеня кристалізації в 1,3-1,4 рази. Отримані результати пояснюються зміною високої молекулярної структури полімеру.

Ключові слова: поліетилен високої щільності, GaAs, GaAs<Te>, композити, метод рентгенівської дифрактометрії.

Muhsin J. Jweeg¹, Emad K. Njim², Orhan S. Abdullah³, Mohsin A. Al-Shammari⁴,
Muhannad Al-Waily⁵, Sadeq H. Bakhy³

Free Vibration Analysis of Composite Cylindrical Shell Reinforced with Silicon Nano-Particles: Analytical and FEM Approach

¹*Al-Farahidi University, College of Technical Engineering, Iraq*

²*Ministry of Industry and Minerals, State Company for Rubber and Tires Industries, Iraq, emad.njim@gmail.com*

³*Mechanical Engineering Department, University of Technology, Iraq*

⁴*University of Baghdad, College of Engineering, Department of Mechanical Engineering, Iraq*

⁵*Department of Mechanical Engineering, Faculty of Engineering, University of Kufa, Iraq*

Previous research presented the effect of nanomaterials on the mechanical properties of composite materials with various volume fraction effects; in addition, their research presented the effect of nanomaterials on the same mechanical characteristics for a composite plate structure, such as vibration and thermal buckling behavior. Therefore, since the use of shell structures is for large applications, it is necessary to investigate the modification of the vibration characteristics of its design with the effect of nanomaterials and study the influence of other reinforced nanoparticle types on its features. Therefore, in this work, silicon nanoparticles were selected to investigate their effect on the vibration behavior of a shell structure. As a result, this work included studying the vibration behavior by testing the shell structure with a vibration test machine. In addition, after manufacturing the composite material shell with various silicon volume fractions, the mechanical properties were evaluated. In addition, the finite element technique with the Ansys program was used to assess and compare the vibration behavior of the shell structure using the numerical technique. The comparison of the results gave an acceptable percentage error not exceeding 10.93%. Finally, the results evaluated showed that the modification with silicon nanomaterials gave very good results since the nanomaterials improved about 65% of the shell's mechanical properties and vibration characteristics.

Keywords: Shell Vibration, Silica Nano, Silica Shell Vibration, Composite Shell, and Nano Composite.

Received 14 July 2022; accepted 23 January 2023.

Introduction

The composite materials investigation in previous years in different applications was due to the high strength to weight ratio; therefore, this investigation for composite materials being modified for mechanical properties for composite materials by reinforcement with different fibers, and then modified for composite by reinforcement with varying concentrations of powder, [1-3]. Then, the investigated different composite materials structures are as a beam, plate, and other facilities with various applications, such as the vibration of the plate with different parameters, [4-5], buckling for a plate with multiple parameters, [6-8], stress analysis for other

structures, fatigue characterization with different applications, [9], and prosthetic and orthotics structures. Thus, due to the impartment for composite materials and application, then it was necessary to investigate the modification of the composite materials with reinforcement by nanoparticle materials since this modification with the composite materials leads to an increase in the material mechanical properties with a high value and with a low increasing for the weight of the material, [10-11]. Therefore, one application for composite materials was for a shell structure under vibration behavior due to impartment for shell structure. So, different nanomaterials can be used to modify the mechanical properties of materials. Then one of the

impairment materials can be used with silica nanoparticle materials since these materials give high modifications and change the structure's dynamic behavior. Also, due to impairment for shell structure, then, work in this paper is to modify the dynamic behavior of shell structure by reinforcement with silica nanomaterials.

Therefore, many researchers studied the dynamic behavior of shell structure with different techniques and parameters effect, as mentioned below. A. A. Hamzah et al. [12] investigated the effect of thermal load on the dynamic characteristics of a cylindrical structure by using the finite element technique.

In 2019, a semi-analytical method was used by Fuzhen Pang et al. [13] to study the vibration characterization of composite laminated cylindrical and spherical shells. Then, in 2019, Haichao Li et al. [14] investigated free vibration analysis of combined spherical and cylindrical shells with non-uniform thickness based on the Ritz method using a semi-analytical solution. Also, in 2019, Zhaoye Qin et al. [15] studied analytically the dynamic model for vibration analysis of a cylindrical shell structure made of functionally graded materials with arbitrary boundary conditions. The Rayleigh-Ritz method was used, and the vibration response of a cylindrical shell based on geometric parameters, the volume fraction of carbon nanotubes, and boundary conditions were also evaluated. M. Azmi et al. [16] studied the effect of SiO₂ nanomaterials on the dynamic response by using an analytical model. Thus, this investigation included determining the dynamic behavior for the column with various nanomaterials amounts; in addition, this study involved the dynamic analysis for different supported columns. The column's dynamic behavior was calculated under the blast load applied. Xiao Li [17] examined the stability conditions of composite laminated nonlinear cylindrical shells under periodic axial loads and a hygrothermal environment. Using experimental, numerical, and analytical techniques, M. Zarei et al. In [18] investigated the vibrational characteristics of joined stiffened conical-cylindrical composite shells.

Kwanghun Kim et al. [19] analyzed the natural frequencies and mode shapes of the coupled laminated composite elliptical-cylindrical-elliptical shells with elastic boundary conditions using the finite element method (FEM). Finally, Giuseppe Sciascia et al. [20] used a multi-domain Ritz method and FEM for investigating vibration characteristics and dynamic instability analysis of stiffness laminated composite shell structures.

A review of studies shows that many researches have been done on static and dynamic behavior for a shell structure with different reinforcement fibers and nanomaterials effect. But, they did not study the impact of Silica nanomaterials reinforcement on the composite shell structure. Therefore, the main aim of this paper is to investigate the effects of different volume fractions for Silica nanoparticle materials on the natural frequency and deformation of a composite shell structure, combined with the unidirectional fiber and epoxy resin materials. The present research includes an experimental technique used to manufacture a composite shell with nanoparticle materials and then a tensile test and vibration rig to calculate the composite material shell's mechanical properties and natural frequency with the nano effect. The

numerical technique will be used to compare the natural frequency results for given agreement with the experimental results and determine the deformation of the shell structure with the nano effect.

I. Experimental Work

The experimental work included using a vibration rig with a vibration machine to measure the natural frequency of a cantilever shell cylinder with various nano silicon volume fractions. Where the experimental work was divided into three parts; firstly, manufacturing the shell cylinder samples with various nanomaterials volume fractions, using nano volume fractions from 0 to 2.5%, secondly, calculating the mechanical properties for the composite materials manufactured with the nanoparticle effect, and finally, calculating the vibration characterization (natural frequency) for the shell structure sample.

1.1. Manufacturing of Samples

The manufacturing of nanocomposite samples included two parts; firstly, samples for tensile test, as shown in Fig. 1, according to the ASTM stander (D3039/D03039M), [21], as shown in Fig. 2 (with sample width=15 mm, overall length = 250 mm, thickness =1 mm, tab length =56 mm, tab thickness =1.5 mm and tab bevel angle =7° or 90°), for fiber direction (0° and 90°), and secondly, the shell samples, as shown in Fig. 3, with dimensions (shell length= 30 cm, shell diameter = 15 cm, and shell thichness = 4 mm). Nanosilica (purity = 99%, particle size = 10–30 nm, surface area = 30–60 m²/gm), obtained from Skyspring Nanomaterials, Inc., is introduced into the matrix. All tensile and shell manufactured samples were made with different volume fractions for nano silicon materials as (0, 0.5, 1, 1.5, 2, and 2.5%) . In addition, the reinforcement fiber used for manufacturing the composite materials was unidirectional glass fiber with (30%) reinforcement fiber volume fraction and (70%) decrease with nano additive) epoxy resin material. Then, the manufacturing of the composite material samples (tensile and shell samples) combined the epoxy resin material with the nano silicon materials to produce a composite matrix using an ultrasonic machine and then reinforced the composite matrix with a unidirectional glass fiber material.

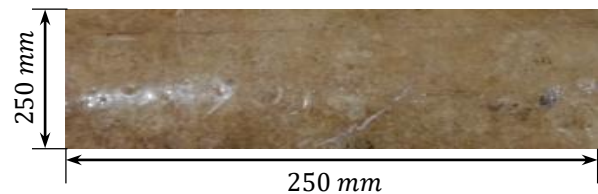


Fig. 1. Composite Tensile Sample.

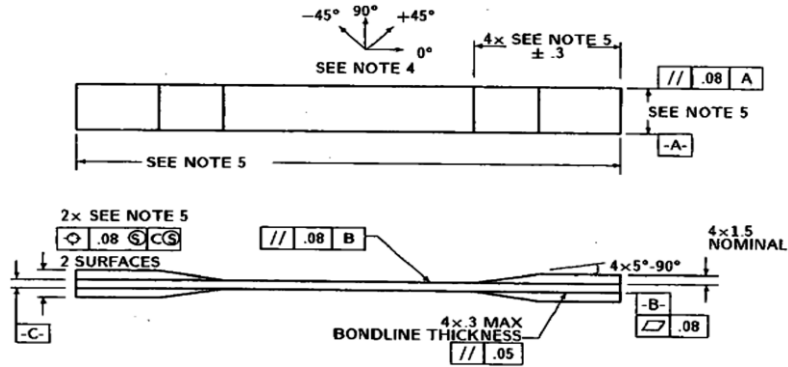


Fig. 2. ASTM (D3039/D03039M), Tensile Sample Drawing.

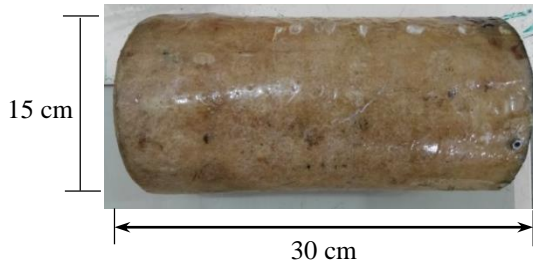


Fig. 3. Shell Composite Structure.

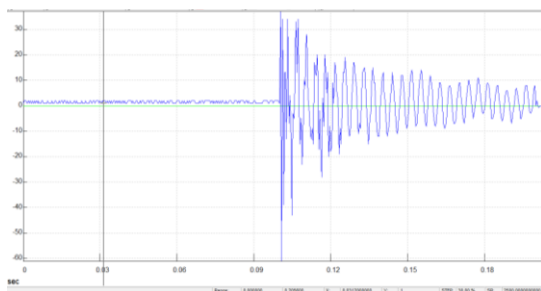
1.2. Mechanical Properties Testing

The mechanical properties testing included calculating the modulus of elasticity for composite materials with and without a nano particles effect. The tensile samples are presented in Fig. 1 to test five models for each volume fraction of nanoparticle effect and then calculate the average value for composite materials, as shown in Table 1. Also, the tensile test was done by using a universal tensile test machine. Therefore, the mechanical properties determined by the experimental work can be used as a numerical technique to obtain the mechanical behavior of the shell structure.

Table 1.

Mechanical Properties for Composite Materials with Different Silica Nanoparticle Volume Fractions

No.	Nano Volume Fraction (%)	Modulus of Elasticity E_1 (GPa)	Modulus of Elasticity E_2 (GPa)
1	0	12.6	3.3
2	0.5	13.3	4.1
3	1	15.9	5.6
4	1.5	17.5	7.3
5	2	18.9	9.2
6	2.5	21.4	11.1



(a) Vibration Signal

1.3. Vibration Characterization Measurement

The vibration testing included using the vibration test rig shown in Fig. 4 to calculate the natural frequency for the shell structure, shown in Fig. 4, with various Nanoparticle volume fractions. The vibration test rig consists of the following parts: structure rig accelerometer, amplifier, oscilloscope, and impact hammer [22]. The natural frequency was calculated by impacting the shell sample using an impact hammer and then reading the voltage signal using (an oscilloscope). Then, the natural frequency was calculated using FFT, using the SIGVIEW program, as shown in Fig. 5.

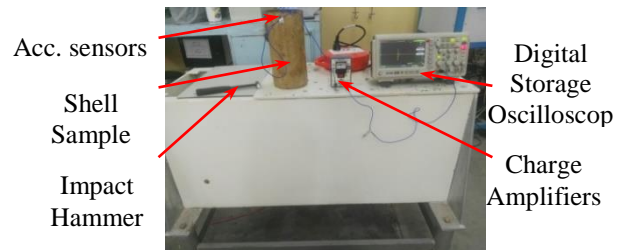
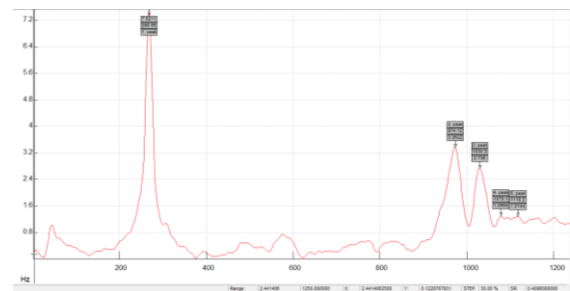


Fig. 4. Vibration test-rig.

II. Finite Element Technique

The numerical technique is an approximate solution for the engineering problem with accepted error, and it can be applied to the static and dynamic behavior of a structure with different boundary conditions [23-24]. A numerical technique used in this work comprised using finite element technique using Ansys program Version 15. The Ansys code needed first select the best element type required for the case applied, input the mechanical properties of the structure calculated from the experimental technique, mesh the structure by section for



(b) FFT Signal

Fig. 5. Sigview Analysis of Signal Vibration.

the best number of elements, depending on the mesh generation technique, and finally calculating the required output for the problem [25-26]. So, the output of this work included calculating the natural frequency and deformation of the composite shell structure, supported as a cantilever, with different silica nanoparticle volume fractions. In addition, a comparison of the numerical natural frequency with the experimental results was made to obtain agreement for the results calculated.

Therefore, the best element can be used for the dynamic analysis of the shell structure is (Shell element with eight nodes and 5 degrees for each node), as shown in Fig. 6, where this element has the global displacement structure that can be listed as,

$$\{U\} = \begin{Bmatrix} u \\ v \\ w \end{Bmatrix} \quad (1)$$

And the local displacement is,

$$\{q\}_i = \begin{Bmatrix} u \\ v \\ w \\ \alpha \\ \beta \end{Bmatrix}_i \quad \text{for } (i = 1, \dots, 8) \quad (2)$$

Therefore, the global displacement can be calculated from the local displacement as:

$$\begin{Bmatrix} u \\ v \\ w \end{Bmatrix} = \sum_{i=1}^8 N_i \begin{Bmatrix} u \\ v \\ w \end{Bmatrix}_i + \sum_{i=1}^8 N_i \zeta \frac{h_i}{2} \mu_i \begin{Bmatrix} \alpha \\ \beta \end{Bmatrix}_i \quad (3)$$

Where, N_i is the shape function, and μ_i can be calculated from

$$\mu_i = \begin{bmatrix} -l_{2i} & l_{1i} \\ -m_{2i} & m_{1i} \\ -n_{2i} & n_{1i} \end{bmatrix} \quad (4)$$

Then, displacement for shell element can be determined by using Eqs. 1 to 4 as:

$$\begin{Bmatrix} u_{,x} \\ u_{,y} \\ u_{,z} \\ v_{,x} \\ v_{,y} \\ v_{,z} \\ w_{,x} \\ w_{,y} \\ w_{,z} \end{Bmatrix} = \sum_{i=1}^8 \begin{bmatrix} a_i & 0 & 0 & -d_i l_{2i} & d_i l_{1i} \\ b_i & 0 & 0 & -e_i l_{2i} & e_i l_{1i} \\ c_i & 0 & 0 & -g_i l_{2i} & g_i l_{1i} \\ 0 & a_i & 0 & -d_i m_{2i} & d_i m_{1i} \\ 0 & b_i & 0 & -e_i m_{2i} & e_i m_{1i} \\ 0 & c_i & 0 & -g_i m_{2i} & g_i m_{1i} \\ 0 & 0 & a_i & -d_i n_{2i} & d_i n_{1i} \\ 0 & 0 & b_i & -e_i n_{2i} & e_i n_{1i} \\ 0 & 0 & c_i & -g_i n_{2i} & g_i n_{1i} \end{bmatrix} \begin{Bmatrix} u \\ v \\ w \\ \alpha \\ \beta \end{Bmatrix}_i \quad (5)$$

Where,

$$\begin{aligned} a_i &= J_{11} N_{i,\zeta} + J_{12} N_{i,\eta} \\ b_i &= J_{21} N_{i,\zeta} + J_{22} N_{i,\eta} \\ c_i &= J_{31} N_{i,\zeta} + J_{32} N_{i,\eta} \\ d_i &= \frac{h_i}{2} (a_i \zeta + J_{13} N_i) \\ e_i &= \frac{h_i}{2} (b_i \zeta + J_{23} N_i) \\ g_i &= \frac{h_i}{2} (c_i \zeta + J_{33} N_i) \end{aligned}$$

Then, by using the strain energy method and using Eq. 5, one can calculate the stiffness matrix as:

$$[K] = \int_{Vol.} [B]^T [D] [B] dV \quad (6)$$

Where,

$$[B]_i = \begin{bmatrix} a_i & 0 & 0 & -d_i l_{2i} & -d_i l_{1i} \\ 0 & b_i & 0 & -e_i m_{2i} & -e_i m_{1i} \\ 0 & 0 & c_i & -g_i n_{2i} & -g_i n_{1i} \\ b_i & a_i & 0 & -(e_i l_{2i} + d_i m_{2i}) & (e_i l_{1i} + d_i m_{1i}) \\ 0 & c_i & b_i & -(g_i m_{2i} + e_i n_{2i}) & (g_i m_{1i} + e_i n_{1i}) \\ c_i & 0 & a_i & -(d_i n_{2i} + g_i l_{2i}) & (d_i n_{1i} + g_i l_{1i}) \end{bmatrix}$$

And, $[D]$ is the rigidity stiffness matrix.

Also, the mass matrix can be calculated as:

$$[M] = \int_V \rho [N]^T [N] dV \quad (7)$$

After this, the natural frequency of the shell structure can be calculated by solution for the general equation for motion by eigenvalue technique as:

$$[M]\{\ddot{U}\} + [K]\{U\} = 0 \quad (8)$$

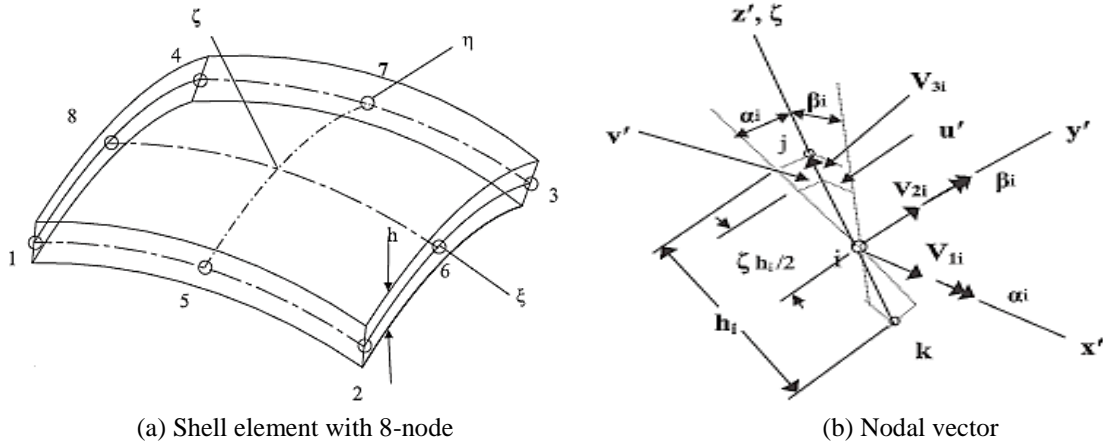


Fig. 6. Element Type used for the Shell Structure

III. Results and Discussion

The present work results include investigating the modification of vibration characterizations for a shell structure using the effect of silica nanoparticle materials made of composite materials combined with resin and unidirectional glass fiber. This work included using experimental and numerical techniques to calculate the

results required. Thus, the experimental results showed the effect of different volume fractions of nanoparticles on the natural frequency of the composite shell structure, supported as a cantilever, as shown in Fig. 7. Also, the numerical technique used comprised calculating the natural frequency of the shell tested in the experimental methods and then comparing the results calculated by the experimental measurements, as presented in Fig. 8. In

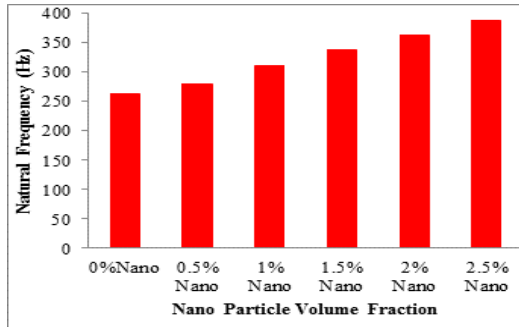


Fig. 7. Natural Frequency for Shell Cylinder with Different Nano Volume Fractions.

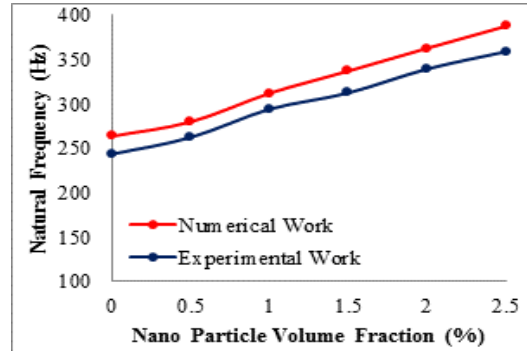
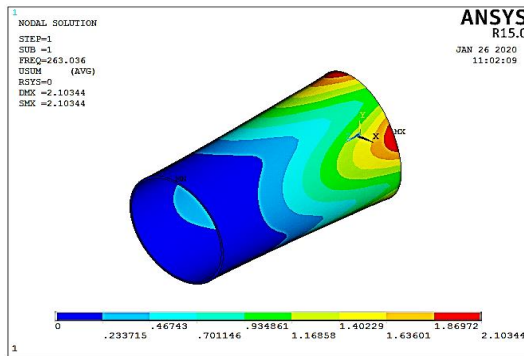
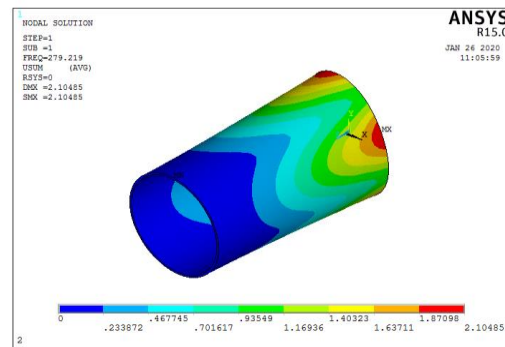


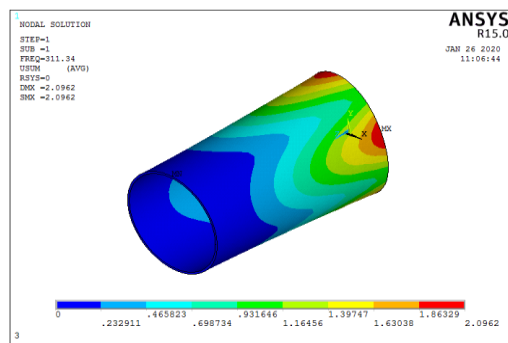
Fig. 8. Comparison between Experimental and Numerical Natural Frequency Results.



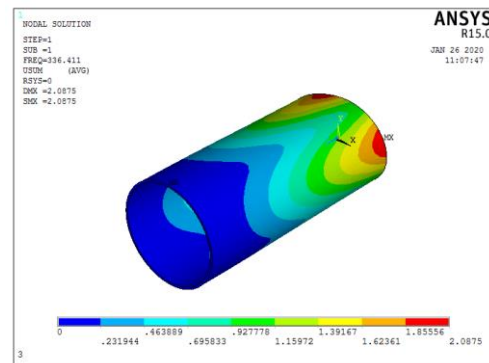
(a) 0% Nano Volume Fraction



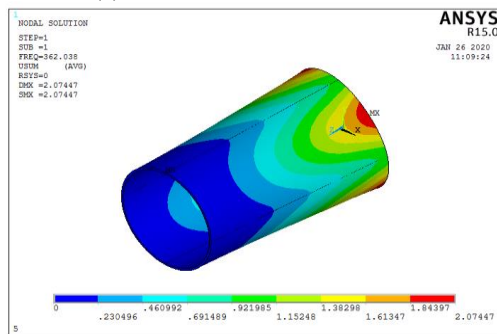
(b) 0.5% Nano Volume Fraction



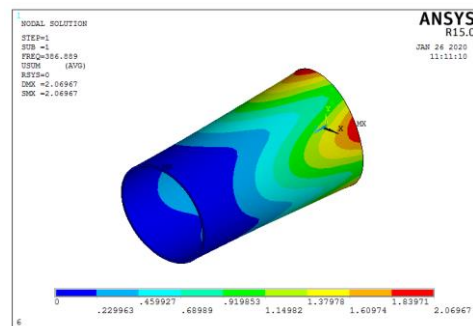
(c) 1% Nano Volume Fraction



(d) 1.5% Nano Volume Fraction



(e) 2% Nano Volume Fraction



(f) 2.5% Nano Volume Fraction

Fig. 9. Deformation for Shell Structure with Various Nanoparticle Reinforcement Volume Fractions.

addition, the numerical technique also included calculating the deformation of the shell structure, with the effect of nanoparticle reinforcement, as in Fig. 9.

Then, from the figures presented, it can be seen that the natural frequency for the shell structure increased with the high values by reinforcing the composite materials using silica nanoparticle materials. In addition, due to increasing the natural frequency, it was found that the deformation stress of the shell decreased with increasing the volume fraction of nanoparticles. As demonstrated in the results recorded in Table 1, the increase in the dynamic response of the shell was caused by the rise in the effective mechanical properties values of the composite materials of the shell structure owing to reinforcement with nanoparticle materials.

Conclusions

In this work, experimental techniques were presented to show the effect of the silica nanoparticle materials on the natural frequency of shell structure. In addition, numerical work was introduced to obtain the agreement for the experimental work by comparing the numerical results of the natural frequency with the experimental results evaluated. Thus, from the current work, the following important conclusions can be drawn:

The experimental work was a perfect technique that can be used to manufacture the composite materials and the shell structure and determine the mechanical properties of the composite materials and the vibration behavior of composite shell structure, with various nano

volume fraction effects.

The comparison between experimental and numerical results for natural frequency gave a good accepting error with a maximum discrepancy that did not exceed (10.93%).

The addition of silica nanoparticle materials improves the mechanical properties (strength and modulus of elasticity) of the entire composite material structure. A nanomaterial-reinforced composite shell structure exhibits extremely high dynamic modifications. A higher nanomaterial volume fraction increases the natural frequency of shell structures.

Due to the modified mechanical properties and dynamic behavior of the composite materials with the reinforcement by silica nanoparticles, the deformation of the shell structure was decreased by increasing the nanoparticle materials.

In future work, it is recommended to examine how nanoparticle sizes and types affect the mechanical performance of cylinders reinforced with nanoparticles.

Muhsin J. Jweeg – Prof. Dr. (Applied Mechanics);
Emad Kadum Njim – PhD, senior researcher (Applied Mechanics);
Orhan S. Abdullah – PhD, Lecturer (Applied Mechanics);
Mohsin Abdullah Al-Shammari– Prof. Dr. (Applied Mechanics);
Muhannad Al-Waily – Prof. Dr. (Applied Mechanics);
Sadeq H. Bakhy – Prof. Dr. (Applied Mechanics).

- [1] K. N. Emad, H. S. Bakhy, and M. Al-Waily, *Analytical and Numerical Investigation of Buckling Behavior of Functionally Graded Sandwich Plate with Porous Core*, Journal of Applied Science and Engineering, 25(2), 339 (2022).
- [2] G.Lin, F. Li, Q. Zhang, P. Chen, W. Sun, I. Saikov, V. Shcherbakov, & M. Alymov, *Dynamic instability of fiber composite cylindrical shell with metal liner subjected to internal pulse loading*, Composite Structures, 280, (2022); <https://doi.org/10.1016/j.compstruct.2021.114906>.
- [3] A. Melaibari, A.A. Daikh, M. Basha, A. Wagih, R. Othman, K.H. Almitani, M.A. Hamed, A. Abdelrahman, M.A. Eltahir, *A Dynamic Analysis of Randomly Oriented Functionally Graded Carbon Nanotubes/Fiber-Reinforced Composite Laminated Shells with Different Geometries*, Mathematics, 10, 408, (2022); <https://doi.org/10.3390/math10030408>.
- [4] M. Q. Wu, W. Zhang, & Y. Niu, *Experimental and numerical studies on nonlinear vibrations and dynamic snap-through phenomena of bistable asymmetric composite laminated shallow shell under center foundation excitation*, European Journal of Mechanics - A/Solids, 89, 2021; <https://doi.org/10.1016/j.euromechsol.2021.104303>.
- [5] H. Bisheh, N.Wu, & T. Rabczuk, *Free vibration analysis of smart laminated carbon nanotube-reinforced composite cylindrical shells with various boundary conditions in hygrothermal environments*, Thin-Walled Structures 149, 106500 (2020); <https://doi.org/10.1016/j.tws.2019.106500>.
- [6] Thakur, S. Nath & C. Ray, *Static and free vibration analyses of moderately thick hyperbolic paraboloidal cross ply laminated composite shell structure*, Structures, 32, 876 (2021); <https://doi.org/10.1016/j.istruc.2021.03.066>.
- [7] X. Miao, C. Li, & Y. Jiang, *Free vibration analysis of metal-ceramic matrix composite laminated cylindrical shell reinforced by CNTs*, Composite Structures, 260, (2021); <https://doi.org/10.1016/j.compstruct.2020.113262>.
- [8] A. Talezadehlari, *Free vibration analysis of perforated composite cylindrical shell and panel using multi-domain generalized differential quadrature (GDQ) method*, Composite Structures, 287, 115337 (2022); <https://doi.org/10.1016/j.compstruct.2022.115337>.
- [9] Y. Zhang, & D. Shi, *Vibration analysis of laminated composite coupled double cylindrical shell-annular-rectangular plate system*, Composite Structures, 281, (2022); <https://doi.org/10.1016/j.compstruct.2021.115020>.
- [10] E. Sobhani, A. R. Masoodi, & A. R. Ahmadi-Pari, *Vibration of FG-CNT and FG-GNP sandwich composite coupled Conical-Cylindrical-Conical shell*, Composite Structures, 273, (2021); <https://doi.org/10.1016/j.compstruct.2021.114281>.
- [11] C. Guo, T. Liu, Q. Wang, B. Qin, & A. Wang, *A unified strong spectral Tchebychev solution for predicting the free*

- vibration characteristics of cylindrical shells with stepped-thickness and internal–external stiffeners*, Thin-Walled Structures, 168, (2021); <https://doi.org/10.1016/j.tws.2021.108307>.
- [12] A. A. Hamzah, H. K. Jobair, O. I. Abdullah, E. T. Hashim, & L. A. Sabri, *An investigation of dynamic behavior of the cylindrical shells under thermal effect*, In Case Studies in Thermal Engineering, 12, 537 (2018); <https://doi.org/10.1016/j.csite.2018.07.007>.
- [13] H. Li, G. Cong, L. Li, F. Pang, & J. Lang., *A semi analytical solution for free vibration analysis of combined spherical and cylindrical shells with non-uniform thickness based on Ritz method*, Thin-Walled Structures, 145, (2019); <https://doi.org/10.1016/j.tws.2019.106443>.
- [14] H. Li, F. Pang, X. Miao, S. Gao, & F. Liu, *A semi analytical method for free vibration analysis of composite laminated cylindrical and spherical shells with complex boundary conditions*, Thin-Walled Structures, 136, 200 (2019); <https://doi.org/10.1016/j.tws.2018.12.009>.
- [15] Z. Qin, X. Pang, B. Safaei, & F. Chu, *Free vibration analysis of rotating functionally graded CNT reinforced composite cylindrical shells with arbitrary boundary conditions*, Composite Structures, 220, 847 (2019); <https://doi.org/10.1016/j.compstruct.2019.04.046>.
- [16] M. Azmi, R. Kolahchi, M.R. Bidgoli, *Dynamic analysis of concrete column reinforced with Sio2 nanoparticles subjected to blast load*, Advances in Concrete Construction, 7(1), 51 (2019).
- [17] Li Xiao, *Parametric resonances of rotating composite laminated nonlinear cylindrical shells under periodic axial loads and hygrothermal environment*, Composite Structures, 255, (2021); <https://doi.org/10.1016/j.compstruct.2020.112887>.
- [18] M. Zarei, G.H. Rahimi, M. Hemmatnezhad, *On the free vibrations of joined grid-stiffened composite conical-cylindrical shells*, Thin-Walled Structures, 161, (2021); <https://doi.org/10.1016/j.tws.2021.107465>.
- [19] K. Kim, Y. Jon, K. An, S. Kwak, & Y. Han, *A solution method for free vibration analysis of coupled laminated composite elliptical-cylindrical-elliptical shell with elastic boundary conditions*, Journal of Ocean Engineering and Science, 7(2), 112 (2022); <https://doi.org/10.1016/j.joes.2021.07.005>.
- [20] G. Sciascia, V. Oliveri, & P. M. Weaver, *Dynamic analysis of prestressed variable stiffness composite shell structures*, Thin-Walled Structures, 175, (2022); <https://doi.org/10.1016/j.tws.2022.109193>.
- [21] D3039/D3039M, *Standard Test Method for Tensile Properties of Polymer Matrix Composite Materials*, ASTM International, (2000)
- [22] E. Njim, S.Bakhi, & M.Al-Waily, *Free vibration analysis of imperfect functionally graded sandwich plates: analytical and experimental investigation*, Archives of Materials Science and Engineering, 111/2 49 (2021); <https://doi.org/10.5604/01.3001.0015.5805>.
- [23] S. E. Sadiq, M. J. Jweeg, and S. H. Bakhy, *Strength analysis of aircraft sandwich structure with a honeycomb core: Theoretical and Experimental Approaches*, Engineering and Technology Journal, 39, 153 (2021).
- [24] J. Jweeg, M., I. Mohammed, A., & S. Jabbar, M., *Investigation of Thickness Distribution Variation in Deep Drawing of Conical Steel Products*, Engineering and Technology Journal, 39, 4A, 586 (2021); <https://doi.org/10.30684/etj.v39i4A.1908>
- [25] E. Njim, S. Bakhi, & M. Al-Waily, *Experimental and Numerical Flexural Properties of Sandwich Structure with Functionally Graded Porous Materials*, Engineering and Technology Journal, 40, 1, 137 (2022); <https://doi.org/10.30684/etj.v40i1.2184>.
- [26] E. Njim, S. Bakhi, & M. Al-Waily, *Experimental and numerical flexural analysis of porous functionally graded beams reinforced by (Al/Al₂O₃) nanoparticles*, International Journal of Nanoelectronics and Materials, 15(2), 91 (2022).

М.Дж. Джвіг¹, Е.К. Нжім², О.С. Абдулла³, М.А. Аль-Шаммарі⁴,
М. Аль-Вайлі⁵, С.Х. Бахі³

Аналіз вільних коливань композитної циліндричної оболонки, армованої кремнієвими наночастинками: аналітичне та FEM наближення

¹Університет Аль-Фарахіді, Технічний інженерний коледж, Ірак;

²Міністерство промисловості та корисних копалин, Державна компанія гумової та шинної промисловості, Ірак,
emad.njim@gmail.com;

³Факультет машинобудування, Технологічний університет, Ірак;

⁴Інженерний коледж Багдадського університету, факультет машинобудування, Ірак;

⁵Кафедра машинобудування, інженерний факультет, Університет Куфи, Ірак

Попередні дослідження показали вплив наноматеріалів на механічні властивості композитних матеріалів з ефектами різних фракцій по об'єму; крім того, дослідження продемонстрували вплив наноматеріалів на такі механічні характеристики композитної пластинчастої структури, як коливання та термічна поведінка. Таким чином, механічні властивості та поведінка модифікуються на високі значення за рахунок зміщення з низькою кількістю для наноматеріалів, яка не перевищує приблизно (3%). Завдання дослідження є встановлення модифікації вібраційних характеристик конструкції з ефектом наноматеріалів і вивчення впливу інших типів армованих наночастинок на характеристики. Наночастинки кремнію обрані для дослідження їх впливу на вібраційну поведінку оболонкової структури. Таким чином, робота включала використання експериментальної методики випробування конструкції оболонки за допомогою вібромашини для вивчення вібраційної поведінки. Після виготовлення оболонки з композитного матеріалу із різними об'ємними частками наночастинок кремнію оцінювали механічні властивості. Використовуючи чисельну техніку, зокрема, метод скінченних елементів за допомогою середовища Ansys, виконано оцінку вібраційної поведінки конструкції оболонки та здійснено порівняння результатів. Порівняння дало прийнятну відсоткову похибку, що не перевищує 10,93%. Оцінені результати показали, що модифікація кремнієвими наноматеріалами дала дуже хороші результати, оскільки наноматеріали покращили приблизно 65% механічних властивостей оболонки та вібраційні характеристики.

N.Ya. Ivanichok¹, P.I. Kolkovskiy², A.M. Soltys¹, V.M. Boychuk¹, V.I. Mandzyuk¹,
L.S. Yablon¹, B.I. Rachiy¹

The effect of orthophosphoric acid on energy-intensive parameters of porous carbon electrode materials

¹Vasyl Stefanyk Precarpathian National University, Ivano-Frankivsk, Ukraine, volodymyr.mandzyuk@pnu.edu.ua

²V.I. Vernadskii Institute of General and Inorganic Chemistry of the NAS of Ukraine, Kyiv, Ukraine

The effect of orthophosphoric acid concentration as an activating agent on the porous structure of carbon materials derived from apricot pits and energy-intensive parameters of electrochemical capacitors formed on their basis is studied. It is found that changing the ratio of the mass of the activating agent to the mass of the raw material in acid-activated porous carbon materials (PCMs), one can control the pore size distribution in the range of 0.5-20 nm and specific surface area in the range of 775-1830 m²/g. The use of cyclic voltammetry, impedance spectroscopy and chronopotentiometry made it possible to set the capacitive nature of charge accumulation processes in acid-activated PCMs, as well as to determine the contribution of a certain size of pores to the specific capacitance of PCM/electrolyte system.

Keywords: porous carbon material, activating agent, specific surface area, pore size distribution, specific capacity, electrochemical capacitor.

Received 27 June 2022; Accepted 25 January 2023.

Introduction

Porous carbon materials (PCMs), having a number of unique properties, are widely used for purification of drinking water from organic impurities [1, 2], separation and storage of gases [3, 4], manufacturing electrodes of electrochemical capacitors (ECs) [5-8] and lithium power sources [9, 10]. Nowadays, PCMs are made from raw materials (RMs) of natural and artificial origin. Preference is given to the former because they are cheap and environmentally friendly. In recent years, research has been conducted to obtain PCMs from agricultural waste, such as cherry and apricot pits [11], coconut shells [12], corn cobs [13], flax and hemp fibers [14] and others. Apricot fruit is an important RM in the food industry, its seeds are used in medicine and cosmetology. Wastes of this production are apricot pits, which can be used as raw material for high-porosity carbon that also solves the problem of disposal of food waste, which leads to environmental pollution.

The most common methods for obtaining PCMs are

physical or chemical activation of carbonaceous RMs [15-17], as well as methods of template synthesis [18, 19].

Chemical activation usually occurs at temperatures (400-800°C) and is accompanied by the use of dehydrating agents (phosphoric acid, zinc chloride, potassium hydroxide). Chemical activation is considered as a reaction between a solid precursor and a chemical reagent. The mass of the final product and its structure depend on the concentration and ratio of the source components, temperature and activation time. A necessary condition for chemical activation is the removal of residual activating reagents and inorganic residue contained in the original carbonized material. When chemically activating plant raw materials with orthophosphoric acid, the latter acts as a dehydrating agent that inhibits the formation of resin, which increases the mass yield of porous carbon and reduces the temperature and activation time compared to physical activation methods [20]. Mixing orthophosphoric acid with crushed apricot pits leads to fragmentation of cellulose, hemicellulose and lignin. The acid separates the cellulose

fibers and causes partial depolymerization of hemicellulose and lignin, which leads to a decrease in the mechanical strength of the particle and its swelling. Orthophosphoric acid leads to the primary carbonization of RM at this stage [20]. When obtaining activated carbon by chemical activation of RM with orthophosphoric acid, the ratio between the amount of acid and the precursor is important for the development of the porous structure of the product obtained. Therefore, the aim of this work is to study the effect of orthophosphoric acid concentration on the structure of PCM and energy-intensive parameters of ECs formed on its basis.

I. Materials and methods

The RM for the production of porous carbon was apricot pits, dried and ground to a fraction of 0.25-1 mm. The resulting material was divided into portions weighing 8 g and mixed with 50 g of orthophosphoric acid. The acid concentration varied from 4 to 32 % in increments of 4 %. The ratio of the mass of the activating agent to the mass of the raw material $Y = m(\text{H}_3\text{PO}_4)/m(\text{RM})$ was respectively 0.25:1; 0.5:1; 0.75:1; 1:1; 1.25:1; 1.5:1; 1.75:1 and 2:1. The resulting mixture was stirred thoroughly for 1-2 hours, then dried at 100°C for 24 hours until a constant mass was reached. Then the mixture was placed in a vertical cylindrical furnace and heated to 550°C at speed of 10°C/min in an argon atmosphere at a gas flow rate of 30 ml/min. When the set temperature was reached, isothermal exposure was performed for 60 minutes. After cooling the material to room temperature, it was washed with hot distilled water to neutral pH and dried at 80°C until a constant mass was reached. The materials obtained are marked according to the ratio of the mass of acid to the mass of raw materials (Table 1).

Thermal transformations of the initial material and materials modified with orthophosphoric acid were studied using a synchronous thermal analyzer STA 449 F3 Jupiter (NETZSCH) in the linear heating mode at a rate of 10°C/min in an argon atmosphere at a gas flow rate of 30 ml/min and temperature range of 20-600°C. The change in mass of the studied samples as a result of heating is represented by the thermogravimetric (TG) curve (measurement accuracy 1 mg), the rate of mass change is represented by the differential thermogravimetric (DTG) curve. An empty crucible of Al_2O_3 was used as a reference standard. The test sample was heated together with the reference sample and the current temperature of the test sample and the temperature difference between the sample and the standard were recorded, which allowed to record the processes associated with the absorption or release of energy.

The textural characteristics of samples were analyzed on the basis of low-temperature (77.4 K) nitrogen

adsorption-desorption isotherms recorded using a Quantachrome Autosorb Nova 2200c adsorption analyzer. Before measurements, the samples were heated at 180°C for 24 h. The specific surface area (S_{BET}) was calculated according to the standard Brunauer-Emmett-Teller (BET) method. The specific surface area (S_{micro}) and volume (V_{micro}) of micropores was calculated by t -method, surface (S_{meso}) and volume (V_{meso}) of mesopores were calculated as the difference between the total surface area (volume) of pores and micropores. The total pore volume V was evaluated from the nitrogen adsorption at $p/p_0 \approx 0.99$, where p and p_0 denote the equilibrium and saturation pressure of nitrogen at 77.4 K, respectively. Calculation of pore size distribution was performed by NLDFT (nonlocal density functional theory) method in the slit-shape pore approximation.

Electrochemical studies of the PCM/electrolyte system were performed in three-electrode cells (Fig. 1). The working electrode (1) was formed of PCM, conductive additive and binder material in a ratio of 75:20:5 wt. %, respectively. A silver chloride (Ag-AgCl) electrode (2) was the reference electrode and the platinum electrode (3) was as the auxiliary one. The silver chloride electrode was placed in a 3.5 M aqueous KCl solution (6) and combined with the working chamber via an agar-agar salt bridge (5). A 30% aqueous solution of KOH was used as the electrolyte (4). The potential of the working electrode against the reference electrode was -0.33 – -0.28 V at room temperature.

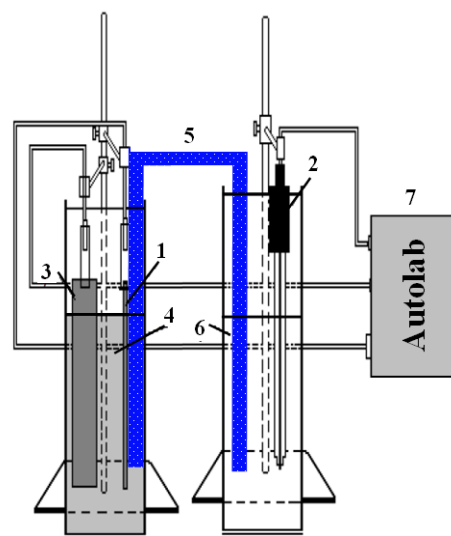


Fig. 1. Scheme of a three-electrode cell for electrochemical research.

The operational characteristics of laboratory samples of ECs were determined in a two-electrode cell (Fig. 2).

Button-type EC electrodes were prepared by pressing a mixture of PCM, conductive additive, and binder material in a ratio of 75:20:5 wt. % respectively into a nickel grid. The formed electrodes were separated by a separator and placed in a two-electrode cell, which was

Table 1.

Designation of acid-activated PCMs								
Y	0.25	0.50	0.75	1.00	1.25	1.50	1.75	2.00
Sample	C025	C050	C075	C100	C125	C150	C175	C200

adsorption-desorption isotherms recorded using a Quantachrome Autosorb Nova 2200c adsorption analyzer. Before measurements, the samples were heated at 180°C

sealed after filling with electrolyte.

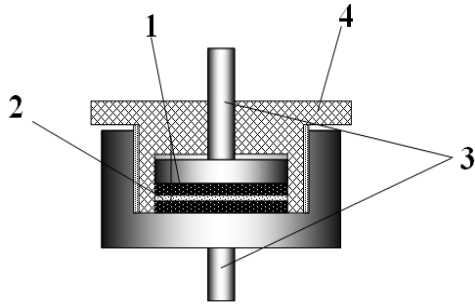


Fig. 2. The scheme of the cell for measuring the capacity of the EC: 1 – electrodes, 2 – separator, 3 – current taps, 4 – insulating cover.

Methods of cyclic voltammetry, impedance spectroscopy and chronopotentiometry were used to study the electrochemical properties of ECs with electrodes on the basis of PCMs. Measurements were performed using an Autolab spectrometer (“ECO CHEMIE”, the Netherlands), equipped with GPES and FRA-2 software.

Cyclic voltammograms were obtained in the potential range from -1 to 0.2 V for three-electrode cells and from 0 to 1 V for two-electrode cells at a scan rate s 1 ÷ 50 mV/s. Voltammetry determines the dependence of current on the applied potential, which changes periodically and linearly over time with a rate $s = \pm \frac{dU}{dt}$. The corresponding current of capacitor with capacitance C is determined as $I = C \frac{dU}{dt} = C \cdot s$. The EC capacity is determined as $C = I/s$ at low scan rate [21]. The total charge accumulated on the electrode surface is calculated by integrating the function $C(U, t)$ over time $q = \int_{u_2}^{u_1} C(U) \frac{dU}{dt} dt = \int_{u_2}^{u_1} C(U) dU$. Capacity is calculated as the ratio of total charge to the magnitude of the potential window $C = q/U$, in which the study is conducted. To estimate the effectiveness of the EC the dependence of the capacity on the scan rate is determined.

Impedance hodographs (or Nyquist diagrams) $Z'' = f(Z')$, where Z' and Z'' are real and imaginary parts of the complex resistance of the system, respectively, were obtained in the frequency range 10^{-2} - 10^5 Hz. The amplitude of the sinusoidal voltage was 10 mV.

Chronopotentiometric studies were performed in the voltage range 0 ÷ 1 V, the charge/discharge current of the capacitor varied in the range from 10 to 50 mA in increments of 10 mA. The specific capacity of the electrode material of the EC was calculated by the formula

$$C = \frac{2It}{(U_{max} - \Delta U)m},$$

where I – charge/discharge current, t – discharge time, U_{max} – maximal voltage, ΔU – voltage drop when the discharge circuit is closed, m – mass of PCM.

II. Results and discussion

Fig. 3 presents TG and DTG curves obtained for plant raw materials due to heating to a temperature of 600°C. In the range of 50-200°C the decrease in the mass of the test samples by 8-10 % is due to the removal of sorbed water contained in the material. When the temperature reaches

250°C, the process of carbonization and decomposition of hemicellulose and cellulose begins, which lasts up to 450°C and is accompanied by 55% weight loss. The next temperature range (450-600°C) is associated with the formation of semi-coke with a small weight loss of 5 %.

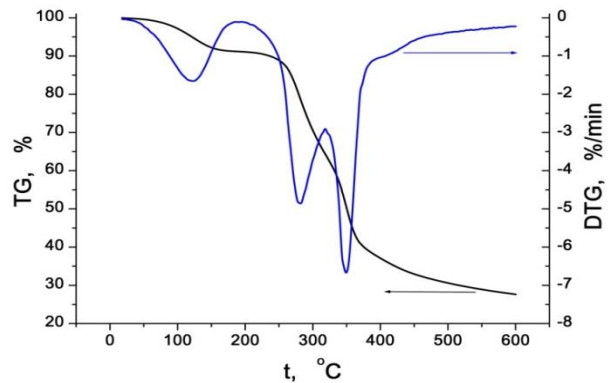


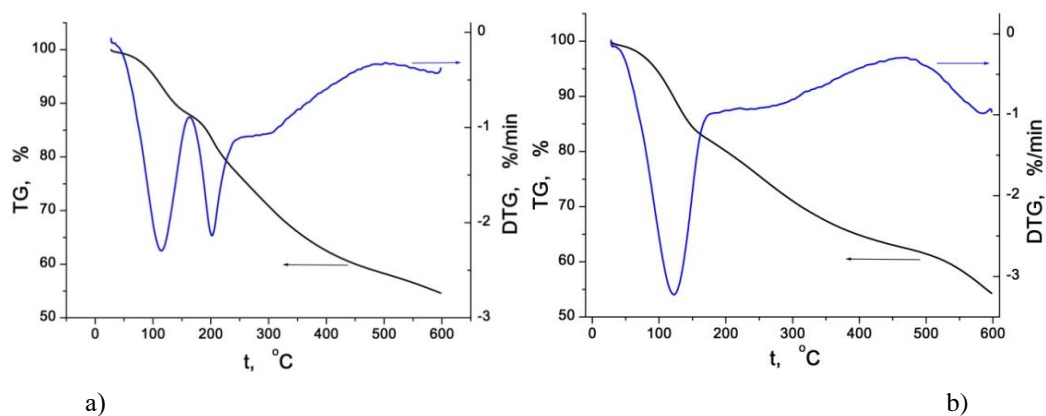
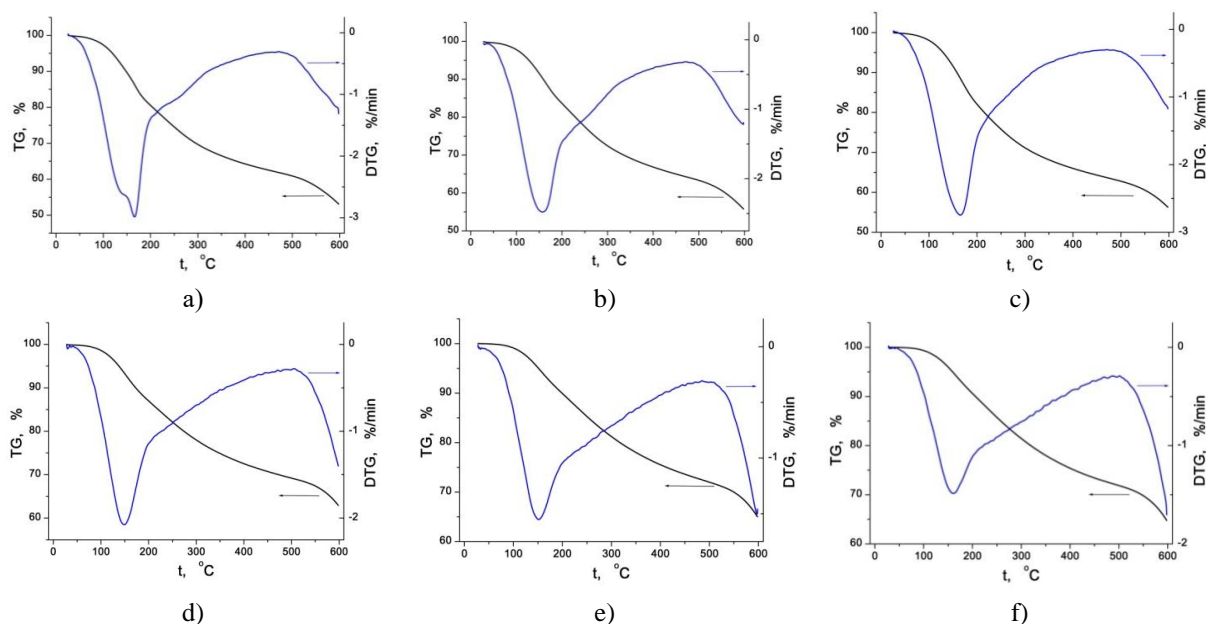
Fig. 3. Thermogram of raw material.

The results of thermogravimetric studies for materials impregnated with orthophosphoric acid at values of $Y = 0.25$ and 0.50 (samples C025, C050) are presented in Fig. 4.

The first region of weight loss due to sorbed forms of water is practically absent on these thermograms. Most probably, orthophosphoric acid at low concentrations first reacts with hemicellulose and lignin, which leads to a sharp drop in mass starting from 100°C (Fig. 4, a). The weight loss with increasing temperature slows down to 0.5 %/min after 450°C. The final oxidation of carbon material after reaction with acid takes place at this stage. The total weight loss of RM is 45% in this temperature range. The temperature of cellulose carbonization decreases at a higher content of orthophosphoric acid, which follows from the presence of only one peak on the DTG curve (Fig. 4, b). In the temperature range of 150-500°C, micro- and mesopores are formed, which is a consequence of the interaction of orthophosphoric acid with biopolymers (lignin, hemicellulose and cellulose). Further increase in the concentration of orthophosphoric acid does not lead to differences in TG and DTG curves for PCMs (Fig. 5). The total weight loss is 40-50 % for all samples, which is less compared to the initial RM.

Orthophosphoric acid acts as an activating agent and promotes dehydration of the primary material, which reduces the degradation temperature of the material, increases the mass of the obtained carbonized carbon material and promotes the formation of its porous structure.

According to low-temperature porometry (Table 2), PCMs are characterized by a microporous structure (the contribution of micropores is 95%) and a developed surface area at low concentrations of orthophosphoric acid (samples C025, C050, C075). Samples C100 and C125 have the maximum value of the specific surface area (1600-1850 m²/g), which is mainly provided by micropores (90-95 %). The maximum total pore volume 1.231 cm³/g, which is provided by mesopores (about 57 %), is typical for the sample C150. As Y increases


Fig. 4. Thermogram of samples C025 (a) and C050 (b).

Fig. 5. Thermogram of samples C075 (a), C100 (b), C125 (c), C150 (d), C175 (e), and C200 (f).

further, both the total surface area and the pore volume of PCMs decrease (samples C175 and C200). Thus, changing the ratio of Y from 0.25 to 1.25, one can obtain microporous carbon material, and when $Y = 1.25 \div 2.00$ mesopores are formed, which are about 50% of the total area and 75% of the total volume.

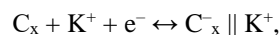
Table 2.

Structural and adsorption characteristics of PCMs

Sample	S_{BET} , m^2/g	S_{micro} , m^2/g	S_{meso} , m^2/g	V , cm^3/g	V_{micro} , cm^3/g	V_{meso} , cm^3/g
C025	775	745	30	0.336	0.303	0.033
C050	880	870	10	0.360	0.354	0.006
C075	1340	1290	50	0.575	0.535	0.040
C100	1635	1520	115	0.804	0.687	0.117
C125	1830	1760	70	0.856	0.779	0.077
C150	1510	645	865	1.231	0.319	0.912
C175	1335	712	623	1.095	0.334	0.761
C200	1120	560	560	0.851	0.243	0.608

According to cyclic voltammetry results (Fig. 6 and Fig. 7) it follows that for acid-activated PCMs there are no redox peaks in the studied potential range that indicates the electrostatic interaction of electrolyte ions with the developed electrode surface. There is a pronounced asymmetry with respect to zero current depending on the

scanning rate s , as well as a difference in the amount of charge during anodic and cathodic polarization at low values s (1-5 mV/s). The asymmetry of these curves with respect to the potential of zero charge indicates the difference between the value of the accumulated charge by K^+ ions and OH^- groups. The magnitude of the current in the negative potential range exceeds the value of the corresponding currents in the positive region by 1.5-2 times, which indicates the dominance of charge accumulation due to K^+ ions, according to the reaction:



where C_x – the surface of the porous structure of the carbon material; K^+ – electrolyte cations; \parallel – double electric layer (DEL), where the charge accumulates due to mechanism of physical adsorption [21].

There is an increase in the specific surface area from 770 to 1800 m^2/g (Fig. 6, b, d, f) when $0.25 \leq Y \leq 1.25$, but a correlation between currents on voltammograms (Fig. 6, a, c, e) and the specific surface area is not observed. The voltammograms of PCMs are almost indistinguishable at low scan rates and $0.25 \leq Y \leq 1.00$, although the surface doubles. Samples C100 and C125 have a larger specific

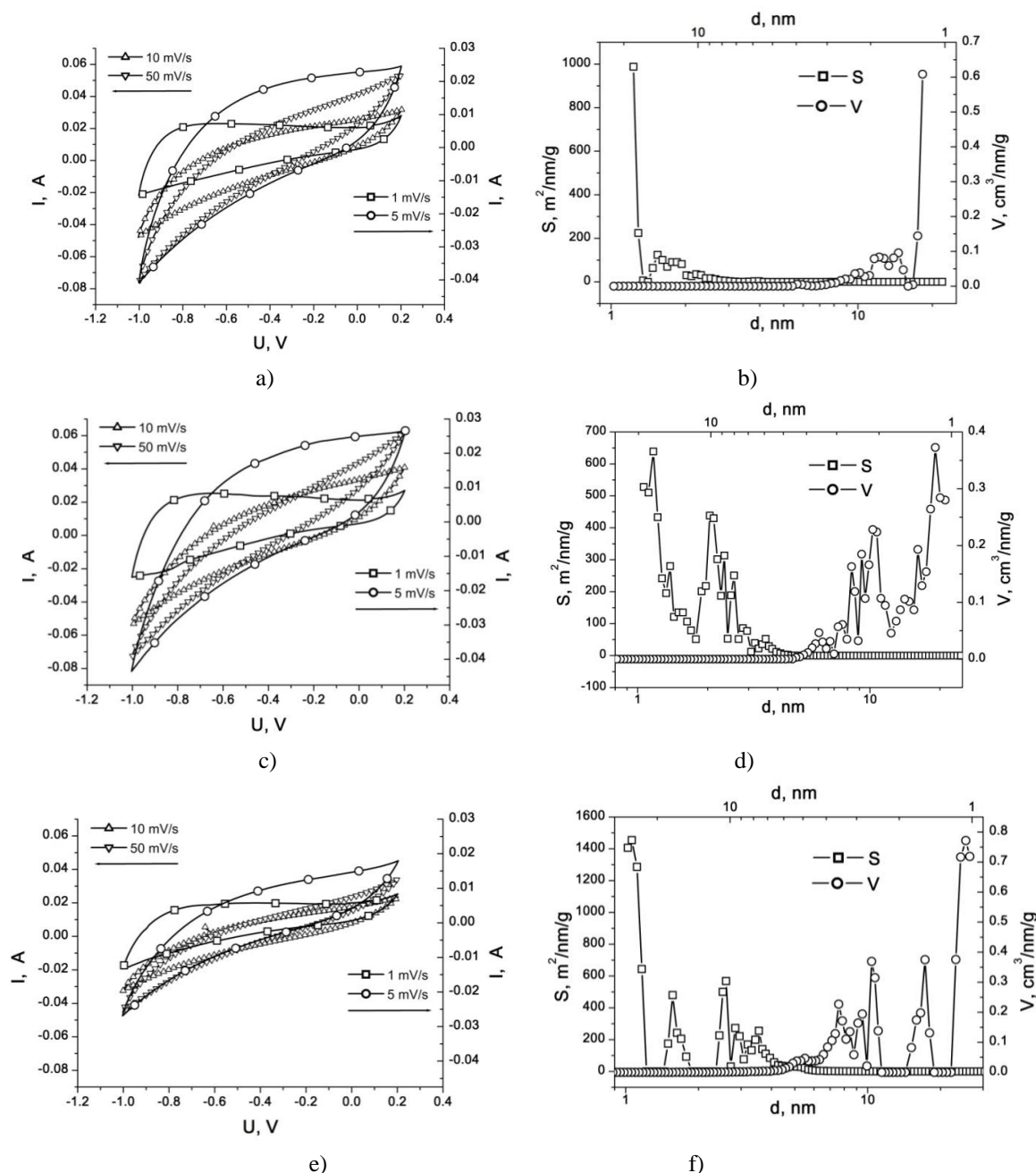


Fig. 6. Cyclic voltammograms and pore size distribution for samples C025 (a, b), C075 (c, d), C125 (e, f).

surface area compared to other materials, but the cycling currents are slightly lower than for samples at $Y < 1$. One of the reasons is the large number of pores smaller than 1 nm (Fig. 6, f), which make significant contribution to the size of the surface area, but are difficult to access for electrolyte ions during cycling. Increasing the scan rate above 10 mV/s leads to distortion of voltammety shapes, which is a consequence of increased internal resistance due to low electrical conductivity of these materials as they are obtained at 550°C.

Voltammograms for mesoporous carbon materials are close to rectangular ones in the positive potential range at low scanning rates (Fig. 7). In this region the charge accumulates due to the formation of DEL by hydroxyl groups on the carbon surface. Low mobility of OH^- groups leads to a change in the course of voltammograms when the scan rate increases slightly.

The values of the specific capacity of PCMs depending on the scan rate are given in Table 3.

According to Table 3, the maximum capacity of the PCM/KOH system is achieved when using PCM with a pore distribution in the range of 1-3 nm, i.e. for microporous materials with a small proportion of transport mesopores.

Laboratory models of EC were made on the basis of samples with the maximum specific capacity (C075, C100, and C125). The cyclic voltammograms of the ECs show that their shape and magnitude of anode and cathode currents are the same at low scan rates (1-5 mV/s) (Fig. 8). An increase in scan rate over 5 mV/s leads to a maximum on the voltammograms in the potential range of 0.2-0.6 V. This effect is especially evident for a series of carbon materials with a microporous structure and a large specific surface area (Fig. 8, c).

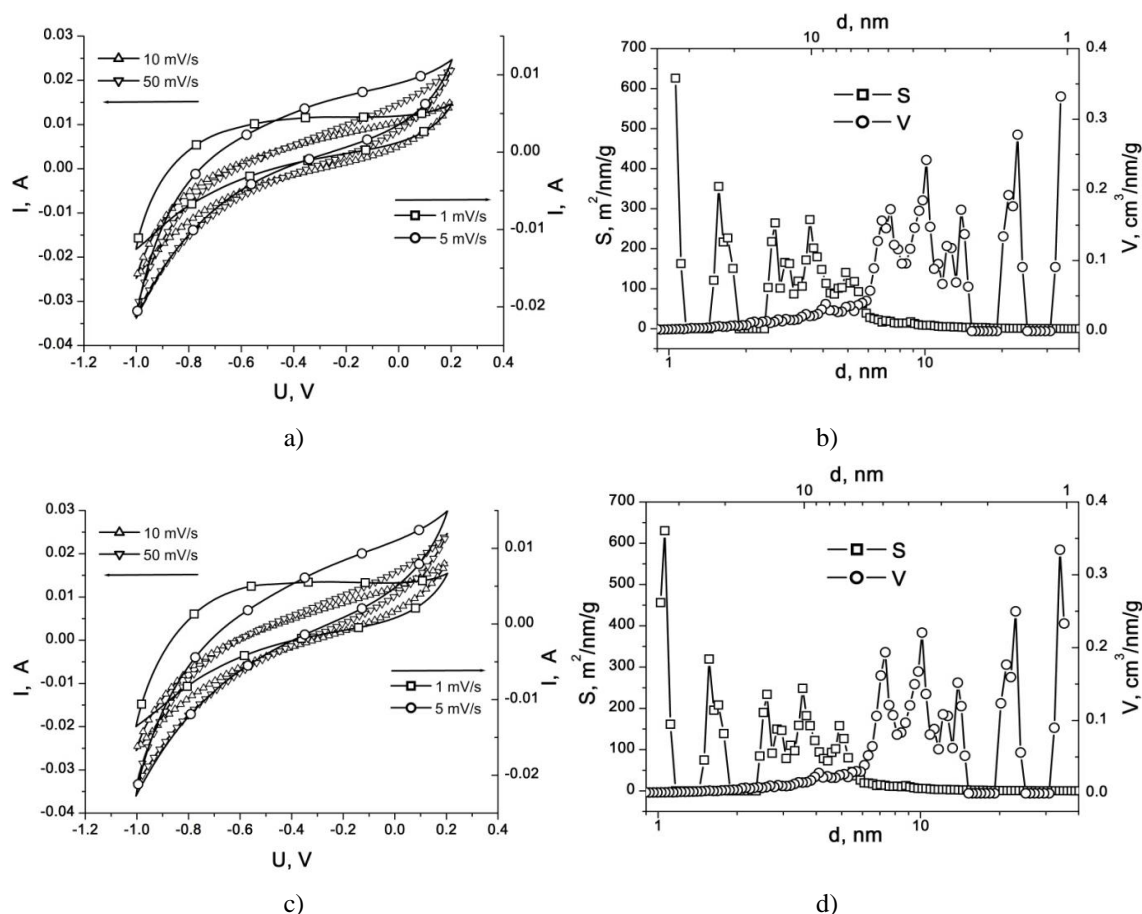


Fig. 7. Cyclic voltammograms and pore size distribution for samples for mesoporous carbon materials C175 (a, b) and C200 (c, d).

Table 3.

Specific capacity (F/g) of acid-activated PCMs at different scan rate and a potential -0.4 V

Sample	1 mV/s	2 mV/s	3 mV/s	4 mV/s	5 mV/s	10 mV/s
C025	99.2	92.7	82.0	69.1	61.0	23.2
C050	132.8	119.8	101.7	84.1	72.8	25.7
C075	140.7	123.8	101.9	82.1	68.7	34.3
C100	148.4	130.4	108.0	85.3	69.7	40.0
C125	99.1	71.3	52.8	39.6	32.0	15.7
C150	61.4	25.9	16.6	11.5	8.8	4.0
C175	76.4	45.3	31.4	22.2	12.4	8.7
C200	68.6	45.8	26.3	18.5	9.3	7.0

The change in the shape of voltammograms is due to the rapid increase in the concentration of ions on the surface of the electrodes with a slight increase in the EC potential, which leads to an increase in the current [22]. The largest value of the current corresponds to a potential of 0.2 V (Fig. 8, c), around which the concentration of ions is maximum. Further accumulation of ions on the surface of the electrodes becomes more complicated and slows down, which is manifested in a decrease in the current value with increasing EC potential.

The internal resistance of the EC increases when $s \geq 20$ mV/s. As a result, the shape of the voltammogram changes during the transition from capacitive to resistive one and the specific capacity of PCM decreases several times (Fig. 9).

The properties of the electrochemical system PCM/electrolyte depending on the applied electrode

potential were studied by impedance spectroscopy method. The obtained Nyquist diagrams (Fig. 10) make it possible to estimate the effect of the porous structure of carbon material and its electrical characteristics on the system parameters depending on the ions of the electrolyte used. The values of the specific capacity and electrical resistance of PCM at different values of the electrode potential provide important information about the effectiveness of its use as an electrode material of EC.

The Nyquist diagrams have the form characteristic of ECs with a dominant capacitive charge accumulation process at the PCM/electrolyte interface in the potential range $-1 \div -0.4$ V (Fig. 10). It is expressed by an almost vertical section on the diagram at low frequencies. When the electrode potential increases from -0.4 to 0.2 V, a semicircle appears on all hodographs in the high-frequency region, which is associated with the passing of

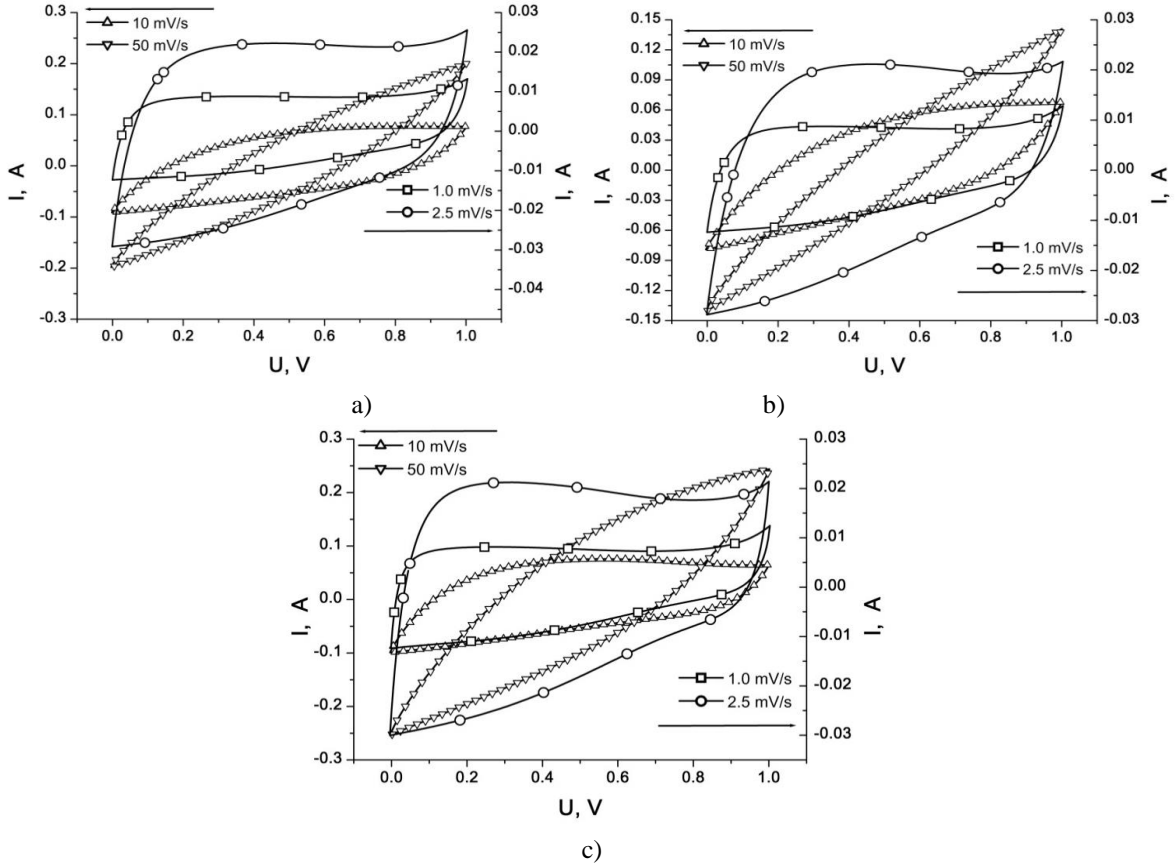


Fig. 8. Cyclic voltammograms for ECs based on samples C075 (a), C100 (b), and C125 (c).

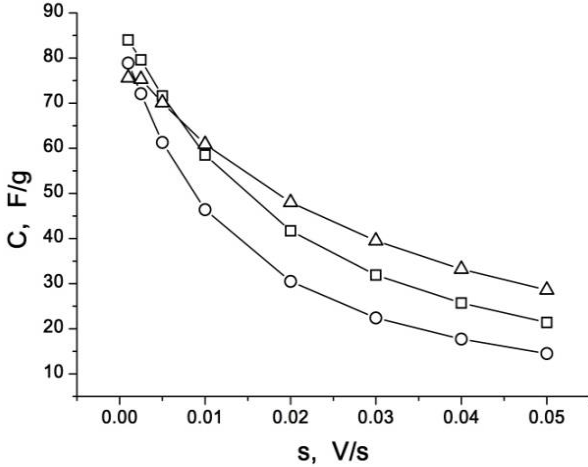


Fig. 9. Dependence of the specific capacity of PCMs on the scan rate for samples C075 (○-), C100 (□-), and C125 (Δ-).

Faraday processes at the electrode [23]. In this case, redox

reactions occur with the participation of OH^- groups. Nyquist diagrams in the range of middle and low frequencies are represented by a straight line with different angles of inclination, which depends on the applied potential, and characterizes the different mechanisms of charge accumulation in the PCM/electrolyte system. The increase of the electrode potential in the positive region leads to a decrease in the angle of inclination of the hodograph within $40^\circ \leq \varphi \leq 50^\circ$, which indicates the diffusion processes in this electrochemical system.

To establish the relationship between the porous structure and the specific capacity of PCM in aqueous solution of KOH, Nyquist diagrams are modeled by an equivalent electrical circuit or determine the specific capacity using calculation formulas that do not require model assumptions [24]. The total complex resistance in an alternating current circuit according to Ohm's law is equal to:

$$Z^* = \frac{U_0 e^{j\omega\tau}}{I_0 e^{j(\omega\tau+\varphi)}} = \frac{U_0}{I_0} e^{-j\varphi} = Z \cos \varphi - jZ \sin \varphi = Z' - jZ'', \quad (1)$$

where U_0, I_0 – voltage and current amplitudes, ω – angular frequency, φ – phase shift angle, j – imaginary unit ($j = \sqrt{-1}$).

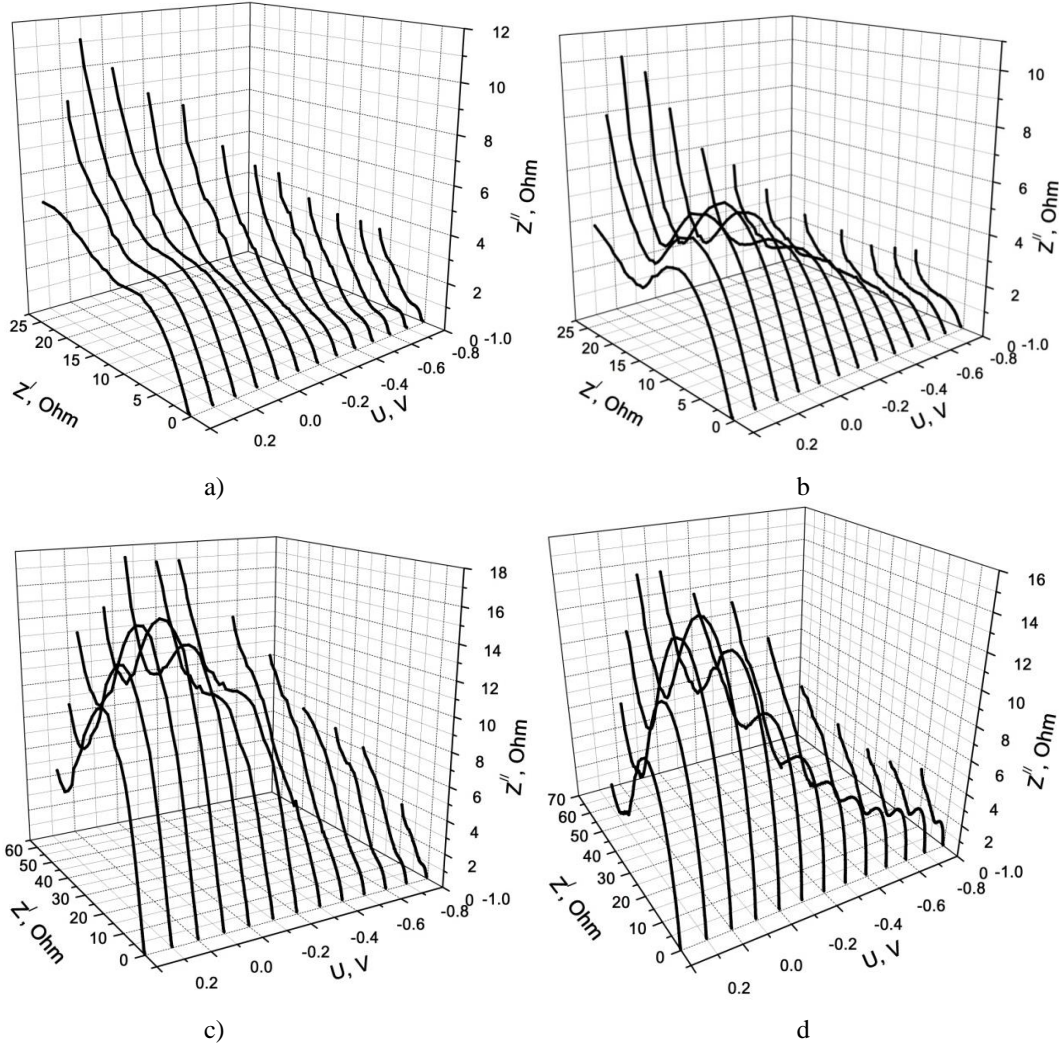


Fig. 10. Nyquist diagrams for PCM/KOH systems based on samples C025 (a), C075 (b), C125 (c), and C200 (d) at different applied potentials.

The electrical resistance R is the main element in impedance models. In the frequency region $Z_R(j\omega) = R$ simulates the proportional relationship between the parameters of the state (current and voltage) and reflects the lack of phase shift between these parameters. The impedance of this element reflects the frequency-independent component of the substance, i.e. $\text{Re } Z_R = R$, and $\text{Im } Z_R = 0$.

The parameter $1/C$ is the coefficient of proportionality between the voltage U_C and the integral from the function of the time dependence of current, which passes through this element and is characterized by the ratio $U_C(t) = \frac{1}{C} \int_{t_0}^t i(t) dt + U_C(t_0)$. This relationship is written as $(j\omega) = \frac{1}{j\omega C} = -\frac{j}{\omega C}$ in the frequency region. Element Z_C contains only the reactive component, which for positive C values is negative one, i.e. reflects the phase delay at $\pi/2$. The impedance Z_C decreases proportionally with increasing frequency. The voltage of the element is proportional to the charge accumulated by it.

Impedance hodographs of studied electrochemical systems (Fig. 10) indicate that there is a pseudo-capacitive accumulation of energy in addition to the DEL capacity. The obtained hodographs can be modeled by equivalent

schemes shown in Fig. 11.

Theoretically, these schemes are described as follows [25]:

$$\frac{1}{Z} = \frac{1}{1/j\omega C_{dl}} + \frac{1}{R_F + 1/j\omega C_p} = j\omega C_{dl} + \frac{j\omega C_p}{j\omega R_F C_p + 1}, \quad (2)$$

where C_{dl} – DEL capacity, C_p – pseudocapacity, R_F – Faraday resistance.

At very low frequencies ($\omega \rightarrow 0$), and/or low R_F

$$\frac{1}{Z} = j\omega(C_{dl} + C_p), \quad C = C_{dl} + C_p.$$

At sufficiently high frequencies ($j\omega R_F C_p \gg 1$)

$$Z = \frac{R_F}{1 + j\omega R_F C_{dl}}$$

The total capacity of the system is calculated using equation (2) at $\omega \rightarrow 0$ (Fig. 12).

The specific capacity of PCMs depends on the magnitude of the electrode potential (Fig. 12), due to changes in the free charge of the surface during its polarization in the positive or negative direction. Conducting electrochemical studies in a three-electrode

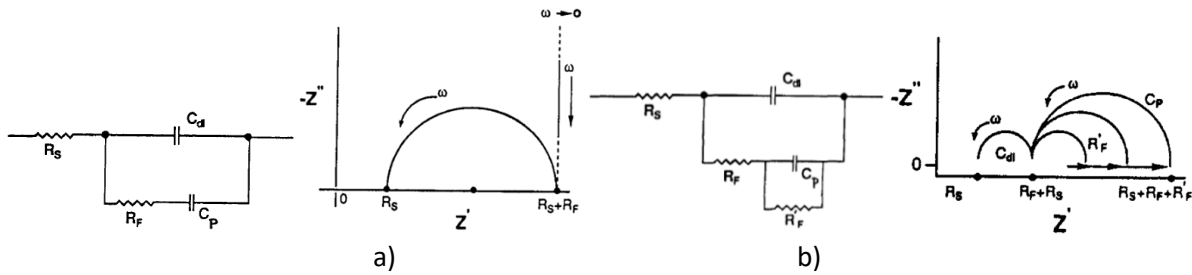


Fig. 11. The simplest equivalent schemes of ECs and their hodographs [25].

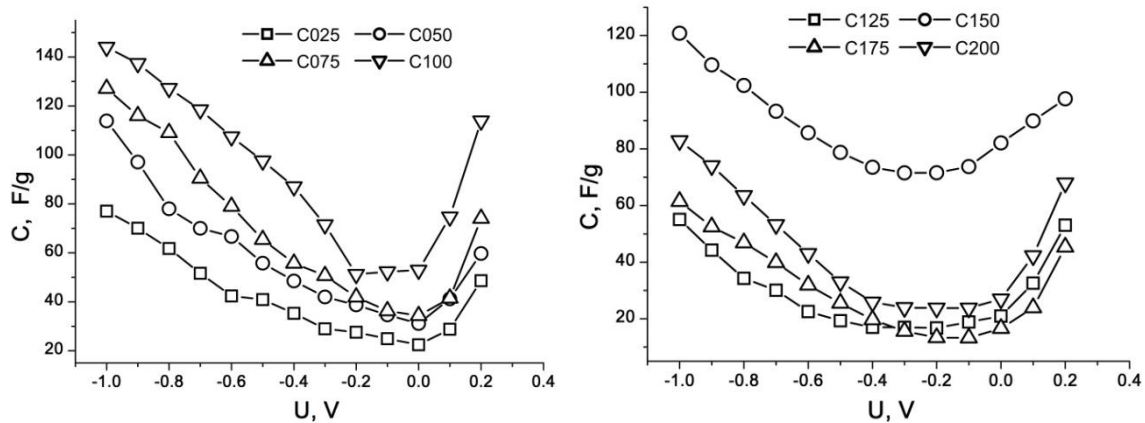


Fig. 12. Dependence of the specific capacity of PCMs on the electrode potential.

cell, it was found that the potential of carbon material against the reference electrode was $-0.33 - 0.28$ V. There is the minimum on volt-farad dependences in range of these potentials. This minimum corresponds to the potential of zero charge in the absence of specific effects on the electrode surface [26] and is shifted to the positive side, which is due to the adsorption of molecular oxygen on the PCM surface in the KOH electrolyte [27]. The specific capacity of PCMs is 15-45 F/g at the potential of zero charge that indicates the ability to spontaneous charge of the porous structure, which occurs according to electrostatic mechanism.

The maximum specific capacitance of PCMs is 150 F/g at negative polarization and decreases with increasing of electrode potential. The capacity is reduced by 25-40 % in the region of positive potentials (0.1-0.2 V). Stationary potentials of carbon materials are in the range of $-0.25 - 0.05$ V, in which DEL is formed by hydrated electrolyte ions [21]. This region is characterized by an increase in capacity at negative polarization and its decreasing at positive polarization. The use of an aqueous solution of KOH as an electrolyte leads to a change in the chemical potentials of ions. As a result the window of potentials of the DEL charge according to the electrostatic mechanism expands from $-0.01 \div -0.25$ V [21] to $-0.01 \div -0.49$ V [27] and the shift of work potentials with the contribution of electrosorption of hydrogen (from $-0.25 \div -0.65$ V to $-0.49 \div -0.9$ V). Positive polarization in the range of $-0.01 \div 0.1$ V leads to electrosorption of hydroxyl groups [27]. At high positive potentials (above 0.2 V) the electrosorption process can lead to an increase in irreversible reactions, such as the formation of water molecules.

To set the correlation between the specific surface area of pores of different diameters and the capacity of the

PCM/electrolyte system, the specific capacity of PCMs was determined by chronopotentiometric method at different operating currents (Fig. 13).

Given that the potassium ion may have two hydrate shells with radii of 0.266 and 0.36 nm [28], it is assumed that pores with a diameter greater than 0.5 nm are electrochemically available for charge in the KOH electrolyte [29]. Both the size of the electrolyte ion and the pore size will affect the maximum DEL. The highest energy of adsorption interaction of PCM with electrolyte molecules is observed in narrow pores of 0.5-1 nm in size. Pores larger than 2 nm are as transport channels for the electrolyte to enter the working pores.

The relationship between the specific surface area of PCM (Table 4) and the specific capacity value (Fig. 13) can be traced.

As follows from Table 4, an increase in the pore area of 1.25-1.65 nm in size leads to an increase in the specific capacity of PCM. For samples C075 and C100, in addition to a given range of pores, a significant contribution to the total area is made by pores of 2.05-2.65 nm in size, which serve as transport channels for the electrolyte. The contribution of transport pores is manifested in the minimal reduction of the specific capacitance with increasing discharge current. Carbon materials C125 \div C175, in which pores with a size of 1.05-1.25 nm predominate, have a specific capacity of 35-50 % lower than previous samples, which is probably due to the presence of pores only in a narrow range. The presence of pores of 1.25-1.45 nm in size with significant area (554 m²/g) for sample C200 provides to the increase in the capacity of PCM. However, a small number of pores in the range of 1.65-1.85 nm leads to a sharp decline in its specific capacity with a slight increase in discharge current. Thus, by changing the ratio of the mass of the

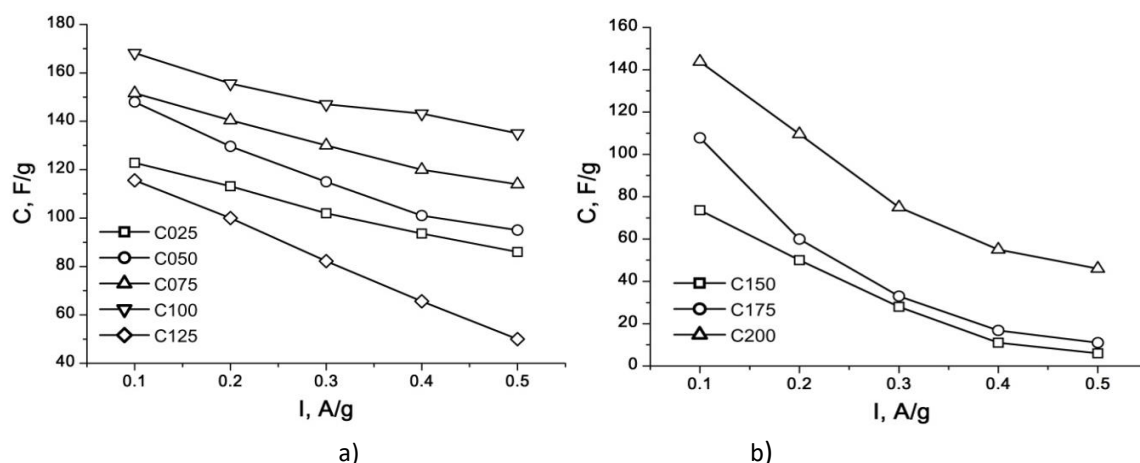


Fig. 13. Dependence of specific capacitance on discharge current for microporous (a) and mesoporous (b) carbon materials.

Table 4.

Dependence of the specific surface area (m^2/g) of PCMs on the pore size

Pore size, nm	Sample							
	C025	C050	C075	C100	C125	C150	C175	C200
1.05-1.25	0	0	0	0	1048	486	414	0
1.25-1.45	620	751	885	790	118	6	15	554
1.45-1.65	9	20	40	54	3	57	1	2
1.65-1.85	2	12	24	26	60	65	43	48
1.85-2.05	7	14	22	13	17	27	21	23
2.05-2.25	27	23	62	67	0	1	0	0
2.25-2.45	26	20	64	107	0	35	0	0
2.45-2.65	15	7	37	75	23	47	9	10
2.65-2.85	12	9	36	68	81	53	36	41
2.85-3.05	6	2	15	40	37	36	26	29
3.05-3.25	4	2	9	32	31	31	23	25

activating agent (orthophosphoric acid) to the mass of plant raw materials, one can effect the pore size distribution of PCM, which in turn allows you to control its specific electrical capacity.

electrode/electrolyte interface and pseudocapacity. The maximum capacity of the PCM/KOH system is achieved by using microporous carbon materials C075-C125 with a small proportion of transport mesopores, which have a pore distribution in the range of 1-3 nm.

Conclusions

According to thermogravimetric studies, the addition of 4-8% orthophosphoric acid to the raw material leads to a sharper drop in mass with increasing temperature compared to the initial material, due to the simultaneous interaction of acid with sorbed water, hemicellulose and lignin. Orthophosphoric acid causes the dehydration of the initial material, which leads to a decrease in the temperature of material degradation, increase the mass of the PCM obtained and promotes the formation of its porous structure.

Carbon material with a microporous structure and a total pore volume $0.86 \text{ cm}^3/\text{g}$ is formed at a growth of Y from 0.25 to 1.25. A further increase Y from 1.25 to 2 results in the formation of mesopores 5-50 nm in size, which is 75 % of the total pore volume.

It was found that the accumulation of capacity in the ECs is due to the formation of DEL at the

Ivanichok N.Y. – Candidate in Physics and Mathematics, Doctoral Student, Leading Specialist of Joint Educational and Scientific Laboratory for Physics of Magnetic Films;
Kolkovskiy P.I. – Candidate in Physics and Mathematics, Senior Researcher;
Soltys A.M. – PhD Student;
Boychuk V.M. – Doctor in Physics and Mathematics, Professor of Department of Physics and Methods of Teaching;
Mandyuk V.I. – Doctor in Physics and Mathematics, Professor of Department of Computer Engineering and Electronics;
Yablon L.S. – Doctor in Physics and Mathematics, Professor of Department of Physics and Methods of Teaching;
Rachiy B.I. – Doctor in Physics and Mathematics, Professor of Department of Materials Science and New Technologies.

- [1] V.D. Canh, S. Tabata, S. Yamanoi, Y. Onaka, T. Yokoi, H. Furumai, H. Katayama, *Evaluation of Porous Carbon Adsorbents Made from Rice Husks for Virus Removal in Water*, *Water*, 13(9), Art. 1280 (2021); <https://doi.org/10.3390/w13091280>.
- [2] J. Li, R. Holze, S. Moyo, S. Wang, S. Li, T. Tang, X. Chen, *Three-dimensional hierarchical porous carbon derived from natural resources for highly efficient treatment of polluted water*, *Environ. Sci. Eur.*, 33, Art. 98 (2021); <https://doi.org/10.1186/s12302-021-00527-6>.
- [3] S. Sircar, T.C. Golden, M.B. Rao, *Activated Carbon for Gas Separation and Storage*, *Carbon*, 34(1) 1 (1996); [https://doi.org/10.1016/0008-6223\(95\)00128-X](https://doi.org/10.1016/0008-6223(95)00128-X).
- [4] Y. Wu, B.M. Weckhuysen, *Separation and Purification of Hydrocarbons with Porous Materials*, *Angew. Chem. Int. Ed.*, 60(35), 18930 (2021); <https://doi.org/10.1002/anie.202104318>.
- [5] B.I. Rachiy, I.M. Budzulyak, E.A. Ivanenko, S.L. Revo, *A composite of nanoporous carbon and thermally exfoliated graphite as an effective electrode material for supercapacitors*, *Surface Engineering and Applied Electrochemistry*, 51(5), 501 (2015); <https://doi.org/10.3103/S1068375515050129>.
- [6] Y.Y. Starchuk, B.I. Rachiy, I.M. Budzulyak, P.I. Kolkovskiy, N.Y. Ivanichok, M.O. Halushchak, *Electrochemical Properties of Hybrid Supercapacitors Formed Based on Nanoporous Carbon and Nickel Tungstate*, *Journal of Nano- and Electronic Physics*, 13(6), Art. 06021 (2021); [https://doi.org/10.21272/jnep.13\(6\).06021](https://doi.org/10.21272/jnep.13(6).06021).
- [7] V. Boichuk, V. Kotsyubynsky, A. Kachmar, B. Rachiy, L. Yablon, *Effect of Synthesis Conditions on Pseudocapacitance Properties of Nitrogen-Doped Porous Carbon Materials*, *Journal of Nano Research*, 59, 112(2019); <https://doi.org/10.4028/www.scientific.net/JNanoR.59.112>
- [8] V.I. Mandzyuk, I.F. Myronyuk, V.M. Sachko, B.I. Rachiy, Yu.O. Kulyk, I.M. Mykytyn, *Structure and Electrochemical Properties of Saccharide-derived Porous Carbon Materials*, *Journal of Nano- and Electronic Physics*, 10(2), Art. 02018 (2018); [https://doi.org/10.21272/jnep.10\(2\).02018](https://doi.org/10.21272/jnep.10(2).02018).
- [9] V.I. Mandzyuk, N.I. Nagirna, R.P. Lisovskyy, *Morphology and Electrochemical Properties of Thermal Modified Nanoporous Carbon as Electrode of Lithium Power Sources*, *Journal of Nano- and Electronic Physics*, 6(1) Art. 01017 (2014).
- [10] R. Wang, R. Wu, C. Ding, Z. Chen, H. Xu, Y. Liu, J. Zhang, Y. Ha, B. Fei, H. Pan, *Porous Carbon Architecture Assembled by Cross-Linked Carbon Leaves with Implanted Atomic Cobalt for High-Performance Li-S Batteries*, *Nano-Micro Letters*, 13(1), Art. 151 (2021); <https://doi.org/10.1007/s40820-021-00676-6>.
- [11] B.I. Rachiy, B.K. Ostafiychuk, I.M. Budzulyak, N.Y. Ivanichok, *Specific Energy Characteristics of Nanoporous Carbon Activated by Orthophosphoric Acid*, *Journal of Nano- and Electronic Physics*, 7(4), Art. 04077 (2015).
- [12] K.-C. Lee, M.S.W. Lim, Z.-Y. Hong, S. Chong, T.J. T., G.-T. Pan, C.-M. Huang, *Coconut Shell-Derived Activated Carbon for High-Performance Solid-State Supercapacitors*, *Energies*, 14, Art. 4546 (2021); <https://doi.org/10.3390/en14154546>.
- [13] S. Yang, K. Zhang, *Converting Corncob to Activated Porous Carbon for Supercapacitor Application*, *Nanomaterials*, 8(4), Art. 181 (2018); <https://doi.org/10.3390/nano8040181>.
- [14] R.Ya. Shvets, I.I. Grygorchak, A.K. Borysyuk, S.G. Shvachko, A.I. Kondyr, V.I. Baluk, A.S. Kurepa, B.I. Rachiy, *New nanoporous biocarbons with iron and silicon impurities: synthesis, properties, and application to supercapacitors*, *Phys. Solid State*, 56(10), 2021 (2014); <https://doi.org/10.1134/s1063783414100266>.
- [15] J. Zhou, A. Luo, Y. Zhao, *Preparation and characterisation of activated carbon from waste tea by physical activation using steam*, *Journal of the Air & Waste Management Association*, 68(12), 1269 (2018); <https://doi.org/10.1080/10962247.2018.1460282>.
- [16] N.Ya. Ivanichok, O.M. Ivanichok, B.I. Rachiy, P.I. Kolkovskiy, I.M. Budzulyak, V.O. Kotsyubynsky, V.M. Boychuk, L.Z. Khrushch, *Effect of the carbonization temperature of plant biomass on the structure, surface condition and electrical conductive properties of carbon nanoporous material*, *Journal of Physical Studies* 25(3), Art. 3801 (2021); <https://doi.org/10.30970/jps.25.3801>.
- [17] I.F. Myronyuk, V.I. Mandzyuk, V.M. Sachko, R.P. Lisovskyy, B.I. Rachiy, *Morphological and Electrochemical Properties of the Lactose-derived Carbon Electrode Materials*, *Journal of Nano- and Electronic Physics* 8(4), Art. 04006 (2016); [https://doi.org/10.21272/jnep.8\(4\(1\)\).04006](https://doi.org/10.21272/jnep.8(4(1)).04006).
- [18] C. Wang, B. Yan., J. Zheng, L. Feng, Z. Chen, Q. Zhang, T. Liao, J. Chen, S. Jiang, C. Du, S. He, *Recent progress in template-assisted synthesis of porous carbons for supercapacitors*, *Advanced Powder Materials* 1(2), Art. 100018 (2022); <https://doi.org/10.1016/j.apmate.2021.11.005>.
- [19] V.I. Mandzyuk, I.F. Myronyuk, V.M. Sachko, I.M. Mykytyn, *Template Synthesis of Mesoporous Carbon Materials for Electrochemical Capacitors*, *Surf. Eng. Appl. Electrochem.* 56(1), 93 (2020); <https://doi.org/10.3103/S1068375520010123>.
- [20] W.C. Lim, C. Srinivasakannan, N. Balasubramanian, *Activation of palm shells by phosphoric acid impregnation for high yielding activated carbon*, *J. Anal. Appl. Pyrolysis*, 88(2), 181 (2010); <https://doi.org/10.1016/j.jaap.2010.04.004>.
- [21] A.I. Belyakov, A.M. Brintsev, N. Khodyrevskaya, *Proc. 14-th International Seminar on Double Layer Capacitors and Hybrid Energy Storage Devices*. Deerfield Beach, USA. 84 (2004).

- [22] H. Wang, L. Pilon, *Physical interpretation of cyclic voltammetry for measuring electric double layer capacitances*, *Electrochim. Acta* 64, 130 (2012); (<https://doi.org/10.1016/j.electacta.2011.12.118>).
- [23] K.D. Pershina, K.O. Kazdobin, *Impedance spectroscopy of electrolytic materials* (Osvita Ukrainy, Kyiv, 2012).
- [24] E. Barsoukov, J.R. Macdonald, *Impedance spectroscopy: theory, experiment, and applications* (John Wiley & Sons Inc., New Jersey, 2018).
- [25] B.E. Conway, *Electrochemical supercapacitors: scientific fundamentals and technological applications* (Kluwer-Plenum, New York, 1999).
- [26] E. Lust, *Encyclopedia of Interfacial Chemistry. Surface Science and Electrochemistry*. Elsevier Inc. 316 (2018); <https://doi.org/10.1016/B978-0-12-409547-2.13613-3>.
- [27] B.P. Bahmatyuk, A.S. Kurepa, I.I. Grygorchak, *Impedance spectroscopy of supercapacitors based on nanoporous activated carbon material*, *Journal of National University "Lvivska Politechnika" "Physical & mathematical sciences"* 687, 188 (2010).
- [28] M.N. Rodnikova, S.A. Zasyplin, G.G. Malenkov, *About the mechanism of negative hydration*, *Reports of the Academy of Sciences*, 324(2), 368 (1992).
- [29] E. Frackowiak, F. Beguin, *Carbon Materials for the Electrochemical Storage of Energy in Capacitors*, *Carbon* 39(6), 937 (2001); [https://doi.org/10.1016/S0008-6223\(00\)00183-4](https://doi.org/10.1016/S0008-6223(00)00183-4).

Н.Я. Іванічок¹, П.І. Колковський², А.М. Солтис¹, В.М. Бойчук¹, В.І. Мандзюк¹,
Л.С. Яблонь¹, Б.І. Рачій¹

Вплив ортофосфорної кислоти на енергоємні параметри пористих вуглецевих електродних матеріалів

¹Прикарпатський національний університет імені Василя Стефаника, Івано-Франківськ, Україна,
volodymyr.mandzyuk@pnu.edu.ua

²Інститут загальної та неорганічної хімії імені В.І. Вернадського НАН України, Київ, Україна

У роботі досліджено вплив концентрації ортофосфорної кислоти як активуючого агента на пористу структуру вуглецевих матеріалів, отриманих із кісточок абрикоса, та енергоємні параметри електрохімічних конденсаторів, сформованих на їх основі. Встановлено, що в кислотноактивованих пористих вуглецевих матеріалах (ПВМ), змінюючи відношення маси активуючого агента до маси вихідної сировини, можна контролювати розподіл пор за розмірами в межах 0,5-20 нм та питому площу поверхні в діапазоні 775-1830 м²/г. Використання методів циклічної вольтамперометрії, імпедансної спектроскопії та хронопотенціометрії дало можливість встановити ємнісний характер процесів накопичення заряду в кислотноактивованих ПВМ, а також визначити вклад пор певного розміру в питому електроємність системи ПВМ/електроліт.

Ключові слова: пористий вуглецевий матеріал, активуючий агент, питома поверхня, розподіл пор за розмірами, питома ємність, електрохімічний конденсатор.

PACS: 81.10.-h; 42.70.-a

ISSN 1729-4428

K. Balakrishnan¹, S. Sakthy Priya^{1,2}, A. Lakshmanan^{1,3}, P. Surendran^{1,4}, Karthik Kannan⁵,
P. Geetha⁶, G. Vinitha⁷, P. Praveen Kumar⁸, P. Rameshkumar^{8*}

Studies on structural, optical nonlinearity and antibacterial activity of Piperazine (bis) p-toluenesulfonate single crystal for optical limiting and biological applications

¹PG and Research Department of Physics, Nehru Memorial College (Autonomous), Affiliated to Bharathidasan University,
Puthanampatti 621 007, India

²Department of Physics, Arignar Anna Government Arts College, Namakkal 637 002, Tamilnadu, India

³Department of Physics, MAM College of Engineering, Siruganur, Tiruchirappalli 621 102, Tamilnadu, India

⁴Department of Physics, Government Arts and Science College, Komarapalayam 638 183, Tamilnadu, India

⁵Chemical Sciences Department and the Radical Research Center, Ariel University, Ariel 40700, Israel

⁶Department of Physics, Quaid-E-Millath Government College for Women (Autonomous), Chennai 600 002, Tamilnadu, India

⁷Division of Physics, School of Advanced Sciences, VIT Chennai 600127, Tamil Nadu, India

⁸Department of Physics, Presidency College (Autonomous), Chepauk, Triplicane, Chennai 600005, Tamilnadu, India,
rameshkumarevr@gmail.com

Piperazine (bis) p-toluenesulfonate (PPTSA), an organic single crystal was synthesized and grown at environmental temperature by slow evaporation process using methanol as the solvent. The grown PPTSA crystal is from the *triclinic* system and belongs to the space group $P\bar{1}$. Powder X-ray diffraction was performed to ensure lattice parameters. Analysis and confirmation of functional groups and bonds were carried out through FT-IR spectral study. The optical characteristics were investigated using the UV-Vis spectrum such as the optical absorption, cut-off wavelength were calculated. The photoluminescence investigation was conducted to assess the luminous characteristics of grown crystal. The calculated NLO parameters like β , n_2 , and $\chi^{(3)}$ were found to be 0.0495×10^{-4} (cm/W), 8.705×10^{-10} (cm²/W), 5.316×10^{-7} (esu) and Optical Limiting threshold value was found to be 3.074×10^{-3} (Wcm⁻²). Antibacterial studies were carried out to investigate the biological significance against selected foodborne germs.

Keywords: Crystal growth, optical material, optical limiting, antibacterial activity.

Received 23 August 2022; Accepted 30 January 2023.

Introduction

Nonlinear optical (NLO) materials received a lot of attention over decades owing to the numerous uses in photonics, such as light-emitting diodes, telecommunication system, high data storage, optical switching and drug delivery [1-3]. Organic nonlinear optical material researches have gained significant attention owing to its usage in optical devices. They have considerable optical susceptibilities and an inherent quick response time as compared to inorganic compound.

Because of the delocalized electrons at π - π^* orbitals, organic materials are anticipated to have rather significant nonlinear optical characteristics. This anticipation motivates the considerable search among organic crystals for improved NLO materials. When compared to inorganic materials, NLO chromophores are implanted in organic materials in a noncentrosymmetric way, revealing excellent nonlinear activity [3-6]. Tosylic acid, also known as p-toluene sulfonic acid, is an organic acid available in solid phase. Charge transfer has been achieved due to the presence of CH₃ group as an electron donor and

sulfonate group serves as an acceptor in the title compound. Complexes including organic and inorganic bases that may aid in the induction of high NLO behavior [7-10]. On the other side of NLO materials, organic molecules with full conjugated bonds agree to form a group. Over the previous two decades, The NLO features of big organic molecules have been the subject of considerable research. Piperazine is an aromatic ring where nitrogen atoms are located in 1, 4 of the ring that makes up an organic molecule [11].

The grown PPTSA crystal was studied by powder X-ray diffraction (PXRD), FTIR, optical absorption, photoluminescence, and Z-scan analysis. Furthermore, the grown crystal was tested for antibacterial activity against some bacterial species.

I. Experimental procedures

1.1. Materials synthesis and crystal growth

PPTSA title crystal was grown by conventional slow evaporation method from the purchased chemicals piperazine and p-toluenesulfonic acid in 1:1 equimolar ratio taking methanol as solvent at ambient temperature. Fig. 1 depicts the chemical reaction process of the produced PPTSA substance. After dissolving the reactants in methanol, the mixture was stirred for 6 hours using a magnetic stirrer to achieve homogeneous solution before being filtered through standard filter paper. The impurities-free saturated solution was wrapped with a perforated sheet and allowed to evaporate in a dust-free environment. The grown crystal was reaped after a span of four weeks and harvested crystal in depicted in Fig. 2.

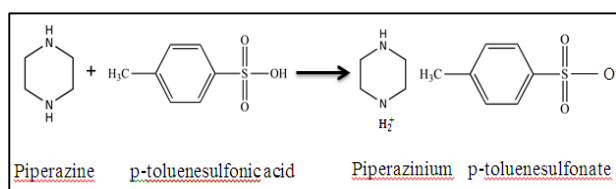


Fig. 1. Reaction scheme of PPTSA.

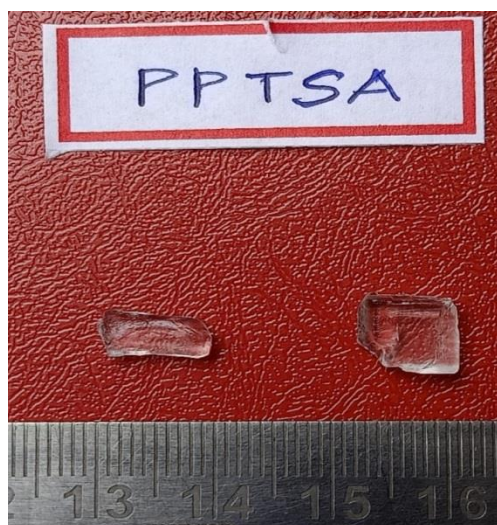


Fig. 2. Photograph of the grown PPTSA single crystal.

1.2. Instrumentation

Investigation of crystal structure was performed by an

XPRT-PRO powder X-ray diffractometer with CuK α radiation ($\lambda=1.5406 \text{ \AA}$, 0.1 min^{-1} , 10° to 80°). Perkin-Elmer (model: Spectrum Two) FTIR spectrophotometer with KBr pellet, the presence of chemical bonding and vibrational modes in the title sample PPTSA were affirmed. The spectra showing optical absorption were recorded using a Perkin Elmer UV-Visible spectrometer (model: Lambda 35) with a wavelength range of 190–1100 nm. The spectra of luminescence were captured using a spectrofluorophotometer (Shimadzu/RF6000) with a xenon lamp as the excitation of cause. Under CW laser (532 nm) stimulation, optical characteristics of nonlinear third-order were determined using a Z-scan experiment. The disc diffusion technique was used to explore the biological activity against chosen bacterial species.

II. Results and discussion

Fig. 3 depicts the powder X-ray diffraction pattern of grown PPTSA crystal. This experiment validated the triclinic crystal structure with the space group $P\bar{1}$ and lattice factors $a = 5.9644 \text{ \AA}$, $b = 13.1731 \text{ \AA}$, $c = 13.5968 \text{ \AA}$, and $V = 934.32 \text{ \AA}^3$, which are similar to the published values Table 1 [12, 13].

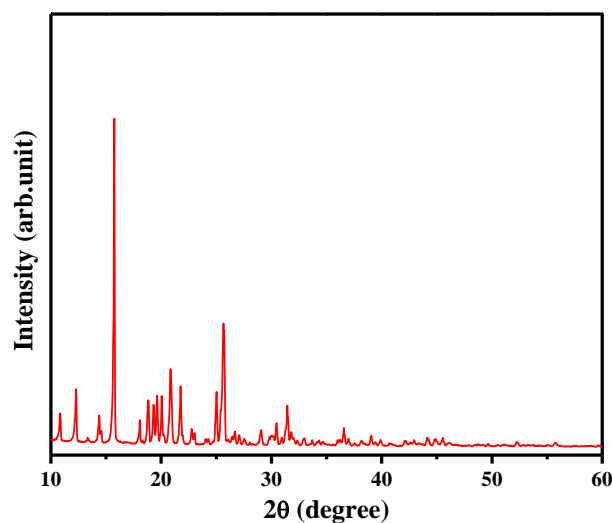


Fig. 3. X-ray diffraction pattern of PPTSA crystal.

$$D = (k\lambda/\beta\cos\theta) \quad (1)$$

$$\beta \cos\theta = \frac{k\lambda}{D} + 4\eta \sin\theta \quad (2)$$

The micro strain (η) in the grown PPTSA crystal's lattice was estimated using the Hall-Williamson equation $\beta \cos\theta = 4\eta\sin\theta + k\lambda/D$. The slope plotted between $\beta \cos\theta$ versus $4\sin\theta$ as depicted in Fig. 4. The existence of tensile strain in the developed crystal is indicated by a positive strain value 6.70×10^{-4} of the grown PPTSA crystal.

$$\delta = \frac{1}{D^2} \quad (3)$$

The dislocation density (δ) influences the characteristics of the crystal and its value is $3.4408 \times 10^{14} \text{ (lines/m}^2\text{)}$ [14].

Table 1.

Crystallographic data for PPTSA single crystal

Parameters	Present work	Reported reference [13]
Unit cell dimensions	a= 5.9644 Å b= 13.1731 Å c= 13.5968 Å $\alpha= 73.680^\circ, \beta = 110.310^\circ,$ $\gamma = 83.390^\circ$	a= 5.9697 Å b= 13.1609 Å c= 13.6027 Å $\alpha= 73.665^\circ, \beta = 110.2650^\circ,$ $\gamma = 83.348^\circ$
Volume	V= 934.32 Å ³	V= 1017.71 Å ³
Space group	P $\bar{1}$	P $\bar{1}$
System	Triclinic	Triclinic
Crystallite Size (D) nm	53.91 nm	
Dislocation Density (δ)	3.4408×10^{14} lines/m ²	

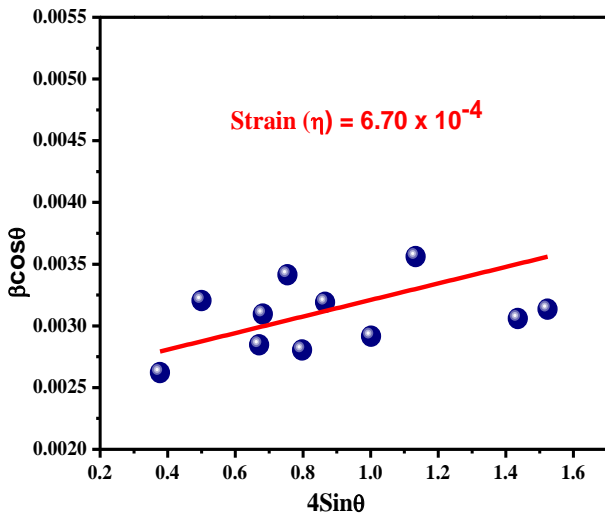


Fig. 4. Williamson-Hall plot of PPTSA crystal.

Fig. 5 displays FT-IR spectrum of grown PPTSA crystal. The N-H stretching of piperazine ions corresponds to vibrations at 3435 cm⁻¹ [15]. The peaks at 3001 cm⁻¹ and 2753 cm⁻¹ suggest the absorption of C-H symmetric and asymmetric bending vibration. The peak of p-toluenesulfonic acid C=C-H stretching mode is 3001 cm⁻¹. Bands at 2816 and 2753 cm⁻¹ suggest attenuation of the C-H stretching mode. The minor peak at 1916 cm⁻¹ is due to the aromatic overtones of p-toluenesulfonic acid [16-17]. The NH₂⁺ deformation is responsible for the peaks at 1624 and 1558 cm⁻¹. At 1459 cm⁻¹, the C=C stretching phase occurred. The peak of the N-H asymmetric bending vibration is 1495 cm⁻¹. Stretching of CH₂ has a peak at 1439 cm⁻¹. At 1396 cm⁻¹, the sulphonate group revealed its stretching vibration. The peak at 1380 cm⁻¹ is caused by CH₂ deformation. The asymmetric and symmetric stretching peaks for the C-N group were 1317 and 1189 cm⁻¹, correspondingly. The C-H group's in-plane and out-of-plane bending modes were 1085 and 737 cm⁻¹, respectively [18]. Table 2 lists all of the wavenumbers as well as the functional groups to which they belong.

The fundamental and crucial quality for piezoelectric, photonic and electro-optic materials is the transparent nature of the formed crystal in the whole spectrum. Electronic transitions in the crystal PPTSA could be understood when incident radiation interacts with the grown crystal. Light absorption allows electrons for the transition in σ and π orbitals from the lower to the higher

energy states. For laser frequency conversion applications, optical transmission window, cut-off wavelength and absorption peak are critical characteristics [19]. The absorption spectrum of PPTSA has been recorded and the lower cut-off wavelength was recorded as 305 nm and no absorbance was found beyond this limit that is displayed in Fig. 6. The suggested value of lower cut-off wavelength should lie between 200-400 nm which could be suitable for the fabrication of laser diodes. The electronic excitations between N and H atoms in piperazine cause the cut-off. The low optical absorption value in the whole visible band implies that grown PPTSA crystals are suited for the production of nonlinear optical systems. The formula is used to calculate the band gap [20],

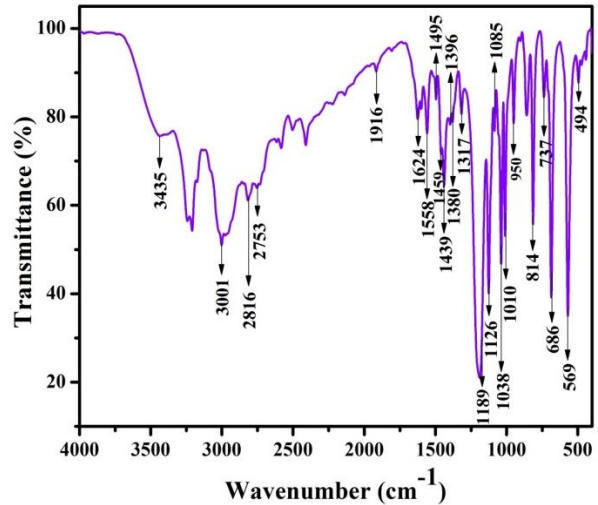


Fig. 5. FTIR spectrum of PPTSA crystal.

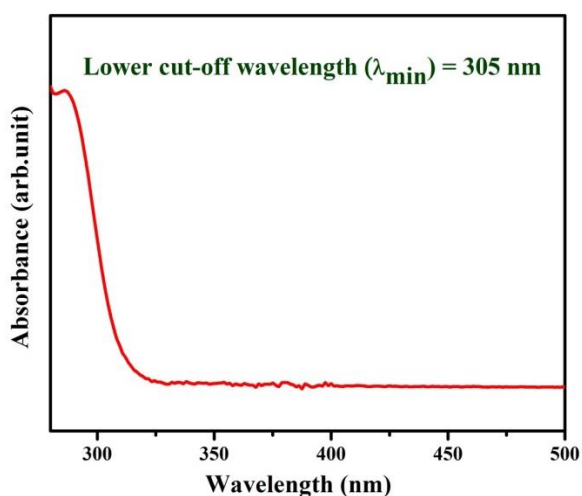
$$E_g = \frac{1240}{\lambda} eV \quad (4)$$

It is determined to be 4.06 eV. The measured spectra and band gap value accord well with the published value. The increased optical transmittance might be owing to fewer flaws, which raises the output intensity. This is more appropriate for NLO applications. The optical absorption co-efficient on photon energy could be calculated using the equation below [21],

$$\alpha = \frac{2.3026}{t} \log_{10} \left(\frac{100}{T} \right) \quad (5)$$

Table 2.

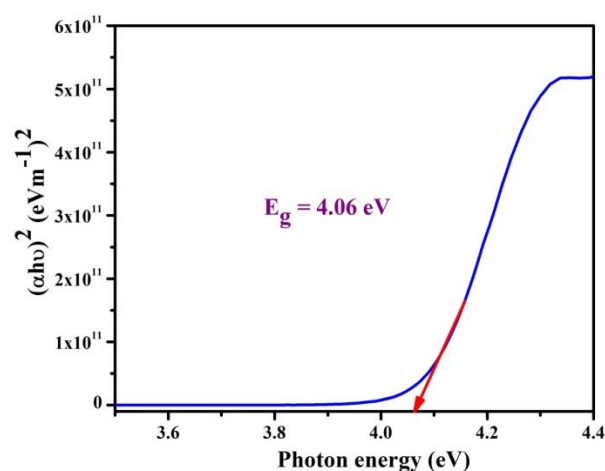
Vibration wavenumbers and their associated assignments of PPTSA title compound	
Wavenumber (cm ⁻¹)	Assignments
3435	N-H stretching
3001	C=C-H symmetric stretching mode
2816	C-H stretching mode
2753	Asymmetric stretching vibrations
1916	p-toluenesulfonic acid
1624	NH ₂ ⁺ deformation
1558	NH ₂ ⁺ deformation
1495	N-H asymmetric bending vibration
1459	C=C stretching
1439	Stretching of CH ₂
1396	Stretching vibration
1380	CH ₂ deformation
1317	C-N group's asymmetric
1189	Symmetric stretching
1126	Asymmetric stretching vibrations of the C-C group
1085	C-H group's in-plane bending modes
1038	C-C group's bending vibration
1010	C-S stretching vibration
950	S-O-C stretching vibration
814	p-toluenesulfonic acid
737	Symmetric and out-of-plane bending modes
686	N-H wagging vibration
596	C-C-N deformations
494	C-N-C deformations


Fig. 6. Absorption spectrum of PPTSA crystal.

Where t is the sample thickness and T is the transmittance (percent). The energy band gap values was calculated using standard relation [22],

$$(\alpha h\nu)^2 = A(h\nu - E_g)^n \quad (6)$$

Where E_g indicates the band gap and A indicates the constant. The band gap values are determined by plotting against $(\alpha h\nu)^2$ versus $h\nu$, as shown in Fig. 7, and it is 4.06 eV. The theoretically computed band gap value agrees with the observed value. The band gap of the PPTSA crystal demonstrates its better visible field properties.


Fig. 7. Tauc's plot of PPTSA crystal.

Fluorescence is vital in medical and scientific studies in aromatic compounds or with many conjugated double bonds that have a high degree of permanence [23]. Good quality of crystal can be analyzed with this instrumentation. The inherent properties of the crystal like crystalline nature, dislocations, structural arrangement and impurities are attributed with the intensity of the emission spectra of the sample [24]. The Photoluminescence spectrum was recorded with the aid of spectrofluorometer for the grown title compound PPTSA and depicted in Fig. 8. When the sample was stimulated with 280 nm, the spectra illustrate a wide elevation pinpointed at 571 nm, indicating yellow radiation. The increased intensity of emission can be used to detect organic organisms. The inclusion of electron-donating group NH and electron-drawing carboxylic group which might increase electron

mobility would result in greater PL emission.

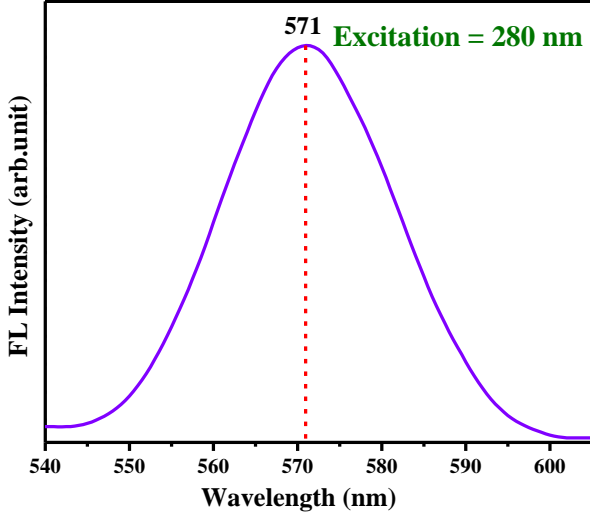


Fig. 8. Luminescence spectra of PPTSA crystal.

The third-order NLO characteristics of PPTSA sample were studied by Z-scan measurements to calculate the nonlinear absorption co-efficient (β), refractive index (n_2), and susceptibility ($\chi^{(3)}$) [25-28]. CW laser (532 nm) with a laser intensity of 100 mW was employed. The title crystal was attached to 90° and displaced along the negative axis. The propagation direction is along the -Z to +Z axis. The sample table can be translated in a variety of ways. Each movement is precisely controlled by a computer. The sample's transmitted intensity was measured and it is sensed by light detector and quantified.

The predicted intensity in a closed aperture (CA) is proportional to the aperture radius (2 mm) and remains

constant throughout the operation. Using an open aperture (OA) approach, intensity was directly recorded by placing a lens in front of the detector to determine the nonlinear absorption co-efficient (β) and an aperture was located between the lens and the front of the detector to determine NLR (n_2). Fig. 9 (a & b) shows the PPTSA crystals CA and OA Z-scan curves, respectively. The refractive index of the grown crystal and their absorption nature directly affect the power of a laser beam. According to the NLR values, the sample generates further focusing or defocusing. The samples CA pattern demonstrates self-defocusing behavior. The OA pattern exhibits reverse saturable absorption. Third-order NLO parameters were calculated using the standard relation [29]. β was determined using OA readings as follows,

$$\beta = \frac{2\sqrt{2}\Delta T}{I_0 L_{\text{eff}}} (m/w) \quad (9)$$

The following equation estimates the samples susceptibility.

$$\chi^{(3)} = \sqrt{(R_e \chi^{(3)})^2 + (I_m \chi^{(3)})^2} \quad (10)$$

Where the components in the expression are given as

$$R_e(\chi^{(3)}) = \frac{10^{-4} \varepsilon_0 c^2 n_0^2 n_2}{\pi} (cm^2/W) \quad (11)$$

$$I_m(\chi^{(3)}) = \frac{10^{-2} \varepsilon_0 c^2 n_0^2 \lambda \beta}{4\pi^2} (cm/W) \quad (12)$$

Where ε_0 (8.854×10^{-12} F/m), n_0 and c are obvious notations. The calculated NLO susceptibility value was found to be 5.316×10^{-7} (esu). Table 3 shows the third-order NLO parameters for the grown PPTSA crystal. The

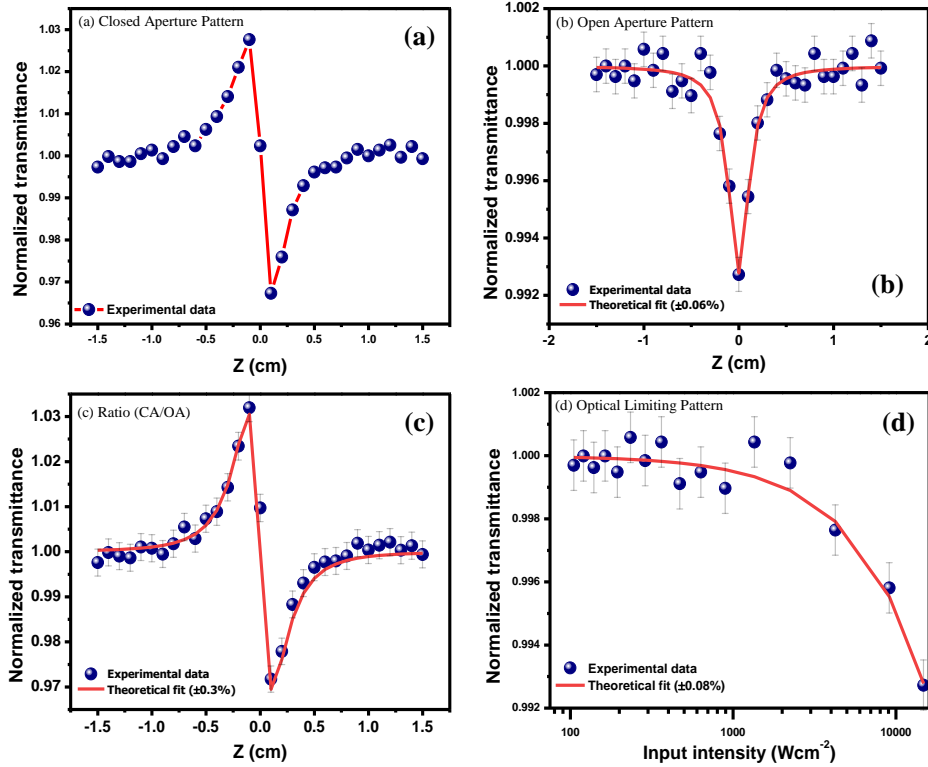


Fig. 9. (a) Closed aperture, (b) Open aperture, (c) Ratio of closed to open aperture z-scan and (d) Optical limiting pattern of PPTSA sample.

material's nonlinear optical properties indicate that it might be employed in optoelectronics devices such as optical limiting, night vision devices, and light emitting diode applications.

The variation of normalized transmittance with respect to the input intensity of laser beam has been displayed in Fig. 9d, is known as optical limiting curve which is plotted from the data extracted from open aperture scan. The plot suggests that the normalized transmittance is linear at low input intensity when the intensity starts increasing at one particular intensity the nonlinearity arises called as onset limiting threshold. The normalized transmittance approaches minimum at $Z=0$. The limiting threshold intensity is found different for different input intensities. This investigation is a valuable tool to fabricate optical limiting devices. The synthesized single crystal has been acknowledged as a potential candidate for optical limiting applications.

In recent years researchers focus on the biomedical

applications in addition to the NLO applications, one among them is antibacterial activity. The titular compound PPTSA was examined against human pathogens gram +Ve (*Klebsiella pneumoniae*, *Escherichia coli*), and gram -Ve (*Streptococcus aureus*, *Streptococcus Pneumoniae*) through disc diffusion method. The observed inhibition zones in the diffusion plate have been displayed in Fig. 10. Zone of inhibition for evaluating antibacterial activity was taken in the order 40, 50, and 60 μ L respectively in which the grown PPTSA shows an excellent response 24.5 mm (60 μ L) against gram negative *Streptococcus aureus*. This result ensures concentration makes significant impact on inhibition zone (Table 4). As a matter of fact commercially available amoxicillin shows only 15 mm (60 μ L). Characteristics such as intermolecular interaction, solubility, and conductivity may be important in antibacterial activity. Investigating the title compound's for antibacterial properties has demonstrate that the existence of hydrogen bonding interactions boost

Table 3.

NLO parameters of the grown PPTSA single crystal

Third-order NLO parameters	Values
Laser wavelength	532 (nm)
Focal length of lens used	130 (mm)
Radius of aperture used	1.5 (mm)
Radius of the beam on aperture	3 (mm)
Intensity of the laser at the focus	0.01478 (MW/cm ²)
Reighley range (Z_R)	1.271 (mm)
Nonlinear absorption coefficient (β)	$0.0495 \times 10^{-4} \text{ cm/W}$
Nonlinear refractive index (n_2)	$8.705 \times 10^{-10} \text{ cm}^2/\text{W}$
Real part of the third order susceptibility [$R_e(\chi^{(3)})$] cm^2/W	$2.039 \times 10^{-7} \text{ esu}$
Imaginary part of the third order susceptibility [$I_m(\chi^{(3)})$] cm/W	$4.910 \times 10^{-7} \text{ esu}$
Third order nonlinear optical susceptibility [$\chi^{(3)}$]	$5.316 \times 10^{-7} \text{ esu}$
Optical Limiting threshold values (OL)	$3.074 \times 10^{-3} (\text{Wcm}^{-2})$

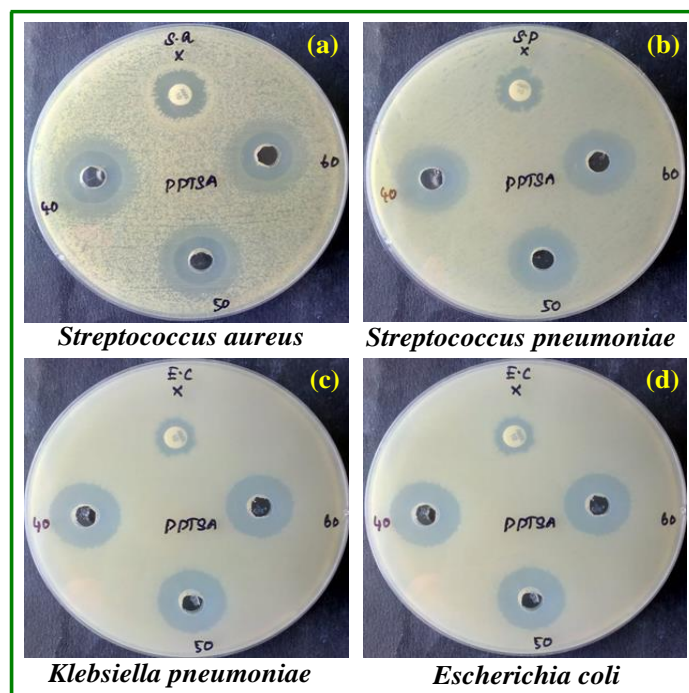


Fig. 10. Antibacterial plate photos of the grown PPTSA crystal (a) *Streptococcus aureus*, (b) *Streptococcus pneumoniae*, (c) *Klebsiella pneumoniae* and (d) *Escherichia coli*.

Table 4

The antibacterial activity of PPTSA single crystal

Test microorganism	Gram reaction	Zone of inhibition (mm)			
		40 (μ L)	50 (μ L)	60 (μ L)	Amx (μ L)
<i>Klebsiella pneumoniae</i>	G+	21	21	22	16
<i>Escherichia coli</i>	G+	19	19	19	11
<i>Streptococcus aureus</i>	G-	24	23	24	15
<i>Streptococcus Pneumoniae</i>	G-	20	20	20	13

antibacterial effectiveness significantly [31-35]. Furthermore, the presence of a free HNCCO moiety promotes the delocalization of π -electrons over the PPTSA molecule, increasing lipophilicity [36]. The enhancement of lipophilicity of the compound retards the normal cell processes via degradation of cell's permeability in turn pathogens are made destroyed. Hence the titular compound could be an effective material for bio medical applications [37-40].

Conclusions

Piperazine (bis) p-toluenesulfonate (PPTSA) crystals were successfully grown at ambient temperature using a slow evaporation approach. Crystallinity of the crystal was confirmed with PXRD and crystallizes *triclinic* and belong to $P\bar{1}$. The functional groups of PPTSA crystal was affirmed by FTIR spectra. The UV-Vis spectrum reveals that the energy band gap value is 4.06 eV. The photoluminescence measurements confirmed that the produced crystal could be used to fabricate LEDs. The grown PPTSA crystal exhibits RSA and self-defocusing nature which are inevitable for optical limiting and switching applications. The title crystal PPTSA was

subjected to antibacterial activity against human pathogen and found that it is a efficient material for drug manufacturing.

Acknowledgements

One of the authors P. Surendran is grateful to UGC-NFHE [F1-17.1/2015-16/NFST-2015-17-ST-TAM-1335] and A. Lakshmanan wish to thank the UGC-RGNF [F1-17.1/2016-17/RGNF-2015-17SC-TAM-21802] New Delhi, India, for the financial support.

Conflicts of interest

We declare that we have no conflicts of interest.

Balakrishnan K. – Ph.D Research Scholar;
Sakthy Priya S. – Ph.D in Physics, Guest Lecturer;
Lakshmanan A. – Ph.D in Physics, Assistant Professor;
Surendran P. – Ph.D in Physics, Guest Lecturer;
Kannan Karthik – Ph.D in Physics, Postdoctoral Fellow;
Geetha P. – Assistant Professor;
Vinitha G. – Assistant Professor;
Kumar P. Praveen – Associate Professor;
Rameshkumar P. – Assistant Professor.

- [1] E. Selvakumar, G. Anandha babu, P. Ramasamy, Rajnikant, T. Uma Devi, R. Meenakshi, A. Chandramohan, *Synthesis, growth, structure and spectroscopic characterization of a new organic nonlinear optical hydrogen bonding complex crystal: 3-Carboxyl anilinium p-toluene sulfonate*, Spectrochim. Acta Part A Mol. Biomol. Spectrosc. 125, 114 (2014); <https://doi.org/10.1016/j.saa.2014.01.035>.
- [2] K. Sangeetha, S. Thamocharan, R.R. Babu, S.M. Kumar, *Linear and nonlinear optical properties of 4-nitrobenzoic acid (4-NBA) single crystals*, Bull. Mater. Sci. 41, 73 (2018); <https://doi.org/10.1007/s12034-018-1583-5>.
- [3] R. Aarathi, P. Umarani, C.R. Raja, *Interpretation of molecular structure and third-order nonlinear optical studies of 4-methylbenzylammonium nitrate single crystal*, Appl. Phys. A. 124, 498 (2018); <https://doi.org/10.1007/s00339-018-1913-x>.
- [4] G. Peramaiyan, R.M. Kumar, G. Bhagavannarayana, *Crystal growth, structural, optical and dielectric studies of ammonium p-toluenesulfonate*, J. Cryst. Growth. 408, 14 (2014); <https://doi.org/10.1016/j.jcrysgro.2014.09.011>.
- [5] V. Thayanithi, P.P. Kumar, *Growth, optical, mechanical and thermal behavior of unidirectionally grown L-Glutaminium p-Toluenesulfonate crystal*, Mater. Res. Express. 6, 46207 (2019); <https://doi.org/10.1088/2053-1591/aafd43>.
- [6] S. Sagadevan, P. Murugasen, *Studies on Optical, Mechanical and Electrical Properties of Organic Nonlinear Optical p-Toluidine p-Toluenesulfonate Single Crystal*, J. Cryst. Process Technol. 4, 99 (2014); <https://doi.org/10.4236/jcpt.2014.42013>.
- [7] C. Amirthakumar, B. Valarmathi, I.M. Zahid, G. Vinitha, V. Seetharaman, A. Ramnathan, R.M. Kumar, *Studies on the third order nonlinear optical properties of a novel o-Phenylenediaminium p-Toluenesulfonate single crystal*, Mater. Lett. 247, 25 (2019); <https://doi.org/10.1016/j.matlet.2019.03.068>.
- [8] G. Shanmugam, S. Brahadeeswaran, *Spectroscopic, thermal and mechanical studies on 4-methylanilinium p-toluenesulfonate – a new organic NLO single crystal*, Spectrochim. Acta - Part A Mol. Biomol. Spectrosc. 95, 177 (2012); <https://doi.org/10.1016/j.saa.2012.04.100>.

- [9] M. Suresh, S. Asath Bahadur, S. Athimoolam, *Synthesis, growth and characterization of a new hydrogen bonded organic tosylate crystal: l-alaninium p-toluenesulfonate for second order nonlinear optical applications*, J. Mater. Sci. Mater. Electron. 27, 4578 (2016); <https://doi.org/10.1007/s10854-016-4334-7>.
- [10] R. Kaliammal, S. Sudhahar, G. Parvathy, K. Velsankar, K. Sankaranarayanan, *Physicochemical and DFT studies on new organic Bis-(2-amino-6-methylpyridinium) succinate monohydrate good quality single crystal for nonlinear optical applications*, J. Mol. Struct. 1212, 128069 (2020); <https://doi.org/10.1016/j.molstruc.2020.128069>.
- [11] A. Rathika, M. Antony Lilly Grace, A. Arun Kumar, R. Subramaniyan, R. Suja, *Organic piperazine p-nitrophenol (PPN) single crystal growth and characterization*, Mater. Today Proc. 47, 4741 (2021); <https://doi.org/10.1016/j.matpr.2021.05.663>.
- [12] A. Suvitha, P. Vivek, P. Murugakoothan, *Nucleation kinetics, growth and characterization of guanidinium 3-nitrobenzoate single crystal*, Opt. - Int. J. Light Electron Opt. 124, 3534 (2013); <https://doi.org/10.1016/j.ijleo.2012.10.069>.
- [13] P. Rekha, G. Peramaiyan, M. NizamMohideen, R. Mohan Kumar, R. Kanagadurai, *Synthesis, growth, structural and optical studies of a novel organic Piperazine (bis) p-toluenesulfonate single crystal*, Spectrochim. Acta Part A Mol. Biomol. Spectrosc. 139, 302 (2015); <https://doi.org/10.1016/j.saa.2014.12.069>.
- [14] S. Sakthy Priya, K. Balakrishnan, P. Surendran, A. Lakshmanan, S. Pushpalatha, G. Ramalingam, P. Rameshkumar, K. Kaviyarasu, T. Ashok Hegde, G. Vinitha, *Investigations on structural, electrical, and third order nonlinear optical properties of benzimidazolium maleate single crystal*, Mater. Today Proc. 36, 163 (2021); <https://doi.org/10.1016/j.matpr.2020.02.680>.
- [15] R.U. Mullai, S.R. Kanuru, R. Arul Jothi, S. Gopinath, S. Vetrivel, *Synthesis, growth, thermal, mechanical and optical studies of piperazinium based cupric sulfate (PCS) single crystals: A third order nonlinear optical material*, Opt. Mater. (Amst). 110, 110482 (2020) <https://doi.org/10.1016/j.optmat.2020.110482>.
- [16] S. Gunasekaran, B. Anita, *Spectral investigation and normal coordinate analysis of piperazine*, Indian J. Pure Appl. Phys. 46, 833 (2008); <http://nopr.niscair.res.in/handle/123456789/3024>.
- [17] S. Chinnasami, M. Manikandan, S. Chandran, R. Paulraj, P. Ramasamy, *Growth, Hirshfeld surfaces, spectral, quantum chemical calculations, photoconductivity and chemical etching analyses of nonlinear optical p-toluidine p-toluenesulfonate single crystal*, Spectrochim. Acta Part A Mol. Biomol. Spectrosc. 206, 340 (2019); <https://doi.org/10.1016/j.saa.2018.08.015>.
- [18] R.R. Kumar, P. Sathya, R. Gopalakrishnan, *Structural, vibrational, thermal and optical studies of organic single crystal: Benzotriazolium p-toluene sulfonate (BTPTS)*, in: AIP Conf. Proc., 20508 (2016); <https://doi.org/10.1063/1.4946559>.
- [19] S.V. Ashvin Santhia, B. Aneeba, S. Vinu, R. Sheela Christy, A.M. Al-Mohaimed, D.A. Al Farraj, *Studies on physicochemical and antibacterial deeds of amino acid based L-Threonine sodium bromide*, Saudi J. Biol. Sci. 27, 2987 (2020); <https://doi.org/10.1016/j.sjbs.2020.09.020>.
- [20] S.S.B. Solanki, R.N. Perumal, T. Suthan, *Growth and characterization of propyl 4-hydroxybenzoate single crystal by vertical Bridgman technique*, Mater. Res. Innov. 22, 144 (2018); <https://doi.org/10.1080/14328917.2016.1266428>.
- [21] G. Feng, L. Li, D. Xu, *Optical Properties of CaNb₂O₆ Single Crystals Grown by OF*, Crystals. 11, 928 (2021); <https://doi.org/10.3390/cryst11080928>.
- [22] A.T. Ravichandran, R. Rathika, M. Kumaresavanji, *Growth and Z-scan analysis of semi-organic Bis(picolinic acetate) Zinc(II) single crystal for third order NLO applications*, J. Mol. Struct. 1224, 129048 (2021); <https://doi.org/10.1016/j.molstruc.2020.129048>.
- [23] V. Subhashini, S. Ponnusamy, C. Muthamizhchelvan, B. Dhanalakshmi, *Growth and characterization of piperazinium 4-nitrophenolate monohydrate (PNP): A third order nonlinear optical material*, Opt. Mater. (Amst). 35, 1327 (2013); <https://doi.org/10.1016/j.optmat.2013.01.032>.
- [24] G. Anandha Babu, P. Ramasamy, *Growth and characterization of 2-amino-4-picolinium toluene sulfonate single crystal*, Spectrochim. Acta Part A Mol. Biomol. Spectrosc. 82, 521 (2011); <https://doi.org/10.1016/j.saa.2011.08.003>.
- [25] V. Siva, S. Asath Bahadur, A. Shameem, A. Murugan, S. Athimoolam, M. Suresh, *Synthesis, supramolecular architecture, thermal and optical behavior of 4-methoxyanilinium perchlorate: A promising third-order NLO material for optical limiting device applications*, Opt. Mater. (Amst). 96, 109290 (2019); <https://doi.org/10.1016/j.optmat.2019.109290>.
- [26] V. Siva, A. Shameem, A. Murugan, S. Athimoolam, M. Suresh, S. Asath Bahadur, *A promising guanidinium based metal-organic single crystal for optical power limiting applications*, Chinese J. Phys. 64, 103 (2020) <https://doi.org/10.1016/j.cjph.2020.01.001>.
- [27] A. Anandhan, C. Sivasankari, M. Saravanabhavan, V. Siva, K. Senthil, *Synthesis, crystal structure, spectroscopic investigations, physicochemical properties of third-order NLO single crystal for optical applications*, J. Mol. Struct. 1203, 127400 (2020); <https://doi.org/10.1016/j.molstruc.2019.127400>.
- [28] K. Pichan, S.P. Muthu, R. Perumalsamy, *Crystal growth and characterization of third order nonlinear optical piperazinium bis(4-hydroxybenzenesulphonate) (P4HBS) single crystal*, J. Cryst. Growth. 473, 39 (2017); <https://doi.org/10.1016/j.jcrysgro.2017.05.018>.

- [29] S. Kamaal, M. Mehkoom, M. Muslim, S.M. Afzal, A. Alarifi, M. Afzal, A. Alowais, M. Muddassir, A.N. Albalwi, M. Ahmad, *Crystal Structure, Topological and Hirshfeld Surface Analysis of a Zn(II) Zwitterionic Schiff Base Complex Exhibiting Nonlinear Optical (NLO) Properties Using Z-Scan Technique*, Crystals. 11, 508 (2021); <https://doi.org/10.3390/cryst11050508>.
- [30] K. Nivetha, K. Aravinth, K. Senthil, S. Kalainathan, *Evaluation of structural, spectral, thermal and optical properties of an efficient centrosymmetric organic single crystal 2-[2-(4-diethylamino-phenyl)-vinyl]-1-methyl pyridinium tetrafluoroborate for nonlinear optical applications*, J. Mol. Struct. 1225, 129082 (2021); <https://doi.org/10.1016/j.molstruc.2020.129082>.
- [31] M. Tamil Elakkiya, K. Anitha, *CCDC 1541880: Experimental Crystal Structure Determination*, Mater. Lett. 235, 202 (2019); <https://doi.org/10.1016/j.matlet.2018.10.015>.
- [32] S. Sakthy Priya, K. Balakrishnan, P. Surendran, A. Lakshmanan, S. Pushpalatha, P. Rameshkumar, P. Geetha, K. Kannan, T.A. Hegde, G. Vinitha, *Investigation on nonlinear optical and antibacterial properties of organic single crystal: p-Toluidinium L-Tartrate*, Chem. Data Collect. 31, 100640 (2021); <https://doi.org/10.1016/j.cdc.2020.100640>.
- [33] V. Revathi, K. Karthik, H. Mahdizadeh, *Antibacterial activity and physico-chemical properties of metal-organic single crystal: Zinc (Tris) thiourea chloride*, Chem. Data Collect. 24, 100279 (2019); <https://doi.org/10.1016/j.cdc.2019.100279>.
- [34] S.S. Priya, K. Balakrishnan, P. Surendran, A. Lakshmanan, P. Geetha, P. Rameshkumar, T.A. Hegde, G. Vinitha, A.A. Raj, *Investigations on Structural, Mechanical, Optical, Electrical, Third-Order Nonlinear Optical and Antibacterial Activity of 4-Aminopyridine Monophthalate Single Crystal*, J. Electron. Mater. 50, 291 (2021); <https://doi.org/10.1007/s11664-020-08497-w>.
- [35] K. Kannan, D. Radhika, S. Vijayalakshmi, K.K. Sadasivuni, A. A. Ojiaku, U. Verma, *Facile fabrication of CuO nanoparticles via microwave-assisted method: photocatalytic, antimicrobial and anticancer enhancing performance*, Int. J. Environ. Anal. Chem. 102, 1095 (2022); <https://doi.org/10.1080/03067319.2020.1733543>.
- [36] G.B. Dani RK, P.R. Srivastava M, Y.R. Gondwal M, *Synthesis, Characterization, Single Crystal Structural Studies, Antibacterial Activity and DFT Investigations of 2-Chloro-5-Ethoxy-3,6- Bis(Methylamino)-1,4-Benzoquinone*, Pharm. Anal. Acta. 6, 1 (2015); <https://doi.org/10.4172/2153-2435.1000418>.
- [37] V. Beena, S. Ajitha, S.L. Rayar, C. Parvathiraja, K. Kannan, G. Palani, *Enhanced Photocatalytic and Antibacterial Activities of ZnSe Nanoparticles*, J. Inorg. Organomet. Polym. Mater. 31, 4390 (2021); <https://doi.org/10.1007/s10904-021-02053-7>.
- [38] P. Surendran, A. Lakshmanan, S.S. Priya, K. Balakrishnan, P. Rameshkumar, K. Kannan, P. Geetha, T.A. Hegde, G. Vinitha, *Bioinspired fluorescence carbon quantum dots extracted from natural honey: Efficient material for photonic and antibacterial applications*, Nano-Structures and Nano-Objects. 24, 100589 (2020); <https://doi.org/10.1016/j.nanoso.2020.100589>.
- [39] K. Kannan, D. Radhika, D. Gnanasangeetha, S.K. Lakkaboyana, K.K. Sadasivuni, K. Gurushankar, M.M. Hanafiah, *Photocatalytic and antimicrobial properties of microwave synthesized mixed metal oxide nanocomposite*, Inorg. Chem. Commun. 125, 108429 (2021); <https://doi.org/10.1016/j.inoche.2020.108429>.
- [40] A. Lakshmanan, P. Surendran, S. Sakthy Priya, K. Balakrishnan, P. Geetha, P. Rameshkumar, T.A. Hegde, G. Vinitha, K. Kannan, *Investigations on structural, optical, dielectric, electronic polarizability, Z-scan and antibacterial properties of Ni/Zn/Fe₂O₄ nanoparticles fabricated by microwave-assisted combustion method*, J. Photochem. Photobiol. A Chem. 402, 112794 (2020) <https://doi.org/10.1016/j.jphotochem.2020.112794>.

К. Балакрішнан¹, С. Сакті Прія^{1,2}, А. Лакшманан^{1,3}, П. Сурендран^{1,4},
Картік Каннан⁵, П. Гіта⁶, Г. Вініта⁷, П. Правін Кумар⁸, П. Рамешкумар^{8*}

Дослідження структурної, оптичної нелінійності та антибактеріальної активності монокристалу піперазину (bis) р-толуолсульфонату для оптичних обмежень та біологічних застосувань

¹Університет Бхаратідасану, Путанампатті, Індія;

²Урядовий коледж мистецтв Арігнар Анна, Намаккал, Тамілнаду, Індія;

³Інженерний коледж МАМ, Сіруганур, Тіручіраппаллі, Тамілнаду, Індія;

⁴Державний коледж мистецтв і науки, Комарапалаям, Тамілнаду, Індія;

⁵Відділ хімічних наук і Центр радикальних досліджень, Аріельський університет, Аріель, Ізраїль;

⁶Державний жіночий коледж Куейд-І-Міллат (автономний), Тамілнаду, Індія;

⁷Школа передових наук, VIT Ченнай, Таміл Наду, Індія;

⁸Президентський коледж (автономний), Ченапук, Триплікан, Ченнай, Тамілнаду, Індія, rameshkumarevr@gmail.com

Органічний монокристал піперазин (bis) р-толуолсульфонат (PPTSA) синтезовано і вирощено при температурі навколишнього середовища шляхом процесу повільного випаровування із використанням метанолу у якості розчинника. Вирощено кристал PPTSA відноситься до *триклінної* системи і належить до просторової групи P1. Для перевірки параметрів ґратки застосовано метод порошкової рентгенівської дифракції. Аналіз і конформацію функціональних груп і зв'язків проводили за допомогою спектрального дослідження FT-IR. Оптичні характеристики досліджено із використанням спектру UV-Vis, зокрема, досліджено оптичне поглинання, розрахована довжина хвилі відсікання. Для оцінки світлових характеристик вирощеного кристала досліджено спектри фотолюмінесценції. Розраховані параметри NLO, такі як β , n_2 та $\chi^{(3)}$, були встановлені, відповідно, як 0.0495×10^{-4} (cm/W), 8.705×10^{-10} (cm²/W), 5.316×10^{-7} (esu), виявлене порогове оптичне обмеження склало 3.074×10^{-3} (Wcm⁻²). Здійснено антибактеріальні дослідження для вивчення біологічної активності проти вибраних мікробів харчового походження.

Ключові слова: вирощування кристалів, оптичний матеріал, оптичне обмеження, антибактеріальна дія.

R.M. Balabai, M.V. Naumenko

Synergistic Properties of β -Ga₂O₃ Nanowire Arrays

Kryvyi Rih State Pedagogical University, Kryvyi Rih, Ukraine, nikemar13@gmail.com

Using the methods of electron density functional and ab initio pseudopotential, the spatial distributions of valence electron density, the density of electronic states, and Coulomb potentials along the specified directions within the arrays of β -Ga₂O₃ nanowires with different cross-sectional shapes and positions in arrays were calculated. Synergistic properties of arrays of wires are established. The degree of influence of the wires on each other is determined depending on the geometric parameters of their mutual location in the array. The electronic characteristics of the array of wires as a whole are determined.

Keywords: β -Ga₂O₃, nanowire arrays, electron density functional, *ab initio* pseudopotential, valence electron density distribution, electron state density distribution, Coulomb potential, synergistic properties.

Received 10 October 2022; Accepted 17 February 2023.

Introduction and formulation of the problem

Today, nanotubes and nanowires are successfully grown from various materials [1-16] and attract attention due to their mesoscopic phases, which provide them with new physical properties for use in devices [17]. Efforts have been made to fabricate β -Ga₂O₃ nanotubes, but the reported [18] nanotubes were mostly disordered or bent.

Growing large-scale arrays of β -Ga₂O₃-based cylindrical structures with uniform morphology is still a huge challenge. At this point, there are few reports on the fabrication of β -Ga₂O₃ nanowire arrays by inductively coupled plasma etching [19-27]; the nanowires synthesized using the chemical vapor deposition technique using hydrogen [28]; the monoclinic, vertically oriented β -Ga₂O₃ nanowires obtained by hydrothermal method and annealed [29] (Fig. 1).

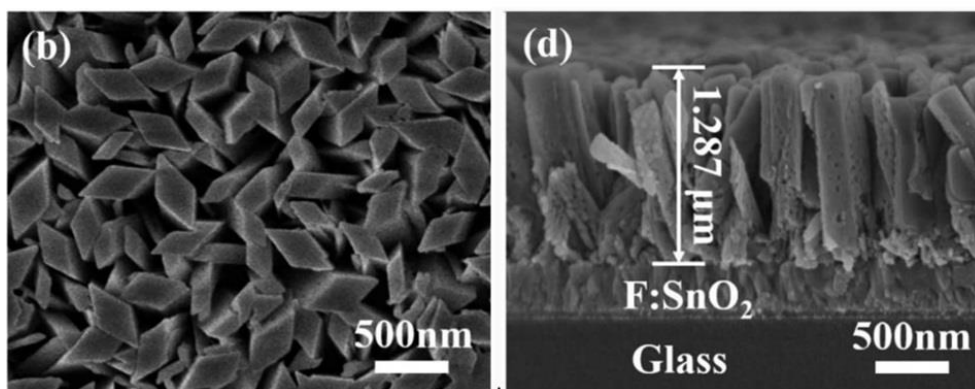


Fig. 1. Scanning electron microscope image at high magnification of vertically aligned arrays of β -Ga₂O₃ nanowires grown on a glass substrate coated with tin oxide with fluorine impurities (left - top view), and a cross-section of the nanowire array (right) [29].

Johnson et al. [30] improved the vapor–liquid–solid growth method for the synthesis of indium oxide, gallium oxide, and tin oxide nanowires by using chemical vapor transport with gold nanoparticles as catalysts. They managed to synthesize single-crystal nanowires with a diameter of 40-100 nm and a length of more than 10-100 microns.

Alkhalayli et al. [31] analyzed the characteristic structure and morphology of β -Ga₂O₃ nanowires for their application in UV photodetectors. Nanowires have a large surface area, small diameter, intrinsic scattering, and high photoconductivity, enabling UV photodetectors to achieve high sensitivity. Also, nanowires minimize the effects of lattice defects and thermal mismatch during the growth process, simplifying high-performance devices' production. In addition, one of the advantages of using nanowires is the ability to enhance light absorption and confine light to increase photosensitivity.

Due to their structural features and potential quantum confinement effects, unique electrical and optical properties are realized in semiconductor nanowires and nanotubes. Matt Low et al. [32], Hao Zeng et al. [33] believe that these semiconductor nanostructures are important elements in a wide range of promising applications for nanoscale devices due to their wide range of compositions and band structures. Current research focuses on rational synthetic control of one-dimensional nanoscale building blocks, novel property characterization and device fabrication based on nanowire building blocks, and integration of nanowire elements into complex functional architecture.

A comprehensive understanding of the synergistic relationship between the structural morphology of β -Ga₂O₃ nanowire arrays and the electronic properties of the array as a whole is necessary. Our work is devoted to the numerical determination of the characteristics of the electronic subsystem of model arrays of β -Ga₂O₃ nanowires of various cross-sections and packing geometries. The main research methods were electron density functional and *ab initio* pseudopotential theories. Using the author's program [34], the spatial distributions of the density of valence electrons, distributions of the density of electronic states, and Coulomb potentials along the specified directions within the array of nanowires were calculated.

I. Models and calculation methods

The numerical experiments from the first principles were performed according to the algorithm described in works [35-37]. Since the calculation algorithm assumed translational symmetry in the studied atomic system, an artificial superlattice of the orthorhombic type was first created. The symmetry of the superlattice made it possible to match the Cartesian system to the crystallographic one. The objects of the study determined the parameters of the unit cell of the superlattice and the atomic basis. The objects of the calculation were infinite arrays of β -Ga₂O₃ nanowires of different diameters, the same height, and different cross-sectional shapes: cylindrical and parallelogram. The wires were located relative to each other with respect to rectangular symmetry.

The ground states of the subsystem of valence electrons of model arrays of nanowires were determined using the self-consistent solution of the Kohn-Sham equations in the local approximation with fixed atomic cores. The calculations were performed under the following conditions: the integration over the Brillouin zone of the artificial superlattice was replaced by the calculation at the Γ -point; self-alignment iterations stopped if the calculation results of the current iteration coincided with the previous one with a predetermined error, their number varied depending on the object being calculated, but usually our results converged after 3-6 iterations; Kohn-Sham wave functions should be written in the form of Bloch functions, expanded on the basis of plane waves; the number of plane waves in the distribution of the wave function was reduced by means of trial calculations and assessment of the physicality of the obtained results (spatial distribution of the electron density, the size of the gap in the energy electronic spectrum between the last occupied state and the first unoccupied one, general ideas about the modeled nanostructure or evaluation of the obtained results in comparison with the results, obtained by other authors), the number of plane waves was chosen to be approximately 20-25 waves per one base atom; the atomic basis was not optimized; the interaction of valence electrons with ionic cores was processed using a pseudopotential from the first principles of Bechelet-Hemann-Schleter.

The synergistic properties of the electronic subsystem of the array of wires were studied, that is, the degree of influence of the wires on each other was determined depending on the geometric parameters of their mutual location in the array and the electronic characteristics of the array of wires as a whole. The influence of the possible growth substrate of the array of wires was not taken into account.

The corresponding values of the parameters of the unit cell of the superlattice and the coordinates of atoms in the basis allowed us to model infinite arrays of β -Ga₂O₃ wires. On Fig. 2 images from different angles of numerically reproduced cylindrical nanowires are given. The nanowires periodically arranged in the XY plane, they have a height equal to $h = 1.57$ nm, different diameters $2 \cdot R$ (0.61 or 0.95 nm, "thin" or "thick"). The nanowires separated by a vacuum and located relative to each other one according to square symmetry at variable distances r (the distance between the centers of the cylinders is marked as "a" in the figure). Wires in the form of a cylinder had a symmetrical cross-section – a circle, other types of wires - prism-shaped - had spatial angles between the limiting faces and the dimensions of the faces corresponding to the monoclinic β -Ga₂O₃ syngonia.

The parameter "c" (Z direction) of the unit cell of the superlattice was chosen so as to avoid the interaction between the atoms of the nanowire array translating in the Z direction, while the interaction in the X, Y directions was detected. The number of atoms in the base was 60 atoms for thin cylindrical and prismatic wires, and 120 atoms for thick cylindrical wires.

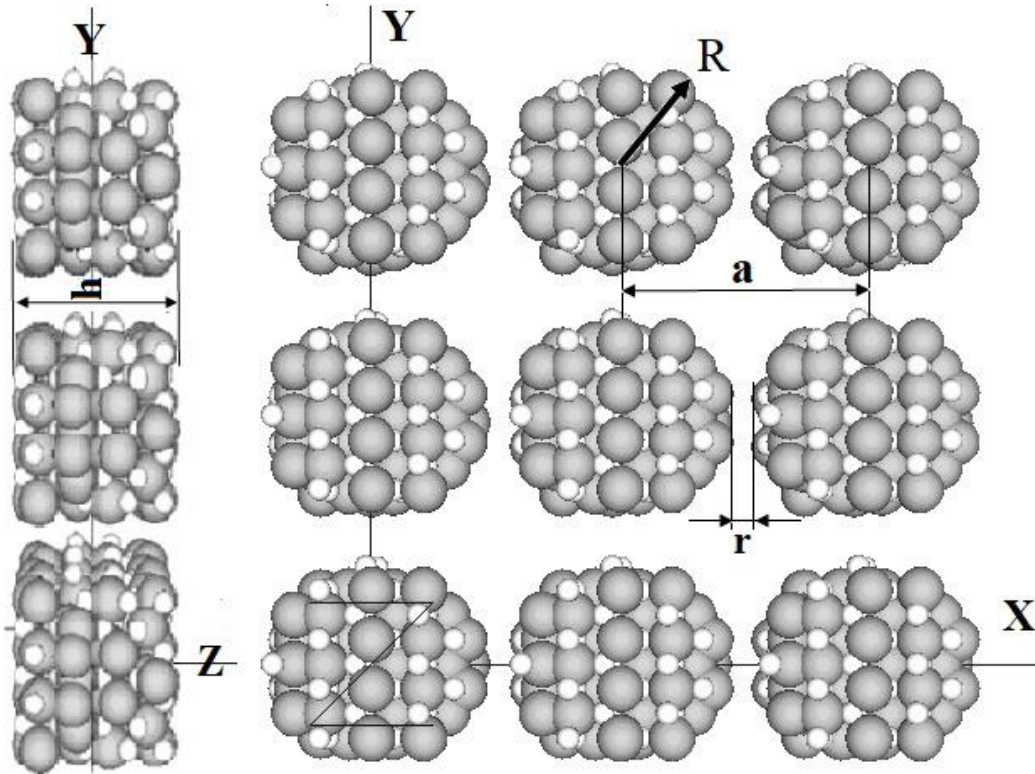


Fig. 2. Fragments of an infinite array of $\beta\text{-Ga}_2\text{O}_3$ wires. Thick nanowires are shown in different angles: on the left – in the ZY plane, on the right – in the XY plane. Gray spheres are Ga atoms, white spheres are O atoms.

II. Results and discussion

To determine the quantitative characteristics of the interaction between nanowires in the array due to long-range electric forces, Coulomb potentials induced by valence electrons were calculated along different directions of nanowire arrays (Fig. 3). As a sign that the interaction between the electronic subsystem of the wires disappears, we considered the equality of the Coulomb potential to be zero in the region between the wires.

It was established that the interaction between the cylindrical wires is manifested starting from the distance between them from 0.71 nm for thin wires, from 0.37 nm for thick ones (Fig. 4-5

An obvious increase in the values of the Coulomb

potentials induced by the electronic subsystem was observed when the wires in the array approached each other. At the same time, this growth occurred more intensively for thin wires. The similarity of the change in the Coulomb potentials, calculated in different directions of the array of cylindrical wires, and the closeness of their numerical values indicate the isotropic nature of the electrical properties of the array, and some difference is associated with an irregular circle in the cross-section of the wire and with different types of atoms lining its side surface. An increase in the values of the Coulomb potentials, induced by the electronic subsystem and proportional to its charge density, in the region between the wires correlates with a decrease in the intensity of the spatial distributions of the density of valence electrons inside the wires, especially this is noticeable in the array of thin wires (Fig. 6).

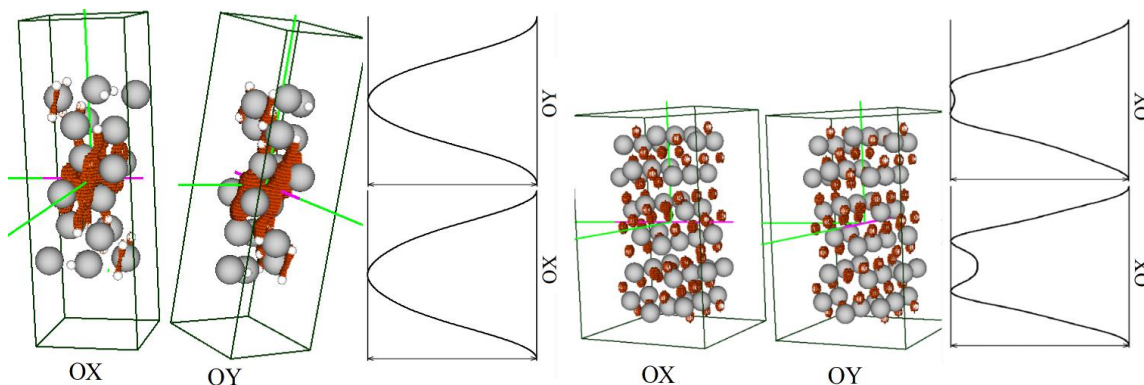


Fig. 3. Directions along arrays of thin (left) and thick (right) nanowires for calculating Coulomb potentials and their designation: OX, OY. A unit cell with the maximum iso-value electron density containing one wire is given; the translation operation involved in the calculation algorithm implements an infinite array of wires in the XY plane. Examples of the obtained potential distributions are given.

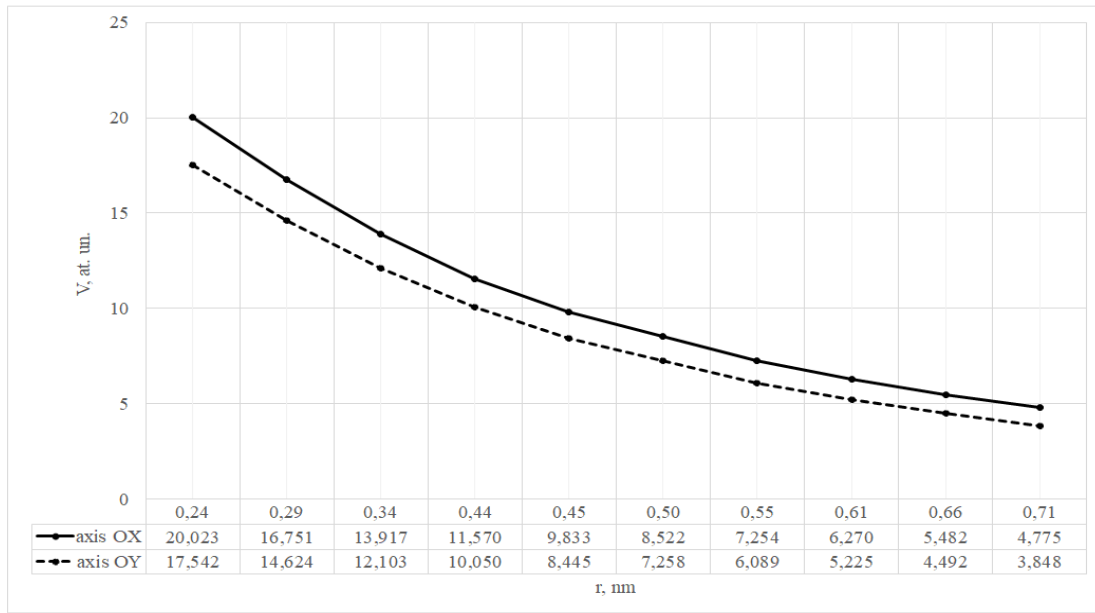


Fig. 4. Values of the Coulomb potentials depending on the distance between thin wires. Coulomb potentials are calculated in the middle between the wires in the directions indicated on fig. 2 in the array of wires.

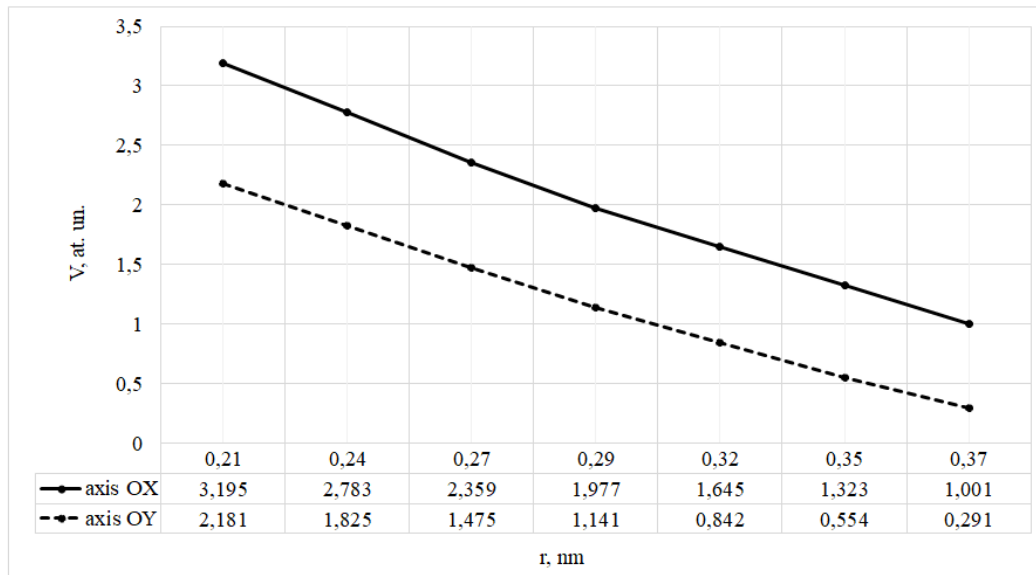


Fig. 5. Values of the Coulomb potentials depending on the distance between thick wires. Coulomb potentials are calculated in the middle between the wires in the directions indicated on fig. 2 in the array of wires.

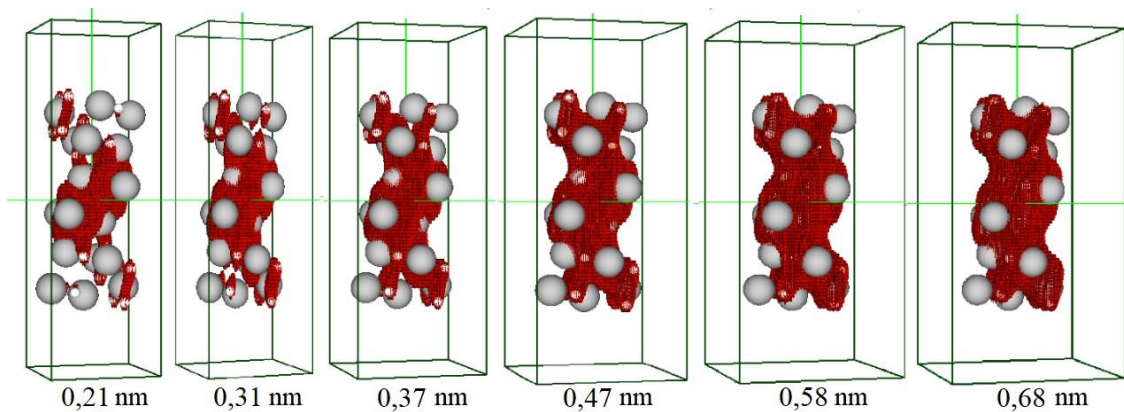


Fig. 6. Spatial distributions of valence electron density in the interval of iso-values 0.8-0.7 from the maximum in the array of thin β -Ga₂O₃ wires when the distance between them changes from 0.21 nm to 0.68 nm.

A decrease in the width of the electronic band gap is evidence of the presence of a synergistic (collective) effect in the electronic properties of an array of closely spaced thick $\beta\text{-Ga}_2\text{O}_3$ wires. Namely, wires located far from each other exhibit the properties of a single cluster and have a significant width of the band gap (HOMO-LUMO) - about 180 eV. Whereas closely located wires demonstrate the properties of an ordered interacting metastructure and a much smaller size of the band gap - about 40 eV (Fig. 7). At the same time, the change in the value of the band gap depending on the reduction in the distance between the wires is monotonic.

As for the array of thin wires, the nature of the change in the value of the electronic band gap depending on the distance between the wires is non-monotonic, and when the distance between them is about 0.50 nm, the value of the band gap was the largest. The rest of the obtained values were almost an order of magnitude smaller than for the array of thick wires (Fig. 8).

Arrays of prism-like wires bounded by faces

characteristic of the $\beta\text{-Ga}_2\text{O}_3$ monoclinic syngony have anisotropic electrical properties, since, firstly, the surface area of the interacting faces of the prism wires in the OY direction is four times larger than in the OX direction and, secondly, the wires are located relative to each other according to rectangular, but not square, symmetry (Fig. 9). This fact is reflected in the distributions of Coulomb potentials (Fig. 10-11). Namely, all distributions are different in shape and numerical values. At the same time, the expected greater intensity of interaction between the faces of the wires, which have a larger area, did not come true. On the contrary, smaller potentials were fixed between these faces, which was apparently determined by incomplete atomic bonds, which were more active on the faces of a smaller area, i.e. in the OX direction. As for the values of the electronic band gap of the array of prism-shaped wires, they are non-monotonic depending on the distance between them.

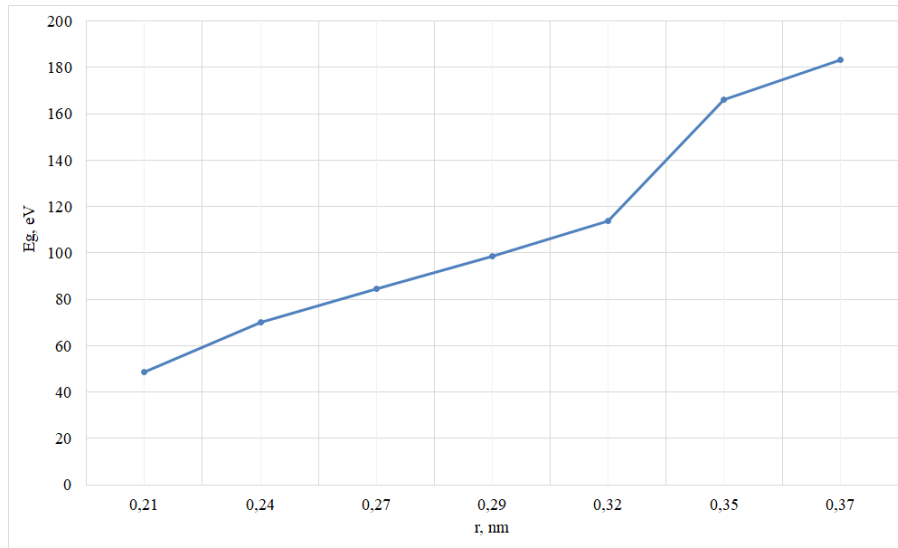


Fig. 7. Dependence of the width of the electronic band gap of the ordered metastructure (an array of thick cylindrical $\beta\text{-Ga}_2\text{O}_3$ wires) on the distance between the wires.

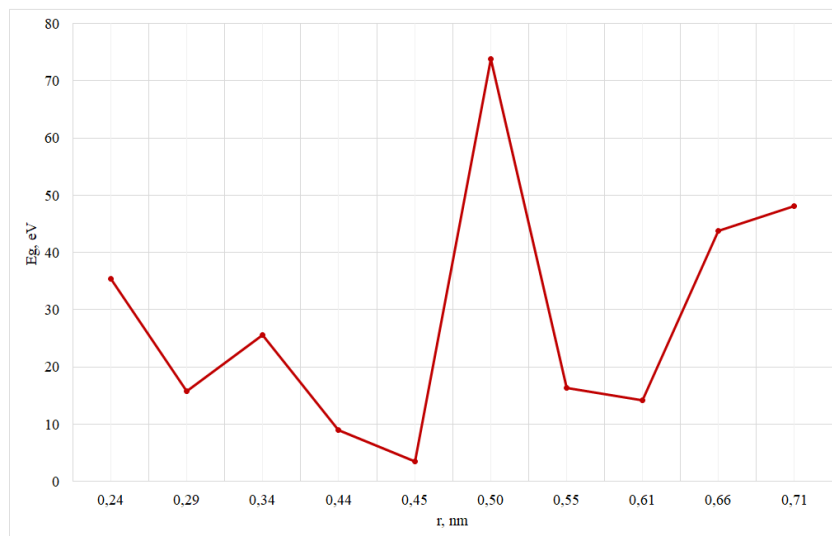


Fig. 8. Dependence of the width of the electronic band gap of the ordered metastructure (an array of thin cylindrical $\beta\text{-Ga}_2\text{O}_3$ wires) on the distance between the wires.

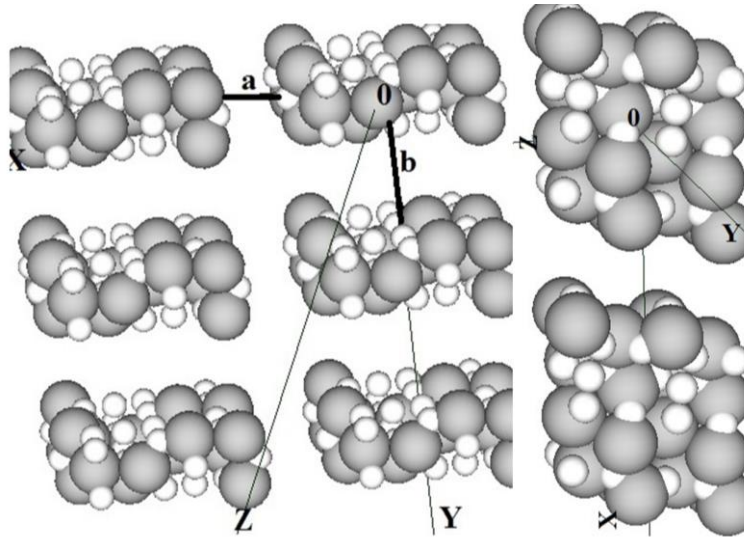


Fig. 9. Directions along arrays of prism-shaped nanowires bounded by faces characteristic of β -Ga₂O₃ monoclinic syngonia for calculation of Coulomb potentials and their designation: OX, OY. The symbols "a", "b" indicate the distances between the wires.

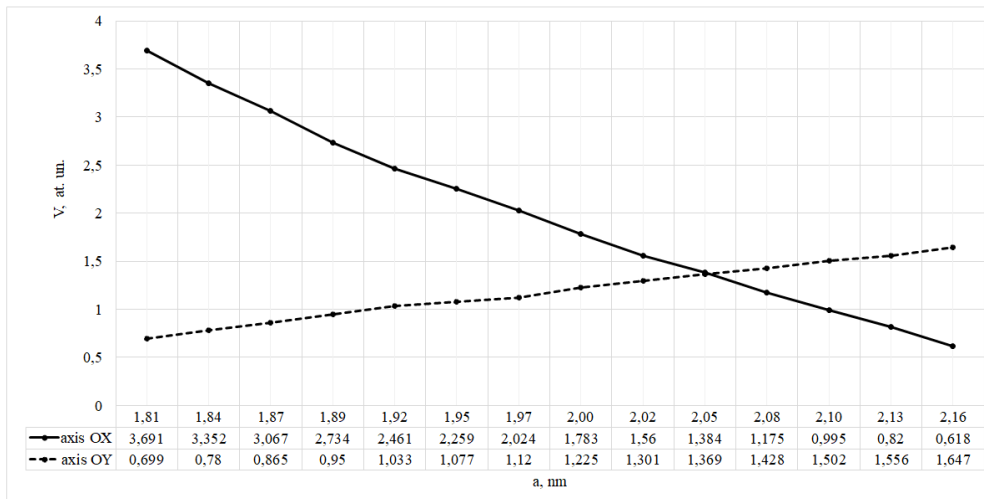


Fig. 10. Values of the Coulomb potentials depending on the distance between the prism-shaped wires. Coulomb potentials are calculated in the middle between the wires in the directions indicated on fig. 9 in the array of wires. The distance "a" between the wires was changed, the distance "b" was fixed at 1.8 nm.

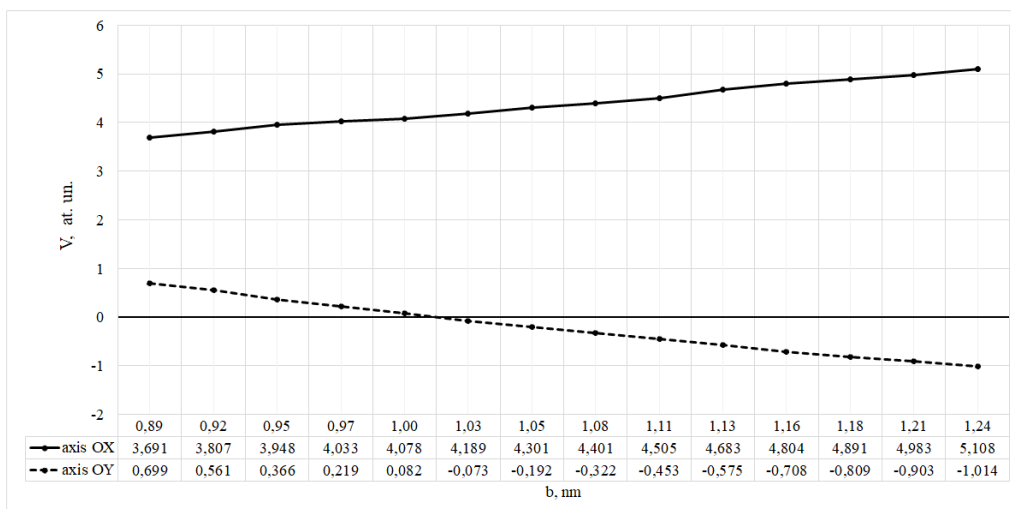


Fig. 11. Values of the Coulomb potentials depending on the distance between the prism-shaped wires. Coulomb potentials are calculated in the middle between the wires in the directions indicated on fig. 9 in the array of wires. The distance "b" between the wires was changed, the distance "a" was fixed at 0.9 nm.

Conclusions

Using the methods of electron density functional theory and *ab initio* pseudopotential, the spatial distributions of the valence electron density, the distributions of the density of electronic states, and the Coulomb potentials along the specified directions within the arrays of β -Ga₂O₃ nanowires of various cross-sectional shapes and positions relative to each other were calculated. Synergistic properties of arrays of wires are established, and the degree of influence of wires on each other is determined depending on the geometric

parameters of their mutual location in the array, and the electronic characteristics of the array of wires as a whole. Arrays of β -Ga₂O₃ wires of cylindrical shape and larger diameter reveal more controlled and physically justified synergistic electronic characteristics than arrays of cylindrical wires of smaller diameter and prismatic shape.

Balabai R.M. – Doctor of Physics and Mathematics of Sciences, Professor of the Department of Physics and Methods of its Teaching;
Naumenko M.V. – Student PhD of the Department of Physics and Methods of its Teaching..

- [1] B. Cheng, E. T. Samulski, *Fabrication and characterization of nanotubular semiconductor oxides In₂O₃ and Ga₂O₃*, Journal of Materials Chemistry, 11, 2901 (2001); <https://doi.org/10.1039/B108167E>.
- [2] B. Zhang, P.-X. Gao, *Metal oxide nanoarrays for chemical sensing: a review of fabrication methods, sensing modes, and their inter-correlations*, Front. Mater. 6(55) (2019); <https://doi.org/10.3389/fmats.2019.00055>.
- [3] Y. Zhang, J. Yang; Q. Li, X. Cao, *Preparation of Ga₂O₃ nanoribbons and tubes by electrospinning*, J. Cryst. Growth, 308, 180 (2007); <https://doi.org/10.1016/j.jcrysgro.2007.07.036>.
- [4] N. W. Gong, M. Y. Lu, C. Y. Wang, Y. Chen, L. J. Chen, *Au(Si)-filled β -Ga₂O₃ nanotubes as wide range high-temperature nanothermometers*. Appl. Phys. Lett., 92, 073101 (2008); <https://doi.org/10.1063/1.2840574>.
- [5] H. Jiang, Y. Chen, Q. Zhou, Y. Su, H. Xiao, L. Zhu, *Temperature dependence of Ga₂O₃ micro/nanostructures via vapor phase growth*, Mater. Chem. Phys., 103, 14 (2007); <https://doi.org/10.1016/j.matchemphys.2007.02.031>.
- [6] T. Braniste, and et al., *Aero-Ga₂O₃ Nanomaterial Electromagnetically Transparent from Microwaves to Terahertz for Internet of Things Applications*, Nanomaterials, 10(6), 1047 (2020); <https://doi.org/10.3390/nano10061047>.
- [7] Ziyao Zhou, Changyong Lan, SenPo Yip, Renjie Wei, Dapan Li, Lei Shu, Johnny C. Ho, *Towards high-mobility In₂xGa_{2-2x}O₃ nanowire field-effect transistors*, Nano Research, 11 (11), 5935 (2018); <https://doi.org/10.1007/s12274-018-2106-9>
- [8] G. F. Yang, and et al. *Fabrication of GaN Nanocolumns with Semipolar Plane Using Ni nano-island masks*, Semicond. Technol., 36, 417 (2011).
- [9] H. S. Kim, G. Y. Yeom, J. W. Lee, T. I. Kim, *Characteristics of inductively coupled Cl₂/BCl₃ plasmas during GaN etching*, J. Vac. Sci. Technol. A, 17, 2214 (1999); <https://doi.org/10.1116/1.581749>.
- [10] M. Y. Hsieh, C. Y. Wang, L. Y. Chen, M. Y. Ke, J. Huang, *InGaN-GaN nanorod light emitting arrays fabricated by silica nanomasks*, IEEE J. Quantum Electron., 44, 468 (2008); <https://doi.org/10.1109/JQE.2007.916665>
- [11] J. Lin, R. Zong, M. Zhou, Y. Zhu, *Photoelectric catalytic degradation of methylene blue by C₆₀-modified TiO₂ nanotube array*, Appl. Catal. B Environ., 89, 425 (2009); <https://doi.org/10.1016/j.apcatb.2008.12.025>.
- [12] T. J. Hsueh, S. J. Chang, C. L. Hsu, Y. R. Lin, I. C. Chen, *ZnO nanotube ethanol gas sensors*, J. Electrochem. Soc., 155, K152 (2008); <https://iopscience.iop.org/article/10.1149/1.2952535>.
- [13] A. Star, Y. Lu, K. Bradley, G. Grüner, *Nanotube optoelectronic memory devices*, Nano Lett., 4, 1587 (2004); <https://doi.org/10.1021/nl049337f>.
- [14] J. Han, Z. Liu, K. Guo, B. Wang, X. Zhang, T. Hong, *High-efficiency photoelectrochemical electrodes based on ZnIn₂S₄ sensitized ZnO nanotube arrays*, Appl. Catal. B Environ., 163, 179 (2015); <https://doi.org/10.1016/j.apcatb.2014.07.040>.
- [15] Z. Zhuang, and et al. *High color rendering index hybrid III-nitride/nanocrystals white light-emitting diodes*, Adv. Funct. Mater., 26, 36 (2016); <https://doi.org/10.1002/adfm.201502870>.
- [16] B. Liu, and et al. *Hybrid light emitters and UV solar-blind avalanche photodiodes based on iii-nitride semiconductors*, Adv. Mater., 32, 1904354 (2020); <https://doi.org/10.1002/adma.201904354>.
- [17] Y. C. Choi, and et al., *Catalytic growth of beta-Ga₂O₃ nanowires by arc discharge*, Adv. Mater., 12 (10), [https://doi.org/10.1002/\(SICI\)1521-4095\(200005\)12:10<746::AID-ADMA746>3.0.CO;2-N](https://doi.org/10.1002/(SICI)1521-4095(200005)12:10<746::AID-ADMA746>3.0.CO;2-N).
- [18] S. Ding, L. Zhang, Y. Li, X. Xiu, Z. Xie, T. Tao, B. Liu, P. Chen, R. Zhang, Y. Zheng, *A selective etching route for large-scale fabrication of β -Ga₂O₃ micro-/nanotube arrays*, Nanomaterials, 11, 3327 (2021); <https://doi.org/10.3390/nano11123327>.
- [19] H. Liang, Y. Chen, X. Xia, C. Zhang, R. Shen, Y. Liu, Y. Luo, G. Du, *A preliminary study of SF₆ based inductively coupled plasma etching techniques for beta gallium trioxide thin film*, Mater. Sci. Semicond. Proc., 39, 582 (2015); <https://doi.org/10.1016/j.mssp.2015.05.065>.
- [20] J. E. Hogan, S.W. Kaun, E. Ahmadi, Y. Oshima, J. S. Speck, *Chlorine-based dry etching of β -Ga₂O₃*, Semicond. Sci. Technol., 31, 065006 (2016); <https://doi.org/10.1088/0268-1242/31/6/065006>.
- [21] J. Yang, S. Ahn, F. Ren, S. Pearton, R. Khanna, K. Bevlín, D. Geerpuram, A. Kuramata, *Inductively coupled plasma etching of bulk, single-crystal Ga₂O₃*, J. Vac. Sci. Technol. B, 35, 031205 (2017); <https://doi.org/10.1116/1.4982714>.

- [22] Z. Lin, X. Xiu, S. Zhang, X. Hua, Z. Xie, R. Zhang, P. Han, Y. Zheng, *Arrays of GaN nano-pillars fabricated by nickel nano-island mask*, Mater. Lett., 108, 250 (2013); <https://doi.org/10.1016/j.matlet.2013.07.005>.
- [23] L. Zhang, X. Xiu, Y. Li, Y. Zhu, X. Hua, Z. Xie, T. Tao, B. Liu, P. Chen, R. Zhang, and et al. *Solar-blind ultraviolet photodetector based on vertically aligned single-crystalline β -Ga₂O₃ nanowire arrays*, Nanophotonics, 9, 4497 (2020); <https://doi.org/10.1515/nanoph-2020-0295>.
- [24] S. Wang, Y. W. Li, X. Q. Xiu, and et al. *Synthesis and characterization of β -Ga₂O₃@GaN nanowires*, Chin. Phys. B, 28, 028104 (2019); <https://doi.org/10.1088/1674-1056/28/2/028104>.
- [25] T. Yamada, J. Ito, R. Asahara, K. Watanabe, M. Nozaki, S. Nakazawa, Y. Anda, M. Ishida, T. Ueda, A. Yoshigoe, and et al., *Comprehensive study on initial thermal oxidation of GaN (0001) surface and subsequent oxide growth in dry oxygen ambient*, J. Appl. Phys., 121, 035303 (2017); <https://doi.org/10.1063/1.4974458>.
- [26] J. H. Choi, M. H. Ham, W. Lee, J. M. Myoung, *Fabrication and characterization of GaN/amorphous Ga₂O₃ nanocables through thermal oxidation*, Solid State Commun., 142, 437 (2007); <https://doi.org/10.1016/j.ssc.2007.03.034>.
- [27] L. Zhang, Y. Li, X. Xiu, G. Xin, Z. Xie, T. Tao, B. Liu, P. Chen, R. Zhang, Y. Zheng, *Preparation of vertically aligned GaN@Ga₂O₃ core-shell heterostructured nanowire arrays and their photocatalytic activity for degradation of Rhodamine B.*, Superlattices Microstruct., 143, 106556 (2020); <https://doi.org/10.1016/j.spmi.2020.106556>.
- [28] [28] J.P. Rex and et al., *The influence of deposition temperature on the structural, morphological and optical properties of micro-size structures of beta-Ga₂O₃*, Results in Physics, 14, 102475 (2019); <https://doi.org/10.1016/j.rinp.2019.102475>.
- [29] W. Shunli, and et al., *β -Ga₂O₃ nanorod arrays with high light-to-electron conversion for solar-blind deep ultraviolet photodetection*, RSC Adv., 9, 6064 (2019); <https://doi.org/10.1039/c8ra10371b>.
- [30] M. C. Johnson, Shaul Aloni, D. E. McCready, E. D. Bourret-Courchesne, *Controlled vapor-liquid-solid growth of indium, gallium, and tin oxide nanowires via chemical vapor transport*, Crystal Growth & Design, 6(8), 1936 (2006); <https://doi.org/10.1021/cg050524g>.
- [31] B. Alhalaili, and et al. *Gallium oxide nanowires for UV detection with enhanced growth and material properties*, Scientific Reports, 10, 21434 (2020); <https://doi.org/10.1038/s41598-020-78326-x>.
- [32] M. Law, J. Goldberger, P. Yang, *Semiconductor nanowires and nanotubes*, Annu. Rev. Mater. Res., 34, 83 (2004); <https://doi.org/10.1146/annurev.matsci.34.040203.112300>.
- [33] Hao Zeng and et al. *Metal-oxide nanowire molecular sensors and their promises*, Chemosensors, 9(2), 41 (2021); <https://doi.org/10.3390/chemosensors9020041>.
- [34] Ab initio calculation. Web source: <http://sites.google.com/a/kdpu.edu.ua/calculationphysics>.
- [35] R. Balabai, M. Naumenko, *Methodology of converting of the coordinates of the basis atoms in a unit cell of crystalline β -Ga₂O₃, specified in a monoclinic crystallographic system, in the laboratory cartesian coordinates for computer applications*, Photoelectronics, 29, 12-20 (2020); <https://doi.org/10.18524/0235-2435.2020.29.225463>.
- [36] R. Balabai, V. Zdeschts, M. Naumenko, *Mechanical modification of electronic properties of ultrathin β -Ga₂O₃ films*, Ukrainian Journal of Physics, 66(12), 1048 (2021); <https://doi.org/10.15407/ujpe66.12.1048>.
- [37] R. Balabai, O. Bondarenko, M. Naumenko, *Energy levels of acceptor impurities in β -Ga₂O₃ nanostructures*, Materials Today: Proceedings, 62(9), 5838-5844 (2022); <https://doi.org/10.1016/j.matpr.2022.05.365>.

Р.М. Балабай, М.В. Науменко

Синергетичні властивості масивів нанодротів β -Ga₂O₃

Криворізький державний педагогічний університет, Кривий Різ, Україна, nikemar13@gmail.com

Методами теорії функціоналу електронної густини та *ab initio* псевдопотенціалу розраховано просторові розподіли густини валентних електронів, розподіли густини електронних станів та Кулонівські потенціали вздовж визначених напрямків у межах масивів нанодротів β -Ga₂O₃ різних форм перерізу та розташування один відносно одного. Встановлені синергетичні властивості масивів дротів, визначена ступінь впливу дротів один на одного в залежності від геометричних параметрів їх взаємного розташування в масиві та електронні характеристики масиву дротів як єдиного цілого.

Ключові слова: β -Ga₂O₃, масиви нанодротів, функціонал електронної густини, *ab initio* псевдопотенціал, розподіл густини валентних електронів, розподіл густини електронних станів, Кулонівський потенціал, синергетичні властивості.

Z. Mykytyuk¹, H. Barylo¹, I. Kremer¹, Y. Kachurak¹, O. Samoilo², I. Kogut³

Nonlinear features of the transition of a liquid crystalline mixture into an isotropic state under the action of alcohol vapors

¹Department of Electronic Engineering, Lviv Polytechnic National University, Lviv, Ukraine, yurii.m.kachurak@lpnu.ua

²Department of Nanostructured Materials, Institute for Scintillation Materials, NAS of Ukraine, Kharkiv, Ukraine, samoilovisma@gmail.com

³Department of Computer Engineering & Electronics, Vasyl Stefanyk Precarpathian National University, Ivano-Frankivsk, Ukraine, igor.kohut@pnu.edu.ua

The work of an optical sensor for determining the concentration of alcohols, in particular methanol, ethanol and isopropanol, based on a liquid crystal sensitive element, was studied. The sensitive element is a mixture of cholesteric liquid crystal CB15 and nematic impurity E7. The detection and reaction of the sensitive element to the presence of alcohol vapors is investigated.

Keywords: optical sensor, E7, alcohols vapor, CB15.

Received 08 October 2022; accepted 23 January 2023.

Introduction

Optical gas sensors based on liquid crystal sensitive elements are a promising research direction in the field of electronics today [1-3]. Such sensors can detect substances in a gaseous state, in particular gases-markers of pathological conditions, as well as a whole range of organic substances, exceeding the concentration of which is unacceptable in production.

Alcohols, particularly methanol, ethanol, and isopropanol, which have been investigated, are flammable, colorless, and readily soluble in water. Their main application is in the medical and chemical industries, and also they can be used as fuel. All these substances are toxic to the human body to varying degrees [4, 5].

Thus, ethanol can be present in the mixture of human exhaled gases and serve as a biomarker of pathological conditions, the most obvious of which is alcohol intoxication. In addition, measurement of ethanol concentration may be necessary in other industries, for example, in chemical industries, distilleries, etc.

Methanol, in turn, is more toxic than ethanol, so it represents a greater danger for people [5]. Measuring its concentration in production is also important, in addition,

due to the liquid crystal sensitive element, it is possible to distinguish between methanol and ethanol by the type of characteristic graphs. Such an opportunity can be useful for detecting low-quality alcohol, where more expensive ethanol can be replaced by methanol.

Chromatography and mass spectrometry methods are currently used to perform the above measurements [6, 7]. These methods require the presence of qualified personnel to perform measurements, are time-consuming, and also require specialized and expensive equipment. The introduction of new technologies for the analysis of the exhaled gases mixture for the diagnosis of diseases is currently limited by a number of factors, in particular, the sensitivity to certain substances and the relative universality of the sensors.

I. Sensitive element

In the conducted research, the sensitive element of the optical sensor is a liquid crystalline cholesteric-nematic mixture consisting of a nematic liquid crystal E7 and an active impurity CB15 [8]. Quantitatively, the presence of an optically active impurity in the mixture is 37%. This

amount of cholesteric impurity allows the mixture to be stable and respond well to changes in the concentration of the analyte substance in the environment.

The determination of the presence and concentration of alcohol vapors in the studied volume is based on the change in the optical properties of the liquid crystal mixture under the influence of the analyte.

Analysis of the interaction of alcohols, as large and structurally similar organic molecules with a liquid crystal mixture of a sensitive element, is close to the interaction of a similar sensor with acetone vapors [9].

Alcohols are derivatives of hydrocarbons in the molecules of which one or more hydrogen atoms are replaced by hydroxyl groups -OH. Alcohols can be classified according to the number of hydroxyl groups present - monoatomic, diatomic, and polyatomic [10, 11]. Thus, in this work, monoatomic alcohols are presented as the studied substances - methyl (CH₃OH), ethyl (C₂H₅OH), and isopropyl (CH₃CH(OH)CH₃).

Alcohols exhibit weak acidic properties, such properties are due to the high polarity of the bond in the hydroxyl group. The polarity of alcohol molecules can be characterized by dipole moments, so ethyl alcohol has a dipole moment of 1.68 D, methyl alcohol - 1.69 D, and isopropyl alcohol - 1.66 D [12, 13].

Thus, considering the E7 liquid crystal mixture, which consists of four different, but structurally similar, liquid crystal substances - derivatives of cyanobiphenyls (4-alkyl-4'-cyanobiphenyls), we can consider it homogeneous, since there is no specific interaction between different components. The general structure and percentage composition of the E7 mixture are shown in Fig. 1.

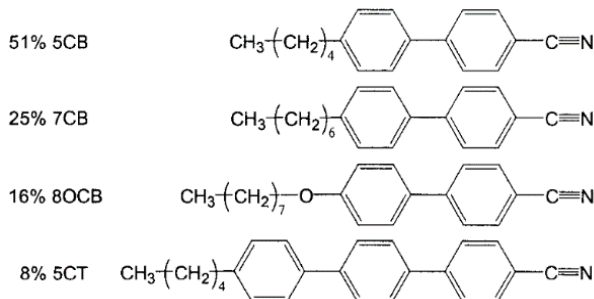


Fig. 1. Liquid crystalline substances contained in the E7 mixture and their percentage ratio.

The optically active admixture of cholesteric liquid crystal CB15 has a general structure similar to the components of the E7 mixture [14]. Namely, CB15 differs from 5CB by replacing the pentyl radical with a branched 2-methylbutyl with an asymmetric carbon atom, thanks to which it induces helical twisting in the system, but significant changes in orientational ordering are not observed. In general, the used liquid crystal mixture E7 and SV15 can be considered qualitatively homogeneous. That is, we get a cholesteric matrix that can interact with alcohol molecules.

The process of changing the optical characteristics of the liquid crystal mixture under the influence of alcohols is based on the change in the pitch of the cholesteric spiral during the interaction, which is described by expression (1). This expression reflects the change in the pitch of the cholesteric spiral in the first approximation.

$$p^{-1} = p_0^{-1}(1 - w) + k_p w(1 - w) + p_a^{-1} w \quad (1)$$

The further principle of the interaction of alcohols with a liquid crystal mixture is similar to the interaction with acetone [15]. Thus, when the concentration of alcohol vapors increases and a certain critical concentration is reached, the orientational order parameter of the liquid crystal mixture decreases to a threshold value, after which the mixture transitions into an isotropic phase [16-18]. The reverse phase transition occurs similarly when the concentration of alcohol vapors decreases, in which case we observe the recovery of the initial color of the liquid crystal mixture. These processes reflect the basis of the operation of the presented liquid crystal optical sensor.

Also, based on previous experiments with similar sensors, it can be concluded that changes over time in the process of absorption of evaporated substances are qualitatively the same for all three color curves and to some extent reflect changes in the degree of optical transmittance [19-21]. We accept these changes as an analytical criterion for the action of alcohols.

II. Photodiode receiver for determining the transient characteristics of a sensitive liquid crystalline element

Determination of the intensities of the three spectral components and subsequent construction of graphs of the transition of the liquid crystal sensitive element to the isotropic state is carried out using the receiving photodiode module TCS3490 [22].

The basis of the receiver is a segmented circular photodiode module consisting of 16 separate photodiodes. 4 photodiodes for each spectral component - red, green, blue and infrared (Fig. 2).

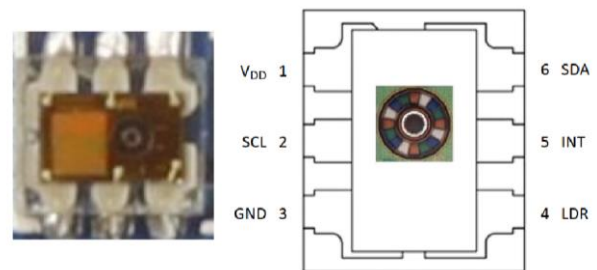


Fig. 2. Appearance and general structure of the TCS34903 photosensitive element

Each spectral component is served by a separate analog-to-digital converter. The high dynamic range of 1 to 1,000,000 and high speed allow the module to be used for measuring the level of ambient light, determining color temperature, controlling industrial processes, and medical diagnostics.

The spectral characteristics of the module are quite satisfactory for obtaining the transient characteristics of the liquid crystal sensitive element. The general spectral characteristics of the receiving module are shown in Fig. 3.

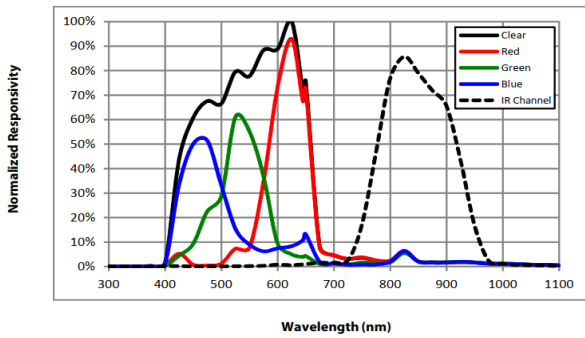


Fig. 3. Spectral characteristics of the receiving photodiode module TCS34903 [22].

In this case, we remove three spectral components for the study. The infrared spectrum is not used, due to the much smaller, about one hundred times, intensity obtained, but in general it repeats the typical appearance and characteristic points of the other three components. Other components and the general structure of the hardware part of the sensor are given in [9]

III. Experiment

The measurements of the change in transmission intensities of the optical liquid crystal sensor under the influence of various alcohols also showed similarities with similar studies of the interaction of the liquid crystal sensor with acetone.

Thus, the experiment with ethanol, the results of which are shown in Fig. 4, 5 clearly visualize the transient processes occurring in the sensitive element.

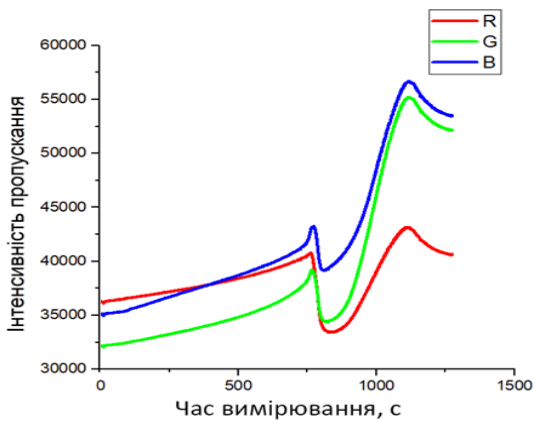


Fig. 4. The curve of change in the transmission intensity of a sensitive liquid crystal element under the influence of ethanol with a concentration of 0.5 ml.

In general, we can observe several typical areas during the transition of a sensitive element to an isotropic state. Thus, the first section represents a slow increase in the transmission intensities of all three components of the spectrum. The second section represents the trigger peak, which indicates the beginning of the intense transition of the mixture into the isotropic state, while the transmission intensities initially decrease slightly, especially for the red component. The next plot shows a sharp transition and increase in transmission intensities, especially for the green and blue components. The next peak reflects the moment

of the beginning of the reverse process and, accordingly, the transition of the sensitive element to the initial state.

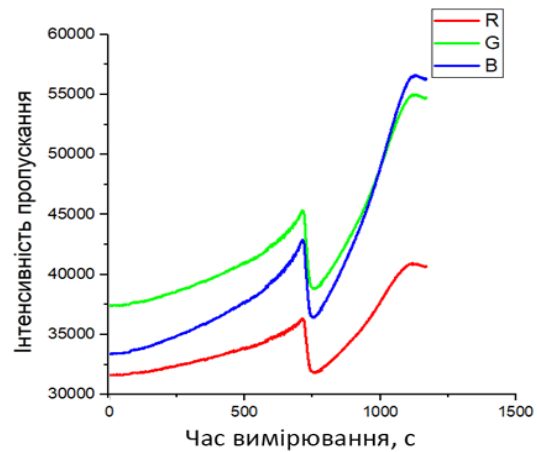


Fig. 5. The curve of changes in transmission intensities for a sensitive liquid crystal element under the influence of ethanol with a concentration of 1 ml.

For the one shown in fig. 5 of the experiment with an increased concentration of ethyl alcohol to 1 ml, a slight decrease in the transition time can be observed. In addition, there is a special characteristic point that appeared in experiments with acetone, namely the intersection of the intensities of the green and blue components of the spectrum.

The interaction with methyl alcohol, as can be seen in Fig. 6, is much weaker - despite the higher concentration (2 ml), the registered changes in transmission intensity are significantly smaller, and there are no signs of a change in the phase state.

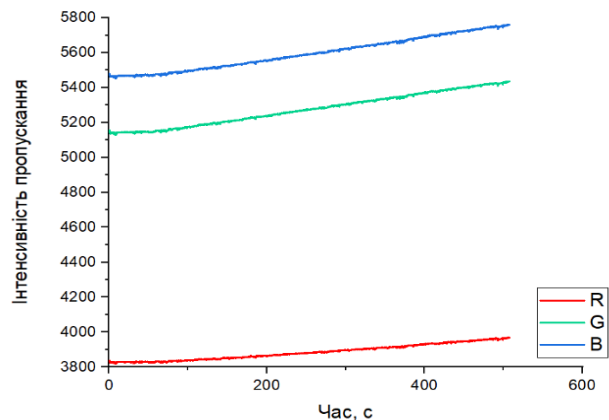


Fig. 6. Graph of changes in transmission intensities of a liquid crystal sensitive element when interacting with vapors of methyl alcohol, concentration 2 ml.

Next, a mixture of methyl and isopropyl alcohol in the proportions of 50 to 50 was placed in the volume of the sensor. The reaction of this mixture is close to the interaction of the sensitive element with ethyl alcohol. The concentration of the mixture in the studies was 0.5 (Fig. 7) and 1 ml (Fig. 8)

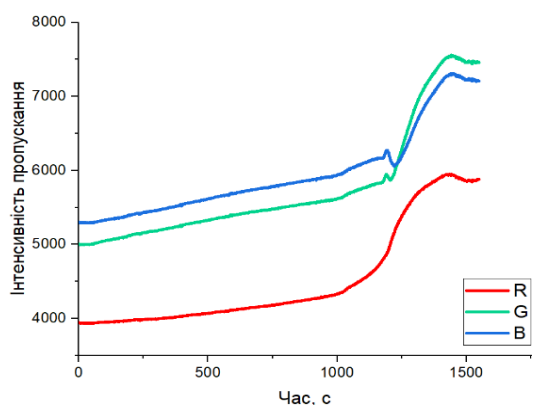


Fig. 7. Graph of the transition to the isotropic state of a sensitive liquid crystal element under the action of a mixture of methyl and isopropyl alcohol with a concentration of 0.5 ml.

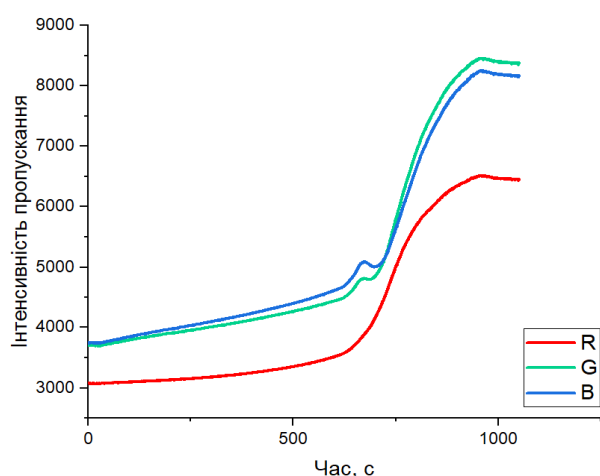


Fig. 8. Graph of the transition to the isotropic state of a sensitive liquid crystal element under the action of a mixture of methyl and isopropyl alcohol with a concentration of 1 ml.

The results of the measurements coincide with the expectations and correspond to similar results that were carried out with other organic solvents, in particular - acetone.

Conclusions

As a result of the study on the interaction of alcohol vapors with a liquid crystal sensitive element, we obtained results that correlate well with previous studies. The relatively low interaction of methyl alcohol with the sensitive element of the sensor can be compensated by heating the alcohol before placing it in the measuring volume of the sensor. In general, when interacting with alcohols, the liquid crystal mixture based on E7 nematic and CB15 cholesteric shows somewhat worse sensitivity than when interacting with acetone.

Another important result is the confirmation of the general typical form of graphs illustrating the transition of a liquid crystal mixture to an isotropic state. In contrast to the predicted linear transition, with a quick jump-like reaction of the sensitive element upon reaching the critical concentration of the analyte substance, already in the second series of experiments we obtained a clear reaction stretched over time, with characteristic points.

The obtained results are very similar to the manifestation of the so-called "blue phase" of the used liquid crystal mixture [23-25]. It was previously established that the "blue phase" for some liquid crystal mixtures is manifested in the vast majority under the influence of temperature, and not during interaction with surrounding substances, but research continues [26]. Further research will be aimed at establishing the correspondence between the known transition of this liquid crystal mixture into the "blue phase" under the influence of temperature, and the resulting transitions during interaction with substances and analytes.

Mykytyuk Z. – Prof., Doctor of Physical and Mathematical Sciences;
Barylo H. – Prof., Doctor of Technical Sciences;
Kremer I. – Associate Prof., Candidate of Technical Sciences;
Kachurak Y. – PhD Student;
Samoilov O. – Researcher, Candidate of Physical and Mathematical Sciences;
Kogut I. – Prof., Doctor of Technical Sciences.

- [1] Lukas Pschyklenk, et al. *Optical gas sensing with encapsulated chiral-nematic liquid crystals*, ACS Applied Polymer Materials, 2.5, 1925(2020); <https://doi.org/10.1021/acsapm.0c00142>.
- [2] Xiaokang Ding and Yang Kun-Lin, *Liquid crystal based optical sensor for detection of vaporous butylamine in air*, Sensors and Actuators B: Chemical, 173, 607 (2012); <https://doi.org/10.1016/j.snb.2012.07.067>.
- [3] O. Aksimientyeva, Z. Mykytyuk, A. Fechan, O. Sushynskyy, & B. Tsizh, *Cholesteric liquid crystal doped by nanosize magnetite as an active medium of optical gas sensor*, Molecular Crystals and Liquid Crystals, 589 (1), 83 (2014); <https://doi.org/10.1080/15421406.2013.872354>.
- [4] I. Rusyn, & R. Bataller, *Alcohol and toxicity*, Journal of hepatology, 59 (2), 387 (2013); <https://doi.org/10.1016/j.jhep.2013.01.035>.
- [5] M. S. Hayreh, S. S. Hayreh, G. L. Baumbach, P. Cancilla, G. Martin-Amat, T. R. Tephly, ... & A. B. Makar, *Methyl alcohol poisoning: III, Ocular toxicity*, Archives of Ophthalmology, 95 (10), 1851 (1977); <https://doi.org/10.1001/archoph.1977.04450100153022>.
- [6] F. W. Karasek, M. J. Cohen, & D. I. Carroll, (1971), *Trace studies of alcohols in the plasma chromatograph—mass spectrometer*, Journal of Chromatographic science, 9 (7), 390 (1971); <https://doi.org/10.1093/chromsci/9.7.390>.
- [7] J. M. E. Quirke, A. C. L. dams, & G. J. Van Berkel, *Chemical derivatization for electrospray ionization mass spectrometry. 1. Alkyl halides, alcohols, phenols, thiols, and amine*, Analytical chemistry, 66 (8), 1302 (1994); <https://doi.org/10.1021/ac00080a016>.

- [8] J. Peláez, & M. Wilson, *Molecular orientational and dipolar correlation in the liquid crystal mixture E7: a molecular dynamics simulation study at a fully atomistic level*, Physical Chemistry Chemical Physics, 9 (23), 2968 (2007); <https://doi.org/10.1039/B614422E>.
- [9] Z. Mykytiuk, H. Barylo, I. Kremer, M. Ivakh, Y. Kachurak & I.Kogut, *Features of the transition to the isotropic state of the liquid crystal sensitive element of the gas sensor under the action of acetone vapor*, Physics and Chemistry of Solid State, 23 (3), 473 (2022); <https://doi.org/10.15330/pcss.23.3.473-477>.
- [10] O. L. Chapman, & R. W. King, *Classification of alcohols by nuclear magnetic resonance spectroscopy*, Journal of the American Chemical Society, 86 (6), 1256 (1964); <https://doi.org/10.1021/ja01060a068>.
- [11] R. J. Bradley, *Chemical properties of alcohols and their protein binding sites*. Cellular and Molecular Life Sciences CMLS, 57(2), 265 (2000); <https://doi.org/10.1007/PL00000689>.
- [12] H. A. Rizk, & I. M. Elanwar, *Dipole moments of glycerol, isopropyl alcohol, and isobutyl alcohol*, Canadian Journal of Chemistry, 46 (4), 507 (1968); <https://doi.org/10.1139/v68-084>.
- [13] M. Jorge, J. R. Gomes & M. C.Barrera, *The dipole moment of alcohols in the liquid phase and in solution*, Journal of Molecular Liquids, 356, 119033 (2022); <https://doi.org/10.1016/j.molliq.2022.119033>.
- [14] G. E. O'Keefe, J. C. De Mello, G. J. Denton, K. J. McEwan, & S. J. Till, *Transient excited-state absorption of the liquid crystal CB15 [4-(2-methylbutyl)-4-cyanobiphenyl] in its isotropic phase*, Liquid crystals, 21 (2), 225 (1996); <https://doi.org/10.1080/02678299608032827>.
- [15] L. Lonhin, *Liquid crystals as sensory and bioequivalent materials*, Monograph, Kh.: ISMA, (2009).
- [16] S. Singh, *Phase transitions in liquid crystals*, Physics Reports, 324 (2-4), 107 (2000); [https://doi.org/10.1016/S0370-1573\(99\)00049-6](https://doi.org/10.1016/S0370-1573(99)00049-6).
- [17] C. P. Fan, & M. J. Stephen, *Isotropic-nematic phase transition in liquid crystals*, Physical Review Letters, 25 (8), 500 (1970); <https://doi.org/10.1103/PhysRevLett.25.500>.
- [18] M. J. Stephen, & J. P. Straley, *Physics of liquid crystals*, Reviews of Modern Physics, 46 (4), 617 (1974); <https://doi.org/10.1103/RevModPhys.46.617>.
- [19] O. Sushynskiy, M. Vistak, V. Dmytrah, *The sensitive element of primary transducer of protein optical sensor* *Modern Problems of Radio Engineering, Telecommunications and Computer Science*, Proceedings of the 13 International Conference on TCSET 2016, art.no.7452075,418 (2016); <https://doi.org/10.1016/j.sna.2015.10.001>.
- [20] W. Wojcik, Z. Mykytyuk, M. Vistak, G. Barylo, R. Politanskyi, I. Diskovskiy, I. Kremer, M. Ivakh, W. Kotsun, *Optical sensor with liquid crystal sensitive element for amino acids detection*, Przegląd Elektrotechniczny, 96 (4), 178 (2020); <https://doi.org/10.1080/15421406.2018.1542108>.
- [21] M. Vistak, V. Dmytrah, R. Fafula, I. Diskovskiy, Z. Mykytyuk, O. Sushynskiy, & Y. Horbenko, *Liquid crystals as an active medium of enzymes optical sensors*. In 2017 IEEE 7th International Conference Nanomaterials: Application & Properties (NAP) (pp. 04NB13-1) (2017, September) IEEE; <https://doi.org/10.1109/NAP.2017.8190326>.
- [22] TCS34903FN Datasheet https://media.ncd.io/sites/2/20170721134410/AMS_TCS3490_Datasheet_1v02-516236.pdf
- [23] I. A. Gvozdozskyy 'Blue phases' of highly chiral thermotropic liquid crystals with a wide range of near-room temperature. *Liq.Cryst.*, 42 (10), 1391 (2015); <https://doi.org/10.1080/02678292.2015.1053001>.
- [24] DL Johnson, JH Flack, PP Crooker, *Structure and properties of the cholesteric blue phases*. *Phys Rev Lett.*, v.45, 641 (1980); <https://doi.org/10.1103/PhysRevLett.45.641>.
- [25] M.D. Asiqur Rahman, S. Mohd Said, S. Balamurugan, *Blue phase liquid crystal: strategies for phase stabilization and device development*, *Sci.Technol.Adv.Mater.*, 16 (3), 033501-1 (2015); <https://doi.org/10.1088/1468-6996/16/3/033501>.
- [26] B. Gurboga, E. Kemiklioglu, *Optical sensing of organic vapor using blue phase liquid crystals*, *Liq.Cryst.*, 49 (11), 1428 (2022); <https://doi.org/10.1080/02678292.2022.2038294>.

З. Микитюк¹, Г. Барило¹, І. Кремер¹, Ю. Качурак¹, О. Самойлов², І. Когут³

Нелінійні особливості переходу рідкокристалічної суміші в ізотропний стан під дією парів спиртів

¹Кафедра електронної інженерії, Національний університет «Львівська політехніка», м. Львів, Україна,
yurii.m.kahcurak@lpnu.ua

²Відділ наноструктурних матеріалів, Інститут сцинтиляційних матеріалів, НАН України, м. Харків, Україна,
samoilovisma@gmail.com

³Кафедра комп'ютерної інженерії та електроніки, Прикарпатський національний університет імені Василя Стефаника, м. Івано-Франківськ, Україна, igor.kohut@pnu.edu.ua

Проведено дослідження роботи оптичного датчика для визначення концентрації спиртів, зокрема, метанолу, етанолу та ізопропанолу, на основі рідкокристалічного чутливого елементу. Чутливий елемент представляє собою суміш холестеричного рідкого кристалу СВ15 та нематичної домішки Е7. Досліджується детектування та реакція чутливого елементу на присутність парів спиртів.

Ключові слова: оптичний сенсор, Е7, пари спиртів, СВ15.

Ya. Saliy¹, L. Nykyruy¹, G. Cempura², O. Soroka³, T. Parashchuk², I. Horichok¹

Periodic nanostructures induced by point defects in $\text{Pb}_{1-x}\text{Sn}_x\text{Te}$

¹Vasyl Stefanyk Precarpathian National University, Ivano-Frankivsk, Ukraine, ihor.horichok@pnu.edu.ua

²AGH University of Science and Technology, Krakow, Poland

³Ivano-Frankivsk National Medical University, Ivano-Frankivsk, Ukraine

Lead tin telluride solid solutions are excellent candidates for the *p*-type conduction legs of the thermoelectric generator modules. The investigation of their microstructure properties is an important issue, that can effectively modify their electronic and thermal transport properties. In this work, we show the experimental dependences of the $\text{Pb}_{1-x}\text{Sn}_x\text{Te}$ component distribution, which were identified as periodic nanostructures with an amplitude of $\lambda \approx 50\text{-}500$ nm. The observed periodicity is explained by the generation and recombination of point defects due to diffusion processes during the synthesis, sintering, and annealing of samples. A model describing the formation of such inhomogeneities in $\text{Pb}_{1-x}\text{Sn}_x\text{Te}$ ternary alloys during isothermal annealing is proposed.

Keywords: point defects, nanostructures, PbSnTe .

Received 17 September 2022; Accepted 19 February 2023.

Introduction

Lead telluride-based compounds are among the best materials for medium-temperature thermoelectric applications [1-4]. The electronic and thermal transport properties of these materials can well-tuned using the point defects and nano-inclusions [5-8]. However, a much more interesting effect is the formation of the self-organized nano-inclusions, which may have a significant effect on the physical properties. Particularly, the formation of periodic structures was observed in PbS , PbSe , and PbTe thin films grown by the thermal deposition method [8-11]. The observed changes of the Seebeck coefficient $S(d)$ and electrical conductivity $\sigma(d)$ at minima and maxima of the thickness dependences of the film were up to ~ 2 times. The authors associated this periodicity ($\Delta d \approx 30$ nm) with the dimensional quantum effect. However, if the amplitude of oscillations at the level of ten nanometers can still be explained by the dimensional quantum effect, the value of Δd at the level of hundreds of nanometers is questionable. In particular, in ref. [11], an increase in the electron concentration by ~ 2 times leads to a decrease in the period of oscillations also by ~ 2 times (from 200 to 100 nm), which is 5 times higher than the values estimated from the quantization

conditions.

The organization of periodic nanostructures not for film material, but bulk CdHgTe crystals, was established in ref. [12]. The authors claimed that the period of oscillation can vary from nanometers to micrometers. The main factor influencing this value is the absolute values and the ratio between concentrations of vacancies and interstitial atoms. The concentration of interstitial atoms may be several orders of magnitude lower than the concentration of vacancies. Therefore, the interstitial atoms, practically without affecting the properties of the material, determine the periodicity of vacancy distribution, which in turn determines the periodicity of nanostructures in the material. Other factors, i.e. the nature of the initial inhomogeneities in material, are less important.

Herein, in the case of the PbTe -based materials, we developed a model, which suggests that the carrier concentration is the main parameter to control the periodicity of the formed nanostructures. By tuning the carrier concentration of $\text{Pb}_{1-x}\text{Sn}_x\text{Te}$ by I-doping we were able to establish the periodic structure of the material with an amplitude $\lambda \approx 50\text{-}500$ nm, which is confirmed by TEM analysis.

I. Experimental section

Synthesis and characterization of materials

Materials were synthesized in quartz ampoules evacuated to a residual pressure of 10^{-5} mbar. The ampoules were subjected to rigorous purification, which included washing in a $1\text{HNO}_3:3\text{HCl}$ concentrated acid mixture and frequent cleaning with distilled water and isopropanol. Polycrystalline $\text{Pb}_{1-x}\text{Sn}_x\text{Te}_{1-y}\text{I}_y$ materials were synthesized by melting Pb (99.999%), Te (99.999%), Sn (99.99%), and PbI_2 (99.999%) at 1273 K. Each ampoule was shaken at the liquid state to force the mixing of the components and then taken from the furnace and quenched in cold water. The obtained ingots were crushed into a fine powder via hand milling in an agate mortar and then densified using the spark plasma sintering technique at 873 K for 20 min in a 10 mm diameter graphite mold under axial compressive stress of 50 MPa in an argon atmosphere. The heating/cooling rate was 50 K/min. For homogenization, all samples were annealed for 20 hours at 873 K in an argon atmosphere.

The structural analyses of the samples were studied using X-ray diffractometer STOE STADI P (by STOE & Cie GmbH, Germany) according to the modified Guinier geometry scheme using the transmission mode ($\text{CuK}\alpha_1$ -radiation, concave Ge-monochromator (111) of the Johann type; $2\theta/\omega$ -scan, angle interval $10.000^\circ \leq 2\theta \leq 85.000^\circ$ with the step of scanning of 0.015° ; the scan time in step 100-230 s). The initial processing of experimental diffraction arrays was performed using PowderCell (version 2.4) software packages.

For SEM and EDX analyses, the samples were embedded in conductive resin, and subsequently polished, using $0.1 \mu\text{m}$ diamond powder in a slurry. The analysis of the samples' chemical composition was carried out using a scanning electron microscope (JEOL JSM-6460LV Scanning Electron Microscope) equipped with energy-dispersive X-ray spectroscopy capabilities.

The specimen for TEM investigations was prepared

with the FIB technique. For TEM investigations, Titan Cubed G2 60-300 (FEI), a probe Cs-corrected (S)TEM was used. The microscope was equipped with the ChemiSTEM EDX system based on four windowless Silicon Drift Detectors (Super X). Phase identification based on Selected Area Electron Diffraction (SAED) patterns was performed using JEMS v4.7830 software (Pierre Stadelmann, JEMS-SAS, Switzerland).

II. Results and discussion

Fig. 1a presents powder X-ray diffraction patterns of pristine PbTe, $\text{Pb}_{0.7}\text{Sn}_{0.3}\text{Te}$, and $\text{Pb}_{0.7}\text{Sn}_{0.3}\text{Te}_{0.99}\text{I}_{0.01}$ solid solutions, normalized to the most intense (200) reflection. XRD results prove that all alloys have a structure of cubic PbTe. The estimated compositional dependence of the lattice parameter a for $\text{Pb}_{1-x}\text{Sn}_x\text{Te}$ agrees well with Vegard's law, as was already observed in earlier works [13].

SEM analysis of sintered samples (Fig. 1b) shows that there are no large macro defects, in particular, micrometer-sized pores, indicating the high homogeneity of the sample. This conclusion is also confirmed by the density measurements. In particular, for the $\text{Pb}_{0.7}\text{Sn}_{0.3}\text{Te}_{0.99}\text{I}_{0.01}$ sample, the value of ρ determined by the Archimedes method was equal to 99% compared with the theoretical XRD density.

The investigation of the structure using TEM indicates the presence of periodic formations (Fig. 2). The distance between them is up to 100 nm. The fact that the formation of these inclusions is caused by periodicity in the distribution of components is confirmed by the quantitative chemical composition analysis using EDX (Fig. 3-4). It is important to note that these inhomogeneities are not inclusions of another phase. Their crystal structure is similar to the structure of the matrix material.

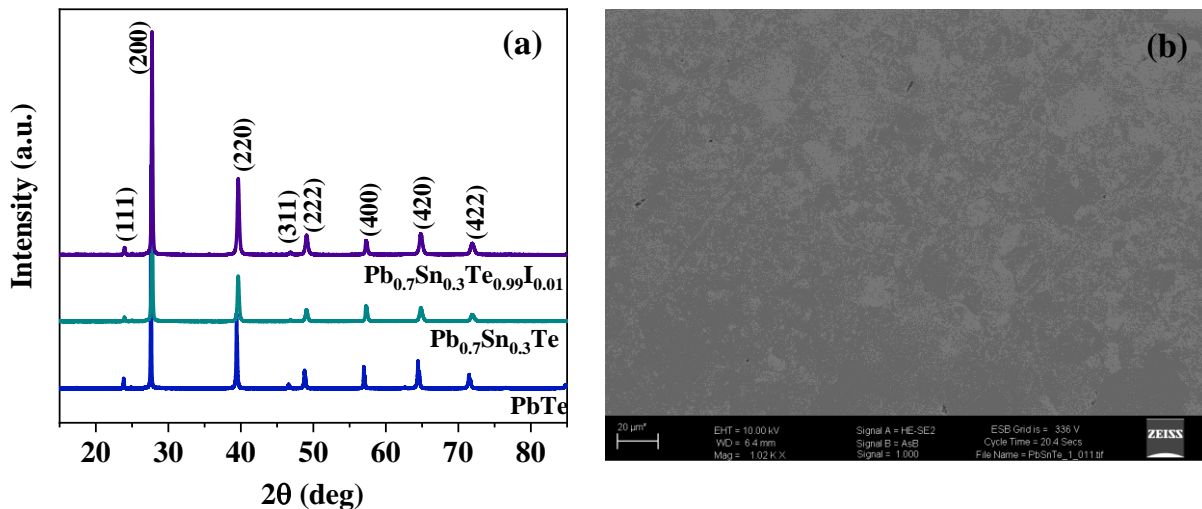


Fig 1. (a) The powder X-ray diffraction patterns for PbTe, $\text{Pb}_{0.7}\text{Sn}_{0.3}\text{Te}$, and $\text{Pb}_{0.7}\text{Sn}_{0.3}\text{Te}_{0.99}\text{I}_{0.01}$ specimens; (b) the Scanning Electronic Microscopy image for the representative $\text{Pb}_{0.7}\text{Sn}_{0.3}\text{Te}_{0.99}\text{I}_{0.01}$ sample.

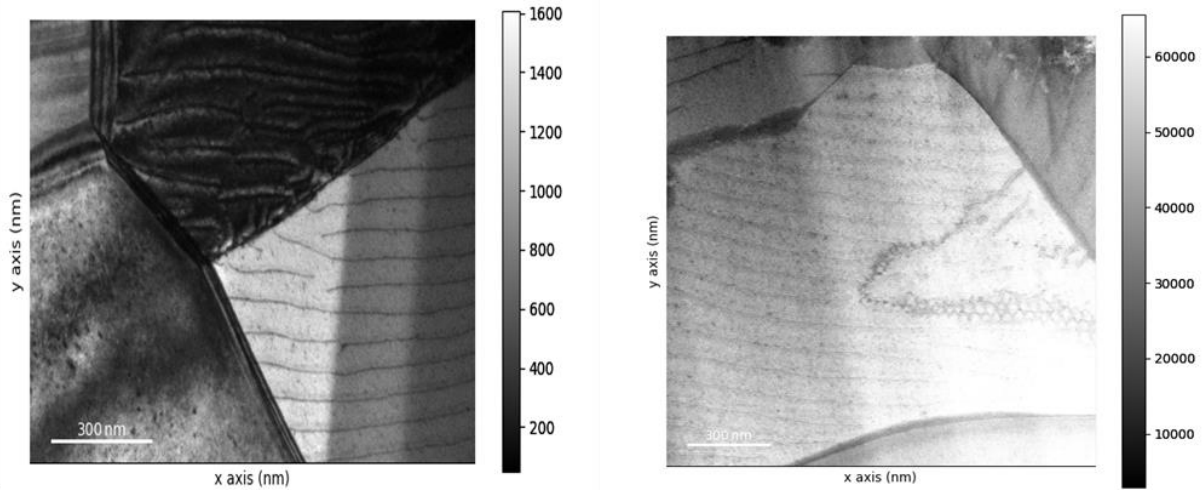


Fig. 2. Transmission electronic microscopy image of the p - $\text{Pb}_{0.7}\text{Sn}_{0.3}\text{Te}_{0.99}\text{I}_{0.01}$ specimen after spark plasma sintering.

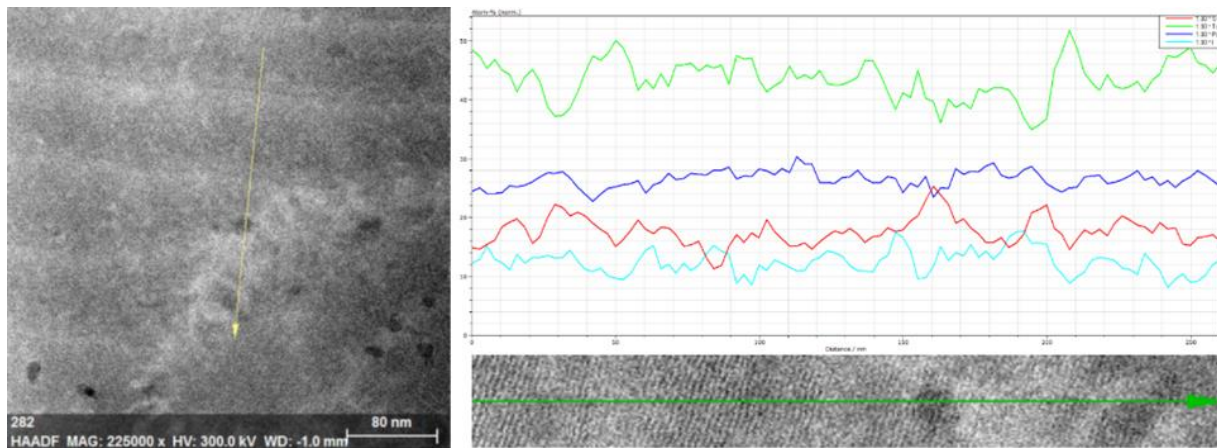


Fig. 3. EDX line scan for the $\text{Pb}_{0.7}\text{Sn}_{0.3}\text{Te}$ specimen after spark plasma sintering.

According to the EDX analysis data presented in Fig. 3, the Fourier analysis was performed. The results are shown in Fig. 4. It can be seen from the calculations that the distribution of the components of the solid solution along the direction of the quantitative elemental analysis has a well-defined periodic character. The theoretically determined oscillation period for tin and tellurium is approximately the same (≈ 42 nm), for lead, it is somewhat larger, but of the same order (≈ 50 nm). The most important thing here is that the distributions of Te and Sn are in antiphase with each other.

It is worth noting that the 1/3 part of the line along which the analysis was carried out is located at the grain boundary. In addition, in this area, a contrasting area is observed, which, according to elemental analysis, is enriched with tin and, accordingly, with a reduced content of lead and tellurium. This explains the slightly more intense oscillations in the concentration of components in this area. It is also important that a satisfactory correlation between the modeled curve and experimental ones was achieved when taking into account two harmonics - the main one, which almost completely determines the main characteristic features of the experimental dependence, and the additional one, which leads to some improvement of the corresponding correlation. Such a regularity may indicate the possibility of the existence of several (at least

two) factors that determine the periodic distribution of components in a solid solution. Moreover, one of them is dominant.

Model for diffusion instability of tellurium atoms distribution in $\text{Pb}_{1-x}\text{Sn}_x\text{Te}$

The essentially nonlinear nature of mutual diffusion processes in the ternary alloys results in the inhomogeneity of the distribution of components and defects [14]. A theoretical model describing the formation of the periodic distribution of mercury atoms in $\text{Cd}_{1-x}\text{Hg}_x\text{Te}$ during post-growth cooling is proposed in ref. [12, 15]. The mechanism of phenomena is based on the diffusion instability in a system containing vacancies and interstitial atoms. It was estimated, that if the initial concentration of interstitial mercury atoms is higher than some limit value of $3 \times 10^{17} \text{ cm}^{-3}$ for $\text{Cd}_{0.8}\text{Hg}_{0.2}\text{Te}$ at long-time annealing ($T=473$ K), the periodic distribution of mercury atoms appears from the insignificant fluctuation. The spatial and temporal scale of the distribution is determined by the equilibrium concentration of vacancies and does not depend on the specific type of fluctuation. The period increases from 10 nm to 3000 nm with a decrease in the equilibrium concentration of vacancies from 10^{19} to 10^{14} cm^{-3} . At low concentrations, the formation of the periodic structures takes a much longer

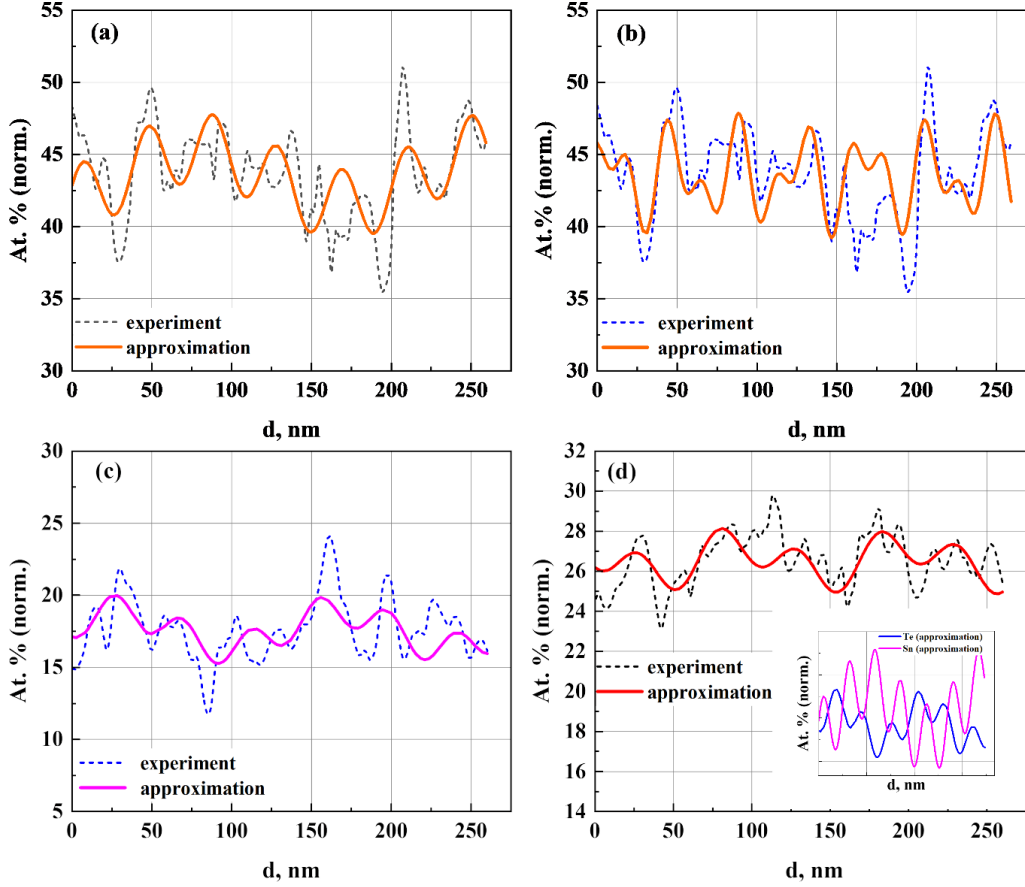


Fig. 4. The element distribution along the EDX line scanning. The dashed line indicates the experimental measurements, the solid lines indicate the simulation using the sinusoidal function. (a) – Te distribution (the main harmonic $\lambda = 40.3$ nm, the amplitude $p_a = 2.4$ at. %, the second harmonic $\lambda = 185$ nm); (b) – Te distribution (the main harmonic $\lambda = 40.3$ nm, the amplitude $p_a = 2.4$ at. %, the second harmonic $\lambda = 23$ nm); (c) Sn distribution (the main harmonic $\lambda = 42.8$ nm, the amplitude $p_a = 1.1$ at. %, the second harmonic $\lambda = 138$ nm); (d) Pb distribution (the main harmonic $\lambda = 50.9$ nm, the amplitude $p_a = 1.0$ at. %, the second harmonic $\lambda = 106.9$ nm). The inset shows that distributions of Te and Sn are in antiphase with an almost identical oscillation period of 41.5 ± 1.2 nm.

time.

Considering the concentration of free charge carriers, we can assume that the $p\text{-Pb}_{0.7}\text{Sn}_{0.3}\text{Te}_{0.99}\text{I}_{0.01}$ semiconductor possesses a concentration of lead acceptor vacancies $V_0 = 2 \times 10^{19} \text{ cm}^{-3}$ and donor interstitial lead atoms $I_{\text{Pb}} = 10^{18} \text{ cm}^{-3}$. This material has a crystalline structure of the NaCl type with a lattice constant $a = 6.4611 \text{ \AA}$ [16], and therefore the concentration of the metal atoms is $S_0 = N_0 = 1.48 \times 10^{22} \text{ cm}^{-3}$. Parameters of the diffusion coefficient of lead vacancies $D_0 = 2.9 \times 10^{-5} \text{ cm}^2 \text{ s}^{-1}$ and $E_D = 0.60 \text{ eV}$ [10] and the diffusion coefficient of interstitial lead atoms $D_0 = 6.64 \times 10^{-2} \text{ cm}^2 \text{ s}^{-1}$ and $E_D = 1.02 \text{ eV}$ [17]. Technological temperatures range from 600 K to 1300 K.

A system of equations describing the evolution of the concentration of Frenkel pairs, which considers the diffusion of each component, as well as their generation with the constant k_1 and recombination with the constant k_2 , has the following form [12,15]:

$$D_v \Delta V = k_1 S - k_2 VI, \quad (2)$$

$$D_i \Delta I = k_2 VI - k_1 S \quad (3)$$

where S , I , and V are the volume concentrations of lead atoms at lattice sites, interstitial lead atoms, and vacancies,

respectively; $k_2 = 4\pi\alpha D_i$, $k_1 = k_2 V_0 I_0 / S_0$. The formation time of the Frenkel pair is $\tau = k_1^{-1}$.

With the change of variables $V = vV_0$, $I = iI_0$, and $S = sS_0$, the original system of equations will be rewritten in the following form:

$$\lambda_v^2 \Delta v = s - vi, \quad (4)$$

$$\lambda_i^2 \Delta i = vi - s, \quad (5)$$

where $\lambda_v^2 = D_v / 4\pi\alpha D_i I_0$, $\lambda_i^2 = 1 / 4\pi\alpha V_0$. Taking the scale length $l = \lambda_i$, in the units of l , we will receive:

$$\gamma \Delta v = s - vi, \quad (6)$$

$$\Delta i = vi - s, \quad (7)$$

where $\gamma = \lambda_v^2 / \lambda_i^2 = 10^{-3}$.

From this system of equations, after summation, it follows that $\gamma \Delta v + \Delta i = 0$. Given that, at zero time, the relative concentrations are unit, we have:

$$\gamma v + i = \gamma + 1, \quad (8)$$

therefore

$$i = 1 + \gamma(1 - v). \quad (9)$$

The connection between s and v is as follows [12,15]:

$$V = V_0 \exp\left(\frac{\Delta E}{kT} \times \frac{s-s_0}{s_0}\right), \quad (10)$$

in dimensionless variables $v = \exp(\alpha(s-1))$, where α is determined by the part of the vacancy formation energy that depends on the deviation of the concentration of lattice site atoms from the equilibrium value, and it is also determined by temperature. Therefore:

$$s = 1 + \frac{\ln(v)}{\alpha} \quad (11)$$

For small deviations, $v = 1 + \delta v$, the system of equations will be reduced to the equation of a harmonic oscillator for the concentration of vacancies in the coordinate space, and the solution will take the form:

$$v = 1 + \delta v_0 \cos\left(\frac{2\pi x}{\lambda}\right), \quad (12)$$

where δv_0 is the amplitude of the initial deviation at the point $x = 0$, and λ is the spatial period of oscillations, which have to be estimated. The concentration of nodal atoms:

$$s = 1 + \frac{\delta v_0 \cos\left(\frac{2\pi x}{\lambda}\right)}{\alpha}, \quad (13)$$

and interstitial

$$i = 1 - \gamma \delta v_0 \cos\left(\frac{2\pi x}{\lambda}\right). \quad (14)$$

Substituting the approximate solutions into the differential equation for the concentration of vacancies, and leaving the terms with linear deviations from the equilibrium value, the period of spatial oscillations can be obtained as follows:

$$\lambda = \frac{2\pi}{\sqrt{\frac{1-\frac{1}{\alpha}}{\gamma}-1}}. \quad (15)$$

From the formula (15), we can see, that a significant impact on the period has γ . If $\gamma \ll 1$ and $\alpha > 1$, then in dimensionless units:

$$\lambda \approx 2\pi\gamma^{1/2}. \quad (16)$$

That is, in the dimensional units:

$$\lambda \approx 2\pi\lambda_v = \sqrt{\frac{D_v\pi}{\alpha D_i I_0}} \quad (17)$$

If $\gamma \rightarrow 1 - 1/\alpha$, then $\lambda \rightarrow \infty$.

Figs. 5-6 show the results of calculations of the distribution period depending on the temperature and vacancy concentration for different energies ΔE .

The solution of the system of equations by numerical methods confirms the received analytical solutions for small deviations at the crystallite boundary.

A strongly inhomogeneous interacting system with

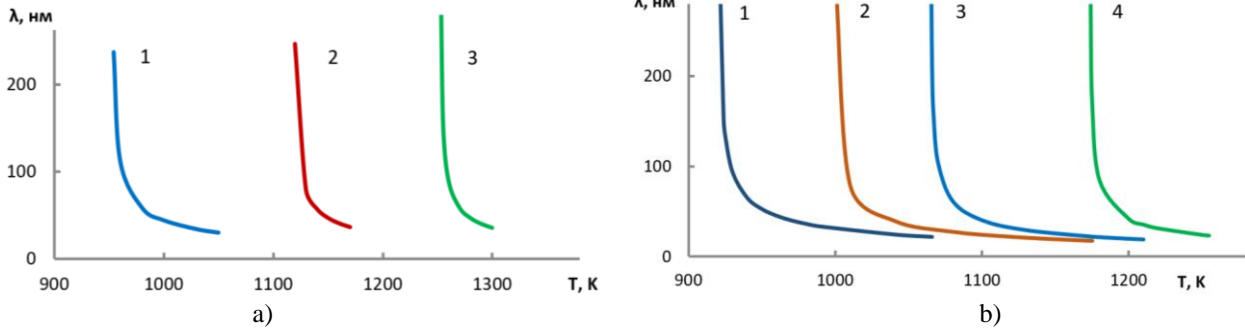


Fig. 5. Dependence of the period of oscillations on the technological temperature for: (a) $\Delta E = 0.3$ eV, with vacancy concentration $1 \cdot 10^{19}$ cm $^{-3}$ (1), $2 \cdot 10^{19}$ cm $^{-3}$ (2), and $3 \cdot 10^{19}$ cm $^{-3}$ (3); (b) $\Delta E = 0.6$ eV, with vacancy concentration $1 \cdot 10^{19}$ cm $^{-3}$ (1), $1.5 \cdot 10^{19}$ cm $^{-3}$ (2), $2 \cdot 10^{19}$ cm $^{-3}$ (3), and $3 \cdot 10^{19}$ cm $^{-3}$ (4).

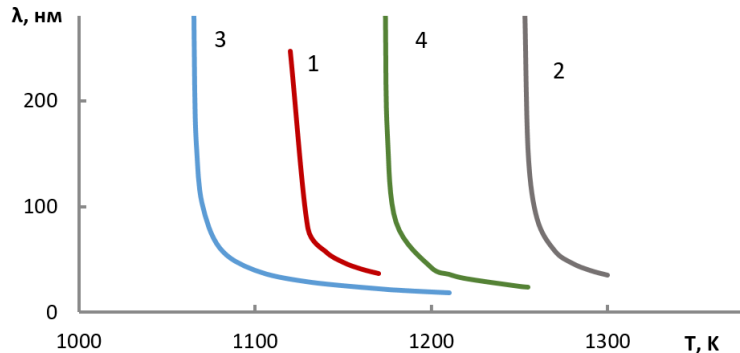


Fig. 6. Dependence of the period of oscillations on the technological temperature and vacancy concentration for $\Delta E = 0.3$ eV (with vacancy concentration $2 \cdot 10^{19}$ cm $^{-3}$ (1) and $3 \cdot 10^{19}$ cm $^{-3}$ (2)) and $\Delta E = 0.6$ eV (with vacancy concentration $2 \cdot 10^{19}$ cm $^{-3}$ (3) and $3 \cdot 10^{19}$ cm $^{-3}$ (4)).

diffusion can undergo a nonequilibrium phase transition. The system is open, it consumes vacancies formed from the outside media. The source of vacancies supports the existence of inhomogeneous structures. The described model was applied to describe the behavior of point defects in $\text{Pb}_{1-x}\text{Sn}_x\text{Te}$. The theoretical prediction suggests that the instability leads to inhomogeneous spatial structures and significant inhomogeneities in the distribution of interstitial lead atoms. Even if relatively small changes around 5 - 10% are observed, the concentration of interstitial defects changes remarkably, up to 2 - 3 times. This may have a crucial effect on the electrophysical properties of $\text{Pb}_{1-x}\text{Sn}_x\text{Te}$ due to possible compensation effects. Areas depleted of interstitial lead are enriched in cationic vacancies and may have p -type of conduction, while the rest of the sample is n -type. In $\text{Pb}_{1-x}\text{Sn}_x\text{Te}$, the degree of compensation is usually quite high, which provides a low concentration of carriers. For example, small (approximately 0.1%) deviations from the homogeneous spatial distribution of donors can lead to significant (several times) differences in the Hall coefficient for two parts of one sample. As a result, the transition to the impurity type when the local concentration of interstitial tellurium atoms changes by 2-3 times is possible and the instability mechanism provides a natural explanation for the formation of n -type inclusions in p -type conductivity materials.

Conclusions

In summary, the diffusion instability of the inhomogeneous distribution of lead in $\text{Pb}_{1-x}\text{Sn}_x\text{Te}$ was

studied. A model for tellurium diffusion which includes two flows (fast interstitial defects and slow substitutions with preservation of lattice nodes) interacting with each other through cationic vacancies, is proposed. Vacancies may come, for example, from the surface, resulting in the fact, that their local concentration is always consistent with the local composition. For the exponential dependence of the concentration of vacancies on the composition, the homogeneous distribution can become unstable and turn into a certain inhomogeneous structure. With the available data for diffusion coefficients, it was found that the instability forms a layered structure with the concentration of internodal lead. Due to the presence of acceptor cationic vacancies, this observation can lead to the formation of internal p - n junctions.

Acknowledgements

The work was supported by the ESTEEM-3 H2020 EU-project, grant agreement No 823717 (AGH University of Science and Technology, Poland).

Saliy Ya. – Doctor of Physical and Mathematical Sciences, Professor;

Nykyruy L. – Ph.D., Professor, Head of Physics and Chemistry of Solids Department;

Cempura G. – Ph.D., Scientist in the Centre of Electron Microscopy for Materials Science;

Soroka O. – Ph.D, Associate Professor;

Parashchuk T. – Ph.D., Department of Inorganic Chemistry;

Horichok I. – Doctor of Physical and Mathematical Sciences, Professor.

- [1] I.V. Horichok, V.V. Prokopiv, R.I. Zapukhlyak, O.M. Matkivskyj, T.O. Semko, I.O. Savelikhina, T.O. Parashchuk, *Effects of oxygen interaction with PbTe surface and their influence on thermoelectric material properties*, J. Nano- Electron. Phys., 10(5) 05006 (2018); [https://doi.org/10.21272/jnep.10\(5\).05006](https://doi.org/10.21272/jnep.10(5).05006).
- [2] T. Parashchuk, I. Horichok, A. Kosonowski, O. Cherniushok, P. Wyzga, G. Cempura, A. Kruk, K.T. Wojciechowski, *Insight into the transport properties and enhanced thermoelectric performance of n-type $\text{Pb}_{1-x}\text{Sb}_x\text{Te}$* , J. Alloys Compd. 860, 158355 (2021); <https://doi.org/10.1016/j.jallcom.2020.158355>.
- [3] R. Knura, T. Parashchuk, A. Yoshiasa, K.T. Wojciechowski, *Evaluation of the double-tuned functionally graded thermoelectric material approach for the fabrication of n-type leg based on $\text{Pb}_{0.75}\text{Sn}_{0.25}\text{Te}$* , Appl. Phys. Lett. 119, 223902 (2021); <https://doi.org/10.1063/5.0075126>.
- [4] T. Parashchuk, L. Chernyak, S. Nemov, Z. Dashevsky, *Influence of Deformation on $\text{Pb}_{1-x}\text{In}_x\text{Te}_{1-y}\text{Iy}$ and $\text{Pb}_{1-x-y}\text{Sn}_x\text{In}_y\text{Te}$ Films*, Phys. Status Solidi B, 18, 1 (2020); <https://doi.org/10.1002/pssb.202000304>.
- [5] I.V. Horichok, M.O. Galushchak, O.M. Matkivskyj, I.P. Yaremij, R.Ya. Yavorskyj, V.S. Blahodry, O.I. Varunkiv, T.O. Parashchuk, *Thermoelectric Properties of Nanostructured Materials Based on Lead Telluride*, J. Nano- Electron. Phys. 9(5), 05022 (2017); [https://doi.org/10.21272/jnep.9\(5\).05022](https://doi.org/10.21272/jnep.9(5).05022).
- [6] B. Naidych, T. Parashchuk, I. Yaremij, M. Moyseyenko, O. Kostyuk, O. Voznyak, Z. Dashevsky & L. Nykyruy, *Structural and Thermodynamic Properties of Pb-Cd-Te Thin Films: Experimental Study and DFT Analysis*, Journal of Elec. Mater., 50, 580 (2021); <https://doi.org/10.1007/s11664-020-08561-5>.
- [7] Taras Parashchuk, Bartłomiej Wiendlocha, Oleksandr Cherniushok, Rafal Knura, and Krzysztof Wojciechowski, *High Thermoelectric Performance of p-Type PbTe Enabled by the Synergy of Resonance Scattering and Lattice Softening*, ACS Appl. Mater. Interfaces, 13, 41, 49027 (2021); <https://doi.org/10.1021/acsami.1c14236>.
- [8] L. Nykyruy, M. Ruvinskiy, E. Ivakin, O. Kostyuk, I. Horichok, I. Kisialiou, Y. Yavorskyj, A. Hrubyak, *Low-dimensional systems on the base of PbSnAgTe (LATT) compounds for thermoelectric application*, Physica E: Low-dimensional systems and nanostructures, 106, 10-18 (2019); <https://doi.org/10.1016/j.physe.2018.10.020>.
- [9] E.I. Rogacheva, O.N. Nashchekina, Y.O. Vekhov, M.S. Dresselhaus, S.B. Cronin, *Effect of thickness on the thermoelectric properties of PbS thin films*, Thin solid films, 423, 115 (2003); [https://doi.org/10.1016/S0040-6090\(02\)00968-9](https://doi.org/10.1016/S0040-6090(02)00968-9).
- [10] E.I. Rogacheva, T.V. Tavrtna, O.N. Nashchekina, S.N. Grigorov, K.A. Nasedkin, *Quantum size effects in PbSe quantum wells*, Applied Physics Letters, 80(15). 2690 (2002); <https://doi.org/10.1063/1.1469677>.

- [11] E.I. Rogacheva, O.N. Nashchekina, S.N. Grigorov, M.S. Dresselhaus, S.B. Cronin, *Oscillatory behavior of the transport properties in PbTe quantum wells*, Institute of Physics Publishing. Nanotechnology, 14, 53 (2003); <https://doi.org/10.1088/0957-4484/14/1/313>.
- [12] A.S. Vasin, M.I. Vasilevsky, *Simulation of diffusion instability of a mercury atomic distribution in the cadmium-mercury-tellurium alloy*, Phys. Solid State, 48, 37 (2006); <https://doi.org/10.1134/S1063783406010082>.
- [13] R. Knura, T. Parashchuk, A. Yoshiasa, K. T. Wojciechowski, *Origins of Low Lattice Thermal Conductivity of Pb_{1-x}Sn_xTe Alloys for Thermoelectric Applications*. Dalt. Trans. 50 (12), 4323 (2021); <https://doi.org/10.1039/d0dt04206d>.
- [14] Y.P. Saliy, R.S. Yavorskyi, *The redistribution modeling of implanted impurity stimulated by vacancies*, Materials Today: Proceedings, 35, 576 (2021); <https://doi.org/10.1016/j.matpr.2019.11.017>.
- [15] M.I. Vasilevskiy and E.V. Anda, *Diffusion instability of homogeneous distribution of mercury in cadmium mercury telluride*, Semicond. Sci. Technol. 10, 157 (1995); <https://doi.org/10.1088/0268-1242/10/2/006>
- [16] Krzysztof T. Wojciechowski, Taras Parashchuk, Bartłomiej Wiendlocha, Oleksandr Cherniushok, and Zinovi Dashevsky, *Highly efficient n-type PbTe developed by advanced electronic structure engineering*, J. Mater. Chem. C, 8, 13270 (2020); <https://doi.org/10.1039/D0TC03067H>.
- [17] Y.I. Ravich, B.A. Efimova, I.A. Smirnov, *Semiconducting Lead Chalcogenides*, Springer US, 1970. <https://doi.org/10.1007/978-1-4684-8607-0>.

Я. Салій¹, Л. Никируй¹, Г. Цемпура², О.Сорока³, Т. Парашук², І.Горічок¹

Періодичні наноструктури, індуковані точковими дефектами в Pb_{1-x}Sn_xTe

¹Прикарпатський національний університет імені Василя Стефаника, Івано-Франківськ, Україна, ihor.horichok@pnu.edu.ua

²Університет науки та технологій AGH, Краків, Польща

³Івано-Франківський національний медичний університет Івано-Франківськ, Україна

Тверді розчини на основі телуридів свинцю та олова є відмінними кандидатами для створення віток р-типу провідності модулів термоелектричного генератора. Дослідження їх мікроструктурних властивостей є важливим питанням, оскільки дозволяє ефективно змінювати їхні електронні властивості та перенесення тепла. У даній роботі показано експериментальні залежності розподілу компонентів Pb_{1-x}Sn_xTe, які ідентифіковані як періодичні наноструктури із амплітудою $\lambda \approx 50-500$ нм. Спостережувана періодичність пояснюється генерацією та рекомбінацією точкових дефектів внаслідок дифузійних процесів під час синтезу, спікання та відпалу зразків. Запропоновано модель, що описує утворення таких неоднорідностей у потрійних сполуках Pb_{1-x}Sn_xTe під час ізотермічного відпалу.

Ключові слова: точкові дефекти, наноструктури, PbSnTe.

A. T. Pathan¹, A. M. Shaikh², S.K.Sushant³, Shridhar N. Mathad^{3*}

Effect of synthesis methods and comparative study of structural properties of micro and nano Ferrites

¹Department of Physics, M.H. SabooSiddik College of Engineering, Mumbai, 400008, India, asrar.pathan@rediffmail.com.

²Department of Electronics, The New College, Kolhapur, 416014, India

³Department of Engineering Physics, K.L.E. Institute of Technology, Gokul Road, Hubballi, 580027 Karnataka, India

physicssiddu@gmail.com, physicssiddu@kleit.ac.in

In this study, $Mn_xZn_{(1-x)}Fe_2O_4$ ferrite samples with $x = 0.4$ and 0.6 were synthesized using a solid-state method and co-precipitation method. In order to determine the effects of various concentrations (x) on the ferrite's structure, particle size, and crystalline phases, prepared samples were analyzed using X-ray diffraction (XRD). The XRD patterns revealed that the synthesized samples display a single-phase cubic spinel structure. FTIR analysis showed for both synthesis method have absorption band in the range 400 to 1000 cm^{-1} . SEM analysis shows extreme homogeneity of all the samples. EDX analysis was used to examine for $Mn_{0.4}Zn_{0.6}Fe_2O_4$. The prepared ferrites powders contain Mn, Zn, and Fe, as shown in both synthesis methods. In this approach, alternative synthesis routes for these ferrites are suggested in this study in order to get around some limitations of the traditional preparation method.

Keywords: Ferrites, XRD, Solid state method, co-precipitation method.

Received 14 January 2023; Accepted 8 March 2023.

Introduction

Ferrites are a class of substances that have attracted a lot of attention recently because of their magnetic [1] and electrical characteristics [2,3], which make them perfect for a variety of applications in industries including electrical engineering, electronics, and tele communications [4,5]. Ferrites have been extensively used as magnetic cores in transformers, inductors, and other electrical components, and have been the subject of many studies due to their potential applications in magnetic data storage, microwave devices, and biomedical engineering. The properties of ferrites can be tailored by controlling the synthesis methods and particle size. In this context, micro and nano-sized ferrites have become increasingly popular due to their unique properties that differ from their bulk counterparts. The small particle size of micro and nano ferrites results in high surface-to-volume ratios, leading to enhanced

magnetic and electrical properties, as well as increased reactivity. The synthesis method used to produce ferrites has a significant impact on the structural and magnetic properties of the resulting material. For example, the synthesis process can determine the particle size, crystalline structure, and magnetic properties of ferrites [6-8]. Solid-state and solution-based approaches are the two primary groups into which ferrites' synthesis techniques may be divided. Solid-state methods, such as ceramic and sintering processes, produce ferrites with a dense and homogeneous structure, while solution-based methods, such as sol-gel, precipitation, and co-precipitation, produce ferrites with a more porous structure [9,10].

In this study, we aim to provide a comprehensive introduction to the effect of synthesis methods on the structural properties of ferrites and a comparative study of the structural properties of micro and nano ferrites [11,12]. The study will focus on the synthesis methods used to produce ferrites and the resulting structural properties,

including particle size, crystalline structure, and magnetic properties. The article will begin by providing an overview of the different synthesis methods used to produce ferrites, including solid-state and solution-based methods. The impact of various synthesis techniques on the crystalline structure, magnetic properties, and particle size of ferrites will thereafter be the main topic of discussion [13]. The structural characteristics of micro and nano ferrites will next be compared, with a focus on the variations in particle size, crystalline structure, and magnetic properties between these two categories of ferrites.

In conclusion, this article will provide a comprehensive overview of the effect of synthesis methods and a comparative study of the structural properties of micro and nano ferrites. By understanding the relationship between synthesis methods and structural properties, it is possible to optimize the synthesis process and tailor the properties of ferrites for specific applications [14,15]. $Mn_xZn_{(1-x)}Fe_2O_4$ Co-precipitation and ceramic methods have been used to synthesis ferrites [10,16,17]. The physical and structural, of these samples have been investigated and the final ferrite product has been identified using established analytical and experimental techniques.

I. Experimental

Samples preparation:

A. Wet-chemical method (co-precipitation method):

Wet chemical (co-precipitation approach) procedure were used to create manganese zinc ferrites from the series of $Mn_xZn_{(1-x)}Fe_2O_4$ ($x = 0.4, \text{ and } 0.6$). The Schematic diagram of co-precipitation method shown in fig 1. NaOH and $FeCl_3$ concentrations for each sample were held constant. Fe:Na ratios were obtained at a 1:4 ratio for each sample. For each sample, varying amounts of the salts

$MnCl_2 \cdot 4H_2O$, $ZnCl_2$, and $FeCl_3$ were dissolved in distilled and deionized water. NaOH solution in a 100 ml beaker was stirred at room temperature using a magnetic stirrer at a speed of 60rpm. Drop by drop, the metallic ion solution was poured into the beaker holding the NaOH solution. Dark grey precipitates were produced during addition. The beaker containing the dark grey precipitates was set into a bath of water and ethylene glycol that had been preheated. Each sample received a different water bath temperature 60 minutes were spent on. After 60 minutes, the particles finally settled to the bottom of the beaker. After being removed from the water bath, the beaker was allowed to cool to a moderate temperature. Filtration was used to obtain the particles. The filtered particles were baked for 18 hours at $80^\circ C$ to dry them out. When the fine materials were finally produced, they were in powder form Cu K α radiation ($\lambda = 1.5405 \text{ \AA}$) was used in the x-ray powder diffraction technique to characterise these materials. These prepared samples ($x = 0.4$ and 0.6) compositions had their lattice parameter computed. The Debye-Scherrer formula was used to estimate the average crystallite size of each sample [18-20].

B. Ceramic method (Solid state method):

The synthesis of $Mn_xZn_{(1-x)}Fe_2O_4$ by solid-state method involves the following steps which showed in Fig 2:

Weighing and mixing: Weigh the required amounts of high-purity MnO , ZnO , Fe_2O_3 , and a suitable dispersant (e.g. polyvinyl alcohol). The powders are then mixed thoroughly in a ball mill or mortar and pestle to ensure a homogeneous mixture.

Grinding and calcination: The powder mixture is then ground to a fine powder and calcined in air at a temperature of $800-1000^\circ C$ for 5 hours to obtain the desired spinel phase.

Milling and pelletizing: The calcined powder is then ground again to obtain a fine powder obtain a dense and homogeneous $Mn_xZn_{(1-x)}Fe_2O_4$ ceramic.

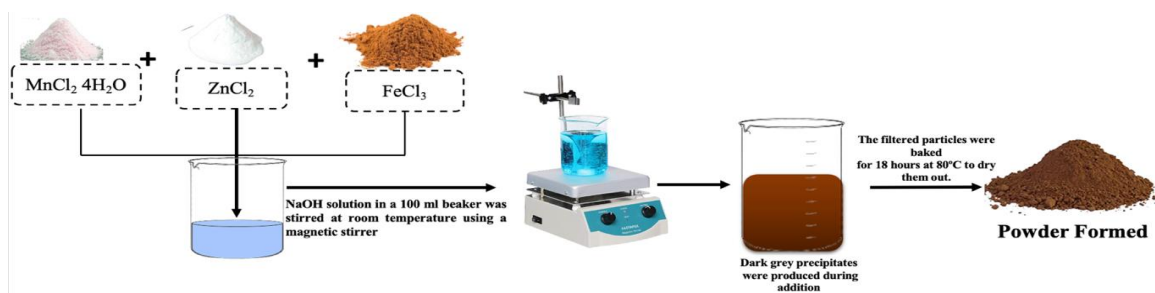


Fig.1. Schematic diagram of co-precipitation method.

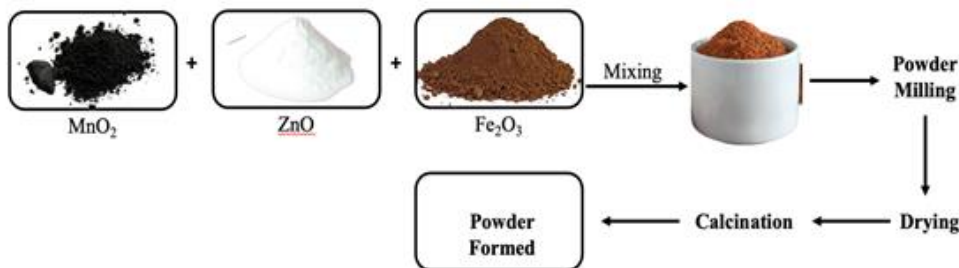


Fig. 2. Schematic diagram of Solid state method.

Characterization: The synthesized ceramic is characterized using techniques such as X-ray diffraction (XRD), scanning electron microscopy (SEM), and EDX analysis to determine its crystal structure, morphology and elemental composition [21,22].

Overall, the solid-state method is a simple and cost-effective method for synthesizing $Mn_xZn_{1-x}Fe_2O_4$ ceramic with good magnetic properties. These samples of $x = 0.4$ and 0.6 compositions had their lattice parameter computed. The Debye-Scherrer formula was used to estimate the average crystallite size of each sample [23].

II. Results and discussion

2.1 X-ray diffraction analysis

The sample was investigated by using X-ray diffraction techniques. The powder X-ray diffraction method observed reflections between 20° and 80° angles. The Mn-Zn ferrite samples were synthesized by conventional solid-state, and the Co-precipitation methods prepared were examined. For all compositions of $Mn_xZn_{1-x}Fe_2O_4$, single-phase cubic spinel structure development is not shown in XRD patterns for all samples created by the ceramic technique but with some impurity peaks are observed its due to low sintering temperature and precursors used as started materials. Fig.3 displays the X-ray spectra of these materials (a and b). The development of ferrites is demonstrated by comparing Figures 3 (a) and 3(b) of the mixture's XRD pattern. As a result, it is discovered that the ceramic approach is not that much helpful in the synthesis of ferrites [24].

The co-precipitation method was used to manufacture samples of $Mn_xZn_{1-x}Fe_2O_4$ with compositions ($x=0.4$ & 0.6) and the X-ray diffraction spectra show that Mn-Zn ferrite formed as a single phase in each case. The patterns observed match the XRD patterns for Mn-Zn ferrite that have been described in the literature. Figures 3 (a) and 3(b)

depict the X-ray diffraction pattern for $Mn_xZn_{1-x}Fe_2O_4$ ($x=0.4, 0.6$) for the samples A1, A2, and S1, S2. The synthesized ferrite sample is supported by the diffraction lines. Wide lines show that the particles are nanoscale. The average particle size for each composition was calculated from the line width of a number of peaks using the Scherrer formula [22]. Table 1 lists the values for the particle size and lattice parameter derived from the X-ray data. The errors listed are the sizes' standard deviations from the mean value. The relative ionic radius can be used to explain why the lattice parameter increases with zinc concentration. Zn^{2+} ions have an ionic radius of 0.82 , which is less than Mn^{2+} ions' ionic radius of 0.91 . As the concentration of Zn^{2+} ions in the Mn-Zn ferrite increases (i.e., x in $Mn_xZn_{1-x}Fe_2O_4$ becomes larger), the average ionic radius of the A and B site metal ions in the crystal structure increases. This is because the ionic radius of Zn (0.74 \AA) is larger than that of Mn (0.83 \AA). When the size of the Zn^{2+} ions increases, the lattice parameter of the crystal also increases, since the larger ions require a larger lattice to maintain the same crystal structure. This is known as the "size effect" [25-27].

The Scherer formula was used to compute the lattice constants 'a' for samples generated using the two different procedures and the results were found to be in good agreement with the reported values. According to calculated lattice parameter values for the ferrite samples, the lattice constant value increased as the concentration (x) of manganese increased (Table 1). For instance, the lattice constant for $Mn_{0.4}Zn_{0.6}Fe_2O_4$ in the ceramic method progressively rises to 8.44 \AA for $Mn_{0.6}Zn_{0.4}Fe_2O_4$. Similar to this, the lattice constant "a" for $Mn_{0.4}Zn_{0.6}Fe_2O_4$, which is 8.45 \AA , climbs to 8.46 \AA for $Mn_{0.6}Zn_{0.4}Fe_2O_4$ when using the wet chemical approach (Table 1). This increase may be a result of the Mn^{2+} and Zn^{2+} cations larger ionic radii. Larger Mn^{2+} cations (0.83 \AA) replace smaller Zn^{2+} cations (0.73 \AA) in the samples when Mn^{2+} concentration rises. In their investigation of Mn-Zn ferrites, various researchers

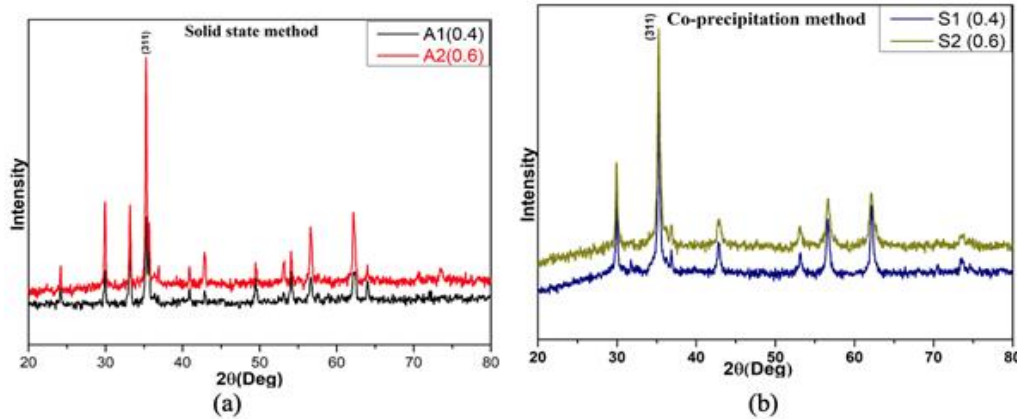


Fig. 3. The X-ray diffraction pattern for $Mn_xZn_{1-x}Fe_2O_4$ ($x = 0.4, 0.6$) prepared by ceramic method and co-precipitation method.

Table 1.

X	Composition	Ceramic method		Co-precipitation method	
		a in \AA (a)	Crystallite size nm(b)	a in \AA (b)	Crystallite size nm(b)
0.4	$Mn_{0.4}Zn_{0.6}Fe_2O_4$	8.44	27.40	8.46	29.76
0.6	$Mn_{0.6}Zn_{0.4}Fe_2O_4$	8.41	37.16	8.45	56.80

reported comparable observations.

2.2 Scanning Electron Microscopic Analysis (SEM)

The properties of ferrites are significantly influenced by the surface shape, grain size, and elemental makeup of the samples. More details on the grain nature of the samples are revealed by looking at the surface morphology and grain size variation of the system $Mn_xZn_{1-x}Fe_2O_4$ ($x=0.4$) with regard to Mn content. Figures 4.1–4.2 display typical micrographs for both series (A2 and S2) for the samples with $x=0.4$ along with the accompanying EDX spectra. The results of the SEM analysis demonstrate the extreme homogeneity of all the samples and shows micro powder with bead like structure formation. Additionally, there are no secondary phases, as seen by the sharp SEM pictures of all the samples. The lack of extra peaks in the XRD patterns supports this. The lack of extra peaks in the XRD patterns supports this. All of the samples' micrographs demonstrate the presence of numerous smaller grains with numerous interfaces, which directly affect the properties of these ferrites [28].

Fig. 4.1 SEM images and EDAX Spectra of $Mn_{0.4}Zn_{0.6}Fe_2O_4$ ($x=0.4$) ferrite sample prepared by co-precipitation method

2.3 EDAX Analysis

EDX analysis was used to examine the compounds' semi-quantitative elemental makeup. In Figures 4.1 and 4.2, the EDX spectra of each sample are displayed (b). The spectra demonstrate that Zn, Mn, and Fe are present in the produced ferrite powders. There is a small variation in the samples compositions levels of Zn, Mn, and Fe, according to the analysis. The mutual quantitative ratio of the elements, however, shows that the composition of the synthesized materials is quite near to the one assumed. Possible Zn evaporation during the synthesis at high temperatures may be the cause of the small disproportions [29,30].

Table 2.

Mass contents of individual ions in Mn-Zn ferrites as determined from EDAX analysis

Element	A2(x = 0.4)		S2(x = 0.4)	
	Weight %	Atomic%	Weight%	Atomic %
O K	24.71	54.57	25.35	55.37
Mn L	12.06	7.76	12.54	7.98
Fe L	37.99	24.03	37.83	23.67
Zn L	25.24	13.64	24.28	12.98

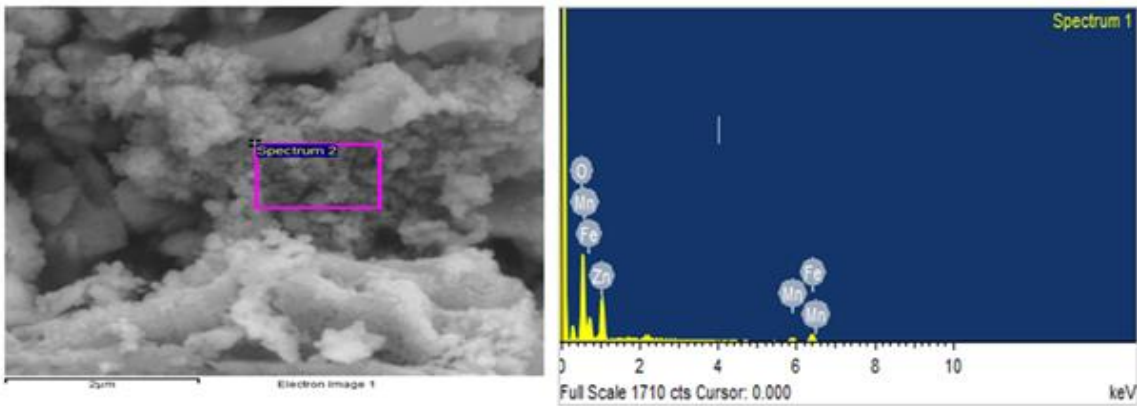


Fig.4.1(a)

Fig.4.1(b)

Fig. 4.1. SEM images and EDAX Spectra of $Mn_{0.4}Zn_{0.6}Fe_2O_4$ ($x = 0.4$) ferrite sample prepared by co-precipitation method.

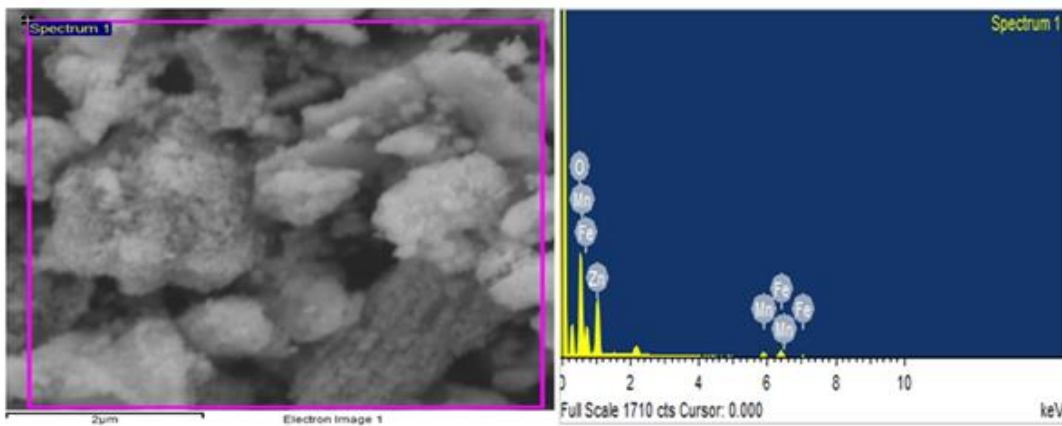


Fig. 4.2 (a)

Fig.4.2 (b)

Fig. 4.2. SEM images and EDAX Spectra of $Mn_{0.4}Zn_{0.6}Fe_2O_4$ ($x = 0.4$) ferrite sample prepared by ceramic method.

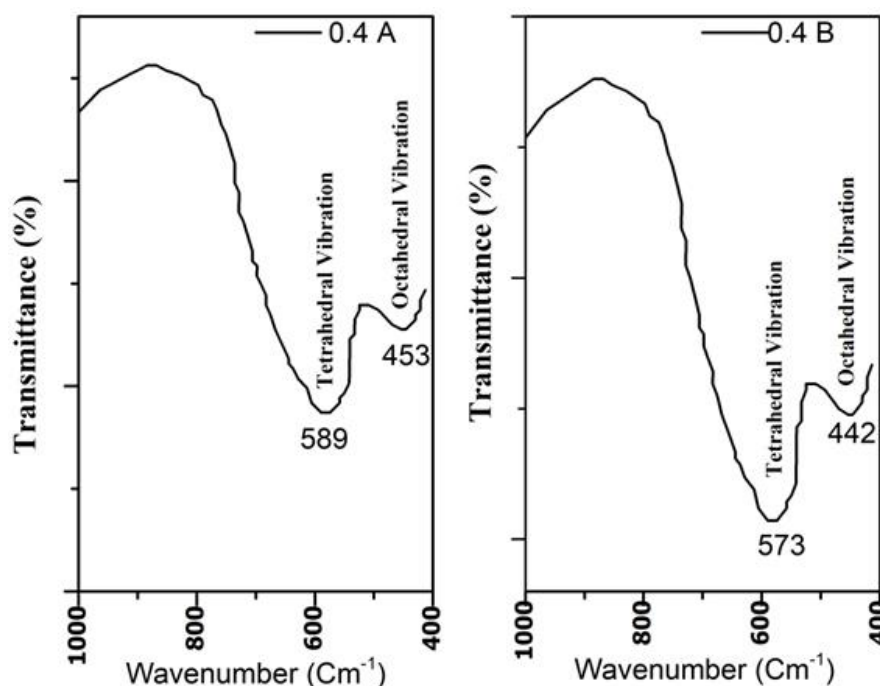


Fig.5. FTIR analysis of $Mn_{0.4}Zn_{0.6}Fe_2O_4$ samples (A- Solid state, B- Co- ppt method).

2.4 FTIR Analysis

Figure 5 demonstrates the FTIR spectra of the solid state (Fig. 5A) and chemical method (Fig.4B) samples ferrite samples with $X = 0.4$ in the range from 400 to 1000 cm^{-1} . The spectra show two main absorption bands below 600 cm^{-1} which is a common characteristic of ferrites[30]. Metal- oxygen stretching vibrations both the samples confirms the cubic structure [31]. The high frequency band lies in the range 573–589 cm^{-1} while the low frequency band lies in the range 442–453 cm^{-1} . Normal ferrites both absorption bands depend on the nature of octahedral Me–O stretching (where Me-metal) vibration and nature of tetrahedral Me–O stretching vibration reveals formation ferrites [33,34]. These two observed bands (ν_1 and ν_2) correspond to the intrinsic vibrations of tetrahedral and octahedral $Fe^{3+}-O^{2-}$ complexes, respectively. Thus FTIR confirms the cubic nature of ferrite samples [35].

have been successfully prepared by both the co-precipitation process and the Solid state method. Samples examined using XRD, SEM and EDX consequences confirmation of formation of pure cubic-phase spinel-type by using Co-precipitation process $Mn_xZn_{1-x}Fe_2O_4$ structure with well-crystalline nature by comparing both the synthesis methods Co-precipitation method is the best Mn-Zn synthesis. The average crystallite size was observed in the range from 27 to 37 nm for the ceramic method and 29 to 56 nm for Co-precipitation method. FTIR analysis showed for both synthesis method have absorption band in the range of 442–453 cm^{-1} (ν_1) and 573–589 cm^{-1} (ν_2).SEM images showed the ferrites samples particles-like morphology of the samples, shows micro powder with bead like structure formation. The quantitative mutual ratio of the elements (EDX) demonstrates that the composition of the synthesized materials.

Conclusions

Cubic Spinel $Mn_xZn_{1-x}Fe_2O_4$ ($x=0.4$ & 0.6) particles

Pathan A. T.–;Assistant Professor, Ph.D.;
Shaikh A. M.–; Professor, Ph.D.;
Sushant S.K. –; Assistant Professor, Ph.D.;
Shridhar N. Mathad – Associate Professor, Ph.D.

- [1] K.P Mudholakar, S. Tambe Vinaykumar, S.S Kakati, S. N. Mathad., *Effect of Sintering condition on Magnetization and Microstructure of $Cu_xCo_{(1-x)}Fe_2O_4$ Ferrites*, Int. J. Adv. Sci. Eng, 9(2), 2678 (2022); <https://doi.org/10.29294/IJASE.9.2.2022.2678-2685>.
- [2] R. S. Totagi, N. J. Choudhari, S. S. Kakati, C. S. Hiremath, S. B. Koujalagi, and R. B. Pujar, *Electrical properties of Ni-Mg-Cu nanoferrites synthesized by sucrose precursor technique*, Scholars Research Library Der Pharma Chemica, 7(3), 11(2015); Accessed: Feb. 21, 2023.
- [3] S. S. Gandhad, P. M. Patil, S. N. Mathad, L. v. Hublikar, P. R. Jeergal, and R. B. Pujar, *Effect of Aluminum Doping on Structural and Mechanical Properties of Ni–Mg Ferrites*, International Journal of Self-Propagating High-Temperature Synthesis, 28(4), 271 (2019); <https://doi.org/10.3103/S1061386219040046/FIGURES/3>.
- [4] A. Kumar, S. Molakeri, S. Kalyane, A. B. Kulkarni, and S. N. Mathad, *Elastic Properties of Nickel Ferrite Synthesized by Combustion and Microwave Method using FT-IR Spectra*, Int. J. Adv. Sci. Eng, 3(422), (2017), Accessed: Feb. 21, 2023.

- [5] M. R. Patil, M. K. Rendale, S. N. Mathad, and R. B. Pujar, *FTIR Spectra and Elastic Properties of Cd-Substituted Ni-Zn Ferrites I*, International Journal of Self-Propagating High-Temperature Synthesis, 26(1), 33 (2017); <https://doi.org/10.3103/S1061386217010083>.
- [6] S. S. Yattinahalli, S. B. Kapatkar, N. H. Ayachit, and S. N. Mathad, *Synthesis and structural characterization of nanosized nickel ferrite*, International Journal of Self-Propagating High-Temperature Synthesis, 22(3), 147 (2013); <https://doi.org/10.3103/S1061386213030114/METRICS>.
- [7] S. N. Adarakatti V S Pattar P K Korishettar, B V Grampurohit, S. N. Mathad. A B Kulkarni, *Synthesis, structural and electrical studies of li-ni-cu nano ferrites*, Acta Chemica Iasi, 26(1), 1 (2018); <https://doi.org/10.2478/achi-2018-0001>.
- [8] Shashidhargouda. H. R. and S. N. Mathad, *Synthesis and structural analysis of Ni_{0.45} Cu_{0.55} Mn₂O₄ by Williamson–Hall and size–strain plot methods*, Ovidius University Annals of Chemistry, 29(2), 122 (2018); <https://doi.org/10.2478/AUOC-2018-0018>.
- [9] S. Vijaykumar, V. R. Hiremath, S. K. Sushant, and S. N. Mathad, *Synthesis, Characterization and Evaluation of δ -Al₂O₃ Nanoparticles Prepared by Chemical Method with Variation of pH*, Journal of Nano- and Electronic Physics, 14 (3), 3027 (2022); [https://doi.org/10.21272/JNEP.14\(3\).03027](https://doi.org/10.21272/JNEP.14(3).03027).
- [10] S. Kakati, M. K. Rendale, and S. N. Mathad, *Synthesis, Characterization, and Applications of CoFe₂O₄ and M-CoFe₂O₄ (M = Ni, Zn, Mg, Cd, Cu, RE) Ferrites: A Review*, International Journal of Self-Propagating High-Temperature Synthesis, 30(4), 189 (2021); <https://doi.org/10.3103/S1061386221040038>.
- [11] S. S. Yattinahalli, S. B. Kapatkar, and S. N. Mathad, *Review of Nanoscience Materials and its applications*, Research Journal of Engineering and Technology, 7(3), 121 (2016); <https://doi.org/10.5958/2321-581X.2016.00024.6>.
- [12] S. S. Yattinahalli, S. B. Kapatkar, and S. N. Mathad, *Structural and Mechanical Properties of a Nano Ferrite*, Advanced Science Focus, 2(1), 42(2014); <https://doi.org/10.1166/ASFO.2014.1079>.
- [13] A. B. Kulkarni and S. N. Mathad, *Effect of Sintering Temperature on Structural Properties of Cd doped Co-Zn Ferrite*, Journal of Nano- and Electronic Physics, 10(1), 1001 (2018); [https://doi.org/10.21272/JNEP.10\(1\).01001](https://doi.org/10.21272/JNEP.10(1).01001).
- [14] R. M. Shedam, A. M. Bagwan, S. N. Mathad, A. B. Gadkari, M. R. Shedam, and R. G. Sonkawade, *Nd³⁺ added Mg–Cd ferrite material study the thick film gas sensing properties*, Mater Chem Phys, 293, 126871 (2023); <https://doi.org/10.1016/j.matchemphys.2022.126871>.
- [15] R. M. Shedam, P. P. Kashid, S. N. Mathad, R. B. Deshmukh, M. R. Shedam, and A. B. Gadkari, *Ferrites gas sensors: A Review*, Physics and Chemistry of Solid State, 23(3), 626 (2022); <https://doi.org/10.15330/PCSS.23.3.626-640>.
- [16] S. U. Durgadsimi, V. R. Kattimani, N. S. Maruti, A. B. Kulkarni, and S. N. Mathad, *Synthesis and structural analysis of nickel ferrite synthesized by co-deposition*, Eurasian Physical Technical Journal, 18(4) (38), 14-19 (2021); <https://doi.org/10.31489/2021NO4/14-19>.
- [17] R. Y. Kolekar, S. B. Kapatkar, and S. N. Mathad, *Nickel-Doped Cobalt Zinc Ferrites Co_{0.8-x}Ni_xZn_{0.2}Fe₂O₄(x=0.0–0.56) by Solid-State Reaction: Synthesis and Characterization*, International Journal of Self-Propagating High-Temperature Synthesis, 29(4), 196 (2020); <https://doi.org/10.3103/S1061386220040044/FIGURES/5>.
- [18] R. Vishwarup and S. N. Mathad, *Facile Synthesis of Nano Mg-Co Ferrites (x=0.15, 0.20, 0.25, 0.30, 0.35, and 0.40) via Co-precipitation Route: Structural Characterization*, Materials International, 2(4) 0471-0476 (2020); <https://doi.org/10.33263/Materials24.471476>.
- [19] M. B. Tahir, T. Iqbal, A. Hassan, and S. Ghazal, *Wet Chemical Co-precipitation Synthesis of Nickel Ferrite Nanoparticles and Their Characterization*, J InorgOrganometPolym Mater, 27(5), 1430 (2017); <https://doi.org/10.1007/S10904-017-0598-5/FIGURES/7>.
- [20] P. Zsabka, G. Leinders, A. Baena, T. Cardinaels, K. Binnemans, and M. Verwerft, *Synthesis of gadolinium-doped thorium dioxide via a wet chemical route: Limitations of the co-precipitation method*, Journal of Nuclear Materials, 489, 211 (2017); <https://doi.org/10.1016/J.JNUCMAT.2017.03.052>.
- [21] Z. Zhang, Y. Liu, G. Yao, G. Zu, and Y. Hao, *Synthesis and Characterization of NiFe₂O₄ Nanoparticles via Solid-State Reaction*, Int J Appl Ceram Technol, 10(1), 142 (2013); <https://doi.org/10.1111/J.1744-7402.2011.02719.X>.
- [22] P. Parhi, T. N. Karthik, and V. Manivannan, *Synthesis and characterization of metal tungstates by novel solid-state metathetic approach*, J Alloys Compd, 465(1-2), 380 (2008); <https://doi.org/10.1016/J.JALLCOM.2007.10.089>.
- [23] S. Mathad, *Solid-State Synthesis and Structural Features of Li_{0.5}Ni_{0.75-x/2}Zn_{x/2}Fe₂O₄ Ferrites*, International Journal of Self-Propagating High-Temperature Synthesis, (2019); <https://doi.org/10.3103/S1061386219010060>.
- [24] J. F. Marco, J. R. Gancedo, M. Gracia, J. L. Gautier, E. Ríos, and F. J. Berry, *Characterization of the Nickel Cobaltite, NiCo₂O₄, Prepared by Several Methods: An XRD, XANES, EXAFS, and XPS Study*, J Solid State Chem, 153(1), 74 (2000); <https://doi.org/10.1006/JSSC.2000.8749>.
- [25] S. S. Kakati, T. M. Makandar, M. K. Rendale, and S. N. Mathad, *Green Synthesis Approach for Nanosized Cobalt Doped Mg–Zn through Citrus Lemon Mediated Sol–Gel Auto Combustion Method*, International Journal of Self-Propagating High-Temperature Synthesis, 31(3), 131 (2022); <https://doi.org/10.3103/S1061386222030049/TABLES/2>.

- [26] S. Kazi, S. Feeda. S. S. Kakati, S. N. Mathad, S. L. Galgali, M. K. Rendale, *Sintering Temperature Dependent Structural and Mechanical Studies of $Ba_xPb_{1-x}TiO_3$ Ferroelectrics*, Journal of Nano- and Electronic Physics, 12(4), 4018 (2020); [https://doi.org/10.21272/JNEP.12\(4\).04018](https://doi.org/10.21272/JNEP.12(4).04018).
- [27] M. C. Dimri, S. C. Kashyap, D. C. Dube, and S. K. Mohanta, *Complex permittivity and permeability of Co-substituted NiCuZn ferrite at rf and microwave frequencies*, J. Electroceram., 16(4), 331 (2006); <https://doi.org/10.1007/s10832-006-9874-4>.
- [28] R. Sen, P. Jain, R. Patidar, S. Srivastava, *Synthesis and characterization of nickel ferrite ($NiFe_2O_4$) nanoparticles prepared by sol-gel method*, Elsevier, 2, 3750 (2015); <https://doi.org/10.1016/j.matpr.2015.07.165>.
- [29] G. Padmapriya, A. Manikandan, V. Krishnasamy, S. K. Jaganathan, and S. A. Antony, *Enhanced Catalytic Activity and Magnetic Properties of Spinel $Mn_xZn_{1-x}Fe_2O_4$ ($0.0 \leq x \leq 1.0$) Nano-Photocatalysts by Microwave Irradiation Route*, J Supercond Nov Magn, 29 (8), 2141 (2016); <https://doi.org/10.1007/S10948-016-3527-X>.
- [30] L. C. Shidaganal, A. B. Kulkarni, S. B. Kapatkar, S. N. Mathad, and R. B. Pujar, *Al-Doped Co-Cd Nanoferrites by Solution-Combustion Synthesis: Preparation and Structural Characterization*, International Journal of Self-Propagating High-Temperature Synthesis, 29(3), 176 (2020); <https://doi.org/10.3103/S1061386220030103>.
- [31] R. D. Waldron, *Infrared spectra of ferrites*, Physical Review, 99(6), 1727(1955); <https://doi.org/10.1103/PHYSREV.99.1727>.
- [32] M. K. Rendale, S. N. Mathad, and V. Puri, *Structural, mechanical and elastic properties of $Ni_{0.7-x}Co_xZn_{0.3}Fe_2O_4$ nano-ferrite thick films*, Microelectronics International, 34(2), 57 (2017); <https://doi.org/10.1108/MI-02-2016-0009/FULL/HTML>.
- [33] S. L. Galagali et al., *Fourier transform infrared spectroscopy and elastic properties of $Mg_{1-x}Cd_xFe_2O_4$ ferrite systems.*, Thaiscience.info, 41(5), 992 (2023).
- [34] M. Patil, M. Rendale, S. Mathad, FTIR spectra and elastic properties of Cd-substituted Ni-Zn ferrites, International Journal of Self-Propagating High-Temperature Synthesis, 26(1), 33 (2017); <https://doi.org/10.3103/S1061386217010083>.
- [35] Ied Mohammed Mnawe , M. Y. Hassaan , Osama Mohmaed Hameda , A.S. Abdel-Moety, *XRD, FTIR and electrical properties investigation of $Ni_{0.6}Zn_{0.4}Cr_xFe_{2-x}O_4$ thin films*, NVEO, 9(1), 1617 (2022).

A.T. Патан¹, А.М.Шейх², С.К. Сушант³, С.Н. Матхад³

Вплив методів синтезу та порівняльне дослідження структурних властивостей мікро- та наноферитів

¹Кафедра фізики, Інженерний коледж Сабу Сіддіка, Мумбаї, 400008, Індія, asrar.pathan@rediffmail.com,

²Кафедра електроніки, Новий коледж, Колхатур, 416014, Індія,

³Кафедра інженерної фізики, К.Л.Е. Технологічний інститут, Хаббали, 580027 Карнатака, Індія

Зразки фериту $Mn_{(x)}Zn_{(1-x)}Fe_2O_4$ із $x = 0,4$ та $0,6$ синтезовано твердотільним методом і методом співосадження. Щоб визначити вплив різних концентрацій (x) на структуру фериту, розмір частинок і кристалічні фази, підготовлені зразки аналізували за допомогою рентгенівської дифракції (XRD). Рентгенограми показали, що синтезовані зразки мають однофазну структуру кубічної шпінелі. Аналіз FTIR показав, що для обох методів синтезу характерною є смуга поглинання в діапазоні від 400 до 1000 cm^{-1} . Аналіз SEM показує надзвичайну однорідність усіх зразків. Для дослідження $Mn_{0,4}Zn_{0,6}Fe_2O_4$ використовували EDX аналіз. Приготовані феритові порошки містять Mn, Zn і Fe, як було показано в обох методах синтезу. У цьому дослідженні пропонуються альтернативні шляхи синтезу цих феритів, щоб обійти деякі обмеження традиційного методу приготування.

Ключові слова: ферити, XRD, твердотільний метод синтезу, метод співосадження.

V.A. Romaka¹, Yu. Stadnyk², L. Romaka², P. Demchenko², A. Horyn², O. Poplavskiy³,
V. Pashkevych¹, P. Haraniuk¹

Peculiarities of structural, electrokinetic, energetic, and magnetic properties semiconductive solid solution $\text{Lu}_{1-x}\text{V}_x\text{NiSb}$

¹National University "Lvivska Politechnika", Lviv, Ukraine, volodymyr.romaka@gmail.com;

²Ivan Franko National University of Lviv, Lviv, Ukraine, lyubov.romaka@gmail.com;

³Vasyl Stefanyk Precarpathian National University, Ivano-Frankivsk, Ukraine

The structural, electrokinetic, energetic, and magnetic properties of the new semiconductive solid solution $\text{Lu}_{1-x}\text{V}_x\text{NiSb}$, $x=0-0.10$, were studied. It was shown that V atoms could simultaneously occupy different crystallographic positions in different ratios, generating structural defects of acceptor and donor nature. This creates corresponding acceptor and donor bands in the bandgap ε_g of $\text{Lu}_{1-x}\text{V}_x\text{NiSb}$. The mechanism of the formation of two acceptor bands with different depths of occurrence has been established: a small acceptor band ε_A^2 , formed by defects due to the substitution of Ni atoms by V ones in the 4c position, and band ε_A^1 , generated by vacancies in the LuNiSb structure. The ratio of the concentrations of generated defects determines the position of the Fermi level ε_F and the conduction mechanisms. The investigated solid solution $\text{Lu}_{1-x}\text{V}_x\text{NiSb}$ is a promising thermoelectric material.

Keywords: semiconductor, electrical conductivity, thermopower coefficient, Fermi level.

Received 09 August 2022; Accepted 16 February 2023.

Introduction

The presented work continues the program of finding new thermoelectric materials based on half-Heusler phases (space group $F\bar{4}3m$ [1]). It is known that thermoelectric materials based on half-Heusler phases have high efficiency in converting thermal energy into electrical energy. The thermoelectric figure of merit Z for some samples of solid solutions reaches values of $ZT \sim 1.4$ at a temperature of $T=800$ K [2], which corresponds to the best characteristics of thermoelectric materials based on tellurides, clathrates, skutterudites, etc. ($Z=\alpha^2 \cdot \sigma / \kappa$, where σ – electrical conductivity, α – coefficient of thermopower, and κ – thermal conductivity) [3].

The study of the structural, electrokinetic, energetic, and magnetic properties of semiconductive substitutional solid solutions based on half-Heusler phases, in particular, based on RNiSb ($R = \text{Y, Gd} - \text{Lu}$) compounds [4-11], allows us to understand the nature of processes of charges transport. After all, the optimization of the electrokinetic

characteristics of thermoelectric materials to increase the efficiency of the conversion of thermal energy into electrical energy is carried out by appropriate doping of half-Heusler phases with donor and/or acceptor impurities [12].

It was shown in Refs. [1, 4-11] that the crystal structure of half-Heusler RNiSb phases is defective. Vacancies are present in crystallographic positions 4a of R atoms and 4c of Ni atoms, which are structural defects of an acceptor nature. The presence of vacancies creates a corresponding acceptor band ε_A^1 in the band gap ε_g of RNiSb , which is indicated by positive values of the thermopower coefficient $\alpha(T)$. Understanding the peculiarities of the spatial arrangement of atoms in the nodes of the unit cell of half-Heusler RNiSb phases, in particular, the degree of occupancy of crystallographic positions, allows us to understand the processes of transformation of crystal and electronic structures and the mechanisms of electrical conductivity during the formation of solid solutions.

Thus, the introduction of Sc atoms ($3d^14s^2$) into the structure of the half-Heusler LuNiSb phase by substituting Lu atoms ($5d^16s^2$) in the $4a$ position simultaneously generates various structural defects in $\text{Lu}_{1-x}\text{Sc}_x\text{NiSb}$, $x = 0-0.10$ [9]. Since Lu and Sc atoms are located in the same group of the Periodic System of chemical elements, the substitution of Lu atoms by Sc atoms in position $4a$ generates structural defects of a neutral nature. In the event that Sc atoms occupy vacancies in position $4a$, structural defects of the acceptor nature caused by the vacancies are eliminated, and defects of the donor nature are generated, and the corresponding donor band ε_D^2 appears. Moreover, at concentrations $x \geq 0.07$, the number of donors in $\text{Lu}_{1-x}\text{Sc}_x\text{NiSb}$ grows ~ 2 times faster than in the range $x = 0-0.07$. However, at all concentrations, the Fermi level ε_F lies in the band gap ε_g near the valence band ε_v , and holes are the main current carriers. Occupation of vacancies by Sc atoms is also accompanied by a slight increase in the lattice parameter $a(x)$ $\text{Lu}_{1-x}\text{Sc}_x\text{NiSb}$.

In the case of introducing into the structure of the half-Heusler LuNiSb phase, the lowest concentration of Zr atoms ($4d^25s^2$), $x = 0.01$, the behavior of the electrokinetic characteristics is fundamentally different than when Sc atoms are introduced [10, 11]. The metallic (non-activation) nature of the behavior of the temperature dependences of the resistivity $\rho(T,x)$ and the negative values of the thermopower coefficient $\alpha(T,x)$ of $\text{Lu}_{1-x}\text{Zr}_x\text{NiSb}$ at all concentrations of Zr atoms indicate that the Fermi level ε_F crossed the percolation level of the conduction band ε_c . This behavior of electrokinetic and energetic properties is caused by the following changes in the crystal and electronic structures:

- substitution of Lu atoms by Zr atoms in the $4a$ position generates structural defects of the donor nature, which is associated with a higher number of d -electrons of Zr. At the same time, a donor band ε_D^1 appears in the band gap ε_g ;

- occupation of vacancies in position $4a$ by Zr atoms simultaneously eliminates structural defects of the acceptor nature generated by the vacancies and generates defects of the donor nature and the donor band ε_D^2 . Occupation of vacancies by Zr atoms is also accompanied by a slight increase in the parameter of the unit cell $a(x)$ of $\text{Lu}_{1-x}\text{Zr}_x\text{NiSb}$ samples.

In this context, it seems interesting to study when V atoms ($3d^34s^2$) will be introduced into the structure of the half-Heusler LuNiSb phase by replacing Lu atoms in the $4a$ position. *A priori*, as in the case of $\text{Lu}_{1-x}\text{Zr}_x\text{NiSb}$ [10, 11], we expected the generation of only donor defects in the $\text{Lu}_{1-x}\text{V}_x\text{NiSb}$ structure, $x=0-0.10$, since the V atom has a higher number of d -electrons than Lu. On the other hand, the atomic radius of V ($r_V=0.134$ nm) is much smaller than that of Lu ($r_{Lu}=0.173$ nm) and close to the atomic radius of Ni ($r_{Ni}=0.125$ nm). This may be a precondition for more complex structural changes in $\text{Lu}_{1-x}\text{V}_x\text{NiSb}$, associated with the possible partial occupation by V atoms of the $4c$ position by occupation of vacancies and/or replacement of Ni atoms. The latter can lead to the generation of defects of an acceptor nature, which will be reflected in the experiment by positive values of the thermopower coefficient $\alpha(T,x)$. In the case of $\text{Lu}_{1-x}\text{Sc}_x\text{NiSb}$ and $\text{Lu}_{1-x}\text{Zr}_x\text{NiSb}$ solid solutions, it was impossible to occupy the crystallographic position $4c$ with atoms of impurities Sc

($r_{Sc}=0.164$ nm) and Zr ($r_{Zr}=0.160$ nm) due to a significant difference with the atomic radius of Ni.

The following results of the study of the structural, electrokinetic, energetic, and magnetic properties of the semiconductive solid solution $\text{Lu}_{1-x}\text{V}_x\text{NiSb}$, $x = 0-0.10$, will allow us to establish the factors that have a decisive influence on the crystal and electronic structures. The latter will make it possible to model and obtain thermoelectric materials with high efficiency in converting thermal energy into electrical energy.

I. Methods and materials

$\text{Lu}_{1-x}\text{V}_x\text{NiSb}$ solid solution samples, $x=0.01-0.10$, were prepared by arc-melting a batch of components weighed with an accuracy of ± 0.001 g in an electric arc furnace with a tungsten electrode (cathode) in purified argon atmosphere under a pressure of 0.1 kPa on a copper water-cooled bottom (anode). For homogenization, the obtained alloys were sealed in vacuumed (up to 1.0 Pa) quartz ampoules and annealed in muffle electric furnaces with temperature control with an accuracy of ± 10 K at a temperature of 1073 K for 720 h, followed by quenching in cold water. For X-ray phase analysis, diffraction data were obtained on a STOE STADI-P powder diffractometer (Cu $K\alpha 1$ radiation). Structural characteristics of $\text{Lu}_{1-x}\text{V}_x\text{NiSb}$ samples were calculated using the Fullprof program package [13]. Control of the chemical and phase composition of the samples was carried out using energy dispersive X-ray spectroscopy (EDRS) (scanning electron microscope Tescan Vega 3 LMU). Measurements of the temperature dependences of the electrical resistivity $\rho(T,x)$ of $\text{Lu}_{1-x}\text{V}_x\text{NiSb}$ were carried out by the two-probe method in the temperature range of 80-400 K on samples in the form of rectangular parallelepipeds measuring $\sim 1.0 \times 1.0 \times 5$ mm³. The values of the thermopower coefficient were measured using the potentiometric method relative to copper. Measurements of the voltage drop on the samples were carried out in different directions of the electric current [2] to reduce the influence of “parasitic” effects at the contact points, as well as the influence of a possible p - n transition. The specific magnetic susceptibility χ of $\text{Lu}_{1-x}\text{V}_x\text{NiSb}$ samples was measured by the relative Faraday method at a temperature of 293 K in magnetic fields up to 10 kOe.

II. Study of the structural properties of $\text{Lu}_{1-x}\text{V}_x\text{NiSb}$

X-ray phase analysis of the samples $\text{Lu}_{1-x}\text{V}_x\text{NiSb}$, $x = 0-0.10$, indicated the absence of traces of impurity phases, except for the main phase, which is indexed in the structure type MgAgAs [1]. According to microprobe analysis data, the concentration of atoms on the surface of $\text{Lu}_{1-x}\text{V}_x\text{NiSb}$ samples corresponds to the initial composition of the charge.

X-ray structural studies of the $\text{Lu}_{1-x}\text{V}_x\text{NiSb}$ solid solution, $x=0-0.10$, exhibited the complex behavior of the unit cell parameter $a(x)$ with an increasing concentration of V atoms (Fig. 1). Based on the fact that the atomic radius of Lu significantly exceeds that of V, it was logical

to expect a decrease in the values of the unit cell parameter $a(x)$ $\text{Lu}_{1-x}\text{V}_x\text{NiSb}$ when replacing Lu atoms with V atoms in the $4a$ position. However, as can be seen from Fig. 1, in the concentration range $x=0-0.03$, the values of $a(x)$ for $\text{Lu}_{1-x}\text{V}_x\text{NiSb}$ increase, pass through a maximum, and rapidly decrease at $x>0.03$. By the way, we observed a similar behavior of the unit cell parameter $a(x)$ in the $\text{Lu}_{1-x}\text{Zr}_x\text{NiSb}$ solid solution [10, 11] (Fig. 1, inset). The presence of maximum on the dependence $a(x)$ of $\text{Lu}_{1-x}\text{V}_x\text{NiSb}$ (Fig. 1) allows us to assume that the V atoms introduced into the matrix of the half-Heusler LuNiSb phase can simultaneously, in different ratios, partially occupy both different crystallographic positions and tetrahedral voids of the structure which make up $\sim 24\%$ of the volume of a unit cell [2].

Since the atomic radius of Ni ($r_{\text{Ni}} = 0.124$ nm) is the smallest among the components of the $\text{Lu}_{1-x}\text{V}_x\text{NiSb}$ solid solution ($r_{\text{Sb}}=0.159$ nm), the increase in the unit cell parameter $a(x)$ in the concentration range $x = 0-0.03$ can be caused by only partial occupation by V atoms crystallographic position $4c$, and also vacancies in position $4a$. In the case of substitution of Ni atoms ($3d^84s^2$) by V atoms ($3d^34s^2$) in $\text{Lu}_{1-x}\text{V}_x\text{NiSb}$, structural defects of an acceptor nature are generated, since the V atom contains fewer d -electrons. At the same time, an additional acceptor band ε_A^2 will appear in the band gap of $\text{Lu}_{1-x}\text{V}_x\text{NiSb}$. On the other hand, the possible occupation of vacancies in position $4c$ by V atoms will also lead to an increase in the values of the lattice parameter $a(x)$ for $\text{Lu}_{1-x}\text{V}_x\text{NiSb}$. At the same time, the structural defect of the acceptor nature (vacancy) and the corresponding acceptor band ε_A^1 disappear. Atom V, occupying a vacancy in position $4c$, generates a structural defect of the donor nature. Therefore, the semiconductor $\text{Lu}_{1-x}\text{V}_x\text{NiSb}$, $x = 0-0.03$, will simultaneously contain donors and acceptors, and their ratio during ionization will determine the sign of the thermopower coefficient $\alpha(x, T)$ and the type of the main current carriers.

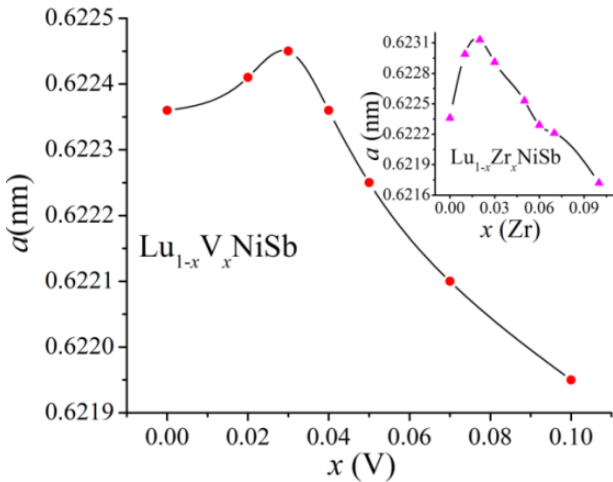


Fig. 1. Variation of the unit cell parameter $a(x)$ with increasing impurity content in $\text{Lu}_{1-x}\text{V}_x\text{NiSb}$ and $\text{Lu}_{1-x}\text{Zr}_x\text{NiSb}$ [11] (upper inset).

A decrease in the values of the unit cell parameter $a(x)$ $\text{Lu}_{1-x}\text{V}_x\text{NiSb}$, which occurs at $x > 0.03$ (Fig. 1), can be caused only by the occupation of crystallographic position $4a$ by V atoms. At the same time, structural defects of a

donor nature will be generated in the crystal both during the substitution of Lu atoms and the occupation of vacancies. The latter eliminates the structural defect in the form of a vacancy and the corresponding acceptor band. The maximum on the dependence $a(x)$ of $\text{Lu}_{1-x}\text{V}_x\text{NiSb}$ at a concentration of $x \approx 0.03$ is the result of two competing processes in the structure of the semiconductor, associated with the simultaneous occupation of crystallographic positions $4c$ and $4a$ by V atoms in different ratios.

Therefore, structural studies of the semiconductive solid solution $\text{Lu}_{1-x}\text{V}_x\text{NiSb}$, $x=0-0.10$, indicate that V atoms can simultaneously occupy different crystallographic positions in different ratios, generating at the same time structural defects of a donor and/or acceptor nature.

The above considerations regarding the changes in the structure of the $\text{Lu}_{1-x}\text{V}_x\text{NiSb}$ solid solution based on the behavior of the unit cell parameter $a(x)$ are of an evaluative nature, since the accuracy of X-ray structural studies does not allow to unambiguously identify the causes of these changes. The results of the study of the electrokinetic, energetic and magnetic properties of $\text{Lu}_{1-x}\text{V}_x\text{NiSb}$, $x = 0-0.10$, presented below, will complement the results of structural studies, which will allow modeling of crystal and electronic structures as close as possible to the real state of the substance.

III. Study of electrokinetic, energetic and magnetic properties of $\text{Lu}_{1-x}\text{V}_x\text{NiSb}$

The temperature dependences of the electrical resistivity $\ln(\rho(1/T, x))$ and the thermopower coefficient $\alpha(1/T, x)$ of the $\text{Lu}_{1-x}\text{V}_x\text{NiSb}$ solid solution, $x = 0-0.10$, are shown in Fig. 2. At all concentrations of $\text{Lu}_{1-x}\text{V}_x\text{NiSb}$, high-temperature activation parts are presented on the temperature dependences $\ln(\rho(1/T, x))$ and $\alpha(1/T, x)$ (Fig. 2). This is evidence that the investigated samples are doped and compensated semiconductors [14]. The presence of high-temperature activation on the dependences $\ln(\rho(1/T, x))$ of $\text{Lu}_{1-x}\text{Sc}_x\text{NiSb}$ indicates the location of the Fermi level ε_F in the band gap ε_g . For samples with concentrations $x = 0-\leq 0.07$, the Fermi level ε_F lies near the valence band ε_V , as indicated by the positive values of the thermopower coefficient α at high temperatures (Fig. 2). At concentrations $x > 0.07$, the Fermi level ε_F moved to the conduction band ε_C , which is indicated by the negative values of the thermopower coefficient α at all temperatures.

The temperature dependences $\ln(\rho(1/T, x))$ of $\text{Lu}_{1-x}\text{V}_x\text{NiSb}$ (Fig. 2) can be described by the well-known expression (1) [14]:

$$\rho^{-1}(T) = \rho_1^{-1} \exp\left(-\frac{\varepsilon_1^p}{k_B T}\right) + \rho_3^{-1} \exp\left(-\frac{\varepsilon_3^p}{k_B T}\right) \quad (1)$$

where the first high-temperature term describes the activation of current carriers $\varepsilon_1^p(x)$ from the Fermi level ε_F into the valence band ε_V , and the second, low-temperature term, describes the jump conduction $\varepsilon_3^p(x)$ with energies

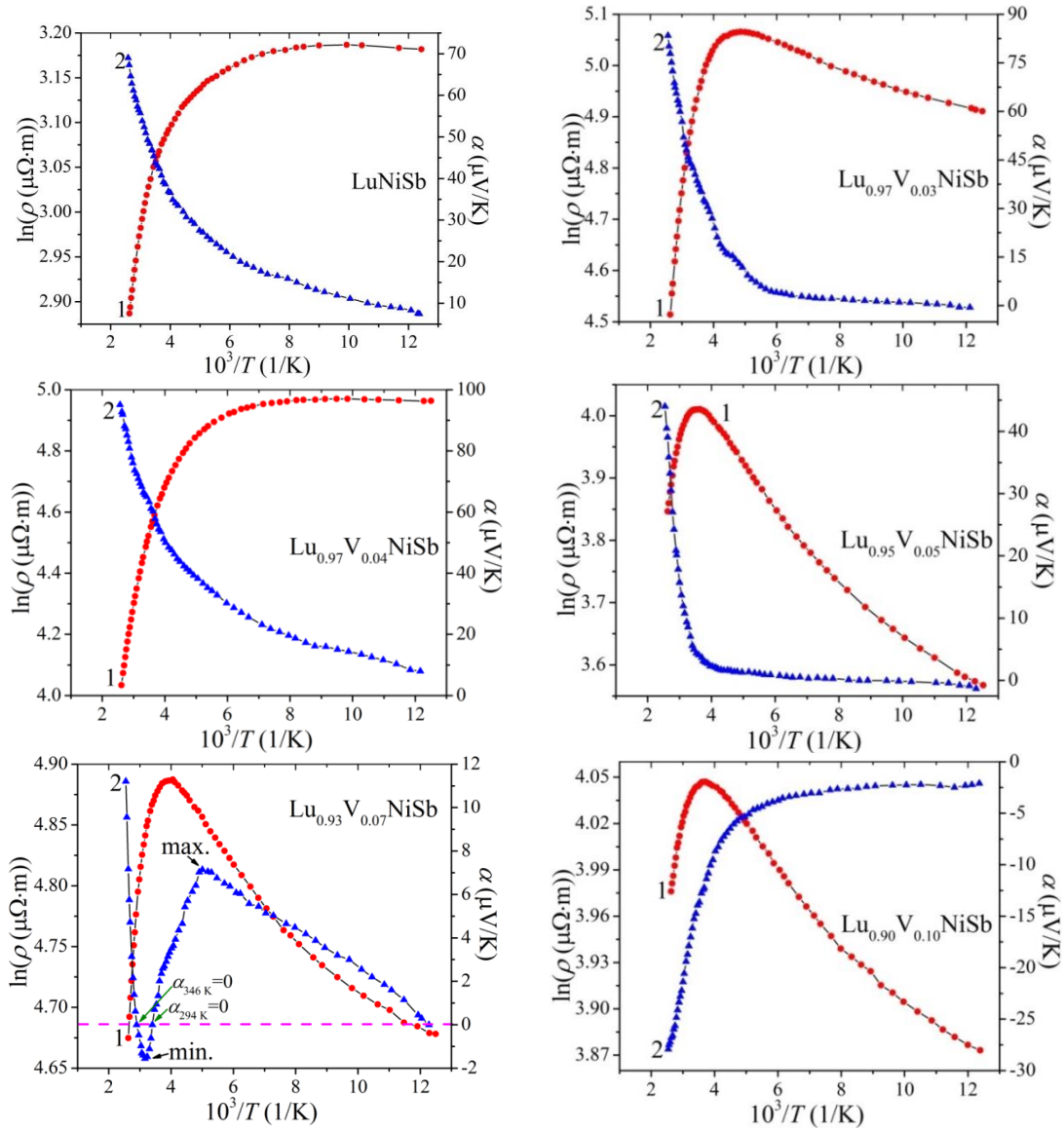


Fig. 2. Temperature dependences of specific electrical resistivity $\ln(\rho(1/T,x))$ (1) and thermopower coefficient $\alpha(1/T,x)$ (2) of $\text{Lu}_{1-x}\text{V}_x\text{NiSb}$.

close to the Fermi level ε_F . The temperature dependence of the thermopower coefficient $\alpha(1/T,x)$ for $\text{Lu}_{1-x}\text{V}_x\text{NiSb}$ (Fig. 2) is described by formula (2) [15]:

$$\alpha = \frac{k_B}{e} \left(\frac{\varepsilon_F^\alpha}{k_B T} - \gamma + 1 \right) \quad (2)$$

where γ is a parameter that depends on the nature of the scattering mechanism. Based on formula (2), the values of activation energies $\varepsilon_1^\alpha(x)$ and $\varepsilon_3^\alpha(x)$ were calculated from the high- and low-temperature activation parts of the dependence $\alpha(1/T,x)$. In Ref. [12], it was established that the values of the activation energies $\alpha(1/T,x)$ are proportional to the amplitude of the large-scale fluctuation of the continuous energy bands and the small-scale fluctuation of the doped and compensated semiconductor. The compensation degree of semiconductor is evaluated by the modulation amplitude of the bands.

The existence of the hopping ε_3^p -conductivity mechanism at low temperatures in the LuNiSb samples indicates the presence of a significant number of ionized acceptors in the semiconductor (positive values of the

thermopower coefficient α) and compensating donors of unknown origin, which actually ensures carrier jumps in localized states in the vicinity of the Fermi energy ε_F . In this case, the Fermi level ε_F in LuNiSb is at a distance of 10.2 meV from the percolation level of the valence band ε_V (Fig. 3). At the same time, a feature of the temperature dependences of the electrical resistivity $\ln(\rho(1/T,x))$ for all doped samples ($x > 0$) of $\text{Lu}_{1-x}\text{V}_x\text{NiSb}$ is the absence of low-temperature activation parts, i.e. the hopping ε_3^p -conductivity mechanism. We can see that in the samples $\text{Lu}_{1-x}\text{V}_x\text{NiSb}$, $x > 0$, at low temperatures, the values of electrical resistivity ρ increase with increasing temperature (Fig. 2), which is characteristic of a metallic type of conductivity.

In doped and compensated semiconductors, the metallization of low-temperature conductivity indicates the closeness of the Fermi energy ε_F and the percolation level of continuous energy bands [14]. In the case of $\text{Lu}_{1-x}\text{V}_x\text{NiSb}$ doped samples, $x=0.01-0.07$, this energy proximity facilitates the ionization of acceptors and the appearance of a significant number of free holes in the

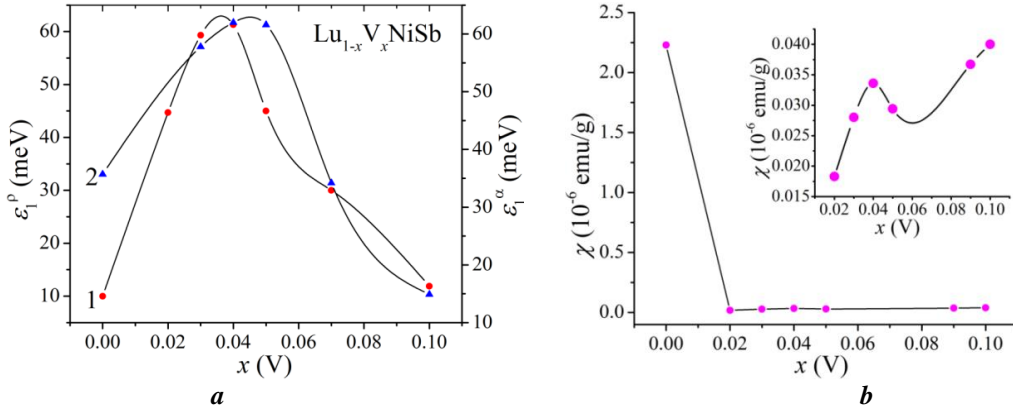


Fig. 3. Variation of activation energies $\varepsilon_1^p(x)$ (1) and $\varepsilon_1^\alpha(x)$ (2) (a), and specific magnetic susceptibility $\chi(x)$ (b) of $\text{Lu}_{1-x}\text{V}_x\text{NiSb}$.

valence band ε_V , which causes the overlap of the wave functions of impurity states near the Fermi energy ε_F .

Using the terminology of the traditional approach to describe semiconductors, let's rephrase what has been said: the ε_A^2 acceptor band, generated by defects due to the substitution of Ni atoms by V ones, intersects with the ε_V valence band, forming a "tail" that leads to the metallization of conductivity.

At higher temperatures, holes are activated from the Fermi level ε_F , which is now fixed by another acceptor band ε_A^1 , generated by vacancies in the structure of the half-Heusler LuNiSb phase. This acceptor band is located deep in the band gap ε_g and the high-temperature activation parts of $\ln(\rho(1/T, x))$ for $\text{Lu}_{1-x}\text{V}_x\text{NiSb}$ reflect the process of hole activation exactly from the acceptor band ε_A^1 . And if in LuNiSb the depth of the Fermi level ε_F relative to the percolation level of the valence band ε_V is ~ 10.2 meV, then, for example, in the semiconductor $\text{Lu}_{0.98}\text{V}_{0.02}\text{NiSb}$ it is about 45 meV (Fig. 3a).

As seen from Fig. 3a, in the concentration range $x = 0-0.03$, the hole activation energy $\varepsilon_1^p(x)$ from the Fermi level ε_F to the percolation level of the valence band ε_V increases almost linearly. This makes it possible to determine the motion rate of the Fermi level ε_F from the valence band ε_V , which is $\Delta\varepsilon_F/\Delta x \approx 16.4$ meV/%V. At concentrations $x \geq 0.07$, the motion rate of the Fermi level ε_F to the percolation level of the conduction band ε_C (negative values of the thermopower coefficient α) is $\Delta\varepsilon_F/\Delta x \approx 6.1$ meV/%V.

The temperature dependence of the thermopower coefficient $\alpha(1/T, x)$ of the semiconductor $\text{Lu}_{0.93}\text{V}_{0.07}\text{NiSb}$ (Fig. 2) revealed two acceptor bands with different depths of occurrence in the band gap ε_g , as well as a donor band, the existence of which we assumed based on results of structural studies. The growth of the thermopower coefficient dependence $\alpha(1/T, x)$ in the temperature range $T = 80-190$ K shows that donors are generated in the semiconductor $\text{Lu}_{0.93}\text{V}_{0.07}\text{NiSb}$ even at low temperatures. The presence of an extremum (maximum) on the dependence $\alpha(1/T, x)$ at $T \approx 190$ K indicates that the growth rate of the concentration of ionized donors is greater than the rate of increase in the concentration of ionized acceptors. Obviously, the depletion of the ε_A^1 acceptor band, generated by vacancies in the structure of the half-Heusler LuNiSb phase, takes place. Such dynamics of growth in the concentration of ionized donors

leads to a change in the sign of the thermopower coefficient $\alpha(1/T, x)$ at $T \approx 294$ K, and the growth of negative values of the thermopower coefficient in the range $T = 294-316$ K indicates a change of type of semiconductor conductivity, when free electrons become the main carriers.

The minimum on the dependence of $\alpha(1/T, x)$ at the temperature $T \approx 316$ K indicates the beginning of ionization of acceptor states ε_A^2 , generated by defects in the replacement of Ni atoms with atoms V and depletion of donor states. Repeated complete compensation of the semiconductor $\text{Lu}_{0.93}\text{V}_{0.07}\text{NiSb}$ occurs at $T \approx 346$ K when the sign of the thermopower coefficient changes from negative to positive. At the same time, at temperatures $T > 346$ K, the holes again become the main current carriers.

The absence at low temperatures of the hopping ε_3^p -conductivity mechanism in $\text{Lu}_{1-x}\text{V}_x\text{NiSb}$, $x > 0.07$, indicates the location of the Fermi level ε_F at a distance of $k_B \cdot T$ from the percolation level of the conduction band ε_C (negative values of the thermopower coefficient $\alpha(1/T, x)$). This leads to an overlap of the wave functions of the impurity states near the Fermi energy ε_F . In the semiconductor $\text{Lu}_{1-x}\text{V}_x\text{NiSb}$, $x > 0.07$, a high concentration of free electrons appears due to the simplified ionization of generated donors as a result of the corresponding structural transformations.

Experimental studies of the magnetic susceptibility $\chi(x)$ showed that the samples of both the LuNiSb compound and the $\text{Lu}_{1-x}\text{V}_x\text{NiSb}$ solid solution at all concentrations are Pauli paramagnets (Fig. 3b). In this case, the similarity of the behavior of the dependences of the resistivity $\rho(x, T)$, the thermopower coefficient $\alpha(x, T)$ (Fig. 4b) and the magnetic susceptibility $\chi(x)$ (Fig. 3b) is clear and associated with a change in the density of states at the Fermi level $g(\varepsilon_F)$.

The behavior of the concentration dependences of the electrical resistivity $\rho(x, T)$ and the thermopower coefficient $\alpha(x, T)$ of $\text{Lu}_{1-x}\text{V}_x\text{NiSb}$ at different temperatures is interesting and informative (Fig. 4). An increase of the electrical resistivity $\rho(x, T)$ in the concentration range $x = 0-0.03$ in a semiconductor of p -type conductivity is possible only if the concentration of free holes decreases. This reason is the generation of donors in the semiconductor that capture holes. This leads to an increase

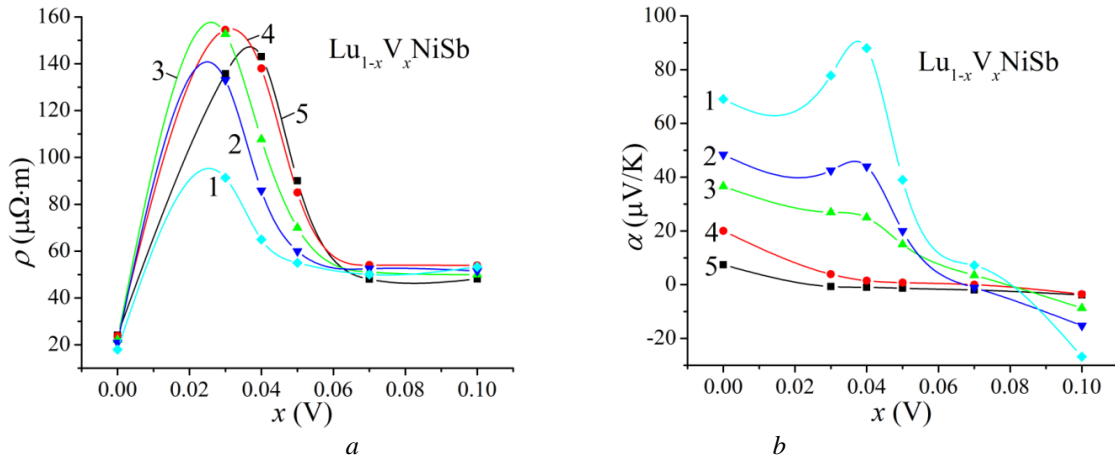


Fig. 4. Variation of the electrical resistivity $\rho(x, T)$ (a) and the thermopower coefficient $\alpha(x, T)$ (b) of $\text{Lu}_{1-x}\text{V}_x\text{NiSb}$ at different temperatures: 1 – $T=380$ K; 2 – $T=300$ K; 3 – $T=250$ K; 4 – $T=160$ K; 5 – $T=80$ K.

in the compensation degree of the semiconductor, as indicated by the behavior of the activation energy $\varepsilon_1^\alpha(x)$, calculated from the high-temperature part of the dependencies $\alpha(1/T, x)$ of $\text{Lu}_{1-x}\text{V}_x\text{NiSb}$ (Fig. 3a, curve 2). At higher modulation amplitude of the continuous energy bands $\varepsilon_1^\alpha(x)$, the higher compensation degree of the semiconductor was observed [14]. We can see that in the concentration range $x=0-0.03$, the values of the activation energy $\varepsilon_1^\alpha(x)$ increase, and the reason is the appearance of donors in the semiconductor.

The results of the electrokinetic and energetic properties of $\text{Lu}_{1-x}\text{V}_x\text{NiSb}$ in the concentration range $x=0-0.03$ are consistent and clarify the conclusions of the structural studies. Thus, based on an analysis of the structural characteristics of $\text{Lu}_{1-x}\text{V}_x\text{NiSb}$, it was established that the increase of the lattice parameter $a(x)$ in the concentration range $x=0-0.03$ can be caused by the only partial occupation of the $4c$ position by V atoms. Since donors are generated in the semiconductor in this case, V atoms in the concentration range $x=0-0.03$ occupy vacancies in position $4c$ (substitution of Ni atoms generates acceptors). At the same time, as follows from the behavior of the thermopower coefficient $\alpha(x, T)$, the concentration of acceptors dominates the concentration of generated donors.

At a concentration $x=0.04$ and temperature of 80 K, an extremum appears on the dependence of the electrical resistivity $\rho(x, T)$, which shifts with increasing temperature to the region of lower concentrations of V atoms. The appearance of an extremum on the $\rho(x, T)$ dependence is the result of changes in the ratio of ionized acceptors and donors available in the semiconductor. The fact that as the temperature increases, the maximum on the $\rho(x, T)$ dependence shifts to the region of lower concentrations of V atoms is understandable, since the increase of temperature simplifies the ionization of acceptors and donors and the increase in the concentration of free carriers. We can assume that at all temperatures in semiconductors $\text{Lu}_{1-x}\text{V}_x\text{NiSb}$, $x > 0.03$, such concentration of free carriers of both types appears that even with a slight increase of the compensation degree up to $x \approx 0.05$ (Fig. 3a, curve 2) the total conductivity of semiconductors increases rapidly and continues up to concentration $x=0.07$.

Since the semiconductor $\text{Lu}_{0.93}\text{V}_{0.07}\text{NiSb}$ simultaneously contains significant concentrations of electrons and holes and is heavily doped and compensated, with an increase of the concentration of V atoms ($x > 0.07$), the type of main carriers changes from holes to electrons (Fig. 3b), however, high concentrations of free electrons provide high conductivity, which has little effect on the change in the values of electrical resistivity $\rho(x, T)$ at all temperatures (Fig. 3a).

Therefore, studies of the electrokinetic, energetic, and magnetic properties of the $\text{Lu}_{1-x}\text{V}_x\text{NiSb}$ solid solution, $x=0-0.10$, confirm the conclusions of structural studies regarding the simultaneous occupation of V atoms in different ratios of crystallographic positions $4a$ and $4c$, generating at the same time structural defects of a donor and/or acceptor nature. Understanding the mechanism of structural transformations in $\text{Lu}_{1-x}\text{V}_x\text{NiSb}$ will make it possible to model and obtain thermoelectric materials with high efficiency in converting thermal energy into electrical energy.

Conclusions

According to the results of a complex study of the structural, electrokinetic, energetic, and magnetic properties of the semiconductive solid solution $\text{Lu}_{1-x}\text{V}_x\text{NiSb}$, obtained by introducing V atoms into the structure of the LuNiSb compound by substitution of Lu atoms in the crystallographic position $4a$, a complicated character of structural changes was revealed. It is shown that V atoms can simultaneously occupy different crystallographic positions in different ratios, generating structural defects of acceptor and donor nature. This gives rise to the corresponding acceptor and donor bands in the band gap ε_g of $\text{Lu}_{1-x}\text{V}_x\text{NiSb}$. The mechanism of the formation of two acceptor bands with different depth of occurrence in $\text{Lu}_{1-x}\text{V}_x\text{NiSb}$ has been established: a small acceptor band ε_A^2 , formed by defects upon the substitution of Ni atoms by V in the $4c$ position, and band ε_A^1 , generated by vacancies in the structure of the half-Heusler LuNiSb phase. The ratio of the concentrations of generated defects determines the position of the Fermi level ε_F and the conduction mechanisms. The investigated solid solution $\text{Lu}_{1-x}\text{V}_x\text{NiSb}$ is a promising thermoelectric

material.

The work was carried out within the framework of the Ministry of Education and Science of Ukraine, grant № 0121U109766.

Romaka V. – Professor of Lviv Polytechnic National University;

Stadnyk Y. – Ph.D., Senior Scientist of Ivan Franko National University of Lviv;

Romaka L. – Ph.D., Senior Scientist of Ivan Franko

National University of Lviv;

Demchenko P. – Ph.D., Senior Scientist of Ivan Franko National University of Lviv;

Horyn A. – Ph.D., Senior Scientist of Ivan Franko National University of Lviv;

Poplavskiy O. – Ph.D., docent of Vasyl Stefanyk Precarpathian National University;

Pashkevych V. – docent of Lviv Polytechnic National University;

Haraniuk P. – docent of Lviv Polytechnic National University.

- [1] K. Hartjes, W. Jeitschko, *Crystal structure and magnetic properties of the lanthanoid nickel antimonides LnNiSb (Ln=La–Nd, Sm, Gd–Tm, Lu)*, J. Alloys Compd. 226, 81 (1995); [https://doi.org/10.1016/0925-8388\(95\)01573-6](https://doi.org/10.1016/0925-8388(95)01573-6).
- [2] V.A. Romaka, Yu.V. Stadnyk, V.Ya. Krayovskyy, L.P. Romaka, O.P. Guk, V.V. Romaka, M.M. Mykyychuk, A.M. Horyn, *The latest heat-sensitive materials and temperature transducers*, Lviv Polytechnic Publishing House, Lviv (2020). ISBN 978-966-941-478-6. [in Ukrainian].
- [3] L.I. Anatyshchuk, *Thermoelements and thermoelectric devices*. Reference book, Naukova dumka, Kyiv (1979). [in Russian].
- [4] I.Karla, J. Pierre, R.V. Skolozdra, *Physical properties and giant magnetoresistance in RNiSb compounds*, J. Alloys Compd, 265, 42 (1998); [https://doi.org/10.1016/S0925-8388\(97\)00419-2](https://doi.org/10.1016/S0925-8388(97)00419-2).
- [5] V.V. Romaka, L. Romaka, A. Horyn, P. Rogl, Yu. Stadnyk, N. Melnychenko, M. Orlovskyy, V. Krayovskyy, *Peculiarities of thermoelectric half-Heusler phase formation in Gd-Ni-Sb and Lu-Ni-Sb ternary systems*, J. Solid State Chem, 239, 145 (2016); <https://doi.org/10.1016/j.jssc.2016.04.029>.
- [6] V.V. Romaka, L. Romaka, A. Horyn, Yu. Stadnyk, *Experimental and theoretical investigation of the Y–Ni–Sb and Tm–Ni–Sb systems*, J. Alloys Compd., 855, 157334 (2021); <https://doi.org/10.1016/j.jallcom.2020.157334>.
- [7] Yu. Stadnyk, L. Romaka, V. A. Romaka, A. Horyn, V. Krayovskii, P. Klyzub, M. Rokomanuk, *Study of semiconducting thermoelectric material Er_{1-x}Zr_xNiSb*, Coll. Abs. XXII Int. Seminar Phys. Chem. Solids. June 17-19, 2020, Lviv, Ukraine. – 2020. – P. 35.
- [8] Yu.V., Stadnyk, L.P. Romaka, A.M. Horyn, V.V. Romaka, M.V. Rokomanuk, V.Z. Pashkevych, *Study of semiconducting thermoelectric material Er_{1-x}Sc_xNiSb*, Coll. Abs. XVIII Int. Freik Conf. Phys., Technol. Thin Films and Nanosystems. October 11-16, 2021, Ivano-Frankivsk, Ukraine. – 2021. – P. 88.
- [9] Yu. Stadnyk, V.A. Romaka, L. Romaka, A. Horyn, V. Pashkevych, M. Rokomanuk, *Experimental studies of thermoelectric material Lu_{1-x}Sc_xNiSb*, Proc. II Intern. Scientific Conference «Current Problems of Chemistry, Materials Science and Ecology», Lutsk, Ukraine, 1-3 June 2022, p. 84-86.
- [10] V.A. Romaka, Yu.V. Stadnyk, L.P. Romaka, V.Z. Pashkevych, V.V. Romaka, A.M. Horyn, P.Yu. Demchenko, *Study of structural, thermodynamic, energy, kinetic and magnetic properties of thermoelectric material Lu_{1-x}Zr_xNiSb*, J. Thermoelectricity, 1, 32 (2021); http://jt.inst.cv.ua/jt/jt_2021_01_en.pdf.
- [11] V.A. Romaka, Yu. V. Stadnyk, L. P. Romaka, A. M. Horyn, V. Z. Pashkevych, M.V. Rokomanuk, *Features of structural, thermodynamic, energetic, kinetic and magnetic characteristic of Lu_{1-x}Zr_xNiSb solid solution*, Coll. Abs. XVIII Int. Freik Conf. Phys., Technol. Thin Films and Nanosystems. October 11-16, 2021, Ivano-Frankivsk, Ukraine. – 2021. – P. 87.
- [12] V.A. Romaka, E.K. Hlil, Ya.V. Skolozdra, P. Rogl, Yu.V. Stadnyk, L.P. Romaka, and A.M. Goryn, *Features of the Mechanisms of Generation and “Healing” of Structural Defects in the Heavily Doped Intermetallic Semiconductor n-ZrNiSn*, Semiconductors, 43, 1115 (2009); <https://doi.org/10.1134/S1063782609090024>.
- [13] T. Roisnel, J. Rodriguez-Carvajal, *WinPLOTR: a windows tool for powder diffraction patterns analysis*, Mater. Sci. Forum, Proc. EPDIC7, 378, 118 (2001); <https://doi.org/10.4028/www.scientific.net/MSF.378-381.118>.
- [14] B.I. Shklovskii and A.L. Efros, *Electronic properties of doped semiconductors*, Springer-Verlag, Berlin, Heidelberg (1984); <https://doi.org/10.1007/978-3-662-02403-4>.
- [15] N.F. Mott and E.A. Davis, *Electron processes in non-crystalline materials*, Clarendon Press, Oxford (1979).

В.А. Ромака¹, Ю. Стадник², Л. Ромака², П. Демченко², А. Горинь², О. Поплавський³,
В. Пашкевич¹, П. Гаранюк¹

Особливості структурних, електрокінетичних, енергетичних та магнітних властивостей напівпровідникового твердого розчину $\text{Lu}_{1-x}\text{V}_x\text{NiSb}$

¹Національний університет "Львівська політехніка", Львів, Україна, volodymyr.romaka@gmail.com;

²Львівський національний університет ім. І. Франка, Львів, Україна, lyubov.romaka@gmail.com;

³Прикарпатський національний університет імені Василя Стефаника, Івано-Франківськ, Україна

Досліджено структурні, електрокінетичні, енергетичні та магнітні властивості нового напівпровідникового твердого розчину $\text{Lu}_{1-x}\text{V}_x\text{NiSb}$, $x = 0-0.10$. Показано, що атоми V можуть одночасно у різних співвідношеннях займати різні кристалографічні позиції, генеруючи структурні дефекти акцепторної та донорної природи. Це породжує у забороненій зоні ϵ_g $\text{Lu}_{1-x}\text{V}_x\text{NiSb}$ відповідні акцепторні та донорні зони. Встановлено механізм формування двох акцепторних зон з різною глибиною залягання: дрібна акцепторна зона ϵ_{A^2} , утворена дефектами при заміщенні у позиції 4c атомів Ni на V, та зона ϵ_{A^1} , породжена вакансіями у структурі LuNiSb . Співвідношення концентрацій генерованих дефектів визначає положення рівня Фермі ϵ_F та механізми провідності. Досліджений твердий розчин $\text{Lu}_{1-x}\text{V}_x\text{NiSb}$ є перспективним термоелектричним матеріалом.

Ключові слова: напівпровідник, електропровідність, коефіцієнт термо-ерс, рівень Фермі.

A.I. Kashuba

Influence of metal atom substitution on the electronic and optical properties of solid-state $\text{Cd}_{0.75}\text{X}_{0.25}\text{Te}$ ($\text{X} = \text{Cu}, \text{Ag}$ and Au) solutions

Department of General Physics, Lviv Polytechnic National University, Lviv, Ukraine, andrii.i.kashuba@lpnu.ua

The solid-state $\text{Cd}_{0.75}\text{X}_{0.25}\text{Te}$ ($\text{X} = \text{Cu}, \text{Ag}$, and Au) solutions crystallize in the cubic structure and are studied in the framework of density functional theory. The theoretical first-principle calculations of the electronic band structure, density of states, and refractive index of solid-state $\text{Cd}_{0.75}\text{X}_{0.25}\text{Te}$ ($\text{X} = \text{Cu}, \text{Ag}$, and Au) solutions are estimated by the generalized gradient approximation (GGA). A Perdew–Burke–Ernzerhof functional (PBE) was utilized. Formation energy is calculated based on the results of the total energy of the study samples. The effective mass of the electrons and holes was calculated based on the electronic band structure. The influence of atom substitution on electron conductivity and mobility is discussed. To study the optical properties was use a complex dielectric function $\epsilon(\hbar\omega)$. The spectral behaviour of the refractive index was calculated based on the dielectric function.

Keywords: density functional theory, electron band structure, formation energy, effective mass, density of state, refractive index.

Received 10 December 2022; Accepted 6 March 2023.

Introduction

Cadmium chalcogenides (CdY , with $\text{Y} = \text{S}, \text{Se}$ and Te) represent the $\text{A}^{\text{II}}\text{B}^{\text{VI}}$ group of crystalline materials that reveal a semiconducting behaviour. These materials embrace large and important research fields because of their wide application potential in various fields of optoelectronic devices [1]. CdTe semiconductor has proven to be a leading compound for manufacturing cost-effective second-generation photovoltaic devices [1]. Cadmium telluride is having a direct band gap with an energy of ~ 1.45 eV and a high absorbance (above 10^5cm^{-1}) [2–4]. This makes it an excellent light-absorbing layer for solar cells. Now, for building solar cells use the low dimensions of the photovoltaic cells. In particular, it's a thin film. Usually, CdTe is deposited on glass, quartz, mica, silicon or many other substrates. But it can also be deposited on substrates like metal foil or polymer sheets [5–7]. Also, Ref. [7] quoted that the formation of a low resistive contact on the CdTe surface is one of the most critical issues for the fabrication of a highly efficient CdTe thin film solar cell. Schottky energy barrier is higher than

~ 0.4 eV, and is formed at the CdTe/metal back contact interface [7–9]. Schottky barrier can be efficiently lowered by doping the CdTe surface using a thin layer of Cu [6, 7, 9]. Cu can diffuse from the back contact into the CdTe thin film. As a result, Cu can enter in CdTe as a doping element, which is a donor. Also, copper can substitute cadmium atoms or free position of Cd vacancy. In literature found many experimental works with studies of Cu and/or Ag doping/substitution in CdTe [10–17]. About identification of Cu and Ag acceptor levels in CdTe was a study in Ref. [18].

A new step in studies of low-dimension systems is quantum dots (QDs) or nanocrystals (NCs) [19, 20]. Also, QDs based on CdTe have potential applications in novel light emitters, next-generation solar cells, sensing, and biomedical diagnostics [19]. This research branch has a perspective using doped QDs, such as $\text{CdTe}:\text{Au}$ [19].

In the present work, the electronic band structure, formation energy, density of states and refractive index of the solid-state $\text{Cd}_{0.75}\text{X}_{0.25}\text{Te}$ ($\text{X} = \text{Cu}, \text{Ag}$ and Au) solutions have been calculated for the first time. In the literature was founded information about studies of physical properties of the CdTe with Cr -doped [21–23], Sn -doped [24], V and P -

doped [25], Cu-doped [26], V-dopes [23, 27], As and P-doped [28], Cl-doped [29]. In the case of substitution of Cd atom in CdTe usually using atoms of Mn [30, 31], Ti [32], Zn [33], et al. Only diffusion of Cd vacancies and interstitials of Cd, Cu, Ag, Au and Mo in CdTe was studied in Ref. [34].

The paper is organized as follows. The next section introduces the calculation techniques used. The first subsection in the second section reports the main results of the structure analysis of solid-state $\text{Cd}_{0.75}\text{X}_{0.25}\text{Te}$ ($X = \text{Cu, Ag and Au}$) solutions. *Ab initio* calculations of the formation energy of solid-state $\text{Cd}_{0.75}\text{X}_{0.25}\text{Te}$ ($X = \text{Cu, Ag and Au}$) solutions are elucidated in the second subsection. The third subsection in the second section is the study of the electronic band structure of the solid solutions. The density of states and refractive index of the solid-state $\text{Cd}_{0.75}\text{X}_{0.25}\text{Te}$ ($X = \text{Cu, Ag and Au}$) solutions are elucidated in the fourth and five subsections, respectively. Finally, the conclusions are drawn in the last section.

I. Methods of calculation

In preview work [35], was reported about electron, phonon, optical and thermodynamic properties of the CdTe crystal. In the present work, the electronic energy spectra of the solid-state $\text{Cd}_{0.75}\text{X}_{0.25}\text{Te}$ ($X = \text{Cu, Ag and Au}$) solutions have been calculated for the first time. The theoretical calculations were performed within the framework of the density functional theory (DFT). To calculate the properties of single-crystalline $\text{Cd}_{0.75}\text{X}_{0.25}\text{Te}$, a crystalline lattice with the basal parameters given below in Table 1 was used. To describe the exchange-correlation energy of the electronic subsystem, we used a functional taken in the approximation of generalized gradient (GGA) and Perdew–Burke–Ernzerhof (PBEsol) parameterization [36]. Ultrasoft Vanderbilt’s pseudopotentials [37] served as ionic potentials.

In our calculations, the value $E_{\text{cut-off}} = 880$ eV was taken for the cutting-off energy of the plane waves (this energy corresponded to the minimum value of the total energy). The convergence of the total energy was about 5×10^{-6} eV/atom. Integration over the Brillouin zone (BZ) was performed on a $2 \times 2 \times 2$ grid of k points, using a Monkhorst–Pack scheme [38]. At the initial stage of our calculations, we optimized a starting CdTe structure for the case of $3 \times 3 \times 3$ supercell (see Ref. [35]). The atomic coordinates and the unit-cell parameters were optimized following a Broyden–Fletcher–Goldfarb–Shanno technique. Optimization was continued until the forces acting on atoms became less than 0.01 eV/Å, the maximum displacement less than 5.0×10^{-4} Å, and the mechanical stresses in the cell less than 0.02 GPa. The energy band diagram was constructed using the points X(0.5, 0, 0.5), R(0.5, 0.5, 0.5), M(0.5, 0.5, 0) and $\Gamma(0,0,0)$ of the Brillouin zone in the reciprocal space (see Fig. 1).

The $\text{Cd}_{0.75}\text{X}_{0.25}\text{Te}$ ($X = \text{Cu, Ag and Au}$) samples were modelled as follows. First formed a $3 \times 3 \times 3$ supercell of the initial compound, CdTe, based on its already optimized structure. The next stage was the theoretical construction of solid-state $\text{Cd}_{0.75}\text{X}_{0.25}\text{Te}$ ($X = \text{Cu, Ag and Au}$) solutions. In the optimization structure CdTe, Cd atoms were gradually replaced by X ($X = \text{Cu, Ag and Au}$). For such

substitution, the crystal structure of optimization structure CdTe was changed on a triclinic with symmetry $P1$. Finally, structures of $\text{Cd}_{0.75}\text{X}_{0.25}\text{Te}$ ($X = \text{Cu, Ag and Au}$) were optimization with finding crystal structure. Obtained of $\text{Cd}_{0.75}\text{Ag}_{0.25}\text{Te}$ structure is drawn in figure 2 for visualization. Optimization lattice parameters and bulk modules (B) are listed in Table 1 (see section 2.1).

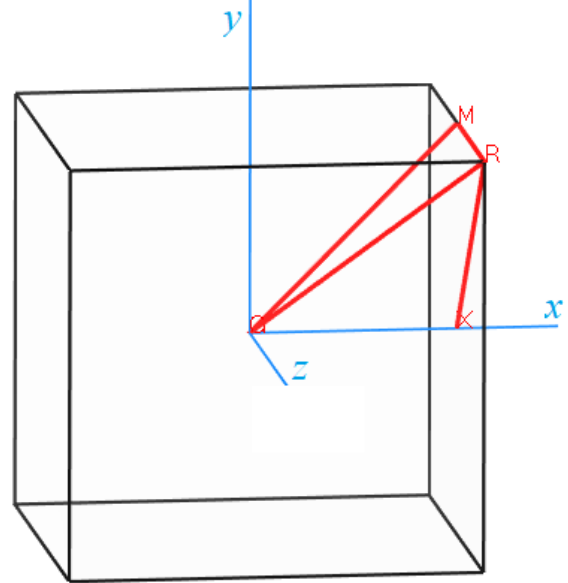


Fig. 1. BZ of cubic $\text{Cd}_{0.75}\text{X}_{0.25}\text{Te}$ ($X = \text{Cu, Ag and Au}$) crystal.

Table 1. Structure parameters of $\text{Cd}_{0.75}\text{X}_{0.25}\text{Te}$ ($X = \text{Cu, Ag and Au}$) crystals

Sample	a , Å	V , Å ³	B , GPa
$\text{Cd}_{0.75}\text{Cu}_{0.25}\text{Te}$	6.39181	261.14	46.3
$\text{Cd}_{0.75}\text{Ag}_{0.25}\text{Te}$	6.45826	269.37	54.9
$\text{Cd}_{0.75}\text{Au}_{0.25}\text{Te}$	6.46845	270.65	43.3

II. Results and Discussion

2.1. Crystal structure of solid-state $\text{Cd}_{0.75}\text{X}_{0.25}\text{Te}$ ($X = \text{Cu, Ag and Au}$) solutions

The X-ray diffraction data (XRD) of solid-state $\text{Cd}_{0.75}\text{X}_{0.25}\text{Te}$ ($X = \text{Cu, Ag and Au}$) solutions was been simulation and shown in figure 3. Theoretical XRD of CdTe crystals with cubic structure is given for comparison.

The XRD (see Fig. 3(a)) show that all samples have one intense reflection peak of approximately between 30° – 30.4° . If compared these data with the cubic CdTe, we can see that the main peak shifts to a higher region. Also, the maximum shifting of the main peak is obtained for sample $\text{Cd}_{0.75}\text{Cu}_{0.25}\text{Te}$ (see Fig. 3(b)).

As result, solid-state $\text{Cd}_{0.75}\text{X}_{0.25}\text{Te}$ ($X = \text{Cu, Ag and Au}$) solutions crystallize in a cubic structure, with the unit-cell dimensions for different samples and atoms position listed in Table 1 and 2, respectively.

In Fig. 4, the structure parameters and bulk modules of the solid-state $\text{Cd}_{0.75}\text{X}_{0.25}\text{Te}$ ($X = \text{Cu, Ag and Au}$) solutions

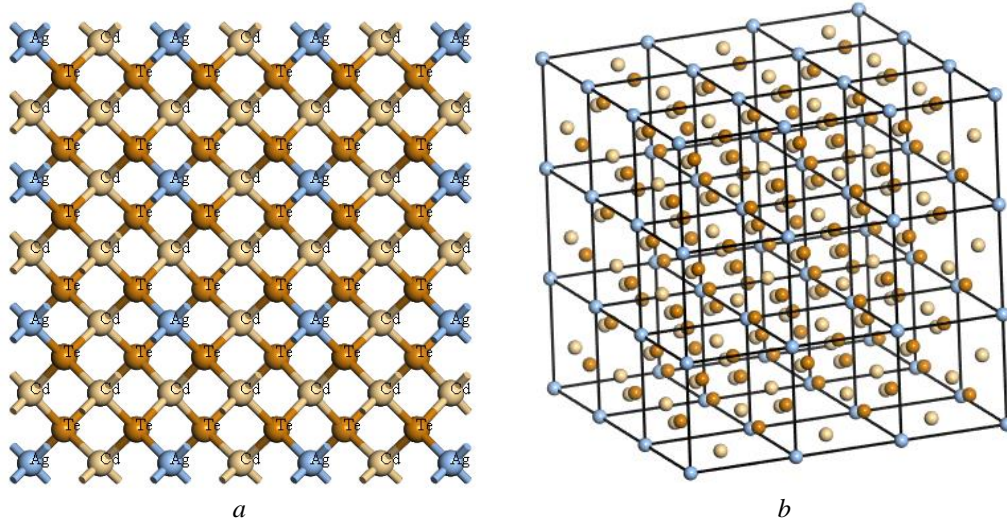


Fig. 2. Crystal structure (a) in (1 1 0) plane and $3 \times 3 \times 3$ supercell (b) of $\text{Cd}_{0.75}\text{Ag}_{0.25}\text{Te}$ crystal.

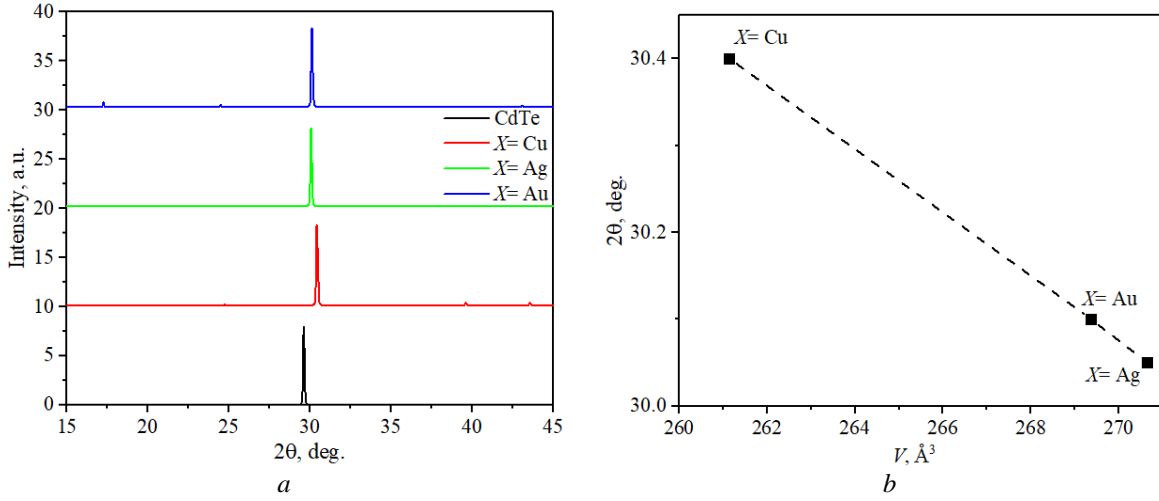


Fig. 3. Theoretical XRD (a) of solid-state $\text{Cd}_{0.75}\text{X}_{0.25}\text{Te}$ ($X = \text{Cu}, \text{Ag}$ and Au) solutions (see information in legend).

Table 2.

Atoms position of $\text{Cd}_{0.75}\text{X}_{0.25}\text{Te}$ ($X = \text{Cu}, \text{Ag}$ and Au) crystals				
Element	Atom Number	x/a	y/b	z/c
$X = \text{Cu/Ag/Au}$	1	0.0	0.0	0.0
Cd	1	0.0	0.5	0.5
Cd	2	0.5	0.0	0.5
Cd	3	0.5	0.5	0.0
Te	1	0.241779	0.241779	0.241779
Te	2	-0.241779	-0.241779	0.241779
Te	3	-0.241779	0.241779	-0.241779
Te	4	0.241779	-0.241779	-0.241779

are shown as a function of the atom radius X ($X = \text{Cu}, \text{Ag}$ and Au). This analysis shows that lattice parameters (a) and volume cell (V) linearly increase with increasing atom radius of substitutions element. But, the bulk module is shown a maximum value, 54.9 GPa, for sample $\text{Cd}_{0.7}\text{Ag}_{0.25}\text{Te}$. Also, the minimum value, 43.3 GPa, was obtained for $\text{Cd}_{0.7}\text{Au}_{0.25}\text{Te}$ and not much higher (46.3 GPa) for $\text{Cd}_{0.7}\text{Cu}_{0.25}\text{Te}$. If compared these data with the data obtained from a calculation using the same method for CdTe (45.13 GPa [35]), we can see that the solid-state $\text{Cd}_{0.75}\text{Cu}_{0.25}\text{Te}$ solution shows a much close value.

2.2 Formation energy of solid-state $\text{Cd}_{0.75}\text{X}_{0.25}\text{Te}$ ($X = \text{Cu}, \text{Ag}$ and Au) solutions

For solid-state $\text{Cd}_{0.75}\text{X}_{0.25}\text{Te}$ solutions was considered only one position of locating X ($X = \text{Cu}, \text{Ag}$ and Au) atoms in the structure of 'parent' CdTe (see information in Table 2). The formation energy of solid-state $\text{Cd}_{0.75}\text{X}_{0.25}\text{Te}$ solutions, when there is a substitution of Cd atom by X ($X = \text{Cu}, \text{Ag}$ and Au) atom is considered, is estimated pursuant to the following equation:

$$E_f = E_{SS} + E_{Cd} - E_{CdTe} - E_X, \quad (1)$$

where E_{SSS} correspond to the total energies of the solid-state $Cd_{0.75}X_{0.25}Te$ ($X= Cu, Ag$ and Au) solutions (SSS denoted as a solid-state solution), E_{CdTe} is the total energies of the 'parent' $CdTe$ compound and E_X and E_{Cd} are total energies of free X ($X= Cu, Ag$ and Au) and Cd atoms, respectively. The optimized free Cd and X ($X= Cu, Ag$ and Au) atoms energies were calculated in the same unit cell as all samples. Positive formation energy denotes the replacement process is endothermic, while negative formation energy denotes the replacement process is exothermic [39]. Formation energy was calculated for all solid-state $Cd_{0.75}X_{0.25}Te$ ($X= Cu, Ag$ and Au) solutions are presented in Table 3. As seen from Table 3, such position of replacements (see Table 2) produces an endothermic process for all studied samples. All studies samples obtained large values of formation energy. Also, high formation energy (1.1–15.0 eV) was reported for cubic SiC samples with different point defects [40]. Defective formation of atomic vacancy in solid-state $Cd_{0.75}X_{0.25}Te$ ($X= Cu, Ag$ and Au) solutions are not studied in this work.

Table 3.
Formation energy of $Cd_{0.75}Me_{0.25}Te$ ($Me= Cu, Ag$ and Au) crystals

Sample	$E_{tot}^{SSS}/E_{tot}^{CdTe}$	E_f , eV
$Cd_{0.75}Cu_{0.25}Te$	0.997	11.05
$Cd_{0.75}Ag_{0.25}Te$	1.491	11.86
$Cd_{0.75}Au_{0.25}Te$	0.949	11.22

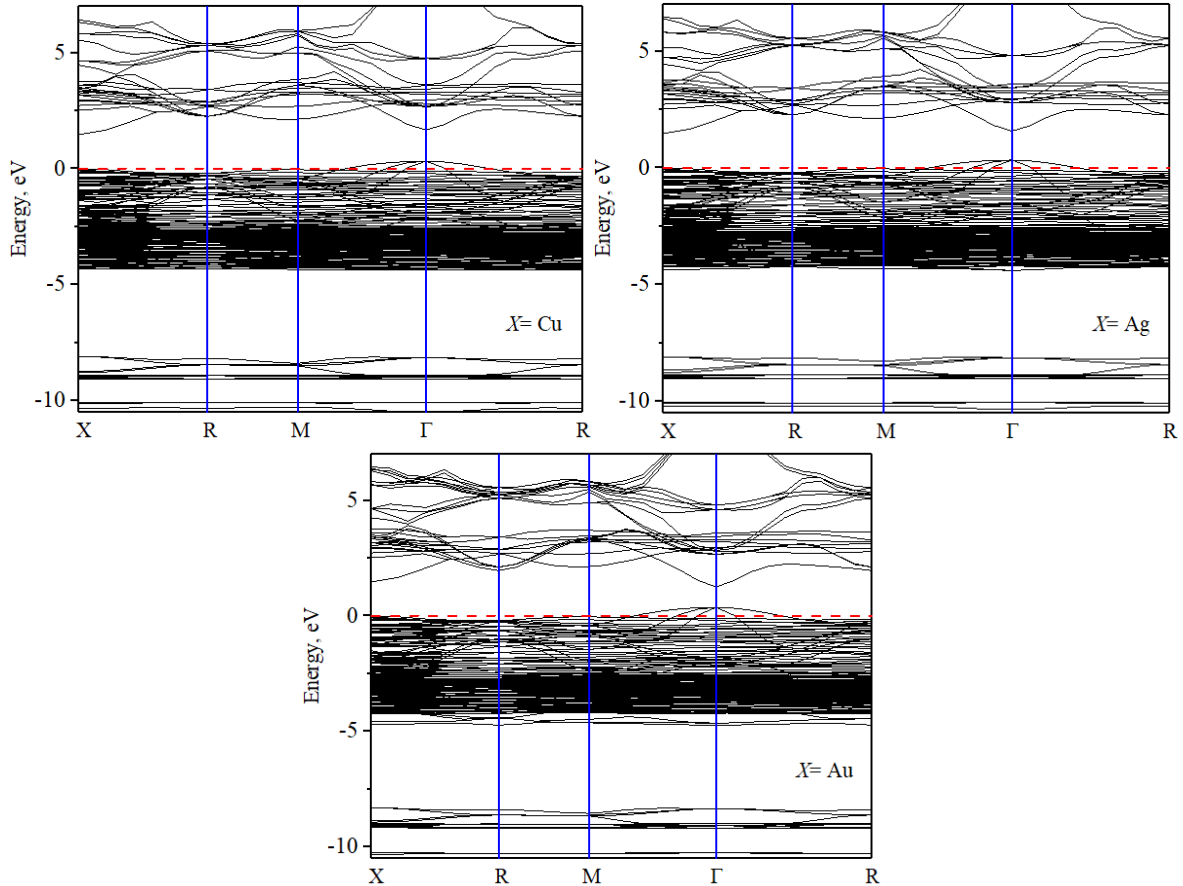


Fig. 5. Electron band energy structure of solid-state $Cd_{0.75}X_{0.25}Te$ ($X= Cu, Ag$ and Au) solutions (see information on legend). The red line corresponded to the position of the Fermi level.

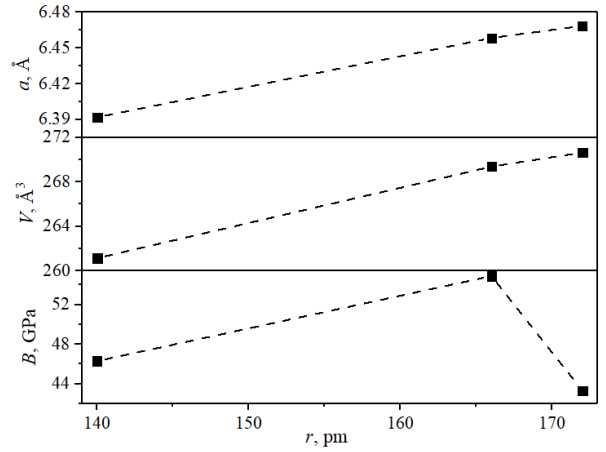


Fig. 4. Crystal cell parameters and bulk modules of solid-state $Cd_{0.75}X_{0.25}Te$ ($X= Cu, Ag$ and Au) solutions as function atom radius of substitutions element.

2.3 Electron band energy structure of solid-state $Cd_{0.75}X_{0.25}Te$ ($X= Cu, Ag$ and Au) solutions

In Fig. 5, the full energy band diagrams of the solid-state $Cd_{0.75}X_{0.25}Te$ ($X= Cu, Ag$ and Au) solutions are shown along the highly symmetric lines of the BZ. The energy in this case is counted from the Fermi level. Analysis of the results of theoretical calculations of the energy band spectrum shows that the smallest optical band gap is localized in the center of the BZ (the point Γ). This means that the crystal is characterized by a direct energy optical band gap.

Position of the higher energy level of the valence band (E_v^{top}), the lower energy level of the conduction band (E_c^{bot}), and their difference (corresponded to optical band gap; $E_c^{\text{bot}} - E_v^{\text{top}}$) at Γ -point of k -space as a function of the atomic number (Z) of X ($X = \text{Cu, Ag and Au}$) for the solid-state $\text{Cd}_{0.75}\text{X}_{0.25}\text{Te}$ ($X = \text{Cu, Ag and Au}$) solutions are presented on figure 6. As we can see from Fig. 6, the Fermi level is shifted to the valence band on 0.32–0.37 eV. Assumed to be this solid-state $\text{Cd}_{0.75}\text{X}_{0.25}\text{Te}$ ($X = \text{Cu, Ag and Au}$) solutions are a degenerate semiconductor. But, this result must be approved by other experimental studies. Also, obtained decrease tendency of optical band gap with increasing atomic number. Such behaviour Fermi level was observed in the defection sample CdTe and with substitution of Te on Cl [29].

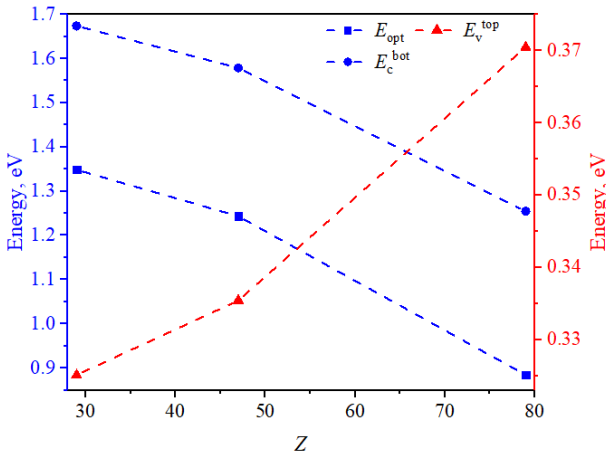


Fig. 6. Position of the higher energy level of the valence band (E_v^{top}), the lower energy level of the conduction band (E_c^{bot}), and their difference (corresponded to optical band gap; $E_c^{\text{bot}} - E_v^{\text{top}}$) for the solid-state $\text{Cd}_{0.75}\text{X}_{0.25}\text{Te}$ ($X = \text{Cu, Ag and Au}$) solutions as a function of the atomic number, obtained from *ab initio* calculations.

2.4 Dispersion of the electron band energy structure of solid-state $\text{Cd}_{0.75}\text{X}_{0.25}\text{Te}$ ($X = \text{Cu, Ag and Au}$) solutions

In addition, one can see a clear anisotropy difference $E(k)$ between the valence and conduction bands (see Fig. 5). The valence complex top is flatter, which is explained by the fact that holes are less mobile than electrons. This behaviour is caused by the inverse relationship between the effective mass (m^*) of the electron (m_e^*)/hole (m_h^*) and the spread $E(k)$ of energy levels [41]:

$$\frac{1}{m^*} = \frac{4 \cdot \pi^2}{h^2} \frac{d^2 E(k)}{dk^2}, \quad (2)$$

where h is the Planck constant, and $E(k)$ is the dependence of the band energy E on the electron wave vector k . As result, we can see that the maximum dispersion of valence and conduction bands was observed for $\Gamma \rightarrow \text{R}$ and $\Gamma \rightarrow \text{M}$ direction.

Information on the quantitative value of m^* for a material is important because this value determines the dynamics of electron conductivity in it and therefore is significant for the corresponding practical applications. The effective masses of electrons and holes in solid-state

$\text{Cd}_{0.75}\text{X}_{0.25}\text{Te}$ ($X = \text{Cu, Ag and Au}$) solutions have been calculated by utilizing the Effective Mass Calculator [42]. The calculated effective masses are presented in Table 4 and figure 7. The resultant absolute value of the $|m^*|$ for the conduction band is lower than that for the valence band. Also, we can see that the value of electron (m_e^*) effective mass increases with the atom radius of X element.

Table 4. Effective mass of the electron (m_e^*) and hole (m_h^*) of $\text{Cd}_{0.75}\text{X}_{0.25}\text{Te}$ ($X = \text{Cu, Ag and Au}$) crystals

Sample	Effective mass	
	m_c/m_0	m_v/m_0
$\text{Cd}_{0.75}\text{Cu}_{0.25}\text{Te}$	0.82	-2.29
$\text{Cd}_{0.75}\text{Ag}_{0.25}\text{Te}$	0.99	-2.44
$\text{Cd}_{0.75}\text{Au}_{0.25}\text{Te}$	0.95	-2.24

In Ref. [43] was reported that the absolute value ($|m^*|$) of electron (m_e^*) and hole (m_h^*) effective mass is $0.096m_0$ and $0.35m_0$. In this study, we obtained the absolute value of the effective mass of the electron and hole value near $(0.82\text{--}0.92)m_0$ and $(2.24\text{--}2.44)m_0$, respectively. This value is much higher than for CdTe . Also, this behaviour will influence the electrical conductivity of solid-state $\text{Cd}_{0.75}\text{X}_{0.25}\text{Te}$ ($X = \text{Cu, Ag and Au}$) solutions. According to the semiconductor theory [41] the specific conductivity σ of a material is dependent on the charged particle's mobility (μ),

$$\sigma = nq\mu, \quad (3)$$

where q is the particle's charge and n is the charged particle's concentration. The electron mobility μ is associated with an impurity of the i -type may be presented by the following relation [44, 45]:

$$\mu_i = \frac{q\tau_i}{m^*}, \quad (4)$$

where τ_i is the relaxation time, which is inversely proportional to the ionized impurity concentration n_i

$$\tau_i \propto n_i^{-1} T^{3/2}. \quad (5)$$

Here T is the thermodynamic temperature. At this time, the electron mobility μ satisfies the following relation:

$$\mu_i \propto \frac{qT^{3/2}}{m^*n_i}. \quad (6)$$

Analysis of Eq. (6) and (3) shows that the electron mobility and conductivity are higher than hole mobility and conductivity ($|m_h^*|/|m_e^*| > 1$) for all studies compound, increases with increasing temperature ($\mu_i \sim T^{3/2}$) and decreases with increasing carrier concentration ($\mu_i \sim n_i^{-1}$).

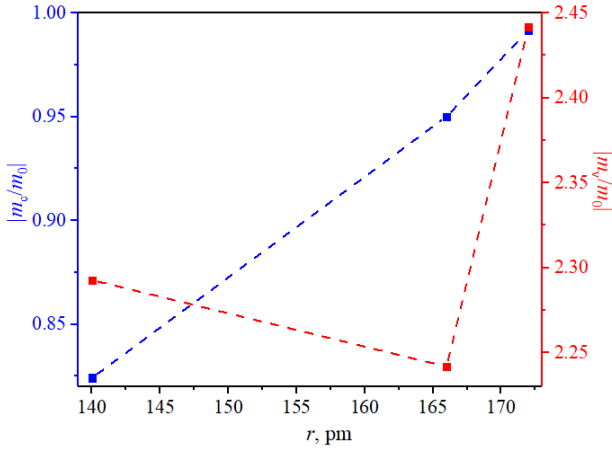


Fig. 7. Effective mass of the electron (m_e^*) and hole (m_h^*) of solid-state $\text{Cd}_{0.75}\text{X}_{0.25}\text{Te}$ ($X = \text{Cu}, \text{Ag}$ and Au) solutions as function atom radius of substitutions element.

2.5 Density of states of the solid-state $\text{Cd}_{0.75}\text{X}_{0.25}\text{Te}$ ($X = \text{Cu}, \text{Ag}$ and Au) solutions

Also, the electron density of states of solid-state $\text{Cd}_{0.75}\text{X}_{0.25}\text{Te}$ ($X = \text{Cu}, \text{Ag}$ and Au) solutions for obtaining the ‘nature’ of the band structure are studied. The analysis of the partial contributions of individual levels to the function of the total density of states (Fig. 8) and the partial contributions of individual bands to the electronic density allows us to find the genesis of the valence and conduction bands for solid-state $\text{Cd}_{0.75}\text{X}_{0.25}\text{Te}$ ($X = \text{Cu}, \text{Ag}$ and Au) solutions.

The lowest band near -10 eV is formed by the s states of Te. The following bands dispersed at the energy marker near -9 eV are formed because of the contributions of the d states of Cd. Electron bands near 4 eV are formed by the s -state of Cd and X element, and the p -state of Te. The peak of the valence complex is practically formed by the p states of Te, with ‘contamination’ of the p states of Cd and X elements. But the conduction band bottom is mainly

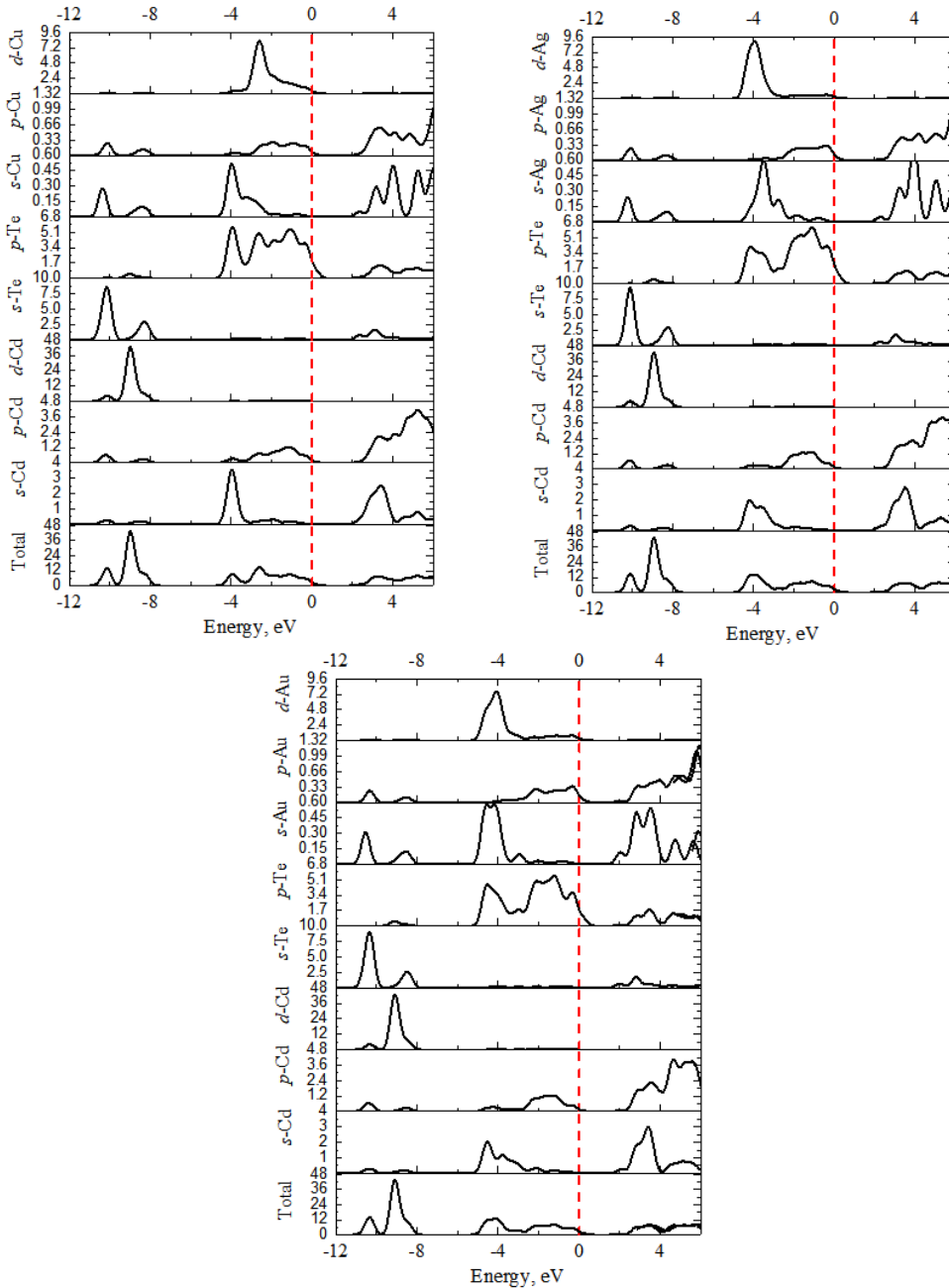


Fig. 8. Partial and total electron density of states of solid-state $\text{Cd}_{0.75}\text{X}_{0.25}\text{Te}$ ($X = \text{Cu}, \text{Ag}$ and Au) solutions.

formed by the s - and p - states of the Cd and X elements.

2.6 Refractive index of the solid-state $\text{Cd}_{0.75}\text{X}_{0.25}\text{Te}$ ($X = \text{Cu}, \text{Ag}$ and Au) solutions

Finally, in this work are present spectral behaviours of the refractive index. To study the optical properties of solid-state $\text{Cd}_{0.75}\text{X}_{0.25}\text{Te}$ ($X = \text{Cu}, \text{Ag}$ and Au) solutions is use a complex dielectric function $\varepsilon(\hbar\omega) = \varepsilon_1 + i\varepsilon_2$. Its imaginary part can be calculated as

$$\varepsilon_2 = \frac{2e^2\pi}{V\varepsilon_0} \sum_{K,v,c} |\langle \psi_K^c | \hat{u} \cdot r | \psi_K^v \rangle|^2 \delta(E_K^c - E_K^v - \hbar\omega), \quad (7)$$

while the real part can be obtained from the Kramers–Kronig relation

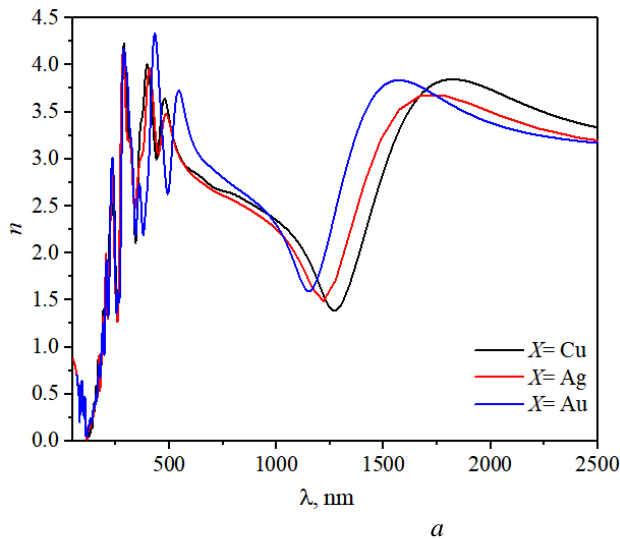
$$\varepsilon_1 - 1 = \frac{2}{\pi} \int_0^\infty \frac{t\varepsilon_2(t)dt}{t^2 - (\hbar\omega)^2}. \quad (8)$$

Using the data obtained for the real and imaginary parts of the dielectric function, one can calculate the spectral dependences of the refractive index n :

$$n = \sqrt{\frac{(\varepsilon_1^2 + \varepsilon_2^2)^{1/2} + \varepsilon_1}{2}}. \quad (9)$$

Fig. 9(a) shows the spectral dependences of the refractive index for solid-state $\text{Cd}_{0.75}\text{X}_{0.25}\text{Te}$ ($X = \text{Cu}, \text{Ag}$ and Au) solutions. Need to be noted that a refractive index below 300 nm are showing practically the same spectral behaviour for all samples. In visible spectral region are obtained three local maximums (see Fig. 9(b)). Also, the maximum value of the refractive index (200–2500 nm) for solid-state $\text{Cd}_{0.75}\text{X}_{0.25}\text{Te}$ solutions was obtained for $X = \text{Cu}$ and Ag near 280 nm, but for $X = \text{Au}$ near 435 nm.

Analysis of the near infrared spectra (IR) region are showing one broad maximum between 1500 and 1800 nm (see Fig. 9(a)). The maximum value of the refractive index in this region is shifting to a higher wavelength region with decreasing atomic number ($\text{Au} \rightarrow \text{Cu}$). The maximum value is obtained for solid-state $\text{Cd}_{0.75}\text{Au}_{0.25}\text{Te}$ solutions and the minimum for $\text{Cd}_{0.75}\text{Ag}_{0.25}\text{Te}$ in this IR region.



Conclusion

The lattice parameters (a , V) linearly increase with increasing atom radius of substitutions element. The bulk module shows a maximum value for the sample with substitutions atoms Cd on the Ag. Solid-state $\text{Cd}_{0.75}\text{Cu}_{0.25}\text{Te}$ solution shows a much close value to ‘pure’ CdTe.

First-principle theoretical studies of the electron energy spectrum for the solid-state $\text{Cd}_{0.75}\text{X}_{0.25}\text{Te}$ ($X = \text{Cu}, \text{Ag}$ and Au) solutions have been carried out using the reliable techniques of density functional theory and known approximations. It has been established that the smallest optical band gap is localized at the center of the BZ and should reveal direct optical transitions. The Fermi level is shifted to the valence band on 0.32–0.37 eV for all studies samples. Formation energy was calculated for solid-state $\text{Cd}_{0.75}\text{X}_{0.25}\text{Te}$ ($X = \text{Cu}, \text{Ag}$ and Au) solutions and changed in the range between 11.05 and 11.86 eV. The absolute value of the effective mass of the electron (0.82–0.99 m_0) and hole (2.24–2.44 m_0) was calculated based on the results of the electronic structure. The electron mobility and conductivity are higher than hole mobility and conductivity ($|m_h^*|/|m_e^*| > 1$) for all studied compounds. The biggest value of the electron mobility and conductivity corresponded to $\text{Cd}_{0.75}\text{Cu}_{0.25}\text{Te}$. Based on the electron density of states was obtained that the peak of the valence complex formed by the p states of Te, with ‘contamination’ of the p states of Cd and X elements. The conduction bottom band is mainly formed by the s - and p - states of the Cd and X elements.

To study the optical properties was use a complex dielectric function $\varepsilon(\hbar\omega)$. Using Kramers–Kronig relation was calculation refractive index. The maximum value of the refractive index for solid-state $\text{Cd}_{0.75}\text{X}_{0.25}\text{Te}$ solutions was obtained for $X = \text{Au}$ near 435 nm.

Acknowledgments

This work was supported by the Project of Young Scientists 0121U108649 of the Ministry of Education and Science of Ukraine.

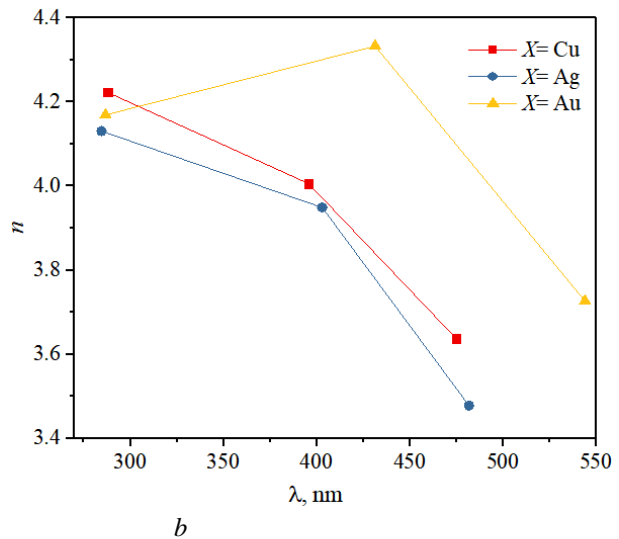


Fig. 9. Spectral behaviour of the refractive index (a) of solid-state $\text{Cd}_{0.75}\text{X}_{0.25}\text{Te}$ ($X = \text{Cu}, \text{Ag}$ and Au) solutions (see information in legend). The three maximum values of the refractive index for the visible spectral region (b).

Kashuba A.I. – Ph.D, Doctoral Student at the Department of General Physics;

- [1] A. Kashuba, I. Semkiv, O. Kushnir, *Basic physical properties of thin films of cadmium chalcogenides*, LAP Lambert Academic Publishing, Riga, Latvia 2021.
- [2] R. Petrus, H. Ilchuk, A. Kashuba, I. Semkiv, E. Zmiiovskaya, *Optical properties of CdTe thin films obtained by the method of high-frequency magnetron sputtering*, *Functional Materials*, 27(2), 342 (2020); <https://doi.org/10.15407/fm27.02.342>.
- [3] Z.R. Zapukhlyak, L.I. Nykyryuk, V.M. Rubish, G. Wisz, V.V. Prokopiv, M.O. Galushchak, I.M. Lishchynskyy, L.O. Katanova, R.S. Yavorskyi, *SCAPS simulation of ZnO/CdS/CdTe/CuO heterostructure for photovoltaic application*, *Physics and Chemistry of Solid State*, 21(4), 660 (2020); <https://doi.org/10.15330/PCSS.21.4.660-668>.
- [4] H. Ilchuk, R. Petrus, I. Semkiv, A. Kashuba, *Directional Synthesis of CdX (X = S, Se, and Te) Thin Films for Solar Cell Application*, *Springer Proceedings in Physics*, 247, 117 (2020). https://doi.org/10.1007/978-3-030-52268-1_9.
- [5] T. Saga, *Advances in Crystalline Silicon Solar Cell Technology for Industrial Mass Production*, *NPG Asia Materials*, 2, 96 (2010); <http://dx.doi.org/10.1038/asiamat.2010.82>.
- [6] Z. Bai, J. Yang, D. Wang, *Thin film CdTe solar cells with an absorber layer thickness in micro- and sub-micrometer scale*, *Appl. Phys. Lett.* 99, 143502 (2011); <https://doi.org/10.1063/1.3644160>.
- [7] Y. Deng, J. Yang, R. Yang, K. Shen, D. Wang, D. Wang, *Cu-doped CdS and its application in CdTe thin film solar cell*, *AIP ADVANCES*, 6, 015203 (2016); <https://doi.org/10.1063/1.4939817>.
- [8] J.L. Freeouf, J.M. Woodall, *Schottky barriers: An effective work function model*, *Appl. Phys. Lett.*, 39, 727 (1981); <https://doi.org/10.1063/1.92863>.
- [9] S.H. Demtsu, J.R. Sites, *Effect of back-contact barrier on thin-film CdTe solar cells*, *Thin Solid Films*, 510, 320 (2006); <https://doi.org/10.1016/j.tsf.2006.01.004>.
- [10] A. Bosioa, R. Ciprian, A. Lamperti, I. Rago, B. Ressel, G. Rosa, M. Stupar, E. Weschke, *Interface phenomena between CdTe and ZnTe:Cu back contact*, *Solar Energy*, 176, 186 (2018); <https://doi.org/10.1016/j.solener.2018.10.035>.
- [11] K.A. Aris, K.S. Rahman, A.M. Ali, B. Bais, I.B. Yahya, Md. Akhtaruzzaman, H. Misran, S.F. Abdullah, M.A. Alghoul, N.Amin, *A comparative study on thermally and laser annealed copper and silver doped CdTe thin film solar cells*, *Solar Energy*, 173, 1 (2018). <https://doi.org/10.1016/j.solener.2018.07.009>.
- [12] T.D. Dzhafarov, S.S. Yesilkaya, N.Y. Canli, M. Caliskan, *Diffusion and influence of Cu on properties of CdTe thin films and CdTe/CdS cells*, *Solar Energy Materials & Solar Cells*, 85, 371 (2005); <https://doi.org/10.1016/j.solmat.2004.05.007>.
- [13] T.A. Gessert, A.R. Mason, P. Sheldon, A.B. Swartzlander, D. Niles, T.J. Coutts, *Development of Cu-doped ZnTe as a back-contact interface layer for thin-film CdS/CdTe solar cells*, *J. Vac. Sci. Technol. A*, 14(3), 806 (1996); <http://dx.doi.org/10.1116/1.580394>.
- [14] D. Grecu, A.D. Compaan, D. Young, U. Jayamaha, D.H. Rose, *Photoluminescence of Cu-doped CdTe and related stability issues in CdS/CdTe solar cells*, *Journal of Applied Physics*, 88, 2490 (2000); <http://dx.doi.org/10.1063/1.1287414>.
- [15] J. Perrenoud, L. Kranz, C. Gretener, F. Pianezzi, S. Nishiwaki, S. Buecheler, A.N. Tiwari, *A comprehensive picture of Cu doping in CdTe solar cells*, *Journal of Applied Physics*, 114, 174505 (2013); <http://dx.doi.org/10.1063/1.4828484>.
- [16] G.H. Tariq, M. Anis-ur-Rehman, *Annealing effects on physical properties of doped CdTe thin films for photovoltaic applications*, *Materials Science in Semiconductor Processing*, 30, 665 (2015); <https://doi.org/10.1016/j.mssp.2014.09.012>.
- [17] H.H. Woodbury, M. Aven, *Some Diffusion and Solubility Measurements of Cu in CdTe*, *Journal of Applied Physics*, 39, 5485 (1968); <http://dx.doi.org/10.1063/1.1655999>.
- [18] J.P. Chamonal, E. Molva, J.L. Pautrat, *Identification of Cu and Ag acceptors in CdTe*, *Solid State Communications*, 43(11), 801 (1982); [https://doi.org/10.1016/0038-1098\(82\)90843-2](https://doi.org/10.1016/0038-1098(82)90843-2).
- [19] V. Dzhagan, O. Kapush, O. Isaieva, S. Budzulyak, O. Magda, P.P. Kogutyuk, L. Trishchuk, V. Yefanov, M. Valakh, V. Yukhymchuk, *Tuning the photoluminescence of CdTe quantum dots by controllable coupling to plasmonic Au nanoparticles*, *Physics and Chemistry of Solid State*, 23(4), 720 (2022); <https://doi.org/10.15330/pcss.23.4.720-727>.
- [20] V. Lesnyak, A. Wolf, A. Dubavik, L. Borchartd, S.V. Voitekhovich, N. Gaponik, S. Kaskel, A. Eychmuller, *3D Assembly of Semiconductor and Metal Nanocrystals: Hybrid CdTe/Au Structures with Controlled Content*, *J. Am. Chem. Soc.*, 133, 13413 (2011); <http://dx.doi.org/10.1021/ja202068s>.
- [21] I. Bouziani, Y. Benhouria, I. Essaoudi, A. Ainane, R. Ahuja, *Magneto-electronic properties of Vanadium impurities co-doped (Cd, Cr)Te compound for spintronic devices: First principles calculations and Monte Carlo simulation*, *Journal of Magnetism and Magnetic Materials*, 466, 420 (2018); <https://doi.org/10.1016/j.jmmm.2018.07.033>.

- [22] N.A. Noor, S. Ali, A. Shaukat, *First principles study of half-metallic ferromagnetism in Cr-doped CdTe*, Journal of Physics and Chemistry of Solids, 72, 836 (2011); <https://doi.org/10.1016/j.jpics.2011.04.008>.
- [23] K.L. Yao, G.Y. Gao, Z.L. Liu, L. Zhu, Y.L. Li, *Half-metallic ferromagnetic semiconductors of V- and Cr-doped CdTe studied from first-principles pseudopotential calculations*, Physica B, 366, 62 (2005); <https://doi.org/10.1016/j.physb.2005.05.024>.
- [24] M.A. Flores, E. Menéndez-Proupin, W. Orellana, J.L. Peña, *Sn-doped CdTe as promising intermediate-band photovoltaic material*, J. Phys. D: Appl. Phys., 50, 035501 (2017); <https://doi.org/10.1088/1361-6463/50/3/035501>.
- [25] F. Goumrhar, L. Bahmad, O. Mounkachi, A. Benyoussef, *Calculated magnetic properties of co-doped CdTe (V,P): First-principles calculation*, Computational Condensed Matter., 13, 87 (2017); <https://doi.org/10.1016/j.cocom.2017.09.009>.
- [26] Jie Ma, Su-Huai Wei, T.A. Gessert, K.K. Chin, *Carrier density and compensation in semiconductors with multiple dopants and multiple transition energy levels: Case of Cu impurities in CdTe*, Physical Review B, 83, 245207 (2011); <https://doi.org/10.1103/PhysRevB.83.245207>.
- [27] M. Sajjad, H.X. Zhang, N.A. Noor, S.M. Alay-e-Abbas, A. Shaukat, Q. Mahmood, *Study of half-metallic ferromagnetism in V-doped CdTe alloys by using first-principles calculations*, Journal of Magnetism and Magnetic Materials, 343, 177 (2013); <http://dx.doi.org/10.1016/j.jmmm.2013.04.045>.
- [28] J.-H. Yang, W.-J. Yin, J.-S. Park, J. Burst, W.K. Metzger, T. Gessert, T. Barnes, S.-H. Wei, *Enhanced p-type dopability of P and As in CdTe using non-equilibrium thermal processing*, Journal of Applied Physics, 118, 025102 (2015); <http://dx.doi.org/10.1063/1.4926748>.
- [29] H. Zhu, M. Gu, L. Huang, J. Wang, X. Wu, *Structural and electronic properties of CdTe:Cl from first-principles*, Materials Chemistry and Physics, 143, 637–641 (2014); <http://dx.doi.org/10.1016/j.matchemphys.2013.09.046>.
- [30] R.Yu. Petrus, H.A. Ilchuk, V.M. Sklyarchuk, A.I. Kashuba, I.V. Semkiv, E.O. Zmiiovska, *Transformation of Band Energy Structure of Solid Solutions CdMnTe*, J. Nano- Electron. Phys., 10(6), 06042-1 (2018); [https://doi.org/10.21272/jnep.10\(6\).06042](https://doi.org/10.21272/jnep.10(6).06042).
- [31] H. Ilchuk, E. Zmiiovska, R. Petrus, I. Semkiv, I. Lopatynskiy, A. Kashuba, *Optical Properties of CdMnTe Film: Experimental and Theoretical Aspects*, Journal of Nano- and Electronic Physics, 12(1), 01027-1 (2020); [https://doi.org/10.21272/jnep.12\(1\).01027](https://doi.org/10.21272/jnep.12(1).01027).
- [32] Q. Mahmood, M. Hassan, *Systematic first principle study of physical properties of Cd_{0.75}Ti_{0.25}Z (Z = S, Se, Te) magnetic semiconductors using mBJ functional*, Journal of Alloys and Compounds, 704, 659 (2017); <https://doi.org/10.1016/j.jallcom.2017.02.097>.
- [33] M.H. Tedjini, A. Oukebdane, M.N. Belkaid, N. Aouail, *The effect of zinc concentration upon electronic structure, optical and dielectric properties of Cd_{1-x}Zn_xTe alloy: TB-mBJ investigation*, Computational Condensed Matter., 27, e00561 (2021); <https://doi.org/10.1016/j.cocom.2021.e00561>.
- [34] J.L. Roehl, S.V. Khare, *Diffusion of Cd vacancy and interstitials of Cd, Cu, Ag, Au and Mo in CdTe: A first principles investigation*, Solar Energy, 101, 245 (2014); <http://dx.doi.org/10.1016/j.solener.2013.12.017>.
- [35] H.A. Ilchuk, L.I. Nykyruy, A.I. Kashuba, I.V. Semkiv, M.V. Solovyov, B.P. Naidych, V.M. Kordan, L.R. Deva, M.S. Karkulovska, R.Y. Petrus, *Electron, Phonon, Optical and Thermodynamic Properties of CdTe Crystal Calculated by DFT*, Physics and Chemistry of Solid State, 23(2), 261 (2022); <https://doi.org/10.15330/pcss.23.2.261-269>.
- [36] J.P. Perdew, K. Burke, and M. Ernzerhof, *Generalized Gradient Approximation Made Simple*, Phys. Rev. Lett., 78(7), 1396 (1997); <https://doi.org/10.1103/PhysRevLett.78.1396>.
- [37] H.J. Monkhorst and J.D. Pack, *Special Points for Brillouin-Zone Integrations*, Phys. Rev. B., 13(12), 5188 (1976); <https://doi.org/10.1103/PhysRevB.13.5188>.
- [38] W. Kohn and L. J. Sham, *Self-Consistent Equations Including Exchange and Correlation Effects*, Phys. Rev. A., 140(4), 1133 (1965); <https://doi.org/10.1103/PhysRev.140.A1133>.
- [39] M. Kovalenko, O. Bovgyra, V. Dzikovskiy, R. Bovhyra, *DFT study for adsorption of CO and H₂ on Pt-doped ZnO nanocluster*, SN Appl. Sci. 2, 790 (2020); <https://doi.org/10.1007/s42452-020-2591-9>.
- [40] C. Wang, J. Bernholc, R.F. Davis, *Formation energies, abundances, and the electronic structure of native defects in cubic SiC*, Phys. Rev. B, 38, 12752(R) (1988); <https://doi.org/10.1103/PhysRevB.38.12752>.
- [41] A. Kashuba, B. Andriyevskyy, I. Semkiv, L. Andriyevska, R. Petrus, E. Zmiiovska, D. Popovych, *Influence of Defective Formations on Photoconductivity of Layered Crystals with Cationic Substitution*, Journal of Nano- and Electronic Physics, 10(6), 06025 (2018); [https://doi.org/10.21272/jnep.10\(6\).06025](https://doi.org/10.21272/jnep.10(6).06025).
- [42] A. Fonari, C. Sutton, Effective Mass Calculator (2012). <https://github.com/afonari/emc>.
- [43] M. Aven, J. Prener, Physics and Chemistry of II-VI Compounds, John Wiley and Sons, New York, 1967.
- [44] Z. Yinnü, Y. Jinliang, X. Chengyang, *First-principles study on electronic structure and conductivity of Sn-doped Ga_{1.375}In_{0.625}O₃*, Journal of Semiconductors, 36, 012003 (2015); <https://doi.org/10.1088/1674-4926/36/1/012003>.
- [45] J. Liu, Q.-Y. Jiang, S.-D. Zhang, H. Zhang, *Carrier mobility and relaxation time in BiCuSeO*, Physics Letters A, 383, 125990 (2019); <https://doi.org/10.1016/j.physleta.2019.125990>.

А.І. Кашуба

Вплив заміщення атомів металу на електронні та оптичні властивості твердих розчинів $\text{Cd}_{0.75}\text{X}_{0.25}\text{Te}$ ($\text{X} = \text{Cu}, \text{Ag}$ та Au)

Кафедра загальної фізики, Національний університет "Львівська політехніка", Львів, Україна, andrii.i.kashuba@lpnu.ua

Тверді розчини $\text{Cd}_{0.75}\text{X}_{0.25}\text{Te}$ ($\text{X} = \text{Cu}, \text{Ag}$ і Au), кристалізовані в кубічній структурі, досліджуються в рамках теорії функціоналу густини. Розрахунки з перших принципів електронної зонної структури, густини станів і показника заломлення твердих розчинів $\text{Cd}_{0.75}\text{X}_{0.25}\text{Te}$ ($\text{X} = \text{Cu}, \text{Ag}$ і Au) оцінені за допомогою узагальненого градієнтного наближення (GGA). Було використано функціонал Пердюю–Берка–Ернзерхофа (PBE). Енергія утворення розрахована за результатами загальної енергії досліджуваних зразків. На основі електронної зонної структури було розраховано ефективну масу електронів і дірок. Обговорено вплив заміщення атомів на електронну провідність і рухливість. Для дослідження оптичних властивостей використовували комплексну діелектричну функцію $\epsilon(\hbar\omega)$. Спектральна поведінка показника заломлення була розрахована на основі діелектричної функції.

Ключові слова: теорія функціонала густини, електронна енергетична структура, енергія формування, ефективна маса, щільність станів, показник заломлення.

M. V. Strikha^{1,2}, D. V. Antoniuk¹

A theoretical model for estimation of work function reduction for MXenes with hydroxyl termination

¹Taras Shevchenko National University of Kyiv, Faculty of radiophysics, electronics and computer systems, Akademika Hlushkova Ave 4g, Kyiv, Ukraine

²V.E. Lashkaryov Institute of Semiconductor Physics, National Academy of Sciences of Ukraine, Nauky Ave, 41 Kyiv, Ukraine, maksym_strikha@hotmail.com

This article presents a simple model that explains significant reduction of work function in MXenes $Ti_{n+1}C_n$ with hydroxyl termination and demonstrates matching results to ones in the existing literature, obtained via complex computing based on the first principles. This model can be applied for results evaluation of the hydroxy functionalization of various MXene types, due to prospects of the creation of novice emission electronics devices

Keywords: MXenes, work function, surface termination, hydroxy group.

Received 17 December 2023; Accepted 10 March 2023.

Introduction

MXenes are a type of two-dimensional materials that has been firstly described in 2011 in work [1] co-authored by Yuri Gogotsi, Ukrainian by origin, who still retains his professor position at Sumy State University. Generalized formula for MXene $M_{n+1}X_nT_x$ includes $n+1$ atomic layers of transition metal M (denoted as M_{n+1}), with n monoatomic layers of carbon or nitrogen in-between them (X_n); such sandwich-like structure can include different terminations (F, O, Cl, OH), denoted as T_x (see Fig. 1). Currently, a term “multi-layer MXene” describes a structure with five or more layers of transition metal.

The distinctive features of MXenes gained public attention: within a decade after the discovery of MXenes, articles about MXenes were published in more than 400 journals by more than 8300 researchers from 1450 institutions in 62 countries (according to estimations in [2]). Due to the varying stoichiometry and surface organization, MXenes have a range of physical and chemical features that can be controlled. MXenes have a variable band gap, which depends on the method of surface termination, high electric conductivity, high Young's modulus, ultra-low optical attenuation etc. Currently MXenes are used in modern energy storage and

conversion devices, electronics, sensors, medicine etc (see review article [3] with references therein).

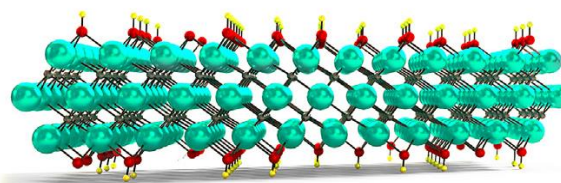


Fig. 1. The first MXenes structure $M_3X_2T_x$, described in [1], that contains three layers of transition metal Ti (big lighter balls), two carbon layers between them (small darker balls), and surface termination of hydroxy groups OH (oxygen atoms are located closer to atoms of metal, while atoms of hydrogen are farther from atoms of metal) above and below.

MXenes can potentially be used for the creation of cathodes with low work function for emission electronics. As per today, caesium is standard material with low work function 2.1 eV [4], its usage, however, is limited due to its high toxicity. Thus, alternative approaches for creation of modern cathodes are considered that are based on the adsorption of alkaline and rare earth metals (Ce, Gd, Eu),

and co-adsorption on surfaces of Si, Ge, and Mo, also in nanostructured state, where double-charged layers can be created, which significantly reduce work function [5, 6].

Work function of MXenes with surface O, F, OH functionalization was estimated in [7] based on the first principles. It shows that oxygen or fluorine functionalization leads to insignificant increase or reduction of work function, while hydroxyl-terminated MXenes can show low work function in 1,6-2,8 eV range. Here, the intrinsic dipole moment of the OH hydroxyl group is the main factor in work function reduction.

The computations in [7] were carried out with the use of bulky computing packages, and therefore lack the necessary clarity. Thus, a simple theoretical model is needed that allows estimate a possible range of changes in work function affected by MXenes' surface functionalization by hydroxy groups.

Theoretical model

Generally, the change in work function under the influence of adsorbates applied to the surface is caused by three factors: a) redistribution of electronic charge between the surface and adsorbates; b) relaxation of the surface caused by adsorbates; c) polarity of adsorbates [8]. In this paper, we consider MXenes that can be associated with lower work function, i.e., MXenes based on titan and carbon layers (the type, first studied in [1]; see Fig. 1).

Generally, unterminated MXenes are metals or semimetals (semiconductors with a zero-band gap); the high value of density of electronic states close to the Fermi level is caused by the outer layers of transition metals (see [3]). However, already in [1] it was experimentally shown that surface termination of Ti_3C_2 by a hydroxy group led to the creation of a band gap of ca 50 meV, turning such MXene into a semiconductor.

Thus, surface concentration of hydroxy groups exceeds concentration of conductivity carriers in this

material. As Fig. 1 demonstrates, these hydroxy groups create on the surface a monolayer with the same number of dipoles as the number of atoms in the transition metal layer under it. Since the band gap width exceeds 26 meV (which is an energy at the room temperature), then under ambient conditions, each of these metal atoms corresponds to less than one conduction electron, while each of the dipoles corresponds to a negative electronic charge localized near the oxygen atom and a positive one localized near the hydrogen atom. Terminalization shown in Fig. 1, is also not accompanied by a noticeable surface reconstruction of Ti atoms. This means that in the first approximation for the functionalized MXenes based on titanium and carbon, we can neglect the redistribution of the electronic charge between the surface and the adsorbates, and the relaxation of the surface caused by the adsorbates, so that the work function reduction will be caused mainly by the dipole moments of the hydroxyl groups.

The energy level structure, which arises at the boundary between hydroxyl terminated MXene and vacuum, is shown in Fig. 2 (We presented a similar model in [9] to explain the reduction of the electron affinity caused by the presence of two layers of adsorbates, negatively and positively charged, on the semiconductor surface, which corresponds to the experimental situation studied in [5, 6]). At the same time, we assume that the Fermi level coincides with the edge of the conduction band in MXenes).

Since the distance between the hydrogen and oxygen atoms in the hydroxyl group is $d = 0.97 \text{ \AA}$, this gap is tunnel-transparent for thermal electrons near the bottom of the conduction band in the MXene (whose wavelength is an order of magnitude longer), and they freely tunnel from the MXene into vacuum. Therefore, the effective work function from hydroxylfunctionalized MXene (see Fig. 2) is equal to:

$$e\Phi_k = e\Phi_0 - e\Delta\Phi. \quad (1)$$

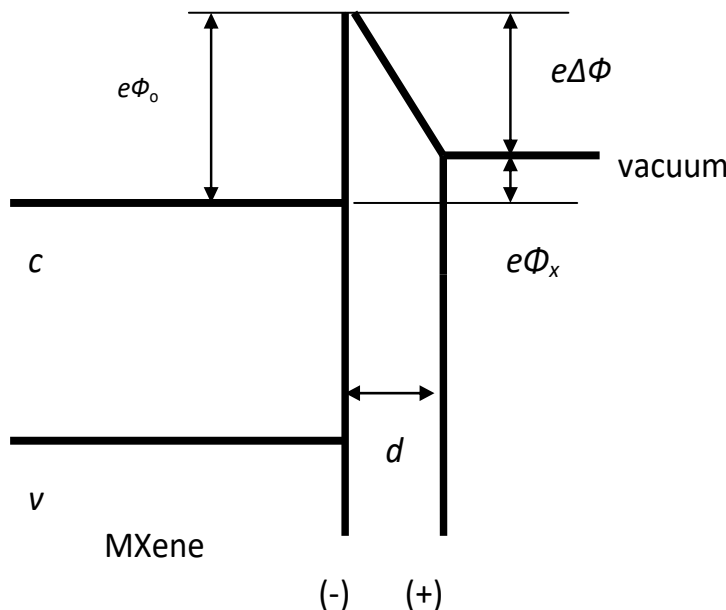


Fig. 2. MXene's work function reduction affected by dipole moment of the hydroxyl group on the surface.

$\Delta\Phi$ in the right-hand side of (1) can be estimated from the flat capacitor formula:

$$\Delta\Phi = \frac{eN_s d}{\varepsilon_0 \varepsilon}, \quad (2)$$

where N_s is surface density of dipoles, ε_0 – a dielectric constant of vacuum, ε – a dielectric permittivity of the gap between charged planes.

Discussion

Assuming that $N_s \sim 5 \cdot 10^{18} \text{ m}^{-2}$, $\varepsilon \sim 10$ (typical value of the dielectric permittivity for semiconductors) and $d \sim 1 \times 10^{-10} \text{ m}$, we obtain $\Delta\Phi \sim 3 \text{ V}$. The value of the work function of MXene non-functionalized by hydroxy groups is equal $\sim 4,5 \text{ eV}$ and does not depend on surface number of Ti and C (in a 1-9 range that could be estimated by computation packages in [7]); after the functionalization, the value lowers to ca 1,6 eV and similarly does not depends on the amount of MXene'

surfaces [7].

Thus, the proposed model not only provide qualitative explanation of the significant work function reduction in $\text{Ti}_{n+1}\text{C}_n$ with hydroxy termination (clearly illustrated in fig. 2), but also matches the results of a complex and cumbersome numerical calculation of [7] based on first principles. This model can be used for evaluation of the hydroxy functionalization results of various MXene types, based on their application prospects in modern emission electronics.

Strikha M. V. – Doctor of Sciences in Physics and Mathematics, Professor, Professor of the Physical electronics department of the Faculty of radiophysics, electronics and computer systems at Taras Shevchenko National university of Kyiv, chief researcher at V.E. Lashkaryov Institute of Semiconductor Physics, National Academy of Science of Ukraine;
Antoniuk D.V. – student of the Faculty of radiophysics, electronics and computer systems at Taras Shevchenko National university of Kyiv.

- [1] M. Naguib, M. Kurtoglu, V. Presser, J. Lu, J. Niu, M. Heon, L. Hultman, Y. Gogotsi, M. W Barsoum, *Two-dimensional nanocrystals produced by exfoliation of Ti_3AlC_2* , *Advanced Materials*, 23 (37): 4248 (2011); <https://doi.org/10.1002/adma.201102306>.
- [2] M. D. Firouzjaei, M. Karimiziarani, H. Moradkhani, M. Elliott, B. Anasori. *MXenes: The two-dimensional influencers*, *Materials Today Advances*, 13, 100202 (2022); <https://doi.org/10.1016/j.mtaadv.2021.100202>.
- [3] X. Jiang, A. V. Kuklin, A. Baev, Y. Ge, H. Ågren, H. Zhang, P. N. Prasad, *Two-dimensional MXenes: From morphological to optical, electric, and magnetic properties and applications*, *Physics Reports*, 848, 1 (2020); <https://doi.org/10.1016/j.physrep.2019.12.006>.
- [4] N. D. Lang and W. Kohn, *Theory of metal surfaces: Work function*, *Phys. Rev. B*, 3, 1215 (1971); <https://doi.org/10.1103/PhysRevB.3.1215>.
- [5] M.G. Nakhodkin, M.I. Fedorchenko, *Interaction of oxygen and gadolinium with Si (100)-2 × 1. Formation of a system with an output function of 1 eV*, *Ukrainian journal of physics*, 60, 97 (2015); <https://doi.org/10.15407/ujpe60.02.0097>.
- [6] T.V. Afanasieva, A.G. Fedorus, A.M. Goriachko et al. *Mesoscopic self-ordering in oxygen doped Ce films adsorbed on Mo (112)*, *Surface Science*, 705, 121766 (2021); <https://doi.org/10.1016/j.susc.2020.121766>.
- [7] M. Khazaei, M. Arai, T. Sasaki, A. Ranjbar, Y. Liang, and S. Yunoki, *OH-terminated two-dimensional transition metal carbides and nitrides as ultralow work function materials*, *Phys. Rev. B*, 92: 075411 (2015); <https://doi.org/10.1103/PhysRevB.92.075411>.
- [8] T. C. Leung, C. L. Kao, W. S. Su, Y. J. Feng, and C. T. Chan, *Relationship between surface dipole, work function and charge transfer: Some exceptions to an established rule*, *Phys. Rev. B*, 68, 195408 (2003); <https://doi.org/10.1103/PhysRevB.68.195408>.
- [9] M.V. Strikha, A.M. Goryachko, *A theoretical model to describe the reduction of work function of a semiconductor/dielectric under the influence of a surface double charged layer*, *Sensor electronics and microsystem technologies*, 19, 3 (2022); <https://doi.org/10.18524/1815-7459.2022.3.265293>.

М.В. Стріха^{1,2}, Д.В. Антонюк¹

Теоретична модель для оцінки зниження роботи виходу максенів з гідроксильною термінацією.

¹Київський національний університет ім. Тараса Шевченка, факультет радіофізики, електроніки і комп'ютерних систем, пр. Глушкова, 42, Київ, Україна;

²Інститут фізики напівпровідників ім. В.Є.Лашкарьова НАН України, пр. Науки, 41, Київ, Україна,
maksym_strikha@hotmail.com

Запропонована проста теоретична модель для пояснення значного зниження роботи виходу в максенах $Ti_{n+1}C_n$ з гідроксильною термінацією. Модель демонструє добрий чисельний збіг із наявними в літературі результатами складного комп'ютерного розрахунку виходячи з першопринципів. Вона може бути використана для оцінки наслідків функціоналізації гідроксильними групами різних типів максенів, з огляду на перспективу створення новітніх приладів емісійної електроніки.

Ключові слова: максени, робота виходу, термінація поверхні, гідроксильна група.

Yu. Nykyruy¹, S. Mudry¹, Yu. Kulyk¹, V. Prunitsa¹, A. Borysiuk²

Magnetic properties and nanocrystallization behavior of Co-based amorphous alloy

¹ Metal Physics Department, Ivan Franko National University of Lviv, Lviv, Ukraine, yuliya.nykyruy@lnu.edu.ua

² Department of Applied Physics and Nanomaterial Science, Lviv Polytechnic National University, Lviv, Ukraine

The magnetic properties of the amorphous $\text{Co}_{57}\text{Fe}_5\text{Ni}_{10}\text{Si}_{11}\text{B}_{17}$ alloy have been studied by a vibrating sample magnetometer. The temperature dependence of saturation magnetization was measured and the Curie point and crystallization onset temperature were determined as 560 K and 760 K respectively. The coercive force was obtained as 200 A/m and saturation magnetization - 65 Am^2/kg . The alloy was produced in the form of a ribbon thickness of 30 μm using the melt spinning method, and its internal amorphous structure was examined by the X-ray diffraction method. The crystallization behavior of the alloy was studied using series of isothermal annealing of the samples of the alloy at temperatures in the range of 723-1023 K for different exposures (up to 240 minutes) and nanocrystalline phases were detected by the X-ray diffraction analysis.

Keywords: Co-based amorphous alloy, DTA, thermo-magnetic curves, hysteresis, magnetic properties, X-ray diffraction, nanocrystallization.

Received 01 November 2022; Accepted 21 February 2023.

Introduction

Co-based amorphous alloys are attractive materials that are already used in various fields of industry. They are very soft magnetic, provide a sufficient high saturation magnetization and are zero-magnetostrictive for appropriate chosen concentration of alloy. Co-based amorphous ribbons are attractive alternative as detection layer in magnetoresistive systems [1]. Depending on the type of hysteresis loop these materials are used in current and power transformers, sensor elements, choke coils, magnetic screens/shielding, high-frequency power applications, etc [2, 3, 4]. Rapidly quenched Co-based alloys were proposed as suitable materials for magnetic cores working at high frequencies. Compositions with zero magnetostriction, magnetic properties and crystallization onset temperatures T_x in $(\text{Fe}_a\text{Co}_{1-a-b}\text{Ni}_b)_{100-y}(\text{Si}_{0.4}\text{B}_{0.6})_y$ system as function of Ni (Mo, Mn) and metalloid content were investigated in [5]. The main disadvantage of these amorphous metal alloys (AMA) was the fact that Curie point exceeds crystallization onset temperature that complicates an effective heat treatment

on hysteresis loop shape. In previous our research the amorphous alloys with similar chemical composition Co-(FeMoMn)-(SiB) were investigated and slightly different thermal stability and magnetic properties were revealed [6]. The Curie point of these alloys doesn't exceed crystallization onset temperature, allowing carrying out the optimization annealing. So, a slight variation in the percentage of elements significantly changes the thermal stability and Curie point of these alloys and Ni doping/absence effect on properties. In this paper, we present the results on studies of magnetic properties and crystallization behavior of $\text{Co}_{57}\text{Fe}_5\text{Ni}_{10}\text{Si}_{11}\text{B}_{17}$ amorphous alloy in comparison with other composition of the system

I. Materials and methods

The amorphous alloy $\text{Co}_{57}\text{Fe}_5\text{Ni}_{10}\text{Si}_{11}\text{B}_{17}$ was produced by rapid cooling from the melt using the melt-spinning technique in the form of the ribbon. The ribbon thickness is about 25 μm and width about 1.5 cm respectively.

Magnetic measurements were performed using a vibrating sample magnetometer. Re-magnetization curves of the studied samples were recorded in a magnetic field from -300 kA/m to $+300$ kA/m. Since the use of saturating magnetic fields is a prerequisite for performing quantitative magnetic phase analysis, the specific saturation magnetization (σ_s) and its temperature dependence were measured in the magnetic field of 800 kA/m. Heating was performed at the rate of 5 K/min within the temperature range of 293 - 950 K.

The as-obtained ribbons were investigated by the DTA-method using synchronous thermal analyzer Linseis STA PT 1600 under dynamic argon atmosphere (~ 6 liters per hour). Heating was performed at the rate of 10 K/min from 293 K up to 973 K.

To study the structural and phase transformations induced by heat treatment, a series of isothermal annealing of samples of the amorphous alloy $\text{Co}_{57}\text{Ni}_{10}\text{Fe}_5\text{Si}_{11}\text{B}_{17}$ were carried out. Annealing was performed in an air atmosphere at temperatures $T=723^\circ\text{K}$, 773°K , and 823°K with different exposure times of up to 240 minutes. The diffraction curves of the annealed samples were measured on a DRON-3 automated X-ray diffractometer using Cu-K_α radiation, monochromatized by reflection from a pyrolytic graphite single crystal mounted on a diffracted beam, which makes it possible to completely to avoid the sample's fluorescent radiation. The back-scattered diffraction curves of the samples were recorded in the mode of continuous movement of the detector at a speed of 2 degrees per minutes with automatic registration of the intensity of scattered radiation.

II. Results and discussions

Re-magnetization curves of the magnetic moment for the $\text{Co}_{57}\text{Ni}_{10}\text{Fe}_5\text{Si}_{11}\text{B}_{17}$ are presented in Fig.1a and show that in the region of weak magnetic fields the magnetization increases in proportion to the external strength magnetic field, and in a strong magnetic field (above 17 - 20 kA/m) the saturation is observed. The specific saturation magnetization was obtained as $\sigma_s=65\text{A}\cdot\text{m}^2/\text{kg}$. The saturation requires quite a strong magnetic field, while the residual magnetization is small.

The coercive force H_C was obtained as about 200 A/m, which corresponds to the average values of coercive force for soft magnetic materials [7], but it is quite larger than the values H_C for some Co-Si-B-based alloys obtained in [8, 9, 10, 11]. Worth noting, the coercive force is structurally sensitive and depends on elastic stresses, shape, and dimension of the ferromagnetic phases. The magnetization of the amorphous ribbon occurs by slightly shifting the boundaries of the domains and the reverse rotation of the vector of spontaneous magnetization.

The temperature dependence of specific saturation magnetization (thermomagnetic curves) $\sigma_s(T)$ for the as-quenched Co-based amorphous alloy (Fig.1b) is typical for amorphous ferromagnets. The saturation magnetization decreased with temperature increasing to Curie point ($T_C = 560$ K). The Curie point of the amorphous alloy was determined by constructing a model of temperature dependence of the spontaneous saturation magnetization of the alloy according to the Weiss-Heisenberg theory. The Curie temperature marks the ferromagnetic - paramagnetic transition, at which $\sigma_s \rightarrow 0$. The temperature interval of ferromagnetic phase existence for $\text{Co}_{57}\text{Fe}_5\text{Ni}_{10}\text{Si}_{11}\text{B}_{17}$ is very wide, about ~ 200 K. Further increase of temperature resulted in σ_s increasing caused by the crystallization of ferromagnetic phase with higher Curie temperature. Thus, the temperature of σ_s increasing indicates the onset of amorphous-crystalline transition and means the crystallization onset temperature of this alloy as $T_x=760\text{K}$, determining the temperature limit of the amorphous state stability. At temperatures above T_x , the thermomagnetic curve displays the crystallization processes of the alloys. In the temperature range 760 - 950 K the curve is characterized by two intervals of increasing that could be interpreted as the formation of two crystallization phases and the crystallization process of the alloy proceeds through a multi-stage model [12]. The crystallization onset temperature of the second phase is determined as about 826 K. Saturation magnetization σ_s , coercive force H_C , Curie temperature T_C , and crystallization onset temperature T_x of the $\text{Co}_{57}\text{Fe}_5\text{Ni}_{10}\text{Si}_{11}\text{B}_{17}$ alloy are summarized in Table 1.

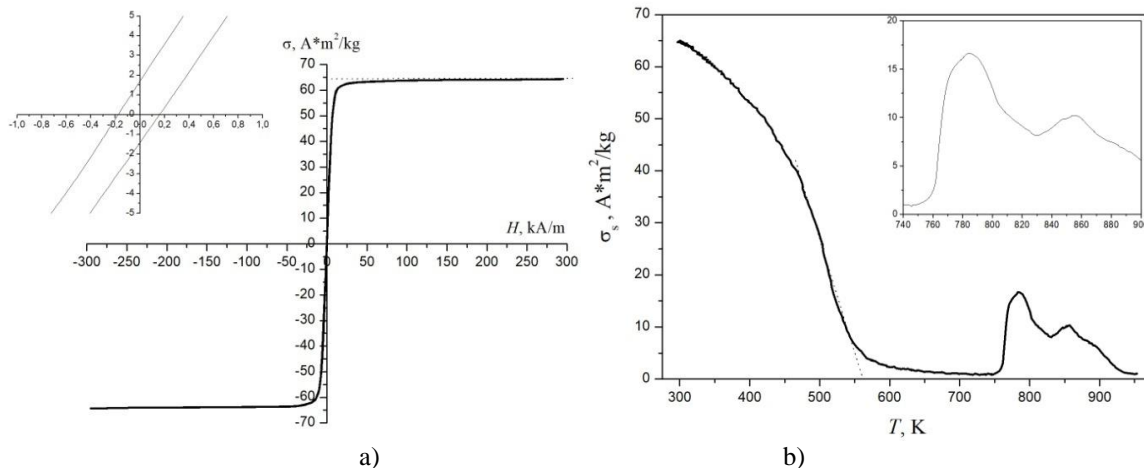


Fig. 1. The hysteresis (a) and thermo-magnetic (b) curves of the $\text{Co}_{57}\text{Fe}_5\text{Ni}_{10}\text{Si}_{11}\text{B}_{17}$ alloy.

Table 1.

Results of magnetic measurements

Alloy composition	σ_s , Am ² /kg	H_c , A/m	T_C , K	T_x^{TM} , K
Co ₅₇ Ni ₁₀ Fe ₅ Si ₁₁ B ₁₇	65	200	560	760 826

The DTA curve for the as-quenched amorphous ribbon (Fig.2) is characterized by two endothermic peaks at a temperature above 780 K that correlates with thermomagnetic curve. The presence of two exothermic peaks has been interpreted as the formation of a second crystallization phase, and the crystallization process of the alloy proceeds through a two-stage model. The onset point of the first peaks specifies the crystallization onset temperature of the alloys indicating the start of the nanocrystallization process as well as the temperature limit of amorphous phase stability. For Co-Fe-Ni-Si-B

alloys, the temperature range of amorphous phase stability is in the range of about 750-850 K and depends on impurities and the production process [13, 14, 15].

The results of thermomagnetic measurements are consistent with the DTA results; however, the value of T_x obtained by the DTA method is higher than T_x obtained by thermomagnetic curve. This difference can be explained partially by different heating rates at DTA and thermomagnetic measurements, because increasing the heating rate contributes to the shift of maxima to higher temperatures [16, 17].

To study the structure and phase transformations in the process of heat treatment, a series of isothermal annealing samples of the amorphous alloy were carried out. Fig. 3 shows the scattering intensity curves of samples annealed at $T=723^\circ\text{K}$ in the time interval from 5 to 240 min. The initial sample is characterized by a completely amorphous structure, which is indicated by the presence of broad maxima without intensity peaks from the

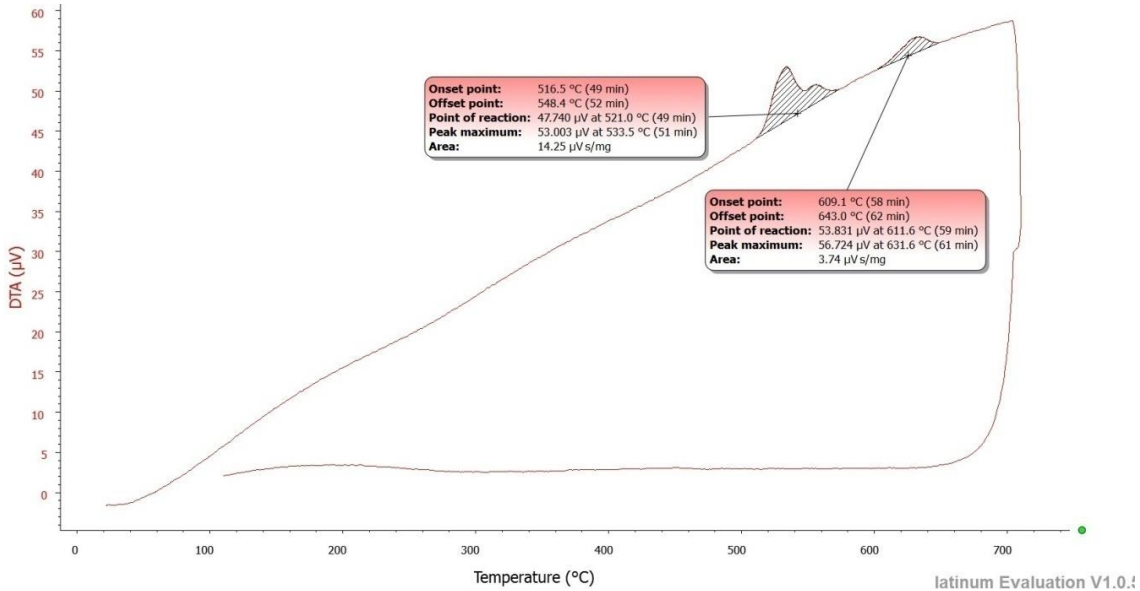


Fig. 2. The DTA curve of the Co₅₇Fe₅Ni₁₀Si₁₁B₁₇ alloy.

Table 2.

Results of DTA measurements

Alloy	Peak	Onset point, K	Offset point, K	Point of reaction, K	Peak maximum, K	Area μVs/mg
Co ₅₇ Fe ₅ Ni ₁₀ Si ₁₁ B ₁₇	1	789,65	821,55	794,15	806,65	14.25
	2	882,25	916,15	884,75	904,75	3.74

Table 3.

Characteristic temperature of phase transformations of the Co-(FeMoMnNi)-(SiB) alloys

Alloy No.	Chemical composition	T_{x1} K (by TM)	T_{x2} K (by TM)	T_{x1} K (by DTA)	T_{x2} K (by DTA)	T_C K	Ref.
1	Co ₅₇ Fe ₅ Ni ₁₀ Si ₁₁ B ₁₇	760	826	790	880	560	This article
2	Co ₇₀ Fe ₃ Mo _{1.5} Mn _{3.5} Si ₁₁ B ₁₁	749	-	789	-	649	[6]
3	Co ₇₃ Fe ₁ Mo ₁ Mn ₃ Si ₁₃ B ₉	704	798	729	824	683	[6]
4	Co _{73.2} Fe _{4.3} Mn _{0.5} Si _{5.3} B _{16.7}	718		710	813	731	[5]
5	Co ₇₃ (Fe,Ni,Mo,Mn) _{5,7} (Si _{0,2} B _{0,8}) _{21,3}	696		700	835	718	[5]
6	Co _{73,3} (Fe,Ni,Mo,Mn) _{5,7} (Si _{0,2} B _{0,8}) ₂₁	698		690	832	720	[5]
7	Co _{58,3} (Fe,Ni,Mn) _{21,6} (Si _{0,2} B _{0,8}) _{20,1}	638		670	801	690	[5]
8	Co _{55,7} (Fe,Ni,Mn) _{24,2} (Si _{0,2} B _{0,8}) _{20,1}	671		671	799	690	[5]

crystalline phase in the diffraction curve.

The position of the main maximum corresponds to the modulus of the wave vector $s_1 = 31.3 \text{ nm}^{-1}$. The average interatomic distance is calculated by the Ehrenfest formula: $R_1 = \frac{7.73}{s_1}$, and is about 0.247 nm which is close to the sum of the atomic radii of Co equal to 0.250 nm. The size of the regions of coherent scattering, estimated according to the formula $L = \frac{2\pi}{\Delta s_1}$, where Δs_1 – the main maximum's full width of half-peak (FWHP), does not exceed 1.5 nm. This value is close to the results obtained for similar alloy composition in [18, 19] where the size of the regions of coherent scattering was 1.3-1.7 nm

Increasing the duration of the isothermal annealing leads to certain structure and phase transformations, which are especially pronounced in the sample annealed for 240 min (Fig. 1a). Against the background of the main maximum of the amorphous phase, a number of features appeared at the positions of $s=29.1 \text{ nm}^{-1}$, 31.2 nm^{-1} , and 32.8 nm^{-1} , which correspond to the diffraction lines (100), (002), and (101) of the $\alpha(\text{Co})$ phase (hexagonal syngony, space group P63/mmc). The obtained result indicates the separation of the nanocrystalline phase of a solid solution based on $\alpha(\text{Co})$ from the amorphous phase. For a more detailed analysis of structure and phase transformations, the difference curves of the scattering intensity were calculated by the formula: $I_d(s) = I(s) - I_0(s)$, where $I_0(s)$ - scattering intensity of the original amorphous alloy (Fig 1b).

As can be seen from Fig. 1b, some structure

changes have begun to appear already during annealing within 15 minutes. Worth noting, the scattering intensity has increased in the region of the main maximum in the samples annealed for 15-30 minutes. The obtained result can be explained by the formation of nanocluster structure units with short-range order characteristic of hexagonal modification of the $\alpha(\text{Co})$ in the amorphous phase. The size of the coherent scattering regions of $\alpha(\text{Co})$ nanoclusters, estimated by FWHP of the maximum of the difference curves, reached $L \approx 3.5 \text{ nm}$, which is significantly larger compared to the original amorphous phase ($L \approx 1.5 \text{ nm}$). Regarding the samples annealed for a longer period of time (60-240 min.), a number of features corresponding to the (100), (002), and (101) lines of $\alpha(\text{Co})$ have appeared on the difference curves. Thus, it can be assumed that an increasing of the duration of isothermal exposure causes the transformation of nanocluster structural units into $\alpha(\text{Co})$ nanocrystals, the average size of which reached about 10 nm when the exposure time increased to 240 min. The volume fraction of the nanocrystalline phase does not exceed 20% of the volume of the amorphous alloy. The formation of $\alpha(\text{Co})$ nanocrystals in the amorphous phase corresponds to the 1st peak on the DTA curve.

Let's consider changes in the structure-phase state of the $\text{Co}_{57}\text{Ni}_{10}\text{Fe}_5\text{Si}_{11}\text{B}_{17}$ amorphous alloy when the exposure temperature increased. As can be seen from Fig. 4, annealing of the samples for 5 min. at $T=773^\circ\text{K}$ has not lead to a change in the phase state of the sample. However, it should be noted that the size of the coherent scattering

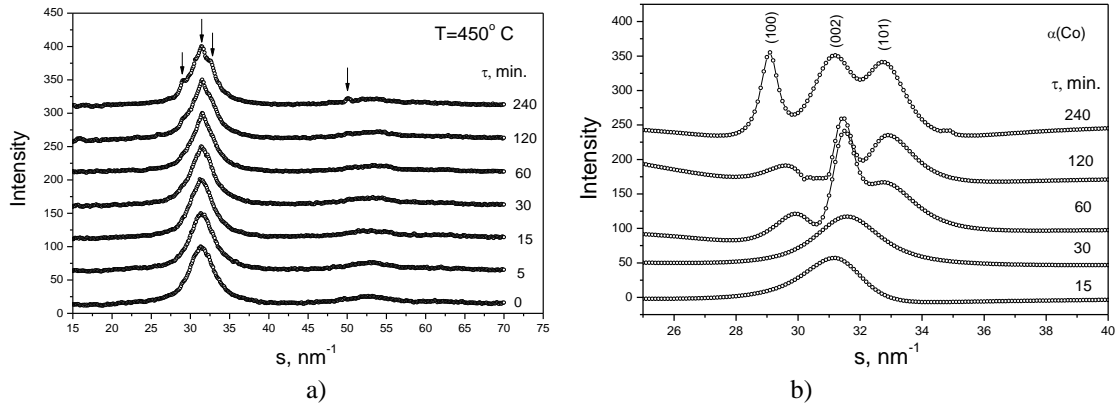


Fig. 3. Diffraction curves of amorphous $\text{Co}_{57}\text{Ni}_{10}\text{Fe}_5\text{Si}_{11}\text{B}_{17}$ alloy annealed at $T=723^\circ\text{K}$ (a), difference curves of scattering intensity (b).

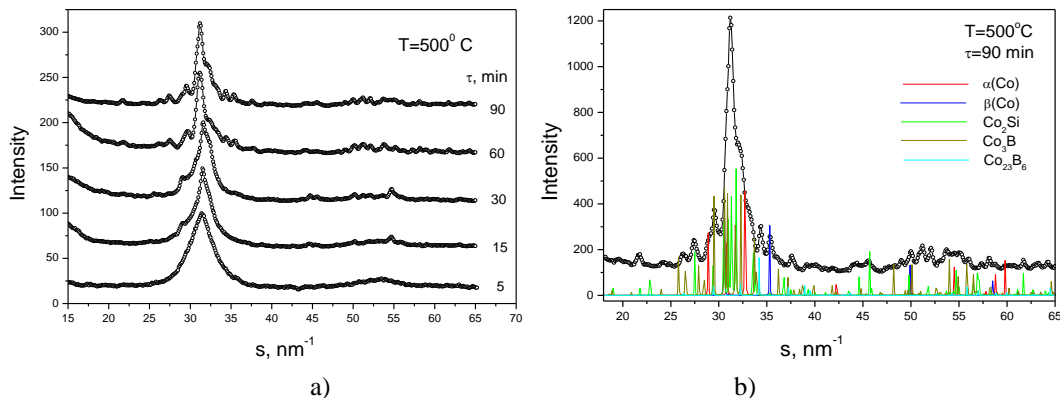


Fig. 4. Diffraction curves of amorphous $\text{Co}_{57}\text{Ni}_{10}\text{Fe}_5\text{Si}_{11}\text{B}_{17}$ alloy annealed at $T=773^\circ\text{K}$ (a), and curve deconvolution for $T=773^\circ\text{K}$ for 90 minutes (b).

regions of the amorphous phase has increased to 2.0 nm, which can be explained by the formation of nanocluster structural units with a short-range order of the $\alpha(\text{Co})$ phase. Phase transformations in the sample started when the duration of annealing increased to 15 min. As can be seen from the diffraction patterns (Fig. 4a), in the time interval of 15-30 minutes the nanocrystals (of the hexagonal phase of an $\alpha(\text{Co})$ based solid solution) are separated from the amorphous phase. Increasing the time of isothermal exposure to 60-90 minutes leads to the complete disintegration of the amorphous phase.

The diffraction spectrum of the sample annealed at

$T=773^\circ\text{K}$ for 90 minutes, compared with the diffraction spectra of the phase components formed as a result of the decomposition of the amorphous phase, is shown in Fig. 4b. It can be represented as a superposition of the spectra of phases $\alpha(\text{Co})$ (hexagonal syngony, group P63/mmc), $\beta(\text{Co})$ (cubic syngony, group Fm3m), silicide Co_2Si (orthorhombic syngony, group Pnma), boride Co_3B (orthorhombic syngonia, group Pnma), and boride Co_{23}B_6 (cubic syngonia, group Fm3m).

The parameters of the crystal structure of the phases are given in the Table. 4. As can be seen from the DTA data, the 1st maximum has a bifurcated form and can be

Table 4.

 Parameters of the structure-phase state of the annealed amorphous alloy $\text{Co}_{57}\text{Ni}_{10}\text{Fe}_5\text{Si}_{11}\text{B}_{17}$

Temperature, annealing time	Phase composition	Unit cell parameters, Å	Average crystallite size, nm
773°K, 30 min.	$\alpha(\text{Co})$	a=2.5184±0.0007 c=4.0706±0.0015	22.0
	Co_2Si	a=4.9146±0.0012 b=3.7402±0.0011 c=7.1344±0.0021	21.5
	Co_3B	a=5.2349±0.0012 b=6.7101±0.0018 c=4.4239±0.0009	24.5
773°K, 90 min.	$\alpha(\text{Co})$	a=2.5044±0.0007, c=4.0193±0.0013	14.5
	$\beta(\text{Co})$	a=3.5484±0.0008	75.0
	Co_2Si	a=4.8924±0.0010 b=3.7684±0.0009 c=7.1434±0.0016	25.5
	Co_3B	a=5.2015±0.0010 b=6.7211±0.001 c=4.4151±0.0008	19.0
	Co_{23}B_6	a=10.8216±0.0018	31.0
823°K, 5 min.	$\alpha(\text{Co})$	a=2.5172±0.0008, c=4.0746±0.0025	17.5
	Co_2Si	a=4.9212±0.0009 b=3.7705±0.0012 c=7.1066±0.0019	27.0
	Co_3B	a=5.2114±0.0013 b=6.7322±0.0016 c=4.4500±0.0009	26.0
823°K, 60 min.	$\alpha(\text{Co})$	a=2.5507±0.0003, c=4.0708±0.0005	125.0
	$\beta(\text{Co})$	a=3.5473±0.0005	60.0
	Co_2Si	a=4.8999±0.0006 b=3.7450±0.0005 c=7.1236±0.0010	25.0
	Co_3B	a=5.2071±0.0008 b=6.6564±0.0011 c=4.3863±0.0007	50.0
	Co_{23}B_6	a=10.7446±0.0011	22.0
1023°K, 60 min.	$\alpha(\text{Co})$	a=2.4977±0.0003, c=4.0868±0.0011	24.0
	$\beta(\text{Co})$	a=3.5273±0.0005	35.5
	Co_2Si	a=4.9271±0.0005 b=3.7596±0.0004 c=7.1468±0.0008	28.0
	Co_3B	a=5.2735±0.0006 b=6.6805±0.0008 c=4.3949±0.0006	34.0

considered as a superposition of two submaxima with different magnitudes of the thermal effect. If the 1st sub-maximum can be associated with the separation of $\alpha(\text{Co})$ solid solution crystals, then the 2nd sub-maximum probably corresponds to the complete decomposition of the amorphous phase.

Let's consider the sequence of structural and phase changes in samples of the amorphous alloy $\text{Co}_{57}\text{Ni}_{10}\text{Fe}_5\text{Si}_{11}\text{B}_{17}$ when the isothermal exposure temperature increases to $T=823^\circ\text{K}$. As can be seen from the series of diffraction patterns (Fig. 5a), crystallization processes occurred already at the early stages of isothermal annealing. Analysis of the phase composition of samples annealed for 2-5 minutes revealed the presence of highly dispersed phases: a solid solution based on $\alpha(\text{Co})$, silicide Co_2Si , and borides Co_3B and Co_{23}B_6 . Complete disintegration of the amorphous phase was observed when the duration of annealing was increased to 15 min. Fig. 5b shows the diffraction pattern of the sample annealed at 823°K for 60 minutes in comparison with reference diffraction spectra of phase components. It should be noted that the sample contains the same phases that we observed in the sample annealed at 773°K for 90 minutes.

Of great interest is the nature of phase transformations of amorphous Co-based alloys in the high-temperature region. Fig. 6 shows the diffraction pattern of a sample of the $\text{Co}_{57}\text{Ni}_{10}\text{Fe}_5\text{Si}_{11}\text{B}_{17}$ amorphous alloy annealed at

$T=1023^\circ\text{K}$ for 60 minutes. As can be seen, the diffraction pattern of the sample can be represented as a superposition of diffraction spectra of phases based on $\alpha(\text{Co})$, $\beta(\text{Co})$, Co_2Si , and Co_3B . It should be noted a significant increase in the proportion of cubic $\beta(\text{Co})$ modification, which is caused by the polymorphic transformation $\alpha(\text{Co})\rightarrow\beta(\text{Co})$ (2nd maximum on the DTA thermogram). In addition, there are no phase lines of the metastable boride Co_{23}B_6 in the diffraction pattern, which indicates its decay and transformation into a stable modification of Co_3B according to the scheme $\text{Co}_{23}\text{B}_6\rightarrow\text{Co}_3\text{B}+\beta(\text{Co})$.

It is known some amorphous-nanocrystalline alloys have physical properties that ~~that~~ are better than the properties of both amorphous and nanocrystalline materials. For example, their magnetic properties are better than the magnetic properties of amorphous ferromagnetic alloys and they have high strength, much higher than the strength of amorphous or crystalline states [20]. The grain size of the nanocrystalline structure of the alloy is determined by the crystallization mechanisms associated with the chemical composition and thermodynamic characteristics. An amorphous-nanocrystalline structure is often achieved by optimization annealing. The crystallization behaviours studies carried out in this work can be used to select optimization annealing modes, which is the aim of our further research.

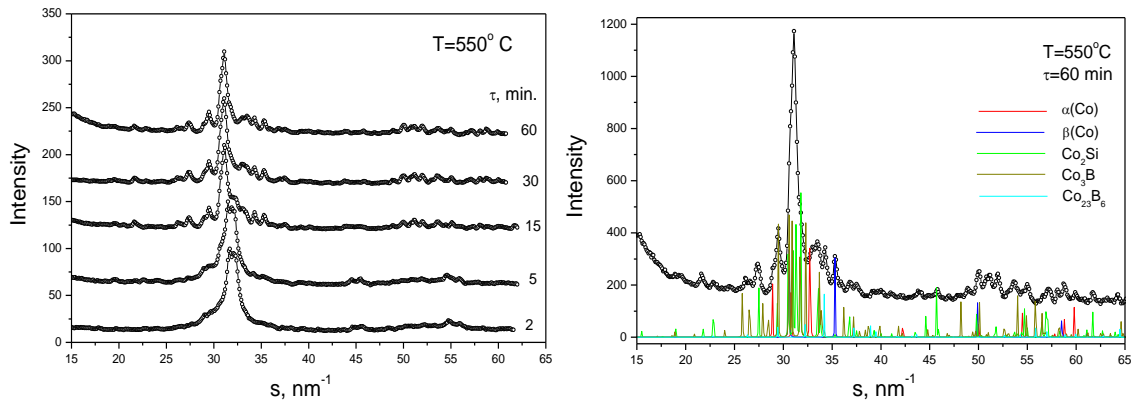


Fig. 5. Diffraction curves of amorphous $\text{Co}_{57}\text{Ni}_{10}\text{Fe}_5\text{Si}_{11}\text{B}_{17}$ alloy annealed at $T=823^\circ\text{K}$ (a), and at $T=823^\circ\text{K}$ for 60 minutes (b).

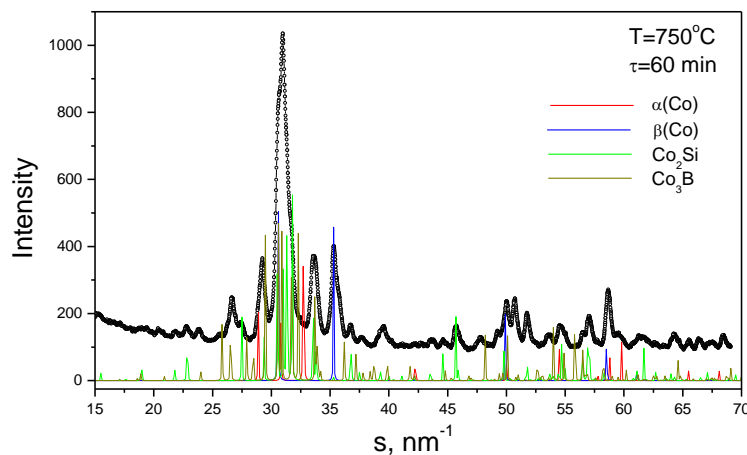


Fig. 6. Diffraction pattern of the sample annealed at $T=1023^\circ\text{K}$ for 60 minutes.

Conclusions

Magnetic properties and crystallization behavior of the $\text{Co}_{57}\text{Ni}_{10}\text{Fe}_5\text{Si}_{11}\text{B}_{17}$ amorphous alloy produced by the melt-spinning technique were studied and parameters that can be useful for practical applications were observed. Our results show that the Curie point of the investigated material is much smaller than the crystallization onset temperature, allowing optimization annealing. The temperature of optimization annealing should not significantly exceed 723 K at the exposure time of 1-4 hours due to the formation of borides.

Funding

This research did not receive any specific grant

Declaration of competing interest

The authors declare that they have no known competing financial interests or personal relationships that could have appeared to influence the work reported in this paper.

Nykyruy Yu. – PhD, Associate Prof. of Metals physics department;
Mudry S. – Prof., D.Sc. Head of Metal physics department;
Kulyk Yu. – PhD, Senior engineer of Metal physics department;
Prunitsa V. – PhD student of Metal physics department
Borisyuk A. – Senior researcher of Department of Applied Physics and Nanomaterial Science.

- [1] A. Kaufler, Y. Luo, K. Samwer, G. Gieres, M. Vieth, J. Wecker, *Tunnel-magnetoresistance system with an amorphous detection layer*, Journ. Appl. Phys. 91, 1701 (2002); <https://doi.org/10.1063/1.1426236>.
- [2] R. Hasegawa, *Applications of amorphous magnetic alloys*, Mater. Sci. Eng., A 375–377,90 (2004); <https://doi.org/10.1016/j.msea.2003.10.258>.
- [3] K. Ackland, A. Masood, S. Kulkarni, P. Stamenov, *Ultra-soft magnetic Co-Fe-B-SiNb amorphous alloys for high frequency power applications*, AIP Adv., 8, 56129(2018); <https://doi.org/10.1063/1.5007707>.
- [4] A.V. Nosenko, V.V. Kyrylchuk, M.P. Semen'ko, M. Nowicki, A. Marusenkov, T. M. Mika, et al., *Soft magnetic cobalt based amorphous alloys with low saturation induction*, J. Magn. Magn Mater. 515, 167328 (2020); <https://doi.org/10.1016/j.jmmm.2020.167328>.
- [5] V K Nosenko, V V Maslov, A P Kochkubey and V V Kirilchuk, *New soft magnetic amorphous cobalt based alloys with high hysteresis loop linearity*, J. Phys.: Conf. Ser. 98, 072006 (2008); <https://doi.org/10.1088/1742-6596/98/7/072006>.
- [6] Y. Nykyruy, S. Mudry, Y. Kulyk, A. Borisyuk, *Magnetic properties and nanocrystallization process in Co-(Me)-Si-B amorphous ribbons*, Applied Nanoscience, (2022); <https://doi.org/10.1007/s13204-022-02746-6>.
- [7] Konieczny, Jaroslaw & A, Borisjuk & M, Pashechko & Dobrzanski, Leszek, *Magnetic properties of Co-based amorphous ribbon under cyclic heating and cooling*, Journal of Achievements in Materials and Manufacturing Engineering, 42 (1-2), 42 (2010);
- [8] Anton V. Nosenko, Vasyl V. Kyrylchuk, Mykhailo P. Semen'ko, Michał Nowicki, Andriy Marusenkov, Taras M. Mika, Oleksandr M. Semyrka, Galyna M. Zelinska, Viktor K. Nosenko, *Soft magnetic cobalt based amorphous alloys with low saturation induction*, Journal of Magnetism and Magnetic Materials, Volume 515, 2020, 167328, ISSN 0304-8853; <https://doi.org/10.1016/j.jmmm.2020.167328>.
- [9] V K Nosenko et al., *New soft magnetic amorphous cobalt based alloys with high hysteresis loop linearity*, J. Phys.: Conf. Ser., 98, 072006 (2008); <https://doi.org/10.1088/1742-6596/98/7/072006>.
- [10] S. Lesz, R. Babilas, M. Nabiałek, M. Szota, M. Dośpiał, R. Nowosielski, *The characterization of structure, thermal stability and magnetic properties of Fe–Co–B–Si–Nb bulk amorphous and nanocrystalline alloys*, Journal of Alloys and Compounds, 509, Supplement 1, S197 (2011); <https://doi.org/10.1016/j.jallcom.2010.12.146>.
- [11] V. V. Girzhon, A. V. Smolyakov, N. I. Zakharenko, N. G. Babich, & M. P. Semen'ko, *Effect of pulsed laser heating on the magnetic properties of amorphous alloy 30KSR*, The Physics of Metals and Metallography, 111(6), 561 (2011); <https://doi.org/10.1134/s0031918x11050061>.
- [12] A.K. Panda, S. Kumari, I. Chattera, P. Svec, A. Mitra, *Effect of Fe addition on the crystallization behaviour and Curie temperature of CoCrSiB-based amorphous alloys*, Philos. Mag. 85 (17), 1835 (2005); <https://doi.org/10.1080/14786430500098934>.
- [13] N. I. Noskova, *Structure and Magnetic Properties of Iron- and Cobalt-Based Amorphous Alloys Versus Nanocrystallization Conditions*. Technical Physics, 50(10), 1311 (2005); <https://doi.org/10.1134/1.2103277>.
- [14] V. I. Lysov, T. L. Tsaregradskaya, A. M. Kurylyuk, O. V. Turkov, G. V. Saenko, *Controlled nanostructuring from an amorphous state in multicomponental alloys based on cobalt*, Journal of physical studies, 22(3), 3702 (2018); <https://doi.org/10.30970/jps.22.3701>.
- [15] N. Bayr, V.S. Kolat, T. Izgi, S. Atalay, H. Gencer and P. Sovak, *Crystallisation Kinetics of $\text{Co}_{75-x}\text{M}_x\text{Si}_{15}\text{B}_{10}$ ($M = \text{Fe}, \text{Mn}, \text{Cr}$ and $x = 0, 5$) Amorphous Alloys*, Acta physica polonica a;); <https://doi.org/10.12693/APhysPolA.129.84>
- [16] M. G. Babych, M. I. Zakharenko, M. P. Semen'ko, Yu. A. Kunyts'ky, and D. S. Leonov, *Peculiarities of Cobalt Based Amorphous Alloys Crystallization*, Nanosystems, Nanomaterials, Nanotechnologies, 6 (1), 237 (2008);
- [17] Bo Han Zhang, Jia Hao Liu, Hai Tao Zhou, *Comprehensive study of the crystallization behavior, thermal stability, and magnetic properties of $\text{Co}_{66.5}\text{Si}_{15.5}\text{B}_{12}\text{Fe}_{4}\text{Ni}_2$ amorphous ribbon*, Journal of Non-Crystalline Solids, 573 (1), 121132 (2021); <https://doi.org/10.1016/j.jnoncrysol.2021.121132>.

- [18] Stepan Mudry, and Yulia Nykyruy, *Laser induced structure transformation in Co₇₀Fe₃Mn_{3.5}Mo_{1.5}B₁₁Si₁₁ amorphous alloy*, Materials Science-Poland, 32 (1), 28 (2014); <https://doi.org/10.2478/s13536-013-0152-2>.
- [19] Yu Nykyruy, S. Mudry, I. Shtablavyi, A. Borisyuk, Ya Tsekhmister, I. Gnilityskiy, *Formation of laser-induced periodic surface structures on amorphous Fe- and Co-based alloys and its impact on magnetic properties*, Materials Chemistry and Physics, 287, (2022); <https://doi.org/10.1016/j.matchemphys.2022.126317>.
- [20] V. I. Lysov, T. L. Tsaregradskaya, A. M. Kurylyuk, O. V. Turkov, G. V. Saenko, *Controlled nanostructuring from an amorphous state in multicomponental alloys based on cobalt*, Journal of Physical Studies 22(3), (2018); <https://doi.org/10.30970/jps.22.3702>.

Ю.С. Никируй¹, С.І. Мудрий¹, Ю.О. Кулик¹, В.В. Пруніца¹, А.К. Борисюк²

Магнітні властивості та нанокристалізація аморфного сплаву на основі кобальту

¹ Львівський національний університет імені Івана Франка, Львів, Україна

² Національний університет «Львівська політехніка», Львів, Україна

Магнітні властивості аморфного сплаву Co₅₇Fe₅Ni₁₀Si₁₁B₁₇ досліджували за допомогою вібраційного магнітометра та було визначено температуру Кюрі (560 К) і температуру початку кристалізації сплаву (760 К). Коерцитивна сила аморфного сплаву - 200 А/м, та намагніченість насичення - 65 Ам²/кг. Аморфний сплав виготовлений у вигляді стрічки товщиною 30 мкм методом спінінгування з розплаву. Внутрішню структуру сплаву та нанокристалізаційну поведінку в мовах ізотермічних відпалів при температурах 723 - 1023 К при різних часах (до 120 хвилин) досліджували методом рентгенівської дифракції і рентгеноструктурного аналізу.

Ключові слова: аморфний сплав на основі кобальту, ДТА, термомагнітні криві, гістерезис, магнітні властивості, рентгенівська дифракція, нанокристалізація.

Ivan Mironyuk¹, Hanna Vasylyeva² Iryna Prokipchuk¹, Igor Mykytyn¹

Adsorption of Sr(II) cations onto titanium dioxide, doped with Boron atoms

¹Department of Chemistry, Vasyl Stefanyk Precarpathian National University, Ivano-Frankivsk, Ukraine, myrif555@gmail.com

²Department of Theoretical Physics, The Section of Nuclear Physics and Elementary particles, Uzhhorod National University, Uzhhorod, Ukraine, h.v.vasylyeva@hotmail.com

The adsorption of Sr(II) cations by Boron-doped TiO₂ was investigated. The adsorbent samples were obtained by liquid-phase sol-gel method using the aqua complex precursor [Ti(OH)₂]₆³⁺ 3Cl⁻ and modifying reagent hydrogen borate H₃BO₃. It was found, that single-phase rutile titanium dioxide or two-phase anatase-rutile oxide materials were formed under the different initial ratios of components.

Boron atoms are combined with Oxygen atoms into triangular structural cell BO₃ in the rutile sample 0.5B-TiO₂ and are localized in the surface layer of the nanoparticle material as a grouping =O₂BOH. The introduction of Boron atoms into the structure of the rutile adsorbent causes an increase in its adsorption capacity for the binding of Sr(II) cations in the aqueous electrolyte medium. The maximal adsorption values for Sr(II) cations by the rutile adsorbent in a neutral electrolyte environment reach 102.3 mg g⁻¹, while it is equal to 68.8 mg g⁻¹ for the unmodified anatase adsorbent a-TiO₂.

The number of acid adsorption centers ≡TiOH^{δ+} on the surface of the rutile adsorbent 0.5B-TiO₂ is ~ 50 units on a surface area of 10 nm², which is twice the number of centers on the surface of the anatase adsorbent a-TiO₂. The ionic strength of the acid centers of the ≡TiOH^{δ+} pK_{a1} and the base centers of the ≡TiOH^{δ-} pK_{a2} of the rutile sample is the largest in comparison with the centers of other investigated adsorbents and, accordingly, are equal to 0.6 and 12.3.

Anatase-rutile adsorbents 1.0B-TiO₂ and 1.5B-TiO₂ contain, respectively, 70% and 57% of the anatase phase. They are significantly inferior in adsorption ability toward cations of Sr(II) compared with the rutile adsorbent 0.5B-TiO₂. This is because Boron atoms are mainly localized in the anatase phase and with oxygen atoms form tetrahedral groups of BO₄⁻. Tetrahedral coordination of Boron atoms with respect to Oxygen atoms in the structure of anatase reduces the induction effect of Boron atoms on the redistribution of electron density in the B-O-Ti bridges and does not lead to the formation of additional acid adsorption centers on the surface of the anatase.

Keywords: Titanium dioxide, Boron, Adsorption, Strontium.

Received 30 August 2022; Accepted 24 January 2023.

Introduction

Adsorption technologies are widely used to solve environmental problems at present time. In particular, the synthetic adsorbents – activated carbon, zeolites, metal oxide-adsorbents Fe₃O₄, ZnO, TiO₂, titanium or zirconium phosphates, ion exchange resins, etc., are often used for the removal of heavy metal cations Pb (II), Cd (II), Ba (II), Hg (II), Sr (II) as well as some anions AsO₄³⁻, SeO₄²⁻, F⁻ from the aquatic environment [1-5]. The disadvantage of

known adsorbents is low adsorption capacity, instability to aggressive media, or complexity of synthesis. In this regard adsorbents based on TiO₂ have unique properties: resistance to acid medium, simplicity of synthesis, and high adsorption capacity toward heavy metal cations. The adsorption binding of metal cations by TiO₂-based adsorbents is carried out by hydroxylated Ti atoms of only a certain type on the surface of TiO₂.

The surface of the anatase modification of TiO₂ with an area of 10 nm² may contain 120-140 ≡TiOH – groups,

but only ~ 30 titanium groups are $\equiv\text{TiOH}^{\delta+}$ acidic centers, which take part in the metal cations adsorption. Most titanium groups, 70-76 (%) percent of the whole amount, demonstrate a neutral nature and are not involved in adsorption.

The authors of publications [6-9] impregnated $\equiv\text{TiO}_2\text{CO}$, $\equiv\text{TiO}_2\text{POOH}$ or $\equiv\text{TiO}_2\text{AsOOH}$ grouping in the amount of 3 to 13 units per 10 nm^2 on the surface of the anatase TiO_2 to increase the number of acid adsorption centers in 2-2.8 times. Exactly the high electronegativity of atoms C (2.5), P (2.1), and As (2.0) in these groupings, compared to the electronegativity of Ti atoms (1.5), causes the formation of additional acidic centers of $\equiv\text{TiOH}^{\delta+}$ capable of binding metal cations around these atoms.

According to our publication [10], sol-gel synthesis of nanoparticle TiO_2 using aqua complex precursor $[\text{Ti}(\text{OH})_6]^{3+}3\text{Cl}^-$ and modifying reagent of borate acid H_3BO_3 (which is also known as hydrogen borate or boric acid) leads to the formation of Boron-containing TiO_2 of different phase composition. In particular, the Boron-containing sample of 0.5B- TiO_2 is a rutile material with a particle shape in the form of villi. Samples with a higher content of Boron atoms 1.0B- TiO_2 and 1.5B- TiO_2 , in addition to rutile, contain 70% and 57% of the mass of anatase, respectively.

Since the electronegativity of atoms B is 2.0 and exceeds the electronegativity of Ti atoms, we can assume a high adsorption capacity of Boron-containing samples of TiO_2 toward metal cations.

In this work, we aim for the following tasks:

- find out the ionic strength of acid $\equiv\text{TiOH}^{\delta+}$ and the base $\equiv\text{TiOH}^{\delta-}$ adsorption centers of the surface of modified TiO_2 samples;
- investigate the adsorption of Sr(II) cations by Boron-containing TiO_2 ;
- determine the average number of acid $\equiv\text{TiOH}^{\delta+}$ and the main $\equiv\text{TiOH}^{\delta-}$ adsorption centers on a surface area of 10 nm^2 of base and modified samples.

I. Experimental techniques

1.1. Synthesis of titanium dioxide samples

Experimental samples of Boron-containing TiO_2 were obtained by the liquid-phase sol-gel method using as a precursor solution of titanium aqua complex $[\text{Ti}(\text{OH})_6]^{3+}3\text{Cl}^-$ and modifying agent – borate acid H_3BO_3 .

The synthesis of investigated samples was carried out at different ratios of components. The conditions for the synthesis of investigated samples and the mechanism of influence of the modifying agent on the course of structure-forming processes are described in detail in the publication [10].

1.2. Investigations of the characteristics of titanium dioxide samples

In this work, special emphasis was placed on the study of the surface characteristics of TiO_2 samples, which can affect the course of adsorption processes.

TEM and IR analyses were conducted; textural characteristics such as surface area and pore size

distribution were determined, as well as the pH of the point of zero charges (pH_{pzc}).

Images of bare a- TiO_2 and Boron-doped TiO_2 were obtained using the LSM 2100F transmission electron microscope (TEM). The accelerating voltage during the operation of the transmission electron microscope was 200 kV or more, which made it possible to record images on a nanometer scale. Light field rendering mode was also used.

The phase composition of the bare a- TiO_2 and modified samples 0.5B- TiO_2 , 1.0B- TiO_2 , 1.5B- TiO_2 , the parameters of the lattice and the dimensions of primary crystallites were investigated using the STOE STADIP diffractometer in the radiation of copper anode. The focus of the rays was carried out according to the Bragg-Brentano scheme. Rietveld's analysis of recorded diffractograms was performed using SHELXL-97 software [11, 12].

The study of the surface area of the samples and their pore size distribution was carried out with the help of isotherms of low-temperature N_2 adsorption-desorption. Quantachrome Autosorb (Nova 2200e) equipment was used for this purpose. Before measurement, the samples were calcined in a vacuum at 180°C for 24 hours. The surface area of the samples was calculated according to the theory of BET (Brunauer-Emmett-Teller). Pore size was estimated using density functional theory (DFT). It should be noted, that when calculating the surface area of adsorbents, the theories of BET and DFT give results that are well consistent with each other. However, since the calculation of surface area using the Brunauer-Emmett-Teller theory is generally accepted, we also used this particular theory.

IR spectroscopy was used, for qualitative and quantitative analysis of samples, with which it is possible to assess the structure of the complex, ions in compounds, phase composition, as well as the different coordination states of Boron atoms in the structure of anatase and rutile. The IR spectra of the samples were obtained on the Double-beam spectrophotometer SPECORD M80 device. To record the spectrum, the sample weight (4 mg) was mixed with KBr at a ratio of 1:100, and crushed in a vibration mill for 10 minutes. The resulting mixture formed a transparent plate size of $20 \times 5\text{ mm}^2$ by pressing.

The pH of the point of zero charges of the surface was determined to assess the surface ability of synthesized adsorbents to attach cations or anions. As a rule, pH_{pzc} is the value of a negative decimal logarithm of the activity of the potential-defining ion of the surface of a solid, that comes into contact with the electrolytic medium. Determination of the pH of the point of zero-charge of the surface a- TiO_2 and samples of TiO_2 doped by the Boron atoms was carried out by the method of drift of the hydrogen indicator of the medium.

1.3. Adsorption research and calculation of the number of adsorption centers of TiO_2 samples

Adsorption studies were carried out in batch conditions. To the 0.05 g of the adsorbent was added 5 ml of the studied aqueous solution of SrCl_2 . The ratio of liquid: solid phase (L:S) was, respectively, 100. Initially, the dependence of the adsorption of strontium ions on the duration of interaction, the so-called kinetics of

adsorption, was investigated. Thus, the duration of the interaction was determined, in which adsorption equilibrium was established in the reaction mixture. In addition, a possible mechanism for the course of adsorption processes was determined using the four most common kinetic models of adsorption.

Adsorption isotherms were measured at a certain time of equilibrium. For this purpose, the initial concentration of strontium ions in the solution was increased. The initial and residual (equilibrium) concentration of strontium ions was determined by direct complexometric titration with the indicator Eriochrom Black T.

In studies of anion adsorption, the equilibrium concentration of adsorbate was defined by Mohr's method, which uses the titration by the standard solution of silver nitrate with potassium chromate as an indicator. The value of adsorption was calculated according to the formula (1):

$$q_e = \frac{[(C_0 - C_e) \cdot V]}{m} \quad (1)$$

For the analytical description of the equilibrium adsorption of the cations Sr (II) by the TiO₂ samples, the Langmuir (2) and Freundlich (3) equations were used [13, 16]:

$$q_e = \frac{A_\infty K C_e}{1 + K C_e} \quad (2)$$

Where, q_e – the amount of adsorbate uptake at equilibrium, mg g⁻¹; A_∞ – maximal adsorption value, which corresponds to filling the whole adsorption centers, mg g⁻¹; K_L – Langmuir equation's constant, (L mg⁻¹) is the value inverse to the concentration of C_e , at which adsorption is $\frac{1}{2} A_\infty$; C_e – adsorbate equilibrium concentration, mg L⁻¹.

$$q_e = K_f C_e^n \quad (3)$$

Where, K_f – Freundlich constant, $\left(\frac{mg/g}{L}\right)^n$; n – intensity parameter of adsorption.

The number of acid adsorption centers N , on the surface of the adsorbent area of 10 nm², was calculated according to equation (4):

$$N = \frac{q_{max} \cdot N_A}{S_{BET} \cdot 10^{17}} \quad (4)$$

Here q_{max} – experimentally defined maximal adsorption of Sr (II) cations, (mole g⁻¹); S_{BET} – the specific surface area of the adsorbent, (m² · g⁻¹); N_A – Avogadro constant (6.022 · 10²³).

Studies of the effect of the acidity of the solution on the adsorption values were performed by adding to the reaction mixture 5 ml of HNO₃ solution or ammonium buffer solution to achieve the required pH value. Accordingly, the L:S ratio increased to 200. The acidity of the solution was controlled using a pH meter with a chlorine-silver electrode.

II. Results and discussion

2.1. The phase composition of the investigated samples

The phase composition of the bare a-TiO₂ and modified samples 0.5B- TiO₂, 1.0B- TiO₂, and 1.5B- TiO₂ the lattice parameters and the dimensions of the primary crystallites of these phases are given in Table 1.

The bare a-TiO₂ contains a single phase – anatase (spatial group I₄₁(amd)). The presence of Boron atoms in the sample of 0.5B-TiO₂ leads to the formation of a single-phase material – rutile (spatial group P₄₂ (mm)) [17]. However, increasing the content of Boron atoms leads to the formation of two-phase samples 1.0B-TiO₂ and 1.5B-TiO₂. These Boron-containing samples consist of anatase and rutile modifications of TiO₂ in quantities of 30 wt., % and 70 wt., % (57 wt., % and 43 wt., %) masses, respectively.

The textural characteristics of the bare a-TiO₂ and Boron-containing samples calculated by the method of low-temperature adsorption-desorption of N₂ molecules (Fig.1) are given in Table 2. They show that according to the specific surface of S_{BET} and the volume of pores V_p , the rutile sample 0.5B-TiO₂ is inferior to the base anatase sample a-TiO₂ and anatase-rutile samples 1.0B-TiO₂ and 1.5B-TiO₂. Thus, S_{BET} and the volume of pores V_p anatase-rutile sample 1.0B-TiO₂ is more than twice as high as these characteristics for 0.5B-TiO₂ rutile. However, the comparison of the rutile sample 0.5B-TiO₂ with the Boron-containing samples of TiO₂ described in the literature [18-20] indicates that the surface area of the sample 0.5B-TiO₂ remains higher than that described for Boron-containing world-wide analogs.

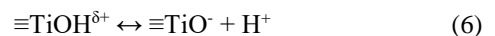
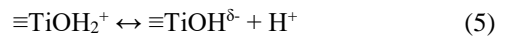
Sol-gel synthesis of investigated samples is special in the aspect of obtaining TiO₂ materials with very small mesopores with a radius of 1.0-3.0 nm and micropores with a radius up to 1.0 nm. (Fig. 1 (b)).

The micropores and mesopores in the samples are the gaps between the primordial particles and their associate or aggregates. The radii of the mesopore of the 0.5B-TiO₂ rutile sample are in the range of 1.0-2.0 nm values. They are smaller in size compared to the radii of other adsorbents. This is because the particles of this sample have the form of villi (Fig. 2 (a)).

Their diameter is 0.8-1.2 nm, and the length is 16-24 nm. The main features are that the villi are folded into "sheaves" in the associates, and this causes the formation of especially small mesoporous. The appearance of such particles is shown in Fig. 2.

2.2. Amphoteric properties of TiO₂

Titanium dioxide belongs to amphoteric oxides of metals, which have both acidic and basic properties. The amphoteric properties of titanium dioxide are manifested in the fact that its surface titanium groups change their chemical state, depending on the pH of the medium:



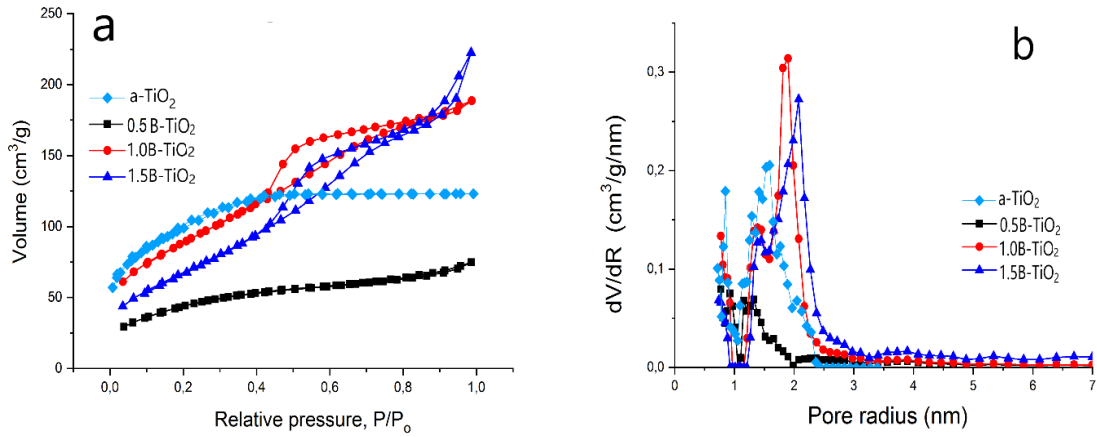


Fig.1. Isotherms of low-temperature N_2 adsorption/desorption of bare a-TiO₂ and Boron-containing TiO₂ samples (a); (b) the pores size distribution in the investigated samples studied by the magnitude of their effective radii.

Table 1.

Textural characteristics of investigated samples and parameters of the lattice of anatase and rutile modification of TiO₂.

Sample	Anatase						Rutile					
	Content, %	a, Å	c, Å	Ti-O (axial), Å	Ti-O (plane), Å	Particle size, nm	Content, %	a, nm	c, nm	Ti-O (axial), Å	Ti-O (plane), Å	Particle size, nm
a-TiO ₂	100	3.784	9.513	1.9787	1.9337	2.9±1.4	—	—	—	—	—	—
0.5B/TiO ₂	—	—	—	—	—	—	100	4.610	2.955	1.9924	1.9466	5.1
1.0B/TiO ₂	70±4	3.796	9.496	1.9752	1.9395	3.5	30±3	4.637	2.946	2.0040	1.9480	6.1
1.5B/TiO ₂	57±2	3.787	9.499	1.9758	1.9351	3.9	43±2	4.602	2.958	1.9889	1.9463	5.7

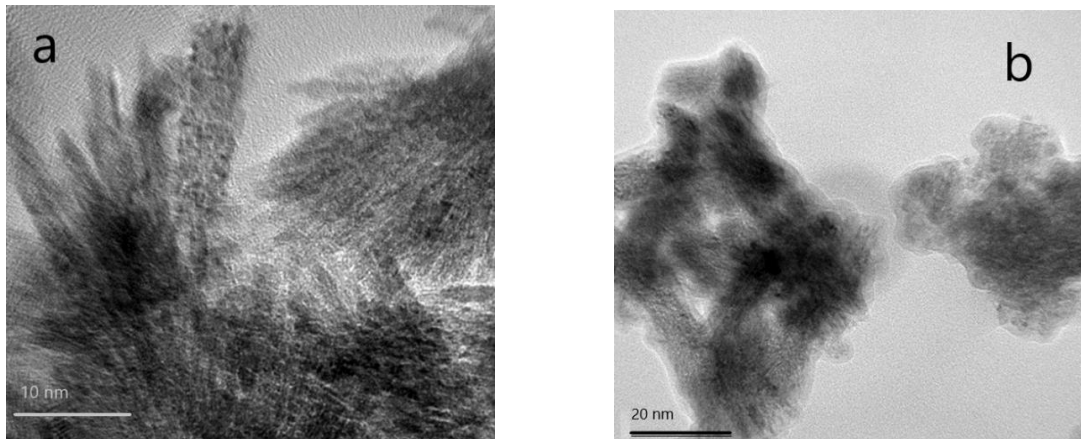


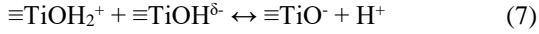
Fig. 2. TEM-image of nanoparticles of the rutile sample 0.5B-TiO₂ (a); and anatase-rutile sample 1.0 B-TiO₂ (b).

Table 2.

Textural characteristics (specific surface area, pore volume).

Sample	S_{BET} (m^2g^{-1})	S_{micro} (m^2g^{-1})	S_{meso} (m^2g^{-1})	V_p (cm^3g^{-1})	V_{micro} (cm^3g^{-1})	V_{meso} (cm^3g^{-1})
a-TiO ₂	239.4	100.5	138.9	0.1519	0.054	0.098
0.5B-TiO ₂	151.6	81.73	69.87	0.1158	0.04175	0.07405
1.0B-TiO ₂	316.1	14.25	301.85	0.2918	0.00661	0.28519
1.5B-TiO ₂	254.1	-	254.1	0.3442	-	0.3442

Titanium surface groups attach the proton H^+ in an acidic environment (scheme 5), and in the alkaline medium, they give it away (Scheme 6). The surface of TiO_2 must contain a proton acceptor, which ensures the transition of the proton from the acid to the base, to reach ionic equilibrium in solution. Therefore, on the surface of the TiO_2 particles, there are both: the base $\equiv TiOH^{\delta-}$ and acid $\equiv TiOH^{\delta+}$ grouping. The establishing of the protolitic equilibrium of the TiO_2 surface can be written in the form of a scheme (7):



The constant of protolitic equilibrium K_n of the surface of TiO_2 is calculated according to the equation:

$$K_n = \frac{[\equiv TiO^{\delta-}][\equiv TiO^-]}{[\equiv TiOH_2^+][\equiv TiOH^{\delta-}]} \quad (8)$$

The values of the constants of acid groups $K_{\alpha 1}$ and the base groups $K_{\alpha 2}$ can be determined accordingly, from the following equations:

$$K_{\alpha 1} = [H^+] \frac{[\equiv TiO^-]}{[\equiv TiOH_2^+]} \quad (9)$$

$$K_{\alpha 2} = [H^+] \frac{[\equiv TiOH^{\delta-}]}{[\equiv TiOH^{\delta+}]} \quad (10)$$

The negative decimal logarithm of the value $K_{\alpha 1}$ ($-\lg K_{\alpha 1} = pK_{\alpha 1}$) characterizes the ion strength of Brønsted's acid centers $\equiv TiOH^{\delta+}$, and the negative decimal logarithm value $K_{\alpha 2}$ ($-\lg K_{\alpha 2} = pK_{\alpha 2}$) that of base centers of Brønsted $\equiv TiOH^{\delta-}$.

The acid-base model of the solid surface was proposed by S. Morrison [21]. According to his model for assessing acidity, pK_{α} is selected – a scale that is limited by the limit values of the dissociation constants of water molecules:

$$-1,76 < pK_{\alpha} < 15,76 \quad (11)$$

The area of the Brønsted centers includes OH^- groups of different acidic strengths, as well as water molecules with different stages of protonation, coordinating with the main and acid centers of Lewis following the pK value of water-acid (-1.76) and the pK of the water-base (15.76). The acid centers of Brønsted are to the left of the neutrality point ($pK_{\alpha} = 7.0$). Their acidity increases from right to left with a decrease in the donor capacity of the orbitals of the metal atom and the displacement of electron density from the atom H to the orbital of the atom O. The bases of Brønsted are situated to the right of the point of neutrality ($pK_{\alpha} = 7.0$). Their basicity increases with a decrease in the donor capacity of the metal atom. There is a shift in electron density from the metal atom to the orbital of the Oxygen atom, which enhances the connection of O-H in the hydroxyl group and increases the basicity of the Brønsted center ($pK_{\alpha} > 7.0$).

The ion strength of the acid and basic titanium groups, respectively, $pK_{\alpha 1}$ and $pK_{\alpha 2}$ of the TiO_2 surface, we calculated by hydrogen indicator – the pH of point of zero charges (pH_{pzc}) of the oxide material and the pH of its suspension. pH_{pzc} is a pH value in which a solid immersed

in an electrolyte has a zero electrical charge on the surface.

According to [21] the average value of the ionic strength of the adsorption centers of the surface $pK_{\alpha \text{ mean}}$ is calculated by the equation (12):

$$pK_{\alpha \text{ mean}} = \frac{1}{2} (K_{\alpha 1} + K_{\alpha 2}) \quad (12)$$

Moreover, the value $pK_{\alpha \text{ mean}}$ identicals the value of pH_{pzc} :

$$pK_{\alpha \text{ mean}} = pH_{pzc} \quad (13)$$

Taking into account the Henderson–Hasselbalch equation [13, 14, 21] (14):

$$\frac{[\equiv TiO^-]}{[\equiv TiOH_2^+]} = 10^{(pH - pH_{pzc})} \quad (14)$$

it is easy to conclude that the ionic force $pK_{\alpha 1}$ of acid centers can be calculated by the equation (15):

$$pK_{\alpha} = pH + |(pH - pH_{pzc})| \quad (15)$$

In the last two equations, pH is a hydrogen index of 1% suspension of oxide material.

The hydrogen indicator of electrolyte in which the surface of the adsorbent acquires a zero electrical charge (pH_{pzc}) is an important parameter since it indicates the areas of pH values within which the adsorbent behaves like cationic or anionic.

The data given in Table 3 show that the pH_{pzc} of the sample 0.5B- TiO_2 is 6.0 and exceeds the values pH_{pzc} of other samples. At the same time, as the number of Boron atoms increases in TiO_2 , the point of zero charges on the pH scale shifts towards an acidic environment.

Table 3.
Properties of bare a- TiO_2 and surface modified TiO_2 samples.

Sample Name	Analytical data			
	pH_{susp}	pH_{pzc}	$pK_{\alpha 1}$	$pK_{\alpha 2}$
a-TiO_2	4.4	5.35	3.4	10.6
0.5B-TiO_2	3.2	6.0	0.4	12.3
1.0B-TiO_2	3.1	3.2	3.0	9.4
1.5B-TiO_2	3.1	2.2	4.0	8.4

For samples 0.5B- TiO_2 , the ionic strength $pK_{\alpha 1}$ of the acid centers $\equiv TiOH^{\delta+}$ is 0.4 and significantly exceeds the ionic strength of these centers in the basic sample a- TiO_2 (3.4) and modified samples 1.0B- TiO_2 (3.0) and 1.5B- TiO_2 (4.0). At the same time, the ionic strength of the base centers $pK_{\alpha 2}$ of the 0.5B- TiO_2 - sample is equal to 12.3 and also exceeds the ionic strength of the base centers of other samples.

The analytical data given in Table 3 may indicate the expected high adsorption capability of the 0.5B- TiO_2 sample for the adsorption of the metal cations in an environment with a $pH > 6.0$. The same sample can effectively adsorb Cl^- , Br^- , I^- anions in an acidic environment with a pH of < 6.0 .

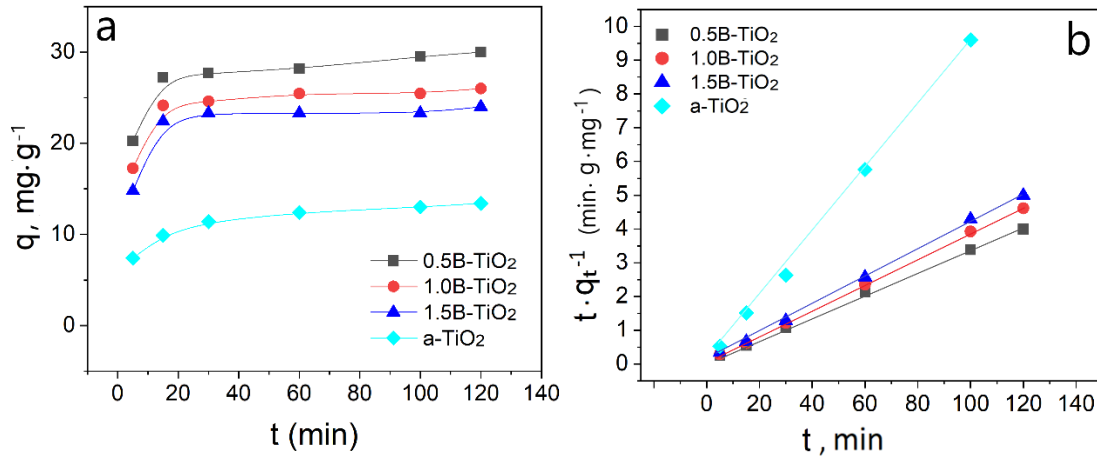


Fig. 4. Dependence of the value of adsorption of strontium ions on the duration of interaction (a); (b) application of the Lagergren model based on the pseudo-second-order equation.

Table 4.

Analytical equations of kinetic models.

Kinetic model	Linear equation
Diffusion	$q_t = K_1 t^{1/2} + K_0$
Elovich	$q_t = \frac{1}{\beta} \ln t + \frac{1}{\beta} \ln (\alpha \cdot \beta)$
Pseudo-first-order	$\text{Lg} (q_p - q_t) = \ln q_p - \frac{k_2}{2.303} t$
Pseudo-second-order	$\frac{t}{q_t} = \frac{1}{K_3 q_p^2} + \frac{t}{q_p}$

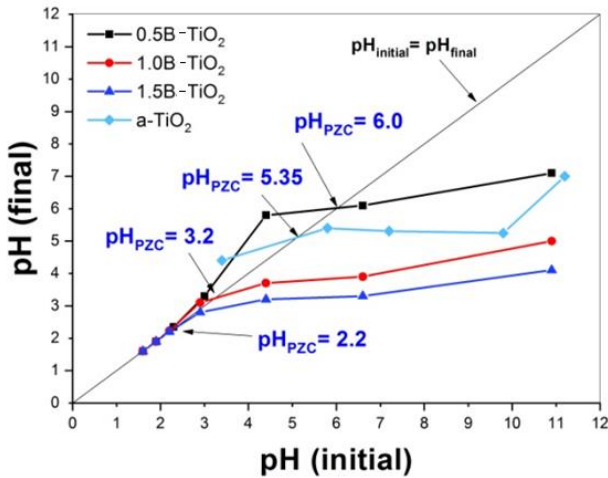


Fig. 3. "Drift" hydrogen suspension indicator during the determination of the pH_{PZC} of investigated TiO₂ samples.

2.3. Adsorption studies. Kinetics of Sr (II) ions adsorption

Kinetic dependences of Sr(II) adsorption from 0.005M solution of SrCl₂ by the investigated TiO₂ samples are shown in Fig. 4. They show that 75% of cations are adsorbed within 30 minutes of contact of the electrolyte with the adsorbent, but the equilibrium state in this process occurs only after 2-2.5 hours.

Four well-known kinetic models: a model of Weber-Morice, Elovich's, and Lagergren's model of pseudo-first and pseudo-second-order [13-16] (Table 4) were used to describe the adsorption of Sr (II) by investigating TiO₂.

In this equations: q_0 and q_t - adsorption capacity at equilibrium and at time t , respectively,

mg g⁻¹; K_1 (mg/g min^{0.5}), K_0 , k_2 (min⁻¹), k_3 (g·mg⁻¹ min⁻¹), α (mg/g min) – rate coefficients of pseudo - first order, pseudo-second order, intra-particle diffusion, and in Elovich kinetic models equations, respectively; β (mg/g)- desorption constant in Elovich equation [16].

The correspondence of the equation of the kinetic model of adsorption with experimental results was estimated by the correlation coefficient R^2 [16]. The results of the approximation of experimental dependences to the theoretical calculations are given in Table 5. They show that the most adequate kinetics of cation adsorption by Boron-doped TiO₂ is described by the Lagergren pseudo-second-order equation. The R^2 for equations is high and equal to 0.9997-0.9994.

2.4. Equilibrium adsorption of strontium ions by TiO₂ samples

Figure 5 (a-d) shows the isotherms of adsorption of cations Sr(II) by TiO₂ samples. They show that the adsorption capacity of modified adsorbents 0.5B-TiO₂; 1.0B-TiO₂ and 1.5B-TiO₂ are higher than the corresponding value for unmodified adsorbent a-TiO₂.

The single-phase rutile adsorbent 0.5B-TiO₂ shows the most effectivity among all Boron-doped samples.

The equations of the Sr (II) adsorption isotherms most reliably describe the adsorption process in the approximation of Langmuir's theory. This is indicated by the high values of the correlation coefficient R^2 (0.9953-0.9905) and the low values of the parameter χ^2 (1.899-12.02). The results are in good agreement with the calculations of kinetic models, according to which, the highest coefficients of linear approximation are obtained

for the pseudo-second-order equation (Table 5).

This significantly increases the reliability of calculations of the number of acid and base adsorption centers on the TiO₂ surface area of 10 nm². The number of acids and base adsorption centers on the TiO₂ surface area of the 10 nm² was calculated by the adsorption values of the Sr(II) cations in a neutral medium (with a pH = 7.0).

At the medium pH equal pH_{pzc} of the corresponding adsorbent, when surface charge equals zero, the number of acid centers is equal to the number of base ones. As the pH of the environment increases concerning the pH_{pzc}, the number of the base centers ≡TiOH^{δ-} is sharply decreasing, and the number of acid centers ≡TiOH^{δ+} remains unchanged. Conversely, with a decreasing the pH of the

Table 5.

Values of parameters and coefficients in equations of kinetic models applied to describe the adsorption of Sr (II) cations.

Equation parameter	0.5B-TiO ₂	1.0B-TiO ₂	1.5B-TiO ₂	a-TiO ₂
Pseudo-first-order				
K₂	-0.0111	-0.0108	-0.0086	0.0042
R²	0.8603	0.7006	0.4664	0.9312
Pseudo-second-order				
K₃	0.0329	0.0381	0.0414	0.0098
R²	0.9994	0.9997	0.9994	0.9968
Elovich				
α	205.2	155.2	60.1	0.271
β	0.376	0.4217	0.414	0.104
R²	0.8446	0.7759	0.7123	0.6442
Intra particle diffusion model				
K₁ step1	2.29	2.27	2.63	0.5588
K₀	16.21	13.24	10.02	8.01
R²	0.8041	0.8005	0.8338	0.9725
K₁ step2	0.394	0.218	0.0937	-
K₀	25.5	23.51	22.67	-
R²	0.9642	0.8581	0.4301	-

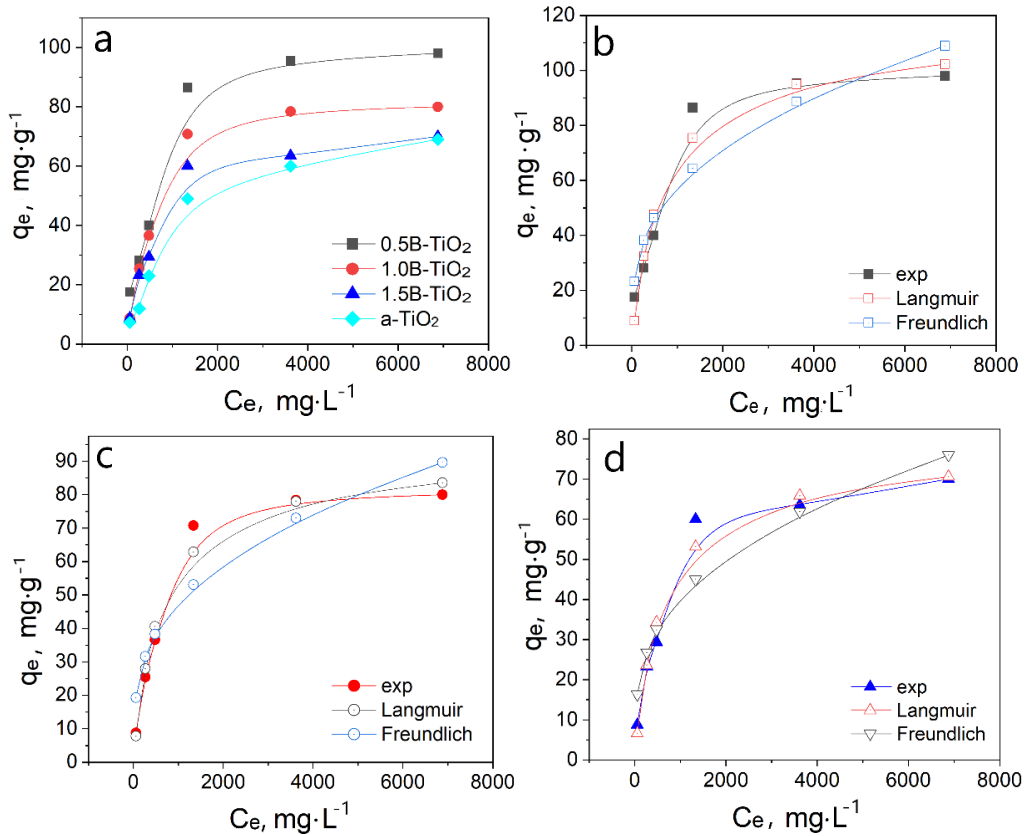


Fig.5. (a) Adsorption isotherms of Sr(II) by investigated samples of TiO₂. Nonlinear approximation of experimental equilibrium results by Langmuir and Freundlich adsorption theories for (b) 0.5B-TiO₂; (c) 1.0B-TiO₂; (d) 1.5B-TiO₂.

Table 6.

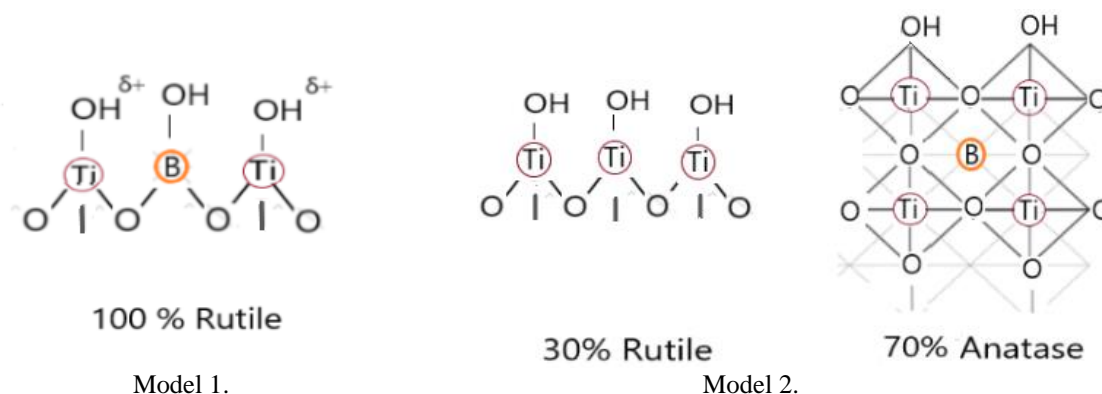
Parameters of Langmuir and Freundlich equations for adsorption of Sr(II) ions by Boron-doped TiO₂.

Adsorption theory	Parameters of equation	Adsorbent			
		0.5B-TiO ₂	1.0B-TiO ₂	1.5B-TiO ₂	a-TiO ₂
Langmuir	K _L	0.001549	0.00169	0.00169	0.00012
	A _{max}	111.92	90.77	76.68	151.66
	Q _{max} calc	102.3	83.58	70.6	68.84
	Q _{max} exp	98	80	70	70.8
	R ²	0.9905	0.9953	0.9944	0.9428
	χ ²	12.02	1.899	2.408	42.38
Freundlich	K _f	6.42	5.34	4.52	0.358
	n	0.32	0.319	0.319	0.5946
	Q _{max} calc	108.9	89.66	75.99	67.58
	Q _{max} exp	98	80	70	70.8
	R ²	0.9730	0.9724	0.9770	0.9574
	χ ²	14.11	14.32	9.74	21.26

Table 7.

The number of acid and base adsorption centers on the TiO₂ surface area of 10 nm².

Adsorbent	The number of adsorption centers on the surface area of 10 nm ²			Percentage of ≡TiOH ^{δ+} , %
	=O ₂ BOH	≡TiOH ^{δ+}	≡TiOH ^{δ-}	
a-TiO ₂	-	19.8	-	15.2
0.5B-TiO ₂	1.6	49.8	46.9	38.3
1.0B-TiO ₂	-	17.3	4.4	13.3
1.5B-TiO ₂	-	18.9	2.3	14.5

Fig. 6. Boron-containing grouping on the surface of particles of the rutile sample 0.5B-TiO₂ (Model 1), and the surface of anatase-rutile particles 1.0B-TiO₂ (Model 2).

environment concerning pH_{pzc} the number of acid centers $\equiv TiOH^{\delta+}$ decreases sharply, and the number of the base centers $\equiv TiOH^{\delta-}$ does not change. The data, which are given in Table 7, show, that the number of acid centers $\equiv TiOH^{\delta+}$ on the surface area of 10 nm² of the rutile sample 0.5B-TiO₂ is 49.8 units and it is the largest compared to other samples.

The number of base centers $\equiv TiOH^{\delta-}$ in this sample is equal to 46.9 units. It is smaller compared to the number of $\equiv TiOH^{\delta+}$. This is due to a greater hydrogen index of the medium compared to the pH_{pzc} of this sample. The number of acid centers of anatase-rutile samples 1.0B-TiO₂ and 1.5B-TiO₂ respectively are equal to 17.3 and 18.9 units on the surface area of 10 nm². The specified number of acid centers is close to the number of these centers in the bare a-TiO₂ sample.

Therefore, the higher adsorption capacity of the rutile sample 0.5B-TiO₂ toward Sr(II) cations than bare a-TiO₂ is due to its crystalline structure and the presence of incorporated Boron atoms in this structure.

Boron atoms in the rutile sample 0.5B-TiO₂ form a grouping =O₂BOH, which are impregnated in the surface layer of titanium dioxide particles. In these groups, atom B is surrounded by three oxygen atoms, two of which are involved in a chemical bond with Ti atoms. Since the electronegativity of atoms B is 2.0 and exceeds the electronegativity of Ti atoms (1.5), therefore, inductive redistribution of the electron density causes the formation of additional acid centers $\equiv TiOH^{\delta+}$ in the vicinity of the impregnated Boron-containing group (see Model 1).

In the IR spectrum of sample 0.5B-TiO₂ (Fig. 7, spectrum 2), fluctuations in groups of BO₃ are weak in

intensity in bands of 1400; 1110, and 974 cm^{-1} . The first two bands belong to the degenerate asymmetric oscillations of BO_3^- groupings, and the third band we attribute to the asymmetric deformation oscillation of B-OH [22, 23].

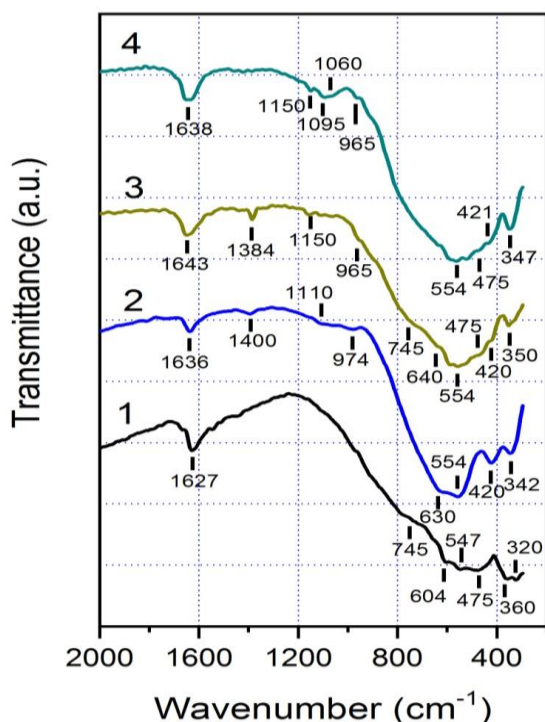


Fig. 7. IR spectra of the basic sample a-TiO₂ (1) and 0.5B-TiO₂ (2), 1.0B-TiO₂ (3), 1.5B-TiO₂ (4).

Titan borate monodentate molecules are creating Ti (OH)₃OB(OH)₂·2H₂O during the synthesis of the sample 0.5B-TiO₂ in the reaction mixture of titanium aqua complex precursor [Ti (OH)₂]₆³⁺·3Cl⁻ and borate acid B(OH)₃. These molecules in the polycondensation process act as a promoter for the formation of rutile, since the length of the Ti-O bond in them, is commensurate with the average length of Ti-O in the octahedra of TiO₆ rutile.

Molecules with a bidentate mononuclear structure Ti (OH)₂O₂BOH · 2H₂O occur, causing the formation of the anatase phase, due to the high chemical potential of the reaction mixture, in the process of synthesis of the samples 1.0B-TiO₂ and 1.5B-TiO₂. The distance of Ti-O in this molecule is commensurate with the average length of the Ti-O bond in the octahedra of the anatase phase. In addition to anatase, these samples contain respectively 30 and 43% percent of rutile. B atoms are in tetrahedral coordination related to Oxygen atoms in anatase TiO₂. The IR spectra of the anatase phase of the anion BO_4^- belong to bands 1150 and 965 cm^{-1} (Fig. 8, spectrums 3 and 4) [22-25].

Anions BO_4^- mainly localized in the volume of the anatase phase (model 2). Tetrahedral coordination of Boron atoms relate to Oxygen atoms reduces the induction effect of Boron atoms on the redistribution of electron density in B-O-Ti bridges and does not lead to the formation of additional acid adsorption centers on the surface of the oxide material.

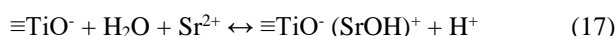
The number of acid centers $\equiv\text{TiOH}^{\delta+}$ on a surface area

of 10 nm^2 in samples 1.0B-TiO₂ and 1.5B-TiO₂ is 17.3 and 18.9 units, respectively (Table 7). This number of acid centers roughly corresponds to the number of centers of unmodified a-TiO₂. These data indicate the absence of Boron atoms in the structure of rutile of two-phase samples.

It should be noted, that the increase in the number of acid centers $\equiv\text{TiOH}^{\delta+}$ in the rutile sample 0.5B-TiO₂ is more than two times due to the impregnation of only 1.6 units of groups =O₂BOH on a surface area of 10 nm^2 . An increase in the number of acid centers on the surface of the investigated adsorbent can be ensured by preventing the formation of titanium-borate molecules with a bidentate structure during synthesis.

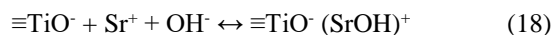
2.5. Mechanism of Sr (II) cations bonding

For adsorption of one Sr(II) cation, one or two adsorption centers may be involved in electrolyte environments with $\text{pH} > \text{pH}_{\text{pzc}}$ (16):



Adsorption of cations according to the scheme (16) is observed in an acidic and slightly acidic electrolyte medium ($\text{pH} = 2 \div 6$). The connection of cations is carried out according to the scheme (17) in a neutral electrolyte medium ($\text{pH} \sim 7$) [6-8, 13, 21].

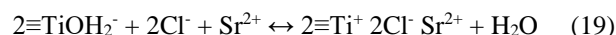
The presence of OH⁻ anions ensures the high efficiency of binding of Sr(II) cations in an alkaline environment ($\text{pH} \sim 8-12$):



Graphical dependences of adsorption of cations Sr(II) from the pH of the medium by investigated samples of TiO₂ are shown in Fig. 8. Fig.8 shows, that there is a tendency of differences in Sr (II) adsorption. In an alkaline environment with a pH of ~ 10-11 adsorption of cations Sr (II) increases, compared with adsorption in a slightly acidic environment, by 1.5-2.0 times.

Adsorption of cations should not be carried out in an environment with $\text{pH} < \text{pH}_{\text{pzc}}$. However, the adsorption value of the Sr(II) cations is 85 mg g^{-1} by the 0.5B-TiO₂, and is equal to the value of adsorption in an environment with a pH of ~ 6.0 is close to corresponding values which are obtained at a pH of ~ 2.0.

This anomaly can be explained by the fact that the adsorption of anions recharges the surface of the adsorbent. The negative charge of anions is not compensated by a completely positive charge of adsorption centers. Therefore, favorable conditions are created for the adsorption of Sr(II) cations. The binding of Sr(II) cations in an acidic environment from SrCl₂ solution occurs according to the scheme (19):



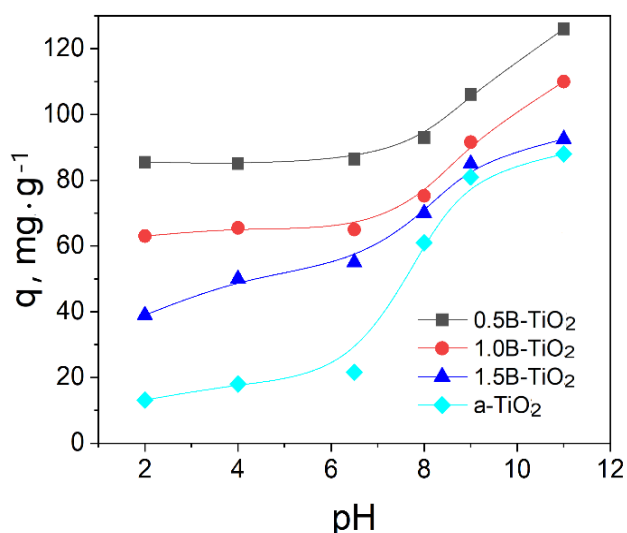


Fig. 8. Adsorption of Sr (II) cations by TiO₂ samples in the medium with different pH.

2.6. Regeneration of the adsorbents

The possibility of the adsorbent regeneration was performed according to the scheme of adsorption-desorption of Sr (II) cations- drying the adsorbent and repeated adsorption. Adsorption of cations was performed from a 0.01M solution of strontium chloride at pH = 8. Removal of adsorbed strontium cations was performed using 0.01M HNO₃ as eluent. Regenerated adsorbents were washed with distilled water, dried, weighed, and again used for adsorption of Sr(II) cations under the same conditions. The value of adsorption of Sr (II) cations remained unchanged, during the seven adsorption-desorption cycles.

In addition, the adsorption value after regeneration was $39.8 \div 7.2 \text{ mg g}^{-1}$ for adsorbent 0.5B-TiO₂ at a confidence level of 95%. The test results indicate the suitability of Boron-doped titanium dioxide in the acid medium and its ability for regeneration [26].

Conclusions

Synthesis of Boron-containing TiO₂ by liquid-phase sol-gel method using aqua complex precursor [Ti(OH)₂]₆³⁺·3Cl⁻ and borate acid H₃BO₃, as a modifying reagent, according to the corresponding ratio of components, leads to the formation of a single-phase rutile

titanium dioxide or a two-phase anatase-rutile oxide material.

In the rutile sample 0.5B-TiO₂, Boron atoms are combined with Oxygen atoms into the triangular structural cell of BO₃ and are localized in the surface layer of the nanoparticle material as a grouping =O₂BOH.

The impregnation of Boron atoms into the structure of the rutile adsorbent causes an increase in its adsorption capacity toward Sr(II) cations. The maximal adsorption of Sr(II) cations by the rutile adsorbent reaches 102.3 mg g⁻¹, compared to the bare a-TiO₂ – 68.8 mg g⁻¹ in a neutral electrolyte environment.

In particular, the number of acid adsorption centers ≡TiOH^{δ+} on the surface of the rutile adsorbent 0.5B-TiO₂ is ~ 50 units on a surface area of 10 nm², which is twice higher than the number of centers on the surface of the base anatase adsorbent a-TiO₂.

The ionic strength of the acid centers of the ≡TiOH^{δ+} pK_{a1} and the main centers of the ≡TiOH^{δ-} - pK_{a2} of the rutile sample is the highest in comparison with the centers of other investigated adsorbents and, accordingly, is equal to 0.6 and 12.3.

Two-phase adsorbents 1.0B-TiO₂ and 1.5B-TiO₂ contain, respectively, 70 and 57% of the anatase phase. They are significantly inferior in adsorption ability toward cations Sr(II) compared with the rutile adsorbent 0.5B-TiO₂. This is because Boron atoms are localized mainly in the anatase phase and form tetrahedral groups of BO₄⁻ with oxygen atoms.

Tetrahedral coordination of Boron atoms concerning Oxygen atoms in the structure of anatase reduces the induction effect of B atoms on the redistribution of electron density in B-O-Ti bridges and does not lead to the formation of additional acid adsorption centers on the surface of the anatase.

Mironyuk Ivan – Head of Department of Chemistry, Vasyl Stefanyk Precarpathian National University;

Mykytyn Igor – Associated professor, Department of Chemistry, Vasyl Stefanyk Precarpathian National University;

Vasylyeva Hanna – Associated professor, Department of Theoretical Physics, The Section of Nuclear Physics and Elementary particles, Uzhhorod National University;

Prokipchuk Iryna – Department of Chemistry, Vasyl Stefanyk Precarpathian National University, leading specialist of the educational laboratory of the Chemistry Department.

- [1] K. Kołacińska, Z. Samczyński, J. Dudek, A. Bojanowska-Czajka, M. Trojanowicz, *A comparison study on the use of Dowex 1 and TEVA-resin in determination of ⁹⁹Tc in environmental and nuclear coolant samples in a SIA system with ICP-MS detection*, Talanta, 184, 527 (2018); <https://www.doi.org/10.1016/j.talanta.2018.03.034>.
- [2] H. Tazoe, H. Obata, et al., *Determination of strontium-90 from the direct separation of yttrium-90 by solid-phase extraction using DGA Resin for seawater monitoring*, Talanta, 152, 219 (2016); <https://www.doi.org/10.1016/j.talanta.2016.01.065>.
- [3] H.V. Vasylyeva, et al., *Radiochemical studies of lanthanum micro-amounts in water solution*, Journal of Molecular Liquids, 1 (3), 41 (2005); <https://www.doi.org/10.1016/j.molliq.2004.07.008>.
- [4] H. Vasylyeva, I. Mironyuk, M. Strilchuk, et al., *Adsorption of zirconium ions by X-type zeolite*, Biointerface Research in Applied Chemistry, 11 (5), 13421, (2021); <http://dx.doi.org/10.33263/BRIAC115.1342113431>.

- [5] T. Tatarchuk, Mu. Naushad, J. Tomaszewska, P. Kosobucki, et al., *Adsorption of Sr (II) ions, and salicylic acid onto magnetic magnesium-zinc ferrites: isotherms and kinetic studies*, Environ Sci Pollut Res Int., 27 (21), 26681 (2020), <https://www.doi.org/10.1007/s11356-020-09043-1>.
- [6] I. Mironyuk, T. Tatarchuk, H. Vasylyeva, V. Gun'ko, I. Mykytyn, Effects of chemisorbed arsenate groups on the mesoporous titania morphology and enhanced adsorption properties towards Sr (II) cations, Journal of Molecular Liquids, 282, 587 (2019); <https://www.doi.org/10.1016/J.MOLLIQ.2019.03.026>.
- [7] I. Mironyuk, T. Tatarchuk, H. Vasylyeva, Mu. Naushad, I. Mykytyn, *Adsorption of Sr (II) cations onto phosphate mesoporous titanium dioxide: mechanism, isotherm, and kinetics studies*, Journal of Environmental Chemical Engineering 7 (6), 103430 (2019); <https://www.doi.org/10.1016/j.jece.2019.103430>.
- [8] I. Mironyuk, T. Tatarchuk, Mu. Naushad, H. Vasylyeva, I. Mykytyn, *Highly Efficient Adsorption Of Strontium Ions By Carbonated Mesoporous TiO₂*, Journal of Molecular Liquids, 285, 742 (2019); <https://www.doi.org/10.1016/j.molliq.2019.04.111>.
- [9] I. Mironyuk, I. Mykytyn, H. Vasylyeva, Kh. Savka, *Sodium-modified mesoporous TiO₂: sol-gel synthesis, characterization, and adsorption activity toward heavy metal cations*, Journal of Molecular Liquids, 316 (10), 113840 (2020); <https://www.doi.org/10.1016/j.molliq.2020.113840>.
- [10] I. Mironyuk, I. Mykytyn, H. Vasylyeva, *Structural and morphological properties of titanium dioxide nanoparticles doped by Boron atoms*, PCSS, 2022 (in production).
- [11] G.M. Sheldrick, *SHELXL-9, Program for the refinement of crystal structures*, Göttingen: Univ. Göttingen, Germany (1997).
- [12] Rodriguez-Carvajal. *FULLPROF: A program for Rietveld refinement and pattern matching analysis*, Abstracts of the satellite meeting on powder diffraction of the XV Congress of the IUCr, Toulouse, France. 127 (1990).
- [13] A.W. Adamson, *Physical chemistry of surfaces*, 3rd edition, Wiley-Interscience, New York, 698 (1976); <https://www.doi.org/10.1002/pol.1977.130151014>
- [14] W. Plazinski, W. Rudzinski, A. Plazinska, *Theoretical models of sorption kinetics including a surface reaction mechanism: a review*, Advances in Colloid and Interface Science, 152 (1-2), 2 (2009); <https://www.doi.org/10.1016/j.cis.2009.07.009>.
- [15] F.-Ch. Wu, R.-L. Tseng, R.-Sh. Juang, *Characteristics of the Elovich equation used for the analysis of adsorption kinetics in dye-chitosan systems*, Chemical Engineering Journal, 150 (2-3), 366 (2009); <https://www.doi.org/10.1016/j.cej.2009.01.014>.
- [16] H.N. Tran, S.-J. You, A. Hosseini-Bandegharai, H.-P. Chao, et al., *Mistakes and inconsistencies regarding adsorption of contaminants from aqueous solutions: a critical review*, Water Res. 120, 88 (2017); <https://www.doi.org/10.1016/j.watres.2017.04.014>.
- [17] D. Hestenes; J. Holt, *The Crystallographic Space Groups in Geometric Algebra*, Journal of Mathematical Physics, 48 (2), 023514. (January 2007); <https://www.doi.org/10.1063/1.2426416>.
- [18] Niu Pingping, Wu Guanghui, Chen Pinghua, et al., *Optimization of Boron Doped TiO₂ as an Efficient Visible Light-Driven Photocatalyst for Organic Dye Degradation With High Reusability*, Frontiers in Chemistry, 8 (2020); <https://www.frontiersin.org/article/10.3389/fchem.2020.00172>.
- [19] Esra Bilgin Simsek, *Solvothermal synthesized boron-doped TiO₂ catalysts: Photocatalytic degradation of endocrine-disrupting compounds and pharmaceuticals under visible light irradiation*, Applied Catalysis B: Environmental, 200, 309 (2017); <https://www.doi.org/10.1016/j.apcatb.2016.07.016>.
- [20] M. Bettinelli, V. Dallacasa, D. Falcomer, P. Fornasiero, V. Gombac, T. Montini, L. Romanò, A. Speghini, *Photocatalytic activity of TiO₂ doped with boron and vanadium*, Journal of Hazardous Materials, 146 (3), 529 (2007); <https://www.doi.org/10.1016/j.jhazmat.2007.04.053>.
- [21] N. Henry, N.M. Senozan. *Henderson–Hasselbalch Equation: Its History and Limitation*, J. Chem. Educ, 78 (11), 1499 (2001), <https://www.doi.org/10.1021/ed078p1499>.
- [22] T. Posch, F. Kerschbaum, D. Fabian, et al, *Infrared properties of solid titanium oxides: exploring potential primary dust condensates*, Astrophys. J. Suppl. Ser., 149, 437 (2003).
- [23] M. Ocaña, V. Fornés, J.V. García Ramos, C.J. Serna, *Factors affecting the infrared and Raman spectra of rutile powders*, Journal of Solid State Chemistry, 75 (2), 364 (1988).
- [24] G.-W. Peng, S.-K. Chen, H.-S. Liu, *Infrared Absorption Spectra and Their Correlation with the Ti-O Bond Length Variations for TiO₂(Rutile), Na-Titanates, and Na-Titanosilicate (Natisite, Na₂TiOSiO₄)*, Appl. Spectrosc., 49, 1646 (1995).
- [25] L.I. Myronyuk, I.F. Myronyuk, V.L. Chelyadyn, V.M. Sachko, M.A. Nazarkovsky, R. Leboda, J. Skubiszewska-Zie, V.M. Gun'ko, *Structural and morphological features of crystalline nano titania synthesized in different aqueous media*, Chemical Physics Letters 583, 103, (2013).
- [26] S. Hamzah, S. Z. Ramli, N.A. Mohammad, et al., *Acid - treated activated carbon for phenolic compound removal in acid pretreatment of lignocellulosic biomass for biogas production*, Biointerface Research in Applied Chemistry, 10, 5466 (2020), <https://www.doi.org/10.33263/briac103.466471>.

Іван Миронюк¹, Ганна Васильєва², Ірина Прокіпчук¹, Ігор Микитин¹

Адсорбція катіонів Sr(II) діоксидом титану, допованим атомами Бору

¹Кафедра хімії, Прикарпатський національний університет ім. В. Стефаника, Івано-Франківськ, Україна, myrif555@gmail.com

²Кафедра теоретичної фізики, Відділення фізики ядра і елементарних частинок, Ужгородський національний університет, Ужгород, Україна, h.v.vasylyeva@hotmail.com

Досліджувалась адсорбція катіонів Sr(II) борвмісними зразками TiO₂, одержаними рідкофазним золь-гель методом з використанням аквакомплексного прекурсора [Ti(OH₂)₆]³⁺ 3Cl⁻ і модифікуючого реагента боратної кислоти H₃BO₃. З'ясовано, що за відповідних співвідношень компонентів утворюється однофазний рутильний діоксид титану або двофазний анатаз-рутильний оксидний матеріал. В рутильному дослідному зразку 0.5B-TiO₂ атоми Бору поєднуються з атомами Оксигену в трикутні структурні мотиви BO₃ і локалізуються у поверхневому шарі наночастинкового матеріалу як групування = O₂ВОH. Інкorporація атомів Бору у структуру рутильного адсорбенту спричинює зростання його адсорбційної спроможності щодо зв'язування катіонів Sr(II) у водному електролітному середовищі. Максимальна адсорбція катіонів Sr(II) в нейтральному електролітному середовищі рутильного адсорбента сягає 102.3 мг·г⁻¹, у той час, як для немодифікованого анатазного адсорбента а-TiO₂ вона рівна 68.8 мг·г⁻¹.

Чисельність кислотних адсорбційних центрів ≡TiOH^{δ+} на поверхні рутильного адсорбента 0.5B-TiO₂ становить ~ 50 одиниць на ділянці поверхні площею 10 нм², що в два рази перевищує чисельність центрів на поверхні базового анатазного адсорбента а-TiO₂. Йонна сила кислотних центрів ≡TiOH^{δ+} рK_{a1} та основних центрів ≡TiOH^{δ-} рK_{a2} рутильного зразка є найбільшою в порівнянні з центрами інших досліджуваних адсорбентів і, відповідно, рівна 0.6 та 12.3.

Анатаз-рутильні адсорбенти 1.0B-TiO₂ та 1.5B-TiO₂ містять відповідно 70 та 57 мас.% анатазної фази. Вони суттєво поступаються за адсорбційною спроможністю зв'язувати катіони Sr(II) рутильному адсорбенту 0.5B-TiO₂. Це зумовлено тим, що атоми Бору в основному локалізуються в анатазній фазі і з атомами Оксигену утворюють тетраедричні групування BO₄. Тетраедрична координація атомів Бору по відношенню до атомів Оксигену в структурі анатазу знижує індукційний вплив атомів Бору на перерозподіл електронної густини в містках В-О-Тi і не приводить до утворення додаткових кислотних адсорбційних центрів на поверхні анатазу.

Ключові слова: Діоксид титану, Бор, Адсорбція, Стронцій.

O. P. Malyk

Transport phenomena in CdTe:Cl and CdTe:Cu - calculation from the first principles

*Semiconductor Electronics Department, Lviv Polytechnic National University, Lviv, 79013, S. Bandera Str., 12, Ukraine.
omalyk@ukr.net*

In the presented article the method of determining the energy spectrum, the wave function of the charge carrier and the crystal potential in CdTe at an arbitrarily given temperature is considered. Using this approach within the framework of the supercell method the temperature dependences of the ionization energies of various types of defects caused by the introduction of chlorine and copper impurities in cadmium telluride are calculated. Also the offered method allows to define the temperature dependence of the optical and acoustic deformation potentials and as well as the dependence on the temperature the charge carrier's scattering parameters on ionized impurities, polar optical, piezooptic and piezoacoustic phonons. Within the framework of short-range scattering models the temperature dependences of the charge carrier's mobility and Hall factor are considered.

Keywords: Transport phenomena, Crystal defects, CdTe, Ab initio calculation.

Received 04 November 2022; Accepted 14 February 2023.

Introduction

Cadmium telluride possesses unique physical properties necessary for photovoltaic converters of solar energy, namely, a required band gap width and needed absorption coefficient value. The structure of intrinsic and impurity defects predominantly determines the electrical and optical properties of this material. Therefore, the study of the defects structure of CdTe is an actual applied problem. In literature there is a wide range of works where the ab initio approach is used to calculate the structure of defects in cadmium telluride [1-7]. However, these works do not specify the way to establish the relationship between the structure of point defects and the kinetic properties of CdTe, which directly determine the electrical properties of the material. In the current work, this problem will be solved in two stages.

At the first stage on the basis of density functional theory (DFT) the calculation from the first principles of energy characteristics of a semiconductor is carried out: energy spectrum, electron (or heavy hole) wave function and potential energy in a crystal lattice. Usually it is assumed that the above characteristics describe the state of

the crystal at $T = 0$ K. In the current article, a method for calculating these characteristics of a sphalerite semiconductor at a predetermined temperature will be proposed. Based on this method the charge carrier (electrons and heavy holes) scattering parameters on different point defects of the crystal will be calculated at a given temperature. At the second stage, the ionization energies of various types of defects caused by the introduction of chlorine and copper impurities into cadmium telluride are determined by the supercell method. Knowing these ionization energies and charge carrier scattering parameters it is possible to calculate the Fermi level and, in turn, the kinetic coefficients of CdTe. It should be noticed that there are a series of works in literature devoting to transport phenomena in semiconductors, in particular in CdTe [8], which are based on ab initio calculations [9-13]. However, in these works the connection between defect structure and kinetic properties is not specified.

I. Calculation of temperature dependences of wave function and crystal potential

When considering the transport phenomena in cadmium telluride, the charge carrier short-range scattering models were used [8, 14-16]. These short-range scattering models include several scattering constants as parameters, which, in turn, require the calculation of the conduction and valence band wave function and the self-

consistent crystal potential. To calculate these above-mentioned constants the method of calculating the electron energy spectrum and the crystal potential, presented in [17,18], was used. This allowed to separate the physical solutions of the Schrödinger equation from the set of mathematical solutions of the Schrödinger equation using the following criterion for selecting physical solutions of the Schrödinger equation, namely: at a given temperature, the theoretical width of the band gap must coincide with its experimental value, which was determined from the experimental expression for solid solution $\text{Hg}_{1-x}\text{Cd}_x\text{Te}$ [19]:

$$E_g(x, T) = -0.302 + 1.93x - 0.81x^2 + 0.832x^3 + 5.35 \times 10^{-4}T(1 - 2x) \quad (1)$$

Using this approach, the following values of the factor α (this parameter defines the mixture of the conventional GGA exchange correlation potentials for Cd and Te, pseudopotentials [20, 21], and the Hartree Fock exchange potential [22]) were obtained for the ideal unit cell (sphalerite structure) of cadmium telluride: $\alpha = 0.397$ corresponds to $T = 0$ K, $\alpha = 0.288$ corresponds to $T = 300$ K. Herewith, the electron wave functions in the conduction and valence band and the crystal potential at temperatures of 0 K and 300 K were obtained.

Accordingly, the following scattering constants for electrons and heavy holes were determined, namely:

1) Scattering constants for charge carrier-polar optical (PO) phonon interaction, charge carrier-piezoacoustic (PAC) phonon and charge carrier-piezo-optic (POP) phonon interaction

$$A_{PO} = A_{PAC} = A_{POP} = \int \psi^*(R^2 - r^2)\psi \, dr \quad (2)$$

2) d_0 is the optical deformation potential constant which choose equal to the maximum value among three optical deformation potential constants corresponding to one longitudinal and two transverse branches of the lattice optical vibrations:

$$d_{0v} = a_0 \int \psi^* \varepsilon_v \cdot V \psi \, dr, \quad v = 1, 2, 3; \quad (3)$$

where the region of integration is the same as in the case of PO scattering; ε_v – unitary contravariant polarization vector of the optical oscillations; vector V is expressed in terms of the derivatives of the self-consistent electron potential energy over the coordinates of the atoms of the unit cell [15].

3) E_{AC} is the acoustic deformation potential constant which was choose equal to the maximum value among three acoustic deformation potential constants corresponding to one longitudinal and two transverse branches of the lattice acoustic vibrations:

$$\begin{aligned} E_{AC\parallel} &= -(-I_1/4 + I_2/2 + I_3/2); \\ E_{AC1\perp} &= -(-I_1/4 + I_2/4 + I_3/2); \\ E_{AC2\perp} &= -(-I_1/2 + I_2/2 + I_3/4); \end{aligned} \quad (4)$$

where $I_1 = \int \psi^* V'_1 \psi \, dr'$; $I_2 = \int \psi^* V'_2 \psi \, dr'$; $I_3 = \int \psi^* V'_3 \psi \, dr'$; V'_1 ; V'_2 ; V'_3 ; are the projections of the vector V in an oblique coordinate system created by the primitive vectors of the zinc blende structure;

4) The ionized impurity scattering constant:

$$A_{II} = \int_{\Omega} \psi^* \frac{1}{r} \psi \, dr \quad (5)$$

It should be noticed that in (2)-(5) integration is carried out according to the method proposed in [17].

Formulas (2) - (5) show that the above mentioned scattering constants are expressed in terms of the integrals over the wave function Ψ and crystal potential U . Calculation of these integrals was made on the base of three-dimensional B-spline interpolation and finite displacement method [23]. The dependence of Ψ and U on temperature causes the temperature dependence of scattering constants. Assuming the simplest, linear, temperature dependence, one can calculate the temperature dependences of the scattering constants for heavy holes and electrons:

$$A_{POhh} = (12.2 + 1.84 \times 10^{-3}T) \times 10^{-20} m^2, \quad A_{POe} = (12.24 + 2.088 \times 10^{-4}T) \times 10^{-20} m^2, \quad (6a)$$

$$d_{0hh} = -43.1 - 0.018T \, eV, \quad d_{0e} = -20.93 - 4.053 \times 10^{-3}T \, eV \quad (6b)$$

$$E_{AChh} = -3.07 - 2.28 \times 10^{-3}T \, eV, \quad E_{ACe} = -2.423 - 4.628 \times 10^{-4}T \, eV \quad (6c)$$

$$A_{IIhh} = (0.442 - 8.90 \times 10^{-6}T) \times 10^{10} m^{-1}, \quad A_{IIe} = (0.4794 - 7.405 \times 10^{-6}T) \times 10^{10} m^{-1} \quad (6d)$$

Using these relations, one can calculate the temperature dependences of electron transition probabilities and in turn the kinetic coefficients of

cadmium telluride.

Note that the temperature dependence of the heavy hole effective mass, which was determined in [17], was

used to calculate the mobility of heavy holes. This temperature dependence has a form:

$$m_{hh} = (0.214 + 9.902 \times 10^{-5}T)m_0 \quad (7)$$

It is possible to note the qualitative similarity of expression (7) to analogous expression for $Cd_xHg_{1-x}Te$ ($x \sim 0.2$), obtained by fitting to experimental data [24].

II. Determination of temperature dependences of ionization energy of different types of impurity defects

The proposed study considers the acceptor defects caused by the introduction of copper impurity were investigated, namely: Cu_{Cd} , $V_{Te} - Cu_{Cd}$, $Cu_{Cd} - Te_{Cd}$, $Cu_{Cd} - V_{Cd}$. The study of the energy spectrum of the defects structure of cadmium telluride was carried out within the framework the supercell method on the basis of the ABINIT code: Cu_{Cd} – supercell Cd_7Te_8Cu ($1 \times 1 \times 2$ sphalerite cubic structure); $V_{Te} - Cu_{Cd}$ – supercell Cd_7Te_7Cu ($1 \times 1 \times 2$ sphalerite cubic structure); $Cu_{Cd} - Te_{Cd}$ – supercell $Cd_{14}Te_{17}Cu$ ($2 \times 1 \times 2$ sphalerite cubic structure); $Cu_{Cd} - V_{Cd}$ – supercell $Cd_{14}Te_{16}Cu$ ($2 \times 1 \times 2$ sphalerite

cubic structure). Next donor defects caused by the introduction of chlorine impurity were considered, namely: Cl_{Te} , $Cl_{Te} - Cd_{Te}$. The energy spectrum of these defect structures was calculated using the supercell method ($1 \times 1 \times 2$ sphalerite cubic structure) based on the ABINIT code: for Cl_{Te} – supercell Cd_8ClTe_7 ; $Cl_{Te} - Cd_{Te}$ – supercell Cd_9ClTe_6 . Analogous calculations were performed for the ideal supercell Cd_8Te_8 ($1 \times 1 \times 2$ sphalerite cubic structure) and $Cd_{16}Te_{16}$ ($2 \times 1 \times 2$ sphalerite cubic structure). At the same time, the following values of the α parameter were obtained for the ideal supercells: Cd_8Te_8 – $\alpha = 0.09$ corresponds to $T=0$ K, $\alpha = 0.0182$ corresponds to $T = 300$ K; $Cd_{16}Te_{16}$ – $\alpha = 0.076$ corresponds to $T=0$ K, $\alpha = 0.00571$ corresponds to $T=300$ K The calculated energy spectra of the above-indicated supercells are presented in Table I.

The next stage of the calculations consists in establishing the temperature dependence of the ionization energy of various types of defects. For this purpose, the method presented in [17] was used. After that, assuming a linear relationship, we obtain the temperature dependences of the defect ionization energy:

$$Cu_{Cd}: \Delta E_A = 1.405 - 5.567 \times 10^{-4} T, \quad (8a)$$

$$V_{Te} - Cu_{Cd}: \Delta E_A = 1.476 - 3.533 \times 10^{-4} T, \quad (8b)$$

Table 1.

Energy spectrum of ideal and defect supercell.

1×1×2 sphalerite cubic structure					
T=0, $E_g=1.65$ eV, exchmix=0.09			T=300 K, $E_g=1.48$ eV, exchmix=0.0182		
Energy levels of ideal Cd_8Te_8 , eV	Energy levels of defect, eV	Ionization energy, eV	Energy levels of ideal Cd_8Te_8 , eV	Energy levels of defect, eV	Ionization energy, eV
E_c - 1×(4.194) (0) E_v - 2× (2.541) (2)*	Cu_{Cd} 1×(3.946) (0) 1×(2.344) (1) 1×(2.344) (2)	At T=0 p- type. At T ≥ 0 $\Delta E_A=1.405$	E_c - 1× (4.108) (0) E_v - 2× (2.620) (2)	Cu_{Cd} 1×(3.858) (0) 1×(2.463) (1) 1×(2.463) (2)	$\Delta E_A = 1.238$
E_c - 1×(4.194) (0) E_v - 2×(2.541) (2)	$V_{Te} - Cu_{Cd}$ 1×(4.017) (0) 1×(2.226) (1) 1×(1.910) (2)	At T=0 p- type. At T ≥ 0 $\Delta E_A=1.476$	E_c - 1×(4.108) (0) E_v - 2× (2.620) (2)	$V_{Te} - Cu_{Cd}$ 1×(3.990) (0) 1×(2.214) (1) 1×(2.054) (2)	$\Delta E_A = 1.370$
E_c - 1×(4.194) (0) E_v - 2×(2.541) (2)	Cl_{Te} 1×(5.073) (0) 1×(3.637) (1) 2×(2.394) (2)	$\Delta E_D=0.557$	E_c - 1×(4.108) (0) E_v - 2×(2.620) (2)	Cl_{Te} 1×(5.070) (0) 1×(3.569) (1) 2×(2.459) (2)	$\Delta E_D = 0.539$
E_c -1×(4.194) (0) E_v -2×(2.541) (2)	$Cl_{Te}-Cd_{Te}$ 1×(4.219) (0) 1×(4.177) (1) 1×(4.177) (2)	$\Delta E_D=0.017$	E_c - 1×(4.108) (0) E_v - 2×(2.620) (2)	$Cl_{Te}-Cd_{Te}$ 1×(4.211) (0) 1×(4.148) (1) 1×(4.148) (2)	$\Delta E_D =-0.040$
2×1×2 sphalerite cubic structure					
T=0, $E_g=1.65$ eV, exchmix=0.076			T=300 K, $E_g=1.48$ eV, exchmix=0.00571		
Energy levels of ideal $Cd_{16}Te_{16}$, eV	Energy levels of defect, eV	Ionization energy, eV	Energy levels of ideal $Cd_{16}Te_{16}$, eV	Energy levels of defect, eV	Ionization energy, eV
E_c -1×(4.130) (0) E_v -2× (2.478) (2)	$Cu_{Cd} - V_{Cd}$ 1× (2.967) (0) 1× (2.360) (1) 1× (1.752) (2)	At T=0 p- type. At T ≥ 0 $\Delta E_A = 0.489$	E_c -1×(4.046) (0) E_v -2×(2.558) (2)	$Cu_{Cd} - V_{Cd}$ 1× (2.881) (0) 1× (2.323) (1) 1× (1.722) (2)	$\Delta E_A = 0.323$
E_c -1×(4.130) (0) E_v -2× (2.478) (2)	$Cu_{Cd} - Te_{Cd}$ 1× (3.085) (0) 1× (3.077) (0) 1× (1.845) (2)	$\Delta E_A = 0.599$	E_c -1×(4.046) (0) E_v -2×(2.558) (2)	$Cu_{Cd} - Te_{Cd}$ 1× (3.012) (0) 1× (3.005) (0) 1× (1.855) (2)	$\Delta E_A = 0.447$

*Recording 2×(2.541) (2) means that there is exist 2-fold degenerate energy level with an occupation number equal 2.

$$Cu_{Cd} - Te_{Cd}: \Delta E_A = 0.599 - 5.067 \times 10^{-4} T, \quad (8c)$$

$$Cu_{Cd} - V_{Cd}: \Delta E_A = 0.489 - 5.533 \times 10^{-4} T, \quad (8d)$$

$$Cl_{Te}: \Delta E_D = 0.557 - 6 \times 10^{-5} T, \quad (8e)$$

$$Cl_{Te} - Cd_{Te}: \Delta E_D = 0.017 - 1.9 \times 10^{-4} T, \quad (8f)$$

It should be noted that only for one type of defects studied, the discrete level of the defect merges with the conduction band, namely: $Cl_{Te} - Cd_{Te}$ at $T = 89$ K. For other types of defects, with the temperature increasing, there is only a decrease in ionization energy without merging with the conduction band.

III. Discussion

Only defects with the lowest ionization energy were taken into account in the calculations of transport properties, as they make the dominant contribution to the transport phenomena. As can be seen from the equations (8a) - (8f) that for copper-doped CdTe such a defect is $Cu_{Cd} - V_{Cd}$, while for chlorine-doped CdTe, it is a defect complex $Cl_{Te} - Cd_{Te}$.

Comparison of theoretical temperature dependences

of heavy holes mobility was made with experimental data presented in [25]. Cadmium telluride parameters used for calculation are presented elsewhere [17]. Therefore, for copper-doped cadmium telluride the Fermi level is determined by the electroneutrality equation, which has the form:

$$p - n = N_A / \{1 + 2 \exp[(E_A - F)/(k_B T)]\}, \quad (9)$$

where N_A – copper impurity concentration and the defect level E_A at a given temperature is choose according to (8d).

The calculation of the temperature dependences of the heavy hole mobility was performed on the basis of short-range scattering models [14,15,17] within the framework of the exact solution of the Boltzmann's kinetic equation [26].

The temperature dependences of the heavy holes mobility in cadmium telluride crystals with a copper impurity concentration of $1 \times 10^{14} \div 1 \times 10^{18} \text{ cm}^{-3}$ were calculated. The results of the calculation are presented in Fig.1. For each value of the concentration of copper atoms N_A , such values of the concentration of the static strain centers N_{SS} were chosen, which would allow to cover all possible values of the heavy holes mobility at low

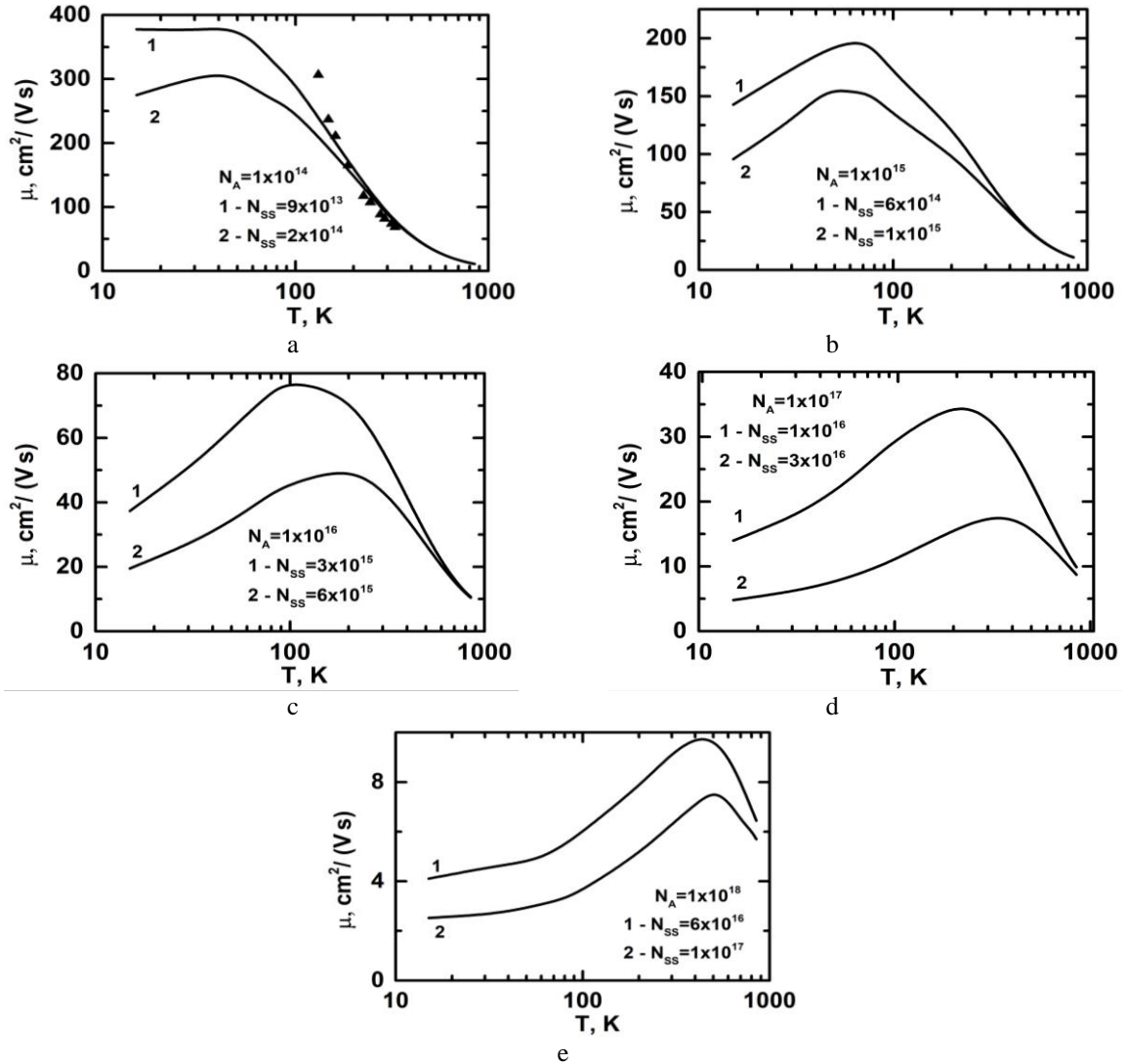


Fig. 1. – The temperature dependences of heavy hole mobility in cadmium telluride crystals with different defect concentration. a – $N_A = 1 \times 10^{14} \text{ cm}^{-3}$; b – $N_A = 1 \times 10^{15} \text{ cm}^{-3}$; c – $N_A = 1 \times 10^{16} \text{ cm}^{-3}$; d – $N_A = 1 \times 10^{17} \text{ cm}^{-3}$; e – $N_A = 1 \times 10^{18} \text{ cm}^{-3}$.

temperatures. Comparison of theoretical curves with experimental data was performed only for the concentration of acceptor defects $1 \times 10^{14} \text{ cm}^{-3}$ (see Fig. 1a). It can be seen that the theoretical curve agrees well enough with the experimental data. Unfortunately, there are no experimental data in the literature for other values of copper impurity concentrations.

For heavy holes, the theoretical curves obtained by two competing approaches were compared: short-range scattering models and long-range scattering models. The results of the calculation are presented in Fig. 2. The dashed lines 1 and 2 represent the results of the calculation of the dependence $\mu(T)$ obtained in the relaxation time approximation using long-range scattering models: curve 2 describes the high-temperature region ($\hbar\omega \ll k_B T$, ω – optical oscillation frequency), curve 1 describes the low-temperature region ($\hbar\omega \gg k_B T$). Regarding curves 1 and 2, the following remark should be made. For cadmium telluride the Debye temperature is $\theta_D = 239 \text{ K}$. Therefore, according to the above inequalities,

the low-temperature region will be determined by the condition $T < 24 \text{ K}$, and the high-temperature region will be determined by the condition $T > 2400 \text{ K}$. As can be seen from Fig. 2(a), the experimental points fall into the region where $T \sim \theta_D$, i.e., where the application of the relaxation time approximation (elastic scattering) is incorrect. On the other hand, the heavy hole short-range scattering models allow to describe inelastic scattering, so their application in this temperature range is correct. In addition, curve 3 differs significantly qualitatively and quantitatively from curves 1 and 2. Given the coincidence of curve 3 with the experiment, it can be argued that the short-range scattering models give a more adequate description of physical reality than long-range models.

Calculated on the basis of the proposed method the dependences of heavy hole's Hall factor on temperature are presented in Fig. 3. It is seen that these dependencies have minimums, which are situated as follows - the higher the concentration of copper impurities, the higher the temperature of minimum.

Theoretical calculations were compared with

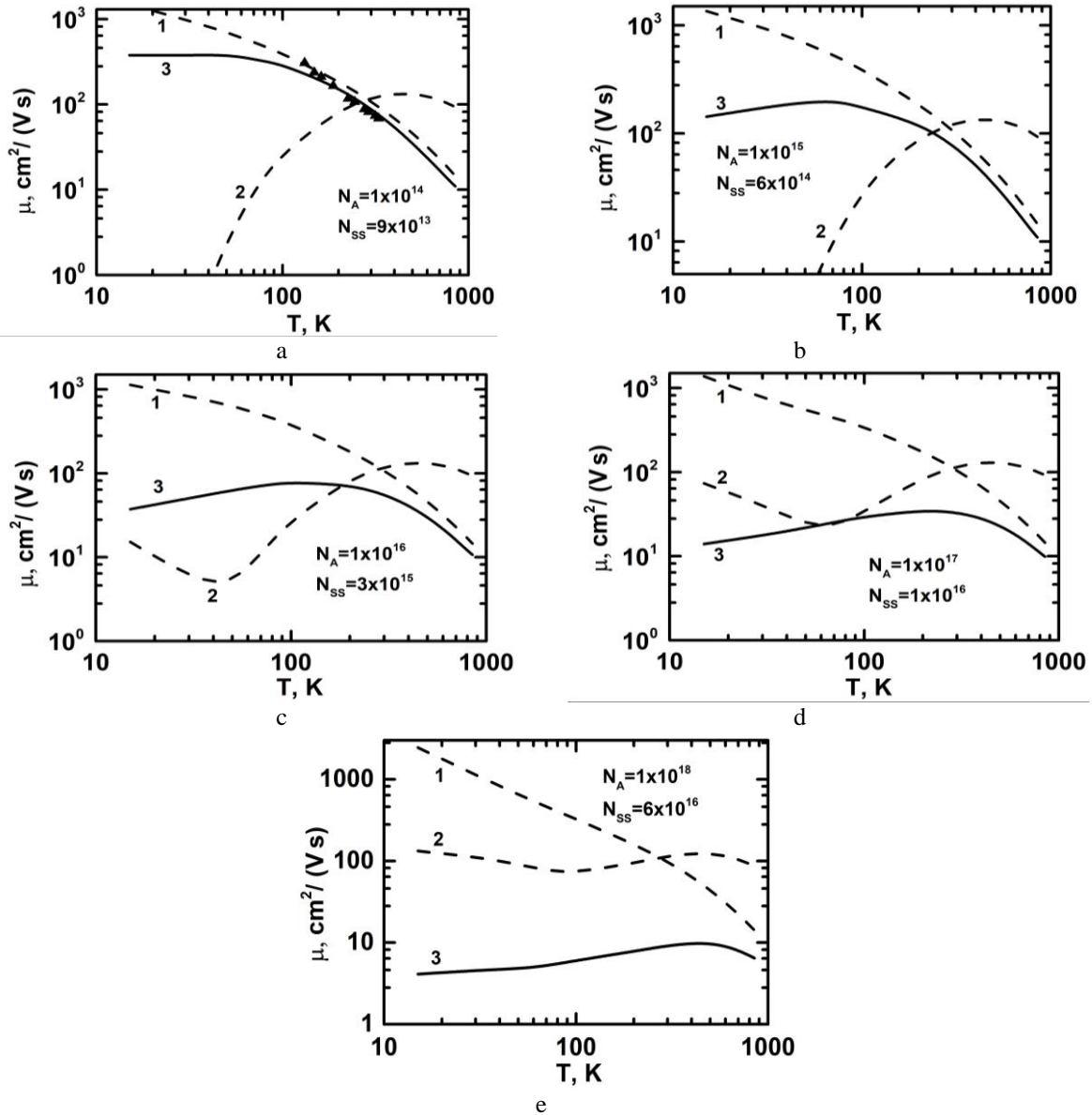


Fig. 2. – Dependencies $\mu(T)$ corresponding to different theoretical approaches. 1, 2 – long-range scattering models (relaxation time approximation); 3– short-range scattering models.

experimental data for chlorine-doped CdTe [27]. As can be seen from (8e)-(8f), the defect with minimum ionization energy is a defect complex $\text{Cl}_{\text{Te}} - \text{Cd}_{\text{Te}}$. Given

$$n - p = N_D / \left[1 + 2 \exp\left(\frac{F - F_D}{k_B T}\right) \right] \text{ - before the merger of the defect level;} \quad (9a)$$

$$n - p = N_D \text{ - after the merger of the defect level,} \quad (9b)$$

where N_D is the chlorine concentration and the defect level E_D at a given temperature is selected according to (8f).

Similar to the case of heavy holes the temperature dependences of the electron mobility were calculated on the basis of short-range scattering models [14,15,17] within the framework of the exact solution of the Boltzmann kinetic equation [26].

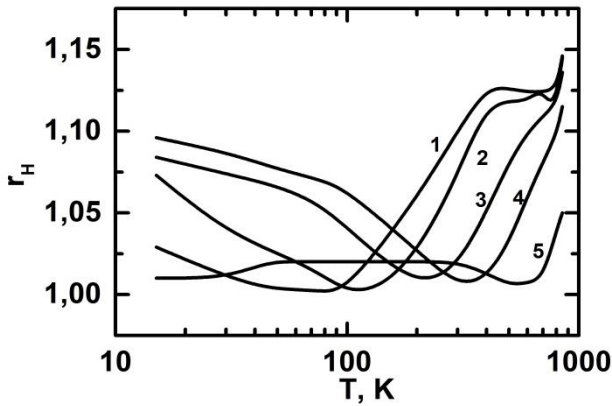


Fig.3. – Heavy hole Hall factor versus temperature in cadmium telluride crystals with different copper concentration. 1 – $N_A=1 \times 10^{14} \text{ cm}^{-3}$; 2 – $N_A=1 \times 10^{15} \text{ cm}^{-3}$; 3 – $N_A=1 \times 10^{16} \text{ cm}^{-3}$; 4 – $N_A=1 \times 10^{17} \text{ cm}^{-3}$; 5 – $N_A=1 \times 10^{18} \text{ cm}^{-3}$.

For chlorine doped samples, theoretical temperature dependences of electron mobility were calculated for the following defect concentrations (see Fig.4):

- sample A – $N_D=5 \times 10^{14} \text{ cm}^{-3}$, $N_{SS}=1.2 \times 10^{15} \text{ cm}^{-3}$;
- sample B – $N_D=5 \times 10^{15} \text{ cm}^{-3}$, $N_{SS}=6 \times 10^{15} \text{ cm}^{-3}$;
- sample C – $N_D=5 \times 10^{16} \text{ cm}^{-3}$, $N_{SS}=8 \times 10^{16} \text{ cm}^{-3}$;
- sample D – $N_D=5 \times 10^{17} \text{ cm}^{-3}$, $N_{SS}=1.8 \times 10^{17} \text{ cm}^{-3}$.

As it is seen, the theoretical curves C and D agree quite well with experimental data at high temperature and high defect concentration. Unfortunately, there are no experimental data in the literature for this type of samples at low defect concentrations.

The abovementioned method of calculation allows the temperature dependence of the electron's Hall factor for chlorine doped samples to be obtained (see Fig. 5). These dependences have minimums that correspond to the temperature at which the transition from the SS-scattering mechanism to the PO-scattering mechanism occurs. From Fig.5 it is seen that the higher the concentration of defects, the higher the transition temperature.

the merger of this defect level with the conduction band, an electroneutrality equation for the Fermi level can be written in the form:

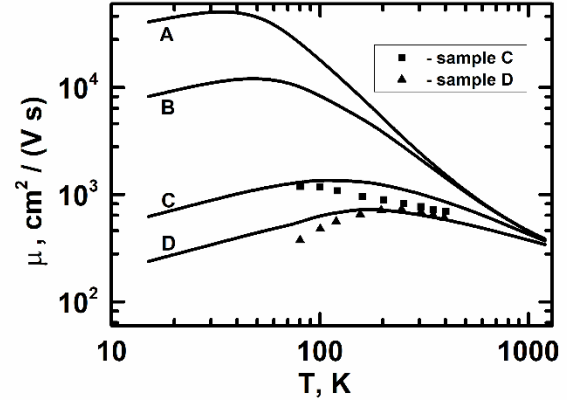


Fig.4. – The temperature dependences of electron mobility in chlorine-doped CdTe. Experimental data – [27].

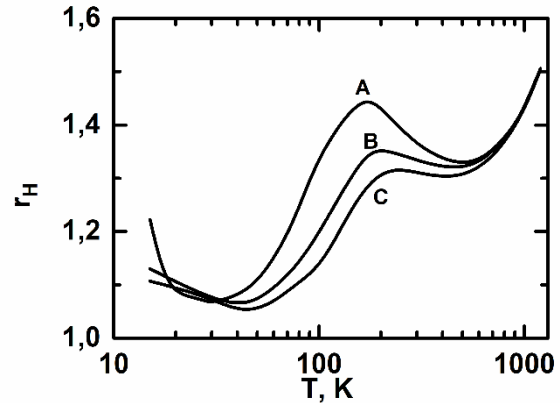


Fig.5. – The temperature dependence of electron's Hall factor in n-CdTe.

If to compare the theoretical curves obtained by the above method with the theoretical curves obtained in the relaxation time approximation (see Fig. 6a-d), one can see that the relaxation time approximation gives theoretical curves that are much less consistent with the experiment (curve 1 corresponds to low temperatures and curve 2 corresponds to high temperatures in the relaxation time approximation) especially in the region of high defects concentrations. This indicates that the method proposed in this article more adequately describes the defect structure of crystals and their kinetic properties.

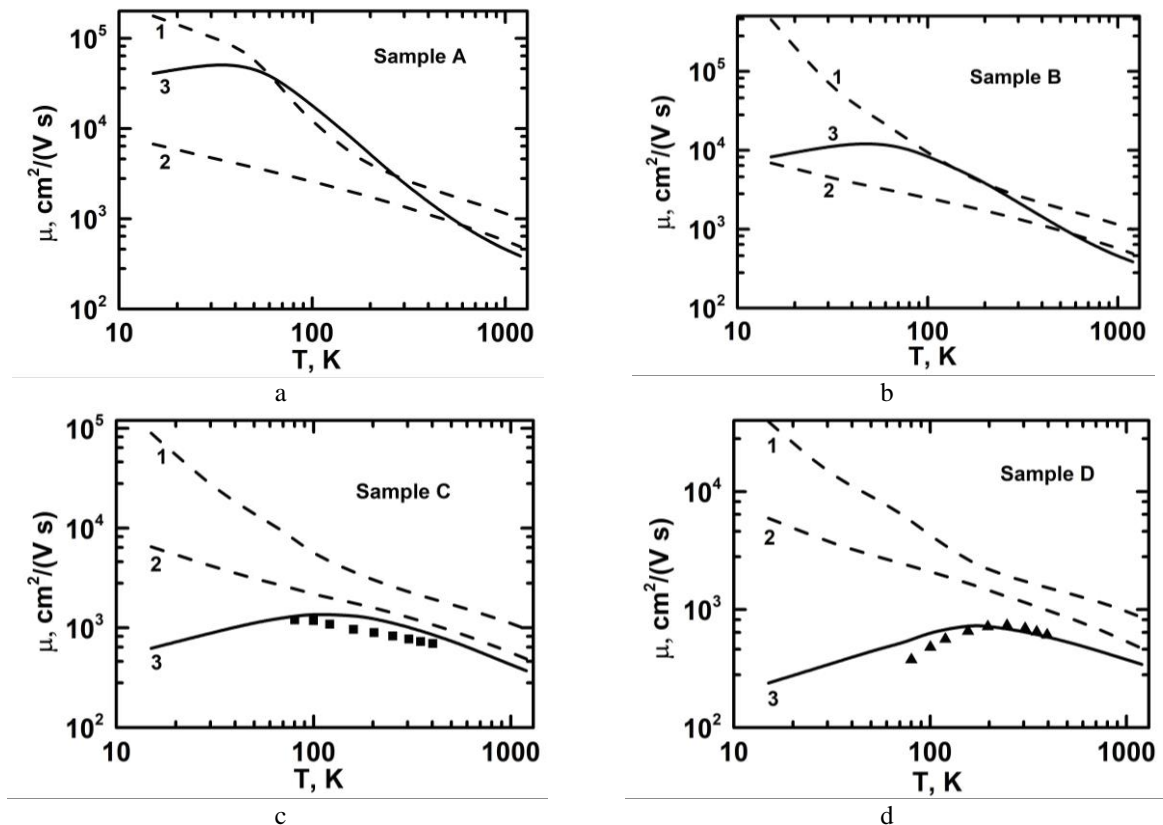


Fig. 6. – Comparing the theoretical curves obtained in the framework of long-range (curves 1 and 2) and short-range (curve 3) scattering models for chlorine doped samples.

Conclusion

The author considers a new scheme for calculating the energy spectrum, wave function and potential energy of an electron in a crystal at a given temperature. Based on this, the temperature dependences of the ionization energies of impurity (Cu and Cl) defects of different types, as well as

the temperature dependences of the kinetic coefficients are determined. It should be noted that the proposed calculation method can be applied to all impurity doped semiconductors with a sphalerite structure.

Malyk O.P. – Doctor of Physical and Mathematical Sciences, Professor, Professor.

- [1] I. Sankin, D. Krasikov, *Kinetic simulations of Cu doping in chlorinated CdSeTe PV absorbers*, Phys. Status Solidi A, 215, 1800887 (2019); <https://doi.org/10.1002/pssa.201800887>.
- [2] Su-Huai Wei, S. B. Zhang, *Chemical trends of defect formation and doping limit in II-VI semiconductors: the case of CdTe*, Phys. Rev. B: Condens. Matter Mater. Phys., 66, 155211 (2002); <https://doi.org/10.1103/PhysRevB.66.155211>.
- [3] Jie Ma, Su-Huai Wei, T. A. Gessert, Ken K. Chin, *Carrier density and compensation in semiconductors with multiple dopants and multiple transition energy levels: Case of Cu impurities in CdTe*, Phys. Rev. B: Condens. Matter Mater. Phys., 83, 245207 (2011); <https://doi.org/10.1103/PhysRevB.83.245207>.
- [4] Ji-Hui Yang, Wan-Jian Yin, Ji.-Sang. Park, Jie Ma, Su-Huai Wei, *Review on first-principles study of defect properties of CdTe as a solar cell absorber*. Semicond. Sci.Technol., 31, 083002 (2016); <https://doi.org/10.1088/0268-1242/31/8/083002>.
- [5] D. Krasikov, A. Knizhnik, B. Potapkin, S. Selezneva, T. Sommerer, *First-principles-based analysis of the influence of Cu on CdTe electronic properties*, Thin Solid Films 535, 322 (2013); <https://doi.org/10.1016/j.tsf.2012.10.027>.
- [6] W. Orellana, E. Menendez-Proupin, M. A. Flores, *Energetics and electronic properties of interstitial chlorine in CdTe*, Phys. Status Solidi B, 256, 1800219 (2019); <https://doi.org/10.1002/pssb.201800219>.
- [7] I. Sankin, D. Krasikov, *Defect interactions and the role of complexes in the CdTe solar cell absorber*, J. Mater. Chem. A 5, 3503 (2017); <https://doi.org/10.1039/C6TA09155E>.
- [8] O.P. Malyk, *The local inelastic electron–polar optical phonon interaction in mercury telluride*, Comput. Mater. Sci., 33/1-3, 153 (2005); <https://doi.org/10.1016/j.commatsci.2004.12.052>.

- [9] K. Kaasbjerg, K.S. Thygesen, K.W. Jacobsen, *Phonon-limited mobility in n-type single-layer MoS₂ from first principles*, Phys. Rev. B, 85, 115317 (2012); <https://doi.org/10.1103/PhysRevB.85.115317>.
- [10] O. Restrepo, K. Varga, S. Pantelides, *First-principles calculations of electron mobilities in silicon: phonon and Coulomb scattering*, Appl. Phys. Lett., 94, 212103 (2009); <https://doi.org/10.1063/1.3147189>.
- [11] O.D. Restrepo, K.E. Krymowski, J. Goldberger, W. A Windl, *A first principles method to simulate electron mobilities in 2D materials*, New J. Phys. 16, 105009 (2014); <https://doi.org/10.1088/1367-2630/16/10/105009>.
- [12] X. Li, J.T. Mullen, Z. Jin, K.M. Borysenko, M. Buongiorno Nardelli, K.W. Kim, *Intrinsic electrical transport properties of monolayer silicene and MoS₂ from first principles*. Phys. Rev. B 87, 115418 (2013); <https://doi.org/10.1103/PhysRevB.87.115418>.
- [13] Wu. Li, *Electrical transport limited by electron-phonon coupling from Boltzmann transport equation: An ab initio study of Si, Al, and MoS₂*, Phys. Rev. B 92, 075405 (2015); <https://doi.org/10.1103/PhysRevB.92.075405>.
- [14] O.P. Malyk, S.V. Syrotyuk, *Local electron interaction with point defects in sphalerite zinc selenide: calculation from first principles*. Journal of Electron. Mater. 47, 4212 (2018); <https://doi.org/10.1007/s11664-018-6068-1>.
- [15] O.P. Malyk, *Prediction of the kinetic properties of sphalerite CdSe_xTe_{1-x} (0.1 ≤ x ≤ 0.5) solid solution: an ab initio approach*. Journal of Electron. Mater. 49, 3080 (2020); <https://doi.org/10.1007/s11664-020-07982-6>.
- [16] O.P. Malyk, *Electron scattering on the short-range potential of the crystal lattice defects in ZnO*. Can. J. Phys. 92, 1372 (2014); <https://doi.org/10.1139/cjp-2013-0075>.
- [17] O.P. Malyk, S.V. Syrotyuk, *Heavy hole scattering on intrinsic acceptor defects in cadmium telluride: calculation from the first principles*, Physics and Chemistry of Solid State, 23(1), 89 (2022); <https://doi.org/10.15330/pcss.23.1.89-95>.
- [18] O.P. Malyk. *Calculation of the electron wave function and crystal potential in a sphalerite semiconductor at a given temperature*, Journal of nano- and electronic physics. 14, 05007 (2022); [https://doi.org/10.21272/jnep.14\(5\).05007](https://doi.org/10.21272/jnep.14(5).05007).
- [19] G.L. Hansen, J.L. Schmit, T.N. Casselman, *Energy gap versus alloy composition and temperature in Hg_{1-x}Cd_xTe*, J. Appl. Phys. 53, 7099 (1982); <https://doi.org/10.1063/1.330018>.
- [20] N.A.W. Holzwarth, A.R. Tackett, G.E. Matthews, *A Projector Augmented Wave (PAW) code for electronic structure calculations, Part I: atompaw for generating atom-centered functions*, Computer Phys. Comm., 135, 329 (2001); [https://doi.org/10.1016/S0010-4655\(00\)00244-7](https://doi.org/10.1016/S0010-4655(00)00244-7).
- [21] A.R. Tackett, N.A.W. Holzwarth, G.E. Matthews, *A Projector Augmented Wave (PAW) code for electronic structure calculations, Part II: pwpaw for periodic solids in a plane wave basis*, Computer Phys. Comm. 135, 348 (2001); [https://doi.org/10.1016/S0010-4655\(00\)00241-1](https://doi.org/10.1016/S0010-4655(00)00241-1).
- [22] J.P. Perdew, K. Burke, M. Ernzerhof, *Generalized gradient approximation made simple*, Phys. Rev. Lett. 77, 3865 (1996); <https://doi.org/10.1103/PhysRevLett.77.3865>.
- [23] C. de Boor, *A Practical Guide to Splines*, (Springer-Verlag, New York, 1978).
- [24] O.P. Malyk, *Electron scattering in Cd_xHg_{1-x}Te at high temperature*, Ukr. J. Phys., 35, 1374 (1990).
- [25] S. Yamada, *On the electrical and optical properties of p-type cadmium telluride crystals*, J. Phys. Soc. Jpn. 15, 1940 (1960); <https://doi.org/10.1143/JPSJ.15.1940>.
- [26] O.P. Malyk, *Nonelastic charge carrier scattering in mercury telluride*. J. Alloys Compd. 371/1-2, 146 (2004); <https://doi.org/10.1016/j.jallcom.2003.07.033>.
- [27] N.V. Agrinskaja, M.V. Alekseenko, O. A. Matveev, *On the mechanism of carrier scattering in chlorine-doped cadmium telluride crystals*, Fiz. Tech. Poluprovod. 5, 1029 (1981).

О.П. Малик

Явища переносу в CdTe:Cl і CdTe:Cu – розрахунок з перших принципів

Кафедра напівпровідникової електроніки, Національний університет «Львівська політехніка», Львів, Україна;
omalyk@ukr.net

У представленій статті розглянуто метод визначення енергетичного спектра, хвильової функції носія заряду та кристалічного потенціалу в CdTe при довільно заданій температурі. За допомогою цього підходу в рамках методу суперкомірки розраховано температурні залежності енергій іонізації різних типів дефектів, спричинених введенням домішок хлору та міді в телурид кадмію. Також запропонований метод дозволяє визначити температурну залежність оптичного та акустичного потенціалів деформації, а також залежність від температури параметрів розсіяння носія заряду на іонізованих домішках, полярних оптичних, п'єзооптичних та п'єзоакустичних фонах. У рамках близькодючих моделей розсіяння розглянуто температурні залежності рухливості носія заряду та фактора Холла.

Ключові слова: явища переносу, кристалічні дефекти, CdTe, розрахунок з перших принципів.

T.M. Mazur¹, M.P. Mazur¹, I.V. Vakaliuk²

Solar cells based on CdTe thin films (II Part)

¹Ivano-Frankivsk National Technical University of Oil and Gas, Ivano-Frankivsk, Ukraine, tetiana.mazur@nung.edu.ua;

²Vasyl Stefanyk Precarpathian National University, Ivano-Frankivsk, Ukraine

This paper discusses the use of semiconductor solar cells based on thin-film cadmium telluride (CdTe) in modern energy production. The advantages and disadvantages of using CdTe thin-film solar cells are analyzed, and arguments are presented in favor of the implementation of mass production technologies for CdTe solar modules, which can compete with silicon analogs in terms of compromise between efficiency and cost. The physical and chemical properties of the binary Cd-Te system are described, and the relationship between the physical, chemical, electrical, and optical properties of CdTe is analyzed, making it attractive for use in thin-film solar cells. Special attention is given to the investigation of photovoltaic properties, which are important parameters for determining photoconductivity, and the advantages and disadvantages of CdTe film photovoltaic properties are discussed. CdTe thin-film heterostructures (HSs), which are important components of modern solar cells, are considered, and their main advantages and disadvantages are described. It is argued that simple methods of manufacturing and forming HSs, which do not require complex and expensive equipment, are an important advantage of CdTe-based solar cell technology.

Keywords: solar cells, thin films, CdTe, photosensitivity, heterostructures.

Received 14 June 2022; Accepted 9 March 2023.

Content

Introduction

1. Requirements for the use of CdTe as thin films for solar cells.
2. Physical and chemical properties of the Cd-Te binary system.
3. Electrical and optical characteristics of CdTe.
4. Photosensitivity of CdTe films.
5. Thin film heterostructures based on CdTe in solar energy.

Conclusions

Introduction

Solar cells (SCs) based on CdTe thin films are a type of photovoltaic solar panels in which the active material for converting solar energy into electricity is a cadmium telluride thin film. CdTe has a high efficiency of converting solar energy and low production cost. It also has good resistance to corrosion and degradation, allowing it to be used in various climate conditions. CdTe is a semiconductor with a bandgap close to the optimum for absorbing sunlight and good electrical conductivity. That is why CdTe is considered one of the most promising

semiconductors for thin-film solar energy.

The technology for manufacturing thin-film solar cells based on CdTe has many advantages over traditional silicon wafers, as CdTe is a semiconductor that efficiently absorbs optical radiation with optimal parameters for solar cells. The production of thin-film CdTe does not require complex microelectronic technology, which makes it more productive and less costly. This is explained not only by the micron thickness of the absorbing layer, but also by the low cost of the substrate, onto which the material is typically deposited, which is usually glass, polymer film, or metal foil. In addition, thin film heterostructures based

on CdTe are a promising technology for solar cell manufacturing.

In field tests, CdTe-based solar panels demonstrated a 17% efficiency that is comparable to silicon-based panels. According to First Solar, the company is capable of achieving an efficiency of 24% in two years and 19% in real-world conditions in three years [1]. In addition, due to the technology of deposition from the vapor phase, First Solar's thin panels are easier to manufacture - the entire process, from transparent glass to the final product, takes only 3.5 hours, while it takes two days to manufacture a silicon element [1].

I. Requirements for the use of CdTe as thin-film solar cells

SCs based on thin films of CdTe have several advantages compared to traditional crystalline solar panels [2]. In particular, they have a higher energy conversion efficiency: CdTe-based solar cells can achieve efficiencies up to 22%, which is significantly higher than traditional crystalline solar panels [2,3]. They are also more resistant to high temperatures: thin CdTe films can operate at high temperatures without significant efficiency loss. Moreover, better performance under low light conditions is provided by CdTe-based thin-film solar cells, which are capable of generating electric current at low light levels, making them effective in cloudy weather or shaded areas [4].

However, thin-film CdTe-based SCs also have some drawbacks, such as high production costs and less resistance to ultraviolet radiation compared to crystalline solar panels [2, 5].

However, CdTe remains one of the materials used to manufacture thin-film solar cells. To use CdTe as a solar cell material, certain requirements must be met. One of the conditions is material purity, meaning that to obtain high-efficiency solar cells, high-purity CdTe with minimal impurities must be used. Another important condition is the thickness of the CdTe film, which must be optimized to achieve maximum efficiency. Typically, films with a thickness of 1 to 2 micrometers are used. To obtain voltage, a heterojunction between CdTe and another material, such as copper (Cu), must be used, ensuring a high-quality junction. It is important to consider the electrical properties, including the optimal concentration of electrons and holes in CdTe, to achieve maximum solar cell efficiency [6, 7]. Additionally, CdTe must be resistant to moisture, temperature changes, ultraviolet radiation, and mechanical damage [6]. From a production standpoint, the use of CdTe must be economically advantageous.

Adherence to these requirements helps achieve maximum efficiency of CdTe-based solar cells and reduces their production cost.

II. Physical and chemical properties of the Cd-Te binary system

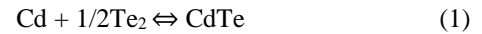
CdTe stands out among II–VI compounds like CdSe,

ZnS, and HgTe due to its unique combination of properties, including the highest average atomic number, lowest melting temperature, least negative enthalpy of formation, largest lattice parameter, and highest ionization potential. In its electronic form, cadmium telluride exhibits amphoteric semiconductor properties, allowing for n- and p-type doping [8]. These factors complement its nearly ideal optical bandgap and absorption coefficient for terrestrial photovoltaic devices, making it easily deposited and controlled in the form of a thin film. Table 1.1 presents the main physical and chemical properties of CdTe.

The crystallization of cadmium telluride occurs in the zinc blende structure. Its existence range is asymmetric. Stoichiometric CdTe has a melting point slightly lower than T_m . For temperatures below 1000 K, the majority of the compound's homogeneity range is on the Cd excess side, and for temperatures above 1000 K, it shifts towards the Te excess side [12]. The maximum melting temperature of the compound is $T_m = 1365$ K and corresponds to a non-stoichiometric composition with an excess of tellurium [10, 12].

The synthesis of II–VI compounds is facilitated by large negative enthalpies of formation (ΔH_f) and, consequently, low vapor pressures (p_{sat}) of the compounds compared to their component elements: for CdTe, $\Delta H_f = -22.4$ kcal/mol and $p_{\text{sat}}(400^\circ\text{C}) = 10^{-5}$ Torr [13, 14].

The equilibrium reaction for solid CdTe and Cd and Te_2 vapors is given by



As a result, deposition of CdTe can be achieved by co-evaporation from elemental sources, direct sublimation from a CdTe source, or transport of Cd and Te_2 vapor using a carrier gas from elemental or CdTe sources. Congruent sublimation of CdTe fixes the gas phase composition for deposition from a CdTe source, and the relatively low vapor pressure of CdTe facilitates the deposition of single-phase solid films over a wide range of substrate temperatures [12].

The partial pressures of the Cd and Te_2 components are related to each other by the equilibrium constant of the reaction [15]:

$$K_p = P_{\text{Cd}}^2 P_{\text{Te}} \quad \text{or} \quad K_p = P_{\text{Cd}} P_{\text{Te}}^{\frac{1}{2}} \quad (2)$$

The temperature dependence of the equilibrium constants K_p varies slightly according to different authors [2, 15].

According to [16], the phase diagram of the Cd-Te system at atmospheric pressure is shown, reflecting the individual vapor-solid equilibria for individual CdTe, Cd, and Te components in the temperature range from 100 to 600°C, which is commonly used for the manufacture of SCs. The congruent evaporation of CdTe simplifies the methods of deposition from the vapor phase, and the relatively high sublimation pressures of Cd and Te ensure a single-phase composition during vacuum deposition at temperatures above approximately 300°C. Additionally, CdTe is a stable product of cathodic reduction from solutions containing Cd and Te ions, due to the similar reduction potentials for Cd and Te and the low solubility

of CdTe [16, 17].

The T-x phase equilibrium of the CdTe system at atmospheric pressure is defined by the end points consisting of Cd (x=0), Te (x=1), and CdTe [16]. The melting temperature of CdTe is much higher than that of Cd ($T_m = 321^\circ\text{C}$) or Te ($T_m = 450^\circ\text{C}$), with a value of $T_m = 1092^\circ\text{C}$ [8,9]. The T-x projections surrounding the stoichiometric composition of CdTe show a very narrow and symmetrical region of existence at $T < 500^\circ\text{C}$, which is approximately $\sim 10^{-6}$ atm.%. At higher temperatures, the region of existence expands and becomes asymmetric on the Cd-enriched side up to 700°C , becoming Te-enriched at higher temperatures. The region of existence and the defect structure are related to the conditions of preparing the bulk material and have been the subject of many studies [8, 18]. Recent theoretical studies on defect levels in CdTe have extended this basis [8, 18]. Currently, the transfer of bulk properties to thin films of CdTe remains an important research topic.

The solid-state properties of CdTe are determined by its ionic bonding. According to the Phillips ionicity scale, CdTe has the highest value of 0.717 among II-VI compounds, which is less than the Phillips threshold value of 0.785 for octahedral coordination [8]. Geometric calculations show that tetrahedral coordination prevails in ionic binary compounds that have a cation/anion radius ratio between 0.225 and 0.732, while octahedral coordination is favored for ratios greater than 0.732 [8, 15]. The cation/anion radius ratio in CdTe is $r(\text{Cd}^{2+})/r(\text{Te}^{2-}) = 0.444$, which favors tetrahedral coordination.

In solid monoatomic substances, tetrahedral coordination of atoms with four nearest neighbors and twelve subsequent neighbor's results in the diamond structure. In double solid substances, this coordination corresponds to the structures of zinc blende and wurtzite. Solid CdTe at atmospheric pressure has a face-centered cubic structure of zinc blende, where the size of the elementary cell is 6.481 Å, and the CdTe bond length is 2.806 Å [9].

Cadmium telluride has two possible structures: sphalerite (cubic B3 structure) and wurtzite (hexagonal B4 structure), with the same number of atoms in the first and second coordination spheres [8]. At room temperature and a pressure of 3.3–3.6 GPa, a phase transition occurs in cadmium telluride from a sphalerite or wurtzite structure to a NaCl-type structure, accompanied by a sudden decrease in electrical conductivity [9].

Band gap of CdTe increases with decreasing temperature ($E_g = 1.5976 - 6.09 \cdot 10^{-4} T^2 / (T + 255)$ – [19], $E_g = 1.622 - 3.5 \cdot 10^{-4} T - 1.1 \cdot 10^{-7} T^2$ – [15], $E_g = 1.65 - 5.35 \cdot 10^{-4} T$ – [8]). The value of the spin-orbital splitting of the valence band becomes 0.9 eV [10], 0.93 eV [19].

Binary equilibrium between Cd and Te reveals only one composition of CdTe, which is formed in the ratio Cd:Te = 50:50% and has a eutectic solution in liquid Te [4]. When studying the phase state of CdTe at high temperatures, an asymmetric expansion of the single-phase region on the Te side was found at $T > 600^\circ\text{C}$. At 750°C , the absence of Cd in the alloy is 10^{18} cm^{-3} , which corresponds to a deficiency. The distance between nearest

Table 1.1.

Basic physical and chemical properties of CdTe [9, 10]

Parameter name, symbol, dimension	Numeric value
1	2
Lattice type	sphalerite
Space group	$T_d^2 - F\bar{4}3m$
Lattice parameter, a , 10^{-10} m	6.481 6.478
Cd-Te bond length, Å	2.806
Density, ρ , kg/m^3	$5.86 \cdot 10^3$
Melting temperature, T_m , K	1365
Thermal expansion coefficient (300K)	$5.9 \times 10^{-6}/\text{K}$
Specific heat, $C_{p,298,15}^0$, J/molK	50.2
Heat of formation, $\Delta H_{f,298,15}^0$, 10^3 J/mol	100.5
Melting heat, ΔH_{m} , 10^3 J/mol	44.4
Heat of sublimation, ΔH , 10^3 J/mol	181.95
Sublimation reaction	$\text{CdTe} \rightarrow \text{Cd} + 1/2\text{Te}_2$
Sublimation pressure p_{sat}	$\log(P_{\text{c}}/\text{bar}) = -10650/T(\text{K})$ $2.56 \log(T) + 15.80$
Standard entropy, $S_{298,15}^0$, 10^3 J/molK	98.61
Entropy of formation, ΔS_f^0 , J/molK	$361.74 (T = 874 \text{ K})$
Entropy changes during melting, ΔS_m , J/molK	32.53
Upper limit of dissociation energy, E , 10^3 J/mol	129.8
Thermal conductivity, χ , W/cm K	0.075
Coefficient of self-diffusion atoms Cd, $D_{\text{self-dif}}^{\text{Cd}}$	$2 \cdot 10^{-8} (T = 1273 \text{ K})$
Coefficient of self-diffusion atoms Te, $D_{\text{self-dif}}^{\text{Te}}$	$8.2 \cdot 10^{-11} (T = 1073 \text{ K})$
Debye temperature, T_θ , K	$200 (T = 80 \text{ K})$

neighbors in the CdTe structure is at the level of 0.28 nm at 300 K. The Hall mobility of electrons at 300 K is up to $n \leq 1050 \text{ cm}^2/\text{Vs}$, and the Hall mobility of holes at 300 K is up to $p \leq 100 \text{ cm}^2/\text{Vs}$. With. The exciton binding energy is 12 meV, the average photon energy is 5.8 meV [8, 20].

III. Electrical and optical characteristics of CdTe

The volumetric optical and electrical properties of CdTe depend on the structure of the electronic bands near the maximum of the valence band (MVB) and the minimum of the conduction band (MCB). For CdTe, the MVB and MCB are located at the same point Γ in the first Brillouin zone, resulting in a direct bandgap width of 1.5 eV at 300 K. The temperature coefficient of the bandgap width for CdTe is approximately -0.4 meV/K , leading to minimal changes in the performance of SCs at typical temperatures. The shape of the bands around the extrema determines the effective mass of electrons in the MCB and holes in the MVB, as well as controls the properties of charge carrier transport and inter-band density of states [21]. Table 1.2 presents the main optical and electrical properties of CdTe.

Compared to other semiconductors such as silicon, CdTe has a higher dielectric constant in the infrared and visible light regions, allowing it to transmit more light and provide higher efficiency for photovoltaic panels. CdTe has good absorption in the infrared and visible light regions [2]. Light reflection on the surface of CdTe depends on its structure and the wavelength of the light. Light scattering in CdTe depends on its defects and impurities, and their presence can be significant, reducing the efficiency of CdTe-based SCs [22]. CdTe photoluminescence occurs when the material absorbs

photons and emits light of the corresponding wavelength.

The mobility and concentration of charge carriers [23, 24], conductivity of the material, energy of radiative transitions [25] and other electrical and optical properties of CdTe strongly depend on its chemical composition and defect structure of the crystal [26]. This structure can be effectively controlled during post-growth high-temperature processing. It has been established that at room and lower temperatures, the predominant scattering mechanism is scattering on ionized centers, while at higher temperatures it is scattering on optical phonons [27].

The band structure of CdTe can be understood by considering its relatively high ionicity, which is explained by the fact that parts of the Bloch functions with periodicity identical to the lattice are associated with the atomic orbitals of Cd and Te. The conduction band arises from the first unoccupied cationic level, namely the 5s level of Cd. The highest valence band consists of the highest occupied level of the anion, namely the 5p level of Te.

In CdTe, the presence of defects disturbs its periodic structure, leading to the formation of localized electronic states within the bandgap and changes in electrical and optical properties [28, 29]. Such defects can be of various types, including intrinsic defects, chemical impurities, and their complexes, which can arise as either substitutional or interstitial defects. For example, cadmium vacancy (V_{Cd}) leads to shallow acceptor states, while cadmium substitution on the tellurium site (Cd_{Te}) leads to shallow acceptor states. Interstitial cadmium (Cd_i) leads to relatively shallow donor states, while interstitial tellurium (Te_i) leads to deep states. Although shallow states can be easily created by acceptors and donors [18], the overall doping effect depends on the probability of formation and ionization degree, which determine the degree of

Table 1.2.

Optical and electrical characteristics of CdTe [7, 20, 22]

Parameter	Value	
Optical range CdTe E_g (300K)	1.50eV \pm 0.01eV	
Optical range. Alloy CdTe _{0.95} S _{0.05}	1.47eV \pm 0.01eV	
Temperature dependence dE_g/dT	-0.4meV/K	
Electronic affinity	4.28eV	
Absorption coefficient (600 nm)	$>5 \times 10^5/\text{sm}$	
Refractive index (600 nm)	~ 3	
High frequency dielectric constant $\epsilon(\infty)$	7.1	
Low frequency (static) dielectric constant ϵ_s	9.65	
	10.9	
	11.0	
Band gap, E_g , eV	1.606 ($T = 4,2 \text{ K}$), 1.5 ($T = 300 \text{ K}$)	
m_e	0.096 m_0	
m_h	0.35 m_0	
μ_e	500–1000 cm^2/Vs	
μ_h	50–80 cm^2/Vs	
Intrinsic concentration of free charge carriers, n , cm^{-3}	$2.0 \cdot 10^6$ – $1.5 \cdot 10^{14}$ ($T = 300$ – 700 K)	
Hall mobility	electron μ_n , $10^{-3} \text{ m}^2 \text{ V}^{-1} \text{ sec}^{-1}$	105
	halls μ_p , $10^{-3} \text{ m}^2 \text{ V}^{-1} \text{ sec}^{-1}$	7

compensation of the desired acceptor state.

One of the most important issues in the processing of CdTe solar cells is achieving high concentrations of acceptors that exceed 10^{14} cm^{-3} . During the thermal processing of the semiconductor system, equilibrium is approached, and first-principles-based studies have shown that p-type doping leads to a self-compensation mechanism [29]. When the Fermi level is shifted towards the MVB, the chemical potential for forming donors increases, which compensates for further acceptor formation and significantly limits the maximum acceptor concentration. On the other hand, deep states can act as traps, reducing carrier lifetime and leading to increased carrier recombination. In [29], the reduction of deep electronic states measured in CdTe and CdZnTe is considered. In article [4] shows a group of shallow and deep defects, including intrinsic, dopant, and complex levels in CdTe. To achieve the desired electrical properties, activation treatments that include certain dopants in CdTe and CdS layers are used. After deposition, CdCl₂, O₂ and Cu can be applied, which in turn activate or passivate intrinsic defects [4].

However, the electrical characteristics of polycrystalline CdTe used in modern solar cells may differ from those of monocrystalline CdTe for several important reasons. In particular, defects between grain boundaries will have different energies in the bandgap and will have different formation energies. This assumption is based on the fact that different post-deposition methods used to improve the efficiency of solar cells mainly affect the grain boundary states rather than the bulk states of CdTe. For example, in the experiment [31], devices with electro-deposited CdTe films were created, which had fibrous grains with a length of 2 μm and a width of 0.15 μm . Both samples received the same CdCl₂ treatment, but one sample underwent a short oxidizing treatment before the CdCl₂ treatment. The cells produced similar open-circuit voltages (V_{OC}), but different photocurrents. The CdTe film in the cell with the oxidation step retained the structure of the deposited grain and the thickness of the CdS film. This cell demonstrated improved performance, with an internal quantum efficiency (IQE) > 90%, indicating improved lifetime of photo-generated carriers compared to the sample without the oxidation step, which showed grain coalescence, loss of the CdS film, and IQE < 60% [8].

This result confirms the correlation between the physical, chemical, and electronic properties of the CdTe/CdS thin-film SC. Since the cells are manufactured in a polycrystalline environment, several critical issues arise that affect the development of thin-film photovoltaic devices. The first is the separation of intragrain effects from grain boundary effects. The second is the detection of the influence of grain boundaries on device performance. The third is the control of film properties over a large area with more than 10^{12} grains per square meter in the CdTe module, where grains have a width of 1 micron. However, during the development of CdTe SCs, these problems were successfully addressed using improved methods for determining characteristics, empirical optimization of film deposition, and post-deposition processing. Today, several powerful methods exist for the quantitative evaluation of film properties, including those for CdTe/CdS SCs, which are discussed in

references [6,32-34]. Some of these methods can also be used as diagnostic sensors for embedded feedback control during the manufacturing process of CdTe/CdS modules.

IV. Photosensitivity of CdTe films

CdTe films are a well-known photosensitive material capable of converting light energy into electrical current. This allows them to be used in solar panels and other photovoltaic devices, such as X-ray detectors, as well as in scientific research.

The main properties of CdTe film photosensitivity include spectral sensitivity, absorption coefficient, conversion efficiency, response time, and stability. CdTe films have high spectral sensitivity in the infrared and visible ranges. Their spectral range depends on the thickness of the film and impurities present in the material. They have high light absorption coefficients compared to other semiconductor materials such as silicon, meaning they can convert more light energy into electrical current. CdTe films have high conversion efficiency of light energy to electrical current, indicating that they can provide high electrical power at low light levels [21, 22, 33]. Additionally, CdTe films have a fast response time to light, allowing them to be used in devices that require a quick response to light. And importantly, CdTe films have good stability against environmental factors such as temperature and humidity.

The photosensitivity of CdTe films is determined by the energy bandgap and defects in the crystalline structure. Since the bandgap of CdTe is approximately 1.5 eV, corresponding to a spectral range of around 800 nm, CdTe films have the highest photosensitivity in the near-infrared and visible spectral ranges.

In addition, the photosensitivity of CdTe films depends on their thickness. The thickness of the film should be sufficient to absorb a sufficient number of photons, but not too large, as this can reduce the charge collection efficiency. Typically, the optimal thickness of CdTe films ranges from 1 to 2 μm .

An important factor affecting the photosensitivity of CdTe films is the quality of the material itself and the technology used to manufacture it. For example, to ensure high efficiency, CdTe films should have high purity and uniformity. The technology used to manufacture CdTe films also affects their photosensitivity: for example, using the chemical deposition from solutions method can produce films with higher photosensitivity than using the physical deposition from vapors method [30].

To ensure high efficiency of CdTe films, they must also have good conductivity and charge carrier transport properties. Additional layers, such as ultra-fast diffusion layers that reduce charge carrier lifetime, or other materials like ZnO layers that provide efficient charge collection, are often used for this purpose.

CdTe films deposited at a temperature of $T_{mel} = 473 \text{ K}$ exhibit photosensitivity. The thickness of the films is set at 400 nm, since the light absorption coefficient is practically inversely proportional to the film thickness, providing better absorption of incident light on the films. Measurements of the I-V (current-voltage) characteristics of CdTe films at different ambient temperatures showed

that they have ohmic properties both in the dark and under illumination. The dark conductivity of the grown CdTe films measured at room temperature is $10^6 \text{ Ohm}^{-1}\text{m}^{-1}$. It is noted that the dark conductivity and photosensitivity of CdTe films increase with an increase in the deposition temperature T_{mel} in the range of 303 to 573 K [35].

The efficiency of the photoconductivity of the film largely depends on natural and external imperfections, which can act as capture or recombination centers. In polycrystalline films, many defects and broken atomic bonds arise between grains, creating additional energy states. These states effectively capture charge carriers, creating a potential barrier at the grain boundary. Due to the uniform structure of the intergranular boundary with an average barrier height E_{bd} , the dark conductivity of the film is determined by the formula [36]

$$\sigma_D = N_C e \mu_0 e^{-(\Delta E + E_{bd})/kT} = N_C e \mu_0 e^{-\Delta E_D/kT} \quad (3)$$

where N_C is the density of states in the conduction band, μ_0 is the carrier mobility in the grain.

During illumination, the conductivity of the film can increase due to an increase in the number of free charge carriers and a decrease in the grain boundary barrier height, which depends on the energy of light. Research [36] has shown that the change in conductivity due to the generation of charge carriers during illumination is insignificant compared to the change in conductivity that arises due to thermal generation of charge carriers. The main factor contributing to the increase in conductivity during illumination is the enhancement of carrier mobility at the grain boundaries, which occurs through barrier modulation. The overall photoconductivity of the films during illumination can be expressed by the formula presented in reference [36]:

$$\sigma_L = N_C e \mu_0 e^{-(\Delta E + E_{bd})/kT} = N_C e \mu_0 e^{-\Delta E_L/kT} \quad (4)$$

$$\Delta E_L = (\Delta E + E_{bd}) \quad (5)$$

Here ΔE_L is the photoactivation energy, E_{bd} is the height of the barrier under illumination.

The barrier height reduction (mobility activation energy) can be expressed as:

$$\Delta E_\mu = (\Delta E_D - \Delta E_L) \quad (6)$$

The energy required to activate the mobility of charge carriers ΔE_μ depends on temperature and light intensity, as well as the lifetime of these carriers. The relationship between photoconductivity and the energy of mobility activation can be expressed using the appropriate equations (3) and (4):

$$\frac{\sigma_L}{\sigma_D} = e^{\Delta E_\mu/kT} \quad (7)$$

The photosensitivity S is determined by the formula

$$S = (\sigma_L - \sigma_D)/\sigma_D \quad (8)$$

It should be noted that the efficiency of photosensitivity depends significantly on defects in the structure, which can act as trapping or recombination centers for charge carriers. In CdTe films with a polycrystalline structure, photoconductivity is mainly determined by processes occurring at grain boundaries. Using atomic force microscopy (AFM) (Fig. 1), the average crystal size was determined, and the efficiency of photosensitivity for films of different thicknesses and structure quality is presented in Fig. 2 [20].

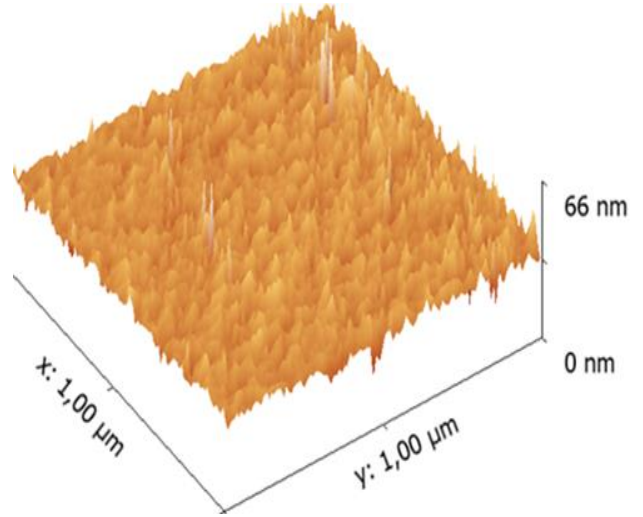


Fig. 1. AFM image of the surface of a 300 nm thick CdTe film on a polished glass substrate.

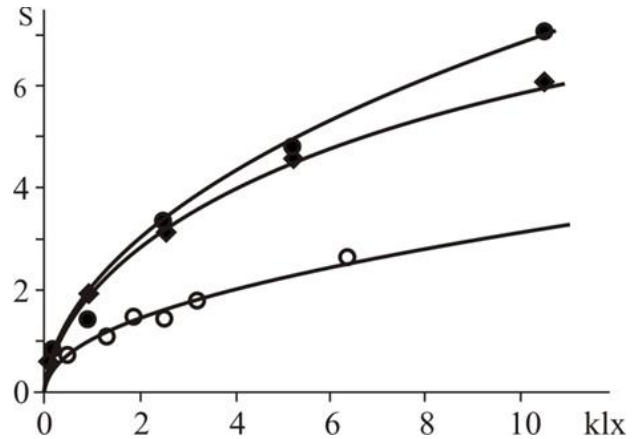


Fig. 2. Dependence of photosensitivity on illumination for thin CdTe films of different thicknesses:

- – thickness 200 nm, lining – polished glass;
 - ◆ – thickness 320 nm, lining – polished glass;
 - – thickness 540 nm, lining – mica;
- the average grain size is 25 nm (●), 30 nm (◆), 90 nm (○).

According to the research results, it can be seen that the photosensitivity of films obtained on polished glass substrates is significantly higher than that of films obtained on fresh mica cleavages (111), and it increases with decreasing film thickness. This is explained by the fact that the specific contribution of intergranular regions increases with decreasing crystallite size [20, 22]. Photoactivation energies decrease in darkness as the

intensity of white light increases. The decrease in photoactivation energy at a higher level of illumination is primarily explained by a decrease in the intergranular boundary potential barrier height. It is expected that the potential barrier strongly affects the mobility of carriers and thus controls photosensitivity.

Using (7) and (8), the photosensitivity can be expressed as a function of the mobility activation energy:

$$S = e^{\Delta E_{\mu}/kT} - 1 \quad (9)$$

On Fig.3 dependences of the calculated activation energies of mobility on illumination are given [20].

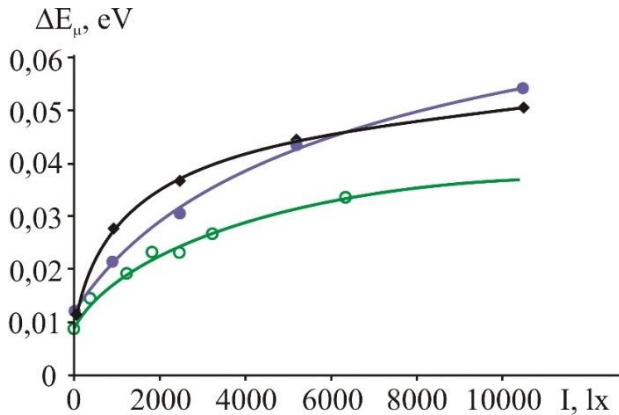


Fig. 3. Dependence of the calculated mobility activation energies on illumination for thin CdTe films of different thicknesses:

- – thickness 200 nm, substrate – mica;
- ◆ – thickness 320 nm, lining – polished glass;
- – thickness 540 nm, lining – mica.

The grain boundary effect explains the decrease in the energy of photoactivation in the dark, since the current lost to recombination at the grain boundaries negatively affects the sensitivity of the films to light. Decreasing the temperature leads to a reduction in the photogeneration process and, accordingly, to a decrease in sensitivity to light. It has been found that the lifetime of minority carriers varies inversely with the intensity of light, confirming the defect-controlled photoconductivity of thin CdTe films.

It is worth noting that the obtained activation energies for films obtained on polished glass are close to each other and are in the range of 0.012–0.05 eV. At the same time, for films obtained on fresh mica cleavages, significantly lower values of mobility activation energies were obtained, which are 0.009–0.03 eV [20, 24].

Despite the high photosensitivity of CdTe films, they also have some drawbacks. For example, CdTe is a toxic material, so special safety measures are required for its production and use. In addition, CdTe films can be sensitive to radiation, which can lead to degradation of their efficiency [2, 3]. However, significant advancements in CdTe film manufacturing technology in recent years have allowed these drawbacks to be minimized.

It is also worth noting that CdTe films have high efficiency in collecting light from small collection areas, making them suitable for creating thin photovoltaic cells. This allows for the creation of more compact and efficient

solar panels.

In summary, the photosensitivity of CdTe films depends on the spectral range, thickness, and quality of the material, as well as the technology used in their manufacture.

V. Thin-film heterostructures based on CdTe in solar energy

CdTe thin film solar cells are important components of modern solar panels that convert solar energy into electricity. They consist of several layers of different semiconductors that are interconnected. Typically, they are made up of a layer of CdS and CdTe, which allows for an energy conversion efficiency (ECE) - the efficiency of converting solar energy into electrical energy.

Thin film solar cells have several advantages over other solar energy technologies. They have an ECE, are able to withstand high temperatures and high levels of illumination and have a low production cost.

One of the main manufacturers of CdTe thin film solar cells is First Solar. The company uses a thin film production process that allows for the production of cells with low cost and HCE. According to the company's data, its SCs have a HCE of over 18%, making them some of the most efficient cells produced [2].

The main advantages of using CdTe thin-film HSs in solar energy are their high efficiency, low cost, ease of production, high stability, and flexibility. CdTe thin-film HSs have a high efficiency of converting solar energy into electrical current, allowing for more power output for the same battery size compared to other materials. In addition, CdTe is a cheap semiconductor, which reduces the production cost of solar panels, particularly CdTe-based thin-film HSs. CdTe thin films can be produced using thin film deposition processes such as chemical bath deposition and physical vapor deposition, which allow for high-quality films to be obtained at low temperatures [29,37]. CdTe thin-film HSs have good stability against environmental and thermal stresses, which ensures the longevity of solar panels [38]. CdTe can be used in flexible solar panels, allowing for the creation of highly efficient solar energy systems that can be applied in various fields such as transportation, aerospace, medicine, and others.

Despite many advantages, thin-film CdTe HSs have certain drawbacks. For example, the low or unsatisfactory stability of the HSs to moisture and acids, which can cause a decrease in their efficiency. Another important aspect of using thin-film CdTe HSs is the issue of cadmium toxicity, which is one of the components of the heterostructure. Additionally, the use of cadmium can cause environmental problems during the disposal of solar panel waste [3]. Despite this, the issues of cadmium toxicity and stability HSs under external factors require further research and the development of effective measures to minimize negative impacts.

Furthermore, there are alternative materials for creating solar cells, such as perovskite materials [39]. These materials have high efficiency in converting solar energy into electricity and are less toxic than cadmium. However, perovskites have their own drawbacks, such as

insufficient stability to moisture, acids, and other factors.

One of the main challenges of CdTe thin-film HSs is their relatively low stability to ultraviolet radiation and high temperatures. This can lead to a decrease in the ECE and a reduction in the service life of the SCs. To mitigate this effect, various protection methods can be used, such as applying protective coatings or using stabilizers [37, 38]. Additionally, there is a limitation on the thickness of CdTe films, which can restrict the effective thickness of the device and thus its ECE. To address this issue, various film strengthening technologies can be employed, or thin heterostructures with other semiconductors, such as CuInGaSe₂ (CIGS), can be utilized [40].

CdTe-based semiconductors have an advantage over Si in that they absorb optical radiation more efficiently, allowing the production of cheaper thin-film CEs. In particular, the average efficiency of the n-CdS/p-CdTe HS is about 16% under AM1.5 illumination conditions and a temperature of 300 K, which is almost half the theoretical value [2].

It is believed that one of the reasons for the low efficiency of CdTe-based SCs is the short lifetime τ_s of non-majority carriers, which leads to a high recombination velocity v_s at the interfaces of the HSs junction and grains in the polycrystalline CdTe film. Reducing the recombination velocity v_s should lead to improvements in the main parameters of solar cells, such as short-circuit current J_{sc} and open-circuit voltage V_{oc} . This is confirmed by experiments that have shown an increase in the open-circuit voltage V_{oc} from 0.84 to 0.93 V when replacing the polycrystalline CdTe film with a single-crystal substrate in n-CdS/p-CdTe heterostructure solar cells [41]. The low values of the short-circuit current and efficiency η of these samples are associated with the high resistance of the p-CdTe base substrates, the concentration of free holes in which does not exceed $7 \cdot 10^{15} \text{ cm}^{-3}$ at 300 K. Improving the structural perfection of the photoactive layer of p-CdTe in thin-film n-CdS/p-CdTe SCs allowed the efficiency η to be increased to ~21%, while V_{oc} increased by only 0.03 V [42, 43].

In this case, the increase in efficiency is associated with an increase in short-circuit current (J_{sc}), which is caused by a significant reduction in the series resistance of the HS through the thin p-CdTe layer. The dependence of the short-circuit current on the level of illumination (L) is linear and changes by more than four orders of magnitude. The open-circuit voltage (V_{oc}) depends on $\lg L$ at low levels of illumination and saturates at high levels, as shown in Fig. 4.

A slight increase in the open-circuit voltage (V_{oc}) indicates that the main factor affecting the minority carrier lifetime (τ_s) is the recombination velocity at the junction interface of the semiconductor components. Various surface passivation methods can be applied to reduce this recombination velocity (v_s) by 1-2 orders of magnitude. These methods can be used for both single crystal and large-grain semiconductor films [38, 44].

The internal quantum efficiency of the CdS/CdTe heterostructure significantly increases with the increase in the charge carrier lifetime and the specific resistance of the CdTe layer. However, it remains at the level of 17–18.5%

for lifetimes within the range of 10^{-9} – 10^{-10} s. To increase the efficiency to the theoretical limit (28–30%), it is necessary to increase the charge carrier lifetime in the CdTe layer to about 10^{-6} s and increase its thickness to several tens of micrometers. However, this is not economically justified [45].

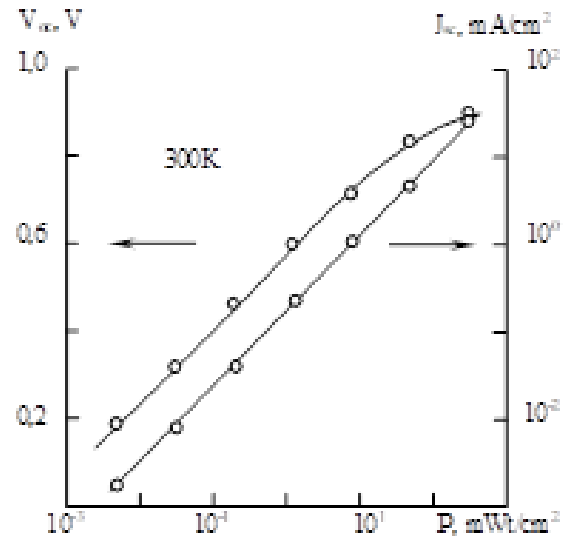


Fig. 4. Dependences of J_{sc} and V_{oc} for surface-barrier diodes on a CdTe:O substrate on the solar energy flux density.

An analysis of optical losses in thin-film CdS/CdTe solar cells with a transparent conducting layer of ITO or SnO₂ showed that even with 100% efficiency of photovoltaic conversion in CdTe and minimal thickness of CdS and ITO layers, the short-circuit current density (J_{sc}) cannot exceed more than 60% of the maximum possible value [46]. If the thickness of CdS and ITO layers is reduced below 30–50 nm, it is impossible to reduce optical losses, and a greater effect can be achieved by improving the transparency of the front electrode using other materials such as Cd₂SnO₄, Zn₂SnO₄ or ZnO. Even in the absence of absorption in CdTe, optical losses at a thickness of 50 nm of CdS reduce the short-circuit current by approximately 35%. The main reason for this reduction is the fundamental absorption in CdS (at $\lambda < 500$ nm), which cannot be eliminated without replacing CdS with a semiconductor material with a wider bandgap [3, 47].

It can be confidently asserted that research on CdTe HSs and other thin-film PV materials for creating SCs is an important direction for science and technology, as it can help reduce dependence on fossil fuels and decrease carbon emissions into the atmosphere. Moreover, the development of solar energy can create new job opportunities and contribute to economic growth. To achieve high ECE and efficiency of CdTe-based SCs, various optimization methods can be used, such as optimization of the thickness and composition of the heterostructure layers, optimization of the element's geometry, using different quality control methods, and developing new production methods. Additionally, it is important to ensure effective recycling of CdTe-based SCs, which will help reduce their environmental impact and contribute to creating a sustainable and environmentally friendly solar energy sector.

Conclusions

CdTe material possesses the necessary properties for creating thin-film SCs, including high energy conversion efficiency, durability, cost-effectiveness, and ease of manufacturing. This makes it an attractive material for PV production. The conductivity coefficient, electron mobility, energy conversion efficiency, transparency, light absorption, scattering coefficient, electrical conductivity, high absorptivity in the near-infrared and visible regions of the spectrum, good chemical and mechanical stability, and other properties of CdTe play an important role in the production of thin-film SCs based on this material.

The photosensitivity of CdTe films depends on several factors, including the film growth method, material purity, and its structure. These films have high sensitivity to light and high-energy radiation, which allows them to be used in various devices, particularly in solar cells. However, the photosensitivity of CdTe films also depends on the presence of defects and impurity levels in the material, so it can be improved through appropriate processing and optimization methods.

Despite the fact that the efficiency of CdTe thin-film solar modules in large-scale production is only around 10–11%, which is significantly lower than the efficiency of silicon-based modules (13–17%), there is still potential for significant improvement of CdTe SCs efficiency through

certain combinations of parameters. The thickness of the absorbing layer, carrier lifetime, specific resistance, and concentration of uncompensated acceptors in CdTe are key factors that can greatly influence efficiency improvement [48].

However, in order to achieve the highest efficiency and ensure resistance to harmful factors, it is necessary to continue developing manufacturing technologies for thin-film PV based on CdTe. This includes the development of new methods for protection against ultraviolet radiation and high temperatures, improvement of the mechanical stability of films, reducing the use of cadmium, and ensuring resistance to the harmful effects of long-term operation.

Research and development conducted over the past decade have enabled the mass production of CdTe-based solar modules that can compete with silicon modules in terms of compromise between efficiency and cost. This contributes to the construction of powerful solar power plants, and rapid development of this industry is expected in the future.

Mazur T.M. – Doctor of Philosophy, Assistant Professor of General and Applied Physics;
Mazur M.P. Associate Professor, Ph.D (Physics and Mathematics), Director of the Institute of architecture, Construction and Power Engineering;
Vakaliuk I.V. – Ph.D. student.

- [1] M.A. Green, E.D. Dunlop, J. Hohl-Ebinger, M. Yoshita, N. Kopidakis, & A.W. Ho-Baillie, *Solar cell efficiency tables (Version 55)*, Progress in Photovoltaics: Research and Applications, 28(1), 3 (2020); <https://doi.org/10.1002/pip.3228>.
- [2] T.M. Mazur, V.V. Prokopiv, M.P. Mazur, U.M. Pysklynets, *Solar cells based on CdTe thin films*, Physics and chemistry of solid state, 22(4), 817 (2021); <https://doi.org/10.15330/pcss.22.4.817-827>.
- [3] L.A. Kosyachenko, & E.V. Grushko, *Prospects for the Use of Thin-Film Cadmium Telluride in Solar Energetics*, Ukr. Phys. Journ., Rev., 7(1), 3 (2012); <http://archive.ujp.bitp.kiev.ua/files/reviews/7/1/r070101pu.pdf>.
- [4] B.E. McCandless, *CdTe solar cells: Processing limits and defect chemistry effects on open circuit voltage*, MRS Online Proceedings Library, 1538(1), 249 (2013); <https://doi.org/10.1557/opl.2013.1017>.
- [5] M.A. Green, E.D. Dunlop, J. Hohl-Ebinger, M. Yoshita, N. Kopidakis, & A. W. Ho-Baillie, *Solar cell efficiency tables (Version 55)*, Progress in Photovoltaics: Research and Applications, 28(1), 3 (2020); <https://doi.org/10.1002/pip.3228>.
- [6] M.A. Green, E.D. Dunlop, J. Hohl-Ebinger, M. Yoshita, N. Kopidakis, & H. Xiaojing, *Solar cell efficiency tables (Version 59)*, Progress in Photovoltaics: Research and Applications, 30(1), 1062 (2021); <https://doi.org/10.1002/pip.3506>.
- [7] V.P. Makhniy, M.M. Berezovskiy, O.V. Kinzerska, M.P. Mazur, T.M. Mazur, V.V. Prokopiv, *Prospects of using surface and barrier CdTe-diodes in solar energy*, Sensor Electronics and Microsystem Technologies, 16(2), 42 (2019); <https://doi.org/10.18524/1815-7459.2019.2.171227>.
- [8] B. E McCandless, & J. R. Sites, *Cadmium telluride solar cells*, Handbook of photovoltaic science and engineering, 600 (2011); <https://kashanu.ac.ir/Files/Content/Handbook.pdf>.
- [9] D.V. Korbutyak, S.V. Melnichuk, E.V. Korbut, & M.M. Borisyuk, (2000). Cadmium telluride: impurity-defect states and detector properties. (Ivan Fedorov: Kyiv, 198 (2000)).
- [10] D.V. Korbutiak, O.V. Kovalenko, S.I. Budzuliak, S.M. Kalytchuk, I.M. Kupchak, *Light-rectifying properties of quantum dots of semiconductor compounds A2B6*, Ukrainian Physical Journal, 7(1), 95 (2012); <http://archive.ujp.bitp.kiev.ua/files/reviews/7/1/r070103pu.pdf>.
- [11] R. Grill, & A. Zappettini, *Point defects and diffusion in cadmium telluride*. Progress in crystal growth and characterization of materials, 48, 209 (2004); <https://doi.org/10.1016/j.pcrysgrow.2005.06.001>

- [12] V.V. Prokopiv, I.V. Horichok, V.V. Prokopiv, & L.V. Turovska. Point defects of Cadmium, Tin and Lead Tellurides. Ivano-Frankivsk, 248 p. (2016); <http://hdl.handle.net/123456789/2541>.
- [13] J. H. Greenberg, *P–T–X phase equilibrium and vapor pressure scanning of non-stoichiometry in the Cd–Zn–Te system*, Progress in crystal growth and characterization of materials, 47(2-3), 196 (2003); <https://doi.org/10.1016/j.pcrysgrow.2005.02.001>.
- [14] R. Fang, & R.F. Brebrick, *CdTe I: Solidus curve and composition-temperature-tellurium partial pressure data for Te-rich CdTe (s) from optical density measurements*, Journal of Physics and Chemistry of Solids, 57(4), 443 (1996); [https://doi.org/10.1016/0022-3697\(95\)00251-0](https://doi.org/10.1016/0022-3697(95)00251-0).
- [15] D.Y. Goswami, S. Vijayaraghavan, S. Lu, & G. Tamm, *New and emerging developments in solar energy*, Solar energy, 76(1-3), 33 (2004); [https://doi.org/10.1016/S0038-092X\(03\)00103-8](https://doi.org/10.1016/S0038-092X(03)00103-8).
- [16] H. Okamoto, & H. Okamoto, *Phase diagrams for binary alloys*, 314, Materials Park, OH: ASM international, (2000); https://www.asminternational.org/documents/10192/1849770/57751G_Frontmatter.pdf.
- [17] O. Knacke, & K. Hesselmann, *Thermochemical properties of inorganic substances*, Springer, (1991); <https://worldcat.org/en/title/644053530>.
- [18] T. Mazur, V. Prokopiv, L. Turovska, *Quasi-chemistry of intrinsic point defects in cadmium telluride thin films*, Molecular Crystals and Liquid Crystals, 671(1), 85 (2018); <https://doi.org/10.1080/15421406.2018.1542088>.
- [19] L. Tsakalakos, J. Balch, J. Fronheiser, B.A. Korevaar, O. Sulima, & J. Rand, *Silicon nanowire solar cells*, Applied physics letters, 91(23), 233117 (2007); <https://doi.org/10.1063/1.2821113>.
- [20] V.V. Prokopiv, O.B. Kostyuk, B.S. Dzundza T.M. Mazur, L.V. Turovska, O.M. Matkivskyi, M.V. Deychakivskyi, *Electrical properties of CdTe<Ca> thin layers*, Physics and chemistry of solid state, 20(4), 372 (2019); <https://doi.org/10.15330/pcss.20.4.372-375>.
- [21] O. Madelung, (Ed.), *Semiconductors: group IV elements and III-V compounds*, Springer Science & Business Media, (2012); <https://doi.org/10.1007/978-3-642-45681-7>.
- [22] V. Prokopiv, I. Horichok, T. Mazur, O. Matkivsky, L. Turovska, *Thermoelectric materials based on samples of microdispersed PbTe and CdTe*, Proceedings of the 2018 IEEE 8th International Conference "Nanomaterials: Applications and Properties", NAP 2018, (2018); <https://doi.org/10.1109/NAP.2018.8915357>.
- [23] B. Naidych, T. Parashchuk, I. Yaremiy, M. Moyseyenko, O. Kostyuk, O. Voznyak, ... & L. Nykyruy, *Structural and thermodynamic properties of Pb-Cd-Te thin films: Experimental study and DFT analysis*, Journal of Electronic Materials, 50, 580-591 (2021); <https://doi.org/10.1007/s11664-020-08561-5>.
- [24] T. Mazur, M. Mazur, *Thickness Dependence of the Kinetic Parameters in CdTe and PbTe Thin Films*, Proceedings of the 2022 IEEE 12th International Conference "Nanomaterials: Applications and Properties", NAP 2022, (2022); <https://doi.org/10.1109/NAP55339.2022.9934352>.
- [25] T. Mazur, M. Slyotov, M. Mazur, O. Slyotov, *Heterolayers of Hexagonal α -CdTe*, Journal of Nano- and Electronic Physics, 14(5), 05029 (2022); [https://doi.org/10.21272/jnep.14\(5\).05029](https://doi.org/10.21272/jnep.14(5).05029).
- [26] R. Grill, J. Franc, P. Hoschl, I. Turkevych, E. Belas, P. Moravec, ... & K.W. Benz, *High-temperature defect structure of Cd- and Te-rich CdTe*, IEEE Transactions on Nuclear Science, 49(3), 1270 (2002); <https://doi.org/10.1109/TNS.2002.1039650>.
- [27] D.M. Freik, V.M. Chobanyuk, O.S. Krynytskyi, & I.V. Horichok, *Photovoltaic transformers of solar irradiation based on cadmium telluride. Part II. Achievements and State of Art. (Review)*. Physics and Chemistry of Solid State, 13(3), 744 (2012); <http://page.if.ua/uploads/pcss/vol13/!1303-29.pdf>.
- [28] T.M. Mazur, V.P. Makhniy, V.V. Prokopiv, M.M. Slyotov, *Thermal annealing effect on optical properties of the cadmium telluride films*, Journal of Nano- and Electronic Physics. 9(5), 05047 (2017); [http://doi.org/10.21272/jnep.9\(5\).05047](http://doi.org/10.21272/jnep.9(5).05047).
- [29] S. H.Wei, S. B.Zhang, & A.Zunger, *First-principles calculation of band offsets, optical bowings, and defects in CdS, CdSe, CdTe, and their alloys*, Journal of applied Physics, 87(3), 1304 (2000); <https://doi.org/10.1063/1.372014>.
- [30] B. Dzundza, O. Kostyuk, & T. Mazur, *Software and Hardware Complex for Study of Photoelectric Properties of Semiconductor Structures*, IEEE 39th International Conference on Electronics and Nanotechnology (ELNANO), Kyiv, 635 (2019); <https://doi.org/10.1109/ELNANO.2019.8783544>.
- [31] H.S. Patel, J.R. Rathod, K.D. Patel, V.M. Pathak, *Structural and surface studies of vacuum evaporated Cadmium Telluride thin films*, American J Mater Sci & Tech, 1, 11 (2012); <https://doi.org/10.7726/ajmst.2012.1002>.
- [32] M.A. Green, K. Emery, D.L. King, S. Igari, & W. Warta, *Solar cell efficiency tables (version 20)*, Progress in photovoltaics, 10(5), 355 (2002); <https://doi.org/10.1002/pip.453>.

- [33] L. Nykyrui, Y. Saliy, R. Yavorskyi, Y. Yavorskyi, V. Schenderovsky, G. Wisz, & S. Górný, *CdTe vapor phase condensates on (100) Si and glass for solar cells*. In 2017 IEEE 7th International Conference Nanomaterials: Application & Properties (NAP), 01PCSI26-1, IEEE (2017); <https://doi.org/10.1109/NAP.2017.8190161>.
- [34] T. Mazur, M. Slyotov, M. Mazur, V. Prokopiv, O. Kinzerska, O. Slyotov, *Features of the cadmium chalcogenide substrates with surface nanostructure*, Materials Today: Proceedings, (2021); <https://doi.org/10.1016/j.matpr.2019.12.112>.
- [35] S. Chander and M.S. Dhaka, *Effect of thickness on physical properties of electron beam vacuum evaporated CdZnTe thin films for tandem solar cells*, Physica E, 84, 112 (2016); <https://doi.org/10.1016/j.physe.2016.05.045>.
- [36] P.K. Kalita, *Temperature dependence of dc photoconductivity in CdTe thin films*, Pramana, 60(6), 1247 (2003); <https://www.ias.ac.in/public/Volumes/pram/060/06/1247-1257.pdf>.
- [37] P.M. Gorley, V.P. Makhniy, P.P. Horley, Yu.V. Vorobiev and J. González-Hernández, *Surface-Barrier Solar Cells Based On Monocrystalline Cadmium Telluride with the Modified Boundary*, Solar Energy [Internet], (2010, Feb 1); <http://dx.doi.org/10.5772/8061>.
- [38] Mykhailo Slyotov, Tetiana Mazur, Volodymyr Prokopiv, Oleksii Slyotov, Myroslav Mazur, *Sources of optical radiation based on ZnTe/ZnSe/ZnS heterostructures*, Materials Today: Proceedings (2022); <https://doi.org/10.1016/j.matpr.2022.03.476>.
- [39] M.I. Elsmami, N. Fatima, M.P.A. Jallorina, S. Sepeai, M.S. Su'ait, N. Ahmad Ludin, M.A. Mat Teridi, K. Sopian, M.A. Ibrahim, *Recent Issues and Configuration Factors in Perovskite-Silicon Tandem Solar Cells towards Large Scaling Production*, Nanomaterials, 11, 3186 (2021); <https://doi.org/10.3390/nano11123186>.
- [40] V.K. Kamble, & V.B. Pujari, *Electrical and micro-structural properties of cadmium chalcogenides: A comparative study*, Int. J. Emerg. Technol. Appl. Eng, 5, 172 (2015); <https://api.semanticscholar.org/CorpusID:16313665>.
- [41] J.N. Duenow, J.M. Burst, D.S. Albin, D. Kuciauskas, S.W. Johnston, R.C. Reedy, & W.K. Metzger, *Single-crystal CdTe solar cells with Voc greater than 900 mV*, Applied Physics Letters, 105(5), 053903 (2014); <https://doi.org/10.1063/1.4892401>.
- [42] M.O. Reese, C.L. Perkins, J.M. Burst, S. Farrell, T.M. Barnes, S.W. Johnston, & W. K. Metzger, *Intrinsic surface passivation of CdTe*, Journal of Applied Physics, 118(15), 155305 (2015); <https://doi.org/10.1063/1.4933186>.
- [43] T.M. Mazur, M.M. Slyotov, V.V. Prokopiv, O.M. Slyotov, M.P. Mazur, *Light emitters based on II-VI chalcogenides with nanostructured surface*, Molecular Crystals and Liquid Crystals, 752, 95 (2022); <https://doi.org/10.1080/15421406.2022.2091276>.
- [44] V.P. Makhniy, *Influence of thermal annealing on physical properties of surface layers of monocrystalline cadmium telluride*, Surface, X-rays, synchrotron and neutron investigation, 2, 108 (2007); <https://naukarus.com/vliyanie-termicheskogo-otzhiga-na-fizicheskie-svoystva-poverhnostnyh-sloev-monokristallicheskogo-tellurida-kadmiya>.
- [45] X. Mathew, L.A. Kosyachenko, V.V. Motushchuk, O.F. Sklyarchuk, *Requirements imposed on the electrical properties of the absorbed layer in CdTe-based solar cells*, J. Materials Science: Materials in Electronics, 18, 1099 (2007); <https://doi.org/10.1007/s10854-007-9317-2>.
- [46] Nowshad Amin, et al., *Encyclopedia of sustainable technologies*, 11, (2017); <https://doi.org/10.1016/B978-0-12-409548-9.10092-2>.
- [47] L. Kosyachenko, *Solar Energy*, edited by R.D. Rugescu, Intech, Croatia, 105 (2010); https://cdn.intechopen.com/pdfs/8547/InTech-Chapter_download.pdf.
- [48] M. A.Green, E. D.Dunlop, J.Hohl-Ebinger, M.Yoshita, N.Kopidakis, & A. W.Ho-Baillie, *Solar cell efficiency tables (Version 55)*, Progress in Photovoltaics: Research and Applications, 28(1), 3 (2021); <https://doi.org/10.1002/ppp.3228>.

Т.М. Мазур¹, М.П. Мазур¹, І.В. Малярська²

Сонячні елементи на основі тонких плівок CdTe (II частина)

¹Івано-Франківський національний технічний університет нафти і газу, Івано-Франківськ, Україна,
tetiana.mazur@nung.edu.ua;

²Прикарпатський національний університет імені Василя Стефаника, Івано-Франківськ, Україна

У роботі проведено дослідження щодо використання напівпровідникових сонячних елементів (СЕ) на основі тонкоплівкового телуриду кадмію (CdTe) в сучасній енергетиці. Проаналізовано переваги та недоліки використання СЕ на основі тонких плівок CdTe, а також приведено аргументи на користь впровадження технологій масового виробництва CdTe сонячних модулів, які можуть конкурувати з кремнієвими аналогами за компромісних значень ефективності та вартості. Описано фізико-хімічні властивості бінарної системи Cd-Te та вказано зв'язок між фізичними, хімічними, електричними та оптичними властивостями CdTe, що робить його привабливим для використання у тонкоплівкових СЕ. Особлива увага приділяється дослідженню фоточутливості, яка є важливим параметром у визначенні фотопровідності, та обговорюються переваги і недоліки фоточутливості плівок CdTe. Розглянуто тонкоплівкові гетероструктури (ГС) CdTe, які є важливими компонентами сучасних сонячних батарей, та описуються їх основні переваги та недоліки. Аргументується, що прості способи виготовлення та формування ГС, які не потребують складного та дорогого обладнання, є важливою перевагою технології СЕ на основі CdTe.

Ключові слова: сонячні елементи, тонкі плівки, CdTe, фоточутливість, гетероструктури.

I.V. Bilynskyi, R.Ya. Leshko, H.Ya. Bandura

Electron and hole spectrum taking into account deformation and polarization in the quantum dot heterostructure InAs/GaAs

Physics Department, Drohobych Ivan Franko State Pedagogical University, Drohobych, Ukraine, galinka.bandura@gmail.com

In the paper InAs spherical quantum dots in a GaAs matrix were investigated. The energies of electrons and holes in single- and multi-band models (with strong, weak, and intermediate spin-orbit interaction) were calculated taking into account both the deformation of the quantum-dot matrix and the polarization charges on the quantum dot surface. The dependence of the energy levels of electrons and holes on the radius of the quantum dot is considered. It is shown that the deformation effects are stronger than polarization for the electron. For holes those effects are opposites. The energies of electrons and holes have been compared in all approximation models.

Keywords: exchange interaction, deformation, 4-band model or multiband hole model, 6-band model, polarization charges, strained heterosystem.

Received 31 October 2022; Accepted 21 February 2023.

Introduction

Recently much attention has been paid to the physics of low-dimensional semiconductor structures. This has been stimulated by the rapid progress in nanometer-scale fabrication technology. Among them, quantum dots, which are also defined as nanocrystals and microcrystallites, or nanoclusters, are of particular interest. The effect of quantum confinement on electrons and holes in semiconductor quantum dots (QD) has been studied in [1-3].

The superlattices of quantum dots InAs in a matrix GaAs has been studied in [4]. The superlattices of spherical and cubic quantum dots (QD) have been studied. Using the method of plane waves for different shapes of QD, analytical expressions for calculating the energy spectrum have been obtained. The dependences of energy zones at high symmetry dots have been constructed. Dependences of the widths of zones have been found.

The basis for the creation of optoelectronic devices is a single-particle character - an electron and a hole. Analytical expressions describing the energy spectrum of electrons and holes for a quantum dot (QD) arising in a self-consistent deformation field created by an array of coherently stressed QDs were obtained in the paper [5]. It

is shown that the internal elastic deformation that occurs at the boundary of the QD matrix affects the energy spectrum of electrons more significantly than the spectrum of holes. The interaction of quantum dots (QDs) between themselves and external electromagnetic fields depends on the size and geometry of quantum dots [6-9]. These dependencies are used in various electronic and optoelectronic devices, including lasers [10-12], single-photon sources [13-15], solar cells [16-18], and photodetectors [19, 20].

Theoretical models for three-dimensional superlattices of cubic and tetragonal InAs/GaAs and Ge/Si quantum dots are proposed in works [21, 22]. Electronic and phonon spectra of such superlattices, densities of electronic states, the effective mass tensor, and conductivity were studied. It was established that the properties of three-dimensional superlattices of quantum dots are more sensitive to the distance between dots than to the shape of the dots.

Real structures can contain various defects. Therefore, conditions may change. For heterosystems in which there is a large difference between the dielectric constants, the effect of polarization charges will be significant. The change in the dielectric properties of the matrix taking into account the polarization or deformation charges leads to a

significant change in the energy of both the electron and the hole. It should be reflected in the optical and other QD properties.

In view of this, in our work we have been calculated the energies of the electron in singleband model, and the hole in both singleband and multiband-band model approximation. And we also have been calculated electron and hole energies with the deformation and polarization at

the same time.

I. Electron energies of semiconductor quantum dots

Let's write the Hamiltonian of the electron in the form

$$\hat{H}_e = -\frac{1}{2} \nabla \frac{1}{m_e} \nabla + U(r_e) = \frac{1}{2} \nabla \frac{1}{m_e} \nabla + U_{conf}(r_e) + U_d(r_e) + U_p(r_e) = \hat{H}_e^0 + U_d(r_e) + U_p(r_e) \quad (1)$$

where

$$m_e = \begin{cases} m_e^{(1)}, & r_e \leq \alpha, \\ m_e^{(2)}, & r_e > \alpha. \end{cases}$$

$$U_{conf}(r_{\{r\}}^{(e)}) = \begin{cases} 0, & r_{\{r\}}^{(e)} \leq \alpha, \\ U_{0;\{r\}}^{(e)}, & r_{\{r\}}^{(e)} > \alpha. \end{cases} \quad (2)$$

$$U_d(r_{\{h\}}^{(e)}) = \begin{cases} 0, & r_{\{h\}}^{(e)} \leq \alpha, \\ U_{0,d;\{h\}}^{(e)}, & r_{\{h\}}^{(e)} > \alpha, \end{cases} = \begin{cases} 0, & r_{\{h\}}^{(e)} \leq \alpha, \\ -|D_{\{h\}}^{(1)} \varepsilon^{(1)}| - |D_{\{h\}}^{(2)} \varepsilon^{(2)}|, & r_{\{h\}}^{(e)} > \alpha, \end{cases} \quad (3)$$

$$U_p(r_{\{h\}}^{(e)}) = \frac{\gamma_0}{4\chi(r_{\{h\}}^{(e)})} \int_0^\infty d r_0 \frac{th(\frac{r_0 - \alpha}{L}) + \frac{r_0}{L} sech^2(\frac{r_0 - \alpha}{L})}{r_0^2 - r_{\{h\}}^{(e)2}} \quad (4)$$

When $U_d(r) = 0$, $U_p(r) = 0$, polarization and deformation can be neglected. The Schrödinger equation with and without account the QD deformation can be solved exactly. It has an expression for the ground state

$$\psi_{e; m_s}(\vec{r}_e) = \frac{1}{\sqrt{4\pi}} S_{e; m_s} \begin{cases} A_e^{(1)} \frac{J_{1/2}(kr_e)}{\sqrt{r_e}}, & r_e \leq \alpha, \\ A_e^{(2)} \frac{K_{1/2}(\eta r_e)}{\sqrt{r_e}}, & r_e > \alpha, \end{cases} = \frac{1}{\sqrt{4\pi}} S_{e; m_s} \begin{cases} A_e^{(1)} \frac{\sin(kr_e)}{r_e}, & r_e \leq \alpha, \\ A_e^{(2)} \frac{\exp(-\eta r_e)}{r_e}, & r_e > \alpha, \end{cases} \quad (5)$$

where $S_{e; m_s}$ is spin function, $m_s = \pm \frac{1}{2}$, $k = \sqrt{2m_e^{(1)} E}$. $\eta = \sqrt{2m_e^{(2)} (U_{0;e} - E)}$ when the QD deformation is neglected and $\eta = \sqrt{2m_e^{(2)} (U_{0;e} + U_{0,d;e} - E)}$ when the QD deformation is accounted. Taking into account the boundary condition and normalize condition, the wave functions and electron energies have been defined. The influence of polarization charges has been calculated in the first-order of perturbation theory. In the same manner the hole energies have been obtained in the case when one can neglect the complex band structure (only heavy hole band is accounted).

In real situation for the InAs/GaAs heterosystem the multiband model for hole states should be used. In the multiband model approximation in the case of intermediate spin-orbit interaction (so-called 6-band model), the solutions of the Schrödinger equation with the Hamiltonian [23-25] have the form like in [23]:

$$\psi_j^+ = \begin{pmatrix} \frac{R_{h2}^+}{\sqrt{2j(2j-1)(2j-2)}} \Phi_{j-3/2}^{(4)} + \frac{R_{h1}^+}{\sqrt{2j(2j+2)(2j+3)}} \Phi_{j+1/2}^{(4)} \\ R_s^+ \Phi_{j+1/2}^{(2)} \end{pmatrix}, \quad (6)$$

$$\psi_j^- = \begin{pmatrix} \frac{R_{h2}^-}{\sqrt{2(j+1)(2j+3)(2j+4)}} \Phi_{j+3/2}^{(4)} + \frac{R_{h1}^-}{\sqrt{2j(2j-1)(2j+2)}} \Phi_{j-1/2}^{(4)} \\ R_s^- \Phi_{j-1/2}^{(2)} \end{pmatrix},$$

where $\Phi_k^{(4)}$, $\Phi_k^{(2)}$ are four-dimensional and two-dimensional vectors-columns [24] based on spherical harmonics $Y_{l,m}(\theta, \varphi)$. We obtain two systems of equations for the radial components of the holes eigenfunctions, R_{h1}, R_{h2}, R_s are located in the QD and outside QD ($j = \frac{1}{2}, \frac{3}{2}, \frac{5}{2}, \dots$).

Systems of differential equations have exact solutions for even and odd states. In the inner region for a spherical QD, the solutions of the equations system (radial functions), are written using the sum of the three spherical Bessel functions of the first kind:

$$\begin{aligned}
 R_{h1}^{j+}(r) &= C_1 J_{j+1/2}(k_l r) + c_2 J_{j+1/2}(k_h r) + C_3 J_{j+1/2}(k_s r), \\
 R_{h2}^{j+}(r) &= -C_1 \sqrt{\frac{3(2j-1)}{2j+3}} J_{j-3/2}(k_l r) + C_2 \sqrt{\frac{3(2j+3)}{3(2j-1)}} J_{j-3/2}(k_h r) - C_3 \sqrt{\frac{3(2j-1)}{2j+3}} J_{j+3/2}(k_s r), \\
 R_s^{j+}(r) &= -C_1 \sqrt{\frac{j}{2j+3}} \frac{2E-(\gamma_1+2\gamma)k_l^2}{\gamma k_l^2} J_{j+\frac{1}{2}}(k_l r) + C_3 \sqrt{\frac{j}{2j+3}} \frac{2E-(\gamma_1+2\gamma)k_s^2}{\gamma k_s^2} J_{j+\frac{1}{2}}(k_s r),
 \end{aligned} \tag{7}$$

and solutions for odd states

$$\begin{aligned}
 R_{h1}^{j-}(r) &= C_4 \sqrt{2j-1} J_{j-1/2}(k_l r) + c_5 \sqrt{2j-1} J_{j-1/2}(k_h r) + c_6 \sqrt{2j-1} J_{j-1/2}(k_s r), \\
 R_{h2}^{j-}(r) &= C_4 \sqrt{3(2j+3)} J_{j+3/2}(k_l r) + C_5 \sqrt{\frac{2j-1}{3(2j+3)}} J_{j+3/2}(k_h r) + C_6 \sqrt{3(2j+3)} J_{j+3/2}(k_s r), \\
 R_s^{j-}(r) &= C_4 \sqrt{j+1} \frac{(\gamma_1+2\gamma)k_l^2-2E}{\gamma k_l^2} J_{j-1/2}(k_l r) + C_6 \sqrt{j+1} \frac{(\gamma_1+2\gamma)k_s^2-2E}{\gamma k_s^2} J_{j-1/2}(k_s r),
 \end{aligned} \tag{8}$$

where

$$\begin{aligned}
 k_h^2 &= \frac{2E}{\gamma_1-2\gamma}, \\
 k_{l,s}^2 &= \frac{2E(\gamma_1+\gamma)-\Delta(\gamma_1+2\gamma) \pm \sqrt{[2E(\gamma_1+\gamma)-\Delta(\gamma_1+2\gamma)]^2-4E(E-\Delta)(\gamma_1-2\gamma)(\gamma_1+4\gamma)}}{(\gamma_1-2\gamma)(\gamma_1+4\gamma)}.
 \end{aligned} \tag{9}$$

Δ is the value of spin-orbit interaction. In the matrix ($r > a$), the solutions of the equations can be represented using modified Bessel functions of the second kind for even and odd states:

$$\begin{aligned}
 R_{h1}^{j+}(r) &= c_1 K_{j+1/2}(k_l r) + c_2 K_{j+1/2}(k_h r) + c_3 K_{j+1/2}(k_s r), \\
 R_{h2}^{j+}(r) &= -c_1 \sqrt{\frac{3(2j-1)}{2j+3}} K_{j-3/2}(k_l r) + c_2 \sqrt{\frac{2j+3}{3(2j-1)}} K_{j-3/2}(k_h r) - c_3 \sqrt{\frac{3(2j-1)}{2j+3}} K_{j+3/2}(k_s r), \\
 R_s^{j+}(r) &= c_1 \sqrt{\frac{j}{2j+3}} \frac{2\varepsilon-(\gamma_1+2\gamma)k_l^2}{\gamma k_l^2} K_{j+1/2}(k_l r) + c_3 \sqrt{\frac{j}{2j+3}} \frac{2\varepsilon-(\gamma_1+2\gamma)k_s^2}{\gamma k_s^2} K_{j+1/2}(k_s r),
 \end{aligned} \tag{10}$$

$$\begin{aligned}
 R_{h1}^{j-}(r) &= c_4 \sqrt{2j-1} K_{j-1/2}(k_l r) + c_5 \sqrt{2j-1} K_{j-1/2}(k_h r) + c_6 \sqrt{2j-1} K_{j-1/2}(k_s r), \\
 R_{h2}^{j-}(r) &= c_4 \sqrt{3(2j+3)} K_{j+3/2}(k_l r) - c_5 \sqrt{\frac{2j-1}{3(2j+3)}} K_{j+3/2}(k_h r) + c_6 \sqrt{3(2j+3)} K_{j+3/2}(k_s r), \\
 R_s^{j-}(r) &= c_4 \sqrt{j+1} \frac{(\gamma_1+2\gamma)k_l^2-2E}{\gamma k_l^2} K_{j-1/2}(k_l r) + c_6 \sqrt{j+1} \frac{(\gamma_1+2\gamma)k_s^2-2E}{\gamma k_s^2} K_{j-1/2}(k_s r),
 \end{aligned} \tag{11}$$

The squares of wave vectors k_l, k_h, k_s are obtained from the formula (9) by substitution $E \rightarrow E - U_{0,h} \gamma_1 \rightarrow \gamma_1^H$, $\gamma \rightarrow \gamma^H$, $\Delta \rightarrow \Delta^H$. γ, γ_1 - are the Luttinger parameters which set the effective masses of heavy and light holes:

$$m_l = m_0/(\gamma_1 + 2\gamma), \quad m_h = m_0/(\gamma_1 - 2\gamma),$$

$$\begin{cases} \gamma_1, & r \leq \alpha, \\ \gamma_1^H, & r > \alpha, \end{cases} \quad \begin{cases} \gamma, & r \leq \alpha, \\ \gamma^H, & r > \alpha. \end{cases}$$

m_0 - is free-electron mass.

If in formulas (7) - (11) the value of Δ is very large, then we obtain the results, which describe multiband hole model in the case of strong spin-orbit interaction (so-called 4-band model) which doesn't take into account the spin-orbital band. If we assume that $m_l = m_h$ and Δ is very large, then we get single band model.

To account the deformation in (7)-(11), the substitution $U_{0,h} \rightarrow U_{o,h} + U_{o,d,h}$ should be done. When we use the boundary condition [23] and normalize condition the hole energy spectrum can be calculated with

take into account the QD-matrix deformation. Polarization charges can be accounted in the perturbation theory.

II. Results

Specific calculations have been performed for heterosystem InAs/GaAs. The parameters are given in table 1. We have proposed the model which accounts for the polarization charges at the QD surface and deformation of the QD and matrix.

Table 1.

The effective masses			
	$m^{(1)}$	$m^{(2)}$	U_0
Electron	0.023	0.067	0.83
heavy hole	0.41	0.51	0.262
light hole	0.026	0.082	0.33

In fig. 1 shows the dependence of the electron energy on the QD radius without polarization and deformation (curve 1), with polarization (curve 2), with deformation (curve 3), with both polarization and deformation (curve 4). We see that for an electron, the energy with only polarization is the highest, and only with deformation is the lowest in compare without them. If we consider the energy with both polarization and deformation, it can be seen that the effects of deformation are stronger for the electron than the effects of polarization. This can be explained as follows: large constants of the hydrostatic deformation potential for electrons and a small difference between the values of the dielectric constant of the QD and the matrix.

In fig. 2 shows the dependence of the heavy hole energy on the radius without polarization and deformation (curve 1), with polarization (curve 2), with deformation (curve 3), and also with polarization and deformation (curve 4). We can see that for the hole the energy plot with only polarization is the highest. And only with deformation is the lowest. But for a hole, the deformation effects are weaker than the polarization effects. The reason for this is the smaller values of the constants of the hydrostatic deformation potential of the holes. And in total energy are lager (curve 4 is higher than curve 1).

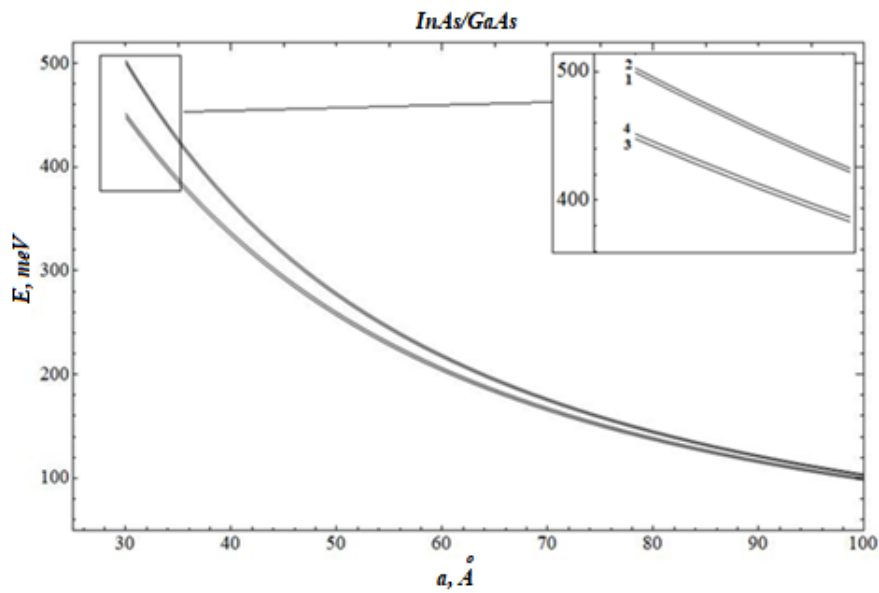


Fig.1. Dependence of the electron ground state energy on the radius of the QD:

- 1 – without taking into account polarization and deformation effects;
- 2 – with account only polarization charges;
- 3 – with account only deformation;
- 4 – with account both polarization and deformation.

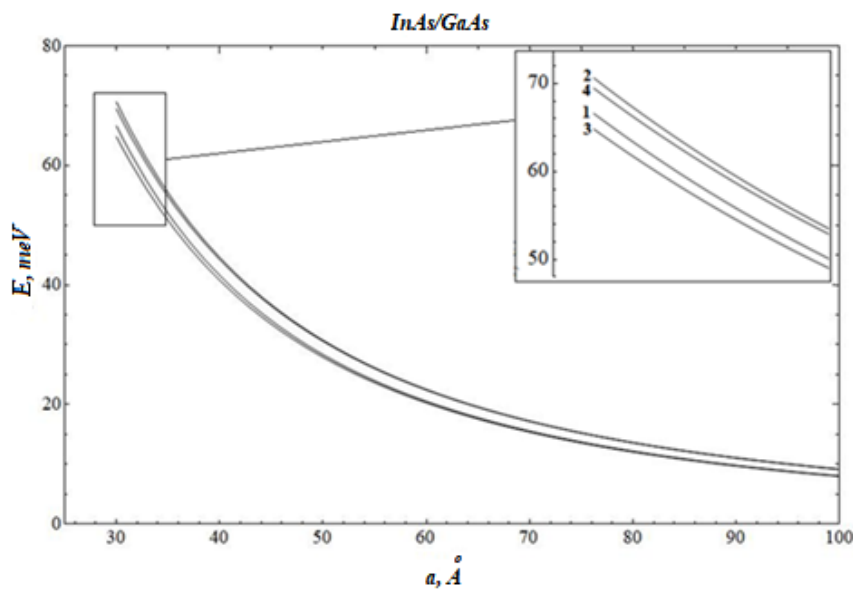


Fig.2. Dependence of the heavy hole ground state energy on the radius of the quantum dot:

- 1 – without taking into account polarization and deformation effects;
- 2 – with account only polarization charges;
- 3 – with account only deformation;
- 4 – with account both polarization and deformation.

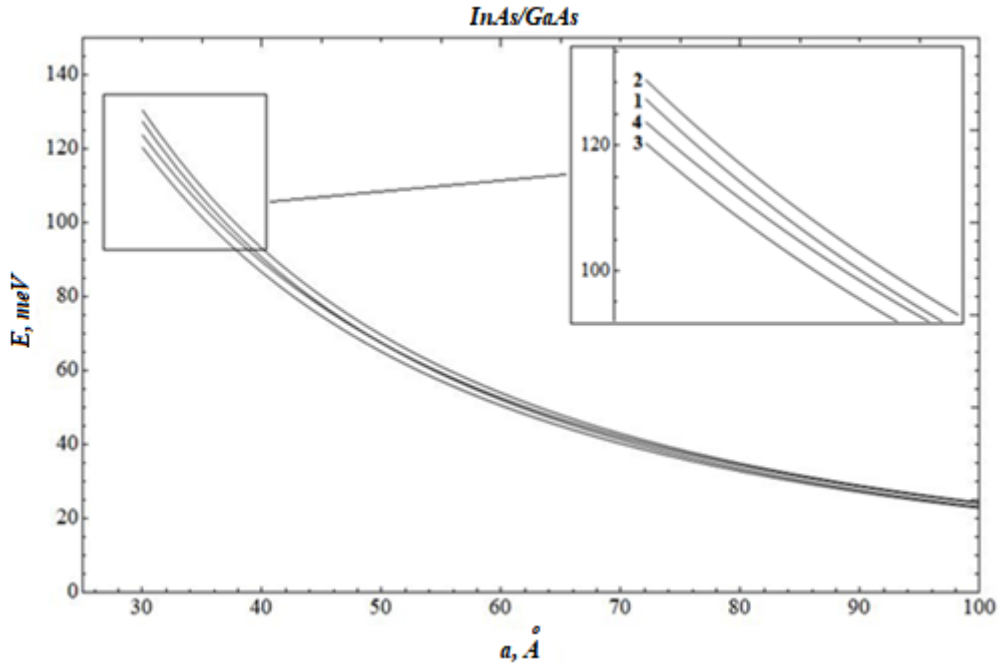


Fig.3. Dependences of ground state hole energies on the QD radius in the 4-band model approximation: 1 – without taking into account polarization and deformation effects; 2 – with account only polarization charges; 3 – with account only deformation; 4 – with account both polarization and deformation.

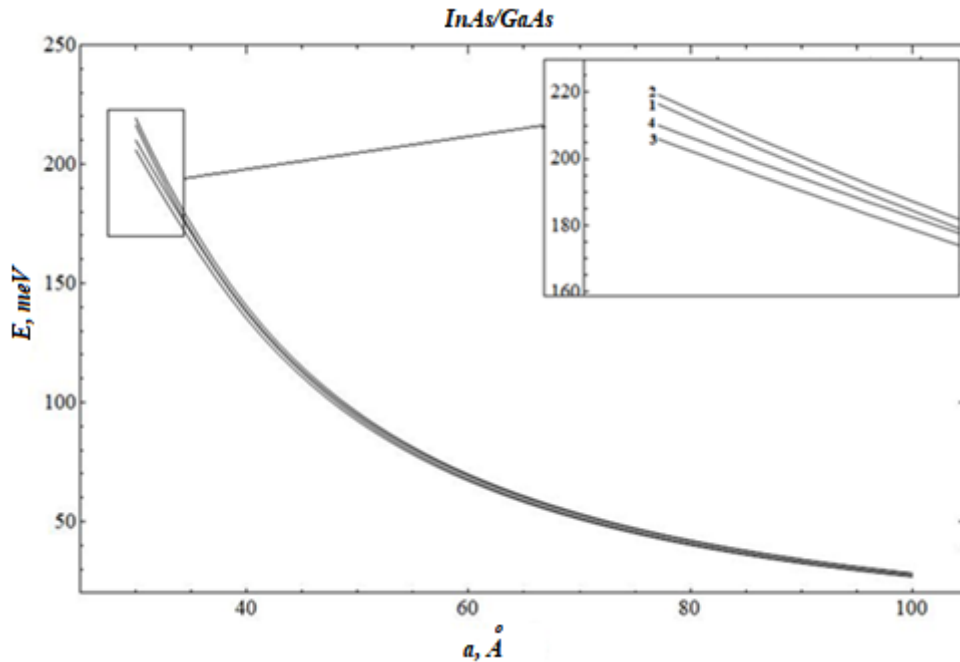


Fig.4. Dependences of ground state hole energies on the QD radius in the 6-band approximation: 1 – without taking into account polarization and deformation effects; 2 – with account only polarization charges; 3 – with account only deformation; 4 – with account both polarization and deformation.

Fig. 3 and fig. 4 show the dependences of the energies on the radius in the 4-band and 6-band approximation. The effects of deformation and polarization are similar to those of an electron, but they are different in magnitude. That is why we compare energies in all presented model for hole (fig. 5). It shows the dependence of the hole energy of various QD radius, taking into account both polarization and deformation. Curve 1 is responsible for the electron, curves 2 and 5 are energies of the light and heavy hole, curve 3 and 4 describe the hole energy in the 4-band and

6-band models, respectively. We can see that the energy for the hole is lower than that for the electron. It caused by effective masses, which for the electron is larger. Also, we have been noted, that in the case of the model with intermediate spin-orbit interaction (6-band model) the energies are larger than in the 4-band model (with large spin-orbit interaction, when spin-off band are neglected). Those result obtained when polarization and deformation are accounted. If polarization and deformation are neglected, the hole energy in the 6-band model are smaller

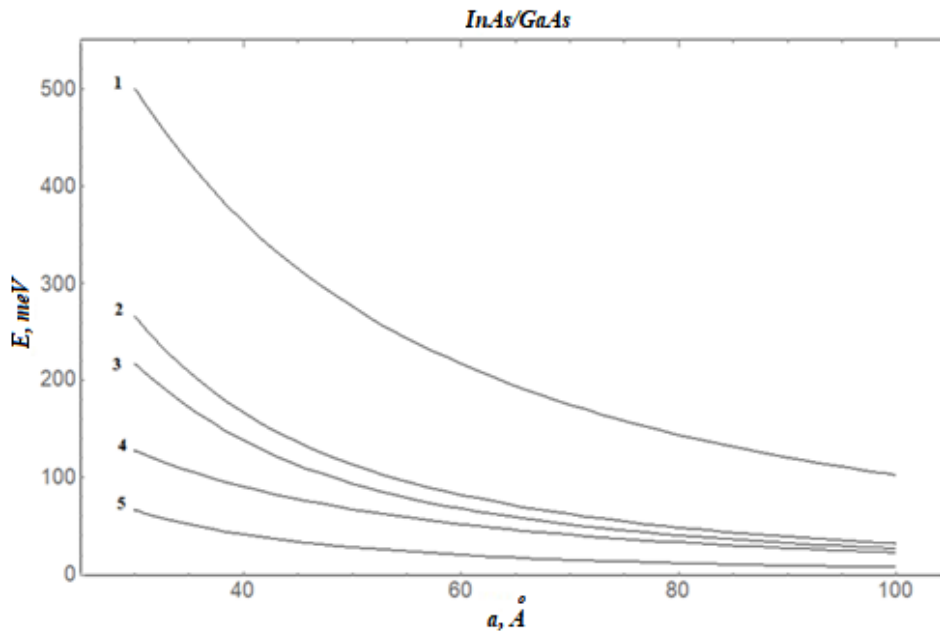


Fig.5. Dependence of ground state energy on QD radius for: 1 – for electron; 2 – singleband model for light hole; 3 – 6-band approximation model for hole; 4 – 4-band approximation model for hole; 5 – singleband model for heavy hole.

than 4-band [23]. Those results for hole are caused by the larger influence of the polarization in the 6-band model than deformation.

Conclusions

In this paper for InAs/GaAs heterosystem we perform calculation of electron and hole energies in single and multiband models with account both QD-matrix deformation and polarization charges on the surface. For electron the deformation effects are stronger. For holes the polarization are stronger. If we compare hole models, the deformation and polarization are partially compensated, but in the total effect the polarization is

stronger (curves 4 are higher than 2 in fig.2-3) in all models. Also, in the 6-band model total hole energies (with account polarization and deformation) are larger than in the case of 4-band model for all QD radiuses, especially for small QD radiuses the difference is signified. For large QD radiuses the difference is vanished.

Bilynskiy I.V. – Doctor of Physical and Mathematical Sciences, Professor of Physics Department;
Leshko R.Ya. – Candidate of Physical and Mathematical Sciences, docent of Physics Department;
Bandura H.Ya. – PhD student of Drohobych Ivan Franko State Pedagogical University.

- [1] J.B. Xia and J.B. Li, *Electronic structure of quantum spheres with wurtzite structure*, Phys. Rev. B, 60, 11 540 (1999); <https://doi.org/10.1103/PhysRevB.60.11540>.
- [2] A. Lochmann, E. Stock, O. Schulz, F. Hopfer, D. Bimberg, V. Haisler, A. Toporov, A. Bakarov, and A. Kalagin, *Electrically driven single quantum dot polarised single photon emitter*, Electron. Lett., 42, 774 (2006); <https://doi.org/10.1049/el:20061076>.
- [3] M. Scholz *et al.*, Non-classical light emission from a single electrically driven quantum dot, Opt. Express, 15, 9107 (2007); <https://doi.org/10.1364/OE.15.009107>.
- [4] I. Bilynskiy, R. Leshko, & H. Bandura, *Influence of quantum dot shape on energy spectra of three-dimensional quantum dots superlattices*, Physics and Chemistry of Solid State, 21(4), 584 (2020); <https://doi.org/10.15330/pcss.21.4.584-590>.
- [5] O. O. Dan'kiv, R. M. Peleshchak, *Strain-renormalized energy spectra of electrons and holes in InAs quantum dots in the InAs/GaAs heterosystem*, Technical Physics Letters, 31, 691 (2005);
- [6] I. D. Rukhlenko *et al.*, *Kinetics of pulse-induced photoluminescence from a semiconductor quantum dot*, Opt. Express 20, 27612 (2012); <https://doi.org/10.1364/OE.20.027612>.
- [7] A.S. Baimuratov, V.K. Turkov, I.D. Rukhlenko, A.V. Fedorov, *Shape-induced anisotropy of intraband luminescence from a semiconductor nanocrystal*, Opt. Lett., 37, 4645 (2012); <https://doi.org/10.1364/OL.37.004645>.
- [8] D. Press, T.D. Ladd, D. P. Y. Yamamoto, B. Zhang, *Complete quantum control of a single quantum dot spin using ultrafast optical pulses*, Nature, 456, 218 (2008); <https://doi.org/10.1038/nature07530>.

- [9] A.V. Baranov, A.V. Fedorov, I.D. Rukhlenko, Y. Masumoto, *Intraband carrier relaxation in quantum dots embedded in doped heterostructures*, Phys. Rev. B, 68, 205318 (2003); <https://doi.org/10.1103/PhysRevB.68.205318>.
- [10] A.J. Shields, *Semiconductor quantum light sources*, Nat. Photon., 1, 215 (2007); <https://doi.org/10.1038/nphoton.2007.46>.
- [11] K.J. Vahala, *Optical microcavities*, Nature, 424, 839 (2003); <https://doi.org/10.1038/nature01939>.
- [12] V.I. Klimov, A.A. Mikhailovsky, S. Xu, A. Malko, *Optical gain and stimulated emission in nanocrystal quantum dots*, Science, 290, 314 (2000); <https://doi.org/10.1126/science.290.5490.314>.
- [13] Z.L. Yuan et al., *Electrically Driven Single-Photon Source*, Science, 295, 102 (2002); <https://doi.org/10.1126/science.1066790>.
- [14] A.J. Bennett et al., *Microcavity single-photon-emitting diode*, Appl. Phys. Lett., 86, 181102 (2005); <https://doi.org/10.1063/1.1921332>.
- [15] P. Michler et al., *A Quantum Dot Single-Photon Turnstile Device*, Science, 290, 2282 (2000); <https://doi.org/10.1126/science.290.5500.2282>.
- [16] K. Tanabe, K. Watanabe, Y. Arakawa, *III-V/Si hybrid photonic devices by direct fusion bonding*, Scientific Rep., 2, 349 (2012); <https://doi.org/10.1038/srep00349>.
- [17] J. Jasieniak, B.I. MacDonald, S. E. Watkins, P. Mulvaney, *Solution-processed sintered nanocrystal solar cells via layer-by-layer assembly*, Nano Lett., 11(7), 2856 (2011); <https://doi.org/10.1021/nl201282v>.
- [18] I. Gur, N.A. Fromer, M.L. Geier, A.P. Alivisatos, *Air-stable all-inorganic nanocrystal solar cells processed from solution*, Science, 310, 462 (2005); <https://doi.org/10.1126/science.1117908>.
- [19] P. Prabhakaran, W.J. Kim, K.-S. Lee, P.N. Prasad, *Quantum dots (QDs) for photonic applications*, Opt. Mater. Express, 2, 578 (2012); <https://doi.org/10.1364/Ome.2.000578>.
- [20] S.A. McDonald et al., *Solution-processed PbS quantum dot infrared photodetectors and photovoltaics*, Nat. Mater., 4, 138 (2005); <https://doi.org/10.1038/nmat1299>.
- [21] O.L. Lazarenkova, A.A. Balandin, *Miniband formation in a quantum dot crystal*, Journal of Applied Physics, 89(10), 5509 (2001); <https://doi.org/10.1063/1.1366662>.
- [22] O.L. Lazarenkova, A.A. Balandin, *Electron and phonon energy spectra in a three-dimensional regimented quantum dot superlattice*, Phys. Rev. B, 66, 245319 (2002); <https://doi.org/10.1103/PhysRevB.66.245319>.
- [23] I. Bilynskiy, R. Leshko, H. Metsan, I. Shevchuk, *Hole States in Spherical Quantum Nanoheterosystem with Intermediate Spin-Orbital Interaction*, Physics and Chemistry of Solid State, 20(3), 227 (2019); <https://doi.org/10.15330/pcss.20.3.227-233>.
- [24] G.B. Grigoryan, E.M. Kazaryan, A.L. Efros, T.B. Yazeva, *Solid State Phys.*, 32(6), 1722 (1990)
- [25] J.M. Luttinger and W. Kohn, *Motion of Electrons and Holes in Perturbed Periodic Fields*, Phys. Rev., 97 (4), 869 (1955).
- [26] E. Menéndez-Proupin and C. Trallero-Giner, *Electric-field and exciton structure in CdSe nanocrystals*, Phys. Rev. B, 69, 125336 (2003); <https://doi.org/10.1103/PhysRevB.69.125336>.
- [27] R.Ya. Leshko, I.V. Bilynskiy, *The hole energy spectrum of an open spherical quantum dot within the multiband model*, Physica E, 1(110), 10 (2019); <https://doi.org/10.1016/j.physe.2019.01.024>.

I.V. Білінський, Р.Я. Лешко, Г.Я. Бандура

Електронно-дірковий спектр з урахуванням деформації та поляризації у квантовій точці гетероструктури InAs/GaAs

Дрогобицький державний педагогічний університет імені Івана Франка, м. Дрогобич, Україна,
galinka.bandura@gmail.com

У роботі досліджено сферичні квантові точки InAs в матриці GaAs. Енергії електронів і дірок в одно- і багатозонних моделях (із сильною, слабкою і проміжною спін-орбітальною взаємодією) розраховано з урахуванням як деформації матриці квантових точок, так і поляризаційних зарядів на поверхні квантових точок. Розглянуто залежність енергетичних рівнів електронів і дірок від радіуса квантової точки. Показано, що для електрона ефекти деформації сильніші, ніж поляризація. Для дірок ці ефекти протилежні. Енергії електронів і дірок порівнювалися в усіх моделях наближення.

Ключові слова: обмінна взаємодія, деформація, 4-зонна модель або багатозонна діркова модель, 6-зонна модель, поляризаційні заряди, напружений гетеросис.

R.G. Abaszade¹, M.B. Babanli¹, V.O. Kotsyubynsky², A.G. Mammadov¹, E. Gür³,
O.A. Kapush⁴, M.O. Stetsenko^{5,4}, R.I. Zapukhlyak²

Influence of gadolinium doping on structural properties of carbon nanotubes

¹Azerbaijan State Oil and Industry University, Baku, Azerbaijan, abaszada@gmail.com

²Vasyl Stefanyk Precarpathian National University, Ivano-Frankivsk, Ukraine, kotsyubynsky@gmail.com

³Eskisehir Osmangazi University, Eskisehir 26040, Turkey, emregur@ogu.edu.tr

⁴V. Lashkaryov Institute of Semiconductor Physics, NASU, Kyiv, Ukraine, savchuk-olja@ukr.net

⁵Key Laboratory of Optoelectronic Devices and Systems, College of Physics and Optoelectronic Engineering, Shenzhen University, Shenzhen, PR China, stetsenkomax@gmail.com

The paper presents an analysis of SEM, EDX, Raman scattering, and FTIR of Gadolinium-doped multi-walled carbon nanotubes obtained by hydrothermal method. The morphological characteristics of the materials were studied and their compositions were analyzed. Hydrothermal doping of MWCNTs with Gd causes the formation of 3D network architecture and sharply increases the content of oxygen surface functionality. An unidentified intense broad peak for Gd-doped material at 2940 cm⁻¹ was observed. The defect state of Gd-doped MWCNTs was studied by Raman spectroscopy.

Keywords: carbon nanotube, gadolinium, SEM, EDX, Raman analysis, FTIR.

Received 10 November 2022; Accepted 9 March 2023.

Introduction

Gadolinium-doped multi-walled carbon nanotubes (MWCNTs) are a type of nanomaterial that has attracted significant interest due to their potential applications in various fields. The doping of gadolinium ions onto the surface of MWCNTs has been studied for potential use in biomedical applications. The incorporation of gadolinium ions onto the surface of MWCNTs has been shown to enhance the magnetic resonance imaging (MRI) contrast of the nanotubes, making them useful for biomedical imaging [1] and drug delivery [2]. Additionally, gadolinium-doped MWCNTs have also been studied for their potential in cancer therapy [3]. Gd-doped multi-walled carbon nanotubes also have shown potential as a sensor material due to their unique properties, including high surface area, chemical stability, and sensitivity to various gases, including hydrogen, ammonia, and nitrogen dioxide [4]. The sensitivity of the material can be tuned by adjusting the

concentration of Gd dopant amounts and the surface functionalization of the nanotubes. By functionalizing the nanotubes with biomolecules such as antibodies or enzymes, the material can detect specific biomarkers or pathogens in biological samples [5].

Overall, the unique properties of gadolinium-doped MWCNTs make them a promising candidate for various applications. However, further research is needed to optimize the material properties depending on the synthesis method. There are several approaches for synthesizing gadolinium-doped MWCNTs, such as co-precipitation, hydrothermal method, chemical vapor deposition (CVD), arc discharge, laser ablation, and chemical functionalization.

The «common synthesis» methods (co-precipitation, chemical vapor deposition) involves the precipitation of gadolinium ions on the carbon nanotubes during the high-temperature catalyst-supported decomposition of carbon source in a pressurized vessel at high temperatures and pressures. Another approach of Gd-doped MWCNTs

obtaining by hydrothermal route allow using the commercial or previously synthesized MWCNTs [6]. The advantage of hydrothermal approach is the simply control of the amount of Gd dopant by adjusting the concentration of gadolinium precursors in the reaction chamber. The doping of MWCNTs with Gd can be realized at respectively low temperatures [7] using previously tested methods for doping graphene materials [8].

This article presents the results of gadolinium-doped MWCNTs obtained using hydrothermal method. A feature of the presented research is the use of a reaction temperature of 220 °C (close to the temperature of Teflon decomposition). The resulting materials were characterized using various techniques, including scanning electron microscopy (SEM), FTIR, and Raman spectroscopy.

I. Experimental details

Multi-walled carbon nanotubes were prepared accordingly to the next protocol. Ferrocene (0.3 g) and thiophene (0.6 ml) were dissolved in 15 ml of xylene to prepare the catalyst precursor solution. The solution was added to a flask and heat it at 100 °C for 1 h under stirring to evaporate the solvent and obtain a dry catalyst precursor. The catalyst precursor was loaded into a quartz vessel and transferred to the center of a quartz tube furnace preheated to 900 °C under an argon gas flow. Once the furnace reaches the desired temperature ethanol was introduced into the furnace using a syringe pump at a flow rate of 0.5 ml/min for 20 min. After the furnace cooled down to room temperature under argon flow the quartz vessel was removed from the furnace and MWCNTs were treated with a mixture of HCl and HNO₃ to remove any residual catalyst. The MWCNTs were rinsed with deionized water several times to remove any residual acids. At the final stage obtained product was washed with ethanol and dried at room temperature for 12 h.

Gadolinium-doped multi-walled carbon nanotubes (Gd-MWCNTs) was obtained using a hydrothermal approach.

Gadolinium nitrate hexahydrate (0.1 g) was dissolved in 50 ml of deionized water and stirred for 30 min to prepare the solution. 1 g of previously obtained MWCNTs was added to the Gd(NO₃)₃·6H₂O solution and sonicated for 1 h to obtain a homogeneous mixture. NaOH (2.5 g) was added to the MWCNTs / Gd(NO₃)₃·6H₂O mixture and stirred for 1 h to adjust the pH to about 12. The obtained colloidal solution was transferred to a Teflon-lined stainless steel autoclave and heat it at 220 °C for 12 h. After autoclave cool down to room temperature precipitate was filtered and a black solid product was collected. The product was rinsed with deionized water and ethanol several times to remove residual impurities. The product was dried at 60-70 °C for 12 h.

The resulting MWCNTs and Gd-MWCNTs were characterized using various techniques, such as scanning electron microscopy (SEM), energy dispersive X-ray spectroscopy (EDS), and Raman spectroscopy. Raman spectra were measured on a confocal Raman spectrometer Nanfinder 30 (Tokyo Inst., Japan) with a 532 nm Nd:YAG laser (resolution about 0.5 cm⁻¹). The laser irradiation

power was less than 1 mW/cm², which made it possible to avoid local overheating of the samples. SEM and EDX analysis was carried out using a Scanning Electron Microscope by JEOL (Oxford Instruments, 15 kV SEI, WD equals 4,5mm). Fourier-IR absorption spectra of carbon nanotube samples were obtained in the range of 4000-1000 cm⁻¹ on a Varian-640IR IR spectrometer. The mixture of MWCNTs or Gd-MWCNTs and KBr (1:300 mass ratio) after vibrating milling was pressed into pellets (50±100 μm) and measured in the transmission mode.

II. Results and discussion

SEM investigations provide valuable information about the morphology as well as structure of MWCNTs, which is useful for understanding their physical and chemical properties and verifying the synthesis results. Figure 1, a-b shows the SEM of MWCNTs and Gd-MWCNTs samples, respectively. Both doped and non-doped MWCNTs show a foam-like morphology. The nanotube diameters in a range of 15-20 nm while the length could reach tens of micrometers were observed. The decrease of average diameter to 12-15 nm for Gd-doped MWCNTs is observed with simultaneous growth of tortuous compared to the non-doped sample. Gd-MWCNTs are wavy, entangled, interconnected with each other, and assembled into 3D network architecture. Similar morphology was analyzed in [9].

Table 1.
EDX data of elemental composition of MWCNTs and Gd-MWCNTs samples

No.	Sample	C Weight %	O Weight %	Gd Weight %
1.	MWCNTs	100	0	0
2.	Gd-MWCNTs	90	9,5	0,5

EDX analysis of pure MWCNTs shows the presence of carbon only with the trace Si (Fig. 1a, Tab.1). As well as the elemental analysis of the Gd-doped MWCNTs demonstrates the presence of C, O, and Gd which is an indication of surface functionalization with an oxygen-containing species as a side effect of the decoration with Gd (Fig. 1b, Tab.1). The presence of Si is a result of thermal treatment in a ceramic vessel. The additional possible reason for oxygen present is the presence of Gd₂O₃ clusters on the surface of the MWCNTs but it's only a minor factor taking into account the mass ratio of oxygen and gadolinium (9.5 and 0.5 mass %, respectively).

FTIR analysis was used to probe the surface functional group's presence for MWCNTs and Gd-MWCNTs samples (Fig.2). The broad peaks observed around 3400 and 1610 cm⁻¹ correspond to the O-H stretching and bending vibration of hydroxyl groups [10]. At the same time, these peaks are completely missing for Gd-MWCNTs which indicates the absence of surface hydroxyl functionalities. The sharp band at 1350 cm⁻¹ also is attributed to the presence of hydroxyl groups (-OH) on the MWCNT surface (the presence of carboxylate groups -COOH is also possible) [11].

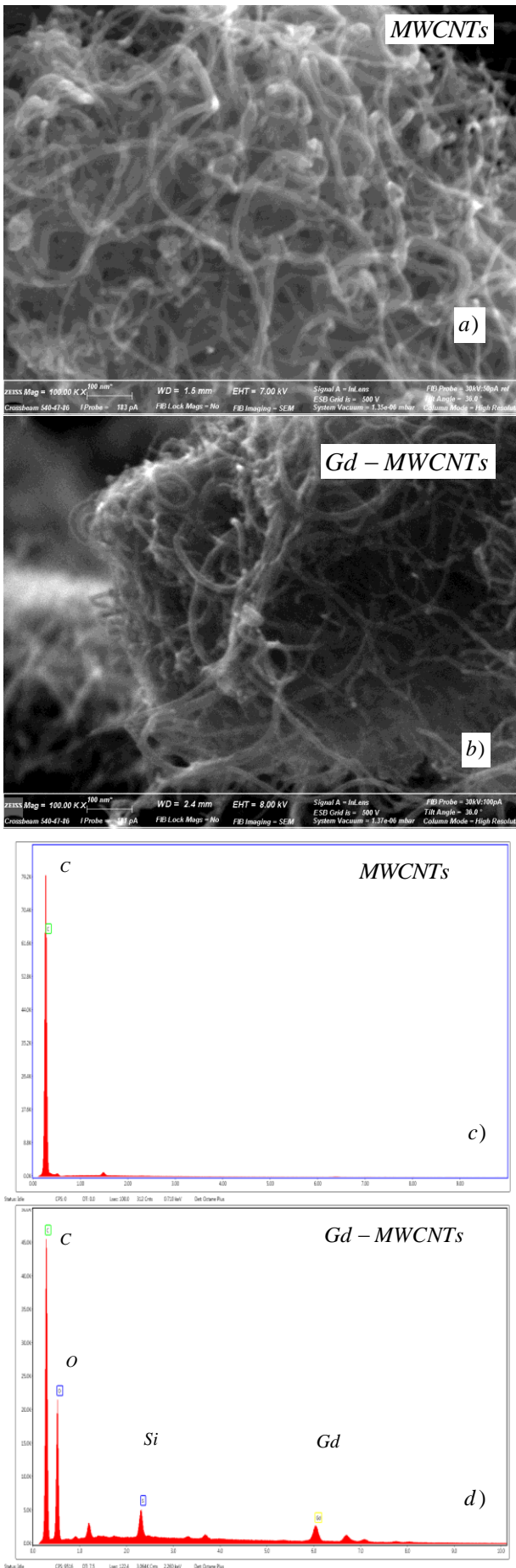


Fig. 1. SEM images (a-b) and EDX spectra (c-d) of MWCNTs and Gd-MWCNTs samples.

The peak at 1350 cm^{-1} is only traced for Gd-MWCNTs. Two intense broad peaks for this Gd-doped material are observed around 2940 and around 1900 cm^{-1} (Fig. 2). The first one can correspond to the overlapped peaks due to the presence of $\text{C}(\text{sp}^3)\text{-H}$ bonds [12]. The other characteristic is not typical for MWCNT and can be attributed to the structural changes induced by the Gd-doping process.

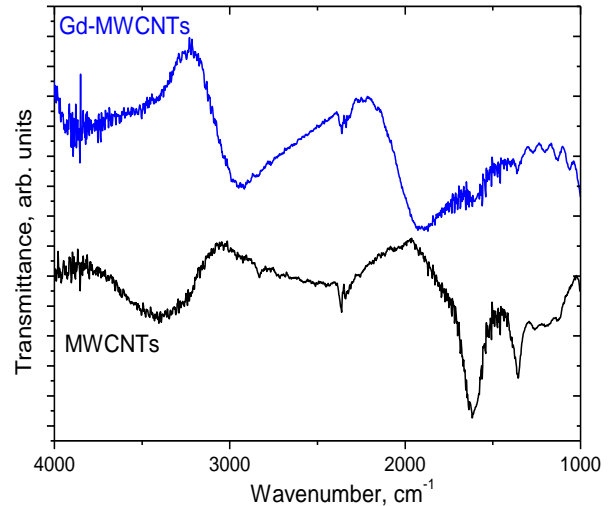


Fig.2. FTIR spectra of MWCNTs and Gd-MWCNTs samples.

For the characterization of the defect structure of MWCNTs and investigation of the influence of Gd doping the Raman spectroscopy was used [13]. Raman scattering spectra for MWCNTs and Gd-MWCNTs samples and also the Lorentz functions deconvolution results are presented in Fig.3.

The spectra consist of two intensive G and D peaks. The G-peak is a first-order high-frequency mode E_{2g} . Its feature for MWCNTs is splitting into two bands: G and its small high-frequency shoulder D' . The last line is associated with disorientation in carbon nanotubes [14]. Disordering and defects in nanotubes are also observed in bands I, D, and D'' . The I band is observed for nanotubes with a highly disordered structure and is recorded as a low-frequency shoulder of the D band [15]. Despite the D and D'' bands being associated with the presence of structural defects, they have different origins. The D'' band takes place when the packaging of a regular layer of graphite is broken by the defects (breaks of graphene sheets in nanotubes and graphene flakes). The D band is associated with lattice disorder or finite-size effects [16]. The analysis of Raman spectra shows that the ratio of intensities of the G and D peaks (I_G/I_D) increases after Gd doping, which indicates a decrease in defects [17] in MWCNT. The 2D and $D+G$ lines were determined as second-order overtones, the presence of which is characteristic of such structures.

The peak intensity ratio I_G/I_D can indicate the level of disorder in graphite structure. Based on a unique opportunity from 2D peak for the characterization of graphene layers number the increasing ratio I_{2D}/I_D for Gd-doped MWCNT can indicate a decrease in the number of graphene sheets.

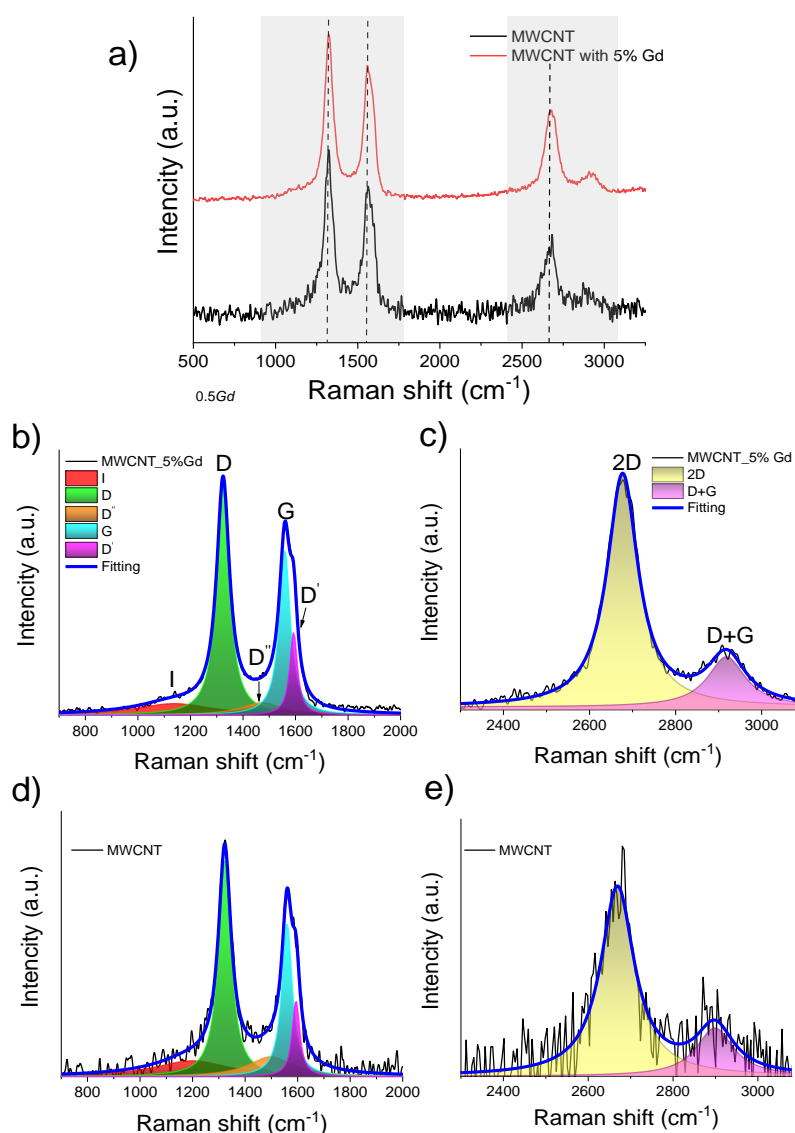


Fig.3. Raman spectra (a) and corresponding results of spectra deconvolution (c-e) for MWCNTs and Gd-MWCNTs samples.

Table 2.

The Raman Spectra Parameters of MWCNTs and Gd-MWCNTs samples

Raman mode parameters, cm ⁻¹	MWCNT	5% Gd doped MWCNT
I (peak position)	1198	1138.2
FWHM	343.8	349
D (peak position)	1322.4	1324.1
FWHM	57.9	58.9
D''(peak position)	1496.9	1472.9
FWHM	203.5	185.9
G (peak position)	1559	1559.3
FWHM	48.5	51.2
D' (peak position)	1594.1	1593
FWHM	35.2	35.5
2D (peak position)	2668.9	2676.9
FWHM	95.9	87.5
D+G (peak position)	2898.5	2918.3
FWHM	106.5	107.5
I _G /I _D	0.59	0.63
I _G /I _{D'}	2.77	2.87
I _{2D} /I _G	1.18	1.26

The properties of Raman scattering analyzes of the studied samples were analyzed and, as can be seen from the results of the studies, changes in the intensities in the scattering spectra and displacement of the peaks at higher frequencies are observed. The change of the peaks in the Raman scattering spectrum is related to the change in the concentration of defects.

The fitting procedure of D and G bands with Lorentzians peaks using OriginPro software allow to calculate the ratio of I_D and I_G integral intensities. These data were used for the average size of graphitic fragments along the basal plane (002) estimate [18]: $L(nm) = (2.4 \times 10^{-10}) \lambda_{0.5Gd}^4 \left(\frac{I_D}{I_G}\right)^{-1}$, where λ is the laser excitation wavelength. In all cases, the average lateral size of graphitic fragments for both samples are close to 20.0±0.3 nm so the doping procedure probably doesn't affect dramatically on the structural properties of the materials

Conclusion

Gd-doped multiwall carbon nanotubes (average Gd content of 0.5 mass %) were obtained by hydrothermal approach (220 °C for 12 h) on the base of previously synthesized MWCNTs (catalytic ethanol decomposition at 900 °C in argon gas flow was used for CNT synthesis). Hydrothermal doping of MWCNTs with Gd causes the formation of 3D network architecture and the presence of oxygen-contained surface functionality (oxygen content of about 9 mass %). Simultaneously the hydroxyl group content for doped material is insignificant compared to the origin MWCNTs. The unidentified intense broad peak for Gd-doped material observed around 2940 cm⁻¹ can be the result of both doping- and hydrothermal treatment-

induced structural changes. The growth of defect concentration for Gd-doped MWCNTs was observed by Raman spectroscopy, but the changes in average lateral sizes of graphene crystallites (along (002) basal plane) were not observed.

Abaszade R.G. – Associate professor, PhD;
Babanli M.B. – Doctor of technical sciences, professor
Kotsyubynsky V.O. – Doctor of sciences, professor;
Mammadov A.G. – Doctor of technical sciences, professor;
Gür E. – Professor, PhD;
Kapush O.A. – Associate professor, PhD;
Stetsenko M.O. – Research, Assistant professor, PhD;
Zapukhlyak R.I. – PhD, Senior Researcher.

- [1] Y. Cao, L. Xu, Y. Kuang, D. Xiong, R. Pei, *Gadolinium-based nanoscale MRI contrast agents for tumor imaging*, Journal of Materials Chemistry B, 5(19), 3431 (2017); <https://doi.org/10.1039/C7TB00382J>.
- [2] S. K. Debnath, R. Srivastava, *Drug delivery with carbon-based nanomaterials as versatile nanocarriers: progress and prospects*, Frontiers in Nanotechnology, 3, 644564 (2021); <https://doi.org/10.3389/fnano.2021.644564>.
- [3] Y. Hwang, S. H. Park, J. W. Lee, Applications of functionalized carbon nanotubes for the therapy and diagnosis of cancer, *Polymers*, 9(1), 13 (2017); <https://doi.org/10.3390/polym9010013>.
- [4] B. Liu, X. Liu, Z. Yuan, Y. Jiang, Y. Su, J. Ma, H. Tai, *A flexible NO₂ gas sensor based on polypyrrole/nitrogen-doped multiwall carbon nanotube operating at room temperature*, Sensors and Actuators B: Chemical, 295, 86 (2019); <https://doi.org/10.1016/j.snb.2019.05.065>.
- [5] M. Pirzada, Z. Altintas, *Nanomaterials for healthcare biosensing applications*, Sensors, 19(23), 5311 (2019); <https://doi.org/10.3390/s19235311>.
- [6] F. Du, L. Zhang, L. Zhang, M. Zhang, A. Gong, Y. Tan, S. Zou, *Engineered gadolinium-doped carbon dots for magnetic resonance imaging-guided radiotherapy of tumors*, Biomaterials, 121, 109 (2017); <https://doi.org/10.1016/j.biomaterials.2016.07.008>.
- [7] R. G. Abaszade, O. A. Kapush, S. A. Mamedova, A. M. Nabiyev, S. Z. Melikova, S. I. Budzulyak, *Gadolinium doping influence on the properties of carbon nanotubes*, Physics and Chemistry of Solid State, 21(3), 404 (2020); <https://doi.org/10.15330/pcss.21.3.404-408>.
- [8] R. G. Abaszade, A. G. Mamedov, I. Y. Bayramov, E. A. Khanmamedova, V. O. Kotsyubynsky, O. A. Kapush, V. M. Boychuk, E. Y. Gur, *Structural and electrical properties of sulfur-doped graphene oxide/graphite oxide composite*, Physics and Chemistry of Solid State, 23(2), 256 (2022); <https://doi.org/10.15330/pcss.23.2.256-260>.
- [9] T. Hajilounezhad, R. Bao, K. Palaniappan, F. Bunyak, P. Calyam, M. R. Maschmann, *Predicting carbon nanotube forest attributes and mechanical properties using simulated images and deep learning*, npj Computational Materials, 7(1), 134 (2021); <https://doi.org/10.1038/s41524-021-00603-8>.
- [10] M. Stetsenko, T. Margitych, S. Kryvyi, L. Maksimenko, Hassan, A.; Filonenko, S., et al. *Nanoparticle Self-Aggregation on Surface with 1,6-Hexanedithiol Functionalization*, Nanomaterials, 10, 512 (2020); <https://doi.org/10.3390/nano10030512>.
- [11] N. Abdolhi, M. Aghaei, A. Soltani, H. Mighani, E. A. Ghaemi, M. B. Javan, H. Balakheyli, *Synthesis and antibacterial activities of novel Hg (II) and Zn (II) complexes of bis (thiosemicarbazone) acenaphthenequinone loaded to MWCNTs*, Journal of Structural Chemistry, 60, 845 (2019); <https://doi.org/10.1134/S0022476619050196>.
- [12] E. Abdel-Fattah, A. I. Alharthi., T. Fahmy, *Spectroscopic, optical and thermal characterization of polyvinyl chloride-based plasma-functionalized MWCNTs composite thin films*, Applied Physics A, 125(7), 475 (2019); <https://doi.org/10.1007/s00339-019-2770-y>.
- [13] A. Sadezky, H. Muckenhuber, H. Grothe, R. Niessner, U. Pöschl, *Raman microspectroscopy of soot and related carbonaceous materials: Spectral analysis and structural information*, Carbon, 43(8), 1731 (2005); <https://doi.org/10.1016/j.carbon.2005.02.018>.
- [14] V. Datsyuk, M. Kalyva, K. Papagelis, J. Parthenios, D. Tasis, A. Siokou, C. Galiotis, *Chemical oxidation of multiwalled carbon nanotubes*, Carbon, 46(6), 833 (2008); <https://doi.org/10.1016/j.carbon.2008.02.012>.
- [15] K. Angon, *Remarks on the structure of carbon materials on the basis of Raman spectra*, Carbon, 31(4), 537 (1993); [https://doi.org/10.1016/0008-6223\(93\)90106-K](https://doi.org/10.1016/0008-6223(93)90106-K).
- [16] K. E. Kim, K. J. Kim, W. S. Jung, S. Y. Bae, J. Park, J. Choi, J. Choo, *Investigation on the temperature-dependent growth rate of carbon nanotubes using chemical vapor deposition of ferrocene and acetylene*, Chemical physics letters, 401(4-6), 459 (2005); <https://doi.org/10.1016/j.cplett.2004.11.113>.

- [17] Y. Yerlanuly, R. Y Zhumadilov, I. V. Danko, D. M. Janseitov, R. R. Nemkayeva, A. V. Kireyev, et al. *Effect of Electron and Proton Irradiation on Structural and Electronic Properties of Carbon Nanowalls*, *ACS omega*, 7(51), 48467 (2022); <https://doi.org/10.1021/acsomega.2c06735>.
- [18] V. O. Kotsyubynsky, V. M. Boychuk, I. M. Budzulyak, B. I. Rachiy, M. A. Hodlevska, A. I. Kachmar, M. A. Hodlevsky, *Graphene oxide synthesis using modified Tour method*, *Advances in Natural Sciences: Nanoscience and Nanotechnology*, 12(3), 035006 (2021); <https://doi.org/10.1088/2043-6262/ac204f>.

Р.Г. Абасзаде¹, М.Б.Бабанлі¹, В.О. Коцюбинський², А.Г. Маммадов¹, Е.Гюр³,
О.А. Капуш⁴, М.О.Стеценко^{5,4}, Р.І.Запужляк²

Вплив допування гадолінієм на структурні властивості вуглецевих нанотрубок

¹Азербайджанський державний університет нафти і промисловості, Баку, Азербайджан, abaszada@gmail.com

²Прикарпатський національний університет імені Василя Стефаника, Івано-Франківськ, Україна, kotsyubynsky@gmail.com

³Університет Ескишехир Османгази, Ескишехир, 26040, Туреччина, emregur@atauni.edu.tr

⁴Інститут фізики напівпровідників ім. В. Лашкарьова, НАНУ, Київ, Україна, savchuk-olja@ukr.net

⁵Ключова лабораторія оптоелектроніки, Коледж фізики та оптоелектроніки, Шеньчженський університет, Шеньжень, Китай, stetsenkomax@gmail.com

В роботі здійснено систематичне вивчення методами SEM, EDX, комбінаційного розсіювання та FTIR багат шарових вуглецевих нанотрубок легованих гадолінієм, отриманих з використанням гідротермального методу. Досліджено морфологічні характеристики матеріалів та проаналізовано їх склад. Гідротермальний варіант легування багат шарових вуглецевих нанотрубок гадолінієм викликає формування тримірної архітектури матеріалу та різко підвищує вміст поверхневих функціональних груп. Спостерігався неідентифікований інтенсивний широкий пік для матеріалу, легованого Gd при 2940 см⁻¹. Методом комбінаційної спектроскопії досліджено дефектний стан багат шарових вуглецевих нанотрубок легованих гадолінієм.

Ключові слова: вуглецеві нанотрубки, допування гадолінієм, SEM, EDX, Раманівська спектроскопія, FTIR.

S. Kovachov, I. Bohdanov, I. Bardus, D. Drozhcha, K. Tikhovod, A. Khrekin,
V. Bondarenko, I. Kosogov, Y. Suchikova

About synthesis mechanism of periodic oxide nanocrystallites on surface of single-crystal

Berdiansk State Pedagogical University Berdiansk, Ukraine, yanasuchikova@gmail.com

We have obtained unique periodic oxide nanocrystallites on the surface of indium phosphide. The morphological characteristics of the structures obtained and their component composition are investigated in the article. The main attention is focused on explaining the mechanism of the periodic structures, which are packed by the ‘parquet floor’ type. The mechanism based on sliding the sources of rectangular-shaped dislocation loops has been proposed. The system of the main and secondary (ingoing) dislocations that cause the formation of the steps has been considered. The mathematical interpretation of the described model has also been proposed.

Keywords: indium phosphide, nanocrystallites, periodic structures, nanowires.

Received 29 October 2022; Accepted 6 March 2023.

Introduction

The need for new “smart” materials is caused by the increasing demand for high-tech electronics [1, 2]. Composite materials have been widely used in photonic devices [3, 4]. The heterostructures are widely used as materials for lasers [5, 6]. Planar nanostructures are of the utmost interest for thin-film technologies, in particular, for the creation of light-emitting diodes [7, 8]. In recent times, the attention of researchers is focused on the materials with the surface architecture [9, 10]. Today, nanoneedles [11], nanowhiskers [12], flower-shaped structures [13], porous surfaces [14, 15], etc., are successfully synthesized. Furthermore, periodic structures are gaining in considerable popularity [16, 17]. The advantage of such structures over other types of nanostructured nanomaterials is caused by the possibility to control wavelengths, radiation angles, etc. [18, 19].

The following tasks are raised to scientists due to understanding of these trends: (1) selection of effective, inexpensive synthesis methods, which allow to create periodic nanostructures with the controlled properties [20, 21]; (2) selection of the components of the substrate/nanostructure system with well-formed

parameters [22].

Today, the synthesis methods of oxide semiconductors and their integration into substrates are being actively investigated [23 – 25]. So, the investigations are concerned with Ga₂O₃ [26, 27], In₂O₃ [28], ZnO [29], CdO [30], TiO₂ [31], etc. Such semiconductors show excellent ability for nanostructuring, as well as being chemically and thermally stable [32, 33]. Furthermore, the surface of the oxide films on the semiconductor show the passivating properties and allow extended service life of the devices [34, 35]. As a rule, the only problem when such heterostructures are formed is the mismatch of the crystal lattices, which causes a large number of stress states at the boundary of two heterostructure components [36]. On the other hand, such situation can be effectively used when structures with non-standard morphology are formed [37, 38]. In this case, the defects of the output semiconductor (substrate) are the source of the nanostructure on the surface [39]. The effective use of this phenomenon is quite a difficult task and requires a further detailed study.

In this study, we report the synthesis of the periodic structures on the surface of indium phosphide, which are packed in the “parquet floor” type. Such structures are promising for study, since periodicity can be effectively

used to create photocatalytic heterostructures and waveguides. We give a qualitative and quantitative interpretation of the mechanism of formation of the parquet oxide structure on the surface of a highly doped indium phosphide.

I. Experiment

The periodic parquet structures were formed by the combined chemical etching methods. A Teflon standard electrochemical cell was used. The cell was filled with the electrolyte. After that, the etching processes were started, with subsequent deposition of the reaction products on the sample surface. The first stage was carried out in the electrochemical anodization at a constant current density. Simple electrochemical etching without the action of a current was used at the second stage. The electrolyte solution was not changed during both stages. Table 1 shows the conditions for the chemical treatment of the samples.

Before carrying out the experiment, the samples were washed in the acetic solution and then degreased with the ethyl alcohol. Immediately after that, the experiment was started. After completion of the experiment, the samples were dried and stored in the open air.

The surface morphology was investigated using a Jeol microscope (Japan), equipped with an NCA Energy 350 spectrometer manufactured by Oxford Instruments Analytical (Great Britain). The topographic images of the synthesized nanostructure surfaces were obtained by raster electron microscopy with the use of secondary electron signals (SEI). Data on the surface inhomogeneity and composition were obtained in the back-scattered electron (BEC) mode. The energy of the electron beam was chosen in the range of (10-15) keV. The elemental composition of the samples was determined using an energy-dispersive spectrometer at an acceleration voltage of (15-20) kV and a beam current of (1-3) nA. The quantitative analysis of the chemical composition of the sample surface was performed by comparing the characteristic lines of the sample with those of standards.

II. Results

Fig. 1 shows the SEM image of InP surface after the electrochemical treatment. It can be seen that massive crystal nanowires, which are organized by “parquet floor” type, were formed on the surface. Table 2 shows the geometric sizes of the formed structures.

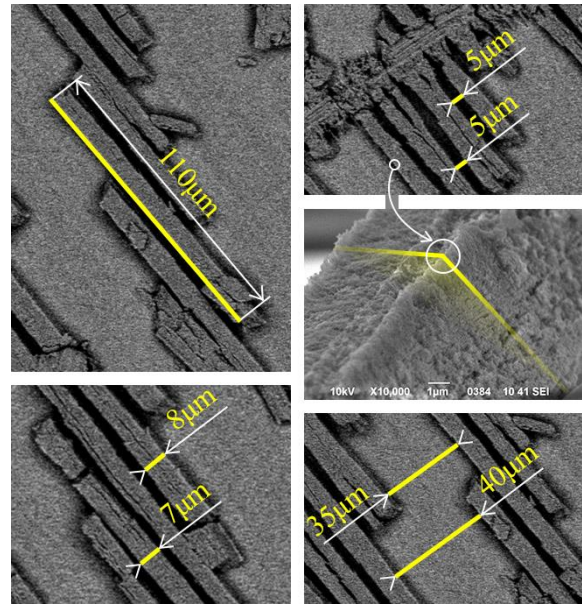


Fig. 1. SEM image of formed periodic structure on the InP surface.

Table 2.

Geometrical sizes of nanowires	
Characteristics	Size, μm
Thickness of nanowire	8-10
Height of nanowire	7-10
Length of nanowire	110-130
Distance between adjacent wires	3
Distance between “parquet layers”	20-50

Thus, it can be seen that the nanowires have the shape of a regular prism. It is interesting to note that the wires have the porous structure with a pore size of 80-120 nm.

Fig. 2 shows the results of the EDX analysis of the formed structure surface at the point on the crystallite surface. We can see that the crystallites were formed by indium oxide with a small content of phosphorus. This certainly points to the formation mechanism of the periodic nanocrystallites on the surface of the indium phosphide. The active etching of the indium and phosphorus atoms, which leads to electrolyte saturation, is observed during the first etching stage. It is followed by an alternative process, namely, the deposition of the reaction products on the surface.

Table 1.

Conditions of experiment				
Stages	Electrolyte	Current density, j , mA/cm^2	Time, min	Additional conditions
1 st stage	$\text{HF}:\text{H}_2\text{O}:\text{C}_2\text{H}_5\text{OH}=1:1:2$	150	10	Mixing of electrolyte; platinum plate was used as cathode
2 nd stage	$\text{HF}:\text{H}_2\text{O}:\text{C}_2\text{H}_5\text{OH}=1:1:2$	0	10	Room temperature, darkness

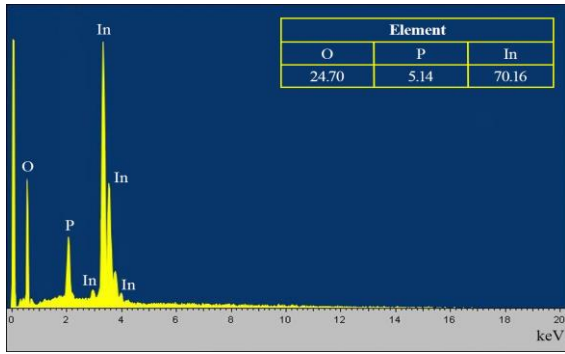


Fig. 2. The results of EDX analysis at the point on the crystallite surface.

III. Discussion

3.1 Mechanism of formation of the periodic structures on the surface of indium phosphide by “parquet floor” type

Single-crystal semiconductors, doped to the high concentrations of minor charge carriers, are characterized by a large number of the dislocations. For the experiment, we used the InP plates with the (111) surface orientation (Fig. 3a). The sources of rectangular-shaped dislocation loops, the sliding system of which can be represented as a parallelogram surface with faces along the (101) and (110) planes, will be observed in the volume of such sample (Fig. 3b).

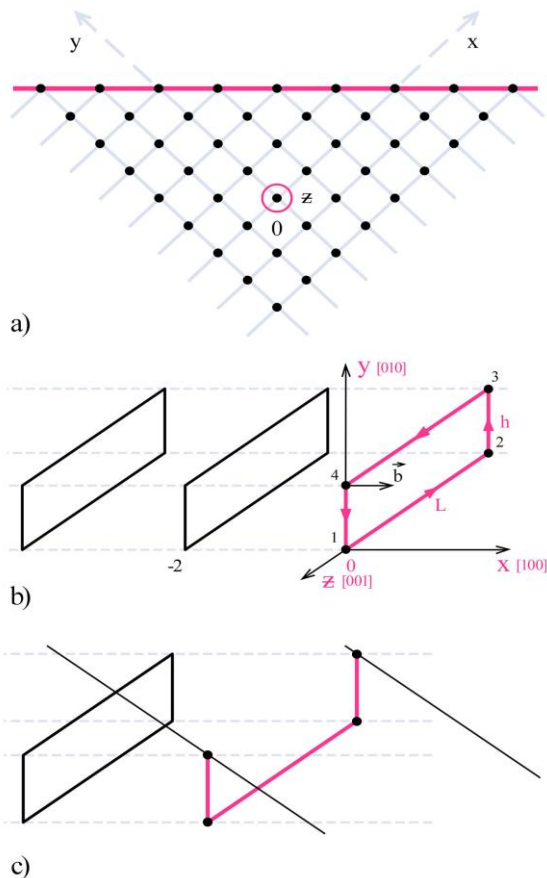


Fig. 3. Fixation model of dislocation loops: a) location of dislocation sliding planes; b) dislocation loops in the volume of n-InP (111); c) fixation of dislocation on sample surface, which will cause the steps.

The dislocation loops tend to spread and move due to the forces of mutual repulsion. This movement occurs in the direction of the sample surface and stops at the moment of emergence of the dislocations (Fig. 3 c). The exit of the first (main dislocation loop) to the surface causes the step. Three other loops (ingoing) in the dislocation system are fixed and their movement stops. Thus, we can observe the accumulations of dislocations.

According to Fig. 3b an important observation can also be made. The dislocation loop does not move along the [010] and [001] directions during movement toward the sample surface (Fig. 3b axes OY and OZ, respectively). In this case, the superposition of the Peach-Koehler force component is zero in all directions except for the [100] direction (OX axis). This will violate the symmetry of the primary and incoming loops, allowing one to displace the ingoing loop along the [010] direction. During further sliding of the ingoing dislocation, it will fall into the obstacle-free sliding system, caused by the main loop of the dislocation accumulations. Then, when exposed to the next dislocation loop, it will advance in the sample volume until it reaches the surface. The next dislocation loops will move according to the same mechanism.

Thus, the sources of the dislocation loops will initiate the steps on the sample surface, which are the periodic areas of the inhomogeneous deformation (Fig. 4a). This, in turn, will allow one to form the sample surface relief with a periodic architecture (Fig. 4b).

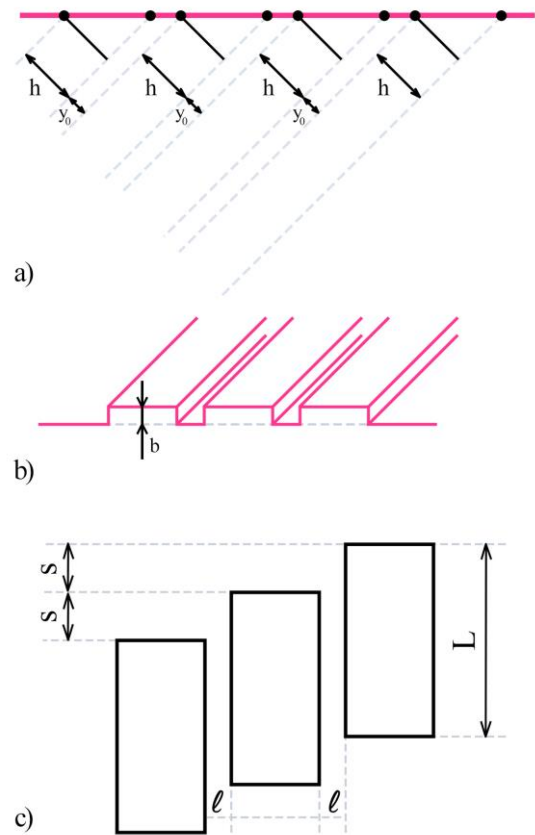


Fig. 4. The system of dislocation loops on the surface of InP (111) (a); schematic diagram of surface relief with parquet periodic crystallites (b) and relative displacement of steps caused by displacement of main and ingoing dislocation loops (c).

In addition to sliding dislocations, the actual crystals also have other type of defects in the volume. The symmetry of the mutual location of the dislocation loops (nonzero superposition of the Pitch-Keller force component) is violated due to this (Fig. 4c). Displacement will occur along the sliding direction [001]. Thus, the arrangement of nanocrystalline wires in the form of parquet steps will be observed on the InP (111) surface.

3.2 Mathematical interpretation of formation of parquet periodic nanostructures

From these considerations, we can present the described mechanism with a mathematical model. Thus, the Pitch-Keller force component acts on the unit length of the dislocation line:

$$f_i = e_{ikl}\tau_k\sigma_{lm}b_m \quad (1)$$

where e_{ikl} is the Levi-Civita symbol; τ_k is the component of the unit vector; σ_{lm} is the components of the mechanical tension tensor; b_m is the components of the Burgers vector.

The superposition of the Pitch-Keller force component, acting on the dislocation loop along the [010] direction, is described by the expression:

$$F_y = -b^2B \frac{h(3d^2+h^2)}{(d^2+h^2)^2}L, \quad (2)$$

$$B = \frac{\mu}{2\pi(1-\sigma)}$$

where b is the Burgers vector; μ is the shear modulus; σ is the Poisson's ratio; h is the size of the dislocation loop along the direction [010]; d is the distance between the dislocation loops; L is the size of the dislocation loop [001].

The Pitch-Keller force component in section (1-2) (Fig. 3b) is described by the expression:

$$F_y^{(1-2)} = -b^2B \frac{(h+y_0)[3d^2+(h+y_0)^2]}{[d^2+(h+y_0)^2]^2}L, \quad (3)$$

where y_0 is the distance module of the dislocation loop from the section (3-4) to the plane ZOx.

Accordingly, for section (3-4), the Pitch-Keller force component (Fig. 3b) is described by the expression:

$$F_y^{(3-4)} = b^2B \frac{y_0(3d^2+y_0^2)}{(d^2+y_0^2)}L. \quad (4)$$

On the basis thereof, the fixation condition of the dislocation loop corresponds to the expression:

$$F_y^{(1-2)} + F_y^{(3-4)} = 0. \quad (5)$$

An important observation is that the length of one parquet step is equal to the length of sections (1-2) and (3-4) of the dislocation loops.

The Pitch-Keller force, acting on the dislocation loop, parallel to the direction [010]:

$$F_y = \pm b^2B \frac{y(3d^2+y^2)}{(d^2+y^2)^2}L, \quad (6)$$

The extremes of the function $F(y)$ have the following values:

$$y_1 = \sqrt{(2\sqrt{3}-3)}d \approx 0,681d,$$

$$y_2 = -\sqrt{(2\sqrt{3}-3)}d \approx -0,681d,$$

The condition of stable equilibrium with respect to the displacement of the dislocation loop along the [010] direction:

$$y_0 = 0,681d - \frac{h}{2}. \quad (7)$$

Taking into account the fact that the angle between the sample surface and the sliding planes of the dislocations is equal to 45° , the step distance is calculated as follows:

$$l = \sqrt{2}y_0 = \sqrt{2}(0,681d - 0,5h) \quad (8)$$

We can also estimate the value of the longitudinal displacement S of the dislocation loop:

$$S = 2(h + y_0) = 2(0,5h) + 0,681d \quad (9)$$

The values of d and h are approximately equal to each other, which gives us the value of the step distance:

$$l \approx 0,256h; \quad S \approx 2,362h. \quad (10)$$

We can see that the conducted simulation gives us the full conformity between the calculated and experimental values.

Conclusions

The mechanism of the periodic nanostructures on the surface of highly doped single-crystal indium phosphide, which are oxide formations and packed on the surface by "parquet floor" type, were described in our paper. The morphological characteristics of the formed nanowires were investigated. In particular, it has been shown that the thickness of the nanowires has the average value of $10 \mu\text{m}$, the length is in the range of $(100 - 130) \mu\text{m}$. EDX analysis showed that the nanowires consist mainly of indium and oxygen atoms. The phase composition of the formed nanocomposites requires further detailed study.

The dislocation mechanism of nanowire formation has been proposed. According to this mechanism, the dislocations move in the direction of the sample surface and stop at the moment of the emergence of the dislocations. This leads to the "run-up" of the next dislocations, resulting in the appearance of the "steps" on the surface. These steps are the sources of the formation of the nanostructures located on the surface with a defined period.

The mathematical interpretation of the proposed

mechanism has been given, and the longitudinal displacement of the dislocation loop and the distance between the steps have been theoretically estimated. The simulation conducted gives us the full conformity between the calculated and experimental values.

Acknowledgements

The study was supported by the Ministry of Education and Science of Ukraine, namely:

the state budget research project No. 0122U000129
The search for optimal conditions for nanostructures synthesis on the surface of A3B5, A2B6 semiconductors and silicon for photonics and solar energy

project No. 0121U10942 Theoretical and methodological bases of the system fundamentalization of the future nanomaterials experts training for productive professional activity.

We also thank the Armed Forces of Ukraine for the safety to carry out this work. This work was only possible thanks to the resilience and courage of the Ukrainian Army.

Kovachov S. – Junior researcher of Berdyansk State Pedagogical University;

Bohdanov I. – Doctor of Pedagogical Sciences, Professor, Rector of the Berdyansk State Pedagogical University;

Bardus I. – Doctor of Pedagogical Sciences, Professor, Professor of the Department of Computer Technologies in Management and Education and Informatics of the Berdyansk State Pedagogical University;

Drozhcha D. – Master's student of the Department of Physics and Teaching Methods of Physics of Berdyansk State Pedagogical University;

Tikhovod K. – Senior laboratory technician of the Department of Physics and Teaching Methods of Physics of Berdyansk State Pedagogical University;

Khrekin A. – Leading specialist of the Department of Physics and Teaching Methods of Physics of Berdyansk State Pedagogical University;

Bondarenko V. – Assistant of the Department of Physics and Teaching Methods of Physics of Berdyansk State Pedagogical University;

Kosogov I. – Senior researcher of the Department of Physics and Teaching Methods of Physics of Berdyansk State Pedagogical University;

Suchikova Y. – Doctor of Technical Sciences, Professor, Vice-Rector for Research of the Berdyansk State Pedagogical University.

- [1] E. Monaico, I. Tiginyanu, V. Ursaki, *Porous semiconductor compounds*, *Semiconductor Science and Technology*, 35(10), 103001 (2020); <https://doi.org/10.1088/1361-6641/ab9477>.
- [2] Z. T. Karipbayev et al., *Optical, Structural, and Mechanical Properties of Gd₃Ga₅O₁₂ Single Crystals Irradiated with 84 Kr⁺ Ions*, *Physica Status Solidi (b)*, 2100415 (2022); <https://doi.org/10.1002/pssb.202100415>.
- [3] Y. He, M. Tsutsui, Y. Zhou, X. S. Miao, *Solid-state nanopore systems: from materials to applications*, *NPG Asia Materials*, 13(1), 1-26 (2021); <https://doi.org/10.1038/s41427-021-00313-z>.
- [4] G.-H. Lee et al., *Multifunctional materials for implantable and wearable photonic healthcare devices*, *Nature Reviews Materials*, 5 (2), 149 (2022); <https://doi.org/10.1038/s41578-019-0167-3>.
- [5] Y. Liu et al., *Room temperature nanocavity laser with interlayer excitons in 2D heterostructures*, *Science Advances*, 5(4), (2019); <https://doi.org/10.1126/sciadv.aav4506>.
- [6] D. Stange et al., *GeSn/SiGeSn Heterostructure and Multi Quantum Well Lasers*, *ACS Photonics*, 5 (11), 4628 (2018); <https://doi.org/10.1021/acsp Photonics.8b01116>.
- [7] Y. Suchikova, V. Kidalov, and G. Sukach, *Blue Shift of Photoluminescence Spectrum of Porous InP*, *ECS Transactions*, 25 (24), 59 (2009); <https://doi.org/10.1149/1.3316113>.
- [8] B. K. SaifAddin et al., *Fabrication technology for high light-extraction ultraviolet thin-film flip-chip (UV TFFC) LEDs grown on SiC*, *Semiconductor Science and Technology*, 34(3), 035007 (2019); <https://doi.org/10.1088/1361-6641/aaf58f>.
- [9] Y. Suchikova, *Provision of environmental safety through the use of porous semiconductors for solar energy sector*, *Eastern-European Journal of Enterprise Technologies*, 6, 5 (84) 26–33 (2016); <https://doi.org/10.15587/1729-4061.2016.85848>.
- [10] T. Sato, X. Zhang, K. Ito, S. Matsumoto, Y. Kumazaki, *Electrochemical formation of N-type GaN and N-type InP porous structures for chemical sensor applications*. In 2016 IEEE SENSORS (1-3) (2016); <https://doi.org/10.1109/ICSENS.2016.7808443>.
- [11] J.-J. Zhang et al., *Oriented arrays of Co₃O₄ nanoneedles for highly efficient electrocatalytic water oxidation*, *Chemical Communications*, 55 (27), 3971 (2019); <https://doi.org/10.1039/c9cc00791a>.
- [12] W. Huang, C. Gatel, Z.-A. Li, and G. Richter, *Synthesis of magnetic Fe and Co nano-whiskers and platelets via physical vapor deposition*, *Materials & Design*, 208, 109914 (2021); <https://doi.org/10.1016/j.matdes.2021.109914>.
- [13] M. Kwoka, E. Comini, D. Zappa, and J. Szuber, *Flower-like ZnO Nanostructures Local Surface Morphology and Chemistry*, *Nanomaterials*, 12 (15), 2666 (2022); <https://doi.org/10.3390/nano12152666>.
- [14] S. Yana, *Porous indium phosphide: Preparation and properties*. Handbook of Nanoelectrochemistry: Electrochemical Synthesis Methods, Properties, and Characterization Techniques, 283 (2016); https://doi.org/10.1007/978-3-319-15266-0_28.

- [15] S. Vambol, et al., *Research into effect of electrochemical etching conditions on the morphology of porous gallium arsenide*, Eastern-European Journal of Enterprise Technologies, 6, 5 (90), 22 (2017); <https://doi.org/10.15587/1729-4061.2017.118725>.
- [16] A. Gapeeva et al., *Electrochemical Surface Structuring for Strong SMA Wire–Polymer Interface Adhesion*, ACS Applied Materials & Interfaces, 13 (18), 21924 (2021); <https://doi.org/10.1021/acsami.1c00807>.
- [17] D. Wu et al., *Self-organization of polymer nanoneedles into large-area ordered flowerlike arrays*, Applied Physics Letters, 95 (9), 091902 (2009); <https://doi.org/10.1063/1.3213394>.
- [18] X. Liang, R. Dong, and J. C. Ho, *Self-Assembly of Colloidal Spheres toward Fabrication of Hierarchical and Periodic Nanostructures for Technological Applications*, Advanced Materials Technologies, 4 (3), 1800541 (2019); <https://doi.org/10.1002/admt.201800541>.
- [19] I.-T. Chen, E. Schappell, X. Zhang, and C.-H. Chang, *Continuous roll-to-roll patterning of three-dimensional periodic nanostructures*, Microsystems & Nanoengineering, 6 (1), (2020); <https://doi.org/10.1038/s41378-020-0133-7>.
- [20] Y.A. Suchikova, V.V. Kidalov, G.A. Sukach, *Influence of type anion of electrolit on morphology porous inp obtained by electrochemical etching*, Journal of Nano- and Electronic Physics, 1(4), 78 (2009).
- [21] S. S. Kovachov et al., *Chemical evaluation of the quality of nanostructures synthesized on the surface of indium phosphide*, Archives of Materials Science and Engineering, 1 (110), 18 (2021); <https://doi.org/10.5604/01.3001.0015.3592>.
- [22] Y. Suchikova, S. Kovachov, I. Bohdanov, *Formation of oxide crystallites on the porous GaAs surface by electrochemical deposition*. Nanomaterials and Nanotechnology, 12, (2022); <https://doi.org/10.1177/18479804221127307>.
- [23] Y. Suchikova, S. Vambol, V. Vambol, N. Mozaffari, and N. Mozaffari, *Justification of the most rational method for the nanostructures synthesis on the semiconductors surface*, Journal of Achievements in Materials and Manufacturing Engineering, 1-2 (92), 19 (2019); <https://doi.org/10.5604/01.3001.0013.3184>.
- [24] S. O. Vambol et al., *Formation of Filamentary Structures of Oxide on the Surface of Monocrystalline Gallium Arsenide*, Journal of Nano- and Electronic Physics, 9 (6), 06016–1 (2017) [https://doi.org/10.21272/jnep.9\(6\).06016](https://doi.org/10.21272/jnep.9(6).06016).
- [25] J. Zhang et al., *Boosting the catalytic activity of a step-scheme $In_2O_3/ZnIn_2S_4$ hybrid system for the photofixation of nitrogen*, Chinese Journal of Catalysis, 43 (2), 265 (2022); [https://doi.org/10.1016/s1872-2067\(21\)63801-9](https://doi.org/10.1016/s1872-2067(21)63801-9).
- [26] A. Usseinov et al., *Vacancy Defects in Ga_2O_3 : First-Principles Calculations of Electronic Structure*, Materials, 14 (23), 7384 (2021); <https://doi.org/10.3390/ma14237384>.
- [27] A. Usseinov et al., *Ab-Initio Calculations of Oxygen Vacancy in Ga_2O_3 Crystals*, Latvian Journal of Physics and Technical Sciences, 58 (2), 3 (2021); <https://doi.org/10.2478/lpts-2021-0007>.
- [28] V. Kumar, S. M. Majhi, K.-H. Kim, H. W. Kim, and E. E. Kwon, *Advances in In_2O_3 -based materials for the development of hydrogen sulfide sensors*, Chemical Engineering Journal, 404, 126472 (2021); <https://doi.org/10.1016/j.cej.2020.126472>.
- [29] I.V. Rogozin, *Nitrogen-doped p-type ZnO thin films and ZnO/ZnSe p-n heterojunctions grown on ZnSe substrate by radical beam gettering epitaxy*, Thin Solid Films, 517(15), 4318 (2009); <https://doi.org/10.1016/j.tsf.2008.12.002>.
- [30] Z. Zhang, M. Wang, F. Wang, *Plasma-assisted construction of CdO quantum dots/CdS semi-coherent interface for the photocatalytic bio-CO evolution*, Chem Catalysis, 2, 1 (2022); <https://doi.org/10.1016/j.cheecat.2022.04.001>.
- [31] V. Serga, R. Burve, A. Krumina, M. Romanova, E. A. Kotomin, A. I. Popov, *Extraction–pyrolytic method for TiO_2 polymorphs production*, Crystals, 11(4), 431 (2021); <https://doi.org/10.3390/cryst11040431>.
- [32] Y. Suchikova, A. Lazarenko, S. Kovachov, A. Usseinov, Z. Karipbaev, and A. I. Popov, *Formation of porous $Ga_2O_3/GaAs$ layers for electronic devices*, in 2022 IEEE 16th International Conference on Advanced Trends in Radioelectronics, Telecommunications and Computer Engineering (TCSET), Lviv-Slavske, Ukraine, Feb. 22–26, (2022); <https://doi.org/10.1109/tcset55632.2022.9766890>.
- [33] B. Khorshidi, I. Biswas, T. Ghosh, T. Thundat, and M. Sadrzadeh, *Robust fabrication of thin film polyamide- TiO_2 nanocomposite membranes with enhanced thermal stability and anti-biofouling propensity*, Scientific Reports, 8 (1), (2018); <https://doi.org/10.1038/s41598-017-18724-w>.
- [34] A. Uzum, I. Kanmaz, *Passivation properties of HfO_2-SiO_2 mixed metal oxide thin films with low reflectivity on silicon substrates for semiconductor devices*, Thin Solid Films, 738, 138965 (2021); <https://doi.org/10.1016/j.tsf.2021.138965>.
- [35] R. J. Theeuwes et al., *PO_x/Al_2O_3 stacks for surface passivation of Si and InP*, Solar Energy Materials and Solar Cells, 246, 111911 (2022); <https://doi.org/10.1016/j.solmat.2022.111911>.
- [36] C. Wang, L. Peng, Q. Qian, J. Du, S. Wang, and Y. Huang, *Tuning the Carrier Confinement in GeS/Phosphorene van der Waals Heterostructures*, Small, 14 (10), 1703536 (2018); <https://doi.org/10.1002/sml.201703536>.
- [37] D. Coelho, J. P. R. S. Gaudêncio, S. A. Carminati, F. W. P. Ribeiro, A. F. Nogueira, and L. H. Mascaro, *Bi electrodeposition on WO_3 photoanode to improve the photoactivity of the $WO_3/BiVO_4$ heterostructure to water splitting*, Chemical Engineering Journal, 399, 125836 (2020); <https://doi.org/10.1016/j.cej.2020.125836>.

- [38] L. Maduro, M. Noordam, M. Bolhuis, L. Kuipers, and S. Conesa-Boj, *Position-Controlled Fabrication of Vertically Aligned Mo/MoS₂ Core-Shell Nanopillar Arrays*, *Advanced Functional Materials*, 32 (5), 2107880 (2021); <https://doi.org/10.1002/adfm.202107880>.
- [39] Y. A. Suchikova, V. V. Kidalov, and G. A. Sukach, *Influence of dislocations on the process of pore formation in n-InP (111) single crystals*, *Semiconductors*, 45(1), 121 (2011); <https://doi.org/10.1134/s1063782611010192>.

С. Ковачов, І. Богданов, І. Бардус, Д. Дрожча, К. Тиховод, А. Хрекін,
В. Бондаренко, І. Косошов, Я. Сичікова

Про механізм синтезу періодичних оксидних нанокристалітів на поверхні монокристалічного InP

Бердянський державний педагогічний університет, Бердянськ, Україна, yanasuchikova@gmail.com

Нами було отримано унікальні періодичні оксидні нанокристаліти на поверхні фосфіду індію. У статті досліджуються морфологічні характеристики одержаних структур та компонентний склад. Основна увага в статті зосереджена на поясненні механізму формування періодичних структур, які упаковані по типу «паркет». Запропоновано механізм, який ґрунтується на ковзанні джерел дислокаційних петель прямокутної форми. Розглянуто систему головної та вторинних (набігаючих) дислокацій, які спричиняють появу сходинок. Також запропоновано математичну інтерпретацію описаної моделі.

Ключові слова: фосфід індію, періодичні структури, дислокації, електрохімічне травлення, поруватий оксид.

A.S. Chernenko, V.V. Kalinchak, A.K. Kopyyka, M.V. Roziznanyi, A.V. Fedorenko

Catalytic oxidation of acetone and ethanol on a platinum wire

Odesa I.I. Mechnikov National University Odesa, Ukraine, tephys@onu.edu.ua

The current-voltage characteristics of a thin long platinum wire in air with small admixtures of acetone or ethanol vapors were obtained. Using the quadratic dependence of platinum resistance on temperature, the temperature-current dependences for the wire were calculated. At concentrations of combustible gas vapors above a certain value, these dependences show a hysteretic character. Using the assumption of complete oxidation of acetone and ethanol on platinum, as a catalyst, and the first order of the oxidation reaction, an analysis of temperature-current dependences was performed. The temperature difference between the high and low-temperature stationary modes of catalytic oxidation on the wire makes it possible to estimate the concentration of the impurity in the mixture. As a result, the experimental dependence of the critical value of the catalytic current ignition and the extinguishing of the gas mixture on platinum on the impurity concentration was constructed. With its analytical description, it is possible to fairly accurately estimate the apparent values of the activation energy and the pre-exponential factor of the oxidation reaction in a wide temperature range. A method of determining the kinetic parameters of the oxidation reaction based on the experimentally found parameters of the degeneracy of critical conditions is proposed.

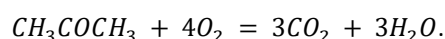
Key words: catalyst, platinum wire, diameter, small admixture of gas, acetone, ethanol, ignition, extinction, combustion.

Received 12 September 2023; Accepted 8 March 2023.

Introduction

Pure metals, especially platinum, are the most common catalysts for the oxidation of volatile organic compounds. Platinum nanoparticles are often added to the surface of the oxide catalyst, which significantly accelerates the oxidation of the compound [1-4].

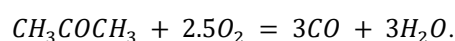
The work [5] investigated the kinetics of catalytic combustion of acetone and toluene at low concentrations in air (partial pressure from 10 to 101 Pa) on $Cu_{0.13}Ce_{0.87}O_y$ catalysts at temperatures from 423 to 483 K. The reaction order and activation energy for acetone combustion are visible and toluene over the catalyst varied depending on the partial pressure of the impurity at the inlet and the reaction temperature, respectively. It was assumed here that the catalytic combustion of acetone in air proceeds according to the gross reaction:



The thermal effect of the reaction is 1829.4 kJ/mol.

The obtained activation energy of the acetone oxidation reaction is 96-109 kJ/mol.

The current characteristics and oxidation of acetone vapors in a corona discharge of atmospheric pressure in the wire-plate system were investigated in [6]. Here, the authors assumed the reaction of complete oxidation of acetone. However, it was also believed that the oxidation of acetone can follow a parallel reaction of incomplete oxidation:



The thermal effect of reaction (II) is 973 kJ/mol.

The authors [7] propose a mechanism for the complete oxidation of acetone on a catalyst of 0.57 wt.% CeO_2 -0.05 wt.% Pt/TiO_2 . Molecules of acetone and oxygen were initially adsorbed on the catalyst. After the reaction temperature increases, acetone decomposes into acetic and formic acids, then these acids turn into carbonate particles. Finally, these particles completely decompose to CO_2 and

H_2O .

The oxidation of acetone on platinum was assumed to be complete, i.e. to CO_2 , and in [4]. At the same time, the concept of low temperatures (up to 300 °C) is introduced for such a process.

Platinum is the earliest catalyst for single-component catalysis in the ethanol oxidation reaction [8, 9]. The authors [8] indicate that such oxidation can be complete (with slow oxidation) to CO_2 and partial to acetaldehyde or acid.

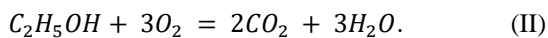
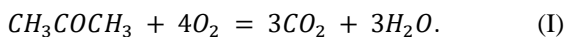
The authors [10] indicate a high percentage (over 90%) of CO_2 formation during the oxidation of methanol and ethanol on a platinum catalyst. By studying the change in the concentration of methanol and ethanol, which exponentially decreased over time during catalytic oxidation with oxygen on a platinum catalyst at room temperatures, the activation energies of these reactions were found. In particular, for ethanol $E = 143$ kJ/mol.

Studies of heterogeneous oxidation of combustible gases on a long and thin wire made of metals of the platinum group, which is heated by an electric current, continue even nowadays [11]. For the occurrence of stable flameless catalytic combustion of gas when the catalyst is heated by current, the correct selection of the diameter and length of the catalyst, the range of combustible gas concentrations, the temperature and speed of the gas-air flow is necessary [12].

A classic example is the oxidation of an admixture of ammonia and hydrogen on a long platinum wire ($L/d = 1000$) with a diameter of 100 μm [13, P. 416]. In a gas-air flow with combustible gas impurities, the heating of the platinum wire (increase in temperature and electrical resistance to steady-state values) was practically carried out by heating with an electric current. Up to a certain value of the heating current, the wire behaved as inert. At different currents for different mixtures (about 0.74 ÷ 0.8 A), there was a sharp increase in the stationary temperature of the catalyst. Increasing the content of combustible gas in the mixture slightly reduces the critical value of current strength, but significantly affects the temperature level of high-temperature states and the critical value of current strength during catalytic extinction.

In this work, the non-isothermal oxidation (combustion) of small impurities of acetone and ethanol in air on a platinum wire will be considered, the critical conditions of catalytic ignition and extinction will be analyzed, and the kinetic parameters of oxidation reactions in air will be evaluated.

In view of the above, this paper assumed that the catalytic combustion of acetone and ethanol in air on a platinum wire is complete oxidation and proceeds according to the following reactions:



Thermal effect of reaction (I) $Q_1 = 1829.4$ kJ/kg, and (II) $Q_2 = 1370$ kJ/kg.

The steady-state level of high-temperature heating of the catalyst T_m during the course of one reaction in the diffusion region according to classical concepts is

determined only by the concentration of the combustible substance in the gas in which the oxidant is in excess:

$$T_m - T_g = T_Q Y_f, \quad T_Q = \frac{Q_f Le^{1-m}}{c_{pg}}, \quad (1)$$

where Q_f is the heat effect of the reaction, calculated for 1 kg of combustible gas, J/kg; Y_f is the relative mass concentration of combustible gas in the gas mixture; c_{pg} – isobaric specific heat of the gas mixture; T_g is the temperature of the gas mixture; $Le = D_f/a_g$ – Lewis number; m is an indicator of the degree of dependence of Nu on Pr and Sh on Sc . For forced convection ($0.1 < Re < 4$) $m = 0.33$.

An interesting feature of the oxidation of these gases is the difference in the Lewis number. Thus, for hydrogen $Le \approx 3$, for ammonia $Le \approx 1$, for acetone $Le = 0.586$, for ethanol $Le = 0.578$.

I. Experimental setup

For the experimental study of the oxidation of acetone and ethanol, a PMT-2 manometric thermocouple transducer was taken (Fig. 1). In it, a platinum wire with a diameter of $d = 95 \mu\text{m}$ and a length of $L = 56$ mm is used as a heater. A glass bulb with an inner diameter was cut off from the PMT-2 stand 30 mm and the upper end of the bulb. The platinum thread was bent in the form of a snake and placed in a plane perpendicular to the axis of the lamp. A tube for supplying the gas-air mixture was inserted through the hole in the lamp holder. After that, the glass bulb was glued to the base. The flask was located vertically. Thus, the incoming mixture moved relative to the thread from top to bottom (acetone and ethanol are heavier than air) and did not accumulate inside the lamp.

The gas mixture was created as follows. A small amount of liquid (acetone or ethanol) was poured into flask 8 (Fig. 1). A flow of air was fed into the liquid using a compressor. At the outlet, an air mixture with vapors of a flammable liquid was obtained. This flow could be diluted with a parallel clean air flow. The total consumption of the mixture was determined by two rotameters on the cold mixture. The temperature of the mixture before entering the chamber and inside it was determined by readings of thermocouples. To ensure the stability of the temperature on the walls of the reaction chamber, it was blown from the outside between the flask 1 and the external chamber 10 (Fig. 1) by a stream of cold air.

The main experimental dependence is the current-voltage characteristic of the wire obtained in the current stabilization mode. The platinum thread was connected to the Picotest 3510A multimeter using a three-wire circuit through the contacts of the PMT-2 lamp. In this case, the multimeter made it possible to measure the voltage and, therefore, the resistance of thread 1 (Fig. 1) together with the contacts of the lamp itself 2 without taking into account the resistance of other connecting conductors. The lamp contacts have a diameter of 1 mm. Their total resistance is $R_k = 0.105 \Omega$, which remains constant in the range of currents for research (they practically do not heat up).

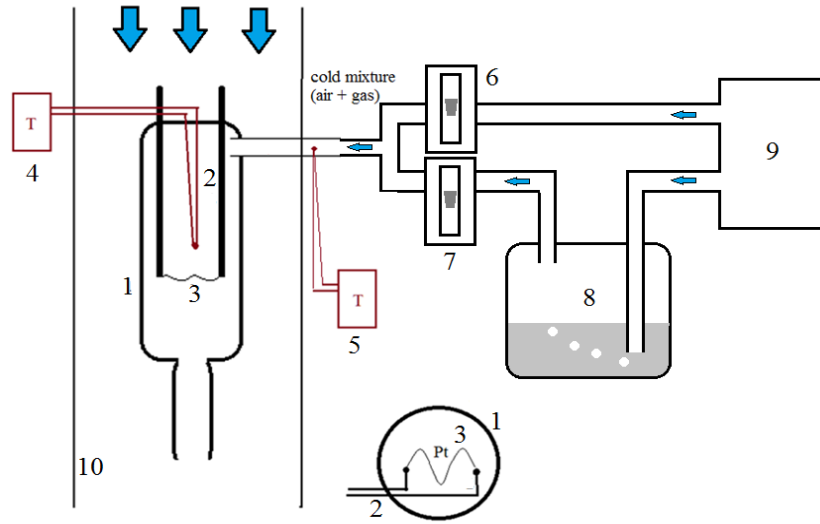


Fig. 1. Scheme of the experimental setup: 1 – PMT-2 glass bulb, 2 – connected contacts, 3 – platinum thread, 4, 5 – millivoltmeters with thermocouples; 6, 7 – rotameters of the float type, 8 – container with liquid; 9 – air compressor; 10 – external camera.

The resistance of the platinum wire is determined according to Ohm's law (without taking into account the resistance of the lamp contacts) and the average

temperature of the wire from the quadratic dependence of the resistance of the wire on temperature:

$$R_c = \frac{U}{I} - R_k, \quad \frac{R_c}{R_{c0}} = 1 + \gamma(T - T_0) - \delta(T - T_0)^2, \quad R_{c0} = \eta_0 \frac{4L}{\pi d^2}.$$

Here, $\gamma = 39.7 \cdot 10^{-4} \text{ 1/K}$, $\delta = 5.841 \cdot 10^{-7} \text{ 1/K}^2$, $\eta_0 = 9.8 \cdot 10^{-8} \text{ } \Omega \cdot \text{m}$. The resistance of a platinum wire with a length of 5.6 cm and a diameter of 95 μm at $T_0 = 273\text{K}$ is $R_0 = 0.775 \text{ } \Omega$.

The volt-ampere characteristic of a platinum wire in a gas-air mixture was recorded with a gradual increase in the strength of the flowing current in steps of 0.1 A (near critical processes in steps of 0.01 A) while establishing a stationary temperature regime of the wire for each current strength. After switching the filament to the catalytic combustion mode (catalytic ignition at 0.58-0.77 A), the current increased to 0.7-0.8 A, and then gradually decreased to 0.01 A.

When reducing the current strength in the catalytic combustion mode, there are two possible qualitatively different options depending on the concentration of the combustible gas: 1) extinction - reverse transition to the low-temperature mode at a lower value of the current strength (curves 2-3, Fig. 2) or self-extinguishing catalytic oxidation at turned off current (curve 4, Fig. 2) [9].

In fig. 2 shows the dependences of the resistance and average temperature of the platinum thread on the power of the heating current at different concentrations of

acetone and ethanol in the gas-air stream blowing the platinum thread.

Reactions (I) and (II) were used to estimate the concentration of acetone and ethanol according to formula (1). For this, the average value of the temperature difference ΔT_{exp} in high- and low-temperature regimes was determined at 3-4 values of the current strength (at the current strength of the catalytic ignition I_i and smaller than it by 0.1, 0.2 and 0.3 A). The concentration of combustible gas was calculated as $Y_f = \Delta T_{exp}/T_0$.

II. Analysis of results

Consider the physical-mathematical model of the heat-mass exchange of a long metal thread, which is heated by an electric current and the catalytic reaction of the oxidation of a small admixture of combustible gas, and is also cooled as a result of molecular-convective heat exchange with a cold gas-air mixture. The equation of unsteady thermodynamics of the metal thread of the catalyst will look like this:

$$\begin{aligned} \frac{V_c}{S_c} c_c \rho_c \frac{dT}{dt} &= q_{eff}, \quad q_{eff} = q_{ch} + q_j - q_g, \quad T(t=0) = T_b \\ q_{ch} &= Q_f \frac{k \rho_{gs} Y_f}{1 + Se}, \quad k = k_0 \exp\left(-\frac{E}{RT}\right), \quad Se = \frac{k}{\beta}, \quad q_g = \alpha(T - T_g), \quad q_j = \frac{I^2 R_c}{\pi d L}, \\ \alpha &= \beta c_p \rho_g Le^{-1+m}, \quad \beta = \frac{D_f Sh}{d}, \quad R_c = \eta \frac{4L}{\pi d^2}, \quad \eta = \eta_0 (1 + \gamma(T - T_0) - \delta(T - T_0)^2), \end{aligned} \quad (2)$$

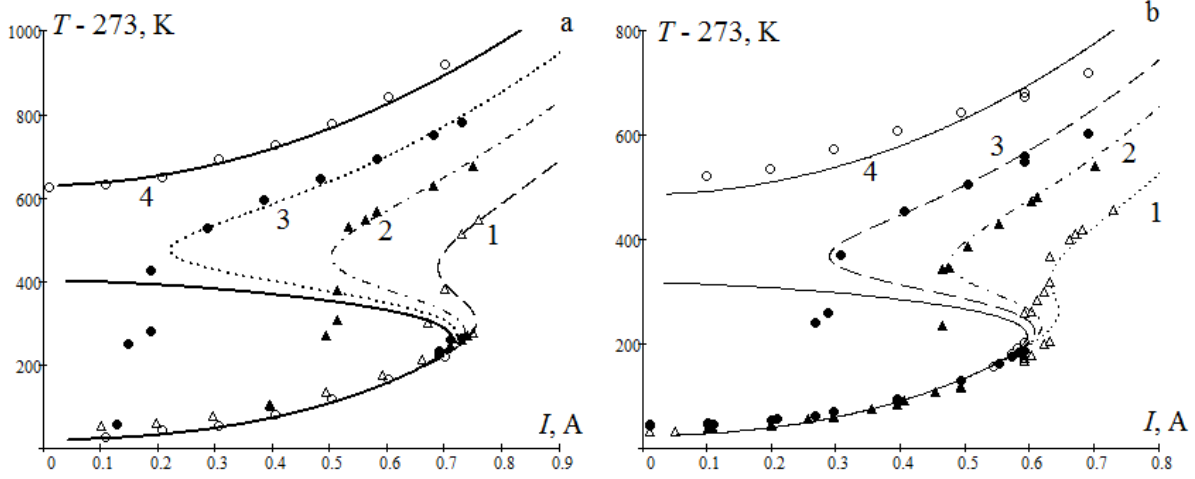


Fig. 2. Dependence of the temperature of a platinum thread (diameter 95 μm) on the strength of the heating current during the catalytic oxidation on it of a) acetone or b) ethanol in a cold gas-air mixture ($T_g = 296\text{ K}$) at different concentrations of Y_f :

a) $\Delta - Y_{f1} = 1.41\%$; $\blacktriangle - Y_{f2} = 2.17\%$; $\bullet - Y_{f3} = 2.83\%$; $\circ - Y_{f4} = 3.53\%$;

b) $\Delta - Y_{f1} = 0.83\%$; $\blacktriangle - Y_{f2} = 1.56\%$; $\bullet - Y_{f3} = 2.12\%$; $\circ - Y_{f4} = 2.91\%$.

Curves 1-4 are theoretical dependences (3).

where V_c is the volume of the catalyst, S_c is the lateral surface of the catalyst, c_c is the specific heat capacity of the catalyst, $J/(\text{kg}\cdot\text{K})$; ρ_c is the density of the catalyst, kg/m^3 ; q_{eff} – effective power density of heat release, W/m^2 ; q_j is the heat released every second when an electric current passes through the cylinder catalyst, calculated per unit of side surface; R_c is the electrical resistance of the wire, Ω .

Suitable lamp contacts are 10 times thicker than a platinum filament and the ratio of the length of the filament to its diameter is almost 600. Therefore, heat dissipation through them is neglected. Considering the fact that the diameter of the platinum wire is less than 100 μm , heat exchange by radiation is also neglected.

The condition for the stationarity of the catalyst temperature $q_{eff} = 0$ is presented in the form of the dependence of the square of the current strength on the stationary temperature at a constant concentration of combustible gas in the air:

$$I = I_0 \sqrt{\frac{T - T_g}{T_0} - \frac{Y_f}{1 + Se} \frac{T_Q k_0}{T_0 \beta} \exp\left(-\frac{E}{RT}\right)}, \quad (3)$$

$$I_0 = \sqrt{\frac{\pi^2 d^2 \lambda_g Nu T_0}{4\eta}}, \quad T_Q = \frac{Q_f Le^{1-m}}{c_{pg}}.$$

The value of I_0 is a weakly decreasing function of temperature. In our case, it lies in the interval from 0.7 to 1.0 A.

Dependence (3) describes the experimental low- and high-temperature steady states. In fig. 2 presents the calculated dependence of the current strength on the steady-state temperature with the parameters of the activation energy and the pre-exponential factor found below. The maximum on this dependence determines the catalytic self-ignition of the combustible gas, and the minimum – catalytic extinction.

The following parameters were used for the

calculations: acetone: $Q_f = 31.5\text{ MJ}/\text{kg}$, $E = 84\text{ kJ}/\text{mol}$, $k_0 = 1.5 \cdot 10^6\text{ 1}/\text{c}$, $D_{j0} = 0.109 \cdot 10^{-4}\text{ m}^2/\text{s}$, $Le = 0.586$, $m = 0$, $n = 1.82$. Ethanol: $Q_f = 29.8\text{ MJ}/\text{kg}$, $E = 92\text{ kJ}/\text{mol}$, $k_0 = 4 \cdot 10^7\text{ 1}/\text{c}$, $D_{j0} = 0.10 \cdot 10^{-4}\text{ m}^2/\text{s}$, $Le = 0.578$. Other parameters: $\rho_{g0} = 1.293\text{ kg}/\text{m}^3$, $c_{g0} = 1005\text{ J}/(\text{kg}\cdot\text{K})$.

The volumetric flow rate of the gas mixture entering the bulb of lamp 1 (Fig. 1) with a thread was 17–23 cm^3/s . This corresponds to a laminar flow speed inside the bulb of 3 cm/s (Reynolds number for the lamp bulb is 58, and for the filament is 0.18). So, in this case, the influence of forced and natural convection can be neglected ($m = 0$). The Sherwood number Sh for a thin long cylinder ranges from 0.45–0.6 [14, P. 325; 13] The choice of the Sh value was determined by matching the inert analytical and experimental $T(I)$ dependences, which is actually determined by the low-temperature branch of the $T(I)$ dependence, on which the chemical reaction practically does not proceed. Thus, with the catalytic oxidation of acetone $Sh = 0.55$, ethanol $Sh = 0.45$. In the catalytic combustion mode, the temperature inside the bulb (thermocouple readings above the platinum thread) increases by 30–40 K, which indicates that natural convection prevails over forced convection on the bulb scale.

Let's apply the extremum condition $\partial I/\partial T = 0$ to dependence (3). As a result, together with (3), we will obtain a system of equations for determining the critical conditions of catalytic self-ignition (i) and extinction (e):

$$\begin{cases} I_{i,e} = I_0 \sqrt{\frac{T_{i,e} - T_g}{T_0} - \frac{RT_{i,e}^2}{ET_0} (1 + Se_{i,e})}, & (4a) \\ Y_f = \frac{RT_{i,e}^2 (1 + Se_{i,e})^2}{ET_Q Se_{i,e}}. & (4b) \end{cases}$$

In fig. 3 shows the solution of system (4). The catalyst temperature $T_{i,e}$ is used as a parameter. The position of dependencies (4) in Fig. 3 depends on the activation energy E and the pre-exponential factor k_0 . The slope of

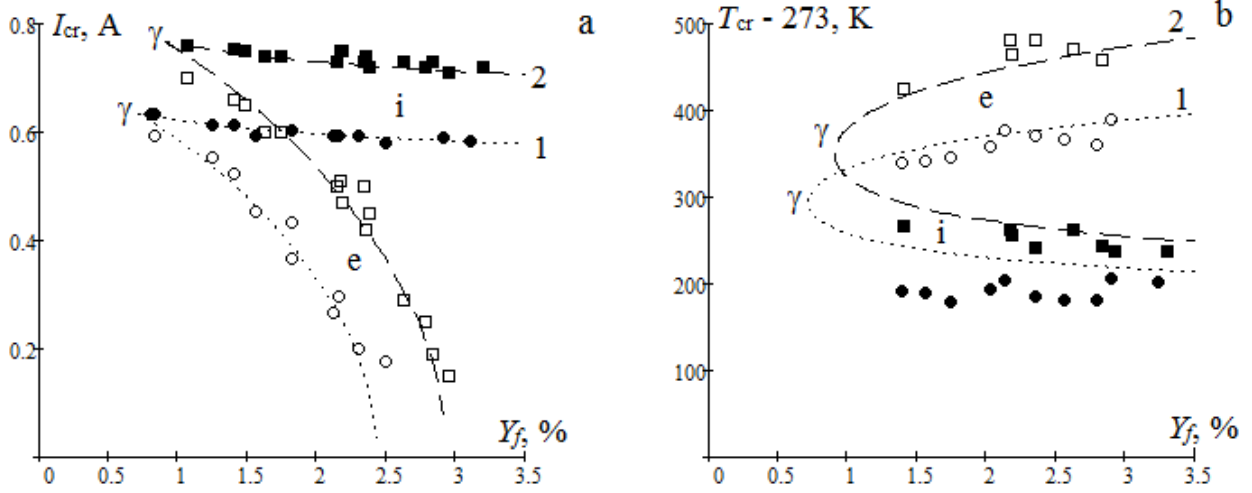


Fig. 3. Dependence of the critical value of a) the power of the heating current (self-ignition and extinction of the catalytic oxidation reaction of 1) ethanol (○, ●) and 2) acetone (□, ■) on a platinum wire with a diameter of 95 μm and b) the temperature of the wire on the concentration of combustible gas in air at room temperature $T_g = 296$ K. Lines are dependences (4).

the extinction curve is significant compared to the self-ignition curve. It is at this stage that it is already possible to find the value of the activation energy and the pre-exponential factor for each of the reactions, which would satisfactorily describe the obtained experimental data. However, let's analyze this dependence.

At the degeneracy points (point γ), the Semenov number $Se_\gamma = 0.75-0.80$. At the points of catalytic self-ignition at a distance from the point of degeneration $Se_i < 0.1$, and at the extinction points $Se_e > 3$.

Therefore, for $Se \ll 1$, the compatible solution of equations (4) leads to

$$T_g + \left(\frac{I_i}{I_0}\right)^2 T_0 = T_i - \frac{RT_{ie}^2}{E}, \quad (5)$$

$$\frac{Q_f L e^{1-m} Y_{fi} E}{c_p g R T_i^2} Se_i = 1$$

$$\frac{T_Q Y_{fi} E}{R T_{g*}^2} \frac{k_0 d}{D_f Sh} \exp\left(-\frac{E}{R T_{g*}}\right) = \frac{1}{e} \quad \text{or} \quad \ln\left(\frac{T_Q Y_{fi}}{T_{g*}^2}\right) = \frac{E}{R} \cdot \frac{1}{T_{g*}} - \ln\left(\frac{E k_0 d}{R D_f Sh}\right).$$

In fig. 4 presents the results of the catalytic ignition of acetone and ethanol on platinum in the form of dependence $\ln\left(\frac{T_Q Y_{fi}}{T_{g*}^2}\right)$ on $\frac{1}{T_{g*}}$. As a result, the data can be described by a linear dependence, from which the value of the activation energy for the oxidation reaction of acetone on platinum was obtained $E = 85$ kJ/mol, and for ethanol $E = 92$ kJ/mol.

For points extinction, we use the schedule in (4) $(1 + Se_e)^2 / Se_e \approx Se_e + 2$. As a result, we get:

$$T_g + \left(\frac{I_e}{I_0}\right)^2 T_0 + T_Q Y_{fe} = T_e + \frac{RT_e^2}{E}, \quad (6)$$

$$\frac{T_Q E}{R T_e^2} \frac{Y_{fe}}{Se_e + 2} = 1$$

The last expression can be used to estimate the activation energy. Let's enter the effective temperature of the environment (the temperature to which an inert conductor would heat up when an electric current is passed through it)

$$T_{g*} = T_g + \left(\frac{I}{I_0}\right)^2 T_0.$$

With catalytic ignition in our case, the current strength I_i is close to I_0 , and almost twice as much as T_g . Using the Frank-Kamenetsky schedule [13] $\exp\left(-\frac{E}{R T_i}\right) \approx \exp\left(-\frac{E}{R T_{g*}}\right) \cdot e$ and approximation $\frac{R T_i^2}{E} \approx \frac{R T_{g*}^2}{E}$ the critical condition of catalytic ignition can be rewritten as:

By connecting both solutions (6), it is not difficult to obtain the dependence

$$T_g + \left(\frac{I_e}{I_0}\right)^2 T_0 = T_e - T_Q Y_{fe} \frac{Se_e + 1}{Se_e + 2},$$

which explains the dependence in fig. 3a. Namely, that at a distance from the point of degeneration of critical conditions, the square of the current strength of the catalytic quench decreases linearly with the increase in the proportion of combustible gas in the mixture.

To find the kinetic parameters, you can also use the found parameters of the degeneracy point of critical conditions. For example, it was shown in [12] that the parameters of the degeneracy point (catalyst diameter and combustible gas concentration) can be represented by the temperature of the gas mixture in the form:

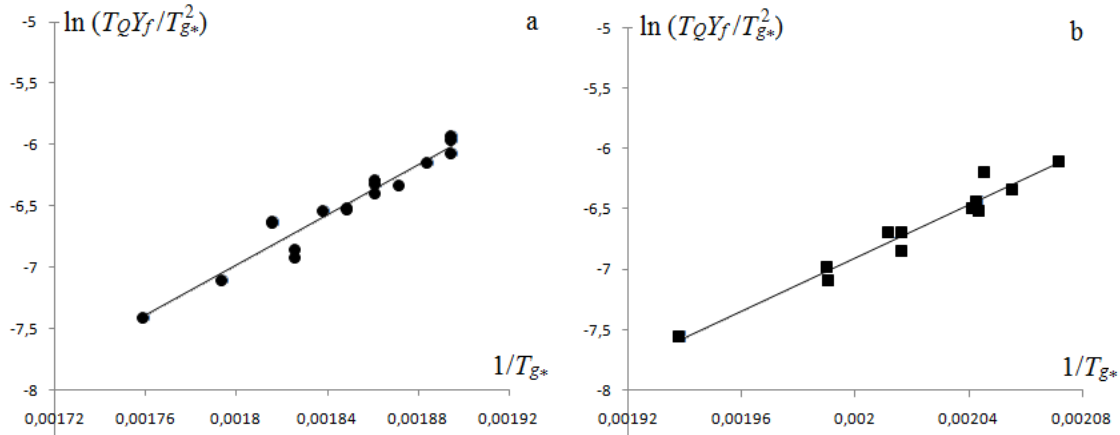


Fig. 4. Dependence $\ln\left(\frac{T_Q Y_f}{T_{g^*}^2}\right)$ on $\frac{1}{T_{g^*}}$ for the oxidation reaction of a) acetone and b) ethanol on a platinum thread.

$$d|_Y = \frac{D_f Sh}{k_0 e^2} \left(1 - 4 \frac{T_{g^*}}{T_E}\right) \exp\left(\frac{T_E}{T_{g^*}}\right), \quad Y_f|_Y = \frac{4}{(1 - 4 T_{g^*}/T_E) T_Q T_E} \frac{T_{g^*}^2}{R}, \quad T_E = \frac{E}{R}.$$

From the second equation we have

$$T_E = 4 T_{g^*} \left(1 + \frac{T_{g^*}}{T_Q Y_f}\right) \Big|_Y \quad \text{or} \quad k_0 = \frac{D_f Sh}{e^2 d} \left(1 - 4 \frac{T_{g^*}}{T_E}\right) \exp\left(\frac{T_E}{T_{g^*}}\right) \Big|_Y.$$

The temperature of the catalyst at degeneration, which needs to be known to determine I_0 and T_{g^*} , can be estimated (Fig. 3b) as the arithmetic mean between the catalytic ignition and extinction temperatures: for acetone $T_\gamma \approx 643$ K, for ethanol $T_\gamma \approx 549$ K.

So, for acetone, the degeneracy parameters $I_\gamma = 0.77$ A, $Y_{f\gamma} = 0.9$ % and, accordingly, the estimated values $E = 85.9$ kJ/mol and $k_0 = 1.4 \cdot 10^6$ m/s. For ethanol $I_\gamma = 0.64$ A, $Y_{f\gamma} = 0.8$ % and, accordingly, the estimated values $E = 91.5$ kJ/mol and $k_0 = 3.0 \cdot 10^7$ m/s. These values are close to those at which agreement of the analytical and experimental data in Fig. 3 was obtained.

Conclusions

Thus, using the assumption of complete oxidation of acetone and ethanol on platinum and the first order of the oxidation reaction, analysis of the current-voltage characteristics platinum wire in a gas mixture with small admixtures of combustible liquid vapors was performed. The temperature difference between the high and low-temperature stationary regimes of catalytic oxidation ΔT_{exp} on the wire makes it possible to estimate the concentration of the impurity in the mixture. The dependence of the critical value of the current strength of catalytic ignition and extinction on the concentration of

the impurity has a wedge-shaped shape, for the analytical description of which the values of the activation energy and the pre-exponential factor of the oxidation reaction can be estimated quite accurately. It is important that the characteristic thermal temperature complex constantly appears in analytical expressions $T_Q Y_f$, which actually is ΔT_{exp} . Therefore, for the determination of kinetic constants by this method, the real gross reaction is unimportant. As a result, it is possible to obtain visible activation energies of oxidation reactions in the given ranges of combustible gas concentrations. If we compare the oxidation of acetone and ethanol on platinum, the catalytic ignition of ethanol is easier. However, the heating of the catalyst during the oxidation of acetone is more significant.

In this thermochemical method of studying current-current characteristics, it is possible to determine the conditions of degeneration of the critical conditions of catalytic oxidation. These parameters also make it possible to evaluate the kinetic characteristics of oxidation reactions in a wide temperature range.

Chernenko A.S. – Dr. Sci., Professor;
Kalinchak V.V. – Dr. Sci., Professor;
Kopiyka A.K. – Ph.D, Ass. Prof.;
Roziznanyi M.V. – Ph.D student;
Fedorenko A.V. – Ph.D, Ass. Prof.

- [1] N. S. Marinkovic, M. Li, & , R. R., Adzic, *Pt-based catalysts for electrochemical oxidation of ethanol*, Topics in Current Chemistry, 377(3), 11 (2019); <https://doi.org/10.1007/s41061-019-0236-5>.
 [2] R. Rizo, S. Pérez-Rodríguez, & G. García, *Well-defined platinum surfaces for the ethanol oxidation reaction*, ChemElectroChem, 6(18), 4725 (2019); <https://doi.org/10.1002/celec.201900600>.

- [3] Guangxing Yang, Qiao Zhang, Hao Yu, Feng Peng, *Platinum-based ternary catalysts for the electrooxidation of ethanol*, Particuology, 58, 169 (2021); <https://doi.org/10.1016/j.partic.2021.01.007>.
- [4] Yunli Ge, Kaixuan Fu, Qian Zhao, Na Ji, Chunfeng Song, Degang Ma, Qingling Liu, *Performance study of modified Pt catalysts for the complete oxidation of acetone*, Chemical Engineering Science, 206, 499(2019); <https://doi.org/10.1016/j.ces.2019.05.051>.
- [5] Chaoquan Hu, *Catalytic combustion kinetics of acetone and toluene over Cu_{0.13}Ce_{0.87}O_y catalyst*, Chemical Engineering Journal, 168, 1185 (2011); <https://doi.org/10.1016/j.cej.2011.02.006>.
- [6] Mikhail N. Lyulyukin, Alexey S. Besov, Alexander V. Vorontsov, *The Influence of Corona Electrodes Thickness on the Efficiency of Plasmachemical Oxidation of Acetone*, Plasma Chem Plasma Process, 31, 23 (2011); <https://doi.org/10.1007/s11090-010-9265-0>.
- [7] Zhiwei Wang, Sha Li, Shaohua Xie, Yuxi Liu, Hongxing Dai, Guangsheng Guo, Jiguang Deng, *Supported ultralow loading Pt catalysts with high H₂O-, CO₂-, and SO₂-resistance for acetone removal*, Applied Catalysis A: General., 579, 106 (2019); <https://doi.org/10.1016/j.apcata.2019.04.018>.
- [8] Guangxing Yang, Qiao Zhang, Hao Yua, Feng Peng, *Platinum-based ternary catalysts for the electrooxidation of ethanol*, Particuology, 58, 169 (2021); <https://doi.org/10.1016/j.partic.2021.01.007>.
- [9] S.G. Babu, P.A. Priyadarsini, R. Karvembu, Copper on boehmite: A simple, selective, efficient and reusable heterogeneous catalyst for oxidation of alcohols with periodic acid in water at room temperature, Appl. Catal. A Gen. 392 (1-2) (2011) 218–224, <https://doi.org/10.1016/j.apcata.2010.11.012>.
- [10] Francisco Jos´e Morales-Leal, Javier Rivera De la Rosa, Carlos J. Lucio-Ortiz, David A. De Haro Del R´ıo, M.A. Garza-Navarro, Wei Tian, Jose E. Herrera, *Monometallic platinum and palladium-based catalysts in the competitive oxidation of methanol over the liquid-phase methanol-ethanol mixtures*, Chemical Engineering Journal, 426, 131623 (2021); <https://doi.org/10.1016/j.cej.2021.131623>.
- [11] Mitu Maria, Razus Domnina, Oancea Dumitru, *Coupled Catalytic/Gas Phase Ignition of Propane-Oxygen-Inert Mixtures on an Isothermally Heated Platinum Filament Supported on Quartz Bar*, Revista de Chimie (Bucharest). 69(4), 870 (2018); <https://doi.org/10.37358/RC.18.4.6218>.
- [12] V.V. Kalinchak, O.S. Chernenko, Thermal physics of flameless combustion of gases (monograph) (Odesa, Astroprint, 2020); <http://dspace.onu.edu.ua:8080/handle/123456789/28625>
- [13] D. A. Frank-Kamenetskiĭ, N. Thon, Diffusion and heat exchange in chemical kinetics (Princeton University Press, Princeton, New Jersey, 1955).
- [14] John H. Lienhard IV and John H. Lienhard V, A heat transfer textbook, 3rd ed (Cambridge, MA : Phlogiston Press, 2001).

О.С. Черненко, В.В. Калінчак, О.К. Копійка, М.В. Розізний, А.В. Федоренко

Каталітичне окислення ацетону і етанолу на платиновому дроті

Одеський національний університет імені І.І. Мечникова, teplophys@onu.edu.ua

Отримані вольт-амперні характеристики тонкого довгого платинового дроту повітрі з малими домішками парів ацетону чи етанолу. Використовуючи квадратичну залежність опору платини від температури розраховані температурно-струмові залежності для дроту. При концентраціях парів горючого газу вище певного значення ці залежності проявляють гістерезисний характер. Використовуючи припущення про повне окислення ацетону та етанолу на платині, як каталізаторі, та перший порядок реакції окислення, виконаний аналіз температурно-струмових залежностей. Різниця температур високо та низькотемпературного стаціонарних режимів каталітичного окислення на дротині дозволяє оцінювати концентрацію домішки в суміші. В результаті побудована експериментальна залежність критичного значення сили струму каталітичного займання та погасання газової суміші на платині від концентрації домішки. При її аналітичному описі можна доволі точно оцінити видимі значення енергії активації та передекспонентного множника реакції окислення в широкому температурному діапазоні. Запропоновано метод визначення кінетичних параметрів реакції окислення по знайдених експериментально параметрам вирождення критичних умов.

Ключові слова: каталізатор, платиновий дріт, діаметр, мала домішка газу, ацетон, етанол, займання, погасання, горіння.

Dhay Ali Sabur¹, Majeed Ali Habeeb², Ahmed Hashim²

Fabrication and Tailoring the Structural and Dielectric Characteristics of GO/Sb₂O₃/PMMA/PC Quaternary Nanostructures For Solid State Electronics Nanodevices

¹*Department of Optics Techniques, Al-Mustaqbal University College, Babylon, Iraq*

²*University of Babylon, College of Education for Pure Sciences, Department of Physics, Iraq, ahmed_tayy@yahoo.com*

In this paper, films of (PMMA-PC/Sb₂O₃-GO) quaternary nanostructures were prepared by casting method with different concentrations of Sb₂O₃/GO NPs are (0, 1.4 %, 2.8 %, 4.2 %, and 5.6 %). The structural and dielectric characteristics of nanostructures system (PMMA-PC/Sb₂O₃-GO) have been explored to use in different solid state electronics nanodevices applications. The morphology of (PMMA-PC/Sb₂O₃-GO) nanostructures films was studied using a scanning electron microscope (SEM). SEM images indicate a large number of uniform and coherent aggregates or chunks. The Fourier transform infrared spectroscopy (FTIR) analysis were studied to show the interactions between the Sb₂O₃/GO NPs and PMMA/PC blend. The dielectric properties of nanostructures films were investigated in the frequency range (100HZ-5MHZ). The dielectric constant, dielectric loss, and A.C electrical conductivity increase with the concentration of (Sb₂O₃-GO) NPs. The dielectric constant and dielectric loss were reduced, whereas electrical conductivity increased with frequency. Finally, results showed the PMMA-PC/Sb₂O₃-GO nanostructures may be considered as promising materials for solid state electronics nanodevices.

Keywords: nanocomposites, Graphene oxide, dielectric properties, blend, nanodevices.

Received 26 July 2022; Accepted 9 March 2023.

Introduction

In recent years, the worldwide community has drawn their consideration towards materials with appropriate and sustainable characteristics. Development of characteristics can be done with a variety of doping substances. The nature and the technique of their fabrication are the factors the most influencing these characteristics. Targeted applications and cost guide researchers on the choice of substances and the technology to be employed in developing the desired devices. Polymers and mainly hybrid composites (organic-inorganic) are attracting growing consideration from researchers as a result of their utilize in numerous industrial sectors [1]. Poly-methylmethacrylate (PMMA) is an significant kind of polymer amid thermoplastics. PMMA is an optically transparent thermoplastic, which is expansively used as a substitute for inorganic glass. PMMA has been prepared using various polymerization

techniques. PMMA is an significant thermoplastic substance with extensive fields in several technological fields due to its unique optical, mechanical, thermal and electrical properties. PMMA is an amorphous polymer with excellent chemical, weather, scratch, and corrosion resistance. It is lightweight, shatter-resistant, and possess favorable processing conditions. PMMA has been used in a range of fields like coatings, additives, sealers, optical fibers, and transparent neutron stoppers [2]. Polycarbonate (PC) has a high degree of transparency. As a result, it may be employed in a variety of industrial applications, including electrical devices, optical fibers, optical storage devices, and glass lenses. However, improving the optical characteristics of polycarbonate is required in contemporary industrial applications. Furthermore, inorganic fillers are promising possibilities for improving the mechanical characteristics, transparency, and toughness of PC without compromising its mechanical qualities. PC appears to be a good host material for a

variety of NPs. Doped Polycarbonate composites containing metal chalcogenides or oxides have distinct optical and structural properties, making them suitable for industrial applications [3]. GO is insulating due to the breaking of the conjugated electronic structure by means of

oxidized functional groups, and it contains permanent defects and disorders. Hence, the electrical characters of GO sheets are dissimilar from those of pristine graphene [4]. Antimony trioxide (Sb_2O_3) is used as a catalyst, a retardant, a conductive substance, a functional filler, and an optical material. Sb_2O_3 is also valuable in plastics, paints, adhesives, and textile back coatings as conductive materials and a high-efficiency flame-retardant synergist [5]. This work aims to prepare of (PMMA-PC/ Sb_2O_3 -GO) nanocomposite film studying the structural and dielectric properties to use in different electronic devices.

I. Materials and Method

Polymethylmethacrylate (PMMA), polycarbonate (PC), antimony trioxide (Sb_2O_3), and graphene oxide (GO) were employed in this study. The casting technique was used to prepare nanocomposites films (PMMA-PC/ Sb_2O_3 -GO). The films were prepared by dissolving 1g of the (PMMA-PC) blend with ratio 80/20 % in

chloroform using a magnetic stirrer. The (Sb_2O_3 -GO) NPs were introduced in the polymeric blend by (1.4%, 2.8%, 4.2%, and 5.8%). The dielectric properties are determined in the frequency range 100Hz-5MHz using an LCR meter.

The dielectric constant (ϵ') is calculated by [6]:

$$\epsilon' = C_p / C_0 \quad (1)$$

C_0 and C_p are vacuum and parallel capacitances. The dielectric loss (ϵ'') is gives by [6]:

$$\epsilon'' = \epsilon' \cdot D \quad (2)$$

D is the dispersion factor. The A.C conductivity was calculated by [7]:

$$\sigma_{A.C} = W \cdot \epsilon'' \cdot \epsilon_0 \quad (3)$$

w is the angular frequency.

II. Results and Discussion

Figure (1) indicates the SEM images of (PMMA-PC/ Sb_2O_3 -GO) nanocomposites. The compatibility of different polymer components with (In_2O_3 , Sb_2O_3) nanoparticles was investigated using scanning electron

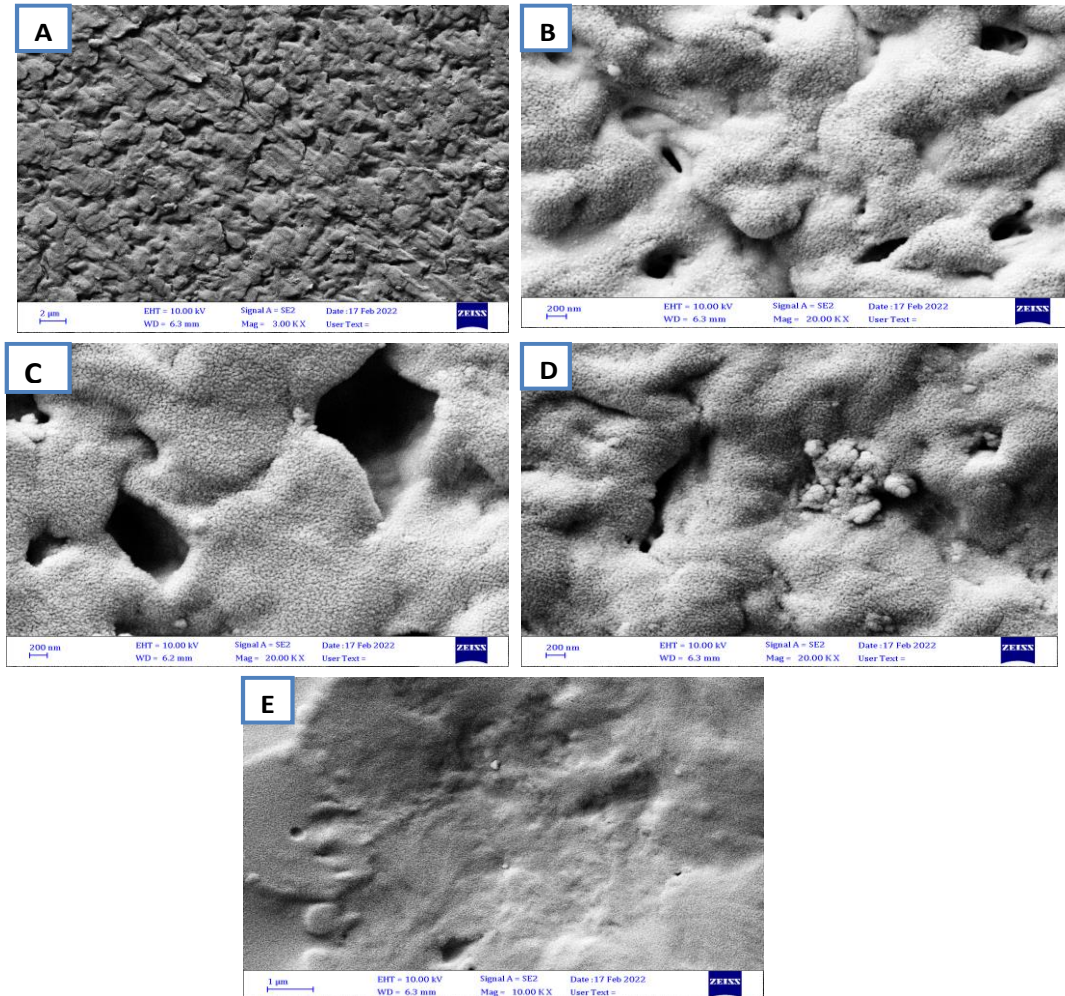


Fig. 1. SEM images for (PMMA-PC/ Sb_2O_3 -GO) Nanocomposites: (A) for pure (B) for 1.4 wt.% Sb_2O_3 -GO NPs (C) for 2.8 wt.% Sb_2O_3 -GO NPs (D) for 4.2wt.% Sb_2O_3 -GO NPs (E) for 5.6 wt.% Sb_2O_3 -GO NPs.

microscopy. The films have a homogeneous grain distribution at surface morphology, whereas the surfaces of the (PMMA-PC/Sb₂O₃-GO) nanocomposites include numerous aggregates or pieces of nanoparticles randomly scattered on the surface. The results are shown when increasing the content of (Sb₂O₃-GO) NPs, the number of aggregations on the surface can be increased [8], also the SEM images show the (Sb₂O₃-GO) nanoparticles have formed the paths network inside the (PMMA-PC) blend where charge carriers are allowed to pass through this the paths [9]. Figure (2) shows the FTIR spectra of (PC-PMMA-Sb₂O₃-GO) nanocomposites at room temperature in the range 4000–500 cm⁻¹. These results reveal that there was no chemical interaction between the components in the (PMMA-PC) blends. The transmittance of the carbonyl and methoxyl stretches of PMMA reduced with increasing in PMMA content, while the transmittance of these peaks increased with an increase in PC concentration, according to a detailed examination of the FTIR spectra for these blends. Because no alterations in the peaks of any of these functional groups in the (PMMA-PC) blend spectra suggest the creation of polymer blends, it may be argued that there is no chemical interaction between component polymers. Thus, these are certainly physical blends. The absorption band at around 1723cm⁻¹ appear C = O stretching band in PMMA. The FTIR bands

at 1434cm⁻¹ attributed to CH₂ scissoring. O – CH₃ stretching resulted in a peak at 1143.66 cm⁻¹ rocking made of vibration. while the peak at 749.63 cm⁻¹ was due to CH₂ rocking made of vibration. Finally, the adding of (Sb₂O₃ and GO) NPs to the polymer blend results in two noteworthy alterations: modest changes in absorption band intensities and vibrational band intensities in peak at 995.79 cm⁻¹ and 749cm⁻¹. This suggests that the interaction between Sb₂O₃ and GO NPs and the two polymers has resulted in a decoupling of the corresponding vibrations.

Figure (3) shows the dielectric constant of (PMMA-PC/Sb₂O₃-GO) nanocomposites varies with frequency, the dielectric constant values decrease with increasing applied frequency, with increasing frequency causing a decrease in space charge polarization to total polarization, with space charge polarization becoming more contributing to polarization at low frequencies and less contributing with increasing frequency, causing a decrease in dielectric constant values for all samples of (PMMA-PC/Sb₂O₃-GO)nanocomposites with polarization. When compared to electronic polarization, ionic polarization reacts somewhat more to changes in field frequencies because the mass of an ion is larger. Figure (4) shows the dielectric constant of (PMMA-PC/Sb₂O₃-GO) nanocomposites vary with the Sb₂O₃-GO NPs content at 100 Hz, The dielectric constant of (PMMA-PC) blend increases with increased

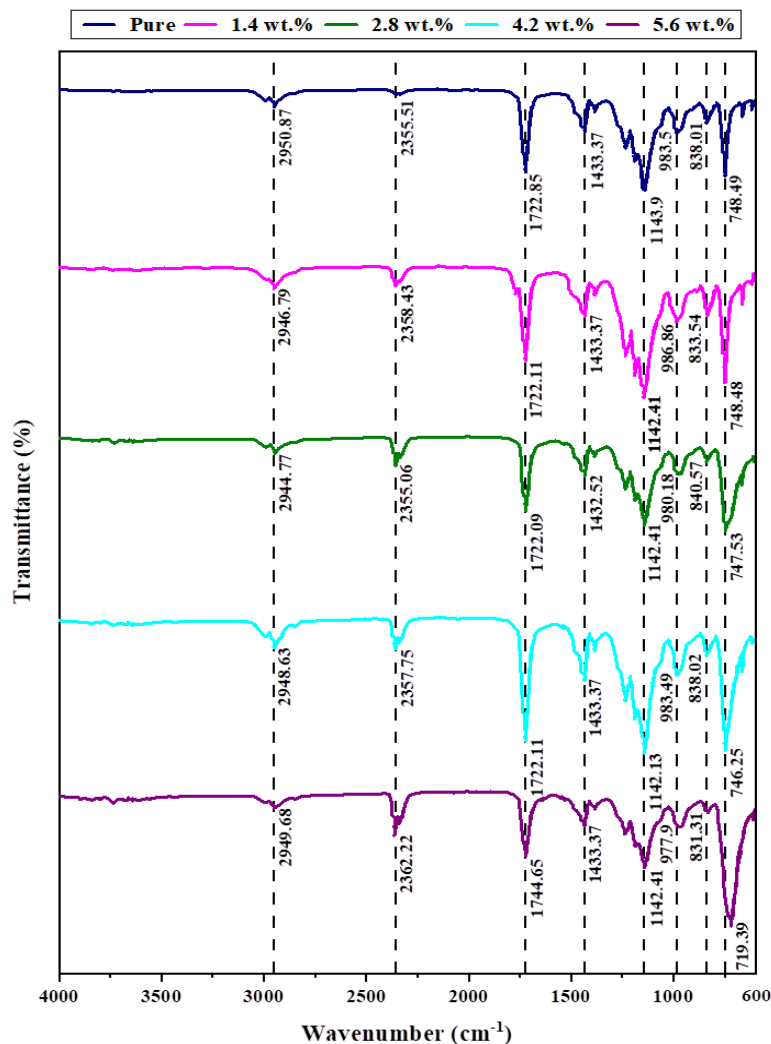


Fig. 2. FTIR spectra for (PC-PMMA-Sb₂O₃-GO) NPs (A) for (PMMA-PC) blend (B) for 1.4wt% (Sb₂O₃-GO) NPs, (C) for 2.8wt% (Sb₂O₃-GO)NPs, (D) for 4.2wt% (Sb₂O₃-GO) NPs, (E) for 5.8wt% (Sb₂O₃-GO) NPs.

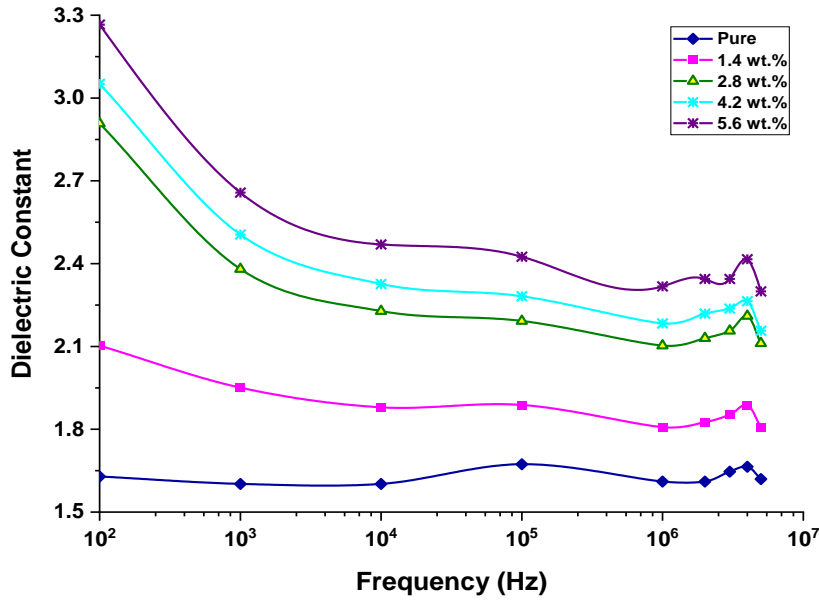


Fig. 3. Variation of dielectric constant for (PMMA-PC/Sb₂O₃-GO) Nanocomposites with frequency at room temperature.

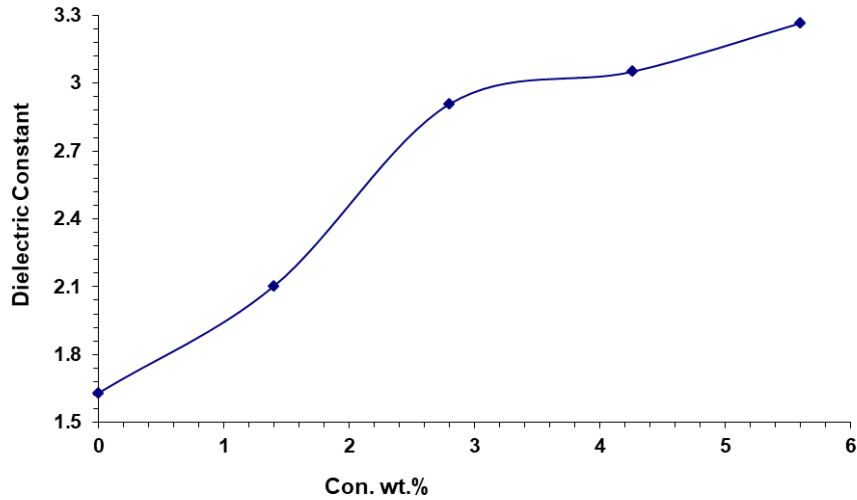


Fig. 4. Effect of (Sb₂O₃-GO) NPs content on dielectric constant for (PMMA-PC) blend at 100Hz.

concentration of Sb₂O₃-GO NPs. This result might be attributed to interfacial polarization inside nanocomposites under an alternating electric field (E1) and, additionally, in charge carriers [10]. Given the high value of the dielectric constant for Sb₂O₃-GO NPs, the dielectric constant (PMMA-PC/Sb₂O₃-GO) nanocomposites are also high [11].

Figure (5) indicates the dielectric loss with frequency for (PMMA-PC) blend with and without different (Sb₂O₃-GO) NPs concentrations. When the frequency is raised, the dielectric loss values for all of the samples tested drop. The creation of free charges occurs at a lower frequency when free charges are generated at the interface between the studied material and the electrode, it also has a maximum value [12]. After a certain frequency value, charge carriers can no longer follow the applied electric field, dielectric loss lowers with increasing frequency, and the fast reduction may be related to polarization for trapped carriers [13]. Figure (6) indicates the dielectric loss increases as the concentration of (Sb₂O₃-GO) NPs increases, a result ascribed to a rise in charge carriers

inside the nanocomposites. Furthermore, the increase in dielectric loss with increasing concentrations of (Sb₂O₃-GO) NPs might be due to the creation of a path of conductive, which would result in leakage current [14,15].

Figure (7) shows the A.C electrical conductivity of (PMMA-PC/Sb₂O₃-GO) nanocomposites changes with the frequency of the electric field at room temperature. Because of charge-carrier mobility and ion hopping from the cluster, A.C electrical conductivity improves with higher electric field frequency. At low frequencies, charge buildup occurs at the electrode-electrolyte interface, resulting in reduced ion mobility and electrical conductivity [16]. Because charge-carrier mobility rises as the frequency field increases [17], the electrical conductivity of nanocomposites improves which is agree with [18-20]. The behavior of A.C electrical conductivity of (PMMA-PC) with Sb₂O₃-GO NPs contents is shown in Figure (8). Because of the composition of dopant NPs, the A.C electrical conductivity of the PMMA -PC blend improves with increased Sb₂O₃-GO NPs concentration,

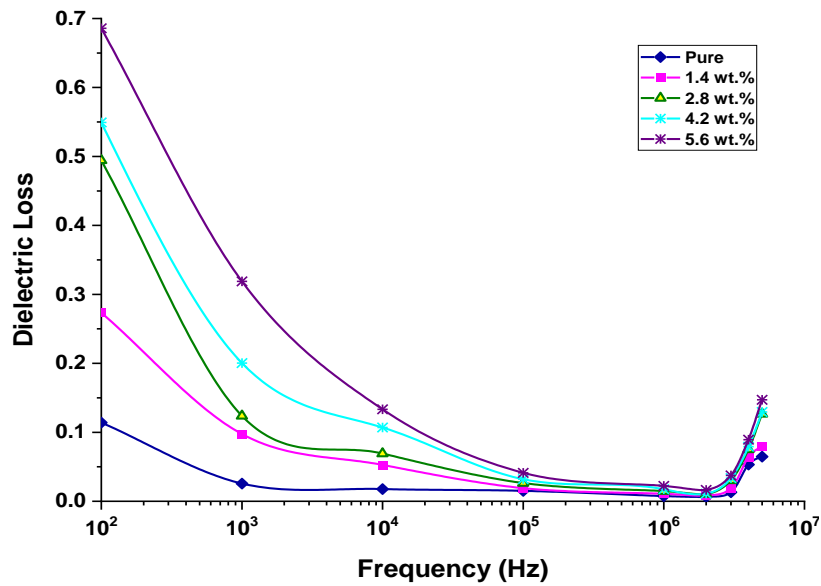


Fig. 5. Variation of dielectric loss for (PMMA -PC/Sb₂O₃-GO) Nanocomposites with frequency at room temperature.

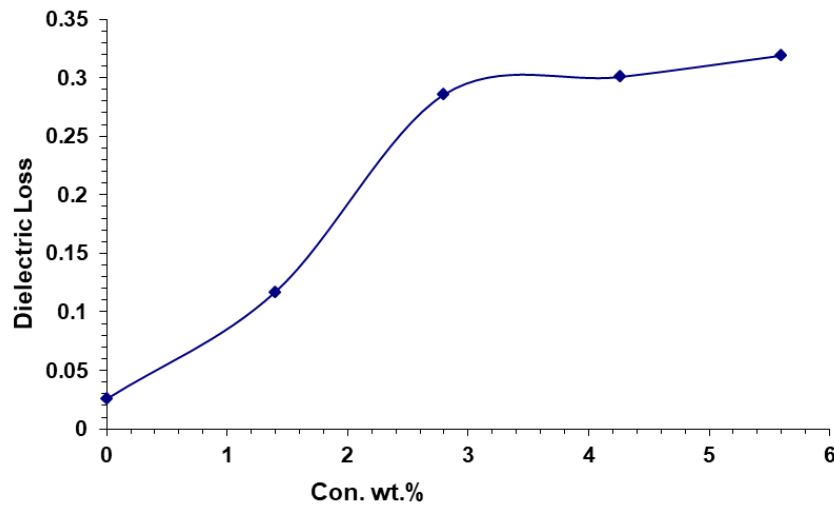


Fig. 6. Effect of(Sb₂O₃ - GO) NPs content on dielectric loss for (PMMA- PC) blend at 100Hz.

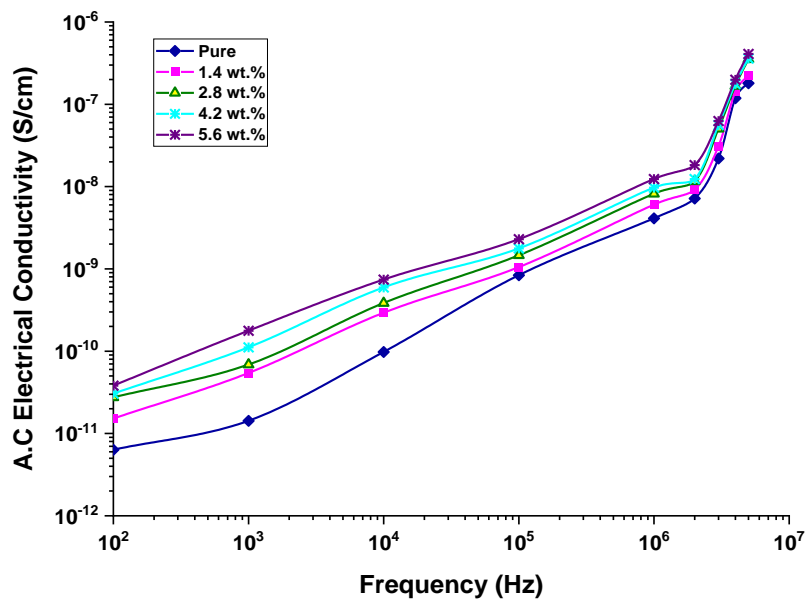


Fig. 7. Variation of A.C electrical conductivity for (PMMA -PC/Sb₂O₃-GO) nanocomposites with frequency at room temperature.

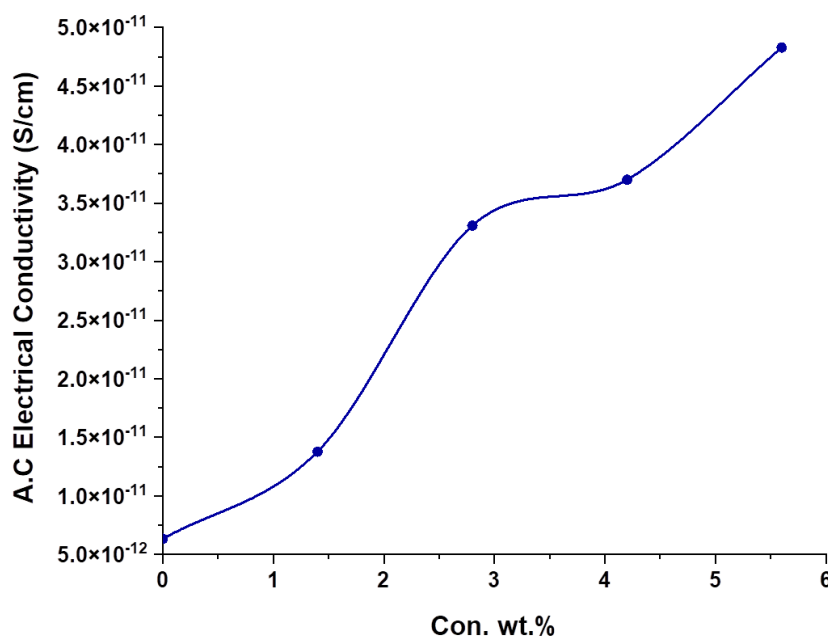


Fig. 8. Effect of (Sb_2O_3 -GO) content on A.C electrical conductivity for (PMMA-PC) blend at 100Hz.

allowing for an increase in charge carriers [21-23]. As a result, the resistance of nanocomposite materials reduces, while A.C electrical conductivity rises. At high concentrations, the nanoparticles in the nanocomposites form a network, which is consistent with agree with [24,25].

Conclusions

Flexible, lightweight and few cost films of (PMMA - PC/ Sb_2O_3 -GO) were prepared using the solution cast technique. The structure and dielectric properties of (PMMA -PC/ Sb_2O_3 -GO) films were studied to use in different electrical applications. SEM micrographs confirm the miscibility of polymers (PMMA -PC/ Sb_2O_3 -GO) in the blend. The growth of (Sb_2O_3 -GO) in (PMMA -PC) blend was confirmed by the presence of irregular-

shaped granular microstructures. The FTIR spectra show the (PMMA-PC) blends did not indicate the existence of any chemical interaction the adding of (Sb_2O_3 and GO) nanoparticles to the polymer blend results in two noteworthy alterations: modest changes in absorption band intensities and vibrational band intensities in peak at 995.79 cm^{-1} and 749 cm^{-1} . The dielectric constant, dielectric loss and A.C electrical conductivity rise as the content of (Sb_2O_3 -GO) increases. The dielectric constant and dielectric loss reduce as frequency rises, although the A.C electrical conductivity increases. The results show that the nanocomposites (PMMA-PC/ Sb_2O_3 -GO) might be employed in a range of electronic applications.

Sabur Dhay Ali – PhD student;
Habeeb Majeed Ali – PhD, Prof.;
Hashim Ahmed – PhD, Prof.

- [1] A. Hashim, M. A. Habeeb, & A. Hadi, *Synthesis of novel polyvinyl alcohol–starch-copper oxide nanocomposites for humidity sensors applications with different temperatures*, Sensor Letters, 15(9), 758 (2017); <https://doi.org/10.1166/sl.2017.3876>.
- [2] A. Hazim, H.M. Abduljalil, & A. Hashim, *Analysis of Structural and Electronic Properties of Novel (PMMA/ Al_2O_3 , PMMA/ Al_2O_3 -Ag, PMMA/ ZrO_2 , PMMA/ ZrO_2 -Ag, PMMA-Ag) Nanocomposites for Low Cost Electronics and Optics Applications*, Trans. Electr. Electron. Mater. 21, 48 (2020); <https://doi.org/10.1007/s42341-019-00148-0>.
- [3] Kaoutar Benthami, Mai ME. Barakat and Samir A. Nouh, *Modification of optical properties of PC-PBT/ Cr_2O_3 and PC-PBT/ CdS nanocomposites by gamma irradiation*, Eur. Phys. J. Appl. Phys., 92 (2), 20402 (2020); <https://doi.org/10.1051/epjap/2020200201>.
- [4] G.G. Politano, C. Versace, *Electrical and Optical Characterization of Graphene Oxide and Reduced Graphene Oxide Thin Films*, Crystals, 12, 1312 (2022); <https://doi.org/10.3390/cryst12091312>.
- [5] A. K. Jha, K. Prasad, and K. Prasad, *A green low-cost biosynthesis of Sb_2O_3 nanoparticles*, Biochem. Eng. J., 43(3), 303 (2009); <https://doi.org/10.1016/j.bej.2008.10.016>.
- [6] T.A. Abdel-Baset, A. Hassen, *Dielectric relaxation analysis and Ac conductivity of polyvinyl alcohol/polyacrylonitrile film*, Physica B, 499, 24 (2016); <http://dx.doi.org/10.1016/j.physb.2016.07.002>.
- [7] P. Beena and H. S. Jayanna, *Dielectric studies and AC conductivity of piezoelectric barium titanate ceramic polymer composites*, Polymers and Polymer Composites, 27(9) 619 (2019); <https://doi.org/10.1177/0967391119856140>.

- [8] A. Qureshi¹, A. Mergen¹ and B. Aktas, *Dielectric and magnetic properties of YIG/PMMA nanocomposites*, Journal of Physics: Conference Series, 153, 1 (2009); <https://doi.org/10.1088/1742-6596/153/1/012061>.
- [9] N.K. Abbas, M.A. Habeeb, and A.J.K. Algidsawi, *Preparation of chloro penta amine cobalt (III) chloride and study of its influence on the structural and some optical properties of polyvinyl acetate*, International Journal of polymer Science, 2015, 926789 (2015); <https://doi.org/10.1155/2015/926789>.
- [10] D.Vaishnav¹ and R. K. Goyal, *Thermal and Dielectric Properties of High-Performance Polymer/ZnO Nanocomposites*, IOP Conf. Series: Journal of Materials Science and Engineering, 64, 1 (2014); <https://doi.org/10.1088/1757-899X/64/1/012016>.
- [11] A. Srivastava, K. Kumar Jana, P. Maiti, D. Kumar, and O. Parkash, *Investigations on Structural, Mechanical, and Dielectric Properties of PVDF/Ceramic Composites*, Journal of Engineering, 2015, Article ID 205490, 9 (2015); <https://doi.org/10.1155/2015/205490>.
- [12] E. Abdelrazek, Elashmawi I, Hezma A, Rajeh A, Kamal M, *Effect of an encapsulate carbon nanotubes (CNTs) on structural and electrical properties of PU/PVC nanocomposites*, Phys B Condens Matter., 502, 48 (2016), <https://doi.org/10.1016/j.physb.2016.08.040>.
- [13] A. Rajeh, HM Ragab, MM Abutalib. *Co doped ZnO reinforced PEMA/PMMA composite: structural, thermal, dielectric and electrical properties for electrochemical applications*, J Mol Struct., 1217, 128447 (2020); <https://doi.org/10.1016/j.molstruc.2020.128447>.
- [14] S. Ju¹, M. Chen¹, H. Zhang and Z. Zhang, *Dielectric properties of nano silica/low-density polyethylene composites: The surface chemistry of nanoparticles and deep traps induced by nanoparticles*, Journal of express Polymer Letters, 8(9), 682 (2014), <https://doi.org/10.3144/expresspolymlett.2014.71>.
- [15] .Chakraborty, K. Gupta, D. Rana and A. Kumar Meikap, *Dielectric relaxation in polyvinyl alcohol–polypyrrole–multiwall carbon nanotube composites below room temperature*, Advances in Natural Sciences, 4, 1 (2014); <http://dx.doi.org/10.1088/2043-6262/4/2/025005>.
- [16] P. Vasudevan, S. Thomas, K. Arunkumar, S. Karthika and N. Unnikrishnan, *Synthesis and dielectric studies of poly (vinyl pyrrolidone) /titanium dioxide nanocomposites*, Journal of Materials, Science and Engineering, 73, 1, (2015); <https://doi.org/10.1088/1757-899X/73/1/012015>.
- [17] I. Tantis, G. Psarras and D. Tasis, *Functionalized graphene poly (vinyl alcohol) nanocomposites: Physical and dielectric properties*, Journal of express Polymer Letters, 6(4), 283 (2012); <https://doi.org/10.3144/expresspolymlett.2012.31>.
- [18] C. M. Mathew, K. Kesavan, and S. Rajendran, *Structural and Electrochemical Analysis of PMMA Based Gel Electrolyte Membranes*, International Journal of Electrochemistry, 2015, Article ID 494308, 7, (2015); <https://doi.org/10.1155/2015/494308>.
- [19] P. Pradeepa and M. Ramesh Prabhu, *Investigations on the Addition of Different Plasticizers in poly (ethylmethacrylate)/poly (vinylidene fluoride-co-hexa fluoro propylene) Based Polymer Blend Electrolyte System*, International Journal of Chemical Technology Research, 7(4), 2077 (2015);
- [20] M.A. Habeeb, A. Hashim, and A. Hadi, *Fabrication of New Nanocomposites: CMC-PAA-PbO₂ Nanoparticles for Piezoelectric Sensors and Gamma Radiation Shielding Applications*, Sensor Letters, 15(9), (2017); <https://doi.org/10.1166/sl.2017.3877>.
- [21] Hojjat and A. Mahmood and Borhani, *Effect of EVA Content upon the Dielectric Properties in LDPE-EVA Films*, International Journal of Engineering Research, 4 (2), 69 (2015); <https://doi.org/10.17950/ijer/v4s2/206>.
- [22] K. J. Kadhim, I. R. Agool, & A. Hashim, *Effect of zirconium oxide nanoparticles on dielectric properties of (PVA-PEG-PVP) blend for medical application*, Journal of Advanced Physics, 6(2), 187 (2017); <https://doi.org/10.1166/jap.2017.1313>.
- [23] O. Abdullah, G. M. Jamal, D. A. Tahir and S. R. Saeed, *Electrical Characterization of Polyester Reinforced by Carbon Black Particles*, International Journal of Applied Physics and Mathematics, 1 (2), 101 (2011); <https://doi.org/10.7763/IJAPM.2011.V1.20>.
- [24] N. Hayder, M.A. Habeeb, and A. Hashim, *Structural, optical and dielectric properties of (PS-In₂O₃/ZnCoFe₂O₄) nanocomposites*, Egyptian Journal of Chemistry, 63, 577 (2020), <https://doi.org/10.21608/EJCHEM.2019.14646.1887>.
- [25] Qayssar M. Jebur, Ahmed Hashim and Majeed A. Habeeb, *Fabrication, Structural and Optical Properties for (PolyvinylAlcohol–Polyethylene Oxide–Iron Oxide) Nanocomposites*, Egypt. J. Chem., 63(2), (2020); <https://doi.org/10.21608/ejchem.2019.10197.1669>.

Д.А. Сабур¹, М.А. Хабіб², А. Хашим²

Виготовлення четвертинних наноструктур GO/Sb₂O₃/PMMA/PC та адаптація їх структурних і діелектричних характеристик для твердотільних електронних нанопристроїв

¹Кафедра оптичної техніки, Університетський коледж Аль-Мустакбал, Вавилон, Ірак

²Вавилонський університет, Освітній коледж чистих наук, факультет фізики, Ірак, ahmed_tayy@yahoo.com

Плівки четвертинних наноструктур (PMMA-PC/Sb₂O₃-GO) отримано методом лиття з різними концентраціями НЧ Sb₂O₃/GO (0, 1,4 %, 2,8 %, 4,2 % та 5,6 %). Структурні та діелектричні характеристики системи наноструктур (PMMA-PC/Sb₂O₃-GO) досліджували для їх використання в різних нанопристроях твердотільної електроніки. Морфологію плівок наноструктур (PMMA-PC/Sb₂O₃-GO) досліджено за допомогою скануючої електронної мікроскопії (SEM). SEM-зображення вказують на велику кількість однорідних і когерентних агрегатів або шматків. Аналіз інфрачервоної спектроскопії з перетворенням Фур'є (FTIR) проводили, щоб показати взаємодію між Sb₂O₃/GO NP та сумішшю PMMA/PC. Досліджено діелектричні властивості плівок наноструктур в діапазоні частот (100Гц-5МГц). Показано, що діелектрична проникність, діелектричні втрати та електропровідність змінного струму зростають зі збільшенням концентрації НЧ (Sb₂O₃-GO). Діелектрична проникність і діелектричні втрати були зменшені, тоді як електрична провідність зростала з частотою. Результати показали, що наноструктури PMMA-PC/Sb₂O₃-GO можна розглядати як перспективні матеріали для твердотільних електронних нанопристроїв.

Ключові слова: нанокompозити, оксид графену, діелектричні властивості, суміш, нанопристрої.

N.A. Smirnova¹, M.S. Maniuk¹, A.V. Korotun^{1,2}, I.M. Titov³

Optical absorption of the composite with the nanoparticles, which are covered with the surfactant layer

¹National University Zaporizhzhia Polytechnic, Zaporizhzhia, Ukraine, andko@zpu.edu.ua

²G.V. Kurdyumov Institute for Metal Physics of the NAS of Ukraine, Kyiv, Ukraine

³UAD Systems, Zaporizhzhia, Ukraine

The optical properties of the nanocomposite with two-layer spherical inclusions “metallic core – surfactant layer” have been studied in the work. The question connected with an influence of the processes at the interface “metal – adsorbate” on the excitation of the surface plasmonic resonances in the nanoparticle has been studied. The fact of splitting of the surface plasmonic resonance due to the influence of the absorption bond near the surface of the metallic nanoparticles and due to the emergence of the additional energy states has been established. The relations for the effective parameters which describe the losses of coherence under the scattering at the chemical interface have been obtained. The calculations for the frequency dependencies of the diagonal components of the dielectric permittivity tensor of two-layer nanoparticle and for the absorption coefficient of the nanocomposite have been performed. It has been shown that the frequency dependencies for the real and imaginary parts of the longitudinal component of the dielectric tensor are close to the similar dependencies for the real and imaginary parts of the dielectric function for the spherical metallic nanoparticle. At the same time the real and imaginary parts of the transverse component weakly depend on the frequency in the visible spectrum and oscillate in the infrared range. It has been established that the absorption coefficient of the composite can have one or two maximums depending on the sizes and on the material of the particles-inclusions.

Keywords: dielectric tensor, absorption coefficient, adsorbate, surface plasmonic resonance, nanocomposite, size dependence, effective relaxation rate.

Received 26 August 2022; Accepted 10 March 2023.

Introduction

Metallic nanoparticles play the significant role in electronic, optoelectronic, thermal and biomedical applications and, precisely for this reason, they attract an attention of the researchers for a long time (see, e.g., [1,2] and references therein). The new trend in optics of metallic nanostructures – nanoplasmonics has appeared due to this fact. One of the important problems of this trend is the study of an optical absorption in the external electromagnetic field [3, 4] and the setting of an optical response which is very useful for the practical applications [5]. An optical absorption of the metallic nanoparticles is induced by the surface plasmonic resonances (SPR), which are the collective oscillations of conduction electrons, excited by the electromagnetic wave [6].

Localized SPR in the metallic nanoparticles of the simplest geometry (spheres, ellipsoids, cylinders) are fundamental for the understanding of the properties of surface plasmons and they have been researched for several decades (see, e.g., [7] and references therein). However, the available in the literature data, connected with the size dependencies for the frequencies of SPR and for the widths of resonance lines, are rather controversial and the dominant physical mechanism, which determines these size dependencies, is the subject of serious debate (see, e.g., [8] and references therein).

The width of the resonance line is directly proportional to the relaxation rate (plasmon decay rate) and the additive contribution into the relaxation rate is given by the different mechanisms, in particular: volumetric damping, scattering on the surface of the

nanoparticle and the radiation damping [9]. The volumetric damping is determined by the processes of electron-electron scattering, electron-photon scattering and also by the scattering of electrons on the impurity atoms and on the defects of the crystal structure [10]. The contribution of the scattering of electrons on the surface of the nanoparticles increases with the decrease in their size [11], while the radiation damping plays an important role for the relatively big particles [12].

It was considered in the majority of experimental [13–15] and theoretical works [11, 12, 16–19] that the width of SPR line varies smoothly with the variation of the dielectric permittivity of the environment. It was established in the work [20] in the frameworks of the finite equations method that the width of SPR line oscillates as the dielectric permittivity function of the environment. The expressions for the surface plasmons lifetime was obtained in the works [11, 12] using the same method and taking into account the surface and radiation relaxation channels. The work [21] contains the numerical studies, based on the independent of time approximation of the local density, which indicate the existence of the size oscillations of the width of SPR line.

The presence of the surfactant (molecules, adsorbed on the surface of the nanoparticles), which is used for the stabilization of the metallic nanoparticles [22], is one more important factor of the shift and the widening of SPR peaks. It is connected with the fact that the additional energy states appear as the result of the adsorption bonding near the surface of metallic nanoparticles. These states contribute into the decay of the surface plasmons, excited in the particle. That is why the presence of the chemically modified surface results in the decrease in amplitude and increase in thickness of SPR peaks in metallic nanoparticles, which was confirmed with the help of two-photon emission spectroscopy [23]. The extension value for SPR line is considered to be one of the main parameters in such applications as sensorics [24], surface-enhanced Romanov scattering [25], field concentration on the ends of nanowires [26], plasmonic nanolithography [27], nanooptics [28] etc.

The study of the optic characteristics of the composites with two-layer nanoparticles-inclusions of the different morphology is of great practical interest from the viewpoint of the production of the materials with the predetermined properties. In previous works [29–31] the absorption by the composites with two-layer spherical nanoparticles, namely: metal-oxide nanoparticles [29], bimetallic nanoparticles [30], shell nanoparticles [31] was studied. In particular, it was established in [29] that the numerical results in the frameworks of the model of the particle with oxide shell are in good agreement with the experimental results as for the absorption spectrum. Moreover, it is known that the optical properties of both metallic nanoparticles and adsorbates, with the help of which these particles are functionalized, are very different from the properties of the composite particle. It should be pointed out that the question connected with the influence of the layer of the surfactant on the absorption properties of nanocomposite with the inclusions of type “metal-adsorbate” is unexplored. That is why the study of the influence of chemical interaction on the interface “metallic core – adsorbate layer” on the adsorption

spectrum of nanocomposite with such layered particles is actual.

I. Basic relations

Let us consider the composite that consists of the dielectric medium with permittivity ϵ_m and the spherical nanoparticles coated in the layer of adsorbed molecules immersed in this medium (fig. 1).

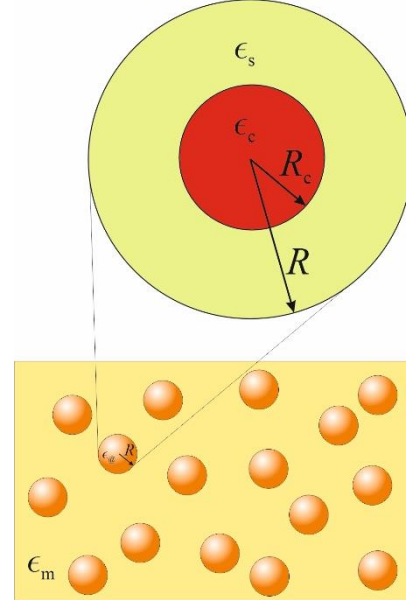


Fig. 1. Geometry of the problem.

The scattering of electrons is anisotropic due to the presence of the adsorbate layer on the nanoparticle, and the absorption coefficient of such composite is equal to [32]

$$\eta(\omega) = \frac{1}{3} (2\eta_{\perp}(\omega) + \eta_{\parallel}(\omega)), \quad (1)$$

Where

$$\eta_{\perp(\parallel)}(\omega) = \frac{9\omega}{c} \beta \epsilon_m^{3/2} \frac{\text{Im}\epsilon_{\text{@}}^{\perp(\parallel)}(\omega)}{[\text{Re}\epsilon_{\text{@}}^{\perp(\parallel)}(\omega) + 2\epsilon_m]^2 + [\text{Im}\epsilon_{\text{@}}^{\perp(\parallel)}(\omega)]^2}. \quad (2)$$

Here ω is the frequency of the incident electromagnetic wave, and c – its velocity; β – the volumetric content of metallic fraction in the dielectric matrix; $\epsilon_{\text{@}}^{\perp(\parallel)}$ – the diagonal components of the dielectric tensor of the composite nanoparticle “metallic core – adsorbed layer of molecules”, which are determined by the relation [33]

$$\epsilon_{\text{@}}^{\perp(\parallel)} = \epsilon_s \frac{\epsilon_c^{\perp(\parallel)} + 2\epsilon_s + 2\beta_c(\epsilon_c^{\perp(\parallel)} - \epsilon_s)}{\epsilon_c^{\perp(\parallel)} + 2\epsilon_s - \beta_c(\epsilon_c^{\perp(\parallel)} - \epsilon_s)}. \quad (3)$$

In formula (3) $\beta_c = (R_c/R)^3$ is the volumetric content of metal in the composite nanoparticle (R_c is the radius of metallic core, R is the total radius of the composite particle), ϵ_s is the dielectric permittivity of adsorbate, and the components of the tensor of the dielectric permittivity

Optical absorption of the composite with the nanoparticles, which are covered with the surfactant layer

of metal core in the frameworks of Drude model have the form

$$\epsilon_c^{\perp(\parallel)} = \epsilon^\infty - \frac{\omega_p^2}{\omega(\omega + i\gamma_{\text{eff}}^{\perp(\parallel)})}, \quad (4)$$

where ϵ^∞ is the contribution of the crystal lattice into the dielectric permittivity; ω_p is the frequency of bulk plasmons, and the expression for the effective relaxation rate has the form

$$\gamma_{\text{eff}}^{\perp(\parallel)} = \gamma_{\text{bulk}} + \gamma_s + \gamma_{\text{rad}} + \gamma_{\text{chem}}^{\perp(\parallel)}. \quad (5)$$

In relation (5) γ_{bulk} is the bulk relaxation rate, which is considered to be constant for each metal; γ_s and γ_{rad} are the surface relaxation rate and radiation decay rate. Let us point out that the value γ_{rad} can be neglected for the relatively small particles.

The surface relaxation rate can be written in the form

$$\gamma_s = \mathcal{S}_{\text{size}} \frac{v_F}{R_c}, \quad (6)$$

where v_F is Fermi electron velocity; R_c is the radius of the nanoparticle,

$$\mathcal{S}_{\text{size}} = \frac{1}{4} \left(\frac{\omega_p}{\omega} \right)^2 \left[1 - \frac{2v_s}{\omega} \sin \frac{\omega}{v_s} + \frac{2v_s^2}{\omega^2} \left(1 - \cos \frac{\omega}{v_s} \right) \right] \quad (7)$$

is an effective parameter which describes the degree of coherence loss under the scattering of electrons on the surface of the nanoparticle [11], $v_s = v_F/2R_c$ is the frequency of the individual oscillations of electrons.

The last addend in formula (5) describes the process

of relaxation, caused by the presence of the interface “metal – adsorbed layer” [34,35]

$$\gamma_{\text{chem}}^{\perp(\parallel)} = \mathcal{S}_{\perp(\parallel)}^{\text{interface}} \frac{v_F}{R_c}. \quad (8)$$

In order to calculate parameters $\mathcal{S}_{\perp(\parallel)}^{\text{interface}}$ let us use the approach, proposed in [34]. In the frameworks of this approach the local density of the states around adsorbed atom (molecule) can be described with the help of Lorentz formula

$$Q_a(\varepsilon) = \frac{1}{\pi} \frac{\Gamma_a/2}{(\varepsilon - \varepsilon_a)^2 + (\Gamma_a/2)^2}, \quad (9)$$

where ε_a and Γ_a are an amplitude and the width of the spectral line, correspondingly.

Thus, the frequency dependencies for the coefficients $\mathcal{S}_{\perp(\parallel)}^{\text{interface}}$ are determined by formulas

$$\mathcal{S}_{\perp}^{\text{interface}} = 4n_a \frac{\omega_{sp}}{v_F} \frac{\varepsilon_s}{\varepsilon^\infty + 2\varepsilon_s} \mathcal{F}_{\perp}(\omega); \quad (10)$$

$$\mathcal{S}_{\parallel}^{\text{interface}} = \frac{3}{8} n_a \sigma_0 \left(\frac{1 + 2\varepsilon_s}{\varepsilon^\infty + 2\varepsilon_s} \right) \mathcal{J}(\omega). \quad (11)$$

In formulae (10) and (11): $\sigma_0 = 64\omega_F Q/3\pi n_e v_F$ (n_e is the concentration of electrons, Q is the number, which depends on the symmetry of the adsorbed resonance state, $Q = 0,2$ for s - and p_z -states, $Q \approx 0,33$ – for p_x - and p_y -states); $\omega_F = \varepsilon_F/\hbar$ (ε_F is Fermi energy); n_a is the surface density of adsorbed atoms; ω_{sp} is the frequency of SPR, and

$$\mathcal{J}(\hbar\omega) = \frac{\pi}{4\varepsilon_F \hbar\omega} \int_{\varepsilon_F - \hbar\omega}^{\varepsilon_F} d\varepsilon [\varepsilon \Gamma_a Q_a(\varepsilon + \hbar\omega)(\varepsilon + \hbar\omega) \Gamma_a Q_a(\varepsilon)]; \quad (12)$$

$$\mathcal{F}_{\perp}(\hbar\omega) = \frac{1}{2\pi^2 \varepsilon_0} (ed)^2 \int_{\varepsilon_F - \hbar\omega}^{\varepsilon_F} d\varepsilon Q_a(\varepsilon) Q_a(\varepsilon + \hbar\omega) \quad (13)$$

Where d is the distance between the center of adsorbed molecule and the image plane.

Calculating the integrals in (12) and (13) and taking into account the expression (9), we obtain

$$\mathcal{S}_{\parallel}^{\text{interface}} = \frac{3\Gamma_a}{16\varepsilon_F} n_a \sigma_0 \left(\frac{1 + 2\varepsilon_s}{\varepsilon^\infty + 2\varepsilon_s} \right)^2 \left\{ \arctg \frac{2(\varepsilon_F - \varepsilon_a)}{\Gamma_a} + \frac{\Gamma_a}{8\hbar\omega} \ln \frac{(\varepsilon_F + \hbar\omega - \varepsilon_a)^2 + (\frac{\Gamma_a}{2})^2}{(\varepsilon_F - \hbar\omega - \varepsilon_a)^2 + (\frac{\Gamma_a}{2})^2} - \frac{1}{2\hbar\omega} \left[(\hbar\omega + \varepsilon_a) \arctg \frac{2(\varepsilon_F - \hbar\omega - \varepsilon_a)}{\Gamma_a} + (\hbar\omega - \varepsilon_a) \arctg \frac{2(\varepsilon_F + \hbar\omega - \varepsilon_a)}{\Gamma_a} \right] \right\} \quad (14)$$

$$\mathcal{S}_{\perp}^{\text{interface}} = \frac{(ed)^2}{2\pi^2 \varepsilon_0} n_a \frac{\omega_{sp}}{v_F} \frac{\varepsilon_s}{\varepsilon^\infty + 2\varepsilon_s} \frac{\Gamma_a^2}{\hbar^2 \omega^2 + \Gamma_a^2} \times \left\{ \frac{2}{\Gamma_a} \left(\arctg \frac{2(\varepsilon_F + \hbar\omega - \varepsilon_a)}{\Gamma_a} - \arctg \frac{2(\varepsilon_F - \hbar\omega - \varepsilon_a)}{\Gamma_a} \right) + \frac{1}{\hbar\omega} \ln \frac{[(\varepsilon_F + \hbar\omega - \varepsilon_a)^2 + (\Gamma_a/2)^2][(\varepsilon_F - \hbar\omega - \varepsilon_a)^2 + (\Gamma_a/2)^2]}{[(\varepsilon_F - \varepsilon_a)^2 + (\Gamma_a/2)^2]^2} \right\} \quad (15)$$

The relations (1) – (3) taking into account formulae (4) – (8) and (14), (15) are going to be used further in order to obtain the numerical results.

II. Results of the calculations and their discussion

The calculations have been performed for the composites with the particles of the different content and size, covered with the layer of oleylamine of the different thickness, situated in different matrices. The parameters of metals and dielectric permittivities of the matrices are given in Tables 1 and 2, and the parameters of oleylamine – in Table 3, correspondingly.

Figure 2 shows the frequency dependencies for the real parts of the diagonal components of the dielectric tensor for the spherical particle Au, covered with the layer of oleylamine. It should be pointed out that the nature of dependencies $Re\epsilon_{\parallel}^{\omega}(\hbar\omega)$ and $Re\epsilon_{\perp}^{\omega}(\hbar\omega)$ is significantly different. The frequency dependencies for the real part of the longitudinal component of dielectric tensor (Fig. 2, *a*) are qualitatively similar to the similar dependencies for the metallic spherical nanoparticles, covered with the layer of an ordinary dielectric [36]. This similarity means the presence of two extrema (maximum and minimum) and the small-scale oscillations in the infrared part of the spectrum due to the manifestation of the kinetic effects, and also means the same character of the shifts of maximums under the increase in radius of the particle (sequence of the curves 1 \rightarrow 2 \rightarrow 3) and in the thickness of the external layer (sequence of the curves 4 \rightarrow 2 \rightarrow 5). As for the dependence $Re\epsilon_{\perp}^{\omega}(\hbar\omega)$, let us point out that this value decreases insignificantly with the increase in frequency in the visible part of the spectrum. At the same time, these dependencies have several minimums and maximums in the infrared part of the spectrum (Fig. 2, *b*). Such behavior can be explained by the significant influence of the local density of the states, generated by adsorbed molecules of oleylamine on $Re\epsilon_{\perp}^{\omega}$, whereas the similar influence on $Re\epsilon_{\parallel}^{\omega}$ is almost absent.

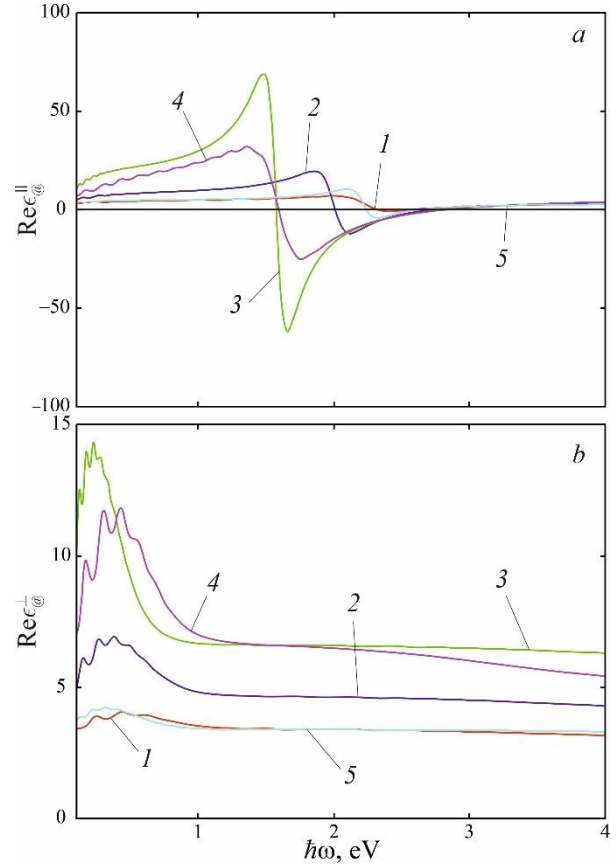


Fig. 2. The frequency dependencies for the real parts of the longitudinal (*a*) and transverse (*b*) components of the dielectric tensor for the particles of different sizes with the core Au: 1 – $R_c = 10$ nm; $t = 5$ nm; 2 – $R_c = 20$ nm; $t = 5$ nm; 3 – $R_c = 50$ nm; $t = 5$ nm; 4 – $R_c = 20$ nm; $t = 2$ nm; 5 – $R_c = 20$ nm; $t = 10$ nm.

Figure 3 shows the curves of the frequency dependencies for the imaginary parts of the diagonal components of the dielectric tensor for particle

The parameters of metals (see, e.g., [36, 37] and the references there)

Metals Parameters	Au	Ag	Cu	Pd	Pt	Al
$n_e, 10^{22} \text{ cm}^{-3}$	5.91	5.85	17.2	2.53	9.1	18.2
ϵ^∞	9.84	3.70	12.03	2.52	4.42	0.7
$\hbar\omega_p, \text{ eV}$	9.07	9.17	12.6	9.7	15.2	15.4
$\hbar\gamma_{bulk}, \text{ eV}$	0.023	0.016	0.024	0.091	0.069	0.082
$\epsilon_F, \text{ eV}$	5.59	5.72	7.56	8.49	13.6	11.03
$v_F, 10^6 \text{ m/s}$	1.41	1.49	1.34	2.84	2.98	1.91

Table 1.

Dielectric permittivities of the matrices [35]

Substance	Air	CaF_2	Teflon	Al_2O_3	TiO_2	C_{60}
T_m	1	1.54	2.3	3.13	4.0	6.0

Table 2.

Parameters of oleylamine [38]

$d, \text{ nm}$	$n_a, \text{ cm}^{-2}$	$\epsilon_a, \text{ eV}$	$\Gamma_a, \text{ eV}$	ϵ_s
10	$1.27 \cdot 10^{12}$	1	1	2.13

Table 3.

Au@OAm. Let us point out that, as in the case of the dependencies $Re\epsilon_{\parallel}^{\parallel}(\hbar\omega)$, the dependencies $Im\epsilon_{\parallel}^{\parallel}(\hbar\omega)$ (Fig. 3, *a*) are qualitatively similar to the similar dependencies for metal-dielectric nanoparticles. The increase in sizes of the metallic core (the increase in content of metal in the nanoparticle) results in the increase in the value of $max(Im\epsilon_{\parallel}^{\parallel})$ and in their shift into the range of smaller frequencies (“red” shift) – sequence of the curves $1 \rightarrow 2 \rightarrow 3$. The increase in the thickness of the adsorbed layer results in the “blue” shift along with the decrease in the value of maximum (sequence of the curves $4 \rightarrow 2 \rightarrow 5$). As for the dependence $Im\epsilon_{\perp}^{\parallel}(\hbar\omega)$, it should be pointed out the weak dependence on the frequency in the visible part of the spectrum and the complicated dependence (the presence of the oscillations) in the infrared region (Fig. 3, *b*). Such behavior of the imaginary part of the transverse component of the dielectric tensor also can be explained by the influence of the local density of the states, induced by the adsorbed molecules.

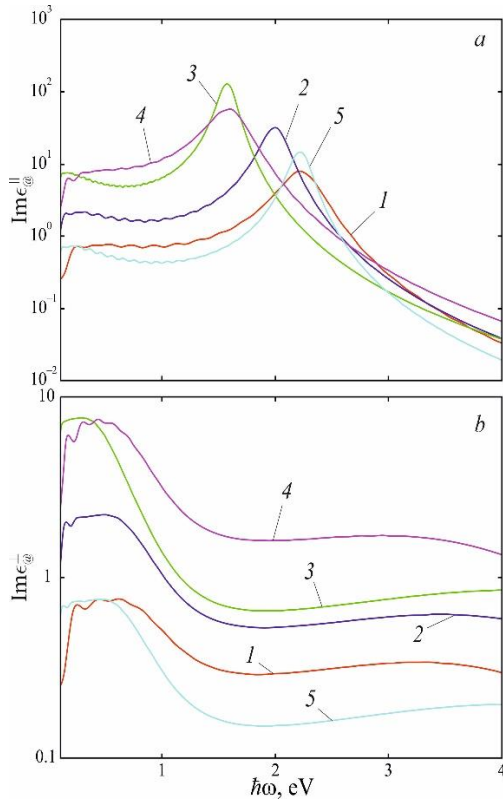


Fig 3. The frequency dependencies for the imaginary parts of the longitudinal (*a*) and transverse (*b*) components of the dielectric tensor for the particles of different sizes with the core Au under the same values of the parameters as in Figure 2.

The Figures 4 and 5 show the curves of the frequency dependencies for the real and imaginary parts of the diagonal components of the dielectric tensor for the particles of the fixed size with the cores of different metals. It should be pointed out that the curves $Re\epsilon_{\parallel}^{\parallel}(\hbar\omega)$ and $Im\epsilon_{\parallel}^{\parallel}(\hbar\omega)$ (Fig 4, *a* i 5, *a*) for the particles with the cores of different metals are qualitatively similar (the presence of two maximums and minimums for $Re\epsilon_{\parallel}^{\parallel}$ and maximums for $Im\epsilon_{\parallel}^{\parallel}$). However, these curves are

quantitatively different in both magnitude and location of extrema. Such quantitative differences result from the significant difference between the contributions of the crystal lattice into the dielectric permittivity and the frequencies of bulk plasmons for different metals. The curves $Re\epsilon_{\perp}^{\perp}(\hbar\omega)$ and $Im\epsilon_{\perp}^{\perp}(\hbar\omega)$ for the particles with the cores of different metals are also qualitatively similar (Fig. 4, *b* and 5, *b*). They depend insignificantly on the frequency in the visible part of the spectrum, and oscillate in the infrared part of the spectrum, and moreover, both the values $Re\epsilon_{\perp}^{\perp}$ and $Im\epsilon_{\perp}^{\perp}$ have the same order for all particles through all frequency region which is under the investigation.

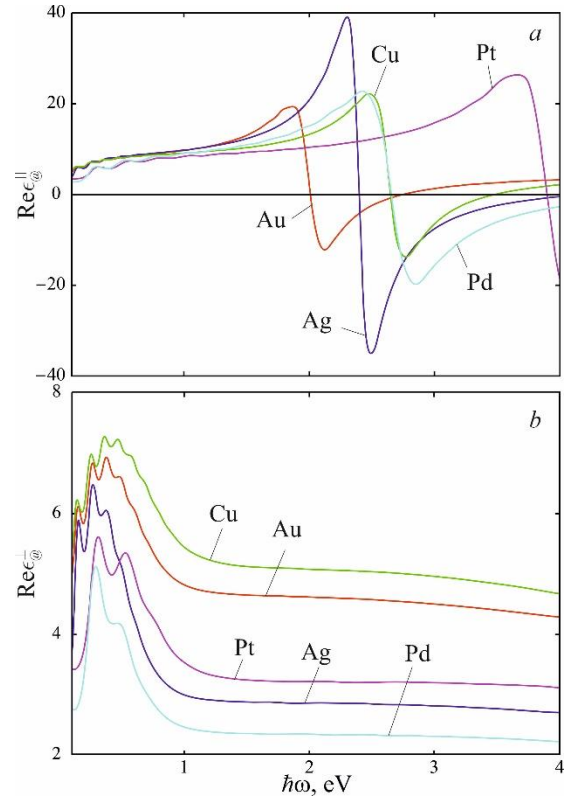


Fig. 4. The frequency dependencies for the real parts of the longitudinal (*a*) and transverse (*b*) components of the dielectric tensor for the particles with the cores of different metals ($R_c = 20 \text{ nm}$; $t = 5 \text{ nm}$).

Figure 6, *a* shows the frequency dependencies for the transverse, longitudinal and integral coefficients of the absorption for the composite with nanoparticles Au@OAm ($R_c = 20 \text{ nm}$, $t = 5 \text{ nm}$). Due to the fact that η_{\perp} has the maximum in the infrared domain of the spectrum, and η_{\parallel} - in the visible domain, an integral coefficient of the absorption η_{Σ} has two maximums, which correspond to the maximums $\eta_{\perp(\parallel)}$. Let us point out that $max \eta_{\parallel}$ is reached at the frequency of the surface plasmonic resonance ω_{sp}^{\parallel} , which is close to the frequency ω_{sp} for the spherical metal-dielectric particle (in the case $\gamma_{chem}^{\perp} = \gamma_{chem}^{\parallel} = 0$ the splitting of the frequencies disappears and $\omega_{sp}^{\parallel} = \omega_{sp}^{\perp} = \omega_{sp}$).

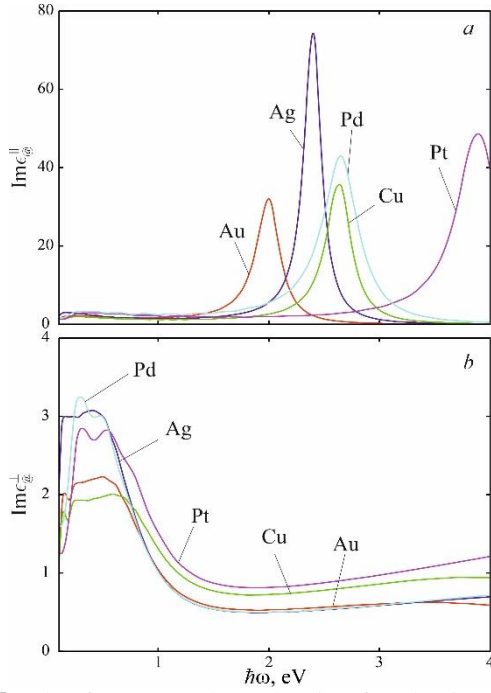


Fig. 5. The frequency dependencies for the imaginary parts of the longitudinal (a) and transverse (b) components of the dielectric tensor for the particles with the cores of different metals ($R_c = 20 \text{ nm}$; $t = 5 \text{ nm}$).

Now let us determine the frequency of the longitudinal surface plasmonic resonance. As is known, the condition of the excitation of SPR is

$$\eta_{\parallel}(\omega) \rightarrow \max,$$

Or

$$\text{Re}\epsilon_{\parallel}^{\text{eff}} + 2\epsilon_m = 0. \quad (16)$$

Using the expressions (3) and (4) and taking into account the fact that in an optical range of frequencies $\omega \gg \gamma_{\text{eff}}^{\parallel}$, we obtain the relation for the frequency of SPR

$$\omega_{sp}^{\parallel} = \frac{\omega_p}{\sqrt{\epsilon_{\infty} + 2\epsilon_s \frac{(1-\beta c)\epsilon_s + (2+\beta c)\epsilon_m}{(1+2\beta c)\epsilon_s + 2(1-\beta c)\epsilon_m}}}. \quad (17)$$

Table 4 gives the calculations for the frequencies of the longitudinal SPR using formula (17) for the particles in teflon and C_{60} with the different metallic cores under the different content of metal. Let us point out that the increase in the dielectric permittivity of the matrix dielectric and in the volumetric content of metallic fraction (decrease in the thickness of the adsorbate layer) results in the decrease in the frequency of SPR. At the same time the frequency of SPR increases, speaking about the sequence of metals $Au \rightarrow Ag \rightarrow Cu \rightarrow Pt$, due to the fact that $\omega_p^{Au} < \omega_p^{Ag} < \omega_p^{Cu} < \omega_p^{Pt}$.

As for $\max \eta_{\perp}$ in the infrared part of the spectrum, it should be pointed out that it can be associated both with SPR at the frequency ω_{sp}^{\perp} , and with the kinetic effects in this domain of the frequencies. The authors plan to deal with the detailed study of this issue and with the development of the corresponding theory in the next work. The results of the calculations of the influence of the dielectric properties of the matrix on the integral

absorption coefficient of the composite with the particles Au@OAm (Fig. 6, b) indicate the presence of the red shift and small increase in value of the maximum of the integral absorption coefficient with the increase in the dielectric permittivity of the matrix medium.

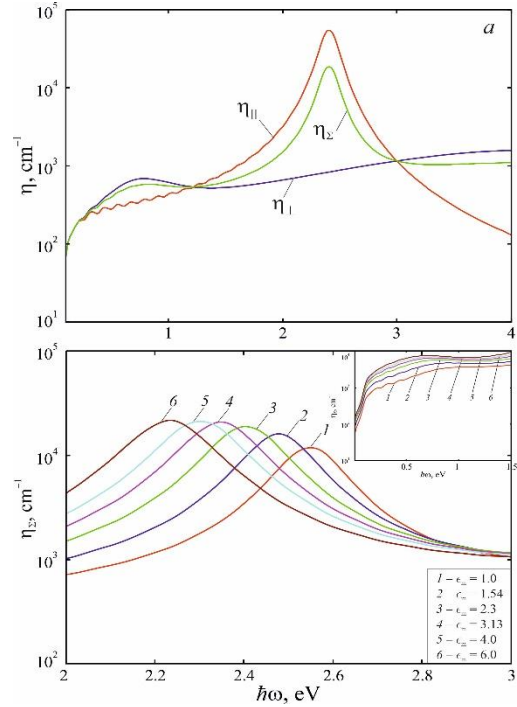


Fig. 6. The frequency dependencies: a – longitudinal, transverse and integral absorption coefficients of the composite with the particles Au@OAm in teflon ($\beta = 0.15$); b – integral absorption coefficient of the composite with the particles Au@OAm ($\beta = 0.15$) in the different matrices ($R_c = 20 \text{ nm}$; $t = 5 \text{ nm}$).

The results of the calculations of the frequency dependence of the integral absorption coefficient for the composite with the nanoparticles Au@OAm of the different sizes indicate the fact that the location of the maximum of the integral absorption coefficient (in the visible part of the spectrum) is practically independent on the radius of the metallic core of the particle and on the thickness of the adsorbed molecules layer (Fig 7, a). At the same time, the increase in the content of metal in the nanoparticle results in the increase in the value of this maximum, and also the other maximum appears in the infrared part of the spectrum. Apart from this, the maximums $\eta_{\Sigma}(\hbar\omega)$ shift towards “blue” side, and their value increases in the sequence of materials of the cores of the particles-inclusions $Au \rightarrow Cu \rightarrow Ag \rightarrow Pt$ (Fig 7, b), due to the fact that the frequencies of the surface plasmonic resonance increase exactly in this order. The second maximum of the integral absorption coefficient (in the infrared part of the spectrum) is noticeable only for the particles-inclusions with the cores Au, Cu, Ag. Also let us point out that $\max \eta_{\Sigma}$ for the composite with the particles Al@OAm shifts towards “blue” side with the decrease in effective electron mass (Fig 7, c), because in this case the frequency of bulk plasmons increases and the frequency of the surface plasmonic resonance increases correspondingly.

Table 4.

The frequencies of SPR for the nanoparticles with the cores of different metals with the different volumetric content of metal

β_c	$\epsilon_m = 2.3$				$\epsilon_m = 6.0$			
	$\omega_{sp}^{\parallel}, eV$				$\omega_{sp}^{\parallel}, eV$			
	Au	Ag	Cu	Pt	Au	Ag	Cu	Pt
0.1	2.413	3.242	3.118	5.159	2.385	3.176	3.086	5.062
0.2	2.410	3.235	3.115	5.150	2.351	3.099	3.049	4.950
0.3	2.407	3.229	3.112	5.140	2.315	3.019	3.007	4.831
0.4	2.404	3.222	3.109	5.130	2.275	2.935	2.963	4.706
0.5	2.402	3.215	3.106	5.120	2.232	2.846	2.913	4.573
0.6	2.399	3.209	3.102	5.110	2.185	2.753	2.859	4.432
0.7	2.396	3.202	3.099	5.100	2.134	2.653	2.799	4.281
0.8	2.393	3.195	3.096	5.091	2.076	2.548	2.731	4.120
0.9	2.390	3.188	3.093	5.081	2.013	2.435	2.656	3.946
1.0	2.387	3.181	3.089	5.070	1.941	2.313	2.570	3.758

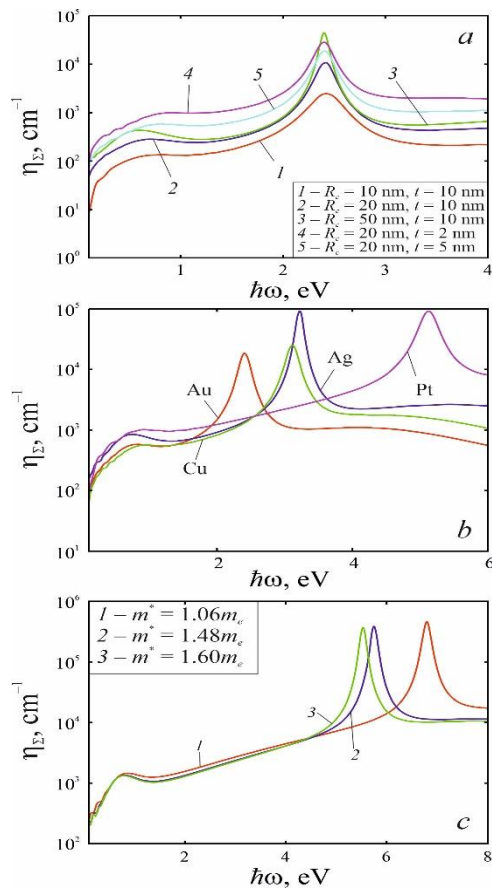


Fig. 7. The frequency dependencies for the integral absorption coefficient of the composite with the particles in teflon ($\beta = 0.15$): *a* – Au@OAm of the different sizes; *b* – of the fixed size ($R_c = 20$ nm; $t = 5$ nm) with the cores of the different metals; *c* – Al@OAm of the fixed size ($R_c = 20$ nm; $t = 5$ nm) under the different values of the effective mass.

Conclusions

The theory of the light wave absorption by the composite with the spherical two-layer nanoparticles of the type “metallic core - surfactant” has been constructed.

The contribution of all mechanisms, in particular, the mechanism connected with the presence of the interface “metal – adsorbed layer” into the widening of the lines of the surface plasmonic resonance has been analyzed.

It has been established that the behavior of the frequency dependencies of the real and imaginary parts of the longitudinal component of the dielectric tensor for the composite spherical nanoparticles is the same as for the frequency dependencies of the real and imaginary parts of the dielectric function of the spherical metallic nanoparticle, namely, the same quantity of the extremums of the real and imaginary parts, the presence of the small-scale oscillations in the infrared part of the spectrum, caused by the kinetic phenomena, and also the red shift of the maximums under the increase in the radius of the particle.

It has been shown that the influence of the local density of the states, formed by molecules of adsorbate, is significant for the real and imaginary parts of the transverse component of the dielectric tensor for two-layer nanoparticle.

It has been demonstrated the presence of two maximums in the frequency dependencies of the integral absorption coefficient of the composite with the spherical layered nanoparticles “metallic core – adsorbate layer”, which are located in the different parts of the spectrum. These maximums correspond to the maximums of the transverse and longitudinal absorption coefficients. Moreover, the maximums of the longitudinal absorption coefficient are reached at the frequencies of the surface plasmonic resonance, which are close to the similar values for the spherical metal-dielectric nanoparticles.

The evolution of the size dependencies of the frequency of the longitudinal SPR for two-layer nanoparticles “metal – adsorbate layer” under the increase in content of metallic fraction for the different dielectric matrices and the cores of different metals has been studied in non-dissipative approximation.

Smirnova N.A. – Senior lecturer of the Department of Micro- and Nanoelectronics in National University Zaporizhzhia Polytechnic;

Maniuk M.S. – Master's degree in Micro- and Nanosystem Engineering, Department of Micro- and Nanoelectronics in National University Zaporizhzhia Polytechnic;

Korotun A.V. – Professor of the Department of Micro- and Nanoelectronics in National University Zaporizhzhia Polytechnic, PhD, Ass. Prof., Senior scientific researcher in the G.V. Kurdyumov Institute for Metal Physics of the National Academy of Sciences of Ukraine;

Titov I.M. – mathematician of the UAD Systems.

- [1] P. Yang, J. Zheng, X. Yong, Q. Zhang, L. Jiang, *Colloidal synthesis and applications of plasmonic metal nanoparticles*, Adv. Mater., 28, 10508 (2016); <https://doi.org/10.1002/adma.201601739>.
- [2] M.C. Mathpal, P. Kumar, A.K. Tripathi, R. Balasubramaniyan, M.K. Singh, J.S. Chung, A. Agarwal, *Facile deposition and plasmonic resonance of Ag-Au nanoparticles in titania thin film*, New J. Chem., 39, (2015); <https://doi.org/10.1039/C5NJ00710K>.
- [3] J. Wang, G. Jia, B. Zhang, H. Liu, C. Liu, *Formation and optical absorption property of nanometer metallic colloids in Zn and Ag dually implanted silica: Synthesis of the modified Ag nanoparticles*, J. Appl. Phys., 113, 034304 (2013); <https://doi.org/10.1063/1.4775820>.
- [4] G. Jia, H. Liu, M. Xiaoyu, H. Dai, C. Liu *Xe ion irradiation induced polycrystallization of Ag nanoparticles embedded in SiO₂ and related optical absorption property*, Opt. Mater. Express, 4(7), 1303 (2014); <https://doi.org/10.1364/OME.4.001303>.
- [5] C.P. Byers, H. Zhang, D.F. Swearer, M. Yorulmaz, B.S. Hoener, D. Huang, A. Hoggard, W.S. Chang, P. Mulvaney, E. Ringe, *From tunable core-shell nanoparticles to plasmonic drawbridges: Active control of nanoparticle optical properties*, Sci. Adv., 1(11), 1500988 (2015); <https://doi.org/10.1126/sciadv.1500988>.
- [6] J. Jana, M. Ganguly, T. Pal, *Enlightening surface plasmon resonance effect of metal nanoparticles for practical spectroscopic application*, RSC Adv., 6(89), 86174 (2016); <https://doi.org/10.1039/C6RA14173K>.
- [7] S. Raza, S.I. Bozhevolnyi, M. Wubs, N.A., *Nonlocal optical response in metallic nanostructures*, J. Phys.: Condens. Matter., 27, 183204 (2015); <https://doi.org/10.1088/0953-8984/27/18/183204>.
- [8] N. A. Mortensen, S. Raza, M.Wubs, T. Sndergaard, and S. I. Bozhevolnyi, *A generalized non-local optical response theory for plasmonic nanostructures*, Nat. Commun., 5, 3809 (2014); <https://doi.org/10.1038/ncomms4809>
- [9] J. Olson, S. Dominguez-Medina, A. Hoggard, L.-Y. Wang, W.-S. Chang, S. Link, *Optical Characterization of Single Plasmonic Nanoparticles*, Chem. Soc. Rev., 44, 40 (2015); <https://doi.org/10.1039/C4CS00131A>.
- [10] M. Liu, M. Pelton, P. Guyot-Sionnest, *Reduced Damping of Surface Plasmons at Low Temperatures*, Phys. Rev. B, 79, 1 (2009); <https://doi.org/10.1103/PhysRevB.79.035418>.
- [11] N.I. Grigorchuk, P.M. Tomchuk, *Optical and transport properties of spheroidal metal nanoparticles with account for the surface effect*, Phys. Rev. B, 84(8), 085448 (2011); <https://doi.org/10.1103/PhysRevB.84.085448>.
- [12] N.I. Grigorchuk, *Plasmon resonant light scattering on spheroidal metallic nanoparticle embedded in a dielectric matrix*, EPL, 97(4), 45001 (2012); <https://doi.org/10.1209/0295-5075/97/45001>
- [13] V.M. Lenart, R.F. Turchiello, G.F. Goya, S.L. Gómez, *Enhanced Thermal Lens Effect in Gold Nanoparticle-Doped Lyotropic Liquid Crystal by Nanoparticle Clustering Probed by Z-Scan Technique*, Braz. J. Phys., 45(2), 213(2015); <https://doi.org/10.1007/s13538-015-0301-7>.
- [14] C. Minnai, P. Milani, *Metal-polymer nanocomposite with stable plasmonic tuning under cyclic strain conditions*, Appl. Phys. Lett., 107(7), 073106. (2015); <https://doi.org/10.1063/1.4928725>
- [15] A. Monti, A. Alù, A.Toscano, F. Bilotti, *Optical invisibility through metasurfaces made of plasmonic nanoparticles*, J. Appl. Phys., 117(12), 123103 (2015); <https://doi.org/10.1063/1.4916257>
- [16] P. Tuersun, *Optimizing the figure of merit of gold nanoshell-based refractive index sensing*, Optik, 127(1), 250 (2016); <https://doi.org/10.1016/j.ijleo.2015.10.069>
- [17] P.M. Tomchuk, M.I. Grigorchuk, *Plasmon fluctuations of electrons in metallic nanoparticles of the ellipsoidal form*, Metallofizika i Noveishie Tekhnologii, 29(5), 623 (2007);
- [18] B.N.J. Persson, *Polarizability of small spherical metal particles: influence of the matrix environment*, Surface Science, 281(1-2), 153 (1993); [https://doi.org/10.1016/0039-6028\(93\)90865-H](https://doi.org/10.1016/0039-6028(93)90865-H).
- [19] E.A. Coronado, G.C. Schatz, *Surface plasmon broadening for arbitrary shape nanoparticles: A geometrical probability approach*, J. Chem. Phys., 119(7), 3926 (2003); <https://doi.org/10.1063/1.1587686>.
- [20] N.I. Grygorchuk, *Behaviour of a line of the surface plasmon resonance in metal nanoparticles*, Metallofizika i Noveishie Tekhnologii, 38(6), 717 (2016); <https://doi.org/10.15407/mfint.38.06.0717>.
- [21] M. Liu, M. Pelton, P. Guyot-Sionnest, *Reduced damping of surface plasmons at low temperatures*, Phys. Rev. B, 79(3), 035418 (2009) <https://doi.org/10.1103/PhysRevB.79.035418>.
- [22] S. Noël, B. Léger, A. Ponchel, K. Philippot, A. Denicourt-Nowicki, A. Roucoux, E. Monflier, *Cyclodextrin-based systems for the stabilization of metallic nanoparticles and their versatile applications in catalysis*, Catal Today, 235, 20 (2014) <https://doi.org/10.1016/j.cattod.2014.03.030>.
- [23] X.-Y. Zhu, *Electron transfer at molecule-metal interfaces: a two-photon photoemission study*, Annu. Rev. Phys. Chem., 53, 221 (2002); <https://doi.org/10.1146/annurev.physchem.53.082801.093725>.

- [24] K.A. Willets, R.P. Van Duyne, *Localized surface plasmon resonance spectroscopy and sensing*, Annual Review of Physical Chemistry, 58, 267 (2007); <https://doi.org/10.1146/annurev.physchem.58.032806.104607>.
- [25] V.M. Rubish, V.K. Kyrylenko, M.O. Durkot, L.I. Makar, M.M. Pop, A.A. Tarnaj, M.L. Trunov, S. Mudry, I. Shtablavyi, *Rapid formation methods of arrays of randomly distributed Au and Ag nanoparticles, their morphologies and optical characteristics*, Physics and Chemistry of Solid State, 22(4), 804 (2021); <https://doi.org/10.15330/pcss.22.4.804-810>.
- [26] D. Li, Y. Xia, *Welding and patterning in a flash*, Nature materials, 3(11), 753 (2004); <https://doi.org/10.1038/nmat1245>.
- [27] W. Srituravanich, N. Fang, C. Sun, Q. Luo, X. Zhang, *Plasmonic nanolithography*, Nano Letters, 4 (6), 1085 (2004); <https://doi.org/10.1021/nl049573q>.
- [28] S. Lal, S. Link, N.J. Halas, *Nano-optics from sensing to waveguiding*, Nature Photonics, 1(11), 641 (2007); <https://doi.org/10.1038/nphoton.2007.223>.
- [29] A.V. Korotun, A.A. Koval', V.I. Reva, *Absorption of Electromagnetic Radiation by Oxide-Coated Spherical Metal Nanoparticles*, J. Appl. Spectr., 86(4), 606 (2019); <https://doi.org/10.1007/s10812-019-00866-6>.
- [30] A.V. Korotun, A.A. Koval', V.I. Reva, I.N. Titov, *Optical Absorption of a Composite Based on Bimetallic Nanoparticles. Classical Approach*, Physics of Metals and Metallography, 120(11), 1040 (2019); <https://doi.org/10.1134/S0031918X19090059>.
- [31] A.V. Korotun, A.A. Koval', I.N. Titov, *Optical Absorption of a Composite Based on Bilayer Metal–Dielectric Spherical Nanoparticles*, J. Appl. Spectr., 87(2), 240 (2020); <https://doi.org/10.1007/s10812-020-00991-7>.
- [32] P.M. Tomchuk, V.N. Starkov, *Influence of shape spread in an ensemble of metal Nanoparticles on their optical properties*, Ukrainian Journal of Physics, 63(3), 204 (2018); <https://doi.org/10.15407/ujpe63.3.204>.
- [33] A.V. Korotun, A.O. Koval, V.V. Pogosov, *Optical parameters of bimetallic nanospheres*, Ukr. J. Phys., 66(6), 518 (2021); <https://doi.org/10.15407/ujpe66.6.518>.
- [34] A. Pinchuk, U. Kreibig, *Interface decay channel of particle surface plasmon resonance*, New J. Phys., 5, 151 (2003); <https://doi.org/10.1088/1367-2630/5/1/151>.
- [35] A. Pinchuk, G. von Plessen, U. Kreibig, *Influence of interband electronic transitions on the optical absorption in metallic nanoparticles*, J. Phys. D: Appl. Phys., 37, 3133 (2004); <https://doi.org/10.1088/0022-3727/37/22/012>.
- [36] A.V. Korotun, N.I. Pavlyshche, *Cross Sections for Absorption and Scattering of Electromagnetic Radiation by Ensembles of Metal Nanoparticles of Different Shapes*, Physics of Metals and Metallography, 122(10), 941 (2021); <https://doi.org/10.1134/S0031918X21100057>.
- [37] A.V. Korotun, A.A. Koval', *Optical Properties of Spherical Metal Nanoparticles Coated with an Oxide Layer*, Optics and Spectroscopy, 127(6), 1161 (2019); <https://doi.org/10.1134/S0030400X19120117>.
- [38] S. Peng, J.M. McMahon, G.C. Schatz, S.K. Gray, Y. Sun, *Reversing the size-dependence of surface plasmon resonances*, Proc. Natl. Acad. Sci. USA, 107(33), 14530 (2010); <https://doi.org/10.1073/pnas.1007524107>.

Н.А. Смирнова¹, М.С. Манюк¹, А.В. Коротун^{1,2}, І.М. Тітов³

Оптичне поглинання композиту з наночастинками, вкритими шаром поверхнево-активної речовини

¹Національний університет «Запорізька політехніка», Україна, andko@zpu.edu.ua

²Інститут металофізики ім. Г. В. Курдюмова НАН України, Київ, Україна

³UAD Systems, Запоріжжя, Україна

В роботі досліджено оптичні властивості нанокompозиту з двошаровими сферичними включеннями «металева ядро – шар поверхнево активної речовини». Розглянуто питання про вплив процесів на інтерфейсі «метал – адсорбат» на збудження поверхневих плазмонних резонансів у наночастинці. Встановлено факт розщеплення поверхневого плазмонного резонансу внаслідок впливу адсорбційних зв'язків поблизу поверхні металевих наночастинок і виникнення додаткових енергетичних станів. Отримано співвідношення для ефективних параметрів, що описують втрати когерентності при розсіюванні на хімічному інтерфейсі. Проведено розрахунки частотних залежностей діагональних компонент тензора діелектричної проникності двошарової наночастинок та коефіцієнта поглинання нанокompозиту. Показано, що частотні залежності дійсної й уявної частин подовжньої компоненти діелектричного тензора близькі до аналогічних залежностей дійсної й уявної частин діелектричної функції сферичної металеві наночастинок, в той час як дійсна й уявна частини поперечної компоненти слабо залежать від частоти у видимій області спектра й осцилюють в інфрачервоній області. Встановлено, що коефіцієнт поглинання нанокompозиту може мати один або два максимуми в залежності від розмірів і матеріалу частинок-включень.

Ключові слова: діелектричний тензор, коефіцієнт поглинання, адсорбат, поверхневий плазмонний резонанс, нанокompозит, розмірна залежність, ефективна швидкість релаксації.

O.M. Popovych¹, I.M. Budzulyak¹, M.M. Khemii¹, R.V. Ilnytskyi¹, L.S. Yablon¹,
D.I. Popovych², I.I. Panko¹

Laser-modified nanocrystalline NiMoO₄ as an electrode material in hybrid supercapacitors

¹Vasyl Stefanyk Precarpathian National University, Ivano-Frankivsk, Ukraine, khemiiolha@gmail.com

²Ya. S. Pidstryhach Institute for Applied Problems of Mechanics and Mathematics, Lviv, Ukraine

The nanocrystalline NiMoO₄ obtained as a result of hydrothermal synthesis was exposed to laser radiation with a pulse energy of 70 mJ/cm² for 5 minutes. The phase composition and size of crystallites of the triclinic structure of NiMoO₄ were determined by X-ray analysis. The average crystallite size was 18 nm for laser-irradiated nickel molybdate. Impedance analysis was used to analyze the temperature dependence of the electrical conductivity of laser-modified NiMoO₄. The frequency index of the power law, determined by the nonlinear approximation method, was 0.5-0.67, which corresponds to the hopping mechanism of charge carriers. The electrochemical behavior of NiMoO₄ was studied using cyclic voltammetry and galvanostatic charge/discharge testing. The laser-irradiated NiMoO₄ reaches a specific capacitance of 553 F/g at a scan rate of 1 mV/s. The hybrid electrochemical system based on electrodes of modified NiMoO₄ and carbon material provides high Coulomb efficiency (95%) for a significant number of charge/discharge cycles.

Keywords: hybrid supercapacitor, laser irradiation, nickel molybdate, electrical conductivity, specific capacitance.

Received 2 October 2023; Accepted 11 March 2023.

Introduction

In the last decades, research in the field of energy storage has significantly increased due to the rapid development of nanotechnology. Energy storage devices are based on electrochemical and electrostatic processes governed by electrons in electrode materials and provide more reliable and flexible power supply while reducing dependence on the fossil fuel industry [1, 2]. The development of hybrid supercapacitors (HSC) is of significant importance for energy accumulation and storage. HSC have several advantages over traditional batteries and supercapacitors [3]. They are capable of achieving higher energy density compared to symmetrical supercapacitors and higher power compared to lithium-ion batteries, making them ideal for applications that require high power output over a long period of time. In a hybrid supercapacitor, the energy storage mechanism is based on both electrochemical and electrostatic principles [4]. A

capacitive electrode stores energy by adsorbing ions, while a battery-type electrode stores energy through an electrochemical reaction. During discharge, both electrodes release the stored energy simultaneously, producing a powerful output current. However, hybrid supercapacitors are still in the early stages of development, and there are challenges that need to be overcome before they can find extensive use. Among them are the optimizations of electrode materials, increasing the energy efficiency of the device, and reducing production costs.

By choosing the optimal methods of obtaining and modifying nanostructure materials, it is possible to increase the energy and power density of accumulation and storage devices [5]. In particular, one of the factors of increasing the surface area, improving the chemical reactivity of the electrode and adsorption of active particles and, accordingly, increasing the performance of devices is the defective structure of electrode materials [6,

7]. However, traditional technologies for obtaining nanomaterials with predetermined structural properties require high temperatures and are energy-intensive. An alternative is laser irradiation of synthesized materials, which is characterized by a much faster and localized thermal effect, allowing for accurate control of the physicochemical properties of the material and its transformation into a more stable energy state [8, 9]. A perspective battery-type material for HSC is the nickel molybdate (NiMoO₄), which stores charge due to the redox reaction of Ni ions and has high electrical conductivity due to Mo ions [10, 11]. By varying the parameters of laser radiation (intensity, pulse duration, operating mode, and wavelength), the structural and morphological properties of nickel molybdate and, accordingly, the capacitive characteristics of electrodes based on it can be significantly improved.

I. Experiment

Nickel molybdate was obtained as a result of hydrothermal synthesis, the procedure of which is presented in [11]. The hydrothermally synthesized nickel molybdate was subjected to laser irradiation. The laser modification was carried out by emission of a Nd–yttrium–aluminum–garnet (Nd-YAG) laser in the near-infrared (1064 nm), which operates in the modulated Q-switched mode with a pulse duration of 10 ns and a pulse repetition rate of 28 Hz. The optimal laser energy in a pulse of 70 mJ/cm² has been experimentally determined, the effect of which does not damage the structure of the material and at the same time stabilizes the energy state. The irradiation duration was 5 minutes.

The crystal structure of the laser-modified material was studied by X-ray diffraction method (DRON powder diffractometer, Cu K α radiation). The temperature behavior of the electrical conductivity of laser-modified nickel molybdate was studied using the AUTOLAB PGSTAT 12 measuring complex in the frequency range of 10⁻²–10⁵ Hz at a voltage of 0 V, in the temperature range of 25–200 °C. The sample was pressed into a cylindrical mold, 14 mm in diameter, with a material thickness of 1 mm. The real conductivity component was determined by the formula: $\sigma = h / (Z' \times S)$, where h is the thickness of the sample, Z' is the experimentally determined real part of the resistivity, S is the surface area of the sample under study. Electrochemical behavior was studied by potentiodynamic and galvanostatic methods using a Tionid charge/discharge stand. Electrochemical studies were carried out in a three-electrode cell using 6 M KOH electrolyte, in which a chlorine-silver electrode was used as a reference electrode, a platinum electrode as an auxiliary electrode, and a nickel molybdate electrode as a working electrode. The working electrode was formed from a mixture of nickel molybdate and acetylene black (80 to 20%) mixed in alcohol and pressed into a nickel mesh, 0.25 cm² in size. The mass of the active material in the electrode was 15 mg.

II. Results and discussions

Fig. 1 shows the X-ray diffraction patterns of the initial and laser-irradiated NiMoO₄ material. The XRD of both NiMoO₄ materials are in agreement with JCPDS 13-0128, which corresponds to a triclinic crystal structure with a $P\bar{1}$ space group [12, 13]. Average crystallite sizes calculated by the Scherer equation: $D = 0.9\lambda / \beta \cos\theta$, where $\lambda = 0.15405$ nm is the wavelength of Cu-K α radiation, β is the FWHM of the most intense maxima, and θ is the Bragg angle, were 17 nm for the initial and 18 nm for the laser-irradiated nickel molybdate. The lack of new bands in the Raman spectra [11] of the laser-irradiated material confirms the stability of the nickel molybdate structure to laser radiation. At the same time, there is a decrease in the integrated intensity and a slight broadening of the XRD bands of the modified material compared to the initial one, indicating the appearance of new structural defects due to laser irradiation.

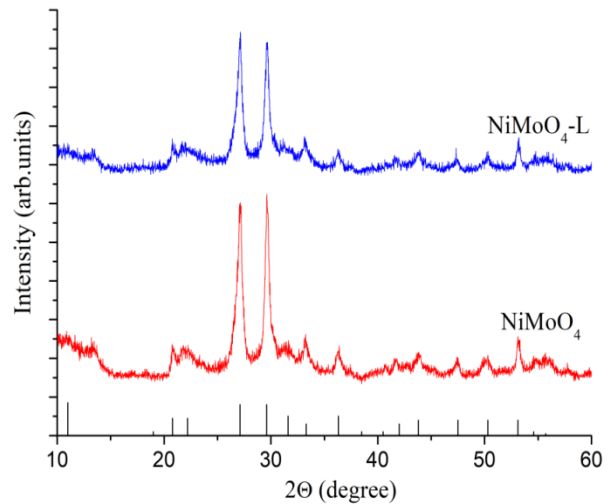


Fig. 1. X-ray diffraction patterns of the initial nickel molybdate (denoted as NiMoO₄) and laser-irradiated material (denoted as NiMoO₄-L).

To determine the effect of laser irradiation on the electrical properties of nickel molybdate, the temperature dependence of the conductivity was studied. The temperature dependence of the electrical conductivity at direct current for the initial and modified NiMoO₄ in the temperature range of 25–150 °C is typical for semiconductor materials (Fig. 2a). The DC electrical conductivity of the initial NiMoO₄ at room temperature is 4·10⁻⁵ S/m, while that of the laser-irradiated one is 3.7·10⁻⁵ S/m. For the initial NiMoO₄, the electrical conductivity increases up to a temperature of 175°C and decreases to 1.6·10⁻⁴ S/m at 200 °C. For laser-modified NiMoO₄, the electrical conductivity reaches its maximum value at 150 °C and decreases to 3.6·10⁻⁵ S/m at 200°C. The decrease in electrical conductivity at higher temperatures may be due to the scattering of charge carriers on lattice vibrations and point defects caused by the presence of higher oxidation states of Ni and Mo, as well as thermally activated defect generation.

The activation energy at DC can be calculated using the Arrhenius equation:

$$\sigma = \sigma_0 \exp(-E/kT),$$

where E is the activation energy, k is the Boltzmann constant, σ_0 is a constant, and T is the temperature. For this purpose, the dependences of $\ln\sigma_{dc}$ on $1/T$ were plotted, and their linear approximation was carried out in the temperature range of 25-150 °C (Fig. 2b). As a result, we obtained activation energy values of 0.13 eV for the initial NiMoO₄ and 0.03 eV in the range of 25-75 °C and 0.17 eV at 100-150 °C for the laser-irradiated NiMoO₄. For the modified material, there is an activation of defects with increasing temperature, which can act as traps for charge carriers, which leads to an increase in the activation energy.

To obtain information on the dynamics of charge carriers and to establish the nature of charge transfer mechanisms in nickel molybdate after laser irradiation, the frequency dependence of conductivity on alternating current in the frequency range 10⁻²-10⁵ Hz was studied (Fig. 3a). The relationship between conductivity and frequency of the applied field is described by the

following equation [14]:

$$\sigma(\omega) = \sigma_{dc} + A\omega^s,$$

where σ_{dc} is the frequency-independent conductivity, A is a constant value, ω is the angular frequency, and s is the frequency index ($0 < s < 1$). At a value of $s < 1$, the electrical conductivity is governed by the hopping mechanism of charge carriers between localized states or defects in the material by tunneling through a potential barrier. Using this law, the conductivity plot was fitted using the method of nonlinear approximation of curves and is shown in Fig. 3a, and the dependence of the fitted parameters is shown in Fig. 3 b.

The numerical value of the frequency degree and its temperature behavior determine the dominant conduction mechanism in the material. Thus, for the laser-irradiated NiMoO₄, the frequency index was 0.5-0.67 and decreased with increasing temperature (Fig. 3b). At higher temperatures, thermal energy can cause a decrease in the density of localized states, as defects and impurities

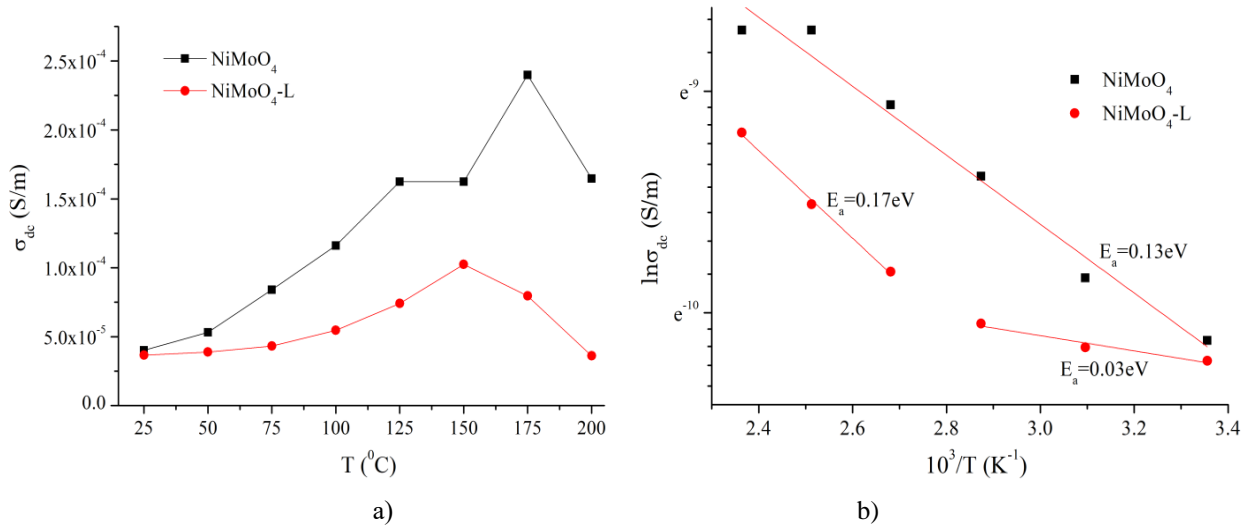


Fig. 2. The temperature dependence of the electrical conductivity (a) and the dependence of $\ln\sigma_{dc}$ on $1/T$ (b) at direct current of the initial and laser-irradiated NiMoO₄.

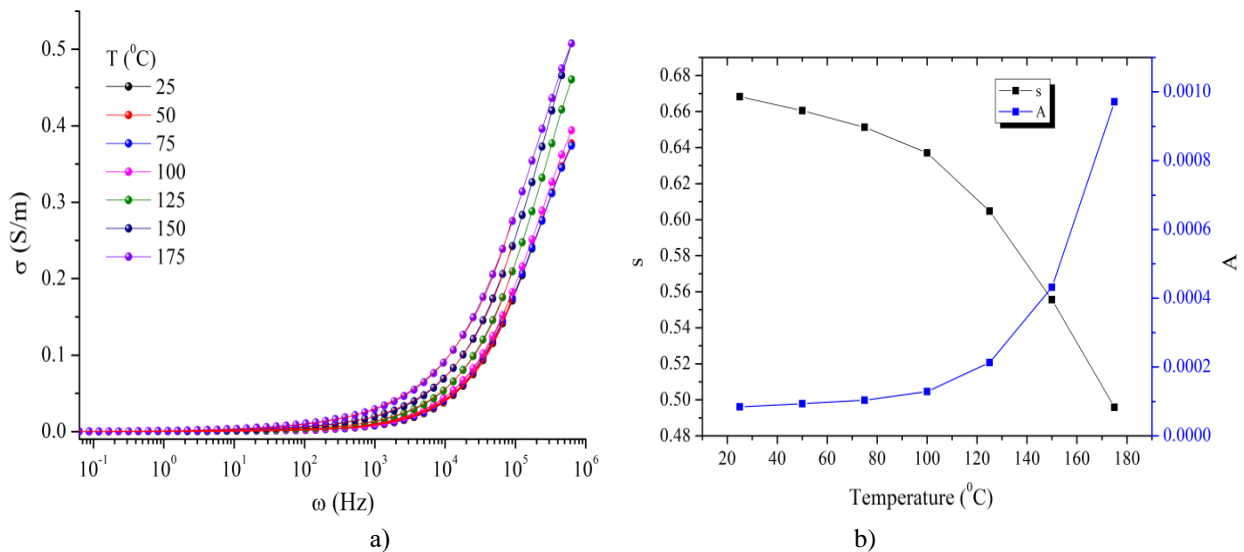


Fig. 3. Temperature dependence of the AC electrical conductivity of laser-irradiated NiMoO₄ (a). Dependence of s and A parameters on temperature (b).

become more mobile and the crystal structure of the material becomes more disordered. This can lead to a decrease in the number of available hopping sites and a corresponding decrease in the value of s . The Jonscher constant A depends on both the type of material and the temperature. The increase in A with increasing temperature (Fig. 3b) is characteristic of many materials with a hopping conduction mechanism and is associated with an increase in thermal energy available to promote the hopping process. At higher temperatures, thermal energy and laser irradiation can help overcome barriers to charge carrier movement by increasing the concentration of charge carriers that can participate in the hopping process, resulting in an increase in the overall electrical conductivity of the material.

The Arrhenius equation was used to determine the activation energy (ΔE_{ac}) of laser-irradiated NiMoO₄ at different frequencies [15]. Fig. 4 shows the linear dependence of $\ln\sigma$ on the inverse temperature. The figure shows that with increasing AC frequency, the activation energy decreases, indicating that at higher frequencies, the charge carriers in the material are subjected to more frequent and rapid changes in the direction of the electric field. This can facilitate the movement of charge carriers and make it easier to overcome the energy barrier. As a result, the activation energy required for the movement of charge carriers will decrease.

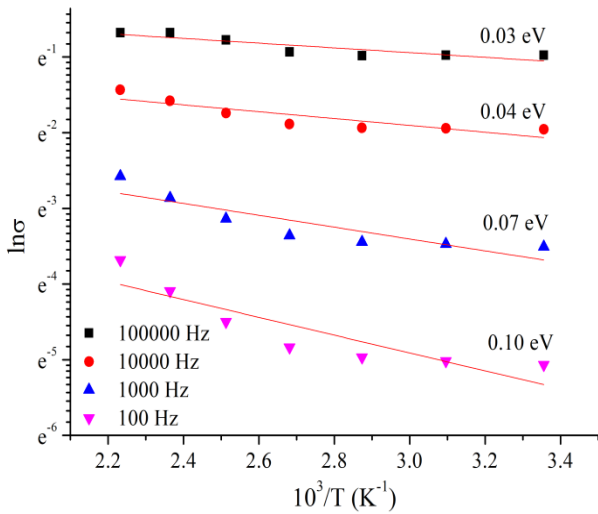
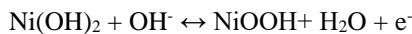
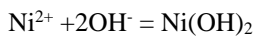


Fig. 4. The variation in σ as a function of inverse temperature (Arrhenius plot) of laser-irradiated NiMoO₄.

To determine the effect of laser irradiation on the capacitive characteristics of nickel molybdate, the electrochemical behavior of two systems was investigated: the initial NiMoO₄ and the laser-irradiated one. Cyclic voltammograms (CV) were recorded in the range of -0.2-0.4 V at a scan rate of 1, 2, 5 and 10 mV/s (Fig. 5a, b). Redox peaks on the CV arise from the interaction of nickel ions from the NiMoO₄ structure with OH⁻ groups from the electrolyte [16]:



One anodic and two cathodic peaks are observed on

the CV of both materials. The appearance of two cathodic peaks indicates that the reduction of NiMoO₄ forms a system with two phases existing at different potentials and is probably γ -NiOOH and β -NiOOH structures [17].

The specific capacitance was calculated using the formula $C=Q/m\Delta U$, where Q is the charge released by the system during cathodic scanning, ΔU is the voltage range, and m is the mass of the active material. The specific discharge capacitance at a scan rate of 1 mV/s was 575 F/g for the initial NiMoO₄ and 553 F/g for the laser-irradiated material and decreased to 242 F/g and 139 F/g at a scan rate of 10 mV/s for NiMoO₄ and NiMoO₄-L, respectively (Fig. 5c). For battery-type electrodes, such as nickel molybdate, the specific capacitance is mainly determined by the redox reactions of the active material and the diffusion of ions into and out of the electrode structure. As the scan rate increases, the time available for ion diffusion decreases, resulting in less efficient transportation of ions to the electrode. As a result, the capacitance decreases. In addition, at higher scan rates (10 mV/s), redox reactions on the electrode surface may not be able to keep up with the potential change, which leads to a decrease in the electrode area involved in the reaction, which also leads to a slight decrease in the capacitance. The laser-modified NiMoO₄ has a slightly lower capacitance compared to the initial material due to the reorganization of defects in the system, which stabilizes after laser irradiation.

Fig. 5 d shows the galvanostatic charge/discharge curves of the initial NiMoO₄ and laser-irradiated at a current of 0.2 A/g in the range of -0.2 to 0.35 V. The asymmetry of the charge/discharge curves is caused by the irreversibility of the electrolyte in the structure of electrode materials due to the passage of Faraday reactions. Thus, the laser modification of NiMoO₄ leads to a decrease in the specific capacitance caused by the destruction of the crystallite surface and a decrease in the intercalation potential of the electrode.

To study the electrochemical parameters of electric energy devices, hybrid supercapacitor was formed with a cathode based on laser-irradiated NiMoO₄ and an anode made of carbon material placed in a 6 M KOH electrolyte. The presence of redox peaks on the CV of the hybrid electrochemical system (Fig. 6a) indicates the accumulation of charge due to Faraday reactions, which is typical for nickel molybdates, while flat areas on the CV correspond to the charge/discharge of the double electric layer of carbon material. As the scan rate increases, the shape of the CV becomes more rounded, which indicates an increase in resistance and a slowdown in the response time of electrochemical reactions.

The specific capacitance was determined from galvanostatic charge/discharge curves (Fig. 6b) at discharge currents of 0.2, 0.5, and 1 A/g by the formula: $C=It/m\Delta U$, where I is the discharge current, t is the discharge time, ΔU is the voltage range, and m is the sum of the masses of carbon material and NiMoO₄. The values of the specific capacitances of the hybrid electrochemical system are presented in Table I. The specific energy and power are calculated by: $E=1/7.2CAU^2$ and $P=E/It$, and the corresponding numerical values are presented in Table I.

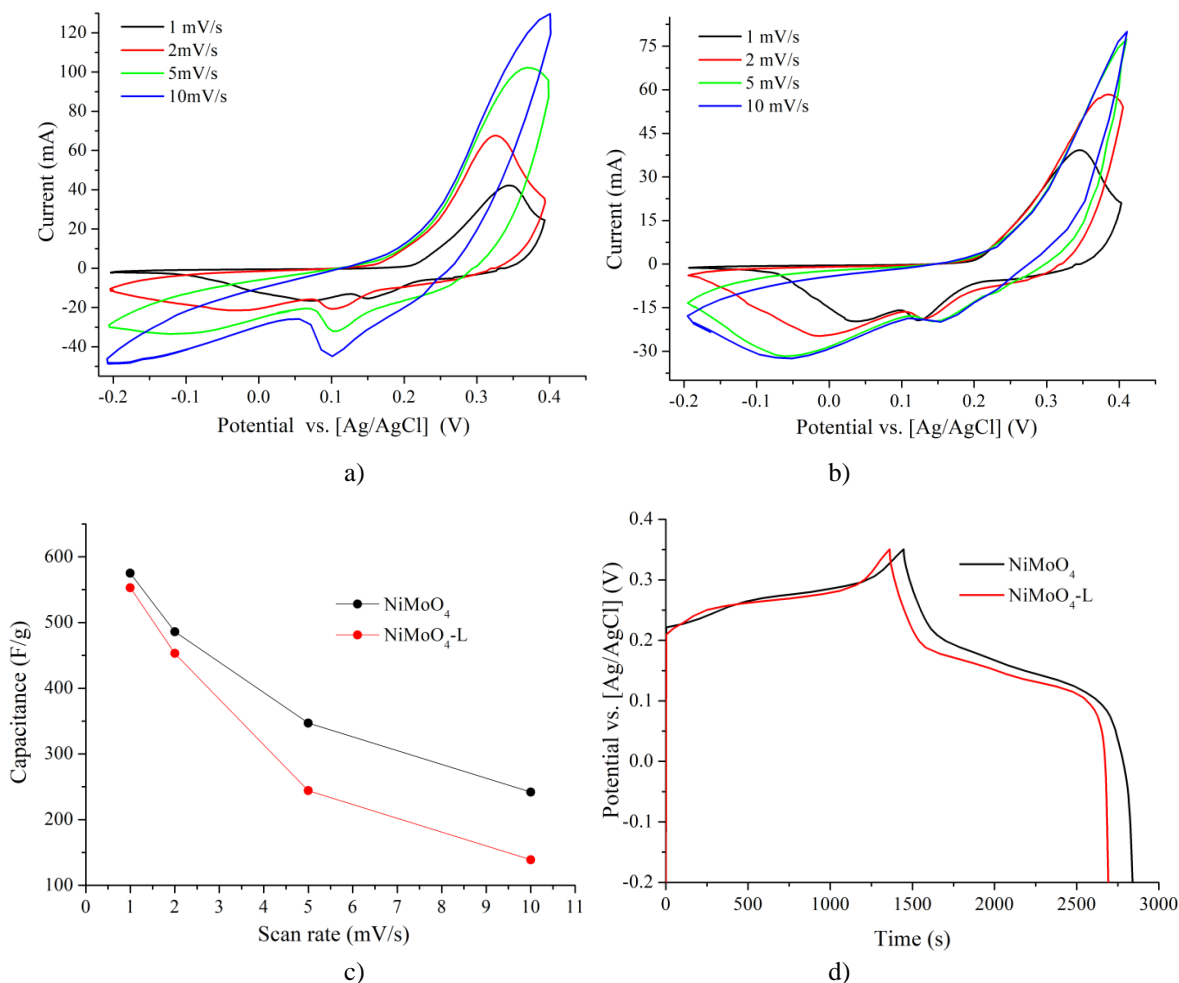


Fig. 5. Cyclic voltammograms of the initial (a) and laser-irradiated NiMoO₄ (b). Dependence of specific capacitances of NiMoO₄ and NiMoO₄-L on scan rate (c). Galvanostatic charge/discharge curves of the initial and laser-irradiated NiMoO₄ at a current of 0.2 A/g (d).

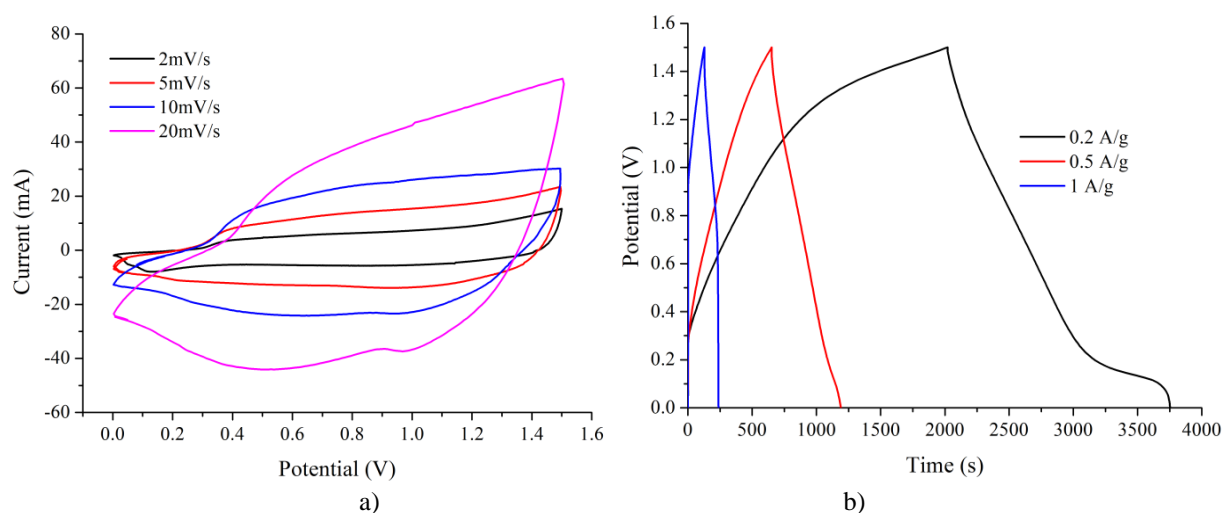


Fig. 6. Cyclic voltammograms (a) and galvanostatic charge/discharge curves (b) of a hybrid electrochemical system based on laser-irradiated NiMoO₄.

The increase in specific capacitance for HSC based on laser-modified material can be explained by the fact that at the initial stages of scanning, the active material is not completely involved in the intercalation of electrolyte ions. During repeated cycling of the hybrid electrochemical system based on NiMoO₄-L, more nickel

is converted to nickel oxyhydroxide, increasing the surface area involved in the redox reaction. This leads to an increase in the discharge time and, accordingly, an increase in the specific capacitance of the material and 95% Coulomb efficiency (Fig. 7).

Table I.
Electrochemical parameters of a hybrid electrochemical system based on laser-irradiated NiMoO₄

Parameter	NiMoO ₄ -L		
Discharge current (A/g)	0,2	0,5	1
Specific capacitance (F/g)	233	185	78
Specific energy (Wh/kg)	73	58	24
Specific power (W/kg)	151	385	792

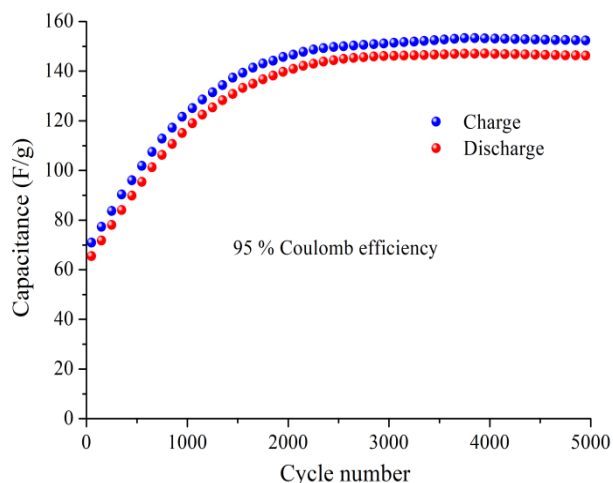


Fig. 7. Specific charge/discharge capacitance and Coulomb efficiency of a hybrid electrochemical system based on laser-irradiated NiMoO₄.

Conclusions

Laser modification of nanocrystalline NiMoO₄ by Nd-YAG laser radiation with a pulse energy of 70 mJ/cm² for 5 min stabilizes the defective nickel molybdate subsystem and leads to the appearance of new structural defects in the material that affect the change in electrical conductivity. It was found that the dc electrical conductivity of laser-irradiated NiMoO₄ decreases to $3.7 \cdot 10^{-5}$ S/m compared to the initial material ($4 \cdot 10^{-5}$ S/m). The study of the temperature dependence of the dc electrical conductivity of the modified material showed that in the range of 100–150°C, defects are activated, which leads to an increase in the activation energy. The mechanism of charge transfer in nickel molybdate after laser irradiation is governed by hopping of charge carriers between localized states or structural defects by stimulating their tunneling through a potential barrier. In addition, the electrode material based on laser-irradiated NiMoO₄ has a high specific capacitance and high Coulomb efficiency (up to 95%) for numerous charge/discharge cycles in a hybrid electrochemical system with a carbon-based electrode, which makes it promising for use in modern electrochemistry.

Popovych O.M. - PhD;

Budzulyak I.M. - Professor, Doctor of Physical and Mathematical Sciences;

Khemii M.M. – PhD student;

Ilnytskiy R.V. – Professor, Doctor of Physical and Mathematical Sciences;

Yablon L.S. – Professor, Doctor of Physical and Mathematical Sciences;

Popovych D.I. – Senior Researcher, Doctor of Physical and Mathematical Sciences;

Panko I.I. - Doctoral student.

- [1] J. Liu, J. Wang, C. Xu, H. Jiang, C. Li, L. Zhang, J. Lin, Z. X. Shen, *Advanced energy storage devices: basic principles, analytical methods, and rational materials design*, *Advanced science*, 5(1), 1700322 (2018); <https://doi.org/10.1002/advs.201700322>.
- [2] P. Simon, Y. Gogotsi, *Perspectives for electrochemical capacitors and related devices*, *Nature materials*, 19(11), 1151 (2020); <https://doi.org/10.1038/s41563-020-0747-z>.
- [3] A. Muzaffar, M. B. Ahamed, K. Deshmukh, J. Thirumalai, *A review on recent advances in hybrid supercapacitors: Design, fabrication and applications*, *Renewable and sustainable energy reviews*, 101, 123 (2019); <https://doi.org/10.1016/j.rser.2018.10.026>.
- [4] B. Rachiy, Yu. Starchuk, P. Kolkovskyy, I. Budzulyak, L. Yablon, V. Kotsyubynsky, O. Morushko, O. Khemiy, *Accumulation of Charge Mechanisms in Electrochemical Systems Based on Carbon and Nickel Tungstate*, *Surface Engineering and Applied Electrochemistry*, 56(6), 697 (2020); <https://doi.org/10.3103/S1068375520060149>.
- [5] H. Liu, X. Liu, S. Wang, H. K. Liu, L. Li, *Transition metal based battery-type electrodes in hybrid supercapacitors: A review*, *Energy Storage Materials*, 28, 122 (2020); <https://doi.org/10.1016/j.ensm.2020.03.003>.
- [6] Y. Zhang, L. Tao, C. Xie, D. Wang, Y. Zou, R. Chen, Y. Wang, C. Jia, S. Wang, *Defect Engineering on Electrode Materials for Rechargeable Batteries*, *Advanced Materials*, 32(7), 1905923 (2020); <https://doi.org/10.1002/adma.201905923>.
- [7] L.S. Yablon, I.M. Budzulyak, M.V. Karpets, V.V. Strelchuk, S.I. Budzulyak, I.P. Yaremiy, O.M. Hemiy, O.V. Morushko, *The structure and physical properties of composites formed from molybdenum sulfide*, *Journal of Nano- and Electronic Physics*, 8(2), 02029 (2016); [https://doi.org/10.21272/jnep.8\(2\).02029](https://doi.org/10.21272/jnep.8(2).02029).
- [8] H. Hu, Q. Li, L. Li, X. Teng, Z. Feng, Y. Zhang, M. Wu, J. Qiu, *Laser irradiation of electrode materials for energy storage and conversion*, *Matter*, 3(1), 95 (2020); <https://doi.org/10.1016/j.matt.2020.05.001>.
- [9] O. Khemii, I. Budzulyak, L. Yablon, D. Popovych, O. Morushko, R. Lisovskiy, *Structure and physical properties of modified β -Ni(OH)₂/C composites*, *Materials Today: Proceedings*, 35, 595(2021); <https://doi.org/10.1016/j.matpr.2019.11.207>.

- [10] R. Xu, J. Lin, J. Wu, M. Huang, L. Fan, Z. Xu, Z. Song, *A high-performance pseudocapacitive electrode material for supercapacitors based on the unique NiMoO₄/NiO nanoflowers*, Applied Surface Science, 463, 721 (2019); <https://doi.org/10.1016/j.apsusc.2018.08.172>.
- [11] O. Popovych, I. Budzulyak, V. Yukhymchuk, S. Budzulyak, D. Popovych, *Raman spectroscopy of nickel molybdate and its modifications*, Fullerenes, Nanotubes and Carbon Nanostructures, 29(12), 1009 (2021); <https://doi.org/10.1080/1536383X.2021.1925253>.
- [12] W. Xiao, J. S. Chen, C. M. Li, R. Xu, X. W. Lou, *Synthesis, Characterization, and Lithium Storage Capability of AMoO₄ (A = Ni, Co) Nanorods*, Chemistry of Materials, 22, 746 (2010); <https://doi.org/10.1021/cm9012014>.
- [13] D. Ghosh, S. Giri, C. K. Das, *Synthesis, Characterization and Electrochemical Performance of Graphene Decorated with 1D NiMoO₄·nH₂O Nanorods*, Nanoscale, 5, 10428 (2013); <https://doi.org/10.1039/C3NR02444J>.
- [14] A.K. Jonscher, *The 'universal' dielectric response*, Nature, 267, 673 (1977); <https://doi.org/10.1038/267673a0>.
- [15] .F. Mott, *Conduction in non-crystalline materials*, Philos. Mag., 19(160), 835 (1969); <https://doi.org/10.1080/14786436908216338>.
- [16] A. Shameem, P. Devendran, V. Siva, R. Packiaraj, N. Nallamuthu, S. Asath Bahadur, *Electrochemical performance and optimization of α-NiMoO₄ by different facile synthetic approach for supercapacitor application*, Journal of Materials Science: Materials in Electronics, 30, 3305 (2019); <https://doi.org/10.1007/s10854-018-00603-3>.
- [17] S. Motupally, C.C. Streinz, J.W. Weidner, *Proton diffusion in nickel hydroxide films: measurement of the diffusion coefficient as a function of state of charge*, Journal of the Electrochemical Society, 142, 1401 (1995); <https://doi.org/10.1149/1.2048589>.

О.М. Попович¹, І.М. Будзуляк¹, М.М. Хемій¹, Р.В. Ільницький¹, Л.С. Яблонь¹,
Д.І. Попович², І.І. Панько¹

Лазерно-модифікований нанокристалічний NiMoO₄ як електродний матеріал в гібридних суперконденсаторах

¹Прикарпатський національний університет імені Василя Стефаника, Івано-Франківськ, Україна,
khemiiolha@gmail.com

²Інститут прикладних проблем механіки і математики ім. Я. С. Підстригача НАН України, Львів, Україна

Нанокристалічний NiMoO₄, отриманий в результаті гідротермального синтезу піддавали впливу лазерного випромінювання з енергією в імпульсі 70 мДж/см² протягом 5 хвилин. Фазовий склад і розміри кристалітів триклінної структури NiMoO₄ визначили методом X-променевого аналізу. Середній розмір кристалітів становив 18 нм для лазерно-опроміненого молібдату нікелю. Для аналізу температурної залежності електропровідності лазерно-опроміненого молібдату нікелю використовували імпедансний аналіз. Частотний показник степеня, визначений за допомогою методу нелінійної апроксимації, становив 0,5-0,67, що відповідає стрибковому механізму носіїв заряду. Електрохімічну поведінку NiMoO₄ досліджували з використанням циклічної вольтамперометрії та гальваностатичного зарядного/розрядного тестування. Лазерно-опромінений NiMoO₄ досягає питомої ємності 553 Ф/г при швидкості сканування 1 мВ/с. Гібридна електрохімічна система, сформована на онові електродів з модифікованого NiMoO₄ та вуглецевого матеріалу демонструє високу кулонівську ефективність (95%) для значної кількості циклів заряду/розряду.

Ключові слова: гібридний суперконденсатор, лазерне опромінення, молібдат нікелю, електропровідність, питома ємність.

O. Paiuk¹, A. Meshalkin², A. Stronski¹, E. Achimova², C. Losmanschii², V. Botnari²,
A. Korchovi¹, M. Popovych¹

Direct magnetic and surface relief patterning using carbazole-based azopolymer

¹V.E. Lashkaryov Institute of Semiconductors Physics, NAS in Ukraine, Kyiv, Ukraine, paiuk@ua.fm

²Institute of Applied Physics, Chisinau, Moldova

The results on using of carbazole-based azopolymer layers (Polyepoxypropylcarbazole: Methyl Red with magnetic particles of Fe₂SO₄) for the recording of 1-D and 2-D surface relief gratings are presented in this report. Morphology study using AFM and MFM of obtained structures has shown their good quality. Surface relief gratings with profile height up to 1.2 μm were obtained during the holographic recording using blue laser. Along with surface relief grating it was shown the direct formation of magnetic relief. Possibility of simultaneous direct fabrication of surface and magnetic relief by optical holographic recording using azopolymer thin films as recording media was shown.

Keywords: azopolymer, polyepoxypropylcarbazole, methyl red, thin films, recording media, holographic gratings, direct recording, surface and magnetic relief.

Received 16 November 2023; Accepted 22 March 2023.

Introduction

Recently, research and the development for new recording media on the base of non-crystalline photosensitive materials have been actively carried out [1-3]. Of particular interest are carbazole-containing copolymers, which could be used for photoinduced formation of surface reliefs [4-6]. Versatile optical elements (refractive elements [7], optical storage elements [8-10]) can be fabricated using such media. Carbazole-containing polymers can be used for both optical and electron-beam recording, which may be of interest for the implementation of combined recording [11]. To increase the light sensitivity of recording materials, their optical sensitization is of great importance [12-14]. Various dyes and additives can be used as spectral sensitizers.

Photostimulated changes in optical and physical properties are the basis for recording and optical information storage [1,3,8]. Substantial materials motions (induced by photoisomerization reactions of azobenzene molecules) can be obtained under light exposure of azopolymers. Carbazole-based azopolymers under the

influence of laser irradiation exhibit changes in thickness, transmission, provide ability to form surface reliefs, high resolution and possibility of optical elements fabrication such as photonic crystals, broad-band antireflection coatings, diffraction gratings, nanostructured polarizers, microlens arrays, holograms, plates, etc. [3]. Carbazole-containing azopolymers are good light-sensitive materials due to high refractive index modulation, high resolution, low absorption for visible and infrared light, high signal-to-noise ratio and good stability of parameters in the environment. However, this recording material is primarily sensitive to the ultraviolet region of the spectrum. Therefore, the problem of expanding the spectral photosensitivity into the visible region of the spectrum to adjust it to the wavelength of recording is topical. To expand the spectral sensitivity, it is necessary to use the optical sensitization of the polymeric recording layer by introducing a dye that has absorption in the desired region of the spectrum.

Exposure by interference intensity pattern is usually used to fabricate diffraction gratings [15-17]. Selective etching usually is used for the surface relief formation

[1,3,15]. Direct fabrication (without a step of selective etching) of gratings by interference pattern exposure was shown in [18-20].

The results on using of carbazole-based azopolymer layers for the direct recording of surface relief gratings are presented in this report.

I. Experiment

Polyepoxypropylcarbazole:Methyl Red (PEPC:MR) with magnetic particles of Fe_2SO_4 was synthesized. As a photosensitizer, the azopolymer contained azodye Methyl Red.

PEPC thin films were fabricated using spin coating. Experiments were carried out at room temperature. Two-beam spectrophotometer SPECORD M40 in the range of wavelengths of 450–900 nm was used for the recording of PEPC:MR films transmission spectra which showed good transparency in the VIS region (Fig.1, curve 1).

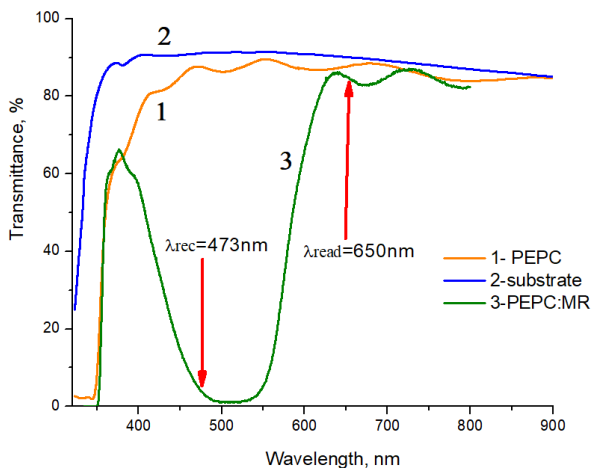


Fig.1. Transmission spectra of PEPC:MR films. 1- PEPC, 2 – substrate transmission, 3 – transmission of PEPC:MR.

By arrows are indicated the wavelength positions used for the gratings recording and diffraction efficiencies measurement. Addition of methyl red provided necessary increase of absorption (curve 3 Fig.1) and sensitivity on the recording wavelength (473 nm), with high transmittance on the reading wavelength (650 nm).

Films thickness was measured using atomic-force microscopy and interference microscope MII-4. Optic Meter program was used for processing of the obtained photographed interference patterns. Thicknesses of films were within 1-3 μm . Atomic Force Microscope (AFM) was used for study of surface relief and morphology of the recorded gratings. Magnetic Force Microscope (MFM) was used for study of magnetic relief of obtained structures.

Holographic gratings (1-D and 2-D) were recorded by standard two laser beams setup with the use of (Fig. 2) linearly p-polarized beams of DPSS laser ($I = 1700 \text{ mW/cm}^2$ and $\lambda = 473 \text{ nm}$). Intensity ratio of beams consisted 1:1, spatial frequency - 170 lines/mm (period $\sim 6.0 \mu m$). Dependence on recording light polarization of the grating relief formation processes was shown in previous works [2, 6]. In present work p-p- configuration of

polarized light was used. Simultaneously with grating formation in-situ diffraction efficiency η measurements were carried out in order to obtain η dependence on time of recording.

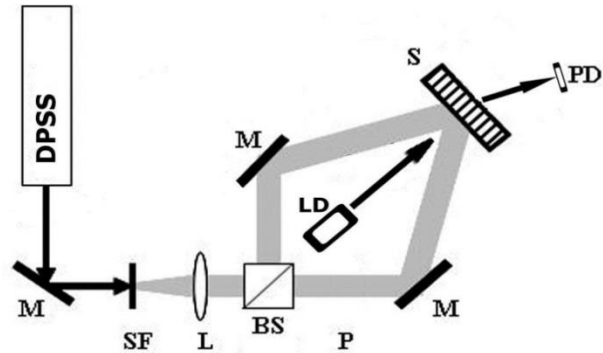
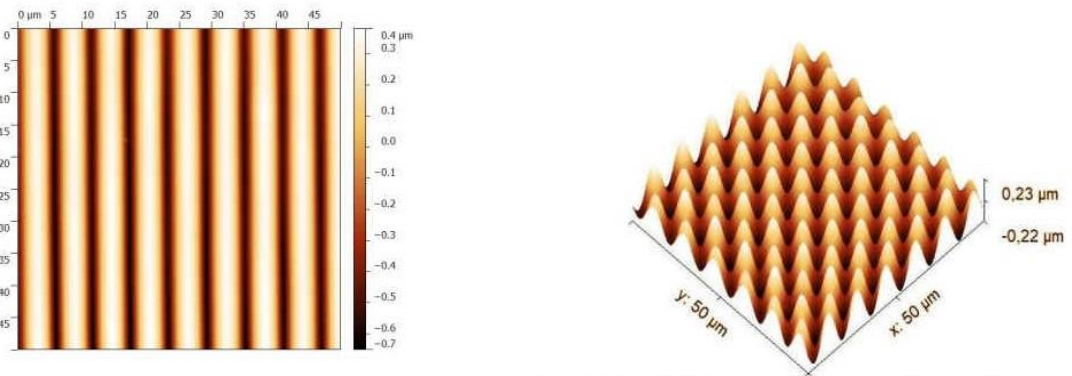


Fig.2. Experimental setup for gratings recording: LD, DPSS and PD are light emitting diode, laser, and registering unit, respectively, BS- beamsplitter, M – flat mirrors, SF and L - collimator, S – sample (registering media).

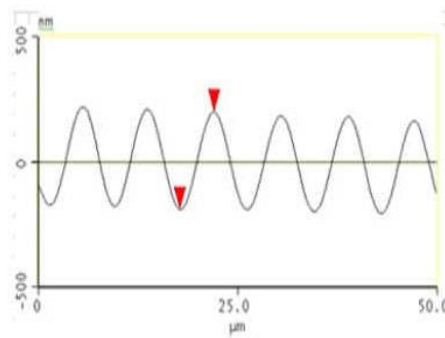
Dependence of the grating formation on exposure time was measured by detecting the intensity of first-order diffraction beam (in transmission) using normally incident light of laser diode (650 nm). Intensities ratio of the first order diffracted beam and the transmitted out of the grating beam was taken as diffraction efficiency value η .

II. Results and Discussion

AFM image of the directly recorded holographic diffraction grating (without selective etching) with the use of PEPC:MR films is shown in Fig.3. Relief heights of the recorded gratings were within 0.3-1.2 μm , that gives relief modulation depth $h/d \sim 0.05 - 0.2$ (h – relief height, d – grating period – 6 μm). Images of gratings in Fig.3-5 show that holographic surface relief gratings with relatively large thickness modulation could be obtained by direct one-step holographic recording without any subsequent processing steps using PEPC layers as recording media. It is also necessary to note that p-p polarization configuration allows to achieve surface relief grating with the largest amplitude up to 50% of original film thickness. In photosensitive azopolymer materials vectorial mass transport during formation of photoinduced surface pattern is known to depend on the excitation wavelength, distribution of intensities and light polarization [1, 6]. Very interesting results were obtained in MFM microscopy studies of the obtained gratings. Amorphous chalcogenides and various photosensitive polymers being non-crystalline materials can be easily doped [16, 19, 21, 22]. Introduced admixtures change physical and chemical (magnetic, optical luminescent, etc.) properties of substances [21]. Such changes enabled to provide direct simultaneous recording of surface and magnetic relief with the use of such substances [23]. Fig. 4 – 5 show that similar result can be obtained with the use of PEPC:MR films with Fe_2SO_4 particles. MFM and AFM images (Fig.4 and 5) show correlation between grating surface relief and distribution and value of magnetic field.



a – 2-D AFM figure of the recorded grating ($d \sim 6.0 \mu\text{m}$) b – 3-D AFM image of the recorded grating



c – grating profile

Fig.3. AMF image of fabricated grating ($d \sim 6 \mu\text{m}$) obtained with the use of PEPC:MR films: a – 2-D image, b– 3-D image, c – grating profile.

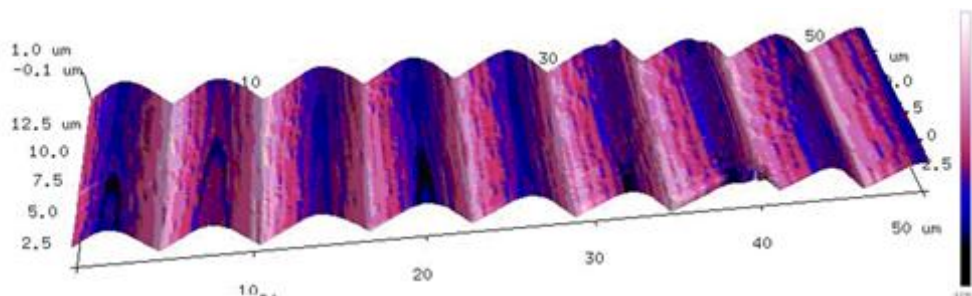


Fig. 4. AFM image of gratings relief and MFM image map (overlapped, colour image, right scale bar) of grating fabricated using PEPC:MR films with Fe_2SO_4 particles [24].

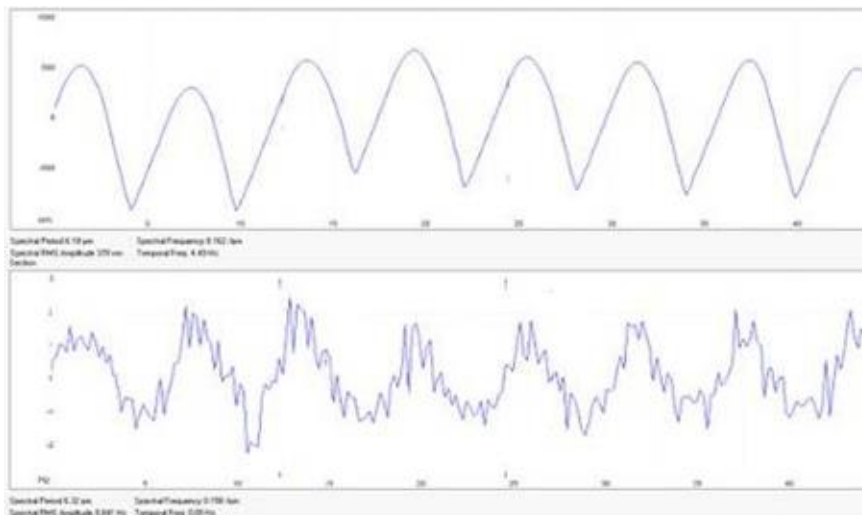


Fig.5. AFM and MFM profiles of grating (shown in Fig.4) directly recorded with the use of PEPC:MR films with Fe_2SO_4 particles.

Nanoparticles redistribution in photopolymer nanoparticle-dispersed matrix as a result of light exposure observed in [25, 26] may also be mechanism of the magnetic relief formation in layers of PEPC:MR with Fe₂SO₄ particles. Direct magnetic relief recording simultaneously with the recording of surface relief by interference pattern using PEPC:MR with Fe₂SO₄ particles as recording media provide possibility for magnetic memory applications and fabrication of optical elements with combination of unique properties.

Conclusions

Holographic grating recording by a direct, one-step process (recording wavelength 473 nm) using polyepoxypropylcarbazole (PEPC): methyl red layers with magnetic particles Fe₂SO₄ was shown in this work. Diffraction efficiency values in transmission of the fabricated gratings were ~ 34%. Simultaneous surface and magnetic relief recording using as recording media polyepoxypropylcarbazole (PEPC) layers: methyl red with Fe₂SO₄ magnetic particles was shown. Obtained results have shown that PEPC films can be used for the

fabrication of high quality optical elements with unique properties using changes of films properties after doping and laser irradiation (changes in absorption, transmission, reflection, in thickness, in magnetic and other physical properties) and for information recording.

Acknowledgements:

Authors appreciate partial financial support from ANCD projects 20.80009.5007.03 & 21.80013.5007.1M and bilateral Moldova-Ukraine project 17.80013.5007.03/UA.

Paiuk Oleksandr – Candidate of Physical and Mathematical Sciences;
Meshalkin Alexei – Senior Scientific Researcher;
Stronski Alexander – Senior Scientific Researcher, Doctor of Physical and Mathematical Sciences;
Achimova Elena – Associate Professor, Doctor of Physical and Mathematical Sciences;
Losmanschii Constantin – PhD student;
Botnari Vladislav – Engineer;
Korchovi Andriy – Candidate of Physical and Mathematical Sciences;
Popovych Mykhailo – PhD student.

- [1] V.M. Kryshenik, Y.M. Azhniuk, V.S. Kovtunencko, *All-optical patterning in azobenzene polymers and amorphous chalcogenides*, Journal of Non-Crystalline Solids, 512, 112 (2019); <https://doi.org/10.1016/j.jnoncrysol.2019.02.019>.
- [2] V.V. Podlipnov, N.A. Ivliev, S.N. Khonina, D.V. Nesterenko, A.Yu. Meshalkin, E.A. Achimova, *Formation of microstructures on the surface of a carbazole-containing azopolymer by the action of laser beams*, J. Phys.: Conf. Ser., 1368, 022069 (2019); <https://doi.org/10.1088/1742-6596/1368/2/022069>
- [3] A. Priimagi, A. Shevchenko, *Azopolymer-based micro- and nanopatterning for photonic applications*, J. Polym. Sci. B Polym. Phys., 52, 163 (2014); <https://doi.org/10.1002/polb.23390>.
- [4] J.V. Grazulevicius, P. Stroehriegl, J. Pielichowski, K. Pielichowski, *Carbazole-containing polymers: synthesis, properties and applications*, Progress in Polymer Science, 28 (9), 1297 (2003); [https://doi.org/10.1016/S0079-6700\(03\)00036-4](https://doi.org/10.1016/S0079-6700(03)00036-4).
- [5] S.G. Sorkhabi, R. Barille, S. Ahmadi-Kandjani, S. Zielinska, E. Ortyl, *A new method for patterning azopolymer thin film surfaces*, Opt. Mater., 66, 573 (2017); <https://doi.org/10.1016/j.optmat.2017.03.004>.
- [6] A. Andries, V. Abaskin, E. Achimova, A. Meshalkin, A. Prisacar, S. Sergheev, S. Robu, L. Vlad, *Application of carbazole-containing polymer materials as recording media*, Phys. Status Solidi A, 208, 1837 (2011); <https://doi.org/10.1002/pssa.201084040>.
- [7] F.T. O'Neill, A.J. Carr, S.M. Daniels, M.R. Gleeson, J.V. Kelly, J.R. Lawrence, J.T. Sheridan, *Refractive elements produced in photopolymer layers*, Journal of Materials Science, 40(15), 4129 (2005); <https://doi.org/10.1007/s10853-005-2567-6>.
- [8] T. Tanaka, *Recording and reading temperature tolerance in holographic data storage, in relation to the anisotropic thermal expansion of a photopolymer medium*, Optics Express, 17(16), 14132 (2009); <https://doi.org/10.1364/OE.17.014132>.
- [9] A. Khan, G.D. Stucky, C.J. Hawker, *High-Performance, Non-diffusive Crosslinked Polymers for Holographic Data Storage*, Advanced Materials, 20(20), 3937 (2008); <https://doi.org/10.1002/adma.200800776>.
- [10] J.T. Sheridan, M.R. Gleeson, C.E. Close, J.V. Kelly, *Optical response of photopolymer materials for holographic data storage applications*, J. Nanosci. Nanotechnol., 7(1), 232 (2007); <https://doi.org/10.1166/jnn.2007.18018>.
- [11] A. Gerbreders, O. Shimane, V. Kolobjonoks, J. Teteris, *UV optical record and electron beam lithography in polymer films*, IOP Conf. Ser.: Mater. Sci. Eng., 38, 012027 (2012); <http://dx.doi.org/10.1088/1757-899X/38/1/012027>.
- [12] J. Guo, S. Liu, M.R. Gleeson, J.T. Sheridan, *Study of photosensitizer diffusion in a photopolymer material for holographic applications*, Optical Engineering, 50(1), 015801 (2011); <https://doi.org/10.1117/1.3526686>.
- [13] K. Curtis, L. Dhar, L. Murphy, A.J. Hill, *Future Developments in Holographic Data Storage: From Theory to Practical Systems*, (Wiley, 2010).

- [14] V.V. Bivol, S.V. Robu, A.M. Prisacari, A.Yu. Meshalkin, L.A. Vlad, M.I. Karaman, *Study of sensitometric and holographic properties of photoresist media based on carbazole-containing polymers sensitized with triiodomethane and pyranphotochromic materials*, High Energy Chemistry, 40(3), 178 (2006); <https://doi.org/10.1134/S001814390603009X>.
- [15] A.V. Stronski and M. Vlček, *Imaging properties of $As_{40}S_{40}Se_{20}$ layers*, Optoelectronics Review, 8(3), 263(2000).
- [16] A. Stronski, L. Revutska, A. Meshalkin, O. Paiuk, E. Achimova, A. Korchovy, K. Shportko, O. Gudymenko, A. Prisacar, A. Gubanova, G. Triduh, *Structural properties of Ag–As–S chalcogenide glasses in phase separation region and their application in holographic grating recording*, Optical Materials, 94, 393 (2019); <https://doi.org/10.1016/j.optmat.2019.06.016>.
- [17] A. Andriesh, S. Sergheev, G. Triduh, A. Meshalkin, *Diffraction optical structures on the basis of chalcogenide glasses and polymers*, J. Optoelectron. Adv. M. 9(10), 3007 (2007).
- [18] M. Vlcek, S. Schroeter, S. Brueckner, S. Fehling, A. Fiserova, *Direct fabrication of surface relief gratings in chalcogenide glasses by excimer laser interference lithography*, Journal of Materials Science: Materials in Electronics, 20(1), 290 (2009); <https://doi.org/10.1007/s10854-008-9584-6>.
- [19] A. Stronski, E. Achimova, O. Paiuk, A. Meshalkin, V. Abashkin, O. Lytvyn, S. Sergeev, A. Prisacar, P. Oleksenko, G. Triduh, *Optical and Electron-Beam Recording of Surface Relief's Using $Ge_5As_{37}S_{58}$ -Se Nanomultilayers as Registering Media*, Journal of Nano Research, 39, 96 (2016); <https://doi.org/10.4028/www.scientific.net/JNanoR.39.96>.
- [20] A. Rahmouni, Y. Bougdid, S. Moujdi, D. V. Nesterenko, and Z. Sekkat, *Photoassisted holography in azodye doped polymer films*, The Journal of Physical Chemistry B, 120(43), 11317 (2016); <https://doi.org/10.1021/acs.jpcc.6b08855>.
- [21] A. Stronski, O. Paiuk, A. Gudymenko, V. Klad'ko, P. Oleksenko, N. Vuichyk, M. Vlček, I. Lishchynskyy, E. Lahderanta, A. Lashkul, A. Gubanova, Ts. Krys'kov, *Effect of doping by transitional elements on properties of chalcogenide glasses*, Ceramics International, 41, 7543 (2015); <http://dx.doi.org/10.1016/j.ceramint.2015.02.077>.
- [22] J. Guo, M.R. Gleeson, J.T. Sheridan, *A Review of the Optimisation of Photopolymer Materials for Holographic Data Storage*, Physics Research International, 2012, 803439 (2012); <https://doi.org/10.1155/2012/803439>.
- [23] A. Stronski, E. Achimova, O. Paiuk, A. Meshalkin, A. Prisacar, G. Triduh, P. Oleksenko, P. Lytvyn, *Direct Magnetic Relief Recording Using $As_{40}S_{60}$: Mn–Se Nanocomposite Multilayer Structures*, Nanoscale Research Letters, 12, 286 (2017); <https://doi.org/10.1186/s11671-017-2060-6>.
- [24] O. Paiuk, A. Meshalkin, A. Stronski, E. Achimova, K. Losmanshii, A. Korchovy, Z. Denisova, V. Goroneskul, P. Oleksenko, *Direct Surface Patterning Using Carbazole-Based Azopolymer*, 5th International Conference on Nanotechnologies and Biomedical Engineering, ICNBME 2021, IFMBE Proceedings, (Springer, Cham, 2022); https://doi.org/10.1007/978-3-030-92328-0_16.
- [25] Yasuo Tomita, Naoaki Suzuki, and Katsumi Chikama, *Holographic manipulation of nanoparticle distribution morphology in nanoparticle-dispersed photopolymers*, Opt. Lett., 30(8), 839 (2005); <https://doi.org/10.1364/OL.30.000839>.
- [26] Yasuo Tomita, Eiji Hata, Keisuke Momose, Shingo Takayama, Xiangming Liu, Katsumi Chikama, Jürgen Klepp, Christian Pruner & Martin Fally, *Photopolymerizable nanocomposite photonic materials and their holographic applications in light and neutron optics*, J.Mod.Opt., 63(53), 511 (2016); <https://doi.org/10.1080/09500340.2016.1143534>.

О. Паюк¹, А. Мешалкін², О. Стронський¹, Є. Акімова², К. Лошманський²,
В. Ботнарі¹, А. Корчовий¹, М. Попович¹

Пряме формування магнітного та поверхневого рельєфу на основі карбазолвмісногоазополімеру

¹Інститут фізики напівпровідників ім. В.Є. Лашкарьова, НАН України, Київ, Україна, paiuk@ua.fm

²Інститут прикладної фізики, Кишинів, Молдова

У роботі представлено результати дослідження шарів карбазолвмісногоазополімерів (поліепоксипропілкарбазол: метиловий червоний з магнітною домішкою Fe_2SO_4) для створення 1-D та 2-D поверхнево рельєфних решіток. Проілюстровано гарну якість отриманих структур на основі результатів досліджень морфології поверхні з використанням АСМ та МСМ. За допомогою синього лазера в процесі голографічного запису отримано поверхнево рельєфні решітки з висотою профілю рельєфу до 1,2 μm . Разом з утворенням поверхнево рельєфної ґратки показано пряме формування магнітного рельєфу решітки. Продемонстровано можливість одночасного прямого формування поверхневого та магнітного рельєфу при оптичному записі решіток на тонких плівках азополімеру.

Ключові слова: азополімер, поліепоксипропілкарбазол, метиловий червоний, тонкі плівки, голографічні решітки, прямий запис, поверхневий і магнітний рельєф.

R. M. Yerojwar^{1,2}, N. S. Kokode², C. M. Nandanwar², D. K. Ingole¹

Synthesis and Photoluminescence characterization of Sr₃La(AlO)₃(BO₃)₄:Eu³⁺, Sm³⁺ Phosphor for n-UV w-LED

¹Department of physics, Mohasinbhai Zaweri Mahavidyalaya, Desaiganj(Wadsa), Gondwana University, Gadchiroli, Maharashtra, India

²Nevjabai Hitkarini Mahavidyalaya, Bramhapuri, Gondwana University, Gadchiroli, Maharashtra, India, yerojwar@gmail.com

A red emitting Eu³⁺ doped Sr₃La(AlO)₃(BO₃)₄ and Sm³⁺ doped Sr₃La(AlO)₃(BO₃)₄ phosphors with high efficiency have been synthesized by combustion method and the photoluminescence properties of samples are investigated in detail. Morphology by scanning electron microscopy and chromaticity by CIE were studied. The results demonstrate the excitation ranges from 340 nm to 420 nm, especially, the strongest excitation (394 nm and 406 nm) locates in the UV region for Eu³⁺ and Sm³⁺ doping, suggesting that the phosphor can match well with LED chips. Under n-UV light excitation of 394 nm the Eu³⁺ doped Sr₃La(AlO)₃(BO₃)₄ and 406 nm Sm³⁺ doped Sr₃La(AlO)₃(BO₃)₄ phosphor can emit bright red light with main emission peaks located at 617 nm and 602 nm are observed. The PL properties indicate that the phosphor has excellent stability. These results imply the importance of Sr₃La(AlO)₃(BO₃)₄:Eu³⁺ and Sr₃La(AlO)₃(BO₃)₄:Sm³⁺ red phosphors in white LEDs under n-UV excitation.

Keywords: Rare earth doped, Combustion synthesis, w-LED, CIE-Coordination, Sr₃La(AlO)₃(BO₃)₄:Eu³⁺, Sr₃La(AlO)₃(BO₃)₄:Sm³⁺, red phosphor.

Received 17 November 2022; Accepted 13 March 2023.

Introduction

Due to advantages of great brightness, low power consumption, and extended operating life, white light-emitting diodes (w-LEDs) have been regarded as significant solid-state light sources [1, 2]. Commercial w-LED currently employ a blue InGaN LED chip to excite a yellow emitting YAG:Ce phosphor, however this method renders colour poorly in the red region, resulting in a very low colour rendering index (CRI) [3]. Additionally, compared to green and blue phosphors, the luminous efficacy of red phosphor triggered by n-UV is significantly lower. As a result, the creation of novel, highly efficient red phosphors triggered by n-UV chips has received a lot of attention in the process of making w-LEDs [4]. Due to ⁵D₀→⁷F_J (J=0, 1, 2, 3, 4) transitions, the Eu³⁺ ion has been identified as one of the best red activators in the phosphors. Examples of this include Eu³⁺ doped Ca₁₂Al₁₄O₃₂F₂ [5], LaBMoO₆ [6], Sr₂LiScB₄O₁₀ [7], Bi₄O₃(BO₃)(PO₄) [8], LiYGeO₄ [9], Sr₅(PO₄)₃F [10],

ZnAl₁₂O₁₉ [11] and NaGdMgWO₆ [12]. They demonstrate effective red emission when excited by n-UV light.

The desire to use Sm³⁺ ions efficient emission in a variety of materials, particularly for phosphors in red and orange, but with the introduction of InGaN and GaN laser diodes in the excitation peak at 405 nm, where Sm³⁺ ions exhibits a quite substantial absorption, visible laser output has also grown. Numerous studies of Sm³⁺ ions in various materials, including phosphors [13, 14], single crystals [15,16], and glasses [17,18]. The Sm³⁺ in phosphors always exhibits a bright reddish emission, which can improve the color-rendering index (CRI) of phosphor-converted w-LEDs [19]. All lanthanide aluminates hosts are promising since they are used to produce white light by increasing the intensity of a red component [20-23].

A Tb³⁺ doped Sr₃La(AlO)₃(BO₃)₄ phosphor that emits a yellowish-green colour and has exceptional thermal stability and very high quantum efficiency, It has a great potential for combining red and blue Sr₃La(AlO)₃(BO₃)₄:Eu³⁺ to obtain an excellent for n-UV w-LED [24]. In this paper, Sr₃La(AlO)₃(BO₃)₄:Eu³⁺ and

$\text{Sr}_3\text{La}(\text{AlO})_3(\text{BO}_3)_4:\text{Sm}^{3+}$ phosphors were prepared by traditional combustion method and their photoluminescence, morphological and CIE properties were studied. The best proportion of the two rare earth ions was investigated also.

I. Experimental

The combustion process was used to create the $\text{Sr}_3\text{La}(\text{AlO})_3(\text{BO}_3)_4$ phosphors doped with Eu^{3+} and Sm^{3+} ions. Every initial component used in the experiment is of analytical (AR) grade. $\text{Sr}(\text{NO}_3)_2$ (Extra pure 98%), $\text{La}(\text{NO}_3)_3 \cdot 6\text{H}_2\text{O}$ (99% AR), $\text{Al}(\text{NO}_3)_3 \cdot 9\text{H}_2\text{O}$ (98.5% AR/ACS), $\text{H}_3(\text{BO}_3)$ (Extra pure 98%), Eu_2O_3 (99.9% AR), Sm_2O_3 (99.9% AR) and NH_2CONH_2 (99.5% AR) were employed as starting materials and fuel, respectively. By combining the proper volume of diluted nitric acid, Eu_2O_3 and Sm_2O_3 are transformed into nitrate form. Every compound in the mixture was combined using the stoichiometric ratio. The mixed colourless solution was then heated at a higher temperature while being stirred (100°C), producing an extremely viscous wet gel. The gel that results is put into a furnace that is kept at 550°C and reheated at 600°C for 2 hr and cooled up to room temp., It takes the flame around 40 seconds to die out. The final product obtained is then crushed with a mortar pestle and the fine powder sample is used for further investigations. SEM Images of the prepared sample is taken and Shimadzu RF5301PC Spectrofluorophotometer was used to measure the PL. A spectral slit width of 1.5 nm was used to record the excitation and emission.

II. Results and Discussion

2.1. SEM studies

SEM investigation of the host $\text{Sr}_3\text{La}(\text{AlO})_3(\text{BO}_3)_4$ phosphor was performed to study the morphology and particle size, as shown in Fig.1. The phosphor is prepared using a combustion method approach and has a solid microcrystalline structure with certain uneven shapes and aggregation between crystalline grains. The average particle size of the $\text{Sr}_3\text{La}(\text{AlO})_3(\text{BO}_3)_4$ sample is determined to be between 2 and 15 micrometers. The majority of commercial phosphors now on the market have particle sizes in the range of a few micrometers [25,26].

2.2. Photoluminescence studies

2.2.1. Photoluminescence properties of $\text{Sr}_3\text{La}(\text{AlO})_3(\text{BO}_3)_4:\text{Eu}^{3+}$ phosphor

Figure 2 displays the excitation spectra of $\text{Sr}_3\text{La}(\text{AlO})_3(\text{BO}_3)_4:\text{Eu}^{3+}$ phosphor were studied in the wavelength range of 350 and 400 nm after the emission peak at 617 nm. The excitation peaks at 362, 380, and 394 nm, corresponding to Eu^{3+} ions transitions ${}^7\text{F}_0 \rightarrow {}^5\text{L}_9$, ${}^7\text{F}_0 \rightarrow {}^5\text{G}_3$, and ${}^7\text{F}_0 \rightarrow {}^5\text{L}_6$ [27]. The maximum excitation peak in the $\text{Sr}_3\text{La}(\text{AlO})_3(\text{BO}_3)_4:\text{Eu}^{3+}$ phosphor was determined to be 394 nm.

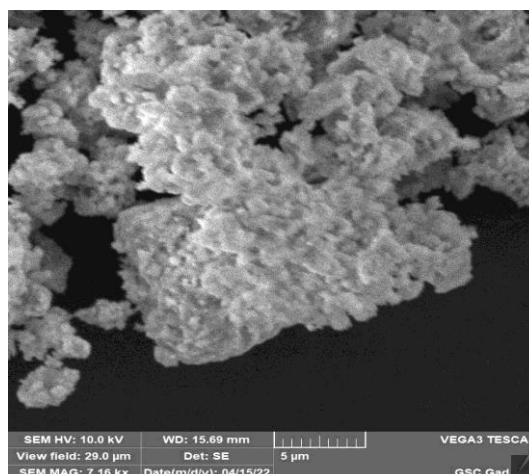


Fig. 1. SEM Photograph of host $\text{Sr}_3\text{La}(\text{AlO})_3(\text{BO}_3)_4$.

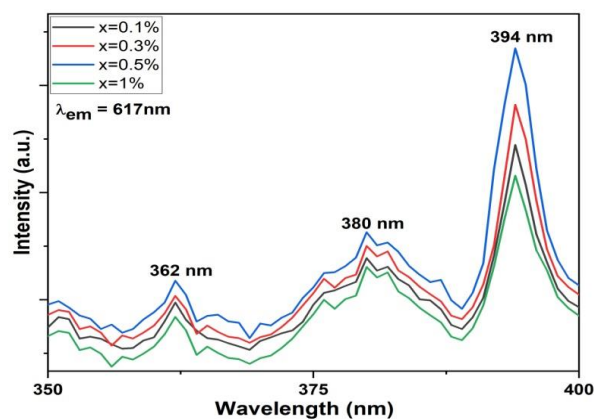


Fig. 2. The excitation spectrum of $\text{Sr}_3\text{La}(\text{AlO})_3(\text{BO}_3)_4:\text{Eu}^{3+}$ (monitored at 617 nm).

Figure 3 displays the emission spectra of $\text{Sr}_3\text{La}(\text{AlO})_3(\text{BO}_3)_4$ phosphors doped Eu^{3+} ions at an excitation wavelength of 394 nm. Two well-resolved emission bands 590 nm (${}^5\text{D}_0 \rightarrow {}^7\text{F}_1$) and 617 nm (${}^5\text{D}_0 \rightarrow {}^7\text{F}_2$) might potentially be seen based on the luminescence spectra, in line with the well-documented Eu^{3+} ions doped phosphor literature of published data. It is widely accepted that the electron dipole and magnetic dipole transitions are responsible for the emission peaks at 617 nm and 590 nm, respectively [28].

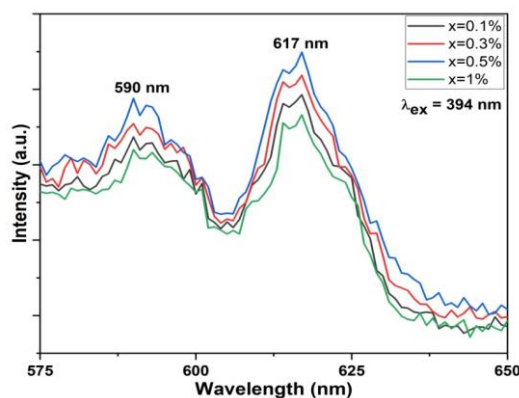


Fig. 3. The emission spectra of $\text{Sr}_3\text{La}(\text{AlO})_3(\text{BO}_3)_4:\text{Eu}^{3+}$ phosphors under 394 nm excitation.

2.2.2. Photoluminescence properties of $\text{Sr}_3\text{La}(\text{AlO})_3(\text{BO}_3)_4:\text{Sm}^{3+}$ phosphor

The photoluminescence excitation spectra of $\text{Sr}_3\text{La}(\text{AlO})_3(\text{BO}_3)_4:\text{Sm}^{3+}$ phosphor are shown in Fig. 4. These materials' PLE spectra were obtained at room temperature by measuring emission wavelength at 602 nm. These spectra exhibit four narrow and strong excitation peaks at 347, 364, 377 and 406 nm ascribed to transitions from ground state $^6\text{H}_{5/2}$ to excited states $^4\text{H}_{9/2}$, $^6\text{D}_{3/2}$, $^4\text{D}_{1/2}$ and $^4\text{F}_{7/2}$ arising from f-f transitions of Sm^{3+} ions [29-33]. The highest excitation peak formed at 406 nm as a result of the $^6\text{H}_{5/2} \rightarrow ^4\text{F}_{7/2}$ transition.

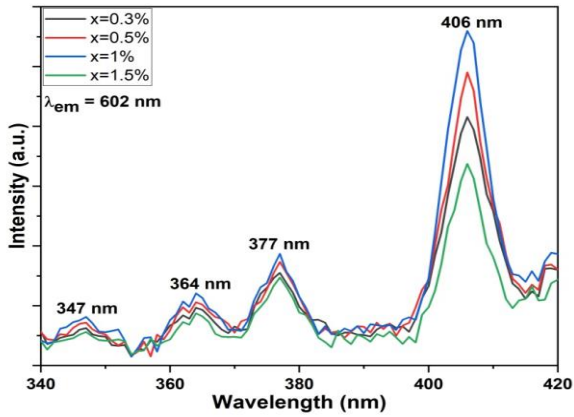


Fig. 4. The excitation spectrum of $\text{Sr}_3\text{La}(\text{AlO})_3(\text{BO}_3)_4:\text{Sm}^{3+}$ (monitored at 602 nm).

The PL spectra of $\text{Sr}_3\text{La}(\text{AlO})_3(\text{BO}_3)_4:\text{Sm}^{3+}$ phosphor stimulated at 406 nm n-UV light are shown in Fig. 5. There are two primary emission peaks in the 525-625 nm range, which are located at 566 and 602 nm, as a result of intra 4f-4f transitions from excited states ($^4\text{G}_{5/2}$) to ground states ($^6\text{H}_{5/2}$ and $^6\text{H}_{7/2}$) respectively. The magnetic dipole (MD) permitted transitions ($^4\text{G}_{5/2} \rightarrow ^6\text{H}_{5/2}$ and $^4\text{G}_{5/2} \rightarrow ^6\text{H}_{7/2}$) detected at 566 and 602 nm dominate the emission spectra and are responsible for the orange-red emission of activator ions, according to the selection rule (change in $j = 0, \pm 1$). [34-36].

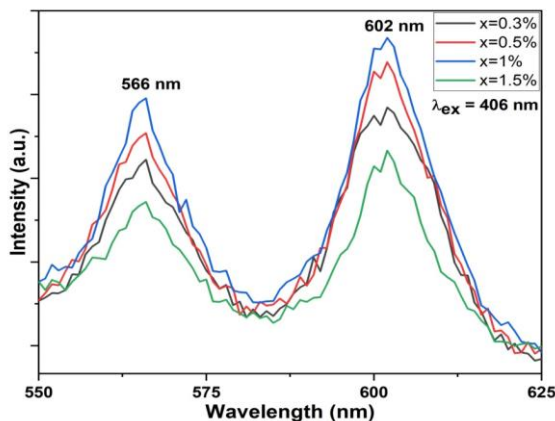


Fig. 5 The emission spectra of $\text{Sr}_3\text{La}(\text{AlO})_3(\text{BO}_3)_4:\text{Sm}^{3+}$ phosphors under 406 nm excitation.

Concentration Quenching

It should be noted that the position of the emission peaks and the form of the emission spectra are similar in each doping concentration; nevertheless, the intensity

factor varied gradually with varying Eu^{3+} and Sm^{3+} ions concentrations in each phosphor. When compared to other concentrations of synthesized phosphors, $\text{Sr}_3\text{La}(\text{AlO})_3(\text{BO}_3)_4$ phosphor (Fig. 6 & 7) has a maximum emission intensity of 1.0 mole % for Eu^{3+} ions and 1.5 mole % for Sm^{3+} doping. The drop in emission intensities was correlated with a rise in Eu^{3+} and Sm^{3+} ions concentrations as a result of the concentration quenching process. As the overall average between the Eu^{3+} and Sm^{3+} ions reduces with increasing ion concentrations in $\text{Sr}_3\text{La}(\text{AlO})_3(\text{BO}_3)_4:\text{Eu}^{3+}$ and $\text{Sr}_3\text{La}(\text{AlO})_3(\text{BO}_3)_4:\text{Sm}^{3+}$ phosphor respectively, a non-radiative energy transfer mechanism occurs via cross-relaxation, enhancing concentration quenching (Fig. 6 & 7) [37, 38, 39].

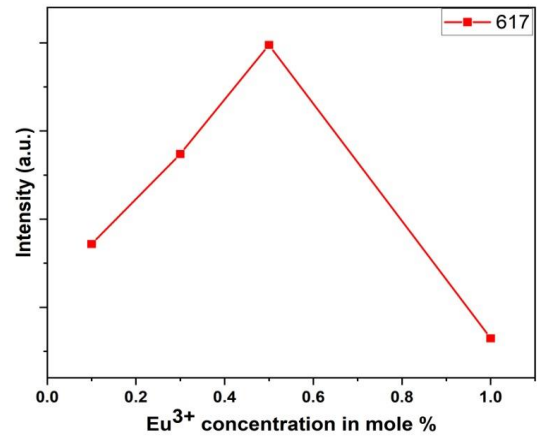


Fig. 6. Variation in the emission intensity 617 nm as function of the Eu^{3+} ion concentration in $\text{Sr}_3\text{La}(\text{AlO})_3(\text{BO}_3)_4:\text{Eu}^{3+}$ phosphor.

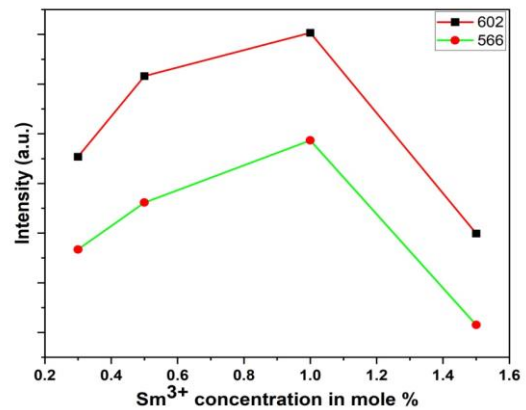


Fig. 7. Variation in the emission intensity 566 nm and 602 nm as function of the Sm^{3+} ion concentration in $\text{Sr}_3\text{La}(\text{AlO})_3(\text{BO}_3)_4:\text{Sm}^{3+}$ phosphor.

2.3. Chromaticity Analysis

Colour coordinates are the essential parameters for examining the phosphor's CIE chromaticity performance. The CIE chromaticity coordinates of $\text{Sr}_3\text{La}(\text{AlO})_3(\text{BO}_3)_4:\text{Eu}^{3+}$ and $\text{Sr}_3\text{La}(\text{AlO})_3(\text{BO}_3)_4:\text{Sm}^{3+}$ Phosphors excited at 394 nm and 406 nm respectively are presented in Fig.7. The corresponding x and y coordinates are (0.684, 0.314) for 617 nm and (0.635, 0.363) for 602 nm. To our observation for all the studied $\text{Sr}_3\text{La}(\text{AlO})_3(\text{BO}_3)_4:\text{Eu}^{3+}$ and $\text{Sr}_3\text{La}(\text{AlO})_3(\text{BO}_3)_4:\text{Sm}^{3+}$

phosphors emission points are found to be located in the red region. Hence, the present red-emitting phosphors find remarkable applications in near ultraviolet excited for w-LEDs [40, 41].

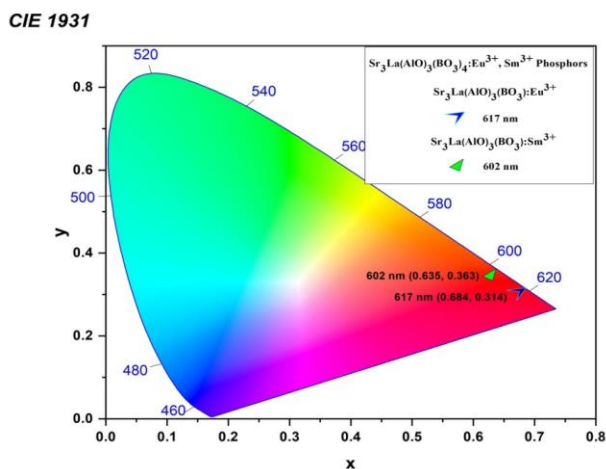


Fig.7. CIE chromaticity diagram of the $\text{Sr}_3\text{La}(\text{AlO})_3(\text{BO}_3)_4:\text{Eu}^{3+}$ and $\text{Sr}_3\text{La}(\text{AlO})_3(\text{BO}_3)_4:\text{Sm}^{3+}$ phosphors.

Conclusion

A Series of $\text{Sr}_3\text{La}(\text{AlO})_3(\text{BO}_3)_4:\text{xEu}^{3+}$ ($x = 0.2, 0.5, 1, 1.5$ mole %) phosphor and $\text{Sr}_3\text{La}(\text{AlO})_3(\text{BO}_3)_4:\text{xSm}^{3+}$ ($x = 0.5, 1.0, 1.5, 2.0$ mole %) phosphor powders were successfully synthesized by the combustion method. The morphological and photoluminescence properties were investigated. The SEM image identifies the irregular morphology of the $\text{Sr}_3\text{La}(\text{AlO})_3(\text{BO}_3)_4$ phosphor samples with micron ranged particles. The photoluminescence properties investigated under photo-excitation showed that the Eu^{3+} doped $\text{Sr}_3\text{La}(\text{AlO})_3(\text{BO}_3)_4$ phosphors exhibited a main red emission peak at 617 nm corresponding to ${}^5\text{D}_0 \rightarrow {}^7\text{F}_2$ transition, also the Sm^{3+} doped

$\text{Sr}_3\text{La}(\text{AlO})_3(\text{BO}_3)_4$ phosphors exhibited main red emission peak at 602 nm corresponding to ${}^4\text{G}_{5/2} \rightarrow {}^6\text{H}_{7/2}$ transition. The optimized concentration of Eu^{3+} and Sm^{3+} ions in the present host is 1% and 1.5% mole respectively. Beyond that concentration, the quenching effect dominates. The CIE of present phosphor doped with Eu^{3+} and Sm^{3+} ions was calculated to be (0.684, 0.314) and (0.635, 0.363) respectively. All results indicate that the as-prepared $\text{Sr}_3\text{La}(\text{AlO})_3(\text{BO}_3)_4:\text{Eu}^{3+}$ and $\text{Sr}_3\text{La}(\text{AlO})_3(\text{BO}_3)_4:\text{Sm}^{3+}$ phosphor have excellent red luminescence properties and is suitable as red-emitting phosphor for w-LEDs application.

Acknowledgement

We are grateful to Dr. N. S. Kokode, Ex. Principal, Nevjabai Hitkarini College, Bramhapuri, for genuinely assisting me and providing inspirational support and IHLR & SS Nevjabai Hitkarini College, Bramhapuri, which was the most valuable contribution to the completion of the work.

The authors would like to thank the Department of Physics of N. H. College in Bramhapuri, (M.S.) India for their helpful advice, India for financial support by the Mahajyoti, Nagpur, fellowship (Outward No. MAHAJYOTI/Nag./Fellowship/2021-22/1042(142) Dated 17/01/2022).

Declaration of Competing Interest

The authors declare that they do not have any known competing financial interests or personal ties that may seem to have influenced the work reported in this paper.

Data availability

No data was used for the research described in the article.

Yerojwar R. M. – M.Sc. SET, Assistant Professor;
Kokode N. S. – Ph.D, Professor;
Nandanwar C. M. – M.Sc. NET, Research Scholar;
Ingole D. K. – Ph.D, Assistant Professor.

- [1] C. C. Lin, R. S. Liu, *Advances in Phosphors for Light-emitting Diodes*, The Journal of Physical Chemistry Letters 2, 1268 (2011); <https://doi.org/10.1021/jz2002452>.
- [2] S. Ye, F. Xiao, Y.X. Pan, Y. Y. Ma, Q. Y. Zhang, *Phosphors in phosphor-converted white light-emitting diodes: Recent advances in materials, techniques and properties*, Material Science and Engineering: R: Reports, 71, 1 (2010); <https://doi.org/10.1016/j.mser.2010.07.001>.
- [3] C. M. Nandanwar, N. S. Kokode, *Synthesis and Photoluminescence Properties of $\text{Ca}_5(\text{PO}_4)_3\text{F}:\text{Ln}$ ($\text{Ln}: \text{Dy}^{3+}, \text{Eu}^{3+}$ and Sm^{3+}) Phosphors for near UV-based solid state lighting*, Physics and Chemistry of solid state, 23 (3), 597 (2022); <https://doi.org/10.15330/pssc.23.3.597-603>.
- [4] S. Neeraj, N. Kijima, A. K. Cheetham, *Novel red phosphors for solid-state lighting: the system $\text{NaM}(\text{WO}_4)_{2-x}(\text{MoO}_4)_x:\text{Eu}^{3+}$ ($M = \text{Gd}, \text{Y}, \text{Bi}$)*, Chemical Physics Letters, 387, 2 (2004); <https://doi.org/10.1016/j.cplett.2003.12.130>.
- [5] H. Peng, Q. Gao, L. Meng, L. Zhang, Q. Pang, L. Liang, *Sol-gel method and optical properties of $\text{Ca}_{12}\text{Al}_{14}\text{O}_{32}\text{F}_2:\text{Eu}^{3+}$ red phosphors*, Journal of Rare Earths, 33, 927 (2015); [https://doi.org/10.1016/S1002-0721\(14\)60507-X](https://doi.org/10.1016/S1002-0721(14)60507-X).
- [6] Z. W. Zhang, D. Q. Ma, Y. Yue, M. Z. Ma, R. P. Liu, *Wide-band excited $\text{LaBMoO}_6:\text{Eu}^{3+}$ red phosphor for white-light-emitting diode*, Journal of Alloys and Compounds, 636, 113 (2015); <https://doi.org/10.1016/j.jallcom.2015.01.134>.
- [7] Q. Chen, B. Miao, P. S. Kumar, S. Xu, *Enhanced luminescence properties and Judd-Ofelt analysis of novel red emitting $\text{Sr}_2\text{LiScB}_4\text{O}_{10}:\text{Eu}^{3+}$ phosphors for WLED applications*, Optical Materials, 116, 111093 (2021); <https://doi.org/10.1016/j.optmat.2021.111093>.

- [8] B. Han, P. J. Li, J. T. Zhang, J. Zhang, Y. F. Xue, X. Y. Suo, Q. Z. Huang, Y. Q. Feng, H. Z. Shi, *First observation of the emission from 5D_J ($J=1, 2, 3$) energy levels of Eu^{3+} in $\text{Bi}_4\text{O}_3(\text{BO}_3)(\text{PO}_4):\text{Eu}^{3+}$ phosphor*, *Material Letters*, 158, 208 (2015); <https://doi.org/10.1016/j.matlet.2015.06.024>.
- [9] Tiansong Dai, Guifang Ju, Yang Lv, Yahong Jin, Haoyi Wu, Yihua Hu, *Luminescence properties of novel dual-emission (UV/red) long afterglow phosphor $\text{LiYGeO}_4:\text{Eu}^{3+}$* , *Journal of Luminescence*, 237, 118193 (2021); <https://doi.org/10.1016/j.jlumin.2021.118193>.
- [10] X. B. Qiao, H. J. Seo, *Luminescence and crystallographic sites for Eu^{3+} ions in $\text{Sr}_5(\text{PO}_4)_3\text{F}$ phosphor*, *Journal of Alloys and Compounds*, 615, 270 (2014); <https://doi.org/10.1016/j.jallcom.2014.06.164>.
- [11] R. M. Yerojwar, N. S. Kokode, C. M. Nandanwar, *Synthesis and Photoluminescence characterization of $\text{ZnAl}_{12}\text{O}_{19}:\text{Sm}^{3+}$ Phosphor for W-LED*, *International Journal of Scientific Research in Science and Technology (IJSRST)*, 9 (3), 811 (2022); [doi:https://doi.org/10.32628/IJSRST](https://doi.org/10.32628/IJSRST).
- [12] L. Zhang, Q. Liu, N. Ding, H. Yang, L. X. Wang, Q. T. Zhang, *Dual-channel enhanced luminescence of double perovskite $\text{NaGdMgWO}_6:\text{Eu}^{3+}$ phosphor based on alternative excitation and delayed quenching*, *Journal of Alloys and Compounds*, 642, 45 (2015); <https://doi.org/10.1016/j.jallcom.2015.04.109>.
- [13] Z. H. Ju, R. P. Wei, J. X. Ma, C. R. Pang, W. S. Liu, *A novel orange emissive phosphor $\text{SrWO}_4:\text{Sm}^{3+}$ for white light-emitting diodes*, *Journal of Alloys and Compounds*, 507, 133 (2010); <https://doi.org/10.1016/j.jallcom.2010.07.138>.
- [14] R. M. Yerojwar, N.S. Kokode, C. M. Nandanwar, *Photoluminescence of – $\text{Ca}_9\text{Al}(\text{PO}_4)_7:\text{Eu}^{3+}$ phosphor*, *International Journal of Scientific Research in Science and Technology (IJSRST)*, 9 (2), 410 (2022); <https://doi.org/10.32628/IJSRST229346>.
- [15] P. Solarz, W. R. Romanowski, *Luminescence and energy transfer processes of Sm^{3+} in $\text{K}_5\text{Li}_2\text{LaF}_{10}:\text{Sm}^{3+}-\text{K}_5\text{Li}_2\text{SmF}_{10}$ single crystals*, *Physics Review B*, 72 075105-8 (2005); <https://doi.org/10.1103/PhysRevB.72.075105>.
- [16] A. Strzep, R. Lisiecki, P. Solarz, G. D. Dzik, W. R. Romanowski, M. Berkowski, *Optical spectra and excited state relaxation dynamics of Sm^{3+} in Gd_2SiO_5 single crystal*, *Applied Physics B*, 106, 85 (2012); <https://doi.org/10.1007/s00340-011-4731-9>.
- [17] R. M. Yerojwar, N. S. Kokode, C. M. Nandanwar, *Luminescence Properties of Rare Earth Sm^{3+} Doped $\text{Ca}_2\text{Mg}_2\text{Al}_{28}\text{O}_{46}$ Phosphor for white light emitting diode*, *International Journal of Scientific Research and Innovative Studies (IJSRIS)*, 1(1), 135 (2022); <https://ijsrisjournal.com/index.php/ojsfiles/article/view/35>.
- [18] C. K. Jayasankar, P Babu, *Optical properties of Sm^{3+} ions in lithium borate and lithium fluoroborate glasses*, *Journal of Alloys and Compounds*, 307 82 (2000); [https://doi.org/10.1016/S0925-8388\(00\)00888-4](https://doi.org/10.1016/S0925-8388(00)00888-4).
- [19] Y.Y. Chen, Q.F. Guo, L.B. Liao, M.Y. He, T.S. Zhou, L.F. Mei, M. Runowski, B. Ma, *Preparation, crystal structure and luminescence properties of a novel single phase red emitting phosphor $\text{CaSr}_2(\text{PO}_4)_2:\text{Sm}^{3+}, \text{Li}^+$* , *Royal Society of Chemistry Advance*, 9 (9), 4834 (2019), <https://doi.org/10.1039/C9RA00264B>.
- [20] A. K. Vishwakarma, M. Jayasimhadri, *Pure orange color emitting Sm^{3+} doped BaNb_2O_6 phosphor for solid-state lighting applications*, *Journal of Luminescence*, 176, 112 (2016); <https://doi.org/10.1016/j.jlumin.2016.03.025>.
- [21] R. Yu, Y. Guo, L. Wang, H. M. Noh, B. K. Moon, B. C. Choi, J. H. Jeong, *Characterizations and optical properties of orange-red emitting Sm^{3+} -doped Y_6WO_{12} phosphors*, *Journal of Luminescence*, 155, 317 (2014); <https://doi.org/10.1016/j.jlumin.2014.06.041>.
- [22] C. M. Nandanwar, N. S. Kokode, A. N. Yerpude, S. J. Dhoble, *Luminescence properties of $\text{LaPO}_4:\text{RE}$ ($\text{RE} = \text{Dy}^{3+}, \text{Eu}^{3+}, \text{Sm}^{3+}$) orthophosphate phosphor for n-UV solid-state lighting prepared by wet chemical synthesis*, *Journal of Materials Science: Materials in Electronics*, 34, 707 (2023); <https://doi.org/10.1007/s10854-023-10119-0>.
- [23] C. M. Nandanwar, A. N. Yerpude, N. S. Kokode, S. J. Dhoble, *Wet chemical synthesis of $\text{BiPO}_4:\text{Eu}^{3+}$ phosphor for w-LED application*, *Luminescence*. 37(10), 1800 (2022); <https://doi.org/10.1002/bio.4340>.
- [24] C. Yue, X. He, Y. Pu, D. Zhu, *Synthesis and properties of a yellowish-green $\text{Sr}_3\text{La}(\text{AlO})_3(\text{BO}_3)_4:\text{Tb}^{3+}$ phosphor with a high thermal stability*, *Journal of Luminescence*, 249, 119046 (2022); <https://doi.org/10.1016/j.jlumin.2022.119046>.
- [25] R. Yu, Y. Guo, L. Wang, H. M. Noh, B. K. Moon, B. C. Choi, et al. *Characterizations and optical properties of orange-red emitting Sm^{3+} -doped Y_6WO_{12} phosphors*. *J Lumin.* 155, 317 (2014); <https://doi.org/10.1016/j.jlumin.2014.06.041>.
- [26] S. Kaur, A. S. Rao, M. Jayasimhadri, *Spectroscopic and Photoluminescence Characteristics of Sm^{3+} doped Calcium Aluminosilicate Phosphor for Applications in w-LEDs*, *Ceramics International*, 43, 7401 (2017); <http://dx.doi.org/10.1016/j.ceramint.2017.02.129>.
- [27] R. M. Yerojwar, N. S. Kokode, C. M. Nandanwar, D. K. Ingole, R.S. Meshram, *Synthesis and Photoluminescence properties of a red emitting $\text{Sr}_4\text{Al}_{14}\text{O}_{25}:\text{Eu}^{3+}, \text{Sm}^{3+}$ phosphors for near UV based w-LEDs*, *Journal of characterization*, 3, 232 (2022); <https://doi.org/10.29228/JCHAR.65059>.
- [28] Z. Wang, S. Lou, P. Li, *Improvement of the red emitting phosphor by introducing A^+ ($\text{A}=\text{Li}, \text{Na}, \text{K}$) into $\text{Sr}_3\text{La}(\text{PO}_4)_3:\text{Eu}^{3+}$* , *Journal of Alloys and Compounds*, 658, 813, (2015); <https://doi.org/10.1016/j.jallcom.2015.11.022>.
- [29] V. Singh, S. Kaur, M. Jayasimhadri, *Luminescence properties of orange emitting $\text{CaAl}_4\text{O}_7:\text{Sm}^{3+}$ phosphor for solid state lighting applications*, *Solid State Sciences*, 101 106049 (2019); <https://doi.org/10.1016/j.solidstatesciences.2019.106049>.

- [30] H. N. Luitel, T. Watari, R. Chand, T. Torikai, M. Yada, *Photoluminescence properties of a novel orange red emitting $\text{Sr}_4\text{Al}_{14}\text{O}_{25}:\text{Sm}^{3+}$ phosphor and PL enhancement by Bi^{3+} co-doping*, *Optical Materias*, 34, 1375 (2012); <https://doi.org/10.1016/j.optmat.2012.02.025>.
- [31] C. M. Nandanwar, N. S. Kokode, A. N. Yerpude, S. J. Dhoble, *Effect of dopant concentration on luminescence properties of a $\text{Ba}_3(\text{PO}_4)_2: \text{RE}$ ($\text{RE} = \text{Sm}^{3+}, \text{Eu}^{3+}, \text{Dy}^{3+}$) phosphor for solid-state lighting*, *Chemical Data Collections* 43, 100979 (2023); <https://doi.org/10.1016/j.cdc.2022.100979>.
- [32] W. T. Carnall, P. R. Fields, K. Rajnak, *Electronic energy levels in the trivalent lanthanide aquo ions. I. $\text{Pr}^{3+}, \text{Nd}^{3+}, \text{Pm}^{3+}, \text{Sm}^{3+}, \text{Dy}^{3+}, \text{Ho}^{3+}, \text{Er}^{3+}$, and Tm^{3+}* , *The Journal of Chemical Physics*, 49, 4424 (1968); <https://doi.org/10.1063/1.1669893>.
- [33] E. Pavitra, G. S. R. Raju, Y. H. Ko, J. S. Yu, *A novel strategy for controllable emissions from Journal Pre-proof 11 Eu^{3+} or Sm^{3+} ions co-doped $\text{SrY}_2\text{O}_4:\text{Tb}^{3+}$ phosphors*, *Physical Chemistry Chemical Physics*, 14, 11296 (2012); <https://doi.org/10.1039/C2CP41722G>.
- [34] S. Devi, V. B. Taxak, S. Chahar, M. Dalal, J. Dalal, A. Hooda, A. Khatkar, R. K. Malik, S. P. Khatkar, *Crystal chemistry and optical analysis of a novel perovskite type $\text{SrLa}_2\text{Al}_2\text{O}_7:\text{Sm}^{3+}$ nanophosphor for white LEDs*, *Ceramics International*, 45, 15571 (2019); <https://doi.org/10.1016/j.ceramint.2019.05.064>.
- [35] S. Chahar, V. B. Taxak, M. Dalal, S. Singh, S. P. Khatkar, *Structural and photoluminescence investigations of Sm^{3+} doped BaY_2ZnO_5 nanophosphors*, *Material Research Bulletin*, 77, 91 (2016); <https://doi.org/10.1016/j.materresbull.2016.01.027>.
- [36] V. R. Bandi, B. K. Grandhe, M. Jayasimhadri, K. Jang, H. S. Lee, S. S. Yi, J. H. Jeong, *Photoluminescence and structural properties of $\text{Ca}_3\text{Y}(\text{VO}_4)_3:\text{RE}^{3+}$ ($\text{RE}^{3+} = \text{Sm}^{3+}, \text{Ho}^{3+}$ and Tm^{3+}) powder phosphors for tri-colors*, *Journal of Crystal Growth*, 326, 120 (2011); <https://doi.org/10.1016/j.jcrysgro.2011.01.075>.
- [37] L. Wang, H. M. Noh, B. K. Moon, S. H. Park, K. H. Kim, J. Shi, and J. H. Jeong, *DualMode Luminescence with Broad Near UV and Blue Excitation Band from $\text{Sr}_2\text{CaMoO}_6:\text{Sm}^{3+}$ Phosphor for White LEDs*, *The Journal of Physical Chemistry C*, 119, 15517 (2015); <https://doi.org/10.1021/acs.jpcc.5b02828>.
- [38] B. Bondzior, D. Stefańska, A. Kubiak, and P. J. Dereń, *Spectroscopic properties of $\text{K}_4\text{SrSi}_3\text{O}_9$ doped with Sm^{3+}* , *Journal of Luminescence*, 173, 38 (2016); <https://doi.org/10.1016/j.jlumin.2015.12.031>.
- [39] T. Wang, W. Bian, D. Zhou, J. Qiu, X. Yu, and X. Xu, *Red long lasting phosphorescence in $\text{Ca}_2\text{Ge}_7\text{O}_{16}:\text{Sm}^{3+}$ via persistent energy transfer from the host to Sm^{3+}* , *Material Research Bulletin*, 74, 151 (2016); <https://doi.org/10.1016/j.materresbull.2015.10.028>.
- [40] C. M. Nandanwar, N. S. Kokode, R. M. Yerojwar, A. N. Yerpude, R. S. Meshram, *Wet chemical synthesis and photoluminescence study of Eu^{3+} activated orthophosphate based phosphor for n-UV based Solid state lighting*, *Journals of optics*, 51, 1 (2023); <https://doi.org/10.1007/s12596-023-01130-z>.
- [41] C. M. Nandanwar, N. S. Kokode, A. N. Yerpude, S. J. Dhoble, *Luminescence properties of $\text{BiPO}_4:\text{Ln}$ ($\text{Ln} = \text{Dy}^{3+}, \text{Tb}^{3+}$ and Sm^{3+}) orthophosphate phosphors for near-UV-based solid-state lighting*, *Bulletin of Materials Science*, 46, 51 (2023); <https://doi.org/10.1007/s12034-023-02900-y>.

P. M. Єроджвар, Н.С. Кокоде, К.М. Нанданвар, Д.К. Інголе

Синтез і фотолюмінесцентні характеристики люмінофору $\text{Sr}_3\text{La}(\text{AlO})_3(\text{BO}_3)_4:\text{Eu}^{3+}, \text{Sm}^{3+}$ для n-УФ w-LED

Університет Гондвани, Махараштра, Індія, yerojwar@gmail.com

Методом спалювання синтезовано високоефективні люмінофори $\text{Sr}_3\text{La}(\text{AlO})_3(\text{BO}_3)_4$, леговані Eu^{3+} і Sm^{3+} , збуджені червоним світлом, а також детально досліджено фотолюмінесцентні властивості зразків. Вивчено морфологію за допомогою скануючої електронної мікроскопії та хроматичність за допомогою СІЕ. Результати демонструють діапазони збудження від 340 нм до 420 нм, особливо, найсильніше збудження (394 нм і 406 нм) знаходиться в УФ-області при допуванні Eu^{3+} і Sm^{3+} , що свідчить про те, що люмінофор може добре поєднуватися зі світлодіодними чіпами. Під дією n-УФ-світла 394 нм люмінофор $\text{Sr}_3\text{La}(\text{AlO})_3(\text{BO}_3)_4$, легований Eu^{3+} , і 406 нм Sm^{3+} , легований $\text{Sr}_3\text{La}(\text{AlO})_3(\text{BO}_3)_4$, може випромінювати яскраво-червоне світло з основними піками випромінювання, розташованими на 617 нм і 602 нм. Властивості ФЛ вказують на чудову стабільність люмінофора. Ці результати вказують на важливість червоних люмінофорів $\text{Sr}_3\text{La}(\text{AlO})_3(\text{BO}_3)_4: \text{Eu}^{3+}$ і $\text{Sr}_3\text{La}(\text{AlO})_3(\text{BO}_3)_4: \text{Sm}^{3+}$ у білих світлодіодах при n-УФ-збудженні.

Ключові слова: легування рідкісноземельними елементами, горіння, w-LED, СІЕ-координація, $\text{Sr}_3\text{La}(\text{AlO})_3(\text{BO}_3)_4:\text{Eu}^{3+}$, $\text{Sr}_3\text{La}(\text{AlO})_3(\text{BO}_3)_4:\text{Sm}^{3+}$, червоний люмінофор.

**Остафійчуку
Богдану Костянтиновичу**

*член-кореспонденту Національної Академії наук України,
заслуженому діячу науки і техніки України,
лауреату Державної премії України в галузі науки і техніки,
доктору фізико-математичних наук, професору,
професору кафедри матеріалознавства і новітніх технологій,
голови спеціалізованої вченої ради по захисту докторських дисертацій,
редактору наукового журналу "Фізика і хімія твердого тіла"
почесному ректору Прикарпатського національного університету
імені Василя Стефаника*



75

Вельмишановний Богдане Костянтиновичу!

*Щиро вітаємо Вас зі славним Ювілеєм.
Бажаємо Вам міцного здоров'я,
насаги до плідної творчої роботи ще на довгі роки,
натхнення у звершенні всього задуманого та запланованого, щирих друзів.
Зичимо добра та щастя на щодень.*

Колеги по роботі, друзі,
редакційна колегія

Персоналії
Остафійчук Богдан Костянтинович

Остафійчук Богдан Костянтинович – член кореспондент НАН України, професор, доктор фізико-математичних наук, завідувач кафедри матеріалознавства і новітніх технологій Прикарпатського національного університету імені Василя Стефаника, ректор Прикарпатського національного університету імені Василя Стефаника (2005-2012 рр.).

Народився 8 лютого 1948 р. у селі Хімчин Косівського району Івано-Франківської області. Після закінчення з відзнакою Рожнівської середньої школи в 1966 році навчався на фізико-математичному факультеті Івано-Франківського державного педінституту, де, після закінчення, працював у науково-дослідній лабораторії. З 1972 по 1975 рік навчався в аспірантурі Інституту металофізики АН України.



*Богдан Остафійчук – випускник
фізико-математичного
факультету*



Богдан Остафійчук – викладач та начальник НДС

педінституту, а також доцентом кафедри фізики. Активно працював у галузі фізики твердого тіла, а саме: створення нових антифрикційних кислотостійких матеріалів та захисних покриттів на металах і сплавах, здійснював керівництво рядом наукових проектів і тем. З 1988 року організував і устаткував унікальним обладнанням наукову лабораторію фізики магнітних плівок і за конкурсом переходить на роботу в Інститут металофізики АН України на посаду завідувача лабораторією, зосередивши свої зусилля на дослідженні і модифікації структури і магнітних властивостей монокристалічних ферит-гранатових плівок. Після захисту докторської дисертації «Структура і магнітні властивості іонно-імплантованих епітаксialних ферит-гранатових плівок» (вчена рада Інституту металофізики НАН України, м. Київ) у 1993 році був запрошений на посаду проректора з наукової роботи Прикарпатського

В 1975 році захистив дисертацію на здобуття наукового ступеня кандидата фізико-математичних наук на тему «Електронна структура інтерметалідів типу фаз Лавеса». З 1976 року працював начальником НДС Івано-Франківського



*Богдан Остафійчук – ректор
Прикарпатського національного
університету
імені Василя Стефаника*

Персоналії. Остафійчук Богдан Костянтинович



*Богдан Остафійчук – проректор
з наукової роботи*

університету імені Василя Стефаника, одночасно виконуючи обов'язки завідувача спільною науково-дослідною лабораторією фізики магнітних плівок Інституту металофізики НАН України і Прикарпатського університету. Рішенням Кабінету Міністрів України в 2001 році даній лабораторії було надано статус національного наукового надбання України.

Його основні наукові інтереси зосереджені в галузі фізики магнітних матеріалів та нанорозмірних систем. Результати, отримані з його участю і під його керівництвом, знаходяться на рівні світових стандартів, а їх практичне застосування дозволило створити генератори і накопичувачі електричної енергії з параметрами, що значно перевищують відомі світові аналоги. Свою наукову роботу професор Остафійчук Б.К. завжди поєднував із педагогічною. Він є автором 8 посібників, 3 підручників, 4 монографій, понад 200 наукових статей і винаходів, під його науковим керівництвом захищено 43 кандидатських і 10 докторських дисертацій, десятки дипломних і магістерських робіт. Професор Остафійчук Б.К. є членом

редколегії двох наукових журналів, головою спеціалізованої вченої ради по захисту докторських дисертацій, експертом з фізики ВАК України, заступником Голови фахової ради МОН України. З 1994 року одночасно завідує кафедрою матеріалознавства і новітніх технологій, успішно керує підготовкою докторських і кандидатських дисертацій, розробкою фундаментальних і прикладних тем в галузі нанотехнологій і фізикотермодинамічних властивостей наносистем. З лютого 2005 року по лютий 2012 року Остафійчук Б.К. – обіймав посаду ректора Прикарпатського національного університету імені Василя Стефаника.

Його вчителями були академік НАН України, доктор фізико-математичних наук, професор Немошкаленко В.В. (Інститут металофізики НАН України, м. Київ); академік НАН України, доктор фізико-математичних наук, професор Барьяхтар В.Г. (Інститут магнетизму НАН України, м. Київ). Нагороди: Державна премія України в галузі науки і техніки (2002); Лауреат рейтингу «Галицькі кмітливіці року» в номінації «Кращий вчений винахідник»; заслужений діяч науки і техніки України (2005); член-кореспондент НАН України (2006).



Богдан Остафійчук – завідувач кафедри матеріалознавства і новітніх технологій Прикарпатського національного університету імені Василя Стефаника

**Когуту
Ігорю Тимофійовичу**

*доктору технічних наук, професору,
члену редакційної колегії наукового журналу "Фізика і хімія твердого тіла",
завідувачу кафедри комп'ютерної інженерії та електроніки
Прикарпатського національного університету імені Василя Стефаника*



70

Вельмишановний Ігоре Тимофійовичу!

*Щиро вітаємо Вас зі славним Ювілеєм.
Бажаємо Вам міцного здоров'я,
наснаги до плідної творчої роботи ще на довгі роки,
натхнення у звершенні всього задуманого та запланованого, щирих друзів.
Зичимо добра та щастя на щодень.*

Колеги по роботі, друзі,
редакційна колегія

Персоналії
Когут Ігор Тимофійович

Когут Ігор Тимофійович – доктор технічних наук, професор, завідувач кафедри комп'ютерної інженерії та електроніки Прикарпатського національного університету імені Василя Стефаника.

Народився 22 лютого 1953 р. у селі Зелене Гусятинського району Тернопільської області.

У 1970 р. закінчив Гримайлівську загальноосвітню середню школу.

У 1970-1975рр. навчався на електрофізичному факультеті Львівського політехнічного інституту за спеціальністю «Напівпровідникові прилади». При кафедрі напівпровідникової електроніки Львівської політехніки Ігор Тимофійович закінчив аспірантуру і докторантуру, захистив кандидатську (1993, Київський політехнічний інститут) та докторську (2010, НУ «Львівська політехніка») дисертації за спеціальністю «Твердотільна електроніка». Його науковими керівниками були доктор технічних наук, професор, завідувач кафедри напівпровідникової електроніки Воронін В.О. та доктор технічних наук, професор Дружинін А.О., науковим консультантом докторської дисертації був завідувач кафедри напівпровідникової електроніки НУ «Львівська політехніка» професор Дружинін А.О.

У 1975-2000 рр. працював в електронній промисловості – у спеціальному конструкторсько-технологічному бюро «Орізон» при ВАТ «РОДОН» (м.Івано-Франківськ), куди був скерований після закінчення Львівського політехнічного інституту. Обіймав посади інженера-конструктора, начальника КБ, начальник відділу мікроелектроніки, консультанта директора СКТБ. У 1995-1997 рр. за сумісництвом працював доцентом кафедри напівпровідникової електроніки НУ «Львівська політехніка»

Неодноразово був головним конструктором НДДКР зі створення нових виробів інтегральної електроніки. Під його керівництвом в СКТБ «ОРИЗОН» (ВАТ «РОДОН», м. Івано-Франківськ) були розроблені спеціалізовані обчислювальні мікросхеми для калькуляторів, спеціалізовані однокристальні ЕОМ управління телевізійними приймачами, мікропроцесорні ВІС, НВІС статичної пам'яті та інші, які випускались у серійному виробництві упродовж багатьох років. Був нагороджений медаллю Виставка досягнень народного господарства СРСР (1988 р.).

З 2000 року працює у Прикарпатському університеті. В 2010 році став професором кафедри радіофізики та електроніки, а з 1 жовтня 2012 року по сьогодні є завідувачем кафедри комп'ютерної інженерії та електроніки. Кафедра є випусковою за 2-ма спеціальностями – «Комп'ютерна інженерія» та «Електроніка». У 2023р. нагороджений медаллю «За заслуги перед Університетом». Є членом експертної ради з наукових проектів МОНУ секція №5 «Електроніка, радіотехніка та телекомунікації», членом спеціалізованої вченої ради із захисту докторських дисертацій за спеціальністю 05.27.01 «Твердотільна електроніка» у НУ «Львівська політехніка».

Сфера наукових інтересів – розроблення і дослідження перспективної елементної бази для мікросистем-на-кристалі на основі структур «кремній-на-ізоляторі». Під його керівництвом захищено 3 кандидатські дисертації, має більше 200 наукових публікацій, з них 43 входять в міжнародну науково-метричну базу даних Scopus та є автором більше 45 патентів.

Всеукраїнський науковий журнал
ФІЗИКА І ХІМІЯ ТВЕРДОГО ТІЛА

Ukrainian Scientific Journal
PHYSICS AND CHEMISTRY OF SOLID STATE

Том 24, № 1
Volume 24, No. 1

Комп'ютерна верстка

Юрчишин Л.Д.

Підписано до друку 26.03.2023 р. Формат 60×84/8.
Гарн. Times New Roman. Умовн. друк. аркушів 12,65
Тираж 100 екземплярів.

Друк: підприємець Голіней О.М.
вул. Галицька, 128, м. Івано-Франківськ, 76008
Тел. +38(0342) 58-04-32